Transactions of the ASME®

Transactions of the ASME, Journal of Engineering for Gas Turbines and Power (ISSN 0742-4795) is published quarterly (Jan., Apr., July, Oct.,) for $130.00 per year by The American Society of Mechanical Engineers, 345 East 47th Street, New York, NY 10017. Second class postage paid at New York, NY and additional mailing offices. POSTMASTER: Send address changes to Transactions of the ASME, Journal of Engineering for Gas Turbines and Power, c/o THE AMERICAN SOCIETY OF MECHANICAL ENGINEERS, 22 Law Drive, Box 2300, Fairfield, NJ 07007-2300.
CHANGES OF ADDRESS must be received at Society headquarters seven weeks before they are to be effective. Please send old label and new address.
PRICES: To members, $40.00, annually: to nonmembers, $136.00.
Add $24.00 for postage to countries outside the United States and Canada.
STATEMENT from By-Laws. The Society shall not be responsible for statements or opinions advanced in papers or . . . printed in its publications (B 7.1, para. 3).

INDEXED by Applied Mechanics Reviews and Engineering Information, Inc.
Canadian Goods & Services Tax Registration #126148048

Journal of Engineering for Gas Turbines and Power

Published Quarterly by The American Society of Mechanical Engineers
VOLUME 115 • NUMBER 2 • APRIL 1993

TECHNICAL PAPERS

(Contents continued on page 260)

Contents (continued)

Generalized Polynomial Expansion Method for the Dynamic Analysis of Rotor-Bearing Systems

T. N. Shiau

J. L. Hwang

Institute of Aeronautics and Astronautics,
National Cheng Kung University,
Tainan, Taiwan

The determination of critical speeds and modes and the unbalance response of rotor-bearing systems is investigated with the application of a technique called the generalized polynomial expansion method (GPEM). This method can be applied to both linear and nonlinear rotor systems; however, only linear systems are addressed in this paper. Three examples including single spool and dual rotor systems are used to demonstrate the efficiency and the accuracy of this method. The results indicate a very good agreement between the present method and the finite element method (FEM). In addition, computing time will be saved using this method in comparison with the finite element method.

Introduction

Various methods for the determination of critical speeds and modes and the unbalance response of rotor-bearing systems have been developed and widely used during the past few decades. These methods may be categorized in two major classes. The first is the discretization method, which approximates a rotor system using a finite number of degrees-of-freedom. In this case, the equations of motions are a set of ordinary differential equations. This category can also be divided into two techniques. One is the state vector-transfer matrix method (Myklestad, 1944; Prohl, 1945; Lund, 1967, 1974a, 1974b). The other is the direct stiffness method (Ruhl and Booker, 1972; Dimaragonas, 1975; Gasch, 1976; Nelson and McVaugh, 1976; Childs, 1978; Nelson, 1980; Adams, 1980; Childs and Graviss, 1982). These techniques have been successfully utilized to analyze the dynamic characteristics of rotor systems. The second is the analytical method (Gladwell and Bishop, 1959; Dimentberg, 1961; Eshleman and Eubanks, 1969; Lee and Jei, 1988), which treats the rotor system as a distributed parameter system with a set of partial differential equations describing the system motion.

At the present time, the state vector-transfer matrix method is limited to linear frequency domain analysis and the direct stiffness method may be the only validated tool available for both linear and nonlinear time domain analysis. However, the use of the direct stiffness method may lead to high computation time and costs for large rotor systems. Kumar and Sankar (1986) proposed a new transfer matrix method for response analysis of large dynamic systems. Gu (1986) introduced an improved transfer matrix–direct integration method to determine the critical speeds and unbalance response. A method combining the methodologies of finite elements and transfer matrix has been applied (Subbiah et al., 1988) for the transient dynamic analysis of rotors. In addition, Crandall and Yeh (1986, 1989) proposed a modeling approach for the multirotor system. It generates the internal modes of each rotor component without solving the eigenvalue problems. Each mode of the rotating shaft is represented by fourth-order polynomials with piecewise constant coefficients. It is noted that for the finite element method (FEM) the deformation of a rotating shaft using a typical beam element is described by third-order polynomials with piecewise constant coefficients. Also, these coefficients are expressed as functions of the deflections at node points.

In this paper, the analysis method introduced by Shiau and Hwang (1989) has been modified and is called the generalized polynomial expansion method (GPEM). The method approximates the displacements of an entire rotating shaft in the global assumed modes sense with $(N_p - 1)$ th order polynomials with time-dependent coefficients. This is different from the finite element method in a subdomain sense and from the modeling approach proposed by Crandall and Yeh (1986, 1989). The present approach can be applied to both linear and nonlinear rotor-bearing systems. The application of the GPEM to nonlinear systems has been investigated and submitted for publication (Hwang and Shiau, 1989). The efficiency and the accuracy of using this method will be demonstrated through examples. The critical speeds, mode shapes, and unbalance response of the examples are shown in this study.

Equation Formulation

The basic configuration of a rotor-bearing system usually consists of the components: rigid disks, flexible shafts, and bearings, such as shown in Fig. 1. The lateral displacements and the rotor eccentricity due to mass unbalance are assumed to be small. To describe the system motion, two reference frames are utilized. One is a fixed reference X-Y-Z and the other is a rotating reference x-y-z. The X and x axes are collinear and coincident with the undeformed bearing centerline. The two reference frames have a single rotation ωt difference about X with ω denoting a whirl speed.

Contributed by the International Gas Turbine Institute and presented at the 36th International Gas Turbine and Aeroengine Congress and Exposition, Orlando, Florida, June 3-6, 1991. Manuscript received at ASME Headquarters January 18, 1991. Paper No. 91-GT-6. Associate Technical Editor: L. A. Riekert.

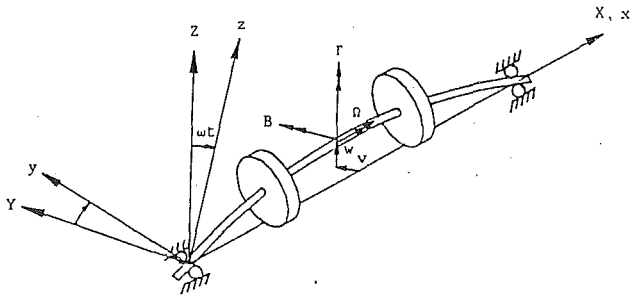

Fig. 1 Typical rotor configuration and coordinates

It is assumed that all the deflections and forces are parallel to the Y-Z plane. The deflection of a cross section of shaft consists of two translations (V, W) and two rotations (B, Γ). It is assumed that the deflections can be expressed as functions of position along the rotating axis x and time t, i.e.,

$$V = V(x, t), \quad W = W(x, t)$$
$$B = B(x, t), \quad \Gamma = \Gamma(x, t) \tag{1}$$

The rotations (B, Γ) are related to the translations (V,W) by the equations

$$B(x, t) = -\frac{\partial W(x, t)}{\partial x}$$
$$\Gamma(x, t) = \frac{\partial V(x, t)}{\partial x} \tag{2}$$

To derive the equations of motion, the Lagrangian approach is employed. This requires the calculation of the kinetic and potential energies of the system. The kinetic and potential energies of the system can be expressed in terms of the displacements and their derivatives. The total kinetic energy (T) and the potential energy (U) of the system can be expressed as

$$T = T_s + T_d + T_e \tag{3}$$
$$U = U_s + U_b \tag{4}$$

where T_s and T_d are the kinetic energy of the shaft and the disk; T_e is the kinetic energy related to the eccentricity; U_s and U_b are the strain energy of the shaft and bearings. They are of the forms:

$$T_s = \frac{1}{2}\int_0^l \rho A(\dot{V}^2 + \dot{W}^2)dx + \frac{1}{2}\int_0^l I_D(\dot{B}^2 + \dot{\Gamma}^2)\,dx + \frac{1}{2}\Omega\int_0^l I_P(\Gamma\dot{B} - B\dot{\Gamma})dx + \frac{1}{2}\Omega^2\int_0^l I_p\,dx \tag{5}$$

$$T_d = \sum_{i=1}^{N_d}\left\{\frac{1}{2}m_i^d(\dot{V}_i^2 + \dot{W}_i^2) + \frac{1}{2}I_{Di}^d(\dot{B}_i^2 + \dot{\Gamma}_i^2) + \frac{1}{2}\Omega I_{pi}^d(\dot{B}\Gamma - \dot{\Gamma}B) + \frac{1}{2}\Omega^2 I_{pi}^d\right\} \tag{6}$$

$$T_e = \int_0^l e(x)\rho(x)A(x)\Omega[-\dot{V}\sin(\Omega t + \phi) + \dot{W}\cos(\Omega t + \phi)]dx + \int_0^l e^2(x)\rho(x)A(x)\Omega^2 dx + \sum_{i=1}^{N_d}\{e_i^d\Omega m_i^d[-\dot{V}_i\sin(\Omega t + \phi_i^d) + \dot{W}_i\cos(\Omega t + \phi_i^d)] + m_i^d(e_i^d)^2\Omega^2\} \tag{7}$$

$$U_s = \frac{1}{2}\int_0^l EI[(V'')^2 + (W'')^2]dx \tag{8}$$

$$U_b = \sum_{j=1}^{N_b}\left\{\frac{1}{2}K_{yyj}^b V_j^2 + \frac{1}{2}K_{zzj}^b W_j^2 + K_{yzj}^b V_j W_j\right\} \tag{9}$$

The dissipation function (F) due to bearing damping is given by

$$F = \sum_{j=1}^{N_b}\left[\frac{1}{2}C_{yyj}^b(\dot{V}_j^b)^2 + \frac{1}{2}C_{zzj}^b(\dot{W}_j^b)^2 + C_{yzj}^b\dot{V}_j^b\dot{W}_j^b\right] \tag{10}$$

The denotations of parameters involved in Eqs. (5)–(10) are given in the Nomenclature.

The assumed mode technique for the undamped rotor-bearing systems, proposed by Shiau and Hwang (1989), has been generalized for damped systems using the following displacement functions:

$$V(x, t) = \sum_{n=1}^{N_p} a_n(t)x^{n-1}$$
$$W(x, t) = \sum_{m=1}^{N_p} b_m(t)x^{m-1} \tag{11}$$

where the $a_n(t)$ and $b_m(t)$ are generalized coordinates. The corresponding rotational displacements, using Eq. (2), are given by

$$\Gamma(x, t) = \frac{\partial V(x, t)}{\partial x} = \sum_{n=2}^{N_p}(n-1)x^{n-2}a_n(t)$$
$$B(x, t) = \frac{-\partial W(x, t)}{\partial x} = -\sum_{m=2}^{N_p}(m-1)x^{m-2}b_m(t) \tag{12}$$

where the integer N_p is the number of polynomials. As noted by Shiau and Hwang (1989), the first two terms of the polynomial expansion of Eq. (11) must exist, i.e., the associated coefficients a_1, a_2, b_1, b_2 cannot be zero. The constant term, the first two terms, and the first three terms of the expansion represent a cylindrical mode, conical mode, and bending mode, respectively. Moreover, if rigid body modes exist in the system,

Nomenclature

$a_n(t)$, $b_m(t)$ = generalized coordinates
$A(x)$ = cross-sectional area of the shaft
c_{yyj}^b, c_{zzj}^b, c_{yzj}^b = damping coefficients of the jth bearing
d = diameter of the shaft
e_i^d = eccentricity of the ith disk
$e(x)$ = eccentricity of the shaft at position x
$E(x)$ = elastic modulus of the shaft
$I(x)$ = cross-sectional area moment
I_D, I_P = diametral and polar mass moment of inertia of the shaft
I_{Di}^d, I_{Pi}^d = diametral and polar mass moment of inertia of the ith disk
k_{yyj}^b, k_{zzj}^b, k_{yzj}^b = elastic constant of the jth bearing
l = total length of the shaft
m_i^d = mass of the ith disk
N_d = total number of disks
N_b = total number of bearings
N_p = total number of polynomials
$\underline{Q}_f$, $\underline{Q}_b$ = magnitude of steady-state forward and backward response
V_i^d, W_i^d = translational displacements of the ith disk
V_j^b, W_j^b = translational displacements of the jth bearing
α_r = real part of eigenvalues
δ_r = log decrements
λ = whirl ratio Ω/ω
$\rho(x)$ = density of the shaft, mass/unit length
Ω = rotating speed of the shaft
ω = whirl speed

the first two terms will be dominant. It should be noted that other types of polynomials may be used as candidates for this method. Trigonometric polynomials have been used with minimal success and other choices are under investigation. The present method is also applicable to those systems with geometric displacement constraints. The additional requirement is to impose the required constraint or constraints. This will be shown in the first example of single uniform shaft.

Substituting Eqs. (11) and (12) and their derivatives into Eqs. (5)–(10) gives the total kinetic energy, potential energy, and dissipation energy in terms of time-dependent polynomial coefficients (a_n, b_m) and their corresponding derivatives ($\dot{a}_n$, $\dot{b}_m$). To find the equations of motion governing the rotor-bearing system, the Lagrangian approach is applied, i.e.,

$$\frac{d}{dt}\left[\frac{\partial}{\partial \dot{q}_i}(T-U)\right]-\frac{\partial}{\partial q_i}(T-U)+\frac{\partial F}{\partial \dot{q}_i}=0 \tag{13}$$

where the generalized coordinates q_i are the a_n and b_m with n, $m = 1, N_p$. For constant rotating speed, the equations of motion may be expressed as follows:

$$\begin{bmatrix} M & O \\ O & M \end{bmatrix}\begin{Bmatrix} \ddot{\mathbf{a}} \\ \ddot{\mathbf{b}} \end{Bmatrix}+\Omega\begin{bmatrix} O & G \\ -G & O \end{bmatrix}\begin{Bmatrix} \dot{\mathbf{a}} \\ \dot{\mathbf{b}} \end{Bmatrix}+\begin{bmatrix} C_{yy} & C_{yz} \\ C_{zy} & C_{zz} \end{bmatrix}\begin{Bmatrix} \dot{\mathbf{a}} \\ \dot{\mathbf{b}} \end{Bmatrix}+\begin{bmatrix} K_s & O \\ O & K_s \end{bmatrix}\begin{Bmatrix} \mathbf{a} \\ \mathbf{b} \end{Bmatrix}+\begin{bmatrix} K_{yy} & K_{yz} \\ K_{zy} & K_{zz} \end{bmatrix}\begin{Bmatrix} \mathbf{a} \\ \mathbf{b} \end{Bmatrix}=\begin{Bmatrix} \mathbf{R}_a \\ \mathbf{R}_b \end{Bmatrix} \tag{14}$$

where the coefficient vectors **a** and **b** are

$$\mathbf{a}=\{a_1,\ldots,a_{N_p}\}^T$$

$$\mathbf{b}=\{b_1,\ldots,b_{N_p}\}^T \tag{15a}$$

and the $N_p \times N_p$ component matrices, M,G, C_{yy}, C_{yz}, C_{zz}, K_s, K_{yy}, K_{yz}, and K_{zz} are shown in the Appendix. The $N_p \times 1$ forcing vectors, $\mathbf{R}_a$ and $\mathbf{R}_b$, are

$$\mathbf{R}_a=\{R_{a1}\ R_{a2}\ \ldots\ R_{aN_p}\}^T$$

$$\mathbf{R}_b=\{R_{b1}\ R_{b2}\ \ldots\ R_{bN_p}\}^T \tag{15b}$$

where

$$R_{aj}=\int_0^l e(x)\rho(x)A(x)\Omega^2\cos(\Omega t+\phi)x^{j-1}dx+\sum_{i=1}^{N_d} e_i^d m_i^d \Omega^2\cos(\Omega t+\phi_i)x_i^{j-1} \tag{15c}$$

$$R_{bj}=\int_0^l e(x)\rho(x)A(x)\Omega^2\sin(\Omega t+\phi)x^{j-1}dx+\sum_{i=1}^{N_d} e_i^d m_i^d \Omega^2\sin(\Omega t+\phi_i)x_i^{j-1}$$

In this work, the shaft eccentricity is considered to be negligible. Then the first term of the expressions R_{aj} and R_{bj}, shown in Eq. (15c), vanishes. In addition, the $N_p \times N_p$ damping and stiffness matrices, C_{yz} and K_{yz}, are considered as symmetric, i.e., $C_{yz} = C_{zy}$ and $K_{yz} = K_{zy}$.

For simplicity and convenience, the $N_p \times 1$ complex vector **p** and its conjugate $\tilde{\mathbf{p}}$ are introduced:

$$\mathbf{p}=\mathbf{a}+i\,\mathbf{b}$$

$$\tilde{\mathbf{p}}=\mathbf{a}-i\,\mathbf{b} \tag{16}$$

and Eq. (14) can then be rewritten as:

$$[M]\ddot{\mathbf{p}}+([C_1]-i\Omega[G])\dot{\mathbf{p}}+([C_2]+i[C_{yz}])\dot{\tilde{\mathbf{p}}}+([K_s]+[K_1])\mathbf{p}+([K_2]+i[K_{yz}])\tilde{\mathbf{p}}=\sum_{j=1}^{N_d} e_j^d m_j^d \Omega^2 \mathbf{R}_j^d e^{i(\Omega t+\phi_j^d)} \tag{17}$$

where the $N_p \times N_p$ matrices $[K_1]$, $[K_2]$, $[C_1]$, and $[C_2]$ are all real and symmetric matrices and of the form

$$[K_1]=\frac{1}{2}([K_{yy}]+[K_{zz}]),\quad [K_2]=\frac{1}{2}([K_{yy}]-[K_{zz}])$$

$$[C_1]=\frac{1}{2}([C_{yy}]+[C_{zz}]),\quad [C_2]=\frac{1}{2}([C_{yy}]-[C_{zz}]) \tag{18a}$$

and the force vector $\mathbf{R}_j^d$ is defined by

$$\mathbf{R}_j^d=\{R_{j1}^d\ R_{j2}^d\ \ldots\ R_{jN_p}^d\}^T$$

$$R_{jk}^d=x_j^{k-1},\quad k=1, N_p \tag{18b}$$

Critical Speeds and Steady-State Unbalance Response

Critical Speeds. The critical speed of the damped system governed by Eq. (17) is calculated using the homogeneous form. Assume the homogeneous solution of Eq. (17) to be of the form

$$\mathbf{p}=\mathbf{R}_f e^{i\omega t}+\mathbf{R}_b e^{-i\omega t} \tag{19}$$

where ω is the natural frequency or the whirl speed of the system and substitute Eq. (19) into the homogeneous form of Eq. (17), to obtain the following equations:

$$(-\omega^2[M]+\omega\Omega[G]+[K_3]+i\omega[C_1])\mathbf{R}_f+([K_2]-\omega[C_{yz}]+i[K_{yz}]+i\omega[C_2])\tilde{\mathbf{R}}_b=0 \tag{20a}$$

$$(-\omega^2[M]-\omega\Omega[G]+[K_3]-i\omega[C_1])\mathbf{R}_b+([K_2]+\omega[C_{yz}]+i[K_{yz}]-i\omega[C_2])\tilde{\mathbf{R}}_f=0 \tag{20b}$$

where $[K_3] = [K_s] + [K_1]$. For undamped orthotropic systems, one can calculate the critical speeds by taking the conjugate of Eq. (20*b*) and combining with Eq. (20*a*) to obtain

$$\left(\begin{bmatrix} [K_3] & [K_2]+i[K_{yz}] \\ [K_2]-i[K_{yz}] & [K_3] \end{bmatrix}-\omega^2\begin{bmatrix} [M]-\lambda[G] & 0 \\ 0 & [M]+\lambda[G] \end{bmatrix}\right)\begin{Bmatrix} \mathbf{R}_f \\ \mathbf{R}_b \end{Bmatrix}=\{0\} \tag{21}$$

where $\lambda = \Omega/\omega$ is the whirl ratio. Setting λ to a specified value and solving the eigenvalue problem governed by Eq. (21) provides the critical speeds of the rotor bearing system. The whirl speeds can also be obtained by rewriting Eq. (14) in the first-order form

$$\begin{bmatrix} [M] & 0 & 0 & 0 \\ 0 & [M] & 0 & 0 \\ 0 & 0 & [I] & 0 \\ 0 & 0 & 0 & [I] \end{bmatrix}\begin{Bmatrix} \ddot{\mathbf{a}} \\ \ddot{\mathbf{b}} \\ \dot{\mathbf{a}} \\ \dot{\mathbf{b}} \end{Bmatrix}+\begin{bmatrix} [C_{yy}] & [C_{yz}]+\Omega[G] & [K_s]+[K_{yy}] & [K_{yz}] \\ [C_{zy}]-\Omega[G] & [C_{zz}] & [K_{zy}] & [K_s]+[K_{zz}] \\ -[I] & 0 & 0 & 0 \\ 0 & -[I] & 0 & 0 \end{bmatrix}\begin{Bmatrix} \dot{\mathbf{a}} \\ \dot{\mathbf{b}} \\ \mathbf{a} \\ \mathbf{b} \end{Bmatrix}=\{0\} \tag{22}$$

and directly solving Eq. (22) for specified rotation speeds.

Steady-State Unbalance Response. The steady state unbalance response of the system governed by Eq. (17) can be assumed of the form

$$\mathbf{p}=\underline{Q}_f e^{i\Omega t}+\underline{Q}_b e^{-i\Omega t} \tag{23}$$

where $\underline{Q}_f$ and $\underline{Q}_b$ are complex vectors that describe the amplitude and phase of forward and backward circular motion, respectively. Substituting Eq. (23) into Eq. (17) gives

$$[A_1]\underline{\mathbf{Q}}_f + [B_1]\underline{\tilde{\mathbf{Q}}}_b = \sum_{j=1}^{N_d} e_j^d m_j^d \Omega^2 \mathbf{R}_j^d e^{i\phi_j^d} \tag{24a}$$

$$[A_2]\underline{\mathbf{Q}}_b + [B_2]\underline{\tilde{\mathbf{Q}}}_f = \mathbf{0} \tag{24b}$$

where the $N_p \times N_p$ matrices $[A_1]$, $[A_2]$, $[B_1]$, and $[B_2]$ are of the form

$$[A_1] = -\Omega^2[M] + \Omega^2[G] + [K_s] + [K_1] + i\Omega[C_1]$$

$$[A_2] = -\Omega^2[M] - \Omega^2[G] + [K_s] + [K_1] - i\Omega[C_1]$$

$$[B_1] = [K_2] - \Omega[C_{yz}] + i([K_{yz}] + \Omega[C_1])$$

$$[B_2] = [K_2] + \Omega[C_{yz}] + i([K_{yz}] - \Omega[C_2]) \tag{25}$$

Solving for $\underline{\tilde{\mathbf{Q}}}_b$ from Eq. (24*b*) in terms of $\underline{\mathbf{Q}}_f$ and substituting into Eq. (24*a*), one obtains

$$\underline{\mathbf{Q}}_f = \sum_{j=1}^{N_d} e_j^d m_j^d \Omega^2 ([A_1] - [B_1][\tilde{T}])^{-1} \mathbf{R}_j^d e^{i\phi_j^d} \tag{26}$$

where the $N_p \times N_p$ matrix $[\tilde{T}]$ is the conjugate of

$$[T] = [A_2]^{-1}[B_2] \tag{27}$$

The backward component of steady-state unbalance response can be obtained by substituting Eq. (26) into Eq. (24*b*) and solving for $\underline{\mathbf{Q}}_b$.

Numerical Examples and Results

Three rotor-bearing systems are used to illustrate the accuracy and the efficiency of the generalized polynomial expansion method (GPEM). The first is a single uniform shaft supported by identical bearings with internal damping. The second is a multistepped rotor system with orthotropic bearings. Finally, a dual rotor system with intershaft bearing is considered. The results for the three examples are presented in tabular and graphic form for various numbers of polynomial terms.

Single Uniform Shaft. A simply supported steel shaft studied by Lund (1974a) and Glasgow and Nelson (1980) is used as a basic example to examine the accuracy and the efficiency of the present method. Firstly, the shaft with two rigid simple supports at two ends is considered. The exact solution for whirl speeds can be derived as

$$\omega = \sqrt{\left(\frac{EI}{\rho A l^4}\right) \frac{(n\pi)^4}{1 + (n\pi)^2 \dfrac{I}{Al^2}(1 - 2\lambda)}}, \quad n = 1, 2, \ldots \tag{28}$$

where all the parameters are defined in the Nomenclature. Before applying the present method, it is noted that the choices of the assumed modes for translational deformations in Eq. (11) are arbitrary, and Eqs. (14) and (21) can be applied to a rotor system with no geometric constraints. However, geometric constraints are introduced to this example as follows:

$$[B]\,\mathbf{a} = \mathbf{0} \quad \text{and} \quad [B]\,\mathbf{b} = \underline{0} \tag{29}$$

where the matrix $[B]$ is of the form

$$[B] = \begin{bmatrix} 1 & (x_1^b) & (x_1^b)^2 & \ldots & (x_1^b)^{N_p-1} \\ 1 & (x_2^b) & (x_2^b)^2 & \ldots & (x_2^b)^{N_p-1} \end{bmatrix} \tag{30}$$

with x_1^b and x_2^b denote the axial positions of the two supports. Then, one can obtain the following expressions

$$\mathbf{a} = \begin{bmatrix} R \\ I \end{bmatrix} \mathbf{a}_I, \quad \mathbf{b} = \begin{bmatrix} R \\ I \end{bmatrix} \mathbf{b}_I \tag{31}$$

where

$$[R] = -\begin{bmatrix} 1 & x_1^b \\ 1 & x_2^b \end{bmatrix}^{-1} \begin{bmatrix} (x_1^b)^2 & (x_1^b)^3 & \ldots & (x_1^b)^{N_p-1} \\ (x_2^b)^2 & (x_2^b)^3 & \ldots & (x_2^b)^{N_p-1} \end{bmatrix} \tag{32}$$

and

$$\mathbf{a}_I^T = \{a_3\ a_4, \ \ldots\ , a_{N_p}\}$$

$$\mathbf{b}_I^T = \{b_3\ b_4, \ \ldots\ , b_{N_p}\} \tag{33}$$

Substituting Eq. (31) into Eq. (14) and premultiplying Eq. (14) with the transpose of the transformation matrix $[R\ I]^T$ in Eq. (31), the governing equations of a rotor system with geometric requirements are obtained. The following numerical results are obtained for the parameter value $I/Al^2 = 1/64$. Tables 1 and 2 show the comparison of whirl speeds obtained by present method, FEM, and the exact solution from Eq. (28) with whirl ratio $\lambda = -1$ and 1, respectively. It should be noted that the FEM employed in this study deals with the same energy contribution as in GPEM. In addition, the same eigensolver, EIGZS (IMSL, 1984), is applied for the calculation of whirl speeds for both methods. The results indicate that with the same degrees of freedom, the whirl speeds obtained by the present method are always more accurate than those obtained by the FEM.

Secondly, the two supports are considered to be identical flexible bearings. The stiffness coefficients of the bearings are $K_{yy} = K_{zz} = 1.7513 \times 10^7$ N/m, $K_{yz} = K_{zy} = -2.917 \times 10^6$ N/m and the damping coefficients are $C_{yy} = C_{zz} = 1.752 \times 10^3$ N • s/m and $C_{yz} = C_{zy} = 0.0$ N • s/m. The shaft is of diameter $d = 10.16$ cm and length $l = 127$ cm. Consider the eigenvalues of Eq. (22) to be $\sigma_r = \alpha_r \pm i\omega_r$ and the log decrements δ_r of the damped precessional modes to be defined by

Table 1 Comparison of whirl speeds of uniform shaft for $\lambda = -1$

$\frac{Whirl\ Speeds\ Obtained\ by\ GPEM}{Whirl\ Speeds\ Obtained\ by\ FEM}$ $unit: \sqrt{\frac{EI}{\rho Al^4}}$

DOF=2	4	6	8	12	16	Exa. Sol.
9.0389 9.0389	8.1631 8.1925	8.1608 8.1673	8.1608 8.1629	8.1608 8.1612	8.1608 8.1609	8.1608
29.135 29.135	23.473 25.842	23.383 23.645	23.383 23.472	23.383 23.401	23.383 23.389	23.383
	54.792 47.319	39.642 43.157	39.098 39.750	39.089 39.238	39.089 39.139	39.089
	85.615 67.403	56.250 62.403	54.539 60.118	54.478 55.078	54.478 54.684	54.478
		121.86 88.225	73.721 77.852	69.611 71.251	69.605 70.209	69.605
		163.71 104.42	92.454 101.96	84.591 93.276	84.561 85.967	84.561
			211.26 127.75	101.04 108.97	99.407 102.09	99.404
			264.57 140.89	117.38 130.62	114.19 125.92	114.17
				158.56 155.27	129.60 140.15	128.39
				184.26 181.44	145.01 160.49	143.56

† DOF = $N_p - 2$ for GPEM & DOF = $2 \times N_e$ for FEM.
‡ GPEM is the present method.

Table 2 Comparison of whirl speeds of uniform shaft for $\lambda = 1$

$\frac{Whirl\ Speeds\ Obtained\ by\ GPEM}{Whirl\ Speeds\ Obtained\ by\ FEM}$ $unit: \sqrt{\frac{EI}{\rho Al^4}}$

DOF=2	4	6	8	12	16	Exa. Sol.
11.926 11.926	10.735 10.771	10.732 10.740	10.732 10.735	10.732 10.732	10.732 10.732	10.732
85.621 85.621	64.233 71.554	63.780 64.615	63.779 64.049	63.779 63.832	63.779 63.796	63.779

† DOF = $N_p - 2$ for GPEM & DOF = $2 \times N_e$ for FEM.
‡ GPEM is the present method.

Table 3 Results of log decrements, whirl speeds, and CPU time using GPEM for Ω = 400.0 rad/s

N_p	Log Decrements (δ_r), Whirl Speeds (ω_r), CPU Time (sec.)				
	Forward		Backward		CPU (sec.)
	δ_r	ω_r(rad/sec)	δ_r	ω_r(rad/sec)	
6	0.0853	540.85	0.1169	497.05	3.08
	0.2924	1160.7	0.3479	1020.7	
	0.2683	2330.6	0.2797	2209.2	
	0.1235	5245.3	0.1224	5180.2	
7	0.0852	540.84	0.1169	497.04	3.96
	0.2924	1160.7	0.3479	1020.7	
	0.2577	2299.4	0.2697	2182.5	
	0.1235	5245.3	0.1224	5180.2	
8	0.0852	540.84	0.1169	497.04	4.79
	0.2923	1160.6	0.3479	1020.7	
	0.2577	2299.4	0.2697	2182.5	
	0.1123	5087.8	0.1114	5028.3	
9	0.0852	540.84	0.1169	497.04	6.30
	0.2923	1160.6	0.3479	1020.7	
	0.2577	2299.3	0.2697	2182.5	
	0.1123	5087.8	0.1114	5028.3	

* N_p = Number of polynomials

Table 4 The results of log decrements, whirl speeds, and CPU time using FEM for Ω = 400.0 rad/s

N_e	Log Decrements (δ_r), Whirl Speeds (ω_r), CPU Time (sec.)				
	Forward		Backward		CPU (sec.)
	δ_r	ω_r(rad/sec)	δ_r	ω_r(rad/sec)	
2	0.0831	545.86	0.1214	492.68	3.28
	0.2951	1183.1	0.3614	1010.4	
	0.2601	2318.6	0.2738	2176.2	
	0.1071	5748.1	0.1062	5681.2	
3	0.0827	544.98	0.1209	492.04	5.35
	0.2881	1175.9	0.3564	1006.1	
	0.2603	2321.4	0.2744	2178.8	
	0.1113	5113.9	0.1100	5046.4	
4	0.0826	544.83	0.1208	491.93	8.02
	0.2892	1174.6	0.3555	1005.3	
	0.2579	2315.0	0.2723	2173.6	
	0.1143	5123.1	0.1130	5053.9	
5	0.0826	544.79	0.1208	491.90	12.23
	0.2879	1174.2	0.3553	1005.0	
	0.2571	2312.7	0.2715	2171.7	
	0.1134	5107.4	0.1122	5038.7	

* N_e = Number of elements

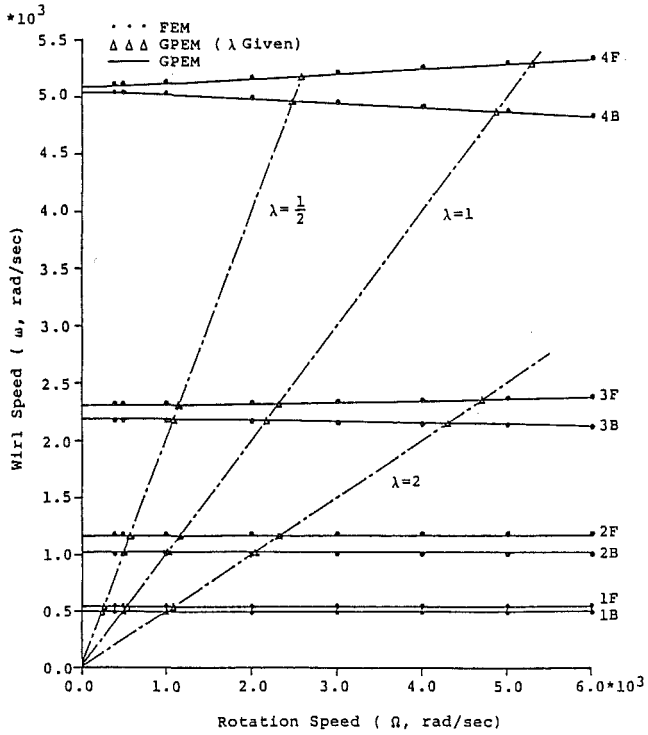

Fig. 2 The whirl map using FEM and GPEM for uniform rotor system

$$\delta_r = \frac{-2\pi\alpha_r}{\omega_r} \tag{34}$$

The density and the elastic modulus are $\rho = 0.7833 \times 10^4$ kg/m^3 and $E = 0.2608 \times 10^{12}$ N/m^2, respectively. The results of the log decrements (δ_r), the whirl speeds (ω_r), and the CPU time on a VAX 785 at a rotation speed of Ω = 400.0 rad/s are shown in Table 3 for the present method and in Table 4 for the finite element method (FEM). It should be noted that the CPU time calculated is based on the same eigensolver, EIGZF (IMSL, 1984). The results indicate that the convergence is very fast using GPEM. A comparison of whirl speeds using GPEM and FEM is shown in Fig. 2. It shows a very good agreement between using GPEM and FEM. However, the results shown in Tables 1–4 indicate that it is computationally more efficiency to use the GPEM. Figures 3–4 show the undamped eigenmodes of the system for Ω = 1000.0, 5000.0 rad/sec, respectively. Each shows four modes with forward (clockwise) motion and backward (counterclockwise) motion at certain rotation speed. The results show that the gyroscopic effect will increase when the rotation speed is increased and the motion will tend to be circular motion if the rotation speed is very large.

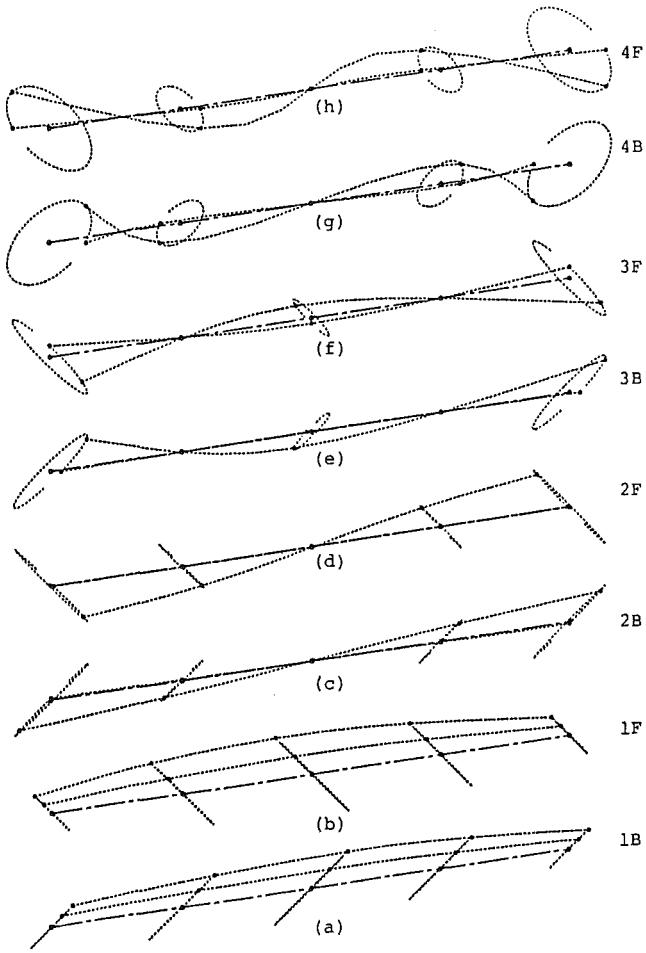

Fig. 3 First four eigenmodes for rotation speed Ω = 1000.0 rad/s

Multistepped Rotor System. The rotor bearing system studied by Nelson and McVaugh (1976) is used to illustrate

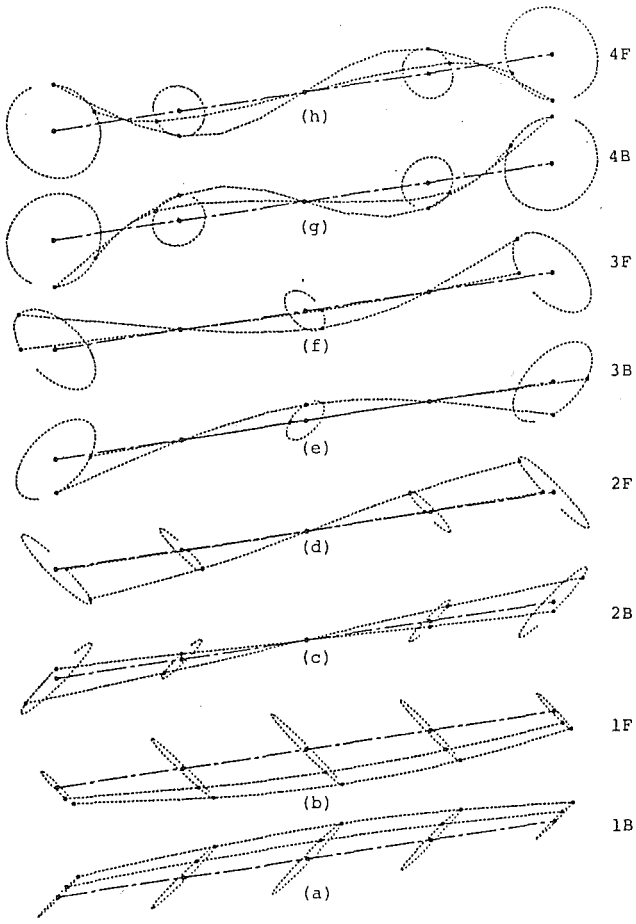

Fig. 4 First four eigenmodes for rotation speed Ω = 5000.0 rad/s

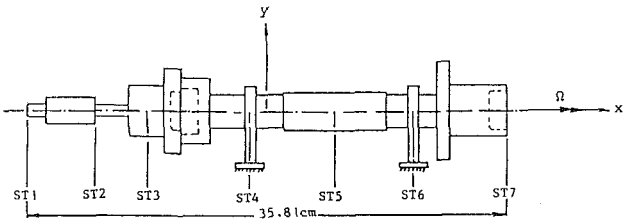

Fig. 5 The configuration of multistepped rotor bearing system

the merits of the present method for the determination of whirl speeds and unbalance response. The configuration of the rotor system and the corresponding data are shown in Fig. 5 and Table 5, respectively. Tables 6 and 7 show the undamped whirl speeds using FEM and GPEM, and the log decrements and damped whirl speeds using FEM and GPEM, respectively. The whirl map for these methods is given in Fig. 6. The results for FEM are obtained from a model with 18 elements and those for GPEM are obtained from 17 polynomial terms. They show that the percentage of difference for the whirl speed is smaller than 6 percent. However, the values of CPU time required are quite different. This indicates that considerable computing time can be saved using GPEM instead of FEM.

Figures 7 and 8 show the first three undamped eigenmodes for the rotation speed Ω = 1000.0, 5000.0 rad/sec, respectively. The results indicate that the increase of rotating speed will significantly influence the second mode. The undamped and damped steady-state unbalance response are shown in Figs. 9 and 10 with unit mass unbalance at the disk location, i.e., e = 1, respectively. The results indicate that for rotation speeds away from the critical speeds, the steady-state responses are approximately the same for both undamped and damped cases.

Table 5 Multistepped rotor configuration data

Element node no.	Node location (cm)	Bearing/ disk	Outer radius (cm)	Inner radius (cm)
1	-17.90		0.51	
2	-16.63		1.02	
3	-12.82		0.76	
4	-10.28		2.03	
5	-9.01	Disk No.1	2.03	
6	-7.74		3.30	
7	-7.23		3.30	1.52
8	-6.47		2.54	1.78
9	-5.20		2.54	
10	-4.44		1.27	
11	-1.39	Bearing No.1	1.27	
12	1.15		1.52	
13	4.96		1.52	
14	8.77		1.27	
15	10.80	Bearing No.2	1.27	
16	12.58		3.81	
17	13.60		2.03	
18	16.64		2.03	1.52
19	17.91			

Distributed rotor:

No.	Density (kg/m^3)	Elastic modulus (N/m^2)
1	7806	2.078×10^{11}

Disk:

No.	Location (cm)	Mass (kg)	Polar inertia (kg m^2)	Diametral inertia (kg m^2)
No.1	-9.01	1.401	0.0020	0.00136

Bearing:

No.	Location (cm)	$k_{yy} = k_{zz}$ (N/m)	$k_{yz} = k_{zy}$ (N/m)	$c_{yy} = c_{zz}$ (Ns/m)	$c_{yz} = c_{zy}$ (Ns/m)
No.1	-1.39	3.503×10^7	-8.756×10^6	1.752×10^3	0
No.2	10.08	3.503×10^7	-8.756×10^6	1.752×10^3	0

Table 6 The whirl speeds and CPU time of undamped multistepped rotor system using FEM and GPEM

Rotating Speed (Ω) \ Undamped Whirl Speed (ω_r)	GPEM		FEM	
	Forward	Backward	Forward	Backward
2000.0	1789.8 5160.8 8601.5	1488.1 4229.6 7245.0	1819.9 5026.2 8149.6	1541.1 4181.1 6833.9
3000.0	1816.5 5159.2 8784.4	1461.8 4227.2 7107.6	1852.6 5023.8 8314.1	1507.9 4176.5 6704.1
4000.0	1847.9 5156.8 8997.3	1430.9 4223.9 6957.9	1889.4 5020.2 8503.2	1470.4 4170.0 6562.6
5000.0	1882.1 5153.5 9229.2	1397.5 4219.6 6806.4	1928.0 5015.4 8705.3	1430.9 4161.6 6420.0
6000.0	1917.8 5149.1 9474.2	1362.7 4214.3 6658.3	1967.4 5008.9 8913.5	1390.6 4151.2 6281.9
CPU Time	58.65 (sec)		474.22 (sec)	

* The unit of Ω and ω_r is rad/sec.

Also, when the rotation speed is large, the steady-state response tends to be in forward synchronous circular motion.

Dual Rotor System. This example considers a dual rotor system with system parameters as shown in Fig. 11 (Rajan et al., 1985). The inner shaft with rotating speed Ω_1 is denoted by Rotor 1, and the outer shaft with rotating speed Ω_2 = 1.5 Ω_1 is denoted by Rotor 2. The bearing supports are considered as isotropic and undamped with stiffness coefficients values 26.2795 $\times$ 10^6 N/m for station 1-0, 17.519 $\times$ 10^6 N/m for

Table 7 Log decrements and the damped whirl speed of multistepped rotor system using FEM and GPEM

Methods / Rotating Speed (Ω)	GPEM				FEM			
	Forward		Backward		Forward		Backward	
	δ_r	ω_r	δ_r	ω_r	δ_r	ω_r	δ_r	ω_r
2000	0.1327	1790.4	0.1972	1489.3	0.1169	1820.5	0.1609	1542.5
	0.4771	5166.2	0.7348	4227.8	0.4266	5034.3	0.6736	4187.6
	0.6227	8538.9	0.6736	7168.8	0.5956	8114.6	0.6833	6770.1
3000	0.1450	1817.0	0.1857	1463.0	0.1302	1853.3	0.1485	1509.3
	0.4778	5163.5	0.7320	4226.3	0.4299	5029.9	0.6686	4184.3
	0.6112	8722.4	0.6824	7032.0	0.5793	8281.8	0.6923	6641.1
4000	0.1568	1848.5	0.1747	1432.1	0.1422	1890.2	0.1378	1471.7
	0.4788	5159.6	0.7282	4224.0	0.4348	5023.5	0.6614	4179.6
	0.5986	8936.4	0.6914	6882.8	0.5603	8474.9	0.7011	6500.4
5000	0.1676	1882.7	0.1651	1398.6	0.1529	1928.9	0.1286	1432.0
	0.4803	5154.3	0.7231	4221.1	0.4416	5015.2	0.6522	4173.4
	0.5852	9169.8	0.7001	6732.0	0.5392	8681.9	0.7089	6358.9
6000	0.1776	1918.4	0.1564	1363.8	0.1628	1968.4	0.1207	1391.7
	0.4825	5147.4	0.7169	4217.5	0.4507	5004.6	0.6408	4165.5
	0.5714	9416.5	0.7083	6584.8	0.5165	8895.7	0.7151	6222.4
CPU Time	60.0 (sec)				500.0 (sec)			

* The unit of Ω and ω_r is rad/sec.

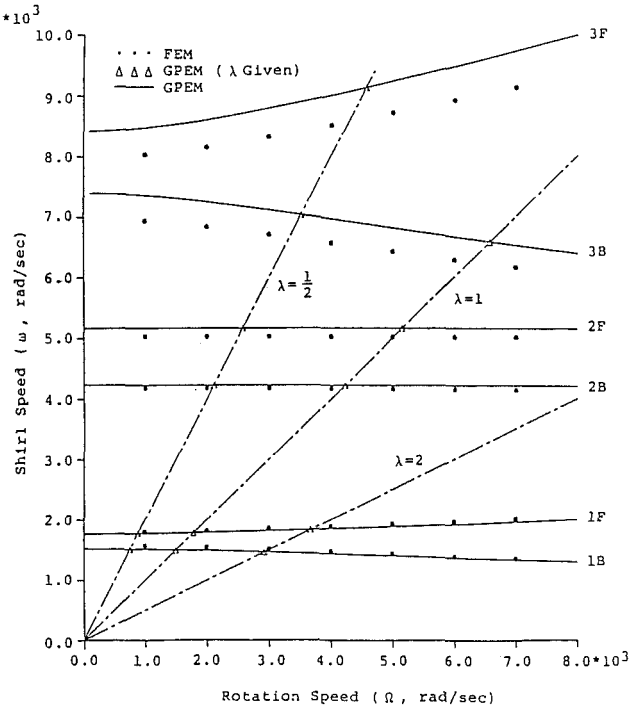

Fig. 6 Whirl map using FEM and GPEM for multistepped rotor system

stations 6-0 and 7-0, and 8.7598×10^6 N/m for station 4-10. The motion of the dual rotor system is modeled by the present method with $N_{p(1)} = 12$ for Rotor 1 and $N_{p(2)} = 8$ for Rotor 2. Moreover, each shaft can be treated as a substructure and the boundary coordinates are defined as the coordinates at bearing positions. The system equations of motion can be obtained by assembling the equations of each component. Table 8 shows the whirl speed results for various levels of modal truncation for $\Omega_1 = 1500.0$ rad/sec. Figure 12 shows the whirl speed map. The results indicate that the first few forward and backward modes can be predicted with high accuracy even with high levels of modal truncation.

Based on the present analysis and numerical results, the following remarks can be made:

1 The equations of motion of a rotor system modeled by the present method generally require no geometric constraints. For some problems, it is necessary to satisfy the geometric boundary conditions. In these cases, Eq. (29) can be introduced to describe the geometric constraints.

2 Numerical instability may occur when a large number of polynomial terms is chosen. To avoid the numerical instability,

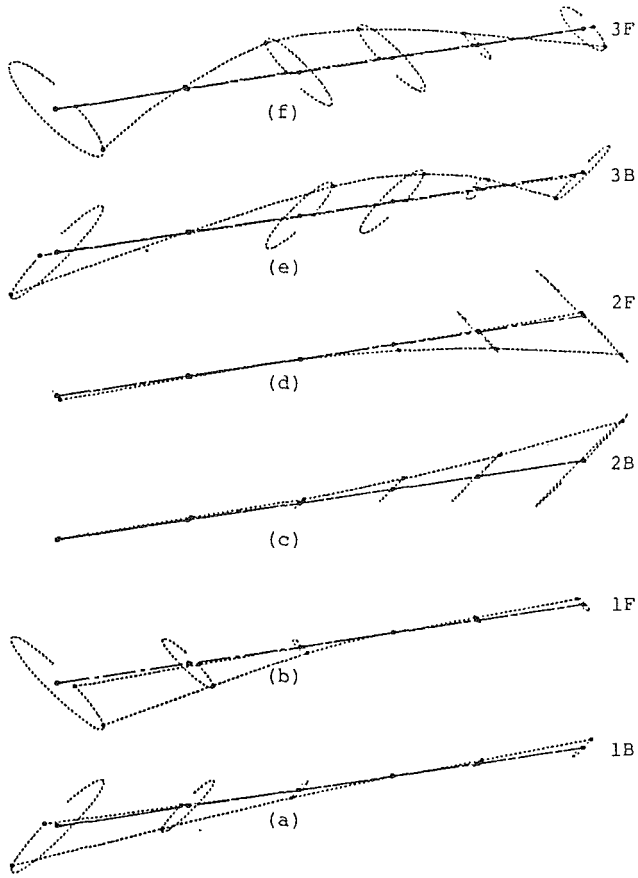

Fig. 7 First three eigenmodes of multistepped rotor system for rotation speed Ω = 1000.0 rad/s

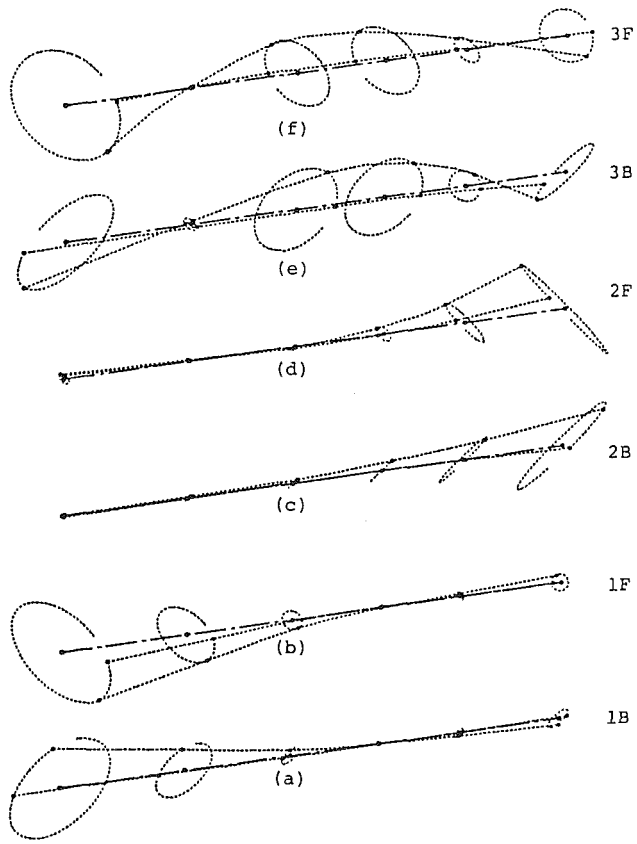

Fig. 8 First three eigenmodes of multistepped rotor system for rotation speed Ω = 5000.0 rad/s

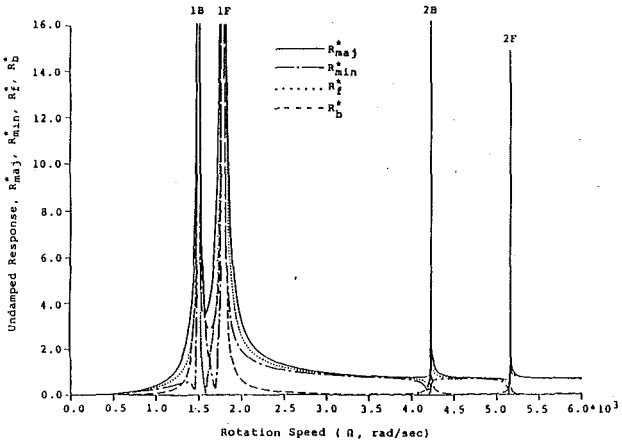

Fig. 9 Undamped steady-state unbalance response due to unit eccentricity

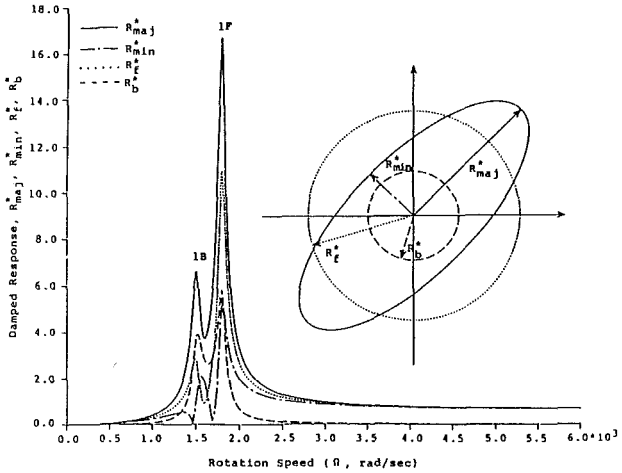

Fig. 10 Damped steady-state unbalance response due to unit eccentricity

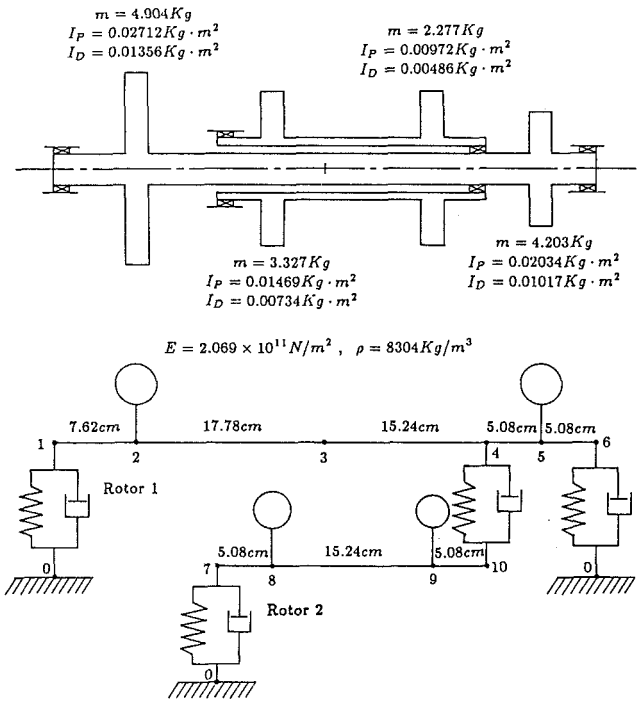

Fig. 11 Schematic plot and parameter values of dual rotor system

Table 8 Whirl speed results for various levels of modal truncation of dual rotor system for Ω_1 = 1500.0 rad/s

Mode No.	M_1/M_2=18/12	10/6	6/4	4/2	2/0
$1^{[B;B]}$	460.483	460.587	461.080	461.827	462.478
$2^{[F;F]}$	931.573	931.587	933.814	935.816	938.144
$3^{[B;B]}$	1500.164	1500.557	1501.162	1502.007	1518.437
$4^{[F;F]}$	1657.883	1657.963	1658.332	1661.702	1684.147
$5^{[B;B]}$	2191.757	2192.673	2198.312	2201.122	2252.444
$6^{[F;F]}$	2273.365	2274.252	2292.499	2299.289	2331.544
$7^{[B;B]}$	2453.515	2454.822	2490.747	2501.737	2501.901
$8^{[B;B]}$	2725.233	2729.219	2775.545	2789.907	2894.072
$9^{[F;F]}$	3224.073	3224.318	3232.292	3273.106	3299.574
$10^{[B;B]}$	3354.284	3357.525	3404.565	3573.703	3966.219
$11^{[F;F]}$	4094.309	4094.792	4099.571	4123.738	4577.460
$12^{[F;F]}$	5880.484	5892.795	5921.292	6068.933	6387.456
Frequency Error			< 1.0%	< 7.0%	

(1). Superscripts $[B;F]$ denote that the whirl motion is backward for Rotor 1 and forward for Rotor 2 respectively.

(2). M_1,M_2 : Number of retained constrained normal modes for Rotor 1 and Rotor 2, respectively.

(3). DOF = $M_1 + M_2 + 10$.

(4). Unit of whirl speed is *rad/sec*.

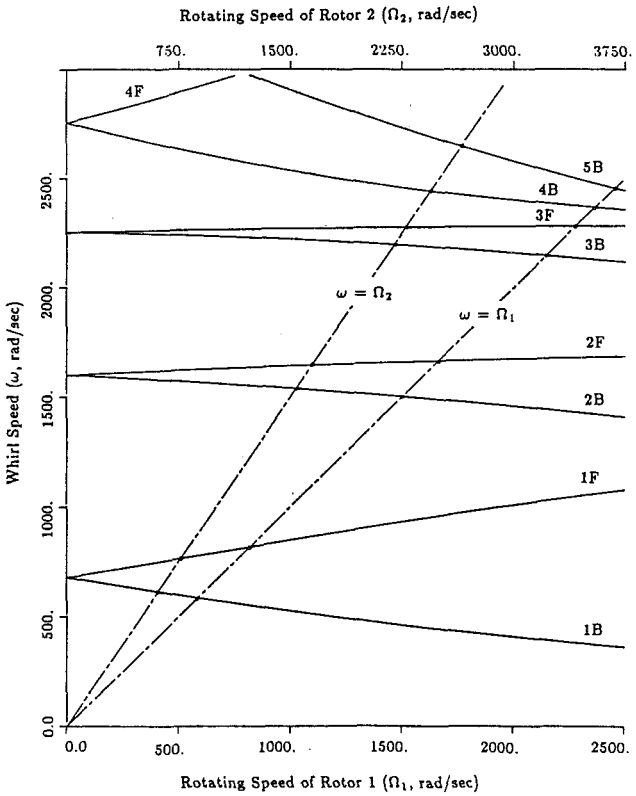

Fig. 12 Whirl map using GPEM for dual rotor system

a similarity transformation can be applied to eliminate the scale of the difference between the elements in system matrices before solving the eigenvalue problem.

3 Other types of function may be chosen as the assumed modes; however, the generalized polynomials appear to be the most convenient and yield accurate solutions.

Conclusions

Three rotor-bearing systems including a single spool rotor and multishaft system have been studied to illustrate the merits of using the generalized polynomial expansion method (GPEM). The results for whirl speeds using the present method

show considerable computing time savings for large rotor systems. The steady-state unbalance response for the undamped and damped system is also studied and satisfactorily compared to those using the FEM. Moreover, the GPEM can be regarded as a global assumed mode method and can be applied to both linear and nonlinear rotor-bearing systems. The merits and procedures for using this method for analyzing nonlinear rotor-bearing systems have been investigated and are presented in a future paper.

Acknowledgments

The authors wish to thank Prof. Harold Nelson from Arizona State University, Tempe, AZ, for his valuable suggestion.

References

Adams, M. L., 1980, "Nonlinear Dynamics of Flexible Multi-Bearing Rotors," *Journal of Sound and Vibration*, Vol. 71(1), pp. 129–144.

Chen, W. J., 1987, "Optimal Design and Parameter Identification of Flexible Rotor-Bearing System," Ph.D. Thesis, Arizona State University, Tempe, AZ.

Childs, D. W., 1978, "The Space Shuttle Main Engine High-Pressure Fuel Turbopump Rotor Dynamic Instability Problem," ASME JOURNAL OF ENGINEERING FOR POWER, Vol. 100, pp. 48–57.

Childs, D. W., and Graviss, K., 1982, "A Note on Critical-Speed Solutions for Finite-Element-Based Rotor Models," ASME *Journal of Mechanical Design*, Vol. 104, pp. 412–415.

Crandall, S. H., and Yeh, N. A., 1986, "Component Mode Synthesis of Multi-rotor Systems," *Proceedings of the Euromech-Colloquium 219, Refined Dynamical Theories of Beams, Plates and Shells and Their Applications*, pp. 44–55.

Crandall, S. H., and Yeh, N. A., 1989, "Automatic Generation of Component Modes for Rotordynamic Substructures," ASME *Journal of Vibration, Acoustics, Stress, and Reliability in Design*, Vol. 111, pp. 6–10.

Dimaragonas, A. D., 1975, "A General Method for Stability Analysis of Rotating Shafts," *Ingenieur-Archiv*, Vol. 44, pp. 9–20.

Dimentberg, F. M., 1961, *Flexural Vibrations of Rotating Shafts*, Butterworth, London.

Eshleman, R. L., and Eubanks, R. A., 1969, "On the Critical Speeds of a Continuous Rotor," ASME *Journal of Engineering for Industry*, Vol. 91, pp. 1180–1188.

Gasch, R., 1976, "Vibration of Large Turbo-rotors in Fluid Film Bearings on Elastic Foundation," *Journal of Sound and Vibration*, Vol. 47(1), pp. 53–73.

Gladwell, G. M. L., and Bishop, R. E. D., 1959, "The Vibration of Rotating Shafts Supported in Flexible Bearings," *Journal of Mechanical Engineering Science*, Vol. 1, pp. 195–206.

Glasgow, D. A., and Nelson, H. D., 1980, "Stability Analysis of Rotor-Bearing Systems Using Component Mode Synthesis," ASME *Journal of Mechanical Design*, Vol. 102, No. 2, pp. 352–359.

Gu, J., 1986, "An Improved Transfer Matrix-Direct Integration Method for Rotor Dynamics," ASME *Journal of Vibration, Acoustics, Stress, and Reliability in Design*, Vol. 108, pp. 182–188.

Hwang, J. L., and Shiau, T. N., 1989, "An Application of Generalized Polynomial Expansion Method to Nonlinear Rotor Bearing System," submitted to ASME *Journal of Vibration and Acoustics*.

IMSL Library, 1984, Mathematical Applications, Inc., Houston, TX.

Kumar, A. S., and Sankar, T. S., 1986, "A New Transfer Matrix Method for Response Analysis of Large Dynamic Systems," *Computers and Structures*, Vol. 23, No. 4, pp. 545–552.

Lee, C.-W., and Jei, Y.-G., 1988, "Modal Analysis of Continuous Rotor-Bearing Systems," *Journal of Sound and Vibration*, Vol. 126, pp. 345–361.

Lund, J. W., and Orcutt, F. K., 1967, "Calculations and Experiments on the Unbalance Response of a Flexible Rotor in Fluid Film Bearing," ASME *Journal of Engineering for Industry*, Vol. 89, No. 4, pp. 705–796.

Lund, J. W., 1974a, "Modal Response of a Flexible Rotor in Fluid-Film Bearings," ASME *Journal of Engineering for Industry*, Vol. 96, No. 2, pp. 525–533.

Lund, J. W., 1974b, "Stability and Damped Critical Speeds of a Flexible Rotor in Fluid-Film Bearings," ASME *Journal of Engineering for Industry*, Vol. 96, pp. 509–517.

Myklestad, N. O., 1944, "A New Method of Calculating Natural Modes of Uncoupled Bending Vibration of Airplane Wings and Other Types of Beams," *Journal of Aeronautical Sciences*, pp. 153–162.

Nelson, H. D., and McVaugh, J. M., 1976, "The Dynamics of Rotor-Bearing Systems Using Finite Elements," ASME *Journal of Engineering for Industry*, Vol. 98, pp. 593–600.

Nelson, H. D., 1980, "A Finite Rotating Shaft Element Using Timoshenko Beam Theory," ASME *Journal of Mechanical Design*, Vol. 102, pp. 793–803.

Prohl, M. A., 1945, "A General Method for Calculating Critical Speeds of Flexible Rotors," ASME *Journal of Applied Mechanics*, Vol. 12, pp. A-142–A-148.

Rajan, M., Nelson, H. D., and Chen, W. J., 1985, "Parameter Sensitivity in the Dynamics of Rotor-Bearing Systems," ASME Paper No. 85-DET-35.

Ruhl, R. L., and Booker, J. F., 1972, "A Finite Element Model for Distributed Parameters Turborotor Systems," ASME *Journal of Engineering for Industry*, Vol. 94, pp. 128–132.

Shiau, T. N., and Hwang, J.-L., 1989, "A New Approach to the Dynamic Characteristic of Undamped Rotor-Bearing Systems," ASME *Journal of Vibration, Acoustics, Stress, and Reliability in Design*, Vol. 111, No. 4, pp. 379–385.

Subbiah, R., Kumar, A. S., and Sankar, T. S., 1988, "Transient Dynamic Analysis of Rotors Using the Combined Methodologies of Finite Elements and Transfer Matrix," ASME *Journal of Applied Mechanics*, Vol. 55, pp. 448–452.

APPENDIX

The components of $N_p \times N_p$ matrices shown in Eq. (14) are of the form

$$M(m, n) = \int_0^l \rho(x)A(x)x^{n+m-2}dx + \int_0^l (n-1)(m-1)I_D x^{n+m-4}dx + \sum_{i=1}^{N_d} [m_i^d (x_i^d)^{n+m-2} + (n-1)(m-1)I_{Di}^d (x_i^d)^{n+m-4}] \quad \text{(A1)}$$

$$G(m, n) = \int_0^l (n-1)(m-1)I_p x^{n+m-4}dx + \sum_{i=1}^{N_d} [(n-1)(m-1)I_{pi}^d (x_i^d)^{n+m-4}] \quad \text{(A2)}$$

$$C_{yy}(m, n) = \sum_{j=1}^{N_b} c_{yyj}^b (x_j^b)^{n+m-2} \quad \text{(A3)}$$

$$C_{yz}(m, n) = \sum_{j=1}^{N_b} c_{yzj}^b (x_j^b)^{n+m-2} \quad \text{(A4)}$$

$$C_{zz}(m, n) = \sum_{j=1}^{N_b} c_{zzj}^b (x_j^b)^{n+m-2} \quad \text{(A5)}$$

$$K_s(m, n) = \int_0^l (n-1)(n-2)(m-1)(m-2)EIx^{n+m-6}dx \quad \text{(A6)}$$

$$K_{yy}(m, n) = \sum_{j=1}^{N_b} k_{yyj}^b (x_j^b)^{n+m-2} \quad \text{(A7)}$$

$$K_{yz}(m, n) = \sum_{j=1}^{N_b} k_{yzj}^b (x_j^b)^{n+m-2} \quad \text{(A8)}$$

$$K_{zz}(m, n) = \sum_{j=1}^{N_b} k_{zzj}^b (x_j^b)^{n+m-2} \quad \text{(A9)}$$

A Study on Stability and Response Analysis of a Nonlinear Rotor System With Mass Unbalance and Side Load

T. N. Shiau
Institute of Aeronautics and Astronautics,
National Cheng Kung University,
Tainan, Taiwan

J. L. Hwang

Y. B. Chang

Group of Structural Mechanics,
ARL/AIDC/CSIST,
Taichung, Taiwan

The stability of steady-state synchronous and nonsynchronous response of a nonlinear rotor system supported by squeeze-film dampers is investigated. The nonlinear differential equations that govern the motion of rotor bearing systems are obtained by using the Generalized Polynomial Expansion Method. The steady-state response of the system is obtained by using the hybrid numerical method, which combines the merits of the harmonic balance and collocation methods. The stability of system response is examined using the Floquet–Liapunov theory. Using the theory, the performance may be evaluated with the calculation of derivatives of nonlinear hydrodynamic forces of the squeeze-film damper with respect to displacement and velocity of the journal center. In some cases, these derivatives can be expressed in closed form and the prediction of the dynamic characteristic of the nonlinear rotor system will be more effective. The stability results are compared to those using a direct numerical integration method and both are in good agreement.

Introduction

Squeeze film dampers (SFD) have been widely used in modern rotating machines to dampen rotor motion and it has been verified that the rotor vibrational amplitudes can be reduced and the system stability can be improved with squeeze-film dampers (Mohan and Hahn, 1974; Gunter et al., 1977; Rabinowitz and Hahn, 1983; Chen, 1987). Because of the complicated hydrodynamic behavior of a squeeze-film damper, it has become a special part of rotor dynamics.

Several investigators (Mohan and Hahn, 1974; Gunter et al., 1977; Hahn, 1979; Taylor and Kumar, 1980; Greenhill and Nelson, 1982; Rabinowitz and Hahn, 1983) have shown that the steady-state response will be a centric circular synchronous motion, if a rotor system is symmetric and vertical, or if a rotor system is preloaded such that the rest journal's center is coincident with the bearing's center. The stability of the centric circular synchronous motion can be studied by first perturbing the equations of motion about the steady-state solution and second solving the eigenvalues problem of the perturbed system. It has been shown by researchers (Hahn, 1979; Athre et al., 1982; Greenhill and Nelson, 1982; Chen, 1987) that the steady-state centric circular motion is unstable if one of the real part of eigenvalues is positive. Another method for studying the stability of steady-state circular motion is to search for the convergent passage by direct numerical integration (Taylor and Kumar, 1980).

The steady-state periodic response of a rotor system with squeeze-film dampers may not be a centric circular motion due to the effects of nonsynchronous excitations and/or asymmetric configuration of a rotor system. Many researchers investigated such periodic response using various methods, such as direct numerical integration (Cookson and Kossa, 1979), perturbation method (Pan and Tonnesen, 1978), trigonometric collocation method (TCM) and harmonic balancing method (HBM) (Saito, 1985; Nataraj and Nelson, 1989; Shiau and Jean, 1990; Jean and Nelson, 1990). However, the stability analysis of such periodic response has not been measured.

The stability of nonlinear steady-state response and the occurrence of nonsynchronous response will be studied in this paper. For noncentric circular synchronous motion, the perturbed dynamic behavior will be governed by a set of linear ordinary differential equations with periodic coefficients. The Floquet–Liapunov theory is used to examine the stability of the periodic system. An improved numerical integration method (Friedmann et al., 1977) is used to calculate the Floquet transition matrix, which is used to determine system stability.

For the analysis of stability, the derivatives of nonlinear squeeze-film forces with respect to journal displacement and velocity will be employed. With the application of short bearing theory, the derivatives of nonlinear squeeze-film forces can be expressed in closed form. A simple example of rigid rotor supported by squeeze-film damper is first employed to demonstrate the stability of the nonlinear periodic response as well as the occurrence of half-subharmonic whirl motion. In addition, the nonlinear response of a flexible rotor system, which consists of multiple rigid disks and bearing supports, is calculated by using the hybrid numerical method (Hwang and

Contributed by the International Gas Turbine Institute and presented at the 37th International Gas Turbine and Aeroengine Congress and Exposition, Cologne, Germany, June 1-4, 1992. Manuscript received by the International Gas Turbine Institute January 16, 1992. Paper No. 92-GT-7. Associate Technical Editor: L. S. Langston.

Shiau, 1991) and the corresponding stability will be examined by using the present algorithm.

Derivation of Governing Equations

A rigid rotor carried in a squeeze-film damper with linear isotropic centering spring and a rotor mass, m, concentrated at the axial center of journal, is shown in Fig. 1. The equations of motion of the rotor system can be expressed in a rotating frame (Mohan and Hahn, 1974; Cookson and Kossa, 1979; Taylor and Kumar, 1980) as follows:

$$m(\ddot{r}-r\dot{\phi}^2)+kr=me\Omega^2\cos(\Omega t-\phi)-F_s\cos\left(\frac{\pi}{2}-\phi\right)+F_r$$

$$m(r\ddot{\phi}+2\dot{r}\dot{\phi})=me\Omega^2\sin(\Omega t-\phi)-F_s\sin\left(\frac{\pi}{2}-\phi\right)+F_\phi \quad (1)$$

where the parameters are defined in the nomenclature and the rotating speed Ω is constant. Alternatively, the equations of motion can be expressed in the inertia frame as

$$m\ddot{v}+kv=F_v+me\Omega^2\cos(\Omega t)$$

$$m\ddot{w}+kw=F_w+me\Omega^2\sin(\Omega t)-F_s \quad (2)$$

It is noted that the forces generated by the squeeze-film damper in the rotating frame (F_r, F_ϕ) and/or in the inertia frame (F_v, F_w), are nonlinear functions of the displacement and velocity of the journal center.

For the flexible rotor system, the Generalized Polynomial Expansion Method (GPEM) proposed by Hwang and Shiau (1991) is employed. The method describes how the deflections of the flexible shaft can be expressed as functions of axial coordinate, x, of flexible shaft and time, t, as follows:

$$v(x,\,t)=\sum_{n=1}^{N_p}a_n(t)x^{n-1}$$

$$w(x,\,t)=\sum_{m=1}^{N_p}b_m(t)x^{m-1}$$

$$\mathrm{B}(x,\,t)=-\frac{\partial w(x,\,t)}{\partial x}=-\sum_{m=2}^{N_p}(m-1)x^{m-2}b_m(t) \quad (3a)$$

$$\Gamma(x,\,t)=\frac{\partial v(x,\,t)}{\partial x}=\sum_{n=2}^{N_p}(n-1)x^{n-2}a_n(t)$$

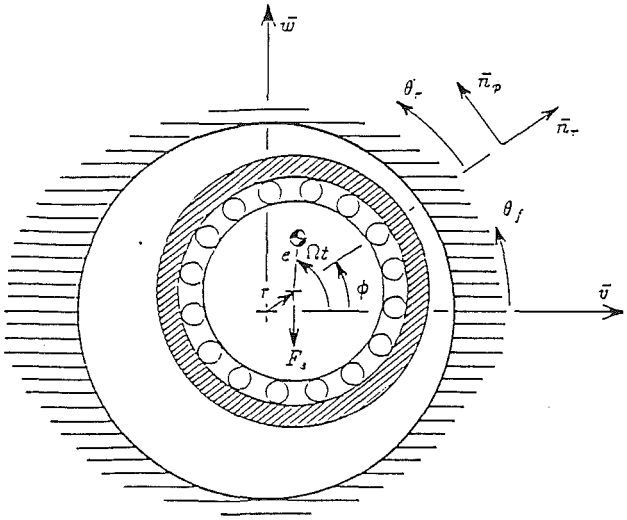

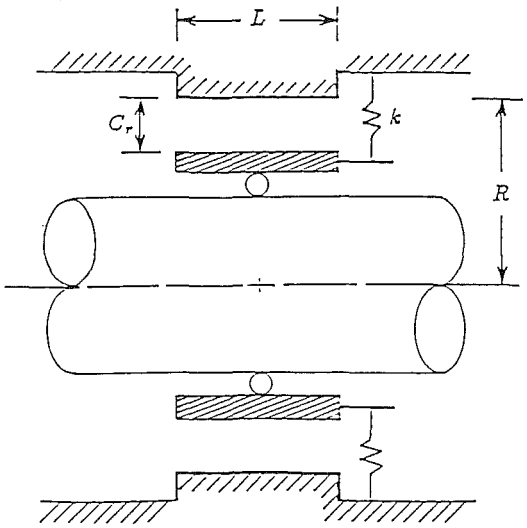

Fig. 1 Model of rigid rotor carried in squeeze-film damper

Nomenclature

a, b = coefficient vectors of polynomials
$[C_{yy}]$, $[C_{yz}]$ $[C_{zy}]$, $[C_{zz}]$ = system generalized damping matrices of bearing
E = modulus of elasticity
e = mass eccentricity
F_a^l, F_b^l = linear generalized force vectors
F_a^n, F_b^n = nonlinear generalized force vectors
$\mathbf{F}_r$, $\mathbf{F}_\phi$ = nonlinear hydrodynamic forces in the radial and tangential directions
$\mathbf{F}_v$, $\mathbf{F}_w$ = nonlinear hydrodynamic forces in the Y and Z directions
F_s = side load
$[K_s]$ = system generalized stiffness matrices of shaft
$[K_{yy}]$,$[K_{yz}]$, $[K_{zy}]$, $[K_{zz}]$ = system generalized stiffness matrices of bearing
k = stiffness of centering spring
$[L(T)]$ = transition matrix
$[M]$, $[G]$ = system generalized mass and gyroscopic matrix, respectively
m = mass of rigid disk
N_P = number of terms of polynomial
N_ω = total number of harmonic terms retained
R, C_r, L = radius, radial clearance, and width of squeeze-film damper, respectively
r = radial displacement of journal center
(v, w) = lateral deflection in (Y, Z) directions
(v_{ss}, w_{ss}) = steady-state response of nonlinear system
B, Γ = rotating deflection in X–Z and X–Y planes
δ = nondimensional mass unbalance = e/C_r
ϵ, ϵ' = nondimensional radial displacement and radial velocity of journal center = r/C_r
Λ = eigenvalues of transition matrix
μ = lubricant viscosity
ρ = mass density per unit volume of the shaft
ϕ = precession angle of journal center
$\dot{\phi}$ = precession velocity of journal center
ω, Ω = whirl speed and rotating speed

where the $a_n(t)$ and $b_m(t)$ are named generalized coordinates and the integer N_p is the total number of polynomials. Using the Lagrangian approach, the equations of motion can be expressed as

$$\begin{bmatrix} M & 0 \\ 0 & M \end{bmatrix}\begin{Bmatrix} \ddot{\mathbf{a}} \\ \ddot{\mathbf{b}} \end{Bmatrix}+\Omega\begin{bmatrix} 0 & G \\ -G & 0 \end{bmatrix}\begin{Bmatrix} \dot{\mathbf{a}} \\ \dot{\mathbf{b}} \end{Bmatrix} + \begin{bmatrix} C_{yy} & C_{yz} \\ C_{zy} & C_{zz} \end{bmatrix}\begin{Bmatrix} \dot{\mathbf{a}} \\ \dot{\mathbf{b}} \end{Bmatrix}+\begin{bmatrix} K_s & 0 \\ 0 & K_s \end{bmatrix}\begin{Bmatrix} \mathbf{a} \\ \mathbf{b} \end{Bmatrix} + \begin{bmatrix} K_{yy} & K_{yz} \\ K_{zy} & K_{zz} \end{bmatrix}\begin{Bmatrix} \mathbf{a} \\ \mathbf{b} \end{Bmatrix}=\begin{Bmatrix} \mathbf{F}_a^l \\ \mathbf{F}_b^l \end{Bmatrix}+\begin{Bmatrix} \mathbf{F}_a^n \\ \mathbf{F}_b^n \end{Bmatrix} \quad (3b)$$

where

$$\mathbf{a}=\{a_1\ a_2\ \ldots\ a_{N_p}\}$$

$$\mathbf{b}=\{b_1\ b_2\ \ldots\ b_{N_p}\}$$

Applying the numerical technique of Hwang and Shiau (1991), the steady-state response of the rotor system can be obtained and expressed by a set of finite terms of trigonometric functions. It should be noted that the linear and nonlinear forces due to the squeeze-film damper are symbolically included in the first and second terms on the right-hand side of Eq. (3*b*), respectively.

Nonlinear Squeeze-Film Forces and Their Derivatives

To obtain the forces of squeeze-film damper, the short bearing approximation is used because most of squeeze-film dampers are of low L/D ratio (Mohan and Hahn, 1974; Gunter et al., 1977), with L the width of bearing and D the diameter of journal. The nonlinear forces of the squeeze-film damper can be obtained by integrating the effective pressure distribution determined from solving the Reynolds equation, along the bearing surface. These nonlinear forces can be expressed as

$$\begin{Bmatrix} F_r \\ F_\phi \end{Bmatrix}=\frac{-\mu RL^3}{C_r^2}\int_{\theta_{r1}}^{\theta_{r2}}\frac{(\dot{\epsilon}\cos\theta_r+\epsilon\dot{\phi}\sin\theta_r)}{(1-\epsilon\cos\theta_r)^3}\begin{Bmatrix}\cos\theta_r\\ \sin\theta_r\end{Bmatrix}d\theta_r \quad (4)$$

$$\begin{Bmatrix} F_v \\ F_w \end{Bmatrix}=\frac{-\mu RL^3}{C_r^2}\int_{\theta_{f1}}^{\theta_{f2}}\frac{(\dot{V}\cos\theta_f+\dot{W}\sin\theta_f)}{(1-V\cos\theta_f-W\sin\theta_f)^3}\begin{Bmatrix}\cos\theta_f\\ \sin\theta_f\end{Bmatrix}d\theta_f$$

$$=\frac{-\mu RL^3}{C_r^w}\int_{\theta_{f1}}^{\theta_{f2}}\frac{(\dot{\epsilon}\cos\theta_r+\epsilon\dot{\phi}\sin\theta_r)}{(1-\epsilon\cos\theta_r)^3}\begin{Bmatrix}\cos\theta_f\\ \sin\theta_f\end{Bmatrix}d\theta_f \quad (5)$$

or

$$\begin{Bmatrix} F_r \\ F_\phi \end{Bmatrix}=\frac{-\mu RL^3\Omega}{C_r^2}\begin{Bmatrix}\epsilon\phi' A_3^{11}+\epsilon' A_3^{02}\\ \epsilon\phi' A_3^{20}+\epsilon' A_3^{11}\end{Bmatrix} \quad (6)$$

where the coefficients A_l^{ij} are defined as follows:

$$A_l^{ij}=\int_{\theta_{r1}}^{\theta_{r2}}\frac{(\sin\theta_r)^i(\cos\theta_r)^j}{(1-\epsilon\cos\theta_r)^l}\,d\theta_r \quad (7)$$

and

$$(')\equiv\left(\frac{\partial}{\partial(\Omega t)}\right)\equiv\frac{1}{\Omega}\frac{\partial}{\partial t}\equiv\frac{1}{\Omega}(\cdot).$$

It is noted that the squeeze film forces will generally depend on the motion of the journal center, which is usually an implicit function of time, as shown in Eqs. (4) and (5). In addition, if the motion orbit of system is synchronous circular and the oil film is fully cavitated (i.e., π-film model), Eq. (6) can be approximately expressed as

$$F_r\approx\frac{-\mu RL^3}{C_r^2}\left(\epsilon\dot{\phi}\,\frac{2\epsilon}{(1-\epsilon^2)^2}+\dot{\epsilon}\,\frac{\frac{\pi}{2}(1+2\epsilon^2)}{(1-\epsilon^2)^{5/2}}\right)$$

$$F_\phi\approx\frac{-\mu RL^3}{C_r^2}\left(\epsilon\dot{\phi}\,\frac{\frac{\pi}{2}}{(1-\epsilon^2)^{3/2}}+\dot{\epsilon}\,\frac{2\epsilon}{(1-\epsilon^2)^2}\right) \quad (8)$$

The dimensionless variables shown in Eq. (5) are given by

$$\epsilon=r/C_r,\quad V=v/C_r,\quad W=w/C_r$$

$$\theta_f=\theta_r+\phi,\ \theta_{f1}=\theta_{r1}+\phi,\quad \theta_{f2}=\theta_{r2}+\phi$$

$$\phi=\tan^{-1}\left(\frac{W}{V}\right) \quad (9)$$

Moreover, the integration limit can be generally expressed as

$$\theta_{r2}=\theta_{r1}+\text{const} \quad (10)$$

which is the case of general application. For example, the constant value is 2π and θ_{r2} can be any constant value for 2π-film bearing model. However, if the constant value is π, θ_{r2} and θ_{f2} will be of the form

$$\theta_{r2}=\tan^{-1}\left(\frac{\epsilon'}{-\epsilon\phi'}\right)$$

$$\theta_{f2}=\tan^{-1}\left(\frac{V'}{-W'}\right) \quad (11)$$

which is the π-film bearing model.

The derivatives of nonlinear squeeze-film forces in either rotating frame or inertia frame can be obtained by differentiating Eqs. (4) and (5) with respect to journal displacement and velocity. They are of the form:

(*a*) *Rotating frame case*

$$\frac{\partial}{\partial\phi}\begin{Bmatrix}F_r\\F_\phi\end{Bmatrix}=\begin{Bmatrix}0\\0\end{Bmatrix} \quad (12)$$

$$\frac{\partial}{\partial\epsilon}\begin{Bmatrix}F_r\\F_\phi\end{Bmatrix}=-\overline{B}\left(\begin{Bmatrix}\phi' A_3^{11}+3\epsilon\phi' A_4^{12}+3\epsilon' A_4^{03}\\ \phi' A_3^{20}+3\epsilon\phi' A_4^{21}+3\epsilon' A_4^{12}\end{Bmatrix}+\frac{\partial\theta_{r1}}{\partial\epsilon}\begin{Bmatrix}\epsilon\phi' L_3^{11}+\epsilon' L_3^{02}\\ \epsilon\phi' L_3^{20}+\epsilon' L_3^{11}\end{Bmatrix}\right) \quad (13)$$

$$\frac{\partial}{\partial\epsilon'}\begin{Bmatrix}F_r\\F_\phi\end{Bmatrix}=-\overline{B}\left(\begin{Bmatrix}A_3^{02}\\A_3^{11}\end{Bmatrix}+\frac{\partial\theta_{r1}}{\partial\epsilon'}\begin{Bmatrix}\epsilon\phi' L_3^{11}+\epsilon' L_3^{02}\\ \epsilon\phi' L_3^{20}+\epsilon' L_3^{11}\end{Bmatrix}\right) \quad (14)$$

$$\frac{\partial}{\partial\phi'}\begin{Bmatrix}F_r\\F_\phi\end{Bmatrix}=-\overline{B}\left(\begin{Bmatrix}\epsilon A_3^{11}\\\epsilon A_3^{20}\end{Bmatrix}+\frac{\partial\theta_{r1}}{\partial\phi'}\begin{Bmatrix}\epsilon\phi' L_3^{11}+\epsilon' L_3^{02}\\ \epsilon\phi' L_3^{20}+\epsilon' L_3^{11}\end{Bmatrix}\right) \quad (15)$$

where

$$\overline{B}=\frac{\mu RL^3\Omega}{C_r^2} \quad (16)$$

$$L_l^{ij}=\left[\frac{(\sin\theta_r)^i(\cos\theta_r)^j}{(1-\epsilon\cos\theta_r)^l}\right]\Bigg|_{\theta_r=\theta_{r1}}^{\theta_r=\theta_{r2}} \quad (17)$$

(*b*) *Inertia frame case*

$$\frac{\partial}{\partial V}\begin{Bmatrix}F_v\\F_w\end{Bmatrix}=-\overline{B}\left(\begin{Bmatrix}3\epsilon' A_4^{01(02)}+3\epsilon\phi' A_4^{10(02)}\\ 3\epsilon' A_4^{01(11)}+3\epsilon\phi' A_4^{10(11)}\end{Bmatrix}+\frac{\partial\theta_{f1}}{\partial V}\begin{Bmatrix}V' L_3^{00(02)}+W' L_3^{00(11)}\\ V' L_3^{00(11)}+W' L_3^{00(20)}\end{Bmatrix}\right) \quad (18)$$

$$\frac{\partial}{\partial W}\begin{Bmatrix}F_v\\F_w\end{Bmatrix}=-\overline{B}\left(\begin{Bmatrix}3\epsilon' A_4^{01(11)}+3\epsilon\phi' A_4^{10(11)}\\ 3\epsilon' A_4^{01(20)}+3\epsilon\rho' A_4^{10(20)}\end{Bmatrix}+\frac{\partial\theta_{f1}}{\partial W}\begin{Bmatrix}V' L_3^{00(02)}+W' L_3^{00(11)}\\ V' L_3^{00(11)}+W' L_3^{00(20)}\end{Bmatrix}\right) \quad (19)$$

$$\frac{\partial}{\partial V'}\begin{Bmatrix}F_v\\F_w\end{Bmatrix}=-\overline{B}\left(\begin{Bmatrix}A_3^{00(02)}\\A_3^{00(11)}\end{Bmatrix}+\frac{\partial\theta_{f1}}{\partial V'}\begin{Bmatrix}V'L_3^{00(02)}+W'L_3^{00(11)}\\V'L_3^{00(11)}+W'L_3^{00(20)}\end{Bmatrix}\right) \quad (20)$$

$$\frac{\partial}{\partial W'}\begin{Bmatrix}F_v\\F_w\end{Bmatrix}=-\overline{B}\left(\begin{Bmatrix}A_3^{00(11)}\\A_3^{00(20)}\end{Bmatrix}+\frac{\partial\theta_{f1}}{\partial W'}\begin{Bmatrix}V'L_3^{00(02)}+W'L_3^{00(11)}\\V'L_3^{00(11)}+W'L_3^{00(20)}\end{Bmatrix}\right) \quad (21)$$

where

$$A_l^{ij(mn)}=\int_{\theta_{r1}}^{\theta_{r2}}\frac{(\sin\theta_r)^i(\cos\theta_r)^j(\sin\theta_f)^m(\cos\theta_f)^n}{(1-\epsilon\cos\theta_r)^l}\,d\theta_r \quad (22)$$

$$L_l^{ij(mn)}=\left[\frac{(\sin\theta_r)^i(\cos\theta_r)^j(\sin\theta_f)^m(\cos\theta_f)^n}{(1-\epsilon\cos\theta_r)^l}\right]\Bigg|_{\theta_r=\theta_{r1},\ \theta_f=\theta_{f1}}^{\theta_r=\theta_{r2},\ \theta_f=\theta_{f2}} \quad (23)$$

Generally, θ_{r1} is a function of ϵ, ϵ', and ϕ'. θ_{f1} is function of V' and W'. The corresponding derivatives shown on the right-hand side of Eqs. (13)–(14) are of the following form:

(*a*) *2π-film bearing model,*

$$\frac{\partial\theta_{r1}}{\partial\epsilon}=\frac{\partial\theta_{r1}}{\partial\epsilon'}=\frac{\partial\theta_{r1}}{\partial\phi'}=\frac{\partial\theta_{f1}}{\partial V}=\frac{\partial\theta_{f1}}{\partial W}=\frac{\partial\theta_{f1}}{\partial V'}=\frac{\partial\theta_{f1}}{\partial W'}=0 \quad (24)$$

(*b*) *π-film bearing model*

$$\frac{\partial\theta_{r1}}{\partial\epsilon}=\frac{\left(\frac{-\epsilon'}{\epsilon\phi'}\right)}{1.0+\left(\frac{-\epsilon'}{\epsilon\phi'}\right)^2}\left(\frac{-1}{\epsilon}\right)$$

$$\frac{\partial\theta_{r1}}{\partial\epsilon'}=\frac{1.0}{1.0+\left(\frac{-\epsilon'}{\epsilon\phi'}\right)^2}\left(\frac{-1}{\epsilon\phi'}\right)$$

$$\frac{\partial\theta_{r1}}{\partial\phi'}=\frac{\left(\frac{-\epsilon'}{\epsilon\phi'}\right)}{1.0+\left(\frac{-\epsilon'}{\epsilon\phi'}\right)^2}\left(\frac{-1}{\phi'}\right) \quad (25)$$

$$\frac{\partial\theta}{\partial V'}=\frac{-W'}{(V')^2+(W')^2}$$

$$\frac{\partial\theta_{f1}}{\partial W'}=\frac{V'}{(V')^2+(W')^2}$$

$$\frac{\partial\theta_{f1}}{\partial V}=\frac{\partial\theta_{f1}}{\partial W}=0 \quad (26)$$

The fomulation of the derivatives shown in Eqs. (12)–(26) will be employed in the stability analysis. The nonlinear forces and their derivatives are expressed in rotating frame because the expressions are simple. However, for studying the stability and the response of system, it is more convenient to use the expressions in fixed frame. Also, it should be noted that the use of the π-film model is only for convenience.

Stability of Steady-State Response

The steady-state solution of Eq. (2) can be approximately described (Saito, 1985; Nataraj and Nelson, 1989; Shiau and Jean, 1990; Jean and Nelson, 1990) by the form

$$v_{ss}=v_0+\sum_{i=1}^{N_w}(v_{ci}\cos\omega_i t+v_{si}\sin\omega_i t)$$

$$w_{ss}=w_0+\sum_{i=1}^{N_w}(w_{ci}\cos\omega_i t+w_{si}\sin\omega_i t) \quad (27)$$

where $\omega_i=i\times\omega$ and N_w is an integer. To examine the stability of the steady-state solution, the motion is perturbed and the resulting motion is expressed as

$$v=v_{ss}+\delta v$$

$$w=w_{ss}+\delta w \quad (28)$$

The perturbed squeeze-film forces can be expressed as

$$\begin{Bmatrix}F_v\\F_w\end{Bmatrix}\approx\begin{Bmatrix}(F_v)_{ss}\\(F_w)_{ss}\end{Bmatrix}+\begin{bmatrix}\left(\frac{\partial F_v}{\partial v}\right)_{ss}&\left(\frac{\partial F_v}{\partial w}\right)_{ss}\\\left(\frac{\partial F_w}{\partial v}\right)_{ss}&\left(\frac{\partial F_v}{\partial w}\right)_{ss}\end{bmatrix}\begin{Bmatrix}\delta v\\\delta w\end{Bmatrix}+\begin{bmatrix}\left(\frac{\partial F_v}{\partial\dot v}\right)_{ss}&\left(\frac{\partial F_v}{\partial\dot w}\right)_{ss}\\\left(\frac{\partial F_w}{\partial\dot v}\right)_{ss}&\left(\frac{\partial F_w}{\partial\dot w}\right)_{ss}\end{bmatrix}\begin{Bmatrix}\delta\dot v\\\delta\dot w\end{Bmatrix} \quad (29)$$

where the subscript *ss* denotes the steady-state solution and the coefficient matrices can be obtained from Eqs. (18)–(21). Substituting Eqs. (27)–(29) into Eq. (2), the perturbed equations are of the form:

$$\begin{bmatrix}m&0\\0&m\end{bmatrix}\begin{Bmatrix}\delta\ddot v\\\delta\ddot w\end{Bmatrix}+\begin{bmatrix}-\left(\frac{\partial F_v}{\partial\dot v}\right)_{ss}&-\left(\frac{\partial F_v}{\partial\dot w}\right)_{ss}\\-\left(\frac{\partial F_w}{\partial\dot v}\right)_{ss}&-\left(\frac{\partial F_w}{\partial\dot w}\right)_{ss}\end{bmatrix}\begin{Bmatrix}\delta\dot v\\\delta\dot w\end{Bmatrix}+\begin{bmatrix}k-\left(\frac{\partial F_v}{\partial v}\right)_{ss}&-\left(\frac{\partial F_v}{\partial w}\right)_{ss}\\-\left(\frac{\partial F_w}{\partial v}\right)_{ss}&k-\left(\frac{\partial F_w}{\partial w}\right)_{ss}\end{bmatrix}\begin{Bmatrix}\delta v\\\delta w\end{Bmatrix}=\begin{Bmatrix}0\\0\end{Bmatrix} \quad (30)$$

The stability of nonlinear steady-state response is governed by Eq. (30), which is a set of homogeneous ordinary differential equations. For the special case of centric circular synchronous motion, i.e.,

$$\omega_1=\Omega,\quad v_0=w_0=0$$

$$v_{ci}=v_{si}=w_{ci}=w_{si}=0\quad\text{for } i\neq 1$$

$$v_{c1}=w_{s1},\quad v_{s1}=-w_{c1} \quad (31)$$

or equivalent to

$$r=\text{const},\ \dot r=0$$

$$\dot\phi=\Omega=\text{const}, \quad (32)$$

Eq. (30) can be written in rotating frame. That yields a set of homogeneous ordinary differential equations with constant coefficients. Thus, the stability problem can be examined by solving the eigenvalues of a constant matrix (Hahn, 1979; Athre et al., 1982; Greenhill and Nelson, 1982; Chen, 1987).

In general, the coefficient matrices shown in Eq. (30) are periodic functions of time with period $2\pi/\omega_1$. The stability problem can be examined by solving the eigenvalues of the transition matrix of the periodic system. Applying the Floquet–Liapunov theory, the steady-state periodic response is stable only when the maximum absolute value of the eigenvalues of transition matrix is smaller than one, i.e.,

$$|\Lambda|_{\max}<1.0 : \textit{Stable}$$

$$|\Lambda|_{\max}\geq 1.0 : \textit{Unstable} \quad (33)$$

For the convenience of analysis, Eq. (30) is cast into the first-order form

$$\{\delta\dot q\}=[S]\{\delta q\} \quad (34)$$

where

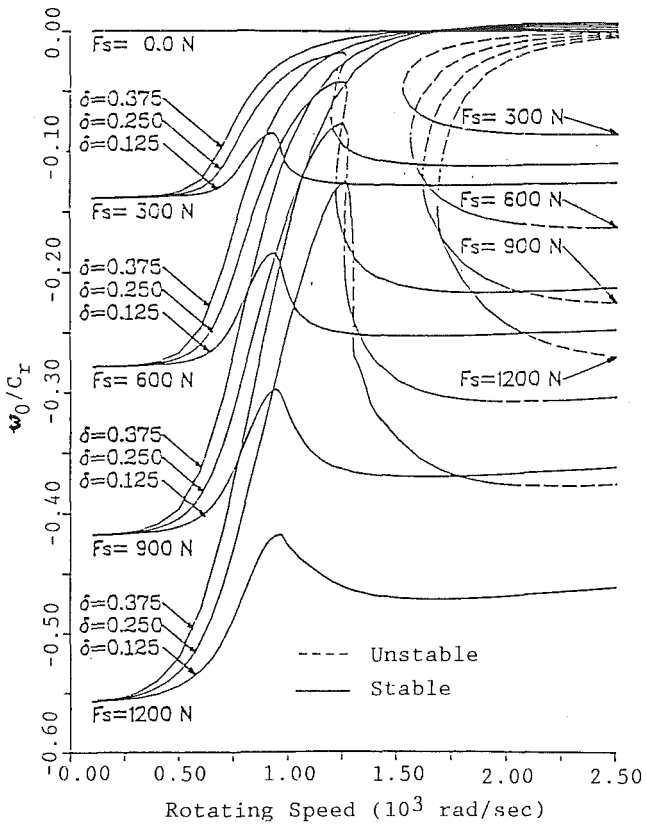

Fig. 2 Nondimensional constant offset in *w* direction versus rotating speed of Example 1

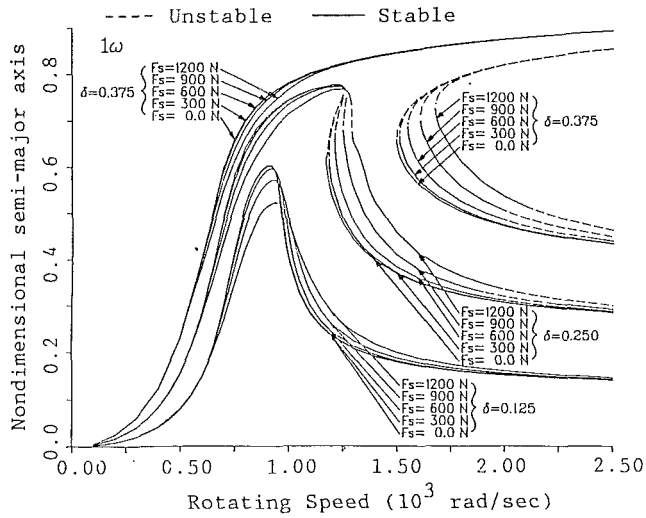

Fig. 3 Nondimensional semimajor axis of the first harmonic response versus rotating speed of Example 1

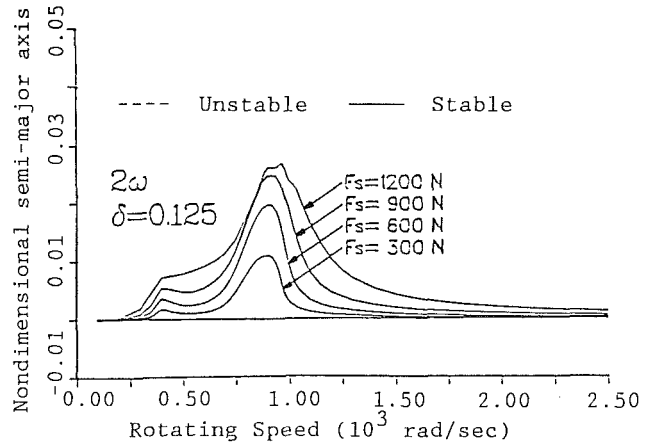

Fig. 4 Nondimensional semimajor axis of the second harmonic response versus rotating speed of Example 1 with δ = 0.125

$$\{\delta q\} = \{\delta \dot{v},\ \delta \dot{w},\ \delta v,\ \delta w\}^T$$

$$[S] = \frac{1}{m}\begin{bmatrix} \left(\frac{\partial F_v}{\partial \dot{v}}\right)_{ss} & \left(\frac{\partial F_v}{\partial \dot{w}}\right)_{ss} & \left(\frac{\partial F_v}{\partial v}\right)_{ss} - k & \left(\frac{\partial F_v}{\partial w}\right)_{ss} \\ \left(\frac{\partial F_w}{\partial \dot{v}}\right)_{ss} & \left(\frac{\partial F_w}{\partial \dot{w}}\right)_{ss} & \left(\frac{\partial F_w}{\partial v}\right)_{ss} & \left(\frac{\partial F_w}{\partial w}\right)_{ss} - k \\ m & 0 & 0 & 0 \\ 0 & m & 0 & 0 \end{bmatrix} \tag{35}$$

Assuming that $[L(t)]$ is a solution matrix of Eq. (34) with initial condition $[L(0)] = [I]$, then the transition matrix of Eq. (34) is defined by $[L(T)]$ with $T = 2\pi/\omega_1$. For a flexible rotor system, the derivatives of nonlinear generalized forces shown in the last term of Eq. (3*b*) can be obtained by the same way for each squeeze-film damper. Knowing the transition matrix, the stability of the system motion can be determined.

Numerical Examples and Results

Example 1. The rotor system studied by Taylor and Kumar (1980) for the response analysis is employed to demonstrate the system stability. The system parameters are given by

Rotor mass	$m = 33.43$ kg
Bearing radius	$R = 64.80$ mm
Bearing width	$L = 22.70$ mm
Bearing clearance	$C_r = 100$ μm
Viscosity of lubricant	$\mu = 2.66 \times 10^{-3}$ N•s/m^2
Stiffness of centering spring	$k = 2.154 \times 10^7$ N/m

The following cases of excitations are studied:

Side load	$F_s = 0.0$, 300, 600, 900, 1200 N
Mass eccentricity	$\delta = e/C_r = 0.125$, 0.250, 0.375

It is assumed that the oil film is fully cavitated and a natural frequency defined as the stiffness of centering spring over the rotor mass is of the value ω_n = 802.7 rad/s.

For various mass eccentricity and side loads, the periodic response of the system can be obtained by individually choosing proper harmonic components. Figure 2 shows the nondimensional constant offset of the journal center in the *w* direction versus journal rotating speed. Figure 3 shows the nondimensional semimajor axis of the first harmonic response versus the journal rotating speed. Figures 4–6 show the nondimensional semimajor axis of the second harmonic response versus journal rotating speed for δ = 0.125, 0.250, and 0.375, respectively. The solid lines shown in Figs. 2–6 represent the stable motion, i.e., $|\Lambda|_{max} < 1.0$ and the dashed lines represent the unstable motion, i.e., $|\Lambda|_{max} \geq 1.0$. The higher harmonic components of response are found to be very small compared to the first harmonic component of response and negligible.

The stability of the synchronous response is shown in Figs. 7–9 for δ = 0.125, 0.250, and 0.375, respectively. For the case of no side load, i.e., F_s = 0, the steady-state response is centric circular synchronous motion. The stability has been studied by Taylor and Kumar (1980) and Greenhill and Nelson (1982). It can be shown that, for small eccentricity (e.g., δ = 0.125), the circular synchronous motion is stable and unique. However, if the eccentricity is increased, different dynamic phenomena will occur. For the case of δ = 0.250, there exist the jump phenomena for the circular synchronous motion when the rotating speeds pass through $\Omega \approx$ 1250.0 rad/s. If the

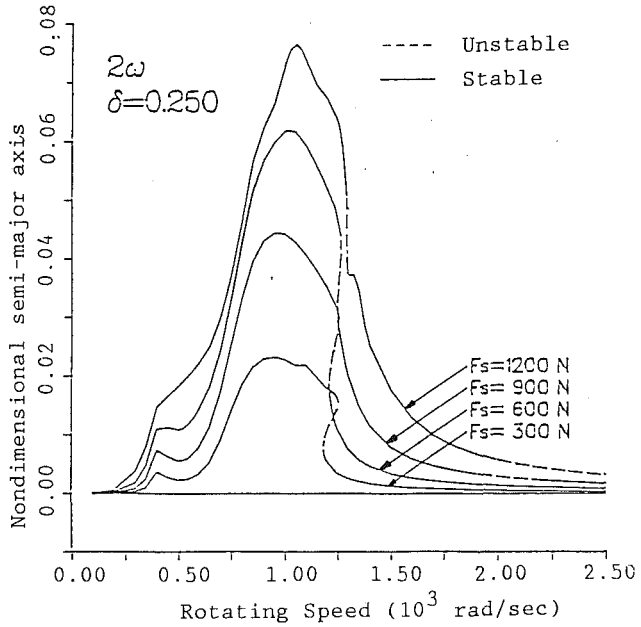

Fig. 5 Nondimensional semimajor axis of the second harmonic response versus rotating speed of Example 1 with $\delta = 0.250$

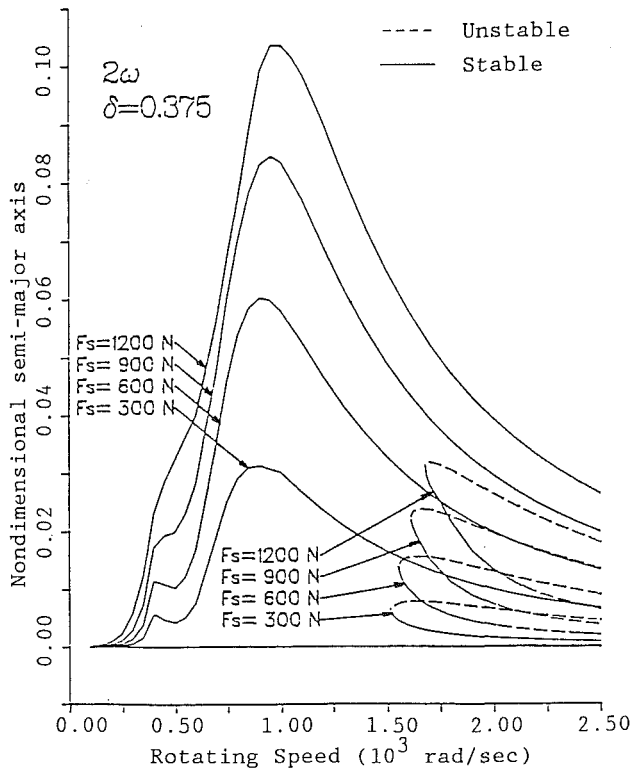

Fig. 6 Nondimensional semimajor axis of the second harmonic response versus rotating speed of Example 1 with $\delta = 0.375$

eccentricity is continuously increased (i.e., $\delta = 0.375$), it is found that the jump phenomena occur at $\Omega \approx 1500.0$ rad/s and a bistable operation behavior appears as $\Omega > 1500.0$ rad/s. The bistable operation behavior and jump phenomena have been shown to be very important (Gunter et al., 1977; Botman and Samaha, 1982; Rabinowitz and Hahn, 1983). The existence of side load will distort the orbits of circular synchronous motion and result in subharmonic whirl motion. In addition, it can destabilize the synchronous motion.

Consider the case of $\delta = 0.250$ and $F_s = 900$N. It is shown that if the journal rotating speed is in the range of 1900–2200

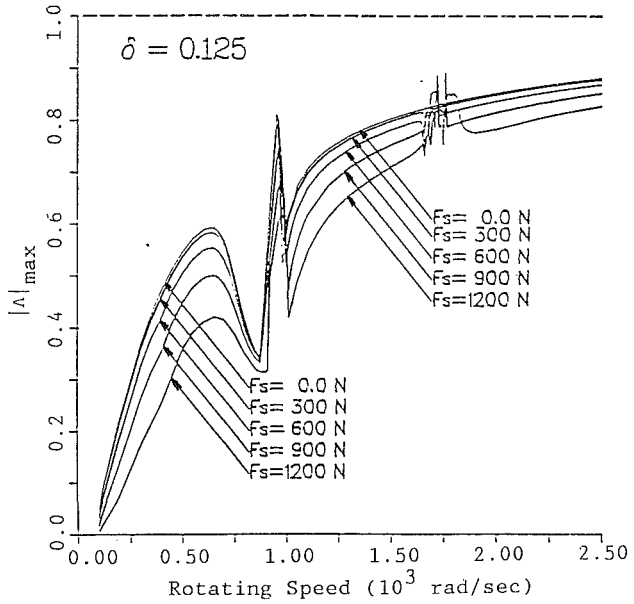

Fig. 7 Stability boundary of the response of Example 1 for $\delta = 0.125$

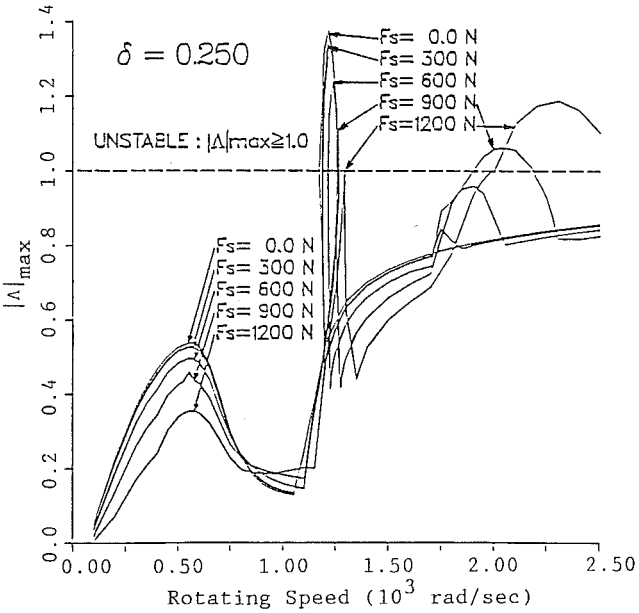

Fig. 8 Stability boundary of the response of Example 1 for $\delta = 0.250$

rad/s, there exists no stable synchronous motion. Using the numerical method proposed by Hwang and Shiau (1991) for solving the subharmonic whirl motions, one will obtain half-subharmonic whirl motion with a period of $T_{1/2} = 2T_1 = 2(2\pi/\Omega)$. A direct numerical integration of the equations of motion has also been applied to compare the results. Figures 10(*a*) and 10(*b*) show the transient behaviors of subharmonic whirl motion calculated by the integration with different initial conditions for the time history from $1T_{1/2}$ to $14T_{1/2}$ with $\Omega = 2000$ rad/s. Figure 10(*c*) shows the orbit of the consecutive five periods of time history from $15T_{1/2}$ to $19T_{1/2}$ for the case of Fig. 10(*a*) and it converges to a limit double-loop motion, which is very consistent with the solution shown in Fig. 10(*d*) by the trigonometric collocation method (TCM). The stability analysis shows $|\Lambda|_{max} = 0.750$. However, when the journal is rotating at a speed $\Omega = 2200$ rad/s, which is near the boundary between half-subharmonic whirl motion and synchronous motion, the behaviors will be significantly changed. Figures 11(*a*) and 11(*b*) show the transient behavior of subharmonic whirl motion obtained by the integration with different initial

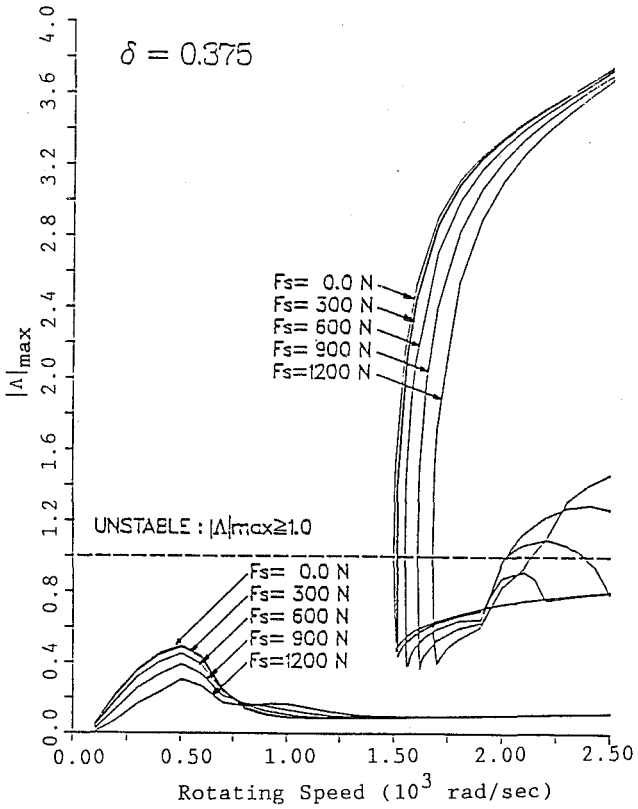

Fig. 9 Stability boundary of the response of Example 1 for $\delta = 0.375$

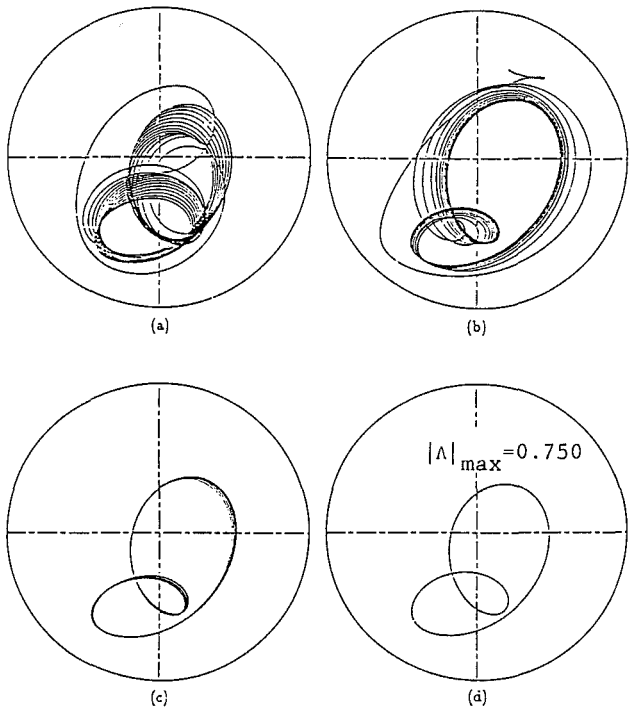

Fig. 10 Orbits of half-subharmonic whirl motion of Example 1 for $\delta = 0.250$, $F_s = 900$ N, and $\Omega = 2000.0$ rad/sec

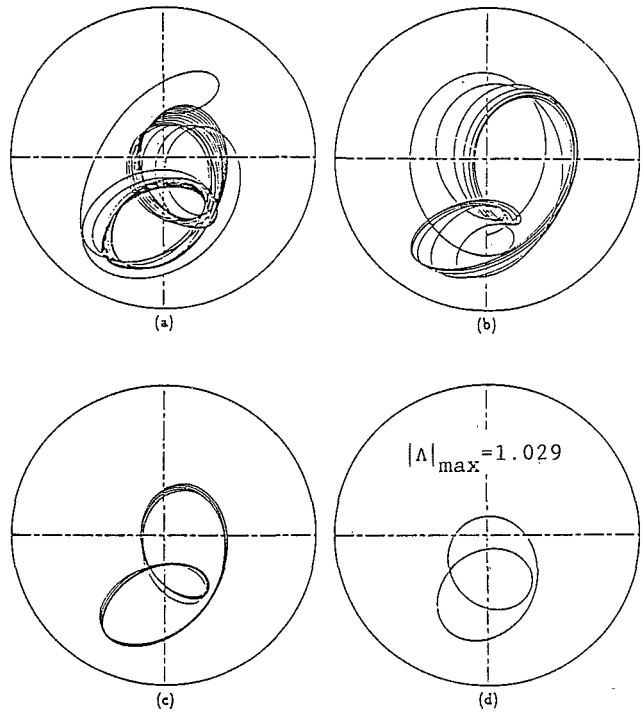

Fig. 11 Orbits of half-subharmonic whirl motion of Example 1 for $\delta = 0.250$, $F_s = 900$ N, and $\Omega = 2200.0$ rad/s

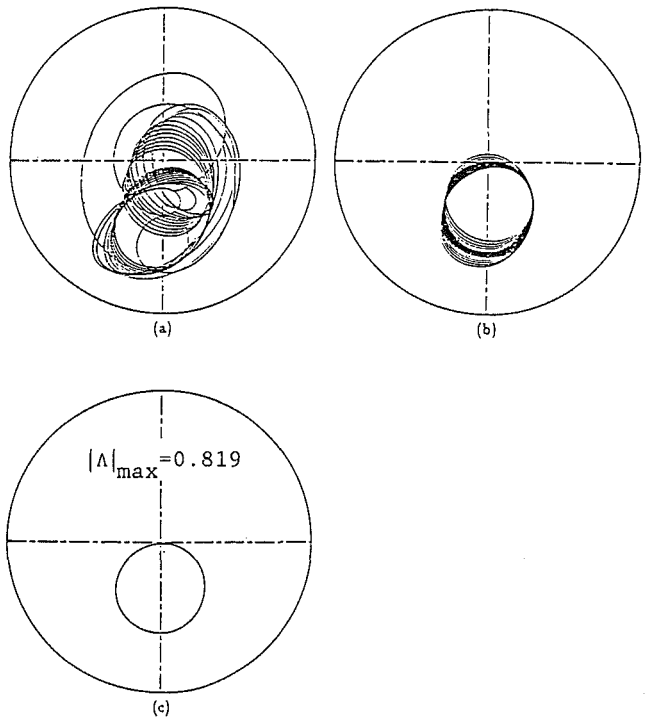

Fig. 12 Orbits of half-subharmonic whirl motion of Example 1 for $\delta = 0.250$, $F_s = 900$ N, and $\Omega = 2300.0$ rad/s

conditions for the time history from $1T_{1/2}$ to $14T_{1/2}$. Figure 11(*c*) shows the consecutive five periods of time history from $15T_{1/2}$ to $19T_{1/2}$ for the case of Fig. 11(*a*). The steady-state solution shown in Fig. 11(*d*) predicted by the TCM is of a maximum absolute eigenvalues of transition matrix, $|\Lambda|_{max} = 1.029$, which implies that the predicted steady-state half-subharmonic whirl motion is unstable. For the case of $\Omega = 2300$ rad/s, Fig. 12(*a*) shows the transient behavior for the time history from $1T_1$ to $28T_1$. Figure 12(*b*) shows the transient behaviors with time history after $28T_1$, and Fig. 12(*c*) shows the final solution. The final solution by integration shows very good agreement with the predicted solution by the TCM. It is stable because of $|\Omega|_{max} = 0.819$.

It is expected that the ultrasubharmonic whirl motion (i.e., 1/3-subharmonic, 1/4-subharmonic, . . . , etc.) will appear at the high rotating speed. The way of the determination of high-order subharmonic whirl motion is the same as that for half-

subharmonic whirl motion or synchronous motion case except that ω_1 is equal to Ω/n, $n = 3, 4, \ldots$.

Example 2. This example considers a flexible rotor system (Hwang and Shiau, 1991) shown in Fig. 13, which consists of rigid disks mounted at stations 1, 4, 5, and 12, and three linear isotropic supports located at stations 3, 6, and 13. Two squeeze-film dampers with centering spring are set at stations 3 and 13. The data of shaft and corresponding material properties are given in Table 1. The mass properties of rigid disks are listed in Table 2. The stiffness properties of the linear isotropic supports and the data of squeeze-film dampers are indicated in Table 3. The rigid disk at station 13 is of mass eccentricity 20.32 μm. In addition, the system is assumed to be horizontal so that the gravitational effect is considered as a side load distribution.

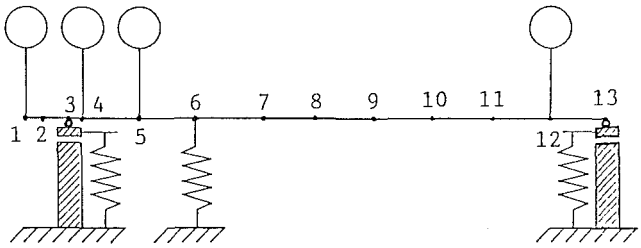

Fig. 13 Rotor model of Example 2

Table 1 Data of the shaft of Example 2

Station No.	Axial Distance to Station (cm)	Inner Radius (cm)	Outer Radius (cm)
1	0.0		
2	4.29		
3	8.89	1.42	
4	10.49		
5	20.17		
6	27.69	1.96	2.95
7	44.20		
8	59.44	2.69	
9	74.68		
10	89.92		
11	105.16	2.26	
12	120.14	1.42	
13	127.94	2.31	
$E = 20.69 \times 10^{10}\ N/m^2$, $\rho = 8193.0\ Kg/m^3$			

Table 2 Mass properties of fixed rigid disk of Example 2

Station No.	Mass (Kg)	Polar Inertia ($Kg \cdot cm^2 \times 10^{-2}$)	Transverse Inertia ($Kg \cdot cm^2 \times 10^{-2}$)
1	11.38	19.53	9.82
4	7.88	16.70	8.35
5	7.70	17.61	8.80
12	21.70	44.48	22.24

Using the modeling approach of the Generalized Polynomial Expansion Method (GPEM) and introducing the idea of component mode synthesis, a set of nonlinear differential equations (Hwang and Shiau, 1991), which govern the system motion, can be obtained. Moreover, the hybrid numerical method, which has the merits of both HBM and TCM, is used to solve for the nonlinear response. Figures 14 and 15 show the nondimensional semimajor axis versus rotating speed for the first and the second-harmonic motions associated with a constant offset relative to eccentricity for stations 3 and 13, respectively. It is also found that the magnitude of nondimensional semimajor axis for the third, fourth, and higher harmonic motions are smaller than 10^{-3}. Since the steady-state response is nearly a circular synchronous motion, the nonlinear squeeze-film forces can be approximated by using Eq. (8). It is indicated that the steady-state responses using Eq. (8) of dashed lines shown in Figs. 14 and 15 are in good agreement with that using Eq. (6), which is the model of noncircular motion. The maximum absolute eigenvalues of the transition matrix $[L(T)]$ are shown in Fig. 16. This indicates that the nonlinear steady-state responses obtained are stable equilibrium.

Discussion and Conclusion

To investigate the dynamic characteristics of a complicate nonlinear system, the direct numerical integration method may be the simplest way. However, it may be inefficient for solving the steady-state response. The methods such as TCM, HBM, and the hybrid numerical method described by Hwang and Shiau (1991) are of better efficiency to predict the steady-state solution. The stability of steady-state synchronous or subhar-

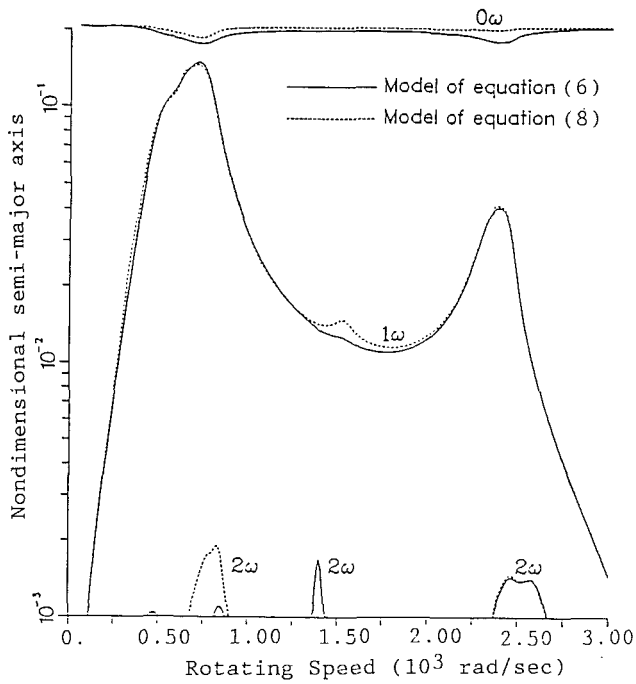

Fig. 14 Nondimensional semimajor axis versus rotating speed for the first and second harmonic at station 3 of Example 2

Table 3 Data of isotropic supports and squeeze-film dampers of Example 2

Station No.	Stiffness of Center Spring (N/m)	Damping of Center Spring (N· sec/m)	Radius of the Journal (mm)	Axial Width of Bearing (mm)	Radius Clearance of Bearing (μm)	Viscosity of Lubricant (N· sec/m^2)
3	0.44×10^7	0.0	50.8	25.4	152.4	1.5×10^{-2}
6	5.72×10^7	0.0	–	–	–	–
13	1.30×10^7	0.0	50.8	25.4	152.4	1.5×10^{-2}

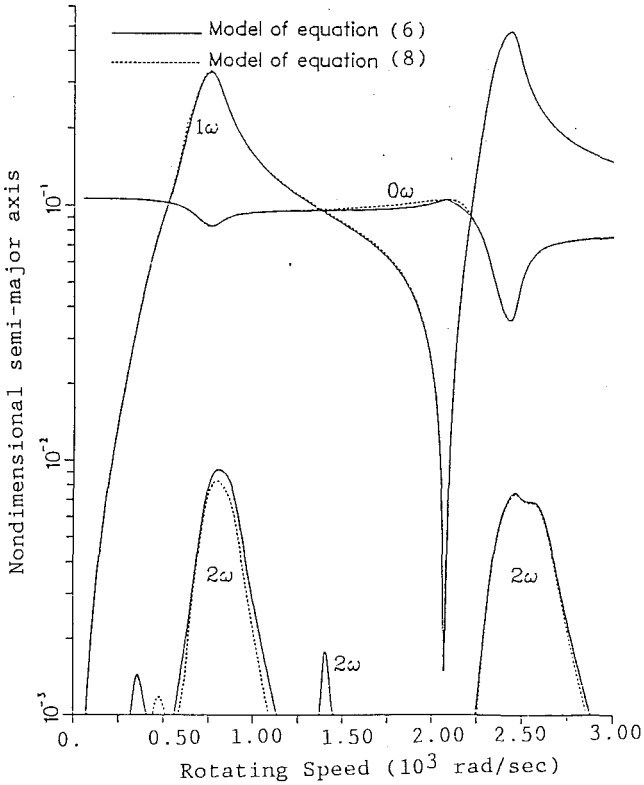

Fig. 15 Nondimensional semimajor axis versus rotating speed for the first and second harmonic at station 13 of Example 2

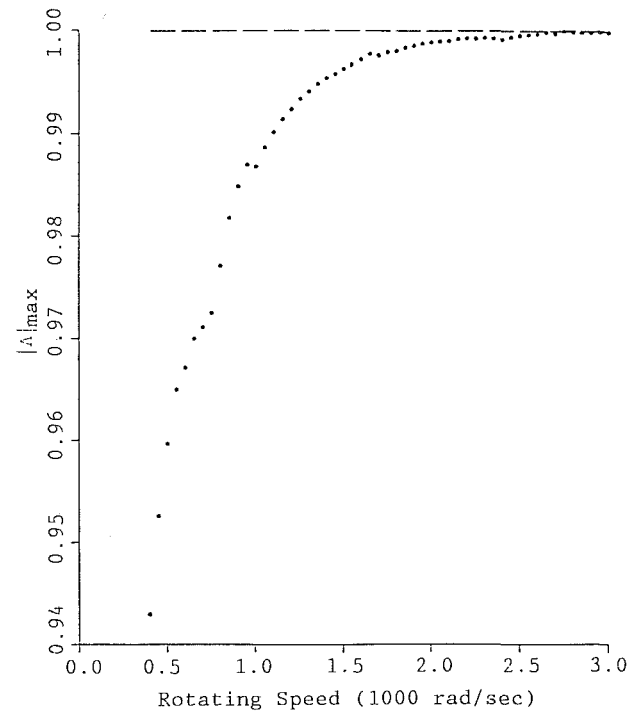

Fig. 16 Maximum absolute eigenvalues of Example 2

monic whirl motions is examined. The derivatives of the nonlinear hydrodynamic forces of a squeeze-film damper with respect to the displacement and velocity of journal center are expressed in closed forms, which are required in the stability analysis.

For the application of methods of TCM, HBM, and the hybrid numerical method, one needs an initial guess of motion for the successive iterations to obtain the steady-state response. If the solution of synchronous motion is assumed, the predicted solution can be found without difficulty. However, if the solution of subharmonic whirl motion is assumed, it requires more computational effort to obtain the predicted solution. It is noted that the motion usually converges first to the response of synchronous motion. To obtain the solution of subharmonic whirl motion, it is suggested to choose the initial value carefully or modify the iterative process. The transition matrix that governs the stability of the rotor bearing system can be determined numerically with desirable accuracy. If the efficiency is concerned, the analysis with component model truncation may be a better choice.

It should be noted that the superharmonic components of a periodic solution are also considered in the response analysis for both synchronous motion and subharmonic whirl motion, except for the centric circular synchronous motion. However, they are small compared to the component of fundamental frequency and negligible. Furthermore, the results conclude that a large unidirectional side load may cause unstable synchronous equilibrium response when the journal is of rotating speed twice the synchronous resonant speed. In this case, the half-subharmonic whirl motion will appear. For small unidirectional side load, the transient behavior will also be a half-subharmonic whirl motion when the journal is rotating at twice the synchronous resonant speed. However, the steady-state response is synchronous.

References

Athre, K., Kurian, J., Gupta, K. N., and Garg, R. D., 1982, "A Numerical Approach to the Stability of Rotor-Bearing Systems," ASME *Journal of Mechanical Design*, Vol. 104, pp. 356–363.

Botman, M., and Samaha, M. A., 1982, "Experiments on the Dynamic Behavior of a Supercritical Rotor," ASME *Journal of Mechanical Design*, Vol. 104, pp. 364–369.

Chen, W. J., 1987, "Optimal Design and Parameter Identification of Flexible Rotor-Bearing Systems," Ph.D. thesis, Arizona State University, Tempe, AZ.

Cookson, R. A., and Kossa, S. S., 1979, "The Effectiveness of Squeeze-Film Damper Bearings Supporting Rigid Rotors Without a Centralising Spring," *Int. J. Mech. Sci.*, Vol. 21, pp. 639–650.

Friedmann, P., Hammond, C. E., and Woo, T. H., 1977, "Efficient Numerical Treatment of Periodic Systems With Application to Stability Problem," *Int. Journal for Numerical Methods in Engineering*, Vol. 11, pp. 1117–1136.

Greenhill, L. M., and Nelson, H. D., 1982, "Iterative Determination of Squeeze Film Damper Eccentricity for Flexible Rotor Systems," ASME *Journal of Mechanical Design*, Vol. 104, pp. 334–338.

Gunter, E. J., Barrett, L. E., and Allaire, P. E., 1977, "Design of Nonlinear Squeeze-Film Dampers for Aircraft Engines," ASME *Journal of Lubrication Technology*, Vol. 99, pp. 57–64.

Hahn, E. J., 1979, "Stability and Unbalance Response of Centrally Preloaded Rotors Mounted in Journal and Squeeze Film Bearing," ASME *Journal of Lubrication Technology*, Vol. 101, pp. 120–128.

Hwang, J. L., and Shiau, T. N., 1991, "An Application of the Generalized Polynomial Expansion Method to Nonlinear Rotor Bearing Systems," ASME *Journal of Vibration and Acoustics*, Vol. 113, No. 3, pp. 299–308.

Jean, A. N., and Nelson, H. D., 1990, "Periodic Response Investigation of Large Order Nonlinear Rotordynamic Systems Using Collocation," *Journal of Sound and Vibration*, Vol. 143, No. 3, pp. 473–490.

Mohan, S., and Hahn, E. J., 1974, "Design of Squeeze Film Damper Supports for Rigid Rotors," ASME *Journal of Engineering for Industry*, Vol. 96, pp. 976–982.

Nataraj, C., and Nelson, H. D., 1989, "Periodic Solutions in Rotor Dynamic Systems With Nonlinear Supports: A General Approach," ASME *Journal of Vibration, Acoustics, Stress, and Reliability in Design*, Vol. 111, pp. 187–193.

Pan, C. H. T., and Tonnesen, J., 1978, "Eccentric Operation of the Squeeze-Film Damper," ASME *Journal of Lubrication Technology*, Vol. 100, pp. 369–378.

Rabinowitz, M. D., and Hahn, E. J., 1983, "Experimental Evaluation of Squeeze Film Supported Flexible Rotors," ASME JOURNAL OF ENGINEERING FOR POWER, Vol. 105, pp. 495–503.

Saito, S., 1985, "Calculation of Nonlinear Unbalance Response of Horizontal Jeffcott Rotors Supported by Ball Bearings With Radial Clearances," ASME *Journal of Vibration, Acoustics, Stress, and Reliability in Design*, Vol. 107, pp. 416–420.

Shiau, T. N., and Jean, A. N., 1990, "Prediction of Steady State Response of Flexible Rotor Systems With Nonlinear Supports: A New Technique," ASME *Journal of Vibration and Acoustics*, Vol. 112, pp. 501–507.

Taylor, D. L., and Kumar, B. R. K., 1980, "Nonlinear Response of Short Squeeze Film Dampers," ASME *Journal of Lubrication Technology*, Vol. 102, pp. 51–58.

Development of a Set of Equations for Incorporating Disk Flexibility Effects in Rotordynamic Analyses

G. T. Flowers
Assistant Professor,
Department of Mechanical Engineering,
Auburn University,
Auburn University, AL 36849-5341

S. G. Ryan
Aerospace Engineer,
Marshall Space Flight Center,
MSFC, AL 35812

Rotordynamic equations that account for disk flexibility are developed. These equations employ free–free rotor modes to model the rotor system. Only transverse vibrations of the disks are considered, with the shaft/disk system considered to be torsionally rigid. Second-order elastic foreshortening effects that couple with the rotor speed to produce first-order terms in the equations of motion are included. The approach developed in this study is readily adaptable for usage in many of the codes that are currently used in rotordynamic simulations. The equations are similar to those used in standard rigid disk analyses but with additional terms that include the effects of disk flexibility. An example case is presented to demonstrate the use of the equations and to show the influence of disk flexibility on the rotor dynamic behavior of a sample system.

Introduction

Modern turbomachinery is used to provide power for a wide range of applications, from steam turbines for electrical power plants to the turbopumps used in the Space Shuttle Main Engine. Such devices are subject to a variety of dynamic problems, including vibration, rotordynamic instability, and shaft whirl. In order to design and evaluate the performance and stability of turbomachinery properly, it is important that appropriate analytical tools be available that will allow for the study of potentially important dynamical effects.

In the modeling of any physical device or process, certain assumptions and restrictions must be made. It is important to assess the validity of such assumptions carefully in order to determine the accuracy and range of applicability of the mathematical model. Rotordynamic analyses are typically performed using models with rigid disks and blades. Studies of rotor models in which the effects of disk flexibility have been included indicate that it may be an important effect for many systems.

The usual procedure for rotordynamic analysis of turbomachinery with complex geometry consists of coupling the free–free rotor and housing modes, obtained through finite element analyses, with constraints to produce a model for the complete turbomachine. This model is then used in stability analyses and for time response simulations. It is considered standard practice in obtaining the free–free rotor modes to neglect disk flexibility. If rotor disk flexibility is an important effect on the free–free rotor modes, significant errors could be introduced into rotor dynamic analyses.

This work presents a technique that incorporates the disk flexibility effects into a modal formulation of a rotordynamic model. Rotordynamic equations are developed that include the effects of rotor disk flexibility. These equations rely on a modal formulation for the rotor shaft and disks (using the free–free modes of the rotor) and are generally applicable to any rotor system. The assumptions and approximations used in the development are presented and discussed. An example case is presented to demonstrate use of the equations developed in this study and to show the influence of disk flexibility on the rotordynamic behavior of a sample system.

Background

There is a large body of research that is available on the dynamic behavior of rotating flexible bodies. The following is not meant to be an exhaustive review of previous work but a discussion of the works that most influenced the current effort.

A classic work by Lamb and Southwell (1921) presented a discussion of the vibrational behavior of a free spinning disk. This work served as the basis for much further work in this area. Southwell (1922) extended this study to examine the vibrational behavior of a spinning disk clamped at its center. Pringle (1969) presented a method for examining the dynamic behavior of a system with connected moving parts. Likins (1974) performed a study of mathematical modeling of spinning elastic bodies for use in modal analyses. Laurenson (1976) discussed methods for performing modal analysis on rotating flexible structures. Meirovitch (1976) presented an analytical study of discretization methods for flexible gyroscopic systems and drew conclusions concerning the appropriateness of various techniques.

There is also a fairly large body of work documented in the literature concerning studies of disk flexibility on rotors and turbomachinery. Klompas (1974) developed a technique for

Contributed by the International Gas Turbine Institute and presented at the 36th International Gas Turbine and Aeroengine Congress and Exposition, Orlando, Florida, June 3–6, 1991. Manuscript received at ASME Headquarters February 12, 1991. Paper No. 91-GT-75. Associate Technical Editor: L. A. Riekert.

studying shaft whirling, which included the effects of flexible disks and blades. Klompas (1983) extended his work by including the effects of disk flexibility in a study of the unbalance response of a turbomachine. This work was primarily aimed at investigating the effects of blade loss. Chivens and Nelson (1975) studied a continuous flexible rotor shaft carrying a continuous flexible plate with a rigid core. They developed the associated governing partial differential equations and presented a number of parameter variation studies. They concluded that, for a rotor with asymmetric supports, disk flexibility is likely to have little effect on critical speeds but may have a significant influence on natural frequencies. Dopkin and Shoup (1974) performed a study of the effects of disk flexibility on the resonant frequencies of an axisymmetric rotating shaft. They found that the effects of disk flexibility may significantly reduce the rotor resonant speeds and that this effect was particularly pronounced at low rotor speeds. Wilgen and Schlack (1977) investigated the effects of disk flexibility on shaft whirl stability using Liapunov techniques. Palladine and Rosettos (1982) developed a finite element method for examining the effects of flexibility on the behavior of a rotor. Sakata et al. (1983) studied the transient vibration behavior of a rotor subjected to a blade loss and included the effects of disk flexibility. Shahab and Thomas (1987) studied finite element models of single and multidisk rotor systems and compared the results to experimental models. This study indicated that coupling effects between the shaft and disk modes can have a significant effect on the dynamical behavior of a rotor. Vance (1988) studied several rotor systems, performing a combined experimental-analytical investigation. His analytical model was configured so that the effects of disk attachment flexibility could be accounted for in an approximate fashion. These studies indicated that, for many cases, the inclusion of rotor disk attachment flexibility could significantly improve the correlation between experimentally measured rotor free-free natural frequencies and calculated values.

Most of these studies have concentrated on qualitative investigations of disk and blade flexibility effects. In many cases, the rotor models used are not readily adaptable to the complicated geometric configurations that are characteristic of practical rotor systems. One of the most direct methods of addressing the modeling issues that arise due to complex rotor geometry is to formulate equations of motion in terms of generalized coordinates using the mode shapes of the nonspinning rotor. Ryan (1989) has developed a rotordynamic analysis package currently used by NASA for study of the SSME turbopumps. The analysis procedure requires the formulation of the rotor model in terms of its free-free mode shapes and frequencies. Rotor disk flexibility is not currently accounted for in this analysis. A finite element study conducted by Flowers (1990) indicated that disk flexibility may significantly affect the free-free rotor modes and frequencies for the SSME high-pressure turbopumps. This implies that significant errors could be introduced into the rotor dynamic analysis by neglecting disk flexibility effects. So, it is important to develop means of accounting for them in the analysis procedures. This study presents a set of rotordynamic equations that account for disk flexibility effects and that can be readily incorporated into a modal-based rotor dynamic analysis program.

Derivation of Equations

The equations of motion will be derived in a very direct manner. The rotor will be modeled as consisting of a series of k_d disks joined by elastic interconnections. All rotor disks are assumed to have equal hub axial displacements and the combined system is assumed to be torsionally rigid. Axial coupling effects between the rotor and flexible disks are neglected. First, the position of an arbitrary point on the ith, rotor disk will be developed in terms of specified variables that describe the rigid body motion (translation and rotation) and the elastic flexing of the point. The rotation sequence for the rigid body rotation of the ith disk is shown below (refer to Fig. 1):

$\theta_{y,i}$ about y

$\theta_{z,i}$ about z'

Ωt about $\bar{x}$

Using this rotation sequence, a position vector for an arbitrary point (the jth) on the ith rotor disk is formed:

$$\mathbf{P}_{i,j} = P_{x,i,j}\hat{x} + P_{y,i,j}\hat{y} + P_{z,i,j}\hat{z} \tag{1}$$

where

$$P_{x,i,j} = h_{i,j} + X_i + u_{i,j} - r\cos(\nu_{i,j} + \Omega t)\sin(\theta_{z,i}) + r_{i,j}\sin(\nu_{i,j} + \Omega t)\sin(\theta_{y,i})$$

$$P_{y,i,j} = Y_i + h_{i,j}\sin(\theta_{z,i}) + r_{i,j}\cos(\nu_{i,j} + \Omega t)\cos(\theta_{z,i}) + u_{i,j}\sin(\theta_{z,i}) + v_{i,j}\cos\Omega t - w_{i,j}\sin\Omega t$$

$$P_{z,i,j} = Z_i + r_{i,j}\sin(\nu_{i,j} + \Omega t)\cos(\theta_{y,i}) - h_{i,j}\cos(\theta_{z,i})\sin(\theta_{y,i}) - u_{i,j}\sin(\theta_{y,i}) + w_{i,j}\cos\Omega t + v_{i,j}\sin\Omega t + r_{i,j}\cos(\nu_{i,j} + \Omega t)\sin(\theta_{y,i})\sin(\theta_{z,i})$$

Nomenclature

$dm_{i,j}$ = mass associated with point (i, j)
$h_{i,j}$ = axial distance of point (i, j) from center of disk
I_a^i = polar mass moment of inertia for ith disk
i = disk index
j = point index for each disk
k, l = mode number indices
k_d = number of rotor disks
M_i = number of points on ith disk
n = number of rotor modes
$q_{y,k}, q_{z,k}$ = kth generalized coordinate in inertial coordinate system
$P_{x,i,j}, P_{y,i,j}, P_{z,i,j}$ = displacement components for jth point on ith rotor disk in terms of generalized coordinates
$r_{i,j}$ = radial coordinate of point (i, j)
$u_{i,j}, v_{i,j}, w_{i,j}$ = elastic deflections of point (i, j)
X_i, Y_i, Z_i = translational coordinates for hub of ith disk
$\Gamma_{k,l} = \sum_{i=1}^{k_d} I_a^i \Psi_i^k \Psi_i^l$
$\epsilon_{i,j}^y, \epsilon_{i,j}^z$ = second-order displacements of point (i, j) in the y and z directions
$\Lambda_{y,i,j}^k, \Lambda_{z,i,j}^k, \Delta_{i,j}^k, \delta_{i,j}^k$ = kth mode shapes for displacements of point (i, j)
$\nu_{i,j}$ = angular coordinate of point (i, j)
$\xi_{y,k}, \xi_{z,k}$ = kth generalized coordinate in rotating coordinate system
Ψ_i^k, Φ_i^k = kth mode shapes for hub displacements of ith disk
Ω = rotor speed
Ω_o = nominal rotor speed
ω_n = natural frequency

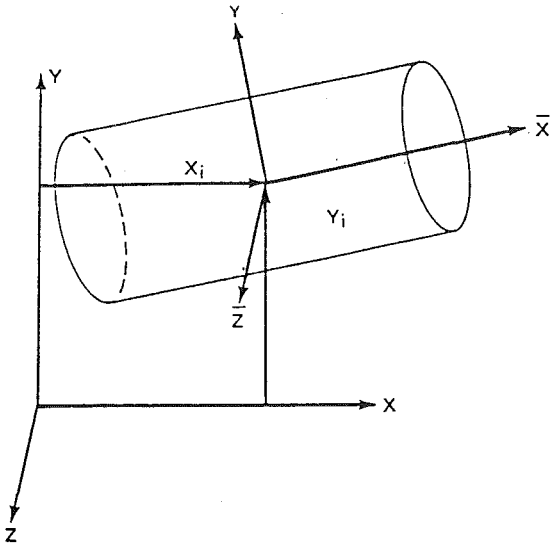

Fig. 1(*a*) *i*th disk hub translation coordinates

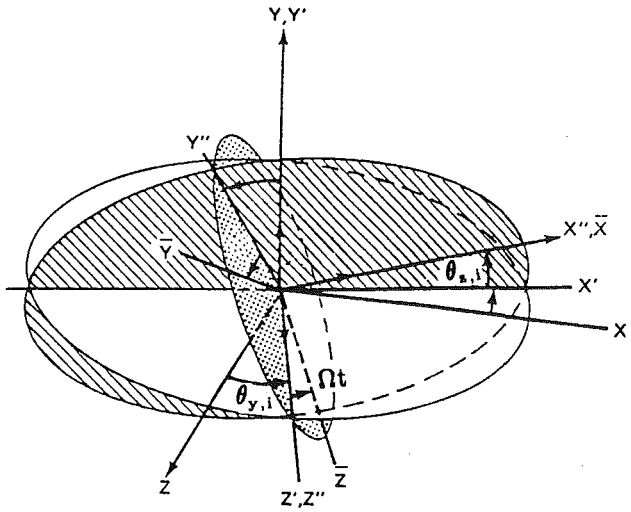

Fig. 1(*b*) *i*th disk hub rotation coordinates

Ordering Scheme. The above expressions are valid for displacements of any arbitrary amplitude. The linearized equations of motion that are the object of this discussion are expressed in terms of generalized coordinates using the free-free mode shapes of the complete rotor. In working toward this result, it becomes necessary to impose an appropriate ordering scheme on the variables used in this development. $\theta_{y,i}$, $\theta_{z,i}$, $u_{i,j}$, $v_{i,j}$, $w_{i,j}$, X_i, Y_i, and Z_i will be taken as first order or "small" quantities for the purpose of this derivation.

Foreshortening Effects. Certain second-order terms in the displacement and velocity expressions will couple with the spinning of the disk to produce first-order terms in the final equations of motion. Notice that such a result is due to the zeroth-order nature of the spin rate and the distance from the center of rotation. In order to develop a correctly linearized set of differential equations, it is necessary to account for such terms adequately. Those second-order terms associated with the rigid body motion of the disk will arise naturally as the position vector is simplified to retain only zeroth, first, and second-order terms. In addition, second-order terms will arise due to flexing of the rotor disk, a phenomenon often referred to as foreshortening. Since linear displacement mode shapes are used in this formulation, second-order displacement effects are not accounted for in the modal transformation.

There have been a number of investigations of foreshortening and related effects in recent years. In addition, there has been considerable debate as to the appropriate manner for including such terms in equation formulations. Some of the work that has been examined in the course of this study is presented by Hodges (1984), Banerjee and Kane (1987), Lips (1987), Banerjee and Dickens (1989), Yoo et al. (1989), London (1989), and Banerjee and Kane (1989a, 1989b).

The magnitude of the foreshortening terms is dependent on the nonlinear deflection of a point on the rotor disk and is, thus, highly dependent on assumptions made about the material behavior. For the purposes of this development, a simplified approach to quantifying the foreshortening effects will be used. It is based upon the following assumptions:

1 Disk material is linearly elastic.

2 The length of a line in the undeformed disk stretches in accordance with the deflection mode shape of that line (only linear stretching).

3 A line in the disk is inextensible due to loading of the disk orthogonal to that line.

The desired foreshortening terms are second-order displacement components for a point. Let $(x^*_{i,j}, y^*_{i,j}, z^*_{i,j})$ be the Cartesian coordinates describing the location after deformation of the disk of point (i, j), located at $(x_{i,j}, y_{i,j}, z_{i,j})$ before deformation of the disk. Examination of Eq. (1) demonstrates that $P_{x,i,j}$ has no zeroth-order terms that are time-varying. Therefore, second-order displacement effects in the axial direction will not couple with zeroth-order terms to produce first-order terms in the linearized equations of motion. So, $x^*_{i,j}$ will not be considered further in this discussion.

Based on the assumptions listed above and in accordance with techniques described by Banerjee and Kane (1989b), it follows that

$$y^*_{i,j} \approx y_{i,j} + v_{i,j} - \frac{1}{2}\int_0^{y_{i,j}} \left(\left(\frac{\delta u}{\delta y}\right)^2 + \left(\frac{\delta w}{\delta y}\right)^2\right) dy \qquad (2a)$$

$$z^*_{i,j} \approx z_{i,j} + w_{i,j} - \frac{1}{2}\int_0^{z_{i,j}} \left(\left(\frac{\delta u}{\delta z}\right)^2 + \left(\frac{\delta v}{\delta z}\right)^2\right) dz \qquad (2b)$$

Therefore, the desired second-order correction terms are

$$\epsilon^y_{i,j} \approx -\frac{1}{2}\int_0^{y_{i,j}} \left(\left(\frac{\delta u}{\delta y}\right)^2 + \left(\frac{\delta w}{\delta y}\right)^2\right) dy \qquad (3a)$$

$$\epsilon^z_{i,j} \approx -\frac{1}{2}\int_0^{z_{i,j}} \left(\left(\frac{\delta u}{\delta z}\right)^2 + \left(\frac{\delta v}{\delta z}\right)^2\right) dz \qquad (3b)$$

Simplified Position Vector. The simplified position vector that results from retaining appropriate zeroth, first, and second-order terms has the following components:

$$P_{x,i,j} = X_i + h_{i,j} + u_{i,j} - r_{i,j}\cos(\nu_{i,j} + \Omega t)\theta_{z,i} + r_{i,j}\sin(\nu_{i,j} + \Omega t)\theta_{y,i} \qquad (4a)$$

$$P_{y,i,j} = Y_i + h_{i,j}\theta_{z,i} + r_{i,j}\left(1 - \frac{\theta^2_{z,i}}{2}\right)\cos(\nu_{i,j} + \Omega t) + u_{i,j}\theta_{z,i} + v_{i,j}\cos\Omega t - w_{i,j}\sin\Omega t + \epsilon^y_{i,j}\cos\Omega t - \epsilon^z_{i,j}\sin\Omega t \qquad (4b)$$

$$P_{z,i,j} = Z_i - h_{i,j}\theta_{y,i} + r_{i,j}\left(1 - \frac{\theta^2_{y,i}}{2}\right)\sin(\nu_{i,j} + \Omega t) + r_{i,j}\cos(\nu_{i,j} + \Omega t)\theta_{y,i}\theta_{z,i} - u_{i,j}\theta_{y,i} + w_{i,j}\cos\Omega t + v_{i,j}\sin\Omega t + \epsilon^z_{i,j}\cos\Omega t + \epsilon^y_{i,j}\sin\Omega t \qquad (4c)$$

Velocity Vector. The position vector of Eq. (4) can now be differentiated to produce the following velocity vector:

$$\mathbf{V}_{i,j} = V_{x,i,j}\hat{x} + V_{y,i,j}\hat{y} + V_{z,i,j}\hat{z} \qquad (5)$$

where

$$V_{x,i,j}=\dot{P}_{x,i,j}$$

$$V_{y,i,j}=\dot{P}_{y,i,j}$$

$$V_{z,i,j}=\dot{P}_{z,i,j}$$

Kinetic Energy. The kinetic energy of the ith disk can be formulated as

$$T_i=\frac{1}{2}\sum_{j=1}^{M_i}(V_{x,i,j}^2+V_{y,i,j}^2+V_{z,i,j}^2)dm_{i,j} \tag{6}$$

The total kinetic energy of the rotor is then

$$T=\sum_{i=1}^{k_d}T_i \tag{7}$$

Free-Free Mode Shapes. The free-free rotor mode shapes will be used in this development to express the kinetic and potential energy in terms of generalized coordinates. These mode shapes are determined for a nonrotating structure and thus serve to describe the deflections in terms of a coordinate system that rotates with the spinning disk. The angular coordinates, $\theta_{y,i}$ and $\theta_{z,i}$, describing the rigid motion of a disk hub are expressed in terms of reference frames that are not spinning with the disk. In order to use the free-free rotor mode shapes appropriately to transform the equation set, it is necessary to transform the generalized coordinates from the rotating reference frame to the inertial reference frame. The free-free mode shapes and the required transformations can be expressed in the following manner.

First, examine a (linearized) displacement vector describing the motion of a point (i, j) on a nonspinning rotor disk.

$$\tilde{\mathbf{P}}_{i,j}=\tilde{P}_{x,i,j}\hat{x}+\tilde{P}_{y,i,j}\hat{y}+\tilde{P}_{z,i,j}\hat{z} \tag{8}$$

where

$$\tilde{P}_{x,i,j}=X_i-r_{i,j}\cos(\nu_{i,j})\theta_{z,i}^{nr}+r_{i,j}\sin(\nu_{i,j})\theta_{y,i}^{nr}+u_{i,j} \tag{9a}$$

$$\tilde{P}_{y,i,j}=Y_i+h_{i,j}\theta_{z,i}^{nr}+v_{i,j} \tag{9b}$$

$$\tilde{P}_{z,i,j}=Z_i-h_{i,j}\theta_{y,i}^{nr}+w_{i,j} \tag{9c}$$

where $\theta_{y,i}^{nr}$ and $\theta_{z,i}^{nr}$ represent $\theta_{y,i}$ and $\theta_{z,i}$ for zero rotor speed.

In terms of the mode shapes, the above components can be expressed in the following manner:

$$\tilde{P}_{x,i,j}=\overline{X}_i+\sum_{k=1}^{n}\Lambda_{y,i,j}^{k}\xi_{y,k}+\sum_{k=1}^{n}\Lambda_{z,i,j}^{k}\xi_{z,k} \tag{10a}$$

$$\tilde{P}_{y,i,j}=\sum_{k=1}^{n}\Delta_{i,j}^{k}\xi_{y,k}+\sum_{k=1}^{n}\delta_{i,j}^{k}\xi_{z,k} \tag{10b}$$

$$\tilde{P}_{z,i,j}=\sum_{k=1}^{n}\Delta_{i,j}^{k}\xi_{z,k}+\sum_{k=1}^{n}\delta_{i,j}^{k}\xi_{z,k} \tag{10c}$$

The generalized coordinates that will be used in the final equations, $q_{z,k}$ and $q_{y,k}$, are related to an inertial reference frame. The generalized coordinates used in the above relations, $\xi_{z,k}$ and $\xi_{y,k}$, are related to a disk-based coordinate system. The following transformation relates the two sets of generalized coordinates:

$$\xi_{y,k}=\cos(\Omega t)q_{y,k}+\sin(\Omega t)q_{z,k} \tag{11a}$$

$$\xi_{z,k}=\cos(\Omega t)q_{z,k}-\sin(\Omega t)q_{y,k} \tag{11b}$$

For the case of an axisymmetric rotor, a restriction that will be imposed on the analysis for the remainder of this development, the following relations hold. The rigid body rotations and translations of the disks (expressed in an inertial reference frame) are transformed in terms of the generalized coordinates as

$$\theta_{y,i}=-\sum_{k=1}^{n}\Psi_i^k q_{z,k} \tag{12a}$$

$$\theta_{z,i}=\sum_{k=1}^{n}\Psi_i^k q_{y,k} \tag{12b}$$

$$Y_i=\sum_{k=1}^{n}\Phi_i^k q_{y,k} \tag{12c}$$

$$Z_i=\sum_{k=1}^{n}\Phi_i^k q_{z,k} \tag{12d}$$

$$X_i=\overline{X} \tag{12e}$$

The following relations are very useful in simplifying the kinetic energy expression:

$$\sum_{j=1}^{M_i}r_{i,j}\cos(\nu_{i,j})\Lambda_{z,i,j}^{k}dm_{i,j}=0 \tag{13a}$$

$$\sum_{j=1}^{M_i}r_{i,j}\sin(\nu_{i,j})\Lambda_{y,i,j}^{k}dm_{i,j}=0 \tag{13b}$$

$$\sum_{j=1}^{M_i}\Lambda_{y,i,j}^{k}\Lambda_{y,i,j}^{l}dm_{i,j}=\sum_{j=1}^{M_i}\Lambda_{z,i,j}^{k}\Lambda_{z,i,j}^{l}dm_{i,j} \tag{13c}$$

$$\sum_{j=1}^{M_i}\Lambda_{z,i,j}^{k}\Lambda_{y,i,j}^{l}dm_{i,j}=0 \tag{13d}$$

$$\sum_{j=1}^{M_i}\Delta_{i,j}^{k}\delta_{i,j}^{l}dm_{i,j}=0 \tag{13e}$$

$$\sum_{j=1}^{M_i}r_{i,j}\cos(\nu_{i,j})\Delta_{i,j}^{k}dm_{i,j}=0 \tag{13f}$$

$$\sum_{j=1}^{M_i}r_{i,j}\sin(\nu_{i,j})\Delta_{i,j}^{k}dm_{i,j}=0 \tag{13g}$$

$$\sum_{j=1}^{M_i}r_{i,j}\cos(\nu_{i,j})\delta_{i,j}^{k}dm_{i,j}=0 \tag{13h}$$

$$\sum_{j=1}^{M_i}r_{i,j}\sin(\nu_{i,j})\delta_{i,j}^{k}dm_{i,j}=0 \tag{13i}$$

Using the above modal relationships and examining the linearized displacement relations for zero rotor speed, the elastic displacement of the point (i, j) are expressed as

$$u_{i,j}=\tilde{P}_{x,i,j}-X_i-\sum_{k=1}^{n}r_{i,j}\sin(\nu_{i,j})\Psi_{i,j}^{k}\xi_{y,k}-\sum_{k=1}^{n}r_{i,j}\cos(\nu_{i,j})\Psi_{i,j}^{k}\xi_{z,k}$$
$$\equiv\sum_{k=1}^{n}\beta_{y,i,j}^{k}\xi_{y,k}+\sum_{k=1}^{n}\beta_{z,i,j}^{k}\xi_{z,k} \tag{14a}$$

$$v_{i,j}=\tilde{P}_{y,i,j}-\sum_{k=1}^{n}h_{i,j}\Psi_{i,j}^{k}\xi_{z,k}\equiv\sum_{k=1}^{n}\tau_{i,j}^{k}\xi_{y,k}+\sum_{k=1}^{n}\kappa_{i,j}^{k}\xi_{z,k} \tag{14b}$$

$$w_{i,j}=\tilde{P}_{z,i,j}-\sum_{k=1}^{n}h_{i,j}\Psi_{i,j}^{k}\xi_{y,k}\equiv\sum_{k=1}^{n}\tau_{i,j}^{k}\xi_{z,k}+\sum_{k=1}^{n}\kappa_{i,j}^{k}\xi_{y,k} \tag{14c}$$

Substitution of the appropriate relations expressed in terms of the generalized coordinates, and simplification based on the relations of Eq. (20), yields the following expression for the kinetic energy of the rotor:

$$T=\frac{1}{2}(M\ddot{\overline{X}}+\{\dot{q}_y\})^T\{\dot{q}_y\}+\{\dot{q}_z\}^T\{\dot{q}_z\})$$
$$-\Omega\{q_{y,k}\}[\Gamma+A+C]\{\dot{q}_z\}+\Omega\{q_{z,k}\}[A-C]\{\dot{q}_y\}$$
$$-\Omega^2\{q_y\}[B]\{q_y\}-\Omega^2\{q_{z,k}\}[B]\{q_{z,k}\} \tag{15}$$

where

$$A_{k,l}=\sum_{i=1}^{k_d}\sum_{j=1}^{M_i}\Lambda_{i,j}^{k}\Lambda_{i,j}^{l}dm_{i,j}+2\sum_{i=1}^{k_d}\sum_{j=1}^{M_i}\delta_{i,j}^{k}\delta_{i,j}^{l}dm_{i,j} \tag{16a}$$

$$B_{k,l}=D_{k,l}-\sum_{i=1}^{k_d}\sum_{j=1}^{M_i}\Lambda_{y,i,j}^{k}\Lambda_{y,i,j}^{l}dm_{i,j}-4\sum_{i=1}^{k_d}\sum_{j=1}^{M_i}\delta_{i,j}^{k}\delta_{i,j}^{l}dm_{i,j} \tag{16b}$$

$$C_{k,l}=\frac{1}{2}\sum_{i=1}^{k_d}\Psi_i^k\Psi_i^l I_a^i \tag{16c}$$

$$\begin{aligned}D_{k,l}&=\sum_{i=1}^{k_d}\sum_{j=1}^{m_i}\int_{y=0}^{y_{i,j}}\left(y_{i,j}\frac{\delta\beta_{y,i,j}^{k}}{\delta y}\frac{\delta\beta_{y,i,j}^{l}}{\delta y}\,dm_{i,j}dy\right)\\&\quad+\sum_{i=1}^{k_d}\sum_{j=1}^{m_i}\int_{y=0}^{y_{i,j}}\left(\left(y_{i,j}\frac{\delta\tau_{i,j}^{l}}{\delta y}\frac{\delta\tau_{i,j}^{k}}{\delta y}+y_{i,j}\frac{\delta\kappa_{i,j}^{l}}{\delta y}\frac{\delta\kappa_{i,j}^{k}}{\delta y}\right)dm_{i,j}\right)dy\\&=\sum_{i=1}^{k_d}\sum_{j=1}^{m_i}\int_{z=0}^{z_{i,j}}\left(z_{i,j}\frac{\delta\beta_{z,i,j}^{k}}{\delta z}\frac{\delta\beta_{z,i,j}^{l}}{\delta z}\,dm_{i,j}dz\right)\\&\quad+\sum_{i=1}^{k_d}\sum_{j=1}^{m_i}\int_{z=0}^{y_{i,j}}\left(\left(z_{i,j}\frac{\delta\tau_{i,j}^{l}}{\delta z}\frac{\delta\tau_{i,j}^{k}}{\delta z}+z_{i,j}\frac{\delta\kappa_{i,j}^{l}}{\delta z}\frac{\delta\kappa_{i,j}^{k}}{\delta z}\right)dm_{i,j}\right)dz\end{aligned} \tag{16d}$$

$$\{q_y\}\equiv\begin{pmatrix}q_{y,1}\\ \cdot\\ \cdot\\ q_{y,k}\\ \cdot\\ \cdot\\ q_{y,n}\end{pmatrix}$$

$$\{q_z\}\equiv\begin{pmatrix}q_{z,1}\\ \cdot\\ \cdot\\ q_{z,k}\\ \cdot\\ \cdot\\ q_{z,n}\end{pmatrix}$$

$\Gamma_{k,l}$, $A_{k,l}$, $B_{k,l}$, $C_{k,l}$, and $D_{k,l}$ are the (k, l) elements for matrices Γ, A, B, C, and D, respectively. $dm_{i,j}$ represents the mass associated with the jth point on the ith disk.

Potential Energy. If the material of the rotor and disks is linear and the modes are properly scaled, the potential energy of the rotor system can be represented in the following form:

$$[V]\equiv\frac{1}{2}\begin{pmatrix}q_y & q_z\end{pmatrix}\begin{pmatrix}[\omega_n^2] & 0\\ 0 & [\omega_n^2]\end{pmatrix}\begin{pmatrix}q_y\\ q_z\end{pmatrix} \tag{17}$$

where

$$[\omega_n^2]\equiv\begin{pmatrix}\omega_{n1}^2 & 0 & \cdot & \cdot & \cdot & 0\\ 0 & \omega_{n2}^2 & \cdot & \cdot & \cdot & 0\\ \cdot & \cdot & \cdot & \cdot & \cdot & \cdot\\ \cdot & \cdot & \cdot & \cdot & \cdot & \cdot\\ 0 & 0 & \cdot & \cdot & \cdot & \omega_{n2}^2\end{pmatrix}$$

and $[\omega_n^2]$ represents the squared natural frequencies of the flexible rotor–flexible disk.

Equations of Motion. The Lagrangian associated with the above system can now be formed as

$$L=T-V \tag{18}$$

The equations of motion can then be formulated using the standard Lagrange equations method. The flexible shaft–flexible disk equations that result are

$$\{\ddot{q}_y\}+\Omega[\Gamma+2A]\{\dot{q}_z\}+[\omega_n^2+\Omega^2B]\{q_y\}=\{\text{interconnection coupling and damping terms}\} \tag{19a}$$

$$\{\ddot{q}_z\}-\Omega[\Gamma+2A]\{\dot{q}_y\}+[\omega_n^2+\Omega^2B]\{q_z\}=\{\text{interconnection coupling and damping terms}\} \tag{19b}$$

where A and B are as previously defined.

For brevity, the interconnection coupling and damping terms account for all dynamic effects acting on the rotor except those explicitly mentioned, including seal forces, bearing forces, and fluid interaction forces.

The rotor equations for the comparable rigid disk system are

$$\ddot{q}_y+\Omega[\Gamma]\{\dot{q}_z\}+[\omega_n^2]\{q_y\}=\{\text{interconnection coupling and damping terms}\} \tag{20a}$$

$$\ddot{q}_z-\Omega[\Gamma]\{\dot{q}_y\}+[\omega_n^2]\{q_z\}=\{\text{interconnection coupling and damping terms}\} \tag{20b}$$

where the respective matrices have been formed using the free–free mode shapes and frequencies obtained from a finite element rotor model in which the disks have been treated as rigid structures.

Example Case

In order to demonstrate the usage of the equations that have been developed in this study, an example case will be investigated. The natural frequencies and critical speeds for equivalent rotor models with and without disk flexibility effects will be presented. The rotor models that will be used for the purposes of this example are for the Space Shuttle Main Engine (SSME) High-Pressure Oxygen Turbopump (HPOTP). The two models are discussed in some detail by Flowers (1990) and are referred to as the "flexible disk rotor model" and the "rigid disk rotor model," respectively.

The rotor models were coded into finite element models and the free–free mode shapes and frequencies calculated. These data were then used to construct the respective matrices in Eqs. (19) and (20). The resulting linear differential equations were coded into a FORTRAN computer program to solve for the system eigenvalues. Bearing stiffness was the only constraint used in this study. A value of 4.0×10^5 lb/in. (2.76×10^9 N/m) was used. No damping terms were included.

Figure 2 is a comparative plot for the natural frequencies as a function of rotor speed for the rotor modeled using rigid and flexible disk models. The natural frequencies and rotor speed are scaled by the nominal operating speed, Ω_o, of 28,200 rpm. Notice that there is an additional mode for the flexible disk model as compared to the rigid disk model. As discussed by Flowers (1990), two second shaft bending modes result from excitation of in-phase and out-of-phase motion of the disk with the respect to the rotor shaft. The in-phase mode corresponds fairly closely to the second bending mode for the rigid disk rotor model. The out-of-phase mode appears as a distinct branch with no corresponding mode from the rigid disk model. The intersections of the synchronous line with the natural frequency curves determine the critical speeds for the rotor system. For this particular case, little variation of the critical speeds is observed for the two models. Only at rotor speeds significantly above the nominal operating speed are significant differences observed. In addition, for low-frequency modes, the respective natural frequencies are close for all rotor speeds. Such behavior indicates that for synchronous excitation, disk flexibility effects do not play a significant role. However, for higher frequency modes, the respective natural frequencies of the rigid and flexible disk models diverge quite a bit, particularly with respect to backward whirling. Thus for superharmonic vibration, which could be excited by nonlinear effects such as rubbing or nonlinear bearing stiffnesses, disk

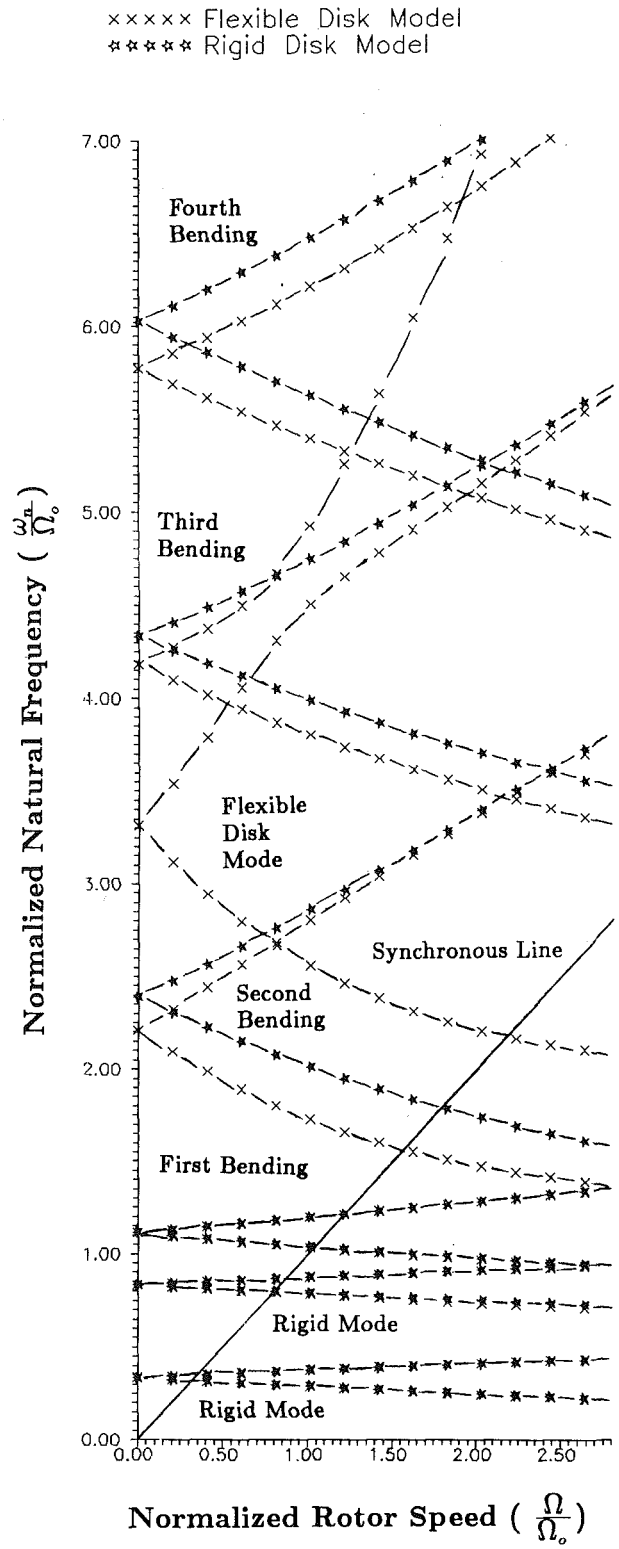

Fig. 2 Comparison of natural frequencies for rigid disk and flexible disk rotor models of the SSME HPOTP

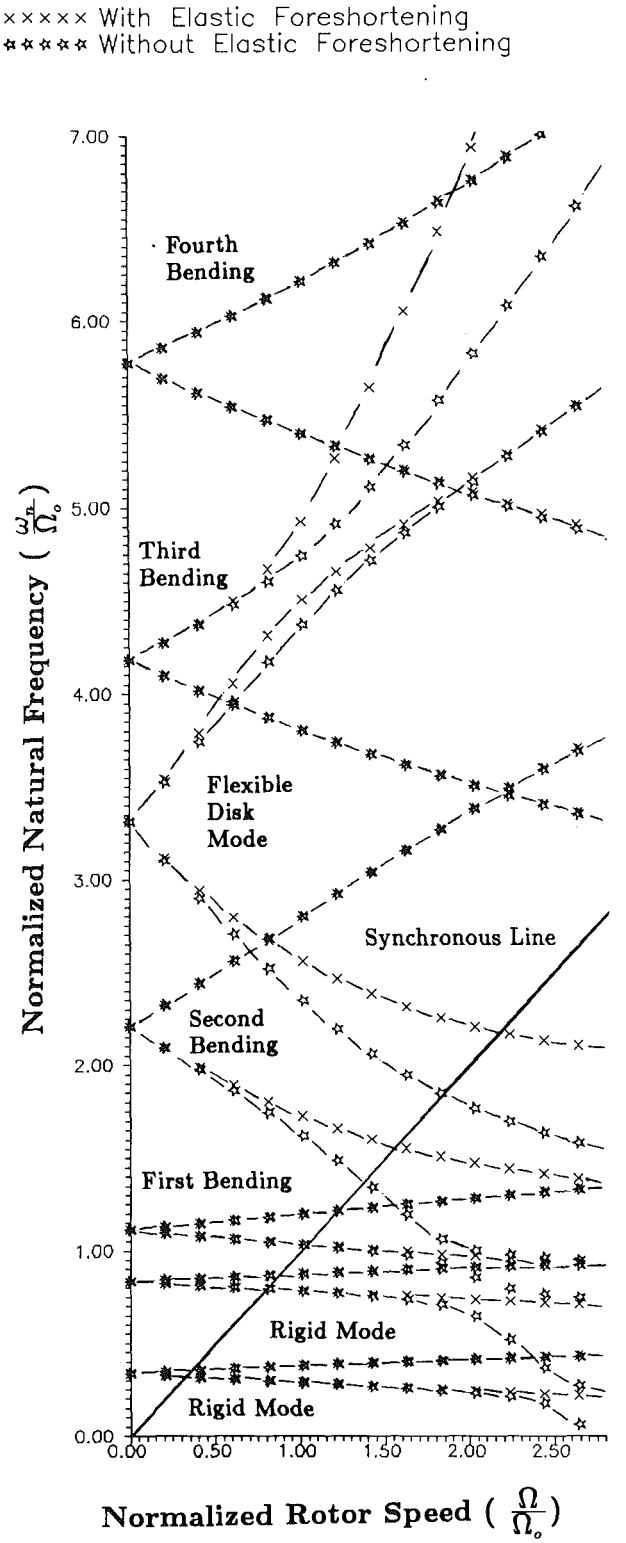

Fig. 3 Comparison of natural frequencies for flexible disk rotor models with and without elastic foreshortening

flexibility can play a very significant role. In fact, such responses have been observed in simulation studies. These results tend to confirm the conclusions of Chivens and Nelson (1975) that disk flexibility does not significantly affect critical speeds for rotors with axisymmetric supports, but may have an important influence on natural frequencies.

The comparable branches for the flexible and rigid disk cases tend to merge for higher rotor speeds. This is due to spin stiffening effects, which are not properly accounted for without the inclusion of foreshortening effects. Figure 3 is a comparative plot for the natural frequencies as a function of rotor speed for the flexible disk rotor model with and without the effects of elastic foreshortening. As is expected, foreshortening does not have an important influence on the lower natural frequencies for relatively low rotor speeds. For the higher natural frequencies and for higher rotor speeds, the natural frequencies predicted by the two models diverge significantly, particularly for backward whirling motion. In fact it can be

seen that, for sufficiently high rotor speeds, the model without foreshortening has a spin softening effect rather than the spin stiffening effect that is expected. So in order to model rotating flexible disk–flexible shaft dynamics adequately, it appears that the inclusion of foreshortening effects can be quite important.

Conclusion

The development of a set of rotordynamic equations that incorporate the effects of rotor disk flexibility has been presented. The derivation has proceeded in a direct fashion from the development of a position vector for an arbitrary point on the rotor to kinetic and potential energy expressions in terms of free-free mode shapes and frequencies for the complete rotor. The energy relations were then used to obtain the associated equations of motion in terms of generalized coordinates by means of the Lagrange equations.

The rotor equations developed in this study are quite similar in form to those typically used for rigid disk models, but two additional matrix terms are included. The two additional terms in these equations, A and B, are modal integrals over each rotor disk and reduce to the corresponding terms in the rigid disk equations when the rigid disk modes are used. Usage of these equations should allow current rigid disk rotordynamic analysis programs using a modal formulation for rotor and housing models to be modified in a relatively easy and straightforward manner to include disk flexibility.

References

Banerjee, A. K., and Kane, T. R., 1987, "Dynamics of a Cantilever Beam Attached to a Moving Base," *Journal of Guidance*, Vol. 10, No. 2, pp. 139–151.

Banerjee, A. K., and Dickens, J. D., 1989, "Dynamics of an Arbitrary Flexible Body Undergoing Large Rotation and Translation With Small Vibration," *Proceedings of the 30th AIAA/ASME/ASCE/AHS/ASC Structures, Structural Dynamics, and Materials Conference*, Apr. 3–5.

Banerjee, A. K., and Kane, T. R., 1989a, "Reply by Authors to K.W. London," *Journal of Guidance*, Vol. 12, No. 2, pp. 286–287.

Banerjee, A. K., and Kane, T. R., 1989b, "Dynamics of a Plate in Large Overall Motion," *Journal of Applied Mechanics*, Vol. 56, pp. 887–892.

Chivens, D. R., and Nelson, H. D., 1975, "The Natural Frequencies and Critical Speed of a Rotating, Flexible Shaft-Disk System," ASME *Journal of Engineering for Industry*, Vol. 97, pp. 881–886.

Dopkin, J. A., and Shoup, T. E., 1974, "Rotor Resonant Speed Reduction Caused by Flexibility of Disks," ASME *Journal of Engineering for Industry*, Vol. 96, pp. 1328–1333.

Flowers, G. T., 1990, "Effects of Rotor Disk Flexibility on the Rotordynamics of the Space Shuttle Main Engine Turbopumps," presented at the AIAA/ASME/ASCE/AHS/ASC 31st SDM Conference, Apr. 2–4.

Hodges, D. H., 1984, "Proper Definition of Curvature in Nonlinear Beam Kinematics," *AIAA Journal*, Vol. 22, pp. 1825–1827.

Klompas, N., 1974, "Theory of Rotor Dynamics With Coupling of Disk and Blade Flexibility and Support Structure Assymmetry," ASME Paper No. 74-GT-159.

Klompas, N., 1983, "Unbalance Response Analysis of a Complete Turbomachine," ASME JOURNAL OF ENGINEERING FOR POWER, Vol. 105, pp. 184–191.

Lamb, H., and Southwell, R. V., 1921, "The Vibrations of a Spinning Disk," *Proceedings of the Royal Society of London*, Series A, Vol. 99, pp. 272–280.

Laurenson, R. M., 1976, "Modal Analysis of Rotating Flexible Structures," *AIAA Journal*, Vol. 14, No. 10, pp. 1444–1450.

Likins, P. W., 1974, "Geometric Stiffness of a Rotating Elastic Appendage," *International Journal of Solids and Structures*, Vol. 10, No. 2, pp. 161–167.

Lips, K. W., 1987, "Approaches and Possible Improvements in the Area of Multibody Dynamics Modeling," Technical report prepared for NASA Marshall Space Flight Center under contract NASA8-34588 by Honeywell Space and Strategic Avionics Division, Clearwater, FL, Oct. 30.

London, K. W., 1989, "Comment on 'Dynamics of a Cantilever Beam Attached to a Moving Base'," *Journal of Guidance*, Vol. 12, No. 2, pp. 284–286.

Palladine, J. A., and Rosettes, J. N., 1982, "Finite Element Analysis of the Dynamics of Flexible Disk Rotor Systems," ASME Paper No. 82-GT-240.

Pringle, R., Jr., 1969, "On the Stability of a Body With Connected Moving Parts," *AIAA Journal*, Vol. 7, No. 6, pp. 1054–1063.

Meirovitch, L., 1967, *Analytical Methods in Vibrations*, Macmillan, New York, pp. 443–445.

Meirovitch, L., 1976, "A Stationarity Principle for the Eigenvalue Problem for Rotating Structures," *AIAA Journal*, Vol. 14, No. 10, pp. 1387–1394.

Ryan, S. G., 1980, "Turbomachinery Rotordynamics Analysis Package," NASA Internal Document, Aug. 20.

Shahab, A. A. S., and Thomas, J., 1987, "Coupling Effects of Disc Flexibility on the Dynamic Behavior of Multi Disc-Shaft Systems," *Journal of Sound and Vibration*, Vol. 114, No. 3, pp. 435–452.

Sakata, M., Aiba, T., and Ohnabe, H., 1983, "Transient Vibration of High-Speed, Lightweight Rotors Due to Sudden Imbalance," ASME JOURNAL OF ENGINEERING FOR POWER, Vol. 105, pp. 480–486.

Southwell, R. V., 1922, "On the Free Transverse Vibrations of a Uniform Circular Disk Clamped at Its Centre; and on the Effects of Rotation," *Proceedings of the Royal Society of London*, Series A, Vol. 101, pp. 133–153.

Vance, J. C., 1988, *Rotordynamics of Turbomachinery*, Wiley, New York, pp. 137–170.

Wilgen, F. J., and Schlack, A. L., 1977, "Effects of Disk Flexibility on Shaft Whirl Stability," *AIAA Journal*, Vol. 15, No. 10, pp. 1531–1533.

Yoo, H. H., Ryan, R. R., and Scott, R. A., 1989, "Use of Assumed Modes in Equations Governing Large Displacement Elastodynamic Plate Behavior," *Proceedings of the 30th AIAA/ASME/ASCE/AHS/ASC Structures, Structural Dynamics, and Materials Conference*, Apr. 3–5.

A Simple Frequency Expression for the In-Plane Vibrations of Rotating Rings

B. L. Koff
Executive Vice President,
Engineering and Technology.

Y. M. El-Aini
Technical Leader,
Vibration and Aeroelasticity Group.

Pratt & Whitney,
West Palm Beach, FL 33410

An approximate but accurate expression for determining the reference in-plane flexural frequencies of rotating rings is presented. The ring reference frequencies are with respect to a coordinate system that rotates with the ring at the mean speed of the forward and backward traveling waves analogous to the standing wave approach for rotating disks. The formula is based on adapting the correction factor for shear, centrifugal stiffening, and centrifugal mass of prismatic bars to be applied to Hoppe's "Classical" formula for stationary, slender, inextensible rings. The result is a closed-form analytical solution applicable to arbitrary shaped rotating rings with distributed loading. The formula has been verified for a wide range of ring radial depths and nodal diameters by comparison to elaborate NASTRAN solid finite element models that account for shear, centrifugal stiffening, and centrifugal mass effects. Excellent correlations, within 1 percent, for all test cases were achieved. Forward and backward traveling-wave frequencies are obtained by using the reference frequency expression into Bryan's "classical" formula for thin rotating rings. Centrifugal mass contribution was shown to be particularly important for thin rings vibrating at low nodal diameters.

1 Introduction

The understanding of the vibration characteristics of rotating rings is of particular importance in turbomachinery as well as numerous other applications. Analysis techniques for the free vibrations of circular rings have been in publication as early as the 19th century when Hoppe (1871) and Bryan (1890) both used inextensional, shearless deformation and negligible rotatory inertia assumptions to investigate the flexural vibrations of stationary and rotating rings, respectively. The formulations by Hoppe and Bryan apply mainly to modes of low circumferential wave numbers and thin rings. To improve accuracy, many investigators (Bickford and Reddy, 1985; Lin and Soedel, 1988; Endo et al., 1984; Lallman, 1980) have attempted to incorporate one or more of the significant factors in their formulations. Unfortunately, accounting for some or all of the factors required to enhance the predictions increases the complexity of the formulation to the extent that simple closed-form solutions are not possible and numerical solutions became the only alternative. With the increased emphasis on accuracy to ensure minimum weight designs, engineers and designers have resorted to the use of state-of-the-art finite element analysis techniques at the expense of increased computer cost and labor and loss of "a feel" for the physics of the problem. Even with today's capabilities of supercomputers and the availability of general purpose advanced finite element codes, the task of computing traveling wave frequencies of rotating rings including the effects of centrifugal stiffening, centrifugal mass, and shear deformations requires a high degree of user expertise. The purpose of this paper is to introduce a useful approximate, yet accurate, formula for the calculation of the in-plane flexural frequencies of rotating circular rings, which include the effects of shear deformations, centrifugal stiffening, and centrifugal mass. These effects are incorporated through a series of correction factors based on prismatic bars and adapted to the classical formula by Hoppe. Having a closed-form solution is a great aid for the design engineer in developing insight into the structural behavior as well as confidence in problem solving ability. It is hoped that this paper will encourage other researchers to develop simplified approaches to other complex structural problems to minimize the total dependence on digital computers to perform basic analyses.

Contributed by the International Gas Turbine Institute and presented at the 36th International Gas Turbine and Aeroengine Congress and Exposition, Orlando, Florida, June 3-6, 1991. Manuscript received at ASME Headquarters February 12, 1991. Paper No. 91-GT-72. Associate Technical Editor: L. A. Riekert.

2 Traveling Waves in Rotating Rings

The dynamic characteristics of rotating rings are inherently different from those of rotating disks. For a given rotational speed, a ring experiencing in-plane vibrations in an n-wave mode will have two natural modes associated with forward and backward traveling waves. A strain gage mounted on the rotating ring will sense two distinct frequencies corresponding to the forward and backward circumferential traveling waves. This is different for the case of a rotating disk where a strain gage mounted on the disk will sense only one frequency for the n-wave natural mode. This basic difference is due to the in-plane flexibility of the ring and the associated radial and

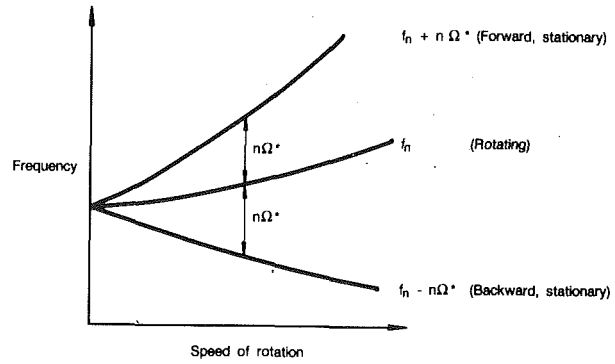

Fig. 1 Campbell diagram for disk

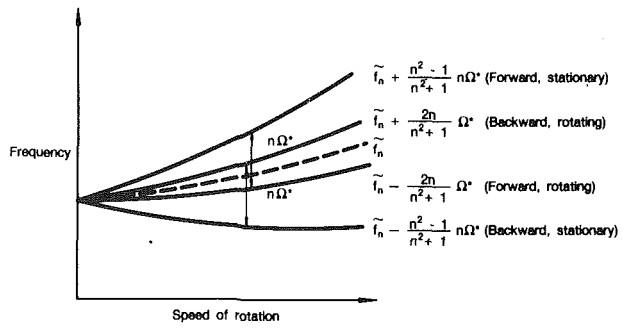

Fig. 2 Campbell diagram for ring

tangential motion of the ring elements due to the rotational effects. A detailed explanation of the phenomenon was presented by Macke (1966). Campbell diagrams, Figs. 1 and 2, compare typical dynamic responses of rotating disks and rings in both the rotating and stationary reference frames. It should be noted that in both cases the relationships between the natural frequencies in the rotating and the stationary (inertial) reference frames are related through the same Galilean transform, namely:

$$f_n^S = f_n^R \pm n\Omega^* \tag{1}$$

where the superscripts S and R indicate stationary and rotating reference frames, respectively, and the (+) sign corresponds to the forward traveling wave.

For the purpose of this paper, the in-plane flexural frequencies of rotating rings are thought of in terms of their *reference* frequencies corresponding to the average of the forward and backward traveling wave frequencies. This pseudo "standing" wave approach is more convenient for correlations with NASTRAN (MacNeal-Schwendler, 1988) finite element modal analysis compared to a transient dynamic analysis. Forward and backward traveling wave frequencies are then obtained using Bryan's formula, namely:

$$f_n^R = \tilde{f}_n \mp \frac{2n\Omega^*}{(n^2+1)} \tag{2}$$

where $\tilde{f}_n$ is the reference frequency corresponding to the n-wave mode and the (−) sign indicates forward traveling wave. Bryan's expression for the reference frequency is given by

$$\tilde{f}_n = \left\{ \frac{1}{4\pi^2} \frac{n^2(n^2-1)^2}{n^2+1} \frac{EIg}{A\gamma a^4} + \frac{n^2(n^2-1)^2}{(n^2+1)^2} \Omega^{*2} \right\}^{1/2} \tag{3}$$

The improvements over Bryan's formula are thus aimed at increasing the accuracy of the reference frequency predictions. This is a valid assumption since shear, centrifugal stiffening, and centrifugal mass corrections are implied in the reference frequency term only.

3 Approximate Formula

The classical formula for in-plane flexural vibration of a circular ring with uniform cross section is given by Hoppe (1871):

$$\tilde{f}_n = \frac{1}{2\pi} \left[\frac{n(n^2-1)}{\sqrt{1+4n^2}} \right] \frac{1}{a^2} \sqrt{\frac{EIg}{A\gamma + q}}; \quad n = 2, 3, \ldots \tag{4}$$

The correction factors to account for shear deformation, centrifugal stiffening, and centrifugal mass are based on the simple analogy to prismatic bars with simply supported ends in equilibrium with an integer number of full sine waves along the beam span corresponding to the same number of nodal diameters on the ring, as shown in Fig. 3.

Shear Factor (K_s). The correction factor for the flexural vibration frequencies of prismatic bars due to shear deformation is given by Timoshenko (1921) as

$$\tilde{f}^2_{n(\text{w/ shear})} = \tilde{f}^2_{n(\text{w/o shear})} \times K_s^2 \tag{5}$$

where

$$K_s^2 = \frac{1}{1 + \frac{I}{A} \frac{E\alpha}{G} \frac{\pi^2}{\lambda_n^2}}$$

This shear correction factor will be used as an approximation for the in-plane flexural vibration of the ring in nodal patterns described by n full waves along the circumference.

Centrifugal Stiffening Factor (K_{cs}). The application of a constant tensile load along the axis of a prismatic bar will result in an increase in its natural frequencies (Woinowsky-Krieger, 1950). Similarly, a rotating circular ring will develop internal direct hoop stresses over the cross section proportional to (Ω^2). This hoop load will have the same effect of increasing the ring natural frequencies as in the case of the prismatic bar. Thus, using the analogy of the simply supported bar, the correction factor for centrifugal stiffening of a ring in n nodal diameter pattern is given by

Nomenclature

A = cross-sectional area
a = radius to ring centerline
b = ring width
E = Young's modulus of elasticity
F = force
f = frequency, Hz
G = shear modulus
g = acceleration of gravity
h = ring radial depth
I = cross-sectional area moment of inertia
i = $\sqrt{-1}$
l = length of ring circumference
M = bending moment
m = mass per unit length
n = ring mode number
o = origin of coordinate axes
P = tensile load at ring section
Q = shear force
q = attached nonstructural weight
R = ring outer radius
t = time
x, y = coordinates
α = section form factor in shear
γ = specific weight
ν = Poisson ratio
ρ = mass density
Ω = rotational speed, rad/s
Ω^* = rotational speed, CPS
ω = frequency, rad/s
$( )'$ = $\partial( )/\partial x$

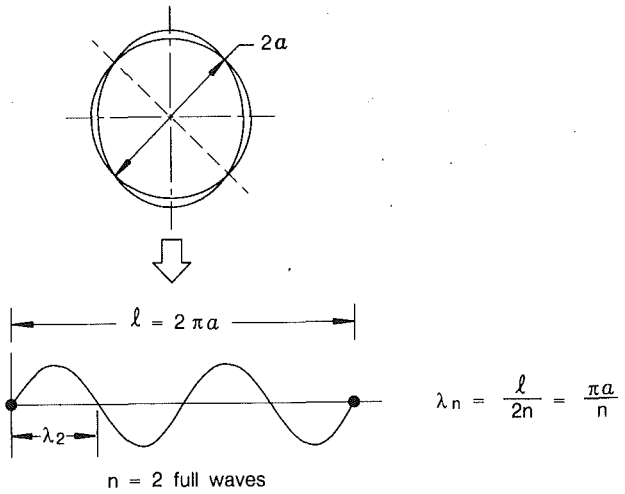

$$\lambda_n = \frac{\ell}{2n} = \frac{\pi a}{n}$$

Fig. 3 Simply supported bar representing a ring in a two-nodal diameter mode

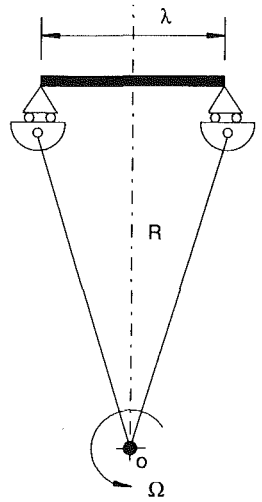

Fig. 4(*a*) A simply supported bar rotating about a fixed origin

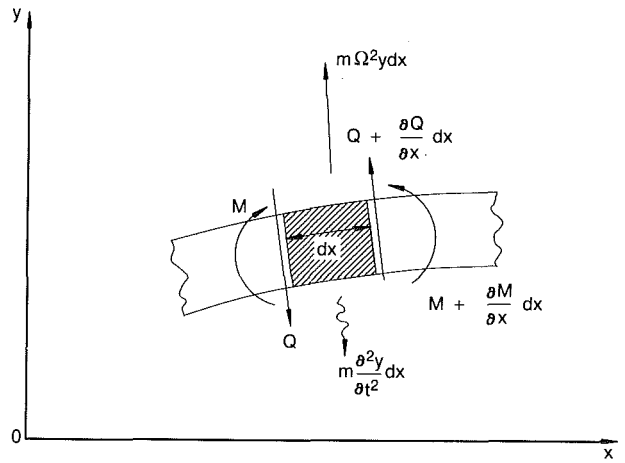

Fig. 4(*b*) Element equilibrium including centrifugal mass term

$$\tilde{f}^2_{n(\mathrm{w/}\,CS)} = \tilde{f}^2_{n(\mathrm{w/o}\,CS)} \times K^2_{CS} \tag{6}$$

where

$$K^2_{CS} = \left(1 + \frac{P\lambda_n^2}{\pi^2 EI}\right)$$

and

$$P = (\gamma A + q)\Omega^2 a^2/g$$

Centrifugal Mass Factor (K_{CM}). Centrifugal mass is a term that accounts for the variation of the centrifugal force as a result of the vibratory motion of the structural element (Dokainish and Rawtani, 1972). The effect of incorporating this term in the equations of motion is a reduction of the elastic restoring force and consequently a reduction in the natural frequencies, as will be illustrated in the following example.

To incorporate the effect of this term, consider the problem of a simply supported beam rotating about a fixed axis through point o with a constant speed Ω, as shown in Fig. 4(*a*). We assume that the ratio R/λ is large such that the direction of the centrifugal force on the beam element along the span is nearly perpendicular to the beam centerline. The equilibrium force, including the centrifugal mass term, is shown in Fig. 4(*b*). The differential equation of equilibrium in the y direction is given by

$$D.E.: \quad EI\frac{\partial^4 y}{\partial x^4} - m\Omega^2 y + m\frac{\partial^2 y}{\partial t^2} = 0, \quad \lambda \geq x \geq 0 \tag{7}$$

$$B.C.(s): \quad y(0, t) = y''(0, t) = 0$$
$$y(\lambda, t) = y''(\lambda, t) = 0$$

Assuming a harmonic solution in the form

$$y = Ye^{i\omega t} \tag{8}$$

reduces Eq. (7) to

$$D.E.: \quad Y^{IV} - \beta^4 Y = 0; \quad \lambda \geq x \geq 0 \tag{9}$$

$$B.C.(s): \quad Y(0) = Y''(0) = 0$$
$$Y(\lambda) = Y''(\lambda) = 0$$

where

$$\beta^4 = \frac{m(\Omega^2 + \omega^2)}{EI} \tag{10}$$

Equation (9) is the classical Euler formulation of the flexural vibrations of a simply supported beam (Thompson, 1981). The eigenvalues, corresponding to the feasible harmonic solutions, are given by:

$$\beta^4 = \left(\frac{n\pi}{\lambda}\right)^4; \quad n = 1, 2, 3,... \tag{11}$$

or

$$\omega_n^2 = \left(\frac{n\pi}{\lambda}\right)^4 \frac{EI}{m} - \Omega^2; \quad n = 1, 2, 3,... \tag{12}$$

Thus, for the ring problem, the correction factor for centrifugal mass will take the form

$$\tilde{f}^2_{n(\mathrm{w/}\,CM)} = \tilde{f}^2_{n(\mathrm{w/o}\,CM)} - K^2_{CM} \tag{13}$$

where

$$K^2_{CM} = \left(\frac{\Omega}{2\pi}\right)^2$$

Combining all three factors, the approximate formula will take the form

$$\tilde{f}^2_n = \tilde{f}^2_{n(\mathrm{Hoppe})} \times K^2_S \times K^2_{CS} - K^2_{CM} \tag{14}$$

or, in expanded form,

$$\tilde{f}_n = \frac{1}{2\pi}\sqrt{\left(\frac{n(n^2-1)}{\sqrt{1+n^2}}\frac{1}{a^2}\right)^2 \frac{\frac{EIg}{A\gamma + q}\left(1 + \frac{P\lambda_n^2}{\pi^2 EI}\right)}{\left(1 + \frac{I}{A}\frac{E\alpha}{G}\frac{\pi^2}{\lambda_n^2}\right)} - \Omega^2}; \quad n = 2, 3,... \tag{15}$$

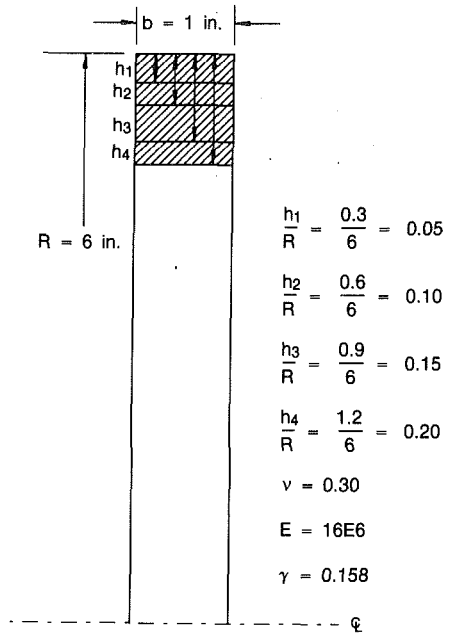

Fig. 5 Ring geometry considered for analysis

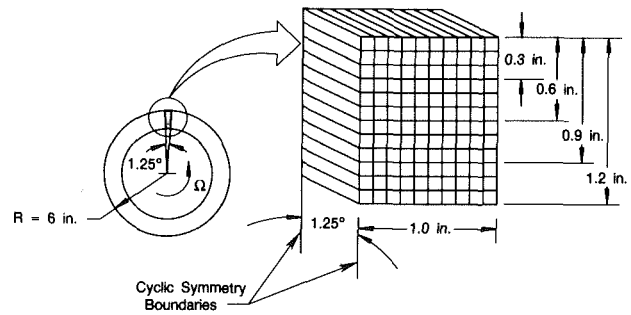

Fig. 6 NASTRAN cyclic symmetry models for five ring configurations

4 NASTRAN Verification

To verify the accuracy of the approximate formula in Eq. (15), a series of analytical test cases were conducted using the MSC/NASTRAN (MacNeal-Schwendler, 1988) version 60A on the IBM-3090 computer. Four ring configurations were considered in the analysis. These configurations are shown in Fig. 5. Thickness-to-radius ratios (h/R) of 0.05, 0.01, 0.15, and 0.20 were used to cover both thin and thick rings.

NASTRAN Models. NASTRAN eight-noded brick elements (CHEXA8) were used to construct a cyclic symmetry model, shown in Fig. 6. The breakup is one element in the circumferential direction covering 1.25 deg of the 360 deg ring, 10 elements along the width, and from 3 to 12 elements through the thickness depending on the thickness ratio (h/R). A special Direct Matrix Abstraction Program (DMAP) that accounts for both differential stiffness and centrifugal mass was used to compute the in-plane natural frequencies of the different ring configurations.

5 Results

NASTRAN models were run for nodal diameters 2, 3, 4, and 5 for four ring configurations with thickness ratios of 0.05, 0.01, 0.15, and 0.20. A comparison between the predictions using the formula in Eq. (15) and NASTRAN, with centrifugal stiffening and centrifugal mass effects included, is shown in Fig. 7. As can be seen, the agreement is excellent

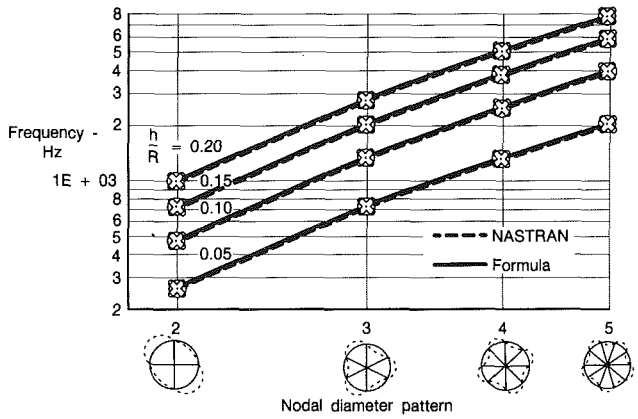

Fig. 7 Comparison between NASTRAN and approximate formula including shear, centrifugal stiffening, and centrifugal mass effects

with the differences being less than 1 percent for all nodal diameters and thickness ratios (see Table 1).

To demonstrate the effect of the centrifugal mass correction, a comparison between NASTRAN and the formula, without the term $(-\Omega^2)$, is shown in Fig. 8. Errors on the order of 19 percent were encountered for the case of a thin ring ($h/R = .05$) at the two-nodal diameter mode. The error is significantly reduced as the ring stiffness increases. This conclusion is obvious by examination of Eq. (15).

To demonstrate the effect of the shear correction on the natural frequency of the different configurations, a comparison between NASTRAN and the formula, without the shear correction factor, is illustrated in Fig. 9. As expected, the largest effect occurs for the ring with the highest thickness ratio and at the highest nodal diameter. The error for this case is on the order of 15 percent.

The improvements of the current formula, Eq. (15), over Bryan's reference frequency, Eq. (3), are evident by comparing Bryan's results in Table 1 to NASTRAN predictions. Bryan's formula indicates a 12 percent error for the two-nodal diameter mode of the thin ring case ($h/R = 0.05$) and a 16 percent error for the thick ring ($h/R = 0.20$) in the five-nodal diameter mode. As anticipated, Bryan's shearless deformation assumption has led to results that closely agree with the current formula without the shear correction factor being incorporated.

6 Concluding Remarks

An approximate, yet accurate, formula for computing the in-plane flexural natural frequencies of rotating circular rings with uniform cross section is presented. Correction factors for centrifugal stiffening, shear deformation, and centrifugal mass are incorporated. The accuracy of the formula has been verified by comparisons to the results of detailed solid finite element models run on MSC/NASTRAN for different ring configurations. The following conclusions are made:

1 The accuracy of the formula is within 1 percent compared to NASTRAN.
2 The formula is more accurate than Bryan's formula for thin rings vibrating at low nodal diameters and for thick rings in high nodal diameters.
3 Centrifugal mass effect is highest for thin rings rotating at high speeds.
4 Shear correction effect is highest for thick rings at high nodal diameters.

It is hoped that this approach of simplifying complicated physical problems can be extended to other structures and dynamics applications to help save designers and engineers the time and effort of running elaborate finite element models for parametric studies during preliminary design.

Table 1 Comparison of NASTRAN frequency predictions with ring formula: $R = 6$ in. $b = 1$ in., $\gamma = 0.158$, $E = 16E6$, $\nu = 0.3$, rpm = 10,000

h/R	Nodal Diam. (n)	NASTRAN (Hz)	Formula ; f_n Shear, Cent. Stiff., Cent. Mass. Eqn. 15	Shear, Cent. Stiff., No Cent. Mass.	No Shear, Cent. Stiff., Cent. Mass.	Bryan's f_n Eqn. 3
0.05	2	262	260	309	261	293
	3	720	716	735	718	725
	4	1301	1291	1301	1298	1300
	5	2026	2008	2015	2026	2027
0.10	2	473	471	500	474	497
	3	1317	1314	1325	1331	1348
	4	2458	2455	2460	2511	2537
	5	3884	3886	3889	4024	4065
0.15	2	720	718	737	728	740
	3	1992	1991	1998	2052	2055
	4	3697	3710	3714	3908	3909
	5	5774	5818	5821	6296	6297
0.20	2	993	989	1003	1015	1023
	3	2709	2712	2717	2865	2867
	4	4968	4985	4988	5474	5474
	5	7629	7687	7688	8835	8835

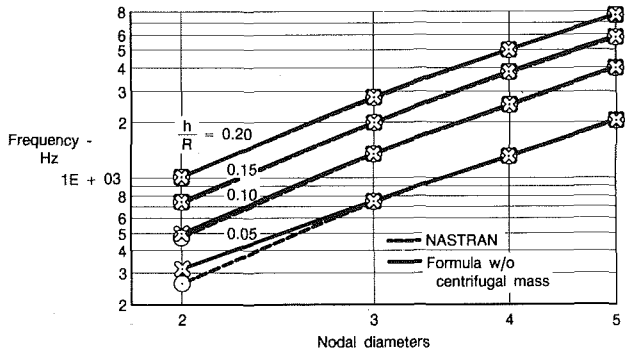

Fig. 8 Effect of neglecting centrifugal mass on ring natural frequencies

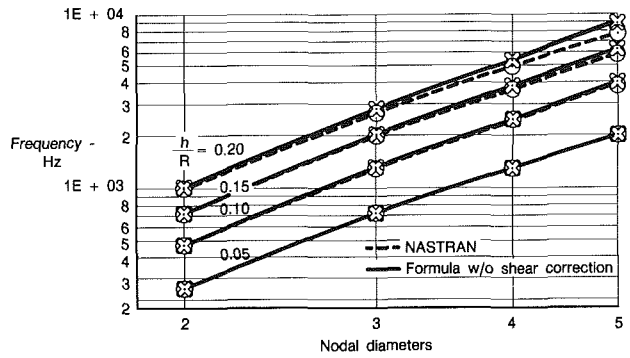

Fig. 9 Effect of neglecting shear correction on ring natural frequencies

Acknowledgments

The authors wish to thank Thomas Hoosac of Pratt & Whitney for performing the NASTRAN finite element analyses used for this study.

References

Bickford, W. B., and Reddy, E. S., 1985, "On the In-Plane Vibrations of Rotating Rings," *Journal of Sound and Vibration*, Vol. 101, No. 1, pp. 13–22.

Bryan, G. H., 1890, "On the Beats in the Vibrations of a Revolving Cylinder or Bell," *Proceedings of the Cambridge Philosophical Society*, Vol. 7, pp. 101–111.

Dokainish, M. A., and Rawtani, S., 1972, "Pseudo-static Deformation and Frequencies of Rotating Turbomachinery Blades," *AIAA Journal*, pp. 1397–1398.

Endo, M., et al., 1984, "Flexural Vibration of a Thin Rotating Ring," *Journal of Sound and Vibration*, Vol. 92, No. 2, pp. 261–272.

Hoppe, R., 1871, "The Bending Vibration of a Circular Ring," *Crelle Journal of Mathematics*, Vol. 73, p. 158.

Lallman, F. J., 1980, "Vibration Characteristics of Steadily Rotating Slender Ring," NASA Tech. Paper No. 1775, Dec.

Lin, J. L., and Soedel, W., 1988, "On General In-Plane Vibrations of Rotating Thick and Thin Rings," *Journal of Sound and Vibration*, Vol. 122, No. 3, pp. 547–570.

Macke, H. J., 1966, "Traveling-Wave Vibration of Gas-Turbine Engine Shells," ASME JOURNAL OF ENGINEERING FOR GAS TURBINES AND POWER, Vol. 88, pp. 179–187.

MacNeal-Schwendler Corp., 1988, "MSC/NASTRAN User's Manual—Version 65," Los Angeles, CA.

Thompson, W. T., 1981, *Theory of Vibrations With Applications*, 2nd ed., Prentice-Hall, Englewood Cliffs, NJ.

Timoshenko, S., 1921, "On the Correction for Shear of the Differential Equation for Transverse Vibration of Prismatic Bars," *Philosophical Magazine*, Series 6, Vol. 41, p. 744.

Woinowsky-Krieger, S., 1950, "The Effect of an Axial Force on the Vibration of Hinged Bars," ASME *Journal of Applied Mechanics*, Vol. 17, pp. 35–36.

Dynamic Response of Rotor-Bearing Systems With Time-Dependent Spin Rates

T. H. Young
Associate Professor.

G. T. Liou
Graduate Research Assistant.

Department of Mechanical Engineering,
National Taiwan Institute of Technology,
Taipei, Taiwan

This paper presents an investigation into the vibration of rotor-bearing systems with time-dependent spin rates. Due to this spin rate, parametric instability may take place in certain situations. In this work, the Galerkin method is used to eliminate the dependence on the spatial coordinates, and then the method of multiple scales is applied to derive periodic solutions and expressions for the boundaries of unstable regions analytically. Numerical results are given for the case where the spin rate is characterized as a small, harmonic perturbation superimposed on a constant rate. The effects of system parameters on the changes of the boundaries of unstable regions are shown.

Introduction

Rotor-bearing systems are widely used assemblies in aerospace and mechanical industries. Power machinery, such as compressors and turbomachines, usually transmits power by means of rotor-bearing systems. In recent years, due to the design trend toward higher spin rates to raise the operating efficiency, lateral vibration of the system becomes aggravated. Therefore, research in the dynamic behavior of rotor-bearing systems has prospered in the past few decades (Vance, 1988).

Previous investigations on the vibration of rotor-bearing systems have dealt primarily with the determination of critical speeds and mode shapes of the systems which spin at a constant rate. According to the methods of analysis, these works can be classified into three groups: (1) the transfer matrix method (Lund, 1974; Bansal and Kirk, 1975; Vance et al., 1987), (2) the finite element method (Ruhl and Booker, 1972; Gasch, 1976; Nelson and McVaugh, 1976; Akella and Craggs, 1986), (3) the assumed mode method (Shiau and Hwang, 1989). Actually the spin rate of a rotor-bearing system is controlled within a small range of variance under external disturbances. Hence, it would be more general and physically realistic to consider a time-dependent spin rate than a constant rate. Due to this time-varying spin rate, the system may bring about parametric instability in certain situations.

Very few works dealing with systems rotating at nonconstant speeds can be found in the literature. The works by Kammer and Schlack (1987a,1987b) appear to be the first ones concerning this topic. In these two papers, the angular speed is expressed as the sum of a constant value and a small periodic perturbation, and the KBM (Krylov–Bogoliubov–Mitropolski) method is used to derive approximate solutions and expressions for the boundaries of unstable regions. Later Young (1991) applied the method of multiple scales of study parametrically the dynamic behavior of a pretwisted, tapered beam with a nonconstant rotating speed, which was assumed in the same way as those in the previous papers by Kammer and Schlack. Furthermore, Young and Liou (1992) investigated the Coriolis effect on the vibration and stability of a cantilever plate that rotates with a time-varying speed. In this paper, the Galerkin method is first applied to eliminate the dependence on the spatial coordinates, and then the method of multiple scales is utilized to derive analytical solutions and expressions for the boundaries of unstable regions of the system. This work extends the past research efforts of the authors to study the vibration of rotor-bearing systems with time-dependent spin rates.

Equations of Motion

A rotor-bearing system consisting of a shaft of length l, a rotor of mass M located at a distance x_o away from the left end of the shaft, and a pair of journal bearings, which are modeled as a combination of springs and dampers at both ends, is shown in Fig. 1. The system spins with respect to the X axis at a rate Ω, where (X, Y, Z) is a fixed coordinate system. (x, y, z) is a rotating coordinate system attached onto the rotor-bearing system with the x axis coinciding with the X axis in the undeformed configuration.

Assume that the axial deformation u is very small in comparison with the lateral deflections v and w, and is negligible. The strain energy of the shaft, after neglecting the shear deformation, can be written as

$$U_s=\frac{1}{2}\left\{\int_0^{x_o^-}[E_yI_y(v_{,xx})^2+E_zI_z(w_{,xx})^2]dx \int_{x_o^+}^{l}[E_yI_y(v_{,xx})^2+E_zI_z(w_{,xx})^2]dx\right\} \quad (1)$$

where E_yI_y and E_zI_z are the flexural rigidities of the shaft in the y and z directions, respectively; "," denotes a partial derivative with respect to x. The strain energy offered by the bearings is given by

Contributed by the Power Division for publication in the JOURNAL OF ENGINEERING FOR GAS TURBINES AND POWER. Manuscript received at ASME Headquarters August 1992. Associate Technical Editor: R. W. Porter.

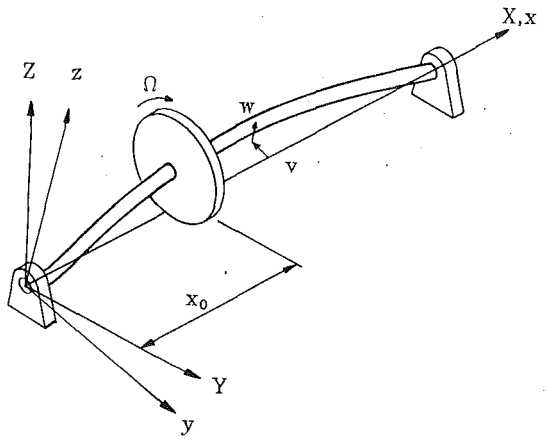

Fig. 1 Configuration of a rotor-bearing system

$$U_b=[k_{yy}v^2+(k_{yz}+k_{zy})vw+k_{zz}w^2]_{x=0}+[k_{yy}v^2+(k_{yz}+k_{zy})vw+k_{zz}w^2]_{x=l} \quad (2)$$

where k_{yy} and k_{zz} are the direct stiffness coefficients of the bearings, while k_{yz} and k_{zy} are the cross-coupling stiffness coefficients. Here the stiffness coefficients of the bearings are assumed as linear functions of the spin rate (Kirk and Gunter, 1976). The shaft is assumed to have no damping and the resistant force induced by the damping in the bearings may be derived from a Rayleigh dissipation function. Therefore, the Rayleigh dissipation function of the system is of the form

$$D=\frac{1}{2}\{[c_{yy}\dot{v}^2+(c_{yz}+c_{zy})\dot{v}\dot{w}+c_{zz}\dot{w}^2]_{x=0}+[c_{yy}\dot{v}^2+(c_{yz}+c_{zy})\dot{v}\dot{w}+c_{zz}\dot{w}^2]_{x=l}\} \quad (3)$$

where "˙" denotes partial differentiation with respect to time. c_{yy} and c_{zz} are the direct damping coefficients of the bearings, while c_{yz} and c_{zy} are the cross-coupling damping coefficients. Usually, the cross-coupling damping coefficients are equal (Kirk and Gunter, 1976). During deformation, the absolute velocity of a point on the neutral axis of the shaft is found to be

$$\mathbf{v}=(\dot{v}-\Omega w)\mathbf{j}+(\dot{w}+\Omega v)\mathbf{k} \quad (4)$$

where $\mathbf{j}$ and $\mathbf{k}$ are the unit vectors along the y and z directions, respectively. By neglecting the rotary inertia, the kinetic energy of the whole system can be written as

$$T=\frac{1}{2}\left\{\int_0^{x_o^-}\rho[(\dot{v}^2+\dot{w}^2)+2\Omega(v\dot{w}-\dot{v}w)+\Omega^2(v^2+w^2)]dx+\int_{x_o^+}^{l}\rho[(\dot{v}^2+\dot{w}^2)+2\Omega(v\dot{w}-\dot{v}w)+\Omega^2(v^2+w^2)]dx\right\}+\frac{1}{2}M[(\dot{v}^2+\dot{w}^2)+2\Omega(v\dot{w}-\dot{v}w)+\Omega^2(v^2+w^2)]_{x=x_o} \quad (5)$$

where ρ is the mass per unit length of the shaft.

The generalized Hamilton principle for viscously damped systems may be written as

$$\delta\int_{t_1}^{t_2}L\,dt-\int_{t_1}^{t_2}\left(\frac{\partial D}{\partial\dot{v}}\delta v+\frac{\partial D}{\partial\dot{w}}\delta w\right)dt=0, \quad (6)$$

where t_1 and t_2 are the time coordinates at which δv and δw vanish, and the Lagrangian $L=T-(U_s+U_b)$. Substituting the expressions for strain energy, kinetic energy, and the dissipation function into the above equations and going through the variation and integration manipulations gives the following equations of motion:

$$\rho\ddot{v}-2\rho\Omega\dot{w}-\rho\Omega^2v-\rho\dot{\Omega}w+(E_yI_yv_{,xx})_{,xx}=0$$
$$\rho\ddot{w}+2\rho\Omega\dot{v}-\rho\Omega^2w+\rho\dot{\Omega}v+(E_zI_zw_{,xx})_{,xx}=0, \quad (7)$$

the following transition conditions at x_o:

$$M\ddot{v}-2M\Omega\dot{w}-M\Omega^2v-M\dot{\Omega}w+(E_yI_yv_{,xx})_{,x}|_{x=x_o^-}^{x_o^+}=0$$
$$M\ddot{w}+2M\Omega\dot{v}-M\Omega^2w+M\dot{\Omega}v+(E_zI_zw_{,xx})_{,x}|_{x=x_o^-}^{x_o^+}=0, \quad (8)$$

and the following boundary conditions at $x=0$ and $x=l$:

$$(E_yI_yv_{,xx})_{,x}+(k_{yy}v+k_{yz}w)+(c_{yy}\dot{v}+c_{yz}\dot{w})=0$$
$$(E_zI_zw_{,xx})_{,x}+(k_{zy}v+k_{zz}w)+(c_{zy}\dot{v}+c_{zz}\dot{w})=0$$
$$E_yI_yv_{,xx}=0$$
$$E_zI_zw_{,xx}=0 \quad (9)$$

Equation (7) together with the transition and boundary conditions written in Eqs. (8) and (9) defines the mathematical model for this problem.

The mathematical problem defined by Eqs. (7)–(9) possesses no exact solution; therefore, approximate methods must be adopted to solve it analytically. In this work, Galerkin's method is first applied to eliminate the dependence on the spatial coordinate x, yielding a set of differential equations in time. Based on this method, the forms of the displacements are assumed as follows:

$$v(x,t)=\sum_{m=0}^{M}a_m(t)\left(\frac{x}{l}\right)^m$$
$$w(x,t)=\sum_{n=0}^{N}b_n(t)\left(\frac{x}{l}\right)^n \quad (10)$$

where a_m and b_n are undetermined functions of time. Since the assumed displacements are not the exact solution of the governing equations and do not satisfy the transition conditions at x_o and the boundary conditions at both ends, on substituting the assumed displacements into the equations of motion, the transition conditions and the boundary conditions yield certain residues. The extended Galerkin method requires that (Leipholz, 1977)

$$\int_0^{x_o^-}[\text{G.E.}]\left(\frac{x}{l}\right)^p dx+\int_{x_o^+}^{l}[\text{G.E.}]\left(\frac{x}{l}\right)^p dx-\left\{[\text{B.F.}]\left(\frac{x}{l}\right)^p-[\text{B.M.}]\times l\frac{\partial}{\partial x}\left(\frac{x}{l}\right)^p\right\}_{x=0}^{x=l}-\left\{[\text{T.F.}]\left(\frac{x}{l}\right)^p\right\}_{x=x_o^-}^{x=x_o^+}=0$$

for each p (11)

where [G.E.], [T.F.], [B.F.], and [B.M.] represent the residues due to the governing equations, the transition conditions, the boundary shearing forces, and bending moments, respectively. Going through a series of laborious manipulations, the above equation yields a set of differential equations in time for the discretized system, i.e.,

$$\rho[M]\ddot{\mathbf{a}}+(c[C]+2\rho\Omega[G])\dot{\mathbf{a}}+\left(\rho\dot{\Omega}[G]+\frac{E_zI_z}{l^4}[K_e]+k\Omega[K_b]+\rho\Omega^2[K_r]\right)\mathbf{a}=0 \quad (12)$$

where $[C]$ and $[G]$ are the damping and the gyroscopic matrices, respectively; $[M]$, $[K_e]$, and $[K_b]$ are the mass matrix and the elastic stiffness matrices of the shaft and the bearings, respectively; $[K_r]$ is the rotating stiffness matrix; $\mathbf{a}$ is a column matrix formed by the undetermined functions a_m and b_n. c and k are constants characterizing the properties of the bearings. Note that the matrix $[C]$ is symmetric, while the matrix $[G]$ is skew-symmetric. The bearing stiffness matrix $[K_b]$ can be decomposed into a symmetric one $[K_b^s]$ and a skew-symmetric one $[K_b^a]$. Assuming that the spin rate can be characterized as a small periodic perturbation $f(t)$ superimposed on the constant rate Ω_o, i.e., $\Omega=\Omega_o+f(t)$, the above equation can be rewritten as

$$\mu^2\{[M]\ddot{\mathbf{a}}+2(\alpha\Omega_o[C]+\Omega_o[G])\dot{\mathbf{a}}\}+\left([K_e]+\frac{k\Omega_o}{\rho}\mu^2[K_b]+\Omega_o^2\mu^2[K_r]\right)\mathbf{a}=-\mu^2\left\{2f[G]\dot{\mathbf{a}}+\dot{f}[G]\mathbf{a}+(2\Omega_o f+f^2)[K_r]\mathbf{a}+\frac{kf}{\rho}[K_b]\mathbf{a}\right\} \quad (13)$$

where $\alpha=\dfrac{c}{2\rho\Omega_o}$ and $\mu=\sqrt{\dfrac{\rho l^4}{E_z I_z}}$.

Equation (13) is a set of simultaneous second-order differential equations. To improve the solvability of the equation and the accuracy of the solution, a modal analysis procedure is utilized to render at least the left-hand side of the equation uncoupled. The modal analysis procedure for a gyroscopic system is different from that for a nongyroscopic system. The procedure used here is based on the method proposed by Meirovitch (1975). First, define a state vector $\mathbf{q}=[\mu\dot{\mathbf{a}},\ \mathbf{a}]^T$, and rewrite the equations of motion as

$$\mu\begin{bmatrix}[M] & [0]\\ [0] & [K_l]\end{bmatrix}\dot{\mathbf{q}}+\left(2\alpha\begin{bmatrix}\mu\Omega_o[C] & [0]\\ [0] & [0]\end{bmatrix}+\begin{bmatrix}2\Omega_o\mu[G] & [K_l]\\ -[K_l] & [0]\end{bmatrix}\right)\mathbf{q}=-\left\{2\frac{f}{\Omega_o}\begin{bmatrix}\Omega_o\mu[G] & [0]\\ [0] & [0]\end{bmatrix}+\frac{\dot{f}}{\Omega_o^2}\begin{bmatrix}[0] & \Omega_o^2\mu^2[G]\\ [0] & [0]\end{bmatrix}+\left(2\frac{f}{\Omega_o}+\frac{f^2}{\Omega_o^2}\right)\begin{bmatrix}[0] & \Omega_o^2\mu^2[K_r]\\ [0] & [0]\end{bmatrix}+\frac{f}{\Omega_o}\begin{bmatrix}[0] & \gamma\Omega_o\mu[K_b^s]\\ [0] & [0]\end{bmatrix}\right\}\mathbf{q}+\left(1+\frac{f}{\Omega_o}\right)\begin{bmatrix}[0] & \gamma\Omega_o\mu[K_b^a]\\ [0] & [0]\end{bmatrix}\mathbf{q} \quad (14)$$

where the matrix $[K_l]=[K_e]+\gamma\Omega_o\mu[K_b^s]+\Omega_o^2\mu^2[K_r]$, and $\gamma=k\mu/\rho$. Next, solve the eigenvalue problem of the corresponding free, undamped gyroscopic system to have the natural frequency ω and the modal vector $\mathbf{x}$. Note that the modal vectors of the problem are in conjugate pairs of complex vectors, i.e., $\mathbf{x}=\mathbf{y}+i\mathbf{z}$.

Now introduce a linear transformation $\mathbf{q}=[P]\zeta$, where $[P]$ is formed by the real and imaginary parts of the normalized eigenvectors. Substituting this transformation into Eq. (14) and premultiplying $[P]^T$ (the transpose of $[P]$) by this equation, using the orthogonality of the modal vectors, yields

$$\mu[I]\dot{\zeta}+[\Lambda]\zeta=-\left\{2\alpha[C^*]+2\frac{f}{\Omega_o}[G^*]+\frac{\dot{f}}{\Omega_o^2}[H^*]+\left(2\frac{f}{\Omega_o}+\frac{f^2}{\Omega_o^2}\right)[K_r^*]+\frac{f}{\Omega_o}[K_s^*]+\left(1+\frac{f}{\Omega_o}\right)[K_a^*]\right\}\zeta \quad (15)$$

where $[I]$ is an identity matrix, and $[\Lambda]$ is a block-diagonal matrix of the form

$$[\Lambda]=\text{diag.}\begin{bmatrix}0 & -\mu\omega_r\\ \mu\omega_r & 0\end{bmatrix}.$$

The other matrices are defined by

$$[G^*]=[P]^T\begin{bmatrix}\Omega_o\mu[G] & [0]\\ [0] & [0]\end{bmatrix}[P],\quad [H^*]=[P]^T\begin{bmatrix}[0] & \Omega_o^2\mu^2[G]\\ [0] & [0]\end{bmatrix}[P],$$

$$[K_r^*]=[P]^T\begin{bmatrix}[0] & \Omega_o^2\mu^2[K_r]\\ [0] & [0]\end{bmatrix}[P],\quad [C^*]=[P]^T\begin{bmatrix}\mu\Omega_o[C] & [0]\\ [0] & [0]\end{bmatrix}[P],$$

$$[K_s^*]=[P]^T\begin{bmatrix}[0] & \gamma\Omega_o\mu[K_b^s]\\ [0] & [0]\end{bmatrix}[P],\quad [K_a^*]=[P]^T\begin{bmatrix}[0] & \gamma\Omega_o\mu[K_b^a]\\ [0] & [0]\end{bmatrix}[P].$$

Note that $[C^*]$ is again a symmetric matrix since $[C]$ is symmetric, and $[G^*]$ is again skew-symmetric since $[G]$ is skew-symmetric. The terms on the left-hand side of the above equation are uncoupled in a block sense; however, those on the right-hand side are still coupled together. To match the form of the matrix $[\Lambda]$, the matrices on the right-hand side are partitioned into $R\times R$ pieces of 2×2 block, where $R=M+N+2$ is the total number of degrees of freedom of the discrete system. If the temporal variable is changed such that the differential equations are in terms of the dimensionless variable $\tau=\Omega_o t$, the above equation can be written as

$$\begin{aligned}\xi_n'-\hat{\omega}_n\eta_n=&-2\alpha\left(\sum_{r=1}^{R}c_{nr}^{11}\xi_r+\sum_{r=1}^{R}c_{nr}^{12}\eta_r\right)-2\frac{f}{\Omega_o}\left(\sum_{r=1}^{R}g_{nr}^{11}\xi_r+\sum_{r=1}^{R}g_{nr}^{12}\eta_r\right)-\frac{f'}{\Omega_o}\left(\sum_{r=1}^{R}h_{nr}^{11}\xi_r+\sum_{r=1}^{R}h_{nr}^{12}\eta_r\right)\\&-\left(2\frac{f}{\Omega_o}+\frac{f^2}{\Omega_o^2}\right)\left(\sum_{r=1}^{R}k_{nr}^{11}\xi_r+\sum_{r=1}^{R}k_{nr}^{12}\eta_r\right)-\frac{f}{\Omega_o}\left(\sum_{r=1}^{R}s_{nr}^{11}\xi_r+\sum_{r=1}^{R}s_{nr}^{12}\eta_r\right)\\&-\left(1+\frac{f}{\Omega_o}\right)\left(\sum_{r=1}^{R}d_{nr}^{11}\xi_r+\sum_{r=1}^{R}d_{nr}^{12}\eta_r\right)\end{aligned}$$

$$\begin{aligned}\eta_n'+\hat{\omega}_n\xi_n=&-2\alpha\left(\sum_{r=1}^{R}c_{nr}^{21}\xi_r+\sum_{r=1}^{R}c_{nr}^{22}\eta_r\right)-2\frac{f}{\Omega_o}\left(\sum_{r=1}^{R}g_{nr}^{21}\xi_r+\sum_{r=1}^{R}g_{nr}^{22}\eta_r\right)-\frac{f'}{\Omega_o}\left(\sum_{r=1}^{R}h_{nr}^{21}\xi_r+\sum_{r=1}^{R}h_{nr}^{22}\eta_r\right)\\&-\left(2\frac{f}{\Omega_o}+\frac{f^2}{\Omega_o^2}\right)\left(\sum_{r=1}^{R}k_{nr}^{21}\xi_r+\sum_{r=1}^{R}k_{nr}^{22}\eta_r\right)-\frac{f}{\Omega_o}\left(\sum_{r=1}^{R}s_{nr}^{21}\xi_r+\sum_{r=1}^{R}s_{nr}^{22}\eta_r\right)\\&-\left(1+\frac{f}{\Omega_o}\right)\left(\sum_{r=1}^{R}d_{nr}^{21}\xi_r+\sum_{r=1}^{R}d_{nr}^{22}\eta_r\right)\end{aligned}$$

$$n=1,\ 2,\ \ldots,\ R \quad (16)$$

where c_{nr}^{ij}, g_{nr}^{ij}, h_{nr}^{ij}, k_{nr}^{ij}, s_{nr}^{ij}, and d_{nr}^{ij} are the $(i-j)$th entries of the $(n-r)$th block matrices of $[C^*]$, $[G^*]$, $[H^*]$, $[K_r^*]$, $[K_s^*]$, and $[K_a^*]$ divided by $\mu\Omega_o$, respectively; ξ_n and η_n are the $(2n-1)$th and $2n$th entries of ζ; "$'$" denotes a differentiation with respect to τ, and $\hat{\omega}=\omega/\Omega_o$. The above equation represents a set of partially uncoupled equations of motion of the discrete system and is the one we will deal with hereafter.

Perturbation Analysis

In this paper, the angular-speed perturbation f is assumed to be periodic. Therefore, it can be expressed in a Fourier series of the form

$$f(t)=\sum_{j=-J}^{J}f_j e^{ij\beta t} \quad (17)$$

where β is called the perturbation frequency, and $i=\sqrt{-1}$. Since the perturbation function f is small compared to the steady-state rate Ω_o, the magnitude of each Fourier coefficient f_j is also small compared to Ω_o. Therefore, the small parameter ϵ appearing in the perturbation technique is defined as $\epsilon=|f_J|/\Omega_o$ in this work, and Eq. (16) can be written as

$$\begin{aligned}\xi_n'-\hat{\omega}_n\eta_n=&-2\alpha\left[\sum_{r=1}^{R}c_{nr}^{11}\xi_r+\sum_{r=1}^{R}c_{nr}^{12}\eta_r\right]-(2\epsilon\tilde{f}+\epsilon^2\tilde{f}^2)\left[\sum_{r=1}^{R}k_{nr}^{11}\xi_r+\sum_{r=1}^{R}k_{nr}^{12}\eta_r\right]-2\epsilon\tilde{f}\left[\sum_{r=1}^{R}g_{nr}^{11}\xi_r+\sum_{r=1}^{R}g_{nr}^{12}\eta_r\right]\\&-i\epsilon\sum_{j=-J}^{J}\hat{\beta}_j\tilde{f}_j e^{i\beta_j\tau}\left[\sum_{r=1}^{R}h_{nr}^{11}\xi_r+\sum_{r=1}^{R}h_{nr}^{12}\eta_r\right]-\epsilon\tilde{f}\left[\sum_{r=1}^{R}s_{nr}^{11}\xi_r+\sum_{r=1}^{R}s_{nr}^{12}\eta_r\right]-(1+\epsilon\tilde{f})\left[\sum_{r=1}^{R}d_{nr}^{11}\xi_r+\sum_{r=1}^{R}d_{nr}^{12}\eta_r\right]\end{aligned}$$

$$\dot{\eta}_n + \hat{\omega}_n \xi_n = -2\alpha\left[\sum_{r=1}^{R} c_{nr}^{21}\xi_r + \sum_{r=1}^{R} c_{nr}^{22}\eta_r\right] - (2\epsilon\tilde{f} + \epsilon^2\tilde{f}^2)\left[\sum_{r=1}^{R} k_{nr}^{21}\xi_r + \sum_{r=1}^{R} k_{nr}^{22}\eta_r\right] - 2\epsilon\tilde{f}\left[\sum_{r=1}^{R} g_{nr}^{21}\xi_r + \sum_{r=1}^{R} g_{nr}^{22}\eta_r\right] - i\epsilon\sum_{j=-J}^{J}\hat{\beta}_j\tilde{f}_j e^{i\hat{\beta}_j\tau}\left[\sum_{r=1}^{R} h_{nr}^{21}\xi_r + \sum_{r=1}^{R} h_{nr}^{22}\eta_r\right] - \epsilon\tilde{f}\left[\sum_{r=1}^{R} s_{nr}^{21}\xi_r + \sum_{r=1}^{R} s_{nr}^{22}\eta_r\right] - (1+\epsilon\tilde{f})\left[\sum_{r=1}^{R} d_{nr}^{21}\xi_r + \sum_{r=1}^{R} d_{nr}^{22}\eta_r\right]$$

$$n = 1, 2, \ldots, R \tag{18}$$

where $\hat{\beta}_j = j\beta/\Omega_o$, and $\tilde{f} = f/|f_J|$.

In the present work, the method of multiple scales is used to find the solution of Eq. (18). One begins by introducing new independent variables $T_j = \epsilon^j \tau$, $j = 0, 1, 2, \ldots$ It follows that the derivatives with respect to τ become expansions in terms of the partial derivatives with respect to T_j (Nayfeh and Mook, 1979). It is assumed that the solution of Eq. (18) can be represented by a uniformly valid expansion having the form

$$\begin{aligned}\xi_n(\tau, \epsilon) &= \xi_{n0}(T_0, T_1, T_2\ldots) + \epsilon\xi_{n1}(T_0, T_1, T_2\ldots) + \ldots \\ \eta_n(\tau, \epsilon) &= \eta_{n0}(T_0, T_1, T_2\ldots) + \epsilon\eta_{n1}(T_0, T_1, T_2\ldots) + \ldots\end{aligned} \tag{19}$$

Due to the complexity of the problem, the expansion is carried out to the order of ϵ^2. Therefore, only T_0 and T_1 are needed. Substituting Eq. (19) into Eq. (18) and equating the coefficients of like power of ϵ yields the following equations:

Order 1:

$$\begin{aligned} D_0\xi_{n0} - \hat{\omega}_n\eta_{n0} &= 0 \\ D_0\eta_{n0} + \hat{\omega}_n\xi_{n0} &= 0\end{aligned} \tag{1}$$

Order ϵ:

$$D_0\xi_{n1} - \hat{\omega}_n\eta_{n1} = -D_1\xi_{n0} - 2\tilde{\alpha}\left[\sum_{r=1}^{R} c_{nr}^{11}\xi_{r0} + \sum_{r=1}^{R} c_{nr}^{12}\eta_{r0}\right] - 2\tilde{f}\left[\sum_{r=1}^{R} \tilde{k}_{nr}^{11}\xi_{r0} + \sum_{r=1}^{R} \tilde{k}_{nr}^{12}\eta_{r0}\right] - 2\tilde{f}\left[\sum_{r=1}^{R} g_{nr}^{11}\xi_{r0} + \sum_{r=1}^{R} g_{nr}^{12}\eta_{r0}\right] - i\sum_{j=-J}^{J}\hat{\beta}_j\tilde{f}_j e^{i\hat{\beta}_j\tau}\left[\sum_{r=1}^{R} h_{nr}^{11}\xi_{r0} + \sum_{r=1}^{R} h_{nr}^{12}\eta_{r0}\right] - \left[\sum_{r=1}^{R} \tilde{d}_{nr}^{11}\xi_{r0} + \sum_{r=1}^{R} \tilde{d}_{nr}^{12}\eta_{r0}\right]$$

$$D_0\eta_{n1} + \hat{\omega}_n\xi_{n1} = -D_1\eta_{n0} - 2\tilde{\alpha}\left[\sum_{r=1}^{R} c_{nr}^{21}\xi_{r0} + \sum_{r=1}^{R} c_{nr}^{22}\eta_{r0}\right] - 2\tilde{f}\left[\sum_{r=1}^{R} \tilde{k}_{nr}^{21}\xi_{r0} + \sum_{r=1}^{R} \tilde{k}_{nr}^{22}\eta_{r0}\right] - 2\tilde{f}\left[\sum_{r=1}^{R} g_{nr}^{21}\xi_{r0} + \sum_{r=1}^{R} g_{nr}^{22}\eta_{r0}\right] - i\sum_{j=-J}^{J}\hat{\beta}_j\tilde{f}_j e^{i\hat{\beta}_j\tau}\left[\sum_{r=1}^{R} h_{nr}^{21}\xi_{r0} + \sum_{r=1}^{R} h_{nr}^{22}\eta_{r0}\right] - \left[\sum_{r=1}^{R} \tilde{d}_{nr}^{21}\xi_{r0} + \sum_{r=1}^{R} \tilde{d}_{nr}^{22}\eta_{r0}\right] \tag{21}$$

where $\tilde{k}_{nr}^{ij} = k_{nr}^{ij} + 1/2 s_{nr}^{ij}$. In the above equations, $\alpha = \epsilon\tilde{\alpha}$ is assumed so that the damping term will appear in the same order as the first nonautonomous term, and $d_{nr}^{ij} = \epsilon\tilde{d}_{nr}^{ij}$ are set in order that the first term of the skew-symmetric part of the bearing stiffness appears in the same order with the damping term.

Equations (20) and (21) have similar forms to Eqs. (20) and (21) in the paper by Young and Liou (1992). Therefore, the solutions of these equations can directly be written as follows:

I The Case of $\hat{\beta}_j$ *Away From* $\hat{\omega}_p \pm \hat{\omega}_q$. In this case, the amplitude of ξ_{n1} is

$$A_n = a_n \exp\left[-\tilde{\alpha}(c_{nn}^{11} + c_{nn}^{22}) - \frac{1}{2}(\tilde{d}_{nn}^{11} + \tilde{d}_{nn}^{22})\right]T_1 \tag{22}$$

where a_n is a constant. Note that $c_{nn}^{12} = c_{nn}^{21}$ because of the symmetry of matrix $[C]$, and $\tilde{d}_{nn}^{12} = \tilde{d}_{nn}^{21} = 0$ is observed during the course of numerical computation. Therefore, A_n will decay with time, and hence the system is always stable if

$$\tilde{\alpha}(c_{nn}^{11} + c_{nn}^{22}) + \frac{1}{2}(\tilde{d}_{nn}^{11} + \tilde{d}_{nn}^{22}) \geq 0 \tag{23}$$

Otherwise, the system is unstable. The above inequality can be used to construct the stability boundary for the rotor-bearing system with constant spin rates.

II The Case of $\hat{\beta}_j$ *Near* $\hat{\omega}_p + \hat{\omega}_q$. In the presence of damping, the transition curves are defined by

$$\hat{\beta}_j = \hat{\omega}_p + \hat{\omega}_q \pm \epsilon(c_p + c_q)\left\{\frac{\Lambda_{pq}\bar{\Lambda}_{qp}}{c_p c_q} - 1\right\}^{1/2} + O(\epsilon^2) \tag{24}$$

where

$$c_p = \tilde{\alpha}(c_{pp}^{11} + c_{pp}^{22}) + \frac{1}{2}(\tilde{d}_{pp}^{11} + \tilde{d}_{pp}^{22}),\quad c_q = \tilde{\alpha}(c_{qq}^{11} + c_{qq}^{22}) + \frac{1}{2}(\tilde{d}_{qq}^{11} + \tilde{d}_{qq}^{22})$$

and

$$\Lambda_{pq} = \sum_{j=1}^{J}\left\{\left[-ik_{pq}^{21} - k_{pq}^{22} - ig_{pq}^{21} - g_{pq}^{22} + \frac{1}{2}\hat{\beta}_j h_{pq}^{21} - \frac{i}{2}\hat{\beta}_j h_{pq}^{22}\right] - \left[-k_{pq}^{11} + ik_{pq}^{12} - g_{pq}^{11} + ig_{pq}^{12} - \frac{i}{2}\hat{\beta}_j h_{pq}^{11} - \frac{1}{2}\hat{\beta}_j h_{pq}^{12}\right]\right\}\tilde{f}_j$$

$$\bar{\Lambda}_{qp} = \sum_{j=1}^{J}\left\{\left[ik_{qp}^{21} - k_{qp}^{22} + ig_{qp}^{21} - g_{qp}^{22} + \frac{1}{2}\hat{\beta}_j h_{qp}^{21} - \frac{i}{2}\hat{\beta}_j h_{qp}^{22}\right] - \left[-k_{qp}^{11} - ik_{qp}^{12} - g_{qp}^{11} - ig_{qp}^{12} - \frac{i}{2}\hat{\beta}_j h_{qp}^{11} - \frac{1}{2}\hat{\beta}_j h_{qp}^{12}\right]\right\}\tilde{f}_j \tag{25}$$

In the above equation, Λ_{pq} and Λ_{qp} are either real or pure imaginary simultaneously. Therefore, transition curves exist if Λ_{pq} and $\bar{\Lambda}_{qp}$ have the same sign when they are real, and the opposite sign when they are pure imaginary.

III The Case of $\hat{\beta}_j$ *Near* $\hat{\omega}_p - \hat{\omega}_q$. In this case, the transition curves are found to be

$$\hat{\beta}_j = \hat{\omega}_p - \hat{\omega}_q \pm \epsilon(c_p + c_q)\left\{\frac{\Lambda_{pq}\Lambda_{qp}}{c_p c_q} - 1\right\}^{1/2} + O(\epsilon^2) \tag{26}$$

where c_p and c_q are defined as stated above, and

$$\Lambda_{pq} = \sum_{j=1}^{J}\left\{\left[-ik_{pq}^{21} + k_{pq}^{22} - ig_{pq}^{21} + g_{pq}^{22} + \frac{1}{2}\hat{\beta}_j h_{pq}^{21} + \frac{i}{2}\hat{\beta}_j h_{pq}^{22}\right] - \left[-k_{pq}^{11} - ik_{pq}^{12} - g_{pq}^{11} - ig_{pq}^{12} - \frac{i}{2}\hat{\beta}_j h_{pq}^{11} + \frac{1}{2}\hat{\beta}_j h_{pq}^{12}\right]\right\}\tilde{f}_j$$

$$\Lambda_{qp} = \sum_{j=1}^{J}\left\{\left[-ik_{qp}^{21} + k_{qp}^{22} - ig_{qp}^{21} + g_{qp}^{22} + \frac{1}{2}\hat{\beta}_j h_{qp}^{21} + \frac{i}{2}\hat{\beta}_j h_{qp}^{22}\right] - \left[-k_{qp}^{11} - ik_{qp}^{12} - g_{qp}^{11} - ig_{qp}^{12} - \frac{i}{2}\hat{\beta}_j h_{qp}^{11} + \frac{1}{2}\hat{\beta}_j h_{qp}^{12}\right]\right\}\tilde{f}_j \tag{27}$$

Again Λ_{pq} and Λ_{qp} are either real or pure imaginary simultaneously. The transition curves exist if Λ_{pq} and Λ_{qp} have the same sign when they are real, and the opposite sign when they are pure imaginary.

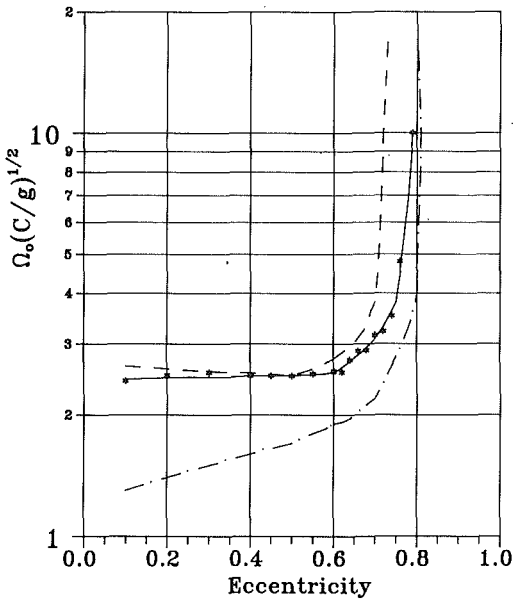

Fig. 2 Stability map of a rigid rotor on a pair of cavitated journal bearings with constants spin rates: —·—: Reddi and Trumpler; - - -: Kirk and Gunter; ——: present work

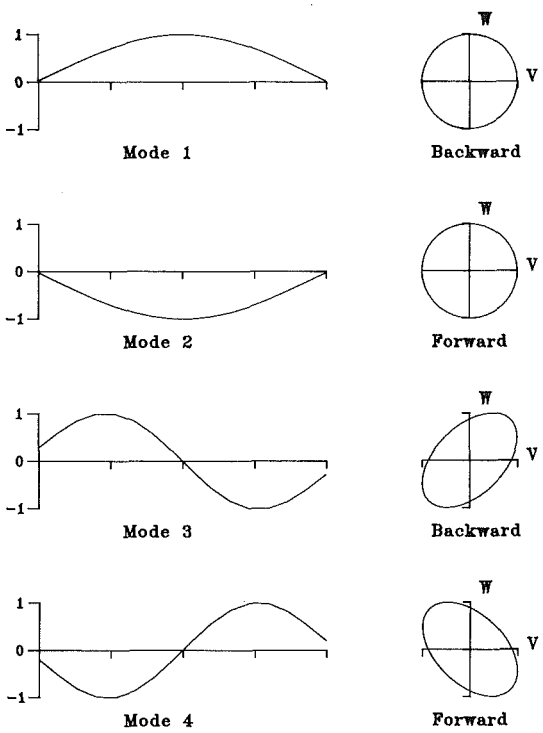

Fig. 3 Mode shapes of a rotor-bearing system spinning at a constant rate with $M/\rho l = 1.0$, $x_o/l = 0.5$, $kl^3/EI\sqrt{C/g} = 200$, and $\Omega_o\sqrt{C/g} = 1.5$

Numerical Results and Discussions

Before presenting the results of this study, a comparison with those in the existing literature is made. Figure 2 shows the stability map of a rigid rotor on a pair of cavitated journal bearings with constant spin rates. The stiffness and damping coefficients of the bearings are determined from the work by Kirk and Gunter (1976). By using only the first two trial functions in the Galerkin method, the displacements represent a rigid-body motion. The result of the present work, which is obtained by Eq. (23), is compared with the results by Kirk and Gunter (1976) and Reddi and Trumpler (1962). In this figure, the region above the stability boundary is stable. It is found

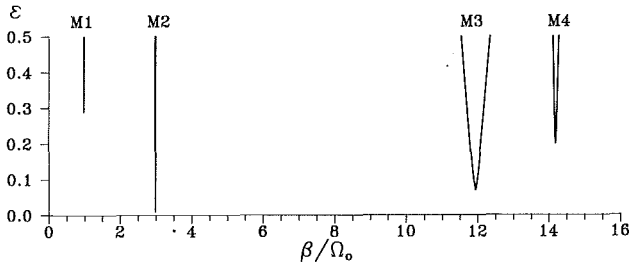

Fig. 4 Transition curves of a rotor-bearing system with $M/\rho l = 1.0$, $x_o/l = 0.5$, $kl^3/EI\sqrt{C/g} = 200$, $\Omega_o\sqrt{C/g} = 1.5$, and $\alpha = 0.1$; $M1$ = first main resonance; $M2$ = second main resonance; $M3$ = third main resonance; $M4$ = fourth main resonance

that the result obtained by the authors lies between these two existing results. During the course of this study, it is also observed that the stability boundary of a flexible rotor with constant spin rates will be lower and much more complicated.

From now on, we will deal with flexible rotors supported by a pair of journal bearings, whose stiffness and damping coefficients are assumed as follows:

$$\begin{pmatrix} k_{xx} & k_{xy} \\ k_{yx} & k_{yy} \end{pmatrix} = k\Omega \begin{pmatrix} 3 & 1.3 \\ -6 & 4.5 \end{pmatrix}, \quad \begin{pmatrix} c_{xx} & c_{xy} \\ c_{yx} & c_{yy} \end{pmatrix} = c \begin{pmatrix} 5 & -3.5 \\ -3.5 & 10 \end{pmatrix},$$

which corresponds to an eccentricity $e = 0.5$, according to Kirk and Gunter (1976). In addition, the shaft is assumed to be isotropic, i.e., $E_y I_y = E_z I_z = EI$. Figure 3 presents the first four mode shapes of a rotor-bearing system with a constant spin rate. Here only the symmetric part of the bearing stiffness matrix is included. The parameters used in this figure are $M/\rho l = 1.0$, $x_o/l = 0.5$, $(kl^3/EI)\sqrt{C/g} = 200$, and $\Omega_o\sqrt{C/g} = 1.5$, where C is the clearance of the bearing, and g is the gravitational acceleration. Eight terms are used for each assumed displacement throughout this work. Due to the effect of unequal bearing stiffness in the transverse directions, the locus of the shaft becomes an ellipse instead of a circle; due to the Coriolis effect, each mode of the corresponding static system divides into two modes in the spinning system. One is called the forward mode with the whirling direction the same as the spin direction, while the other is called the backward mode with the whirling direction opposite to the spin direction. The first two modes are symmetric with respect to the midspan of the shaft, while the third and fourth modes are antisymmetric.

As an example of the application of the general solutions, the perturbation of the spin rate is taken as $f(t) = F\cos\beta t$, where F is assumed to be small compared to Ω_o. If the small parameter ϵ is defined as $\epsilon = F/\Omega_o$, the function f is given by the Fourier series $f = 1/2(e^{i\bar{\beta}_1\tau} + e^{-i\bar{\beta}_1\tau})$ with Fourier coefficients $f_{-1} = f_1 = 1/2$. The transition curves of a rotor-bearing system with the nonconstant spin rate are depicted in Fig. 4. In this figure, the damping factor $c/2\rho\Omega_o$ is 0.1, while the other parameters are the same as those used in Fig. 3. The figure reveals that the unstable regions corresponding to the first two main resonances are very small in comparison with the third and forth ones. The unstable regions for higher modes are even larger, but the higher modes are generally less important because their frequencies are much higher beyond the normal operating frequencies. In addition, unstable regions corresponding to the backward modes are larger than those of the corresponding forward modes except for the first two modes. The reason may be attributed to the following: From Eqs. (24)–(27), the size of the unstable region is decided by the entries of the Coriolis, rotating stiffness, and bearing stiffness matrices, and the effects of rotating stiffness bearing stiffness are opposite. In the course of the numerical studies, the effects of the rotating stiffness and the symmetric part of the bearing stiffness on the stability of the system are approximately of equal importance at the first two modes, and the latter is found to be dominant at higher modes. Moreover, the effect of this

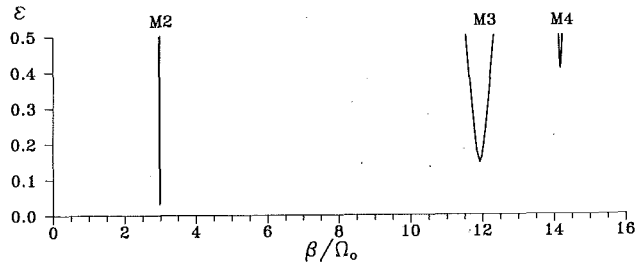

Fig. 5 Transition curves of a rotor-bearing system with $M/\rho l = 1.0$, $x_o/l = 0.5$, $kl^3/EI\sqrt{C/g} = 200$, $\Omega_o\sqrt{C/g} = 1.5$, and $\alpha = 0.2$; $M1$ = first main resonance; $M2$ = second main resonance; $M3$ = third main resonance; $M4$ = fourth main resonance

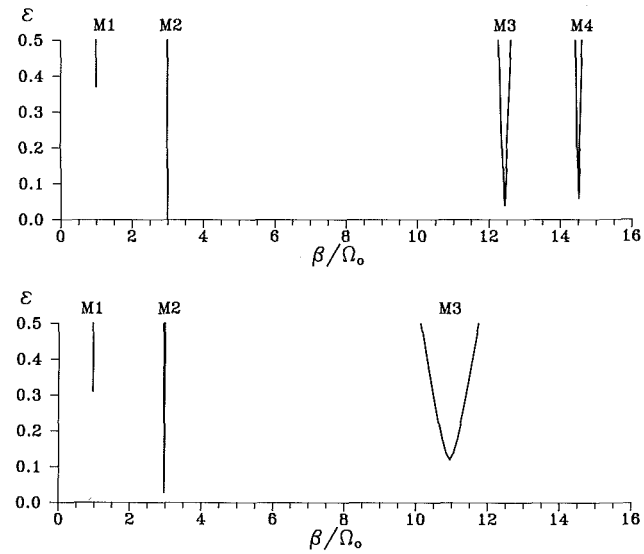

Fig. 6 The effect of the bearing-to-shaft stiffness ratio on the transition curves of a rotor-bearing system with $M/\rho l$ 1.0, $x_o/l = 0.5$, $\Omega_o\sqrt{C/g} = 1.5$, and $\alpha = 0.1$: (*a*) $kl^3/EI\sqrt{C/g} = 400$; (*b*) $kl^3/EI\sqrt{C/g} = 100$; $M1$ = first main resonance; $M2$ = second main resonance; $M3$ = third main resonance; $M4$ = fourth main resonance

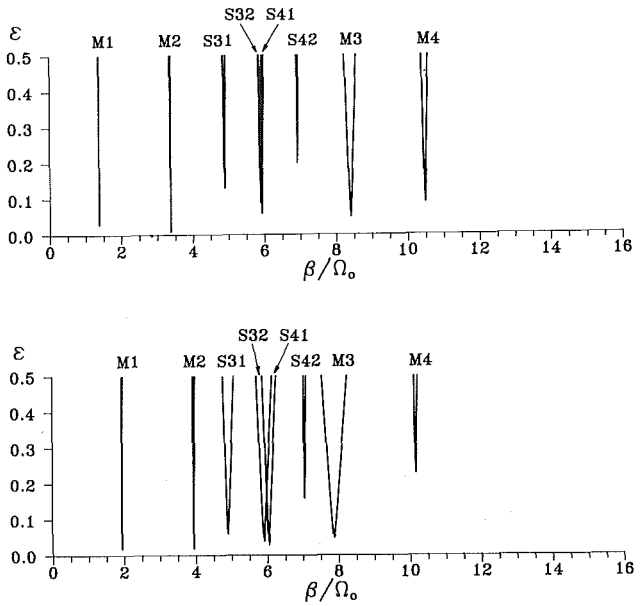

Fig. 7 Effect of the disk location on the transition curves of a rotor-bearing system with $M/\rho l = 1.0$, $kl^3/EI\sqrt{C/g} = 200$, $\Omega_o\sqrt{C/g} = 1.5$, and $\alpha = 0.1$: (*a*) $x_o/l = 0.25$; (*b*) $x_o/l = 0.125$; $M1$ = first main resonance; $M2$ = second main resonance; $M3$ = third main resonance; $M4$ = fourth main resonance; $S31$ = summed-type resonance near $\omega_1 + \omega_3$; $S32$ = summed-type resonance near $\omega_2 + \omega_3$; $S41$ = summed-type resonance near $\omega_1 + \omega_4$; $S42$ = summed-type resonance near $\omega_2 + \omega_4$

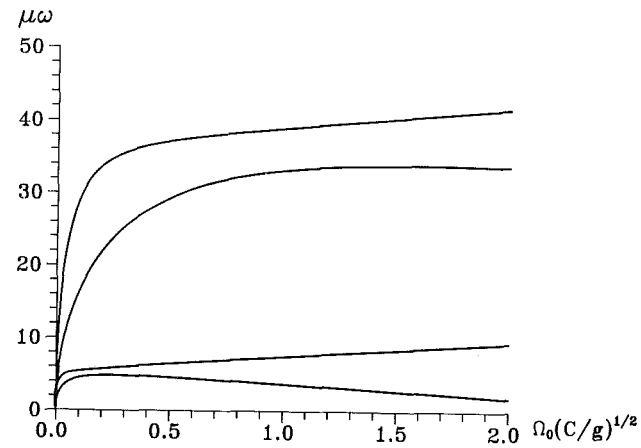

Fig. 8 The natural frequencies of the rotor-bearing system versus the steady-state spin rate; $M/\rho l = 1.0$, $x_o/l = 0.5$, $kl^3/EI\sqrt{C/g} = 200$

dominant factor is increasing for higher modes and is larger for backward modes.

The effect of bearing damping on the changes of the boundaries of unstable regions is illustrated in Fig. 5. Here the damping factor is 0.2, while all the other parameters remain the same as those used in the previous figure. Comparing with Fig. 4, it is found that an increase in bearing damping causes all the unstable regions to shrink upward. Consequently, the effect of bearing damping is stabilizing.

The effect of the bearing-to-shaft stiffness ratio on the stability of the rotor-bearing system discussed above is shown in Fig. 6. An increase in the bearing stiffness makes the support more rigid, and hence raises all the natural frequencies of the system. Moreover, an increase in this ratio makes the entries of all the matrices involved in the stability analysis, i.e., $[C^*]$, $[G^*]$, $[H^*]$, $[K_r^*]$, $[K_s^*]$, and $[K_a^*]$, smaller. The smaller s_{nr}^{ij} are, the narrower the unstable regions are; the smaller c_{nr}^{ij} are, the lower the unstable regions are. Therefore, an increase in this ratio generally causes the unstable regions to shift toward a higher frequency range, to narrow in size and to lower in position, as shown in the figure. In addition, the effect is more profound at higher modes than at lower modes.

The effect of the disk location on the unstable regions of the rotor-bearing system studied in Fig. 4 with the same nonconstant spin rate is shown in Fig. 7. Since the disk is not located at the middle, none of the modes possess a symmetric property. Moreover, since the shapes of the third and fourth modes resemble more and more those of the first and the second modes as the disk location moves closer to the end, a summed type of combination resonance occurs between these modes, and the size of these unstable regions becomes larger as the disk location gets closer to the end. As to the effect of the disk location on the unstable regions corresponding to the main resonances, no evident trend is observed. The effect of the disk mass on the stability of the rotor-bearing system is found to be insignificant at any location if the disk mass is of the same order as that of the shaft.

Figure 8 presents the first four natural frequencies of the abovementioned rotor-bearing system versus the steady-state spin rate. Again only the symmetric part of the bearing stiffness matrix is included, and all the other parameters used are the same as those used in Fig. 3. When the system is static, the first two modes are the rigid-body modes since the bearing stiffness coefficients are zeros at zero spin rate. As the spin rate begins to increase, each mode of the static system divides into forward and backward modes, and the frequencies of these two modes separate farther away with increasing spin rates due to the Coriolis effect. Figure 9 depicts the effect of the steady-state spin rate on the stability of the same rotor-

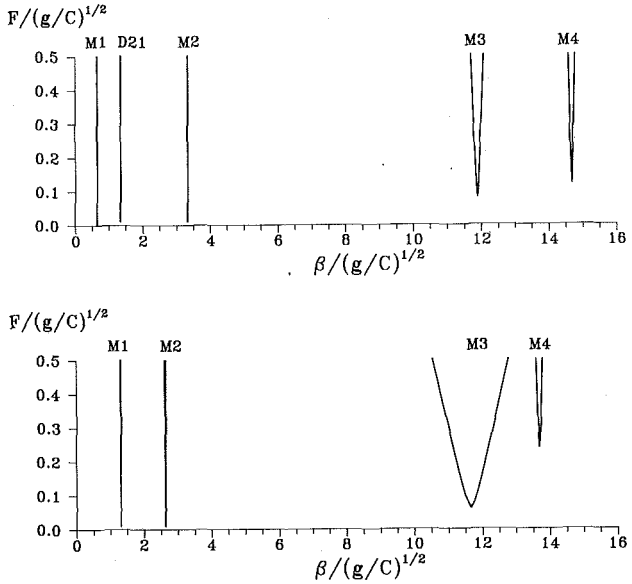

Fig. 9 The effect of the steady-state spin rate on the transition curves of a rotor-bearing system with $M/\rho l = 1.0$, $x_o/l = 0.5$, $kl^3/EI\sqrt{C/g} = 200$, and $\alpha = 0.1$: (a) $\Omega_o l\sqrt{g/C} = 2.0$; (b) $\Omega_o l\sqrt{g/C} = 1.0$; $M1$ = first main resonance; $M2$ = second main resonance; $M3$ = third main resonance; $M4$ = fourth main resonance; $D21$ = difference-type resonance near $\omega_2 - \omega_1$

bearing system. To have a justified basis, the units of the coordinate axes are changed to $F/\sqrt{g/C}$ and $\beta/\sqrt{g/C}$, which are independent of the spin rate. An increase in this rate makes the unstable regions corresponding to the forward modes larger and those of the backward modes smaller, and it brings about the different type of resonance between the first two modes, which belong to the same class of symmetry, due to an increase in the Coriolis effect. The fact that an increase in the steady-state spin rate will raise the natural frequencies of the forward modes and enlarge the size of the unstable regions agrees with the result already observed by the authors (Young and Liou, 1992).

For a different value of eccentricity, which will result in different values of bearing stiffness and damping coefficients, similar phenomena already shown in this work are again observed. If the bearing stiffness coefficients are independent of the spin rate, such as roller bearings, all the unstable regions of the rotor-bearing system will be very small.

Conclusions

A study of the vibration of a rotor-bearing system with time-dependent spin rate has been presented in this paper. In this study, parametric main resonances and combination resonances were shown to arise in the nonresonant solutions as a result of the time dependence of the spin rate. Resonant solutions were then derived from which the expressions for the boundaries of the unstable regions were obtained. Due to the complexity of the problem, only the first-order solutions were presented, and a simple perturbation function $f(t) = F\cos\beta t$ was considered to demonstrate the general solutions numerically. However, solutions for more general periodic functions can be generated easily.

Based on the assumptions made in this work, the following conclusions can be drawn from the above numerical results:

1 The stability of the rotor-bearing system with constant spin rates is determined by the skew-symmetric part of the bearing stiffness, while it is dominated by the symmetric part of the bearing stiffness for the system with nonconstant spin rates.

2 The unstable regions become larger for higher modes, and the unstable regions corresponding to the backward modes are larger than those of the corresponding forward modes except for the first two modes.

3 If the system preserves geometric symmetry, the mode shapes of the system will have the symmetric class, and combination resonances may bring about between the modes belonging to the same class of symmetry. Otherwise, they may exist between neighboring modes, and the size of the combination resonances depends on the similarity of the shapes of the modes involved in the resonances.

4 An increase in the steady-state spin rate will make the unstable regions corresponding to the forward modes larger in size and those of the backward modes smaller.

5 The effect of bearing damping is stabilizing.

References

Akella, S., and Craggs, A., 1986, "Modifications to a Timoshenko Beam-Shaft Finite Element to Include Internal Disks and Changes in Cross-Section," *J. Sound Vib.*, Vol. 126, No. 2, pp. 227–238.

Bansal, P. N., and Kirk, R. G., 1975, "Stability and Damped Critical Speeds of Rotor-Bearing Systems," ASME *Journal of Engineering for Industry*, Vol. 97, pp. 1325–1332.

Gasch, R., 1976, "Vibration of Large Turbo-Rotors in Fluid-Film Bearings on an Elastic Foundation," *J. Sound Vib.*, Vol. 47, No. 1, pp. 538–573.

Kammer, D. C., and Schlack, A. L., Jr., 1987a, "Effects of Nonconstant Spin Rate on the Vibration of a Rotating Beam," ASME *Journal of Applied Mechanics*, Vol. 54, pp. 305–310.

Kammer, D. C., and Schlack, A. L., Jr., 1987b, "Dynamic Response of a Radial Beam With Nonconstant Angular Velocity," ASME *Journal of Vibration, Acoustics, Stress, and Reliability in Design*, Vol. 109, pp. 138–143.

Kirk, R. G., and Gunter, E. J., 1976, "Stability and Transient Motion of a Plain Journal Mounted in Flexible Damped Supports," ASME *Journal of Engineering for Industry*, Vol. 98, pp. 576–594.

Leipholz, H., 1977, *Direct Variational Methods and Eigenvalue Problems in Engineering*, Noordhoff Int. Pub., The Netherlands.

Lund, J. W., 1974, "Stability and Damped Critical Speeds of a Flexible Rotor in Fluid-Film Bearings," ASME *Journal of Engineering for Industry*, Vol. 96, pp. 509–517.

Meirovitch, L., 1975, "A Modal Analysis for the Response of Linear Gyroscopic Systems," ASME *Journal of Applied Mechanics*, Vol. 42, No. 2, pp. 446–450.

Nayfeh, A. H., and Mook, D. T., 1979, *Nonlinear Oscillations*, Wiley, New York.

Nelson, H. D., and McVaugh, J. M., 1976, "The Dynamics of Rotor-Bearing Systems Using Finite Elements," ASME *Journal of Engineering for Industry*, Vol. 98, pp. 593–600.

Reddi, M. M., and Trumpler, P. R., 1962, "Stability of the High Speed Journal Bearing Under Steady Load—1: The Incompressible Film," ASME *Journal of Engineering for Industry*, Vol. 84, pp. 351–358.

Ruhl, R. L., and Booker, J. F., 1972, "A Finite Element Model for Distributed Parameter Turborotor Systems," ASME *Journal of Engineering for Industry*, Vol. 94, pp. 126–132.

Shiau, T. N., and Hwang, J. L., 1989, "A New Approach to the Dynamic Characteristics of Undamped Rotor-Bearing Systems," ASME *Journal of Vibration, Acoustics, Stress, and Reliability in Design*, Vol. 111, pp. 379–385.

Vance, J. M., Murphy, B. T., and Tripp, H. A., 1987, "Critical Speeds of Turbomachinery: Computer Predictions Versus Experimental Measurements—Part I: The Rotor Mass-Elastic Model," ASME *Journal of Vibration, Acoustics, Stress, and Reliability in Design*, Vol. 109, pp. 1–7.

Vance, J. M., 1988, *Rotordynamics of Turbomachinery*, Wiley, New York.

Young, T. H., 1991, "Dynamic Response of a Pretwisted, Tapered Beam With Nonconstant Rotating Speed," *J. Sound Vib.*, Vol. 150, No. 3, pp. 435–446.

Young, Y. H., and Liou, G. T., 1992, "Coriolis Effect on the Vibration of a Cantilever Plate With Time-Varying Rotating Speed," ASME *Journal of Vibration and Acoustics*, Vol. 114, pp. 232–241.

Multi-objective Optimization of Rotor-Bearing System With Critical Speed Constraints

T. N. Shiau

J. R. Chang

Institute of Aeronautics and Astronautics,
National Cheng Kung University,
Tainan, Taiwan

An efficient optimal design algorithm is developed to minimize, individually or simultaneously, the total weight of the shaft and the transmitted forces at the bearings. These factors play very important roles in designing a rotor-bearing system under the constraints of critical speeds. The cross-sectional area of the shaft, the bearing stiffness, and the positions of bearings and disks are chosen as the design variables. The dynamic characteristics are determined by applying the generalized polynomial expansion method and the sensitivity analysis is also investigated. For multi-objective optimization, the weighting method (WM), the goal programming method (GPM), and the fuzzy method (FM) are applied. The results show that the present multi-objective optimization algorithm can greatly reduce both the weight of the shaft and the forces at the bearings with critical speed constraints.

Introduction

In the design of modern turbomachinery, it is often necessary to increase the performance of rotor-bearing systems. This requires the design of more compact and lightweight systems, which will greatly save the fuel spent during the service life. Moreover, if the transmitted forces through the bearings can be reduced, the lifetime of the rotor-bearing system will be increased. Since the critical speed range influences the performance and safety of the whole system, it may be necessary and better to constrain the critical speeds in the design process to avoid large vibrations. The present study will focus on the design of a rotor-bearing system with minimum shaft weight and transmitted forces through the bearings under the critical speed constraints.

To perform the optimum design, the first step is to analyze the system dynamic behavior. The transfer matrix method (Myklestad, 1944; Prohl, 1945; Lund, 1974) and the direct stiffness method (Childs, 1978; Nelson, 1980; Adams, 1980; Childs and Graviss, 1982) may be the validated tools for this system. However, as discussed by Shiau and Hwang (1989, 1993), the generalized polynomial expansion method is of better merit compared with those methods and will be employed to analyze the dynamic characteristics of the system.

Some authors (Gunter, 1970; Childs and Graviss, 1982; Shiau and Hwang, 1988, 1990) have shown that the system parameters including the geometry of the system, coefficients of bearing, inertia properties of rigid disk, and the distribution of the mass and stiffness of rotating assemblies have significant influences on the dynamic characteristics of a rotor-bearing system. The parameter sensitivity analysis for a rotor-bearing system has been investigated by Lund (1979), Feitzen and Nordman (1982), Rajan et al. (1986), and Shiau and Hwang (1988, 1990). It should be noted that the design variables considered in this paper are not only the cross-sectional area of shaft and the bearing stiffnesses studied by Shiau and Hwang (1989, 1990) but also the positions of bearings and disks.

The single objective optimization, i.e., weight minimization, of rotor-bearing system under the constraints on critical speeds, dynamic stress, and/or steady-state unbalance response has been studied by Shiau and Hwang (1988, 1990) using a finite element approach for dynamic analysis with optimization methods of the Sequential Unconstrained Minimization Technique and method of feasible direction (Zoutendijk, 1960). In this study, the generalized polynomial expansion method developed by Shiau and Hwang (1989, 1993) is applied for the dynamic analysis and the weighting method (Chankong and Haimes, 1983), the goal programming method (Kaplan and Rao, 1987), and the fuzzy method (Rao, 1984, 1987) are applied together with the method of feasible direction for the multi-objective optimization. Examples are employed to demonstrate the merits of the present design algorithm.

Dynamic Analysis

A typical rotor-bearing system is shown in Fig. 1 consisting of disks, shaft elements with distributed mass and stiffness, and discrete bearings. Two reference frames are adopted: the Newtonian reference frame X–Y–Z, and the rotating reference frame x–y–z. Both the X and x axes are collinear and coincident with the undeformed bearing centerline. The rotating frame rotates about the X axis with a whirl speed of ω.

The dynamic behavior of the rotor-bearing system is analyzed based on the following assumptions: (1) The shear effect of the flexible shaft is neglected; (2) the disks are rigid and

Contributed by the International Gas Turbine Institute and presented at the 36th International Gas Turbine and Aeroengine Congress and Exposition, Orlando, Florida, June 3-6, 1991. Manuscript received at ASME Headquarters February 20, 1991. Paper No. 91-GT-117. Associate Technical Editor: L. A. Riekert.

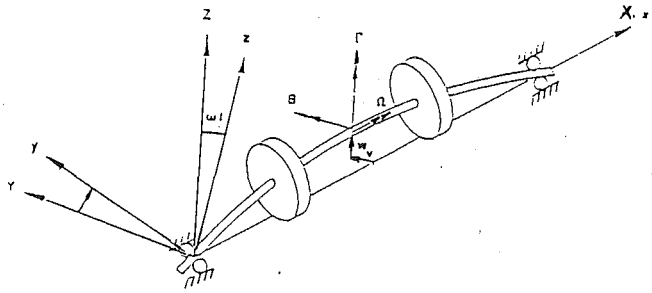

Fig. 1 Typical rotor configuration and coordinates

attached to the flexible shaft, which is supported by the isotropic bearings; (3) lateral displacements are very small so that all the deflections and forces are assumed to parallel to the Y-Z plane; and (4) torsional vibration and axial vibration are neglected. Consider the displacements of two translations and two rotations of any shaft cross section, which are denoted by (V, W) and (B, Γ), respectively. Based on the assumptions, the displacements can be expressed as

$$V = V(x, t), \quad W = W(x, t) \tag{1a}$$

$$\mathrm{B} = \mathrm{B}(x, t), \quad \Gamma = \Gamma(x, t) \tag{1b}$$

The rotations (B, Γ) are geometrically related to the translations (V, W) by the following equations:

$$\mathrm{B}(x, t) = -\frac{\partial W(x, t)}{\partial x}$$

$$\Gamma(x, t) = \frac{\partial V(x, t)}{\partial x} \tag{2}$$

The derivation of the equations of motion using the Lagrangian approach requires the calculation of the kinetic energy and the potential energy of the system. These energy functions can be expressed in terms of the displacements and their derivatives. Since it is often difficult to measure accurately the damping of the bearings, the attention of this study is on the undamped system. Thus, the dissipation energy due to the damping effect of the bearings is neglected. The total kinetic energy (T) consists of the kinetic energy of the shaft (T_s), the disk (T_d), and the eccentricity (T_e). Similarly, the total potential energy (U) has the components of the strain energy of the shaft (U_s) and bearings (U_b). They are expressed as

$$T = T_s + T_d + T_e \tag{3}$$

$$U = U_s + U_b, \tag{4}$$

and the components of the energy are of the forms

$$T_s = \frac{1}{2}\int_0^l \rho A(\dot{V}^2 + \dot{W}^2)dx + \frac{1}{2}\int_0^l I_D(\dot{\mathrm{B}}^2 + \dot{\Gamma}^2)dx + \frac{1}{2}\Omega\int_0^l I_P(\Gamma\dot{\mathrm{B}} - \mathrm{B}\dot{\Gamma})dx + \frac{1}{2}\Omega^2\int_0^l I_P dx \tag{5}$$

$$T_d = \sum_{i=1}^{N_d}\left\{\frac{1}{2}m_i^d(\dot{V}_i^2 + \dot{W}_i^2) + \frac{1}{2}I_{Di}^d(\dot{\mathrm{B}}_i^2 + \dot{\Gamma}_i^2) + \frac{1}{2}\Omega I_{Pi}^d(\Gamma\dot{\mathrm{B}} - \mathrm{B}\dot{\Gamma}) + \frac{1}{2}\Omega^2 I_{Pi}^d\right\} \tag{6}$$

$$T_e = \int_0^l e(x)\rho(x)A(x)\Omega[-\dot{V}\sin(\Omega t + \phi) + \dot{W}\cos(\Omega t + \phi)]dx + \int_0^l e^2(x)\rho(x)A(x)\Omega^2 dx + \sum_{i=1}^{N_d}\{e_i^d\Omega m_i^d[-\dot{V}_i\sin(\Omega t + \phi_i^d) + \dot{W}_i\cos(\Omega t + \phi_i^d)] + \frac{1}{2}m_i^d(e_i^d)^2\Omega^2\} \tag{7}$$

$$U_s = \frac{1}{2}\int_0^l EI[(V'')^2 + (W'')^2]dx \tag{8}$$

$$U_b = \sum_{j=1}^{N_b}\frac{1}{2}k_j^b(V_j^2 + W_j^2) \tag{9}$$

As shown by Shiau and Hwang (1993), the generalized polynomial expansion method describes the translations and the rotations of the shaft in the following expressions:

$$V(x, t) = \sum_{n=1}^{N_p} a_n(t)x^{n-1}$$

$$W(x, t) = \sum_{m=1}^{N_p} b_m(t)x^{m-1} \tag{10}$$

Nomenclature

A = cross-sectional area of the shaft
$a_n(t)$, $b_m(t)$ = generalized coordinates
E = elastic modulus of the shaft
$e(x)$ = eccentricity of the shaft at position x
e_i^d = eccentricity of the ith disk
$F_i(\mathbf{Z})$ = ith objective function
$\mathbf{F}_j^b$ = transmitted force at the jth bearing
g_j = jth constraint
$[G]$ = gyroscopic matrix
I = cross-sectional area moment of inertia
I_D, I_P = diametral and polar mass moment of inertia of the shaft per unit length
I_{Di}^d, I_{Pi}^d = diametral and polar mass moment of the ith disk
$[K]$ = stiffness matrix of the bearing
$[K^s]$ = stiffness matrix of the shaft
$[K^*]$ = stiffness matrix
k_j^b = stiffness of the jth bearing
l = total length of the shaft
l_i = length of the ith shaft element
$[M]$ = mass matrix
N_b, N_d, N_e = total number of disks, bearings, and shaft elements
N_o = number of objectives
N_P = number of terms of polynomial
r_o, r_I = outer and inner radius of the shaft element
T = total kinetic energy
U = total potential energy
(V, W) = translational displacement in (Y, Z) directions
$W(\mathbf{Z})$ = total shaft weight
X-Y-Z = fixed reference frame
x-y-z = rotating reference frame
x_i^b, x_i^d = positions of the ith bearing and disk
z_i, $\mathbf{Z}$ = design variables and vector
B, Γ = angle rotations about Y, Z axes
λ = whirl ratio = Ω/ω
ρ = mass density per unit volume of the shaft
ω, Ω = whirl speed and spin speed
ω_n^c = nth critical speed

$$B(x, t) = -\frac{\partial W(x, t)}{\partial x} = -\sum_{m=2}^{N_p} (m-1)x^{m-2}b_m(t)$$

$$\Gamma(x, t) = \frac{\partial V(x, t)}{\partial x} = \sum_{n=2}^{N-p} (n-1)x^{n-2}a_n(t) \tag{11}$$

where the $a_n(t)$ and $b_m(t)$ are generalized coordinates and the integer N_p is the number of polynomials. Substituting Eqs. (10) and (11) and their derivatives into Eqs. (5)–(9) and applying the Lagrangian approach, i.e.,

$$\frac{d}{dt}\frac{\partial}{\partial \dot{q}_i}(T-U) - \frac{\partial}{\partial q_i}(T-U) = 0, \tag{12}$$

where the generalized coordinates q_i can be any of a_n or b_m with n, $m = 1, N_p$, one can obtain, for any given rotating speed, the equations of motion as

$$\begin{pmatrix} M & 0 \\ 0 & M \end{pmatrix}\begin{pmatrix} \ddot{\mathbf{a}} \\ \ddot{\mathbf{b}} \end{pmatrix} + \Omega\begin{pmatrix} 0 & G \\ -G & 0 \end{pmatrix}\begin{pmatrix} \dot{\mathbf{a}} \\ \dot{\mathbf{b}} \end{pmatrix} + \begin{pmatrix} K_s+K & 0 \\ 0 & K_s+K \end{pmatrix}\begin{pmatrix} \mathbf{a} \\ \mathbf{b} \end{pmatrix} = \begin{pmatrix} \mathbf{R}_a \\ \mathbf{R}_b \end{pmatrix} \tag{13}$$

where the $N_p \times 1$ vectors $\mathbf{a}$, $\mathbf{b}$, $\mathbf{R}_a$, and $\mathbf{R}_b$ are of the forms

$$\mathbf{a} = \{a_1, a_2, \ldots, a_{N_p}\}^T$$

$$\mathbf{b} = \{b_1, b_2, \ldots, b_{N_p}\}^T \tag{14}$$

$$\mathbf{R}_a = \{R_{a1}, R_{a2}, \ldots, R_{aN_p}\}^T$$

$$\mathbf{R}_b = \{R_{b1}, R_{b2}, \ldots, R_{bN_p}\}^T \tag{15}$$

and the expressions of the $N_p \times N_p$ matrices M, G, K_s, and K, and the components of $\mathbf{R}_a$ and $\mathbf{R}_b$ are shown in the appendix.

For simplicity, the $N_p \times 1$ complex vector $\mathbf{P}$ is introduced, which is defined as

$$\mathbf{P} = \mathbf{a} + i\mathbf{b} \tag{16}$$

and the shaft is considered without eccentricity. Equation (13) can be rewritten as

$$[M]\ddot{\mathbf{P}} - i\Omega[G]\dot{\mathbf{P}} + [K+K_s]\mathbf{P} = \mathbf{R}e^{i\Omega t} \tag{17}$$

where the $N_p \times 1$ vector $\mathbf{R}$ is defined as

$$\mathbf{R} = \{R_1, R_2, \ldots, R_{N_p}\}^T \tag{18}$$

and the components of $\mathbf{R}$ are listed in the appendix.

To solve the critical speeds of the system, the homogeneous part of Eq. (17) is considered. Assuming the solution to be of the form

$$\mathbf{P} = \mathbf{C}e^{i\omega t} \tag{19}$$

where ω is the natural frequency or the whirl speed of the system and substituting Eq. (19) into Eq. (17), one can obtain the equation as

$$\{[K^*] - \omega^2([M] - \lambda[G])\}\mathbf{C} = \mathbf{0} \tag{20}$$

where $\lambda = \Omega/\omega$ is the whirl ratio. Setting $\lambda = 1$ or other values and solving the eigenvalue problem governed by Eq. (20), one can obtain the critical speeds and the associated mode shapes. Since the system governed by Eq. (17) is isotropic and the spin speed is constant (i.e., $\dot{\Omega} = 0$), the steady-state unbalance response is a circular motion, which can be assumed as

$$\mathbf{P} = \mathbf{Q}e^{i\Omega t} \tag{21}$$

in which $\mathbf{Q}$ is a vector describing the forward circular motion. Substituting Eq. (21) into Eq. (17), one can obtain the equation as

$$(-\Omega^2[M] + \Omega^2[G] + [K^*])\mathbf{Q} = \mathbf{R} \tag{22}$$

with $[K^*] = [K_s + K]$. Solving for $\mathbf{Q}$ in Eq. (22) with given unbalances and combining Eqs. (21), (16), and (10), one can obtain the steady-state unbalance response of the system.

The response at the jth bearing can be obtained by substituting $x = x_j^b$ into Eq. (10) and the corresponding transmitted force at the jth bearing, which can be expressed as

$$\mathbf{F}_j^b = k_j^b\begin{pmatrix} \sum_{n=1}^{N_p} a_n(t)(x_j^b)^{n-1} \\ \sum_{m=1}^{N_p} b_m(t)(x_j^b)m-1 \end{pmatrix} = k_j^b\begin{pmatrix} \mathbf{B} & 0 \\ 0 & \mathbf{B} \end{pmatrix}\begin{pmatrix} \mathbf{a} \\ \mathbf{b} \end{pmatrix} \tag{23}$$

where

$$\mathbf{B} = \{1 x_j^b (x_j^b)^2 \ldots (x_j^b)^{N_p-1}\} \tag{24}$$

Optimization Approach

The multi-objective optimization problem usually requires the descriptions of the objective functions as well as the side and behavior constraint functions. In this study, the objective functions $F_i(\mathbf{Z})$ are the weight of the shaft $W(\mathbf{Z})$ and the jth bearing's transmitted force $\|F_j^b(\mathbf{Z})\|$. The constraints on the critical speeds are taken as follows:

$$g_1(\mathbf{Z}) = \omega_2^c - \frac{\Omega_{\text{low}}}{a_1} \le 0$$

$$g_2(\mathbf{Z}) = a_2 \cdot \Omega_{\text{high}} - \omega_3^c \le 0 \tag{25}$$

where Ω_{low} and Ω_{high} are the lower and upper bounds of the operating speed range of the existent rotor system. The second and the third critical speeds are denoted by ω_2^c and ω_3^c, respectively. Both are usually associated with the second rigid body mode and the first bending mode, although the significant bending may occur at all critical speeds.

The cross-sectional area of the shaft and the bearing stiffnesses are primarily taken as the design variables since they play a very important role for the determination of critical speeds and transmitted forces through the bearings. However, in this study, the positions of the disks and the bearings are also considered as the design variables to increase the system design capability. The optimum design problem can be expressed as follows:

$$\textit{Minimize:} \quad W(\mathbf{Z}) = \sum_{i=1}^{N_e} \rho_i l_i A_i \tag{26a}$$

$$\text{and } \|F_j^b(\mathbf{Z})\| \tag{26b}$$

$$\textit{Subject to:} \quad g_1(\mathbf{Z}) = \omega_2^c - \frac{\Omega_{\text{low}}}{a_1} \le 0$$

$$g_2(\mathbf{Z}) = a_2 \cdot \Omega_{\text{high}} - \omega_3^c \le 0 \tag{27}$$

$$\mathbf{Z} = \{A_i, k_j^b;\ i = 1, N_e, j = 1, N_b\} \tag{28a}$$

$$\text{or } \mathbf{Z} = \{A_i, k_j^b, x_k^b, x_l^d;\ i = 1, N_e, \quad j, k = 1, N_b, l = 1, N_d\} \tag{28b}$$

$$z_i^l \le z_i \le z_i^u, \quad i = 1, n \tag{29}$$

where N_e, N_b, and N_d are the total numbers of shaft elements, bearings, and disks, respectively. The total number of design variables is denoted by n. The definitions of parameters are given in the Nomenclature. The ith component of design vector $\mathbf{Z}$ is denoted by z_i.

The concept of multi-objective optimization in this study is to transform the vector optimization to a scalar optimization and then the MFD is applied to solve the scalar optimization incorporated with one-dimensional search. Three methods including the *weighting method* (WM), the *goal programming method* (GPM), and the *fuzzy method* (FM) are applied to perform the multiobjective optimization.

(*i*) The weighting method (WM) transforms the multi-objective optimization problem to the reduced single objective form:

$$\textit{Minimize:} \quad \sum_{i=1}^{N_o} w_i F_i(\mathbf{Z})$$

$$\textit{Subject to:} \quad \mathbf{Z} \in C \tag{30}$$

where w_i are positive real numbers and the components of $\mathbf{Z}$ satisfy Eqs. (27) and (29). The corresponding set of $\mathbf{Z}$ is defined by C. For convenience and simplicity, all w_i are chosen to be unity. This implies that all the objective functions play an equally important role in the design.

(*ii*) For the goal programming method (GPM), the objectives are driven to attain the prescribed goals that the designer wishes to achieve. Thus, the solution $\mathbf{Z}^*$ is defined as the one that minimizes the deviations from the goals. Mathematically it is expressed as follows:

$$\textit{Minimize:} \quad \left[\sum_{i=1}^{N_o} (\alpha_i^+ + \alpha_i^-)^P\right]^{1/P}, \quad P \geq 1 \tag{31}$$

$$\textit{Subject to:} \quad \mathbf{Z} \in C \tag{32a}$$

$$F_i - \alpha_i^+ + \alpha_i^- = b_i, \quad i = 1, N_o \tag{32b}$$

$$\alpha_i^+ \geq 0 \tag{32c}$$

$$\alpha_i^- \geq 0 \tag{32d}$$

$$\alpha_i^+ \cdot \alpha_i^- = 0 \tag{32e}$$

where b_i is the goal for the ith objective, and α_i^+ and α_i^- are the under- and overachievement of the ith goal, respectively. In addition, the value of P is chosen to be two, F_i is the value of the ith objective function, and the goal b_i is set to be F_i^*, which is the optimum value from the case of single objective design.

(*iii*) For the fuzzy method (FM), if the original optimization is expressed as

$$\textit{Minimize:} \quad F_i(\mathbf{Z}), \quad i = 1, N_o \tag{33a}$$

$$\textit{Subject to:} \quad g_j(\mathbf{Z}) \in G_j, \quad j = 1, J, \tag{33b}$$

the fuzzy optimization problem can be expressed as

$$\textit{Minimize:} \quad F_i(\mathbf{Z}), \quad i = 1, N_o \tag{34a}$$

$$\textit{Subject to:} \quad g_j(\mathbf{Z}) \in \tilde{G}_j \tag{34b}$$

where $\tilde{G}_j \equiv [-\infty, b_j + d_j]$, $G_j \equiv [-\infty, b_j]$, and d_j is the permissible variation of g_j. The tilde denotes the fuzzy information. Based on the algorithm of fuzzy optimization, the solution of Eq. (34*a*) and (34*b*) is the same as solving for the nondominated solution of the following equations (Rao, 1987):

$$\textit{Maximize:} \quad \lambda$$

$$\textit{Subject to:} \quad \lambda \leq \mu_{fi}(\mathbf{Z}), \quad i = 1, N_o$$

$$\lambda \leq \mu_{gj}(\mathbf{Z}), \quad j = 1, J \tag{35}$$

where μ_{fi} and μ_{gj} represent the membership functions (degree of satisfaction) of the objectives and constraints, respectively, and parameter λ is an added variable. The membership functions μ_{fi} and μ_{gj} are defined as

$$\mu_{fi}(\mathbf{Z}) = \begin{cases} 0, & \text{if } F_i(\mathbf{Z}) > F_i^{\max} \\ 1 - \left(\dfrac{F_i(\mathbf{Z}) - F_i^{\min}}{F_i^{\max} - F_i^{\min}}\right), & \text{if } F_i^{\min} \leq F_i(\mathbf{Z}) \leq F_i^{\max} \\ 1, & \text{if } F_i(\mathbf{Z}) \leq F_i^{\min}, \quad i = 1, N_o \end{cases} \tag{36}$$

$$\mu_{gj}(\mathbf{Z}) = \begin{cases} 0, & \text{if } g_j > b_j + d_j \\ 1 - \left(\dfrac{g_j - b_j}{d_j}\right), & \text{if } b_j \leq g_j \leq b_j + d_j \\ 1, & \text{if } g_j < b_j, \quad j = 1, J \end{cases} \tag{37}$$

The $F_i^{\min}$ and $F_i^{\max}$ shown in Eq. (36) are given by

$$F_i^{\min} = F_i(\mathbf{Z}_i^*)$$

$$F_i^{\max} = \max_k F_i(\mathbf{Z}_k^*) \tag{38}$$

To obtain $F_i^{\min}$ and $F_i^{\max}$, we first minimize each single objective function $F_i(\mathbf{Z})$ subject to the constraints $g_j \leq b_j$, $j = 1, J$. If the solutions are $\mathbf{Z}_i^*$, $i = 1, N_o$, one can employ Eq. (38) to find $F_i^{\min}$ and $F_i^{\max}$.

Sensitivity Analysis

The algorithms of optimization techniques described above require the calculation of sensitivity for each design variable to search the optimum design. It is necessary to calculate the derivatives of objective and constraint functions with respect to design variables. The derivatives of objective functions can be obtained by differentiating Eqs. (26*a*) and (26*b*) with respect to design variables, for the following cases:

1 When the objective function is the weight of the shaft, the gradient can be expressed as

$$\frac{\partial W(\mathbf{Z})}{\partial z_i} = \begin{cases} \rho_i l_i, & \text{if } z_i = A_i; \\ 0, & \text{if } z_i = k_i, x_i^b, \text{ or } x_i^d. \end{cases} \tag{39}$$

2 When the objective function is the transmitted force at the jth bearing, the sensitivity is given by the following cases:

(*i*) The design variable is cross-sectional area A_i:

$$\frac{\partial \|F_j^b(\mathbf{Z})\|}{\partial A_i} = \frac{\partial \|F_j^b(\mathbf{Z})\|}{\partial A_i}\bigg|_{I=\text{const}} + \frac{\partial \|F_j^b(\mathbf{Z})\|}{\partial I_i}\frac{\partial I_i}{\partial A_i} \tag{40}$$

where $\mathbf{I}$ is a vector of moment of inertia. The terms on the right-hand side of Eq. (40) can be obtained by differentiating Eq. (23) with respect to A_i and expressed as

$$\frac{\partial \|F_j^b(\mathbf{Z})\|}{\partial A_i}\bigg|_{I=\text{const}} = k_j^b \{(\mathbf{B}^T\mathbf{a})^2 + (\mathbf{B}^T\mathbf{b})^2\}^{-1/2}\mathbf{B}^T \left\{\mathbf{a}\mathbf{B}^T\frac{\partial \mathbf{a}}{\partial A_i} + \mathbf{b}\mathbf{B}^T\frac{\partial \mathbf{b}}{\partial A_i}\right\} \tag{41a}$$

$$\frac{\partial \|F_j^b(\mathbf{Z})\|}{\partial I_i} = k_j^b \{(\mathbf{B}^T\mathbf{a})^2 + (\mathbf{B}^T\mathbf{b})^2\}^{-1/2}\mathbf{B}^T \left\{\mathbf{a}\mathbf{B}^T\frac{\partial \mathbf{a}}{\partial I_i} + \mathbf{b}\mathbf{B}^T\frac{\partial \mathbf{b}}{\partial I_i}\right\} \tag{41b}$$

$$\frac{\partial \mathbf{I}_i}{\partial A_i} = -\frac{A}{2\pi} + \frac{r_{oi}^2}{2} \tag{41c}$$

(*ii*) The design variable is bearing stiffness k_i^b:

$$\frac{\partial \|F_j^b(\mathbf{Z})\|}{\partial k_i^b} = k_j^b \{(\mathbf{B}^T\mathbf{a})^2 + (\mathbf{B}^T\mathbf{b})^2\}^{-1/2}\mathbf{B}^T \left\{\mathbf{a}\mathbf{B}^T\frac{\partial \mathbf{a}}{\partial k_i^b} + \mathbf{b}\mathbf{B}^T\frac{\partial \mathbf{b}}{\partial k_i^b}\right\}, \quad \text{if } i \neq j \tag{42a}$$

or

$$\frac{\partial \|F_j^b(\mathbf{Z})\|}{\partial k_i^b} = k_j^b \{(\mathbf{B}^T\mathbf{a})^2 + (\mathbf{B}^T\mathbf{b})^2\}^{-1/2}\mathbf{B}^T \left\{\mathbf{a}\mathbf{B}^T\frac{\partial \mathbf{a}}{\partial k_i^b} + \mathbf{b}\mathbf{B}^T\frac{\partial \mathbf{b}}{\partial k_i^b}\right\} + \{(\mathbf{B}^T\mathbf{a})^2 + (\mathbf{B}^T\mathbf{b})^2\}^{1/2}, \quad \text{if } i = j \tag{42b}$$

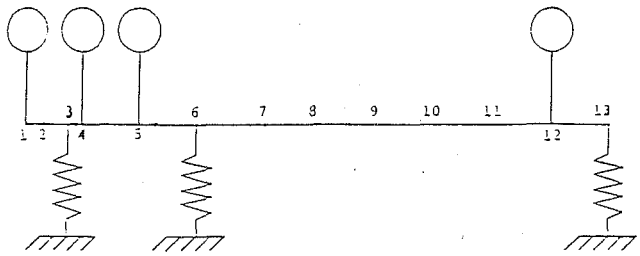

Fig. 2 · Rotor schematic

(*iii*) If the design variable is bearing position x_i^b:

$$\frac{\partial \|F_j^b(\mathbf{Z})\|}{\partial x_i^b} = k_j^b \{(\mathbf{B}^T\mathbf{a})^2 + (\mathbf{B}^T\mathbf{b})^2\}^{-1/2} \mathbf{B}^T \left\{ \mathbf{a}\mathbf{B}^T \frac{\partial \mathbf{a}}{\partial x_i^b} + \mathbf{b}\mathbf{B}^T \frac{\partial \mathbf{b}}{\partial x_i^b} \right\} \tag{43}$$

(*iv*) If the design variable is disk position x_i^d:

$$\frac{\partial \|F_j^b(\mathbf{Z})\|}{\partial x_i^d} = k_j^b \{(\mathbf{B}^T\mathbf{a})^2 + (\mathbf{B}^T\mathbf{b})^2\}^{-1/2} \mathbf{B}^T \cdot \left\{ \mathbf{a}\mathbf{B}^T \frac{\partial \mathbf{a}}{\partial x_i^d} + \mathbf{b}\mathbf{B}^T \frac{\partial \mathbf{b}}{\partial x_i^d} \right\} \tag{44}$$

All the components $\partial\mathbf{a}/\partial z_i$ and $\partial\mathbf{b}/\partial z_i$ shown in Eqs. (41)–(44) can be calculated by the following procedures: First, taking the derivative of Eq. (22) with respect to the variables z_i, one obtains the equation

$$(-\Omega^2[M]\Omega^2[G] + [K^*]) \frac{\partial \mathbf{Q}}{\partial z_i} = \left(\Omega^2 \frac{\partial [M]}{\partial z_i} - \Omega^2 \frac{\partial [G]}{\partial z_i} - \frac{\partial [K^*]}{\partial z_i} \right) \mathbf{Q} \tag{45}$$

The terms of derivatives shown on the right-hand side of Eq. (45) are listed in the appendix, which are known. On the left-hand side, the term $\partial\mathbf{Q}/\partial z_i$ can be obtained by solving Eq. (45). Since the vectors **a** and **b** are the real and imaginary parts of $\mathbf{Q}e^{i\Omega t}$, respectively, the corresponding gradients ($\partial\mathbf{a}/\partial z_i$, $\partial\mathbf{b}/\partial z_i$) are of the form

$$\frac{\partial \mathbf{a}}{\partial z_i} = \frac{\partial Re(\mathbf{Q}e^{i\Omega t})}{\partial z_i} = Re \frac{\partial \mathbf{Q}}{\partial z_i} \cos \Omega t - Im \frac{\partial \mathbf{Q}}{\partial z_i} \sin \Omega t \tag{46a}$$

$$\frac{\partial \mathbf{b}}{\partial z_i} = \frac{\partial Im(\mathbf{Q}e^{i\Omega t})}{\partial z_i} = Re \frac{\partial \mathbf{Q}}{\partial z_i} \sin \Omega t + Im \frac{\partial \mathbf{Q}}{\partial z_i} \cos \Omega t \tag{46b}$$

Similarly the gradients of the constraint functions can be found, by differentiating Eq. (27) with respect to the design variables z_i. The derivatives of critical speed constraints are expressed as follows:

$$\frac{\partial g_1(\mathbf{Z})}{\partial z_i} = \frac{\partial \omega_2^c}{\partial z_i} \tag{47a}$$

$$\frac{\partial g_2(\mathbf{Z})}{\partial z_i} = -\frac{\partial \omega_3^c}{\partial z_i} \tag{47b}$$

By differentiating Eq. (20) with respect to design variables z_i and premultiplying $\mathbf{C}_n^T$ of the nth mode, one can obtain the gradients of critical speeds as

$$\frac{\partial \omega_n^c}{\partial z_i} = \frac{\mathbf{C}_n^T \left(\frac{\partial [K^*]}{\partial z_i} - (\omega_n^c)^2 \frac{\partial [M^*]}{\partial z_i} \right) \mathbf{C}_n}{2\omega_n^c \mathbf{C}_n^T [M^*] \mathbf{C}_n} \tag{48}$$

where $[M^*]$ is defined as $[M^*] \equiv [M] - \lambda[G]$, and the whirl ratio λ is chosen to be unity to obtain the synchronous critical speeds. The terms $\partial[K^*]/\partial z_i$ and $\partial[M^*]/\partial z_i$ are given in the appendix.

Table 1 Initial configuration data of rotor system

Station No.	Axial Distance to Station 1 (cm)
1	0.0
2	4.29
3	8.89
4	10.49
5	20.17
6	27.69
7	44.20
8	59.44
9	74.68
10	89.92
11	105.16
12	120.14
13	127.94
$E = 20.69 \times 10^6 N/cm^2$ $\rho = 8193.0 kg/m^3$ $r_{oi} = 2.95 cm, i = 1, 12$	

Table 2 Fixed rigid disk data

Station No.	Mass (kg)	Polar Inertia (kg-$cm^2 \times 10^2$)	Diametral Inertia (kg-$cm^2 \times 10^2$)
1	11.38	19.53	9.82
4	7.88	16.70	8.35
5	7.70	17.61	8.80
12	21.70	44.48	22.24

Numerical Results and Discussion

The rotor-bearing system shown in Fig. 2 consists of a single spool and three bearings located at stations 3, 6, and 13. The bearings are referred to as No. 1, No. 2, and No. 3, respectively. The shaft is divided into 12 elements and the outer radius of each element is fixed and has the value of 2.95 cm. Moreover, four disks with constant masses are located at stations 1, 4, 5, and 12. The fourth disk is of unbalance $e_4^d = 5 \times 10^{-5}$ m. The details of rotor configuration are listed in Tables 1 and 2. The constants, a_1 and a_2, shown in Eq. (30) are chosen such that the second critical speed ω_2^c is at least lower than Ω_{low} by a factor 1.2 while the third critical speed is at least 30 percent higher than the high end of original operating speed range, i.e., $a_1 = 1.2$, $a_2 = 1.3$. The operating speed range is given by $\Omega_{low} = 830.0$ rad/s and $\Omega_{high} = 1770.0$ rad/s. Thus Eq. (30) can be rewritten as

$$g_1(\mathbf{Z}) = \omega_2^c - 691.67 \text{ rad/s} \le 0 \tag{49a}$$

$$g_2(\mathbf{Z}) = 2301.00 \text{ rad/s} - \omega_3^c \le 0 \tag{49b}$$

The side constraints of design variables are given by

$$1.42 \text{ cm} \le r_{Ii} \le 2.69 \text{ cm}, \quad i = 1, 12 \tag{50a}$$

$$3.50 \times 10^6 \text{ N/m} \le k_i^b \le 1.75 \times 10^8 \text{ N/m}, \quad i = 1, 3 \tag{50b}$$

$$6.00 \text{ cm} \le x_1^b \le 9.00 \text{ cm};$$

$$25.00 \text{ cm} \le x_2^b \le 35.00 \text{ cm};$$

$$125.00 \text{ cm} \le x_3^b \le 127.94 \text{ cm} \tag{50c}$$

Table 3 Initial and final design of example 1 for single objective optimization: (3*a*) inner radius of shaft element and bearing stiffness; (3*b*) critical speed, shaft weight, transmitted forces, and CPU time

	Initial	Final	
Shaft Element		W	F_3^b
	Inner Radius (cm)		
1	1.882	2.690	1.882
2	1.940	2.690	1.993
3	1.466	2.109	1.454
4	1.660	2.690	1.748
5	2.151	2.660	2.263
6	2.690	2.690	2.690
7	2.690	2.690	2.689
8	2.690	2.690	2.685
9	2.690	2.690	2.593
10	2.690	2.690	2.363
11	1.420	2.624	1.420
12	1.880	2.690	1.880
Bearing	Bearing Stiffness (N/m)		
1	3.50×10^6	3.60×10^6	3.68×10^6
2	1.27×10^8	1.28×10^8	1.27×10^8
3	1.20×10^7	1.23×10^7	3.50×10^6

(3a)

	Initial	Final	
		W	F_3^b
	Critical Speed (rad/sec)		
ω_2^c	685.84	691.03	525.15
ω_3^c	2646.14	2302.06	2390.15
	Shaft Weight (kg)		
W	10.235	5.110	10.905
	Transmitted Force (N)		
F_1^b	13.562	13.300	13.781
F_2^b	475.599	473.023	464.873
F_3^b	461.366	544.562	119.441
VAX-8600 CPU (sec)		18.21	10.42

(3b)

$$0.00 \text{ cm} \le x_1^d \le 3.00 \text{ cm};$$

$$10.00 \text{ cm} \le x_2^d \le 13.00 \text{ cm};$$

$$17.00 \text{ cm} \le x_3^d \le 23.00 \text{ cm};$$

$$117.00 \text{ cm} \le x_r^d \le 123.00 \text{ cm} \qquad (50d)$$

The behavior constraints of Eqs. (49*a*) and (49*b*) and the side constraints of Eqs. (50*a*) and (50*b*) are considered as the system constraints for the first example. For the second example, Eqs. (50*c*) and (50*d*) are considered as extra side constraints added to example 1. It should be noted that for the fuzzy method, the parameters g_j, b_j, and d_j, $j = 1, 2$, in Eq. (35) are chosen as $g_1 = \omega_2^c$, $g_2 = -\omega_3^c$; $b_1 = 591.67$ rad/s, $b_2 = -2451.00$ rad/s; $d_1 = 100.00$ rad/s, $d_2 = 150.00$ rad/s. The values of b_1, b_2, d_1, and d_2 could be arbitrarily chosen. The computing system used in this study is VAX-8600.

(*i*) *Example 1.* In this example, the objectives are the total shaft weight and the transmitted force at the No. 3 bearing. The design variables are chosen to be the cross-sectional area of each shaft element and the bearing stiffnesses. The

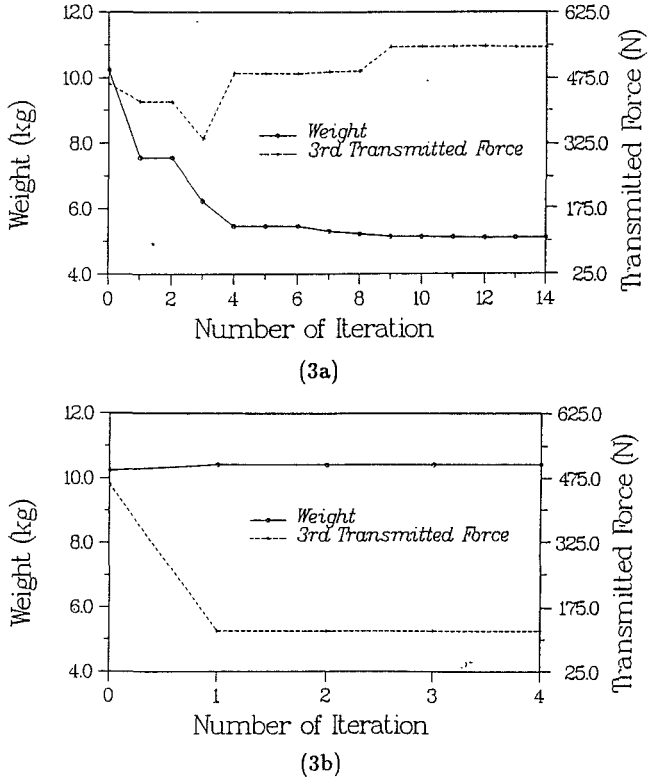

Fig. 3 Histories of optimum design of: (3*a*) the total shaft weight; (3*b*) the third transmitted force

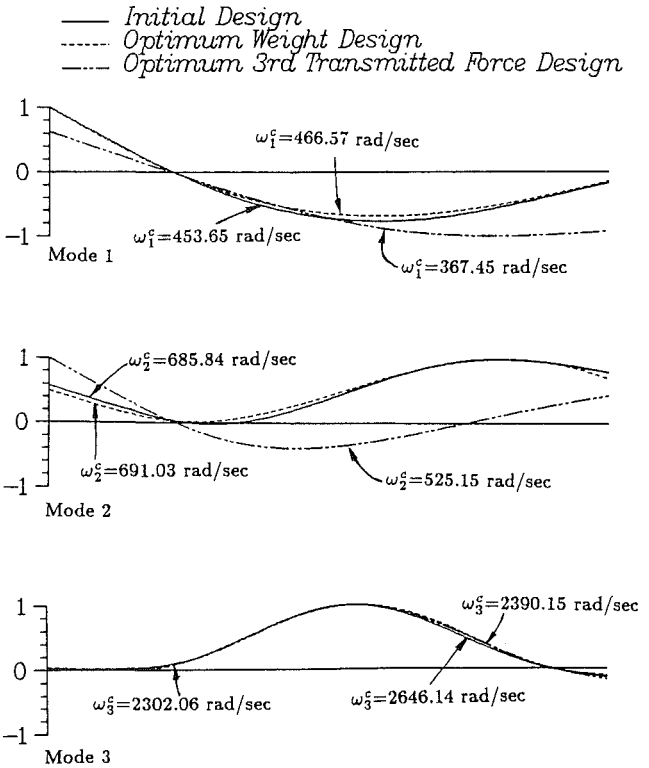

Fig. 4 Mode shapes of initial and optimum design of example 1 (Single objective case)

weighting method (WM), the goal programming method (GPM), and the fuzzy method (FM) are employed for the multiobjective optimization. The single objective optimization is also carried out in this study. The results shown in Table 3 indicate that the optimal weight is increased when the trans-

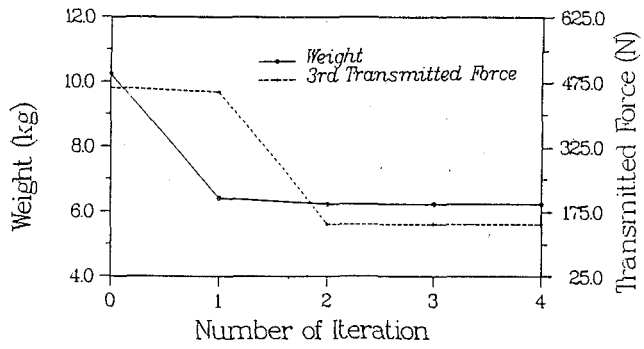

(5a)

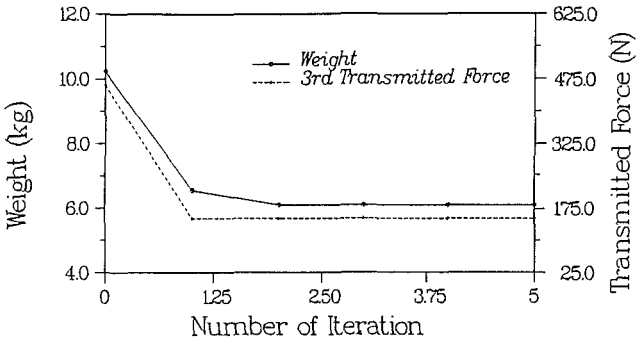

(5b)

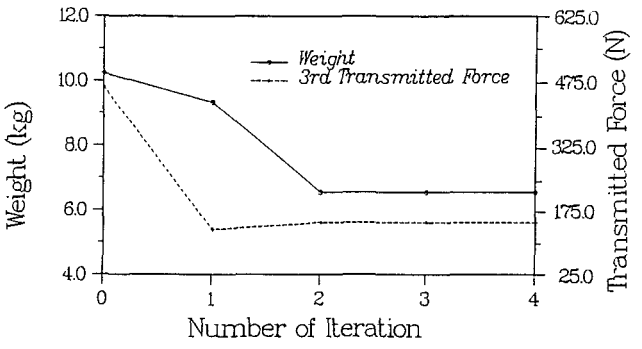

(5c)

Fig. 5 Histories of optimum design of weight and third transmitted force with: (5*a*) Weighting Method; (5*b*) Goal Programming Method; (5*c*) Fuzzy Method

mitted force of the bearing is minimized. This implies that the additional weight is required for the shaft to reduce the dynamic response at the bearing concerned. On the other hand, if the shaft weight is the only objective to be minimized, the transmitted force will increase, although the weight may be considerably reduced. The histories of the design weight and the transmitted force at the No. 3 bearing are shown in Fig. 3 and the mode shapes corresponding to initial and optimum stages are shown in Fig. 4.

One may find that the inner radii of the design with optimum transmitted force are smaller than those with optimum weight case. This is because the former case requires higher stiffness of the shaft to reduce the response of the shaft at corresponding bearing position. Furthermore the stiffness value of the No. 3 bearing for optimum transmitted force case is much smaller than that for the optimum weight case.

For the multi-objective optimization, the total shaft weight and the transmitted force at the No. 3 bearing are considered

Table 4 Initial and final design of example 1: (4*a*) inner radius of shaft element and bearing stiffness; (4*b*) critical speed, shaft weight, transmitted forces, and CPU time

Multiobjective : W and F_3^b				
	Initial	Final		
Shaft Element		WM	GPM	FM
	Inner Radius (cm)			
1	1.882	2.296	2.690	2.155
2	1.940	2.369	2.281	2.224
3	1.466	2.690	2.690	1.582
4	1.660	2.618	2.396	2.614
5	2.151	2.690	2.651	2.690
6	2.690	2.690	2.690	2.690
7	2.690	2.690	2.690	2.690
8	2.690	2.690	2.690	2.690
9	2.690	2.690	2.690	2.690
10	2.690	2.690	2.690	2.690
11	1.420	2.441	2.547	2.422
12	1.880	2.287	2.382	2.354
Bearing	Bearing Stiffness (N/m)			
1	3.50×10^6	3.50×10^6	4.14×10^6	3.50×10^6
2	1.27×10^8	1.28×10^8	1.27×10^8	1.27×10^8
3	1.20×10^7	3.50×10^6	3.50×10^6	3.50×10^6

(4a)

	Initial	Final		
		WM	GPM	FM
	Critical Speed (rad/sec)			
ω_2^c	685.84	514.44	539.05	511.98
ω_3^c	2646.14	2365.15	2352.40	2368.86
	Shaft Weight (kg)			
W	10.235	6.228	6.084	6.550
	Transmitted Force (N)			
F_1^b	13.562	9.303	11.718	9.121
F_2^b	475.599	338.591	340.419	335.634
F_3^b	461.366	146.158	149.991	145.823
VAX-8600 CPU (sec)		8.28	8.33	10.59

(4b)

as the objectives to be minimized. The optimum design can be achieved by using WM, GPM, and FM and the results are shown in Table 4. It indicates that the optimum design weight of multi-objective optimization, compared to the single objective optimization, is smaller than that of optimum transmitted force case but larger than that of the optimum weight case. This implies that if one considers the case of optimum transmitted force as single objective, the weight will be increased in order to make the system stiffer and reduce the system deflection as well as the transmitted force. Furthermore, it is also shown in Table 4 that the final stiffness at the No. 3 bearing for multi-objective optimization is much smaller than that of the optimum weight case. It is because the transmitted force at the No. 3 bearing is also considered as one of the objectives. The optimization histories of the weight and the transmitted force at the No. 3 bearing by using these methods are shown in Fig. 5. The mode shapes corresponding to initial and optimum design of these methods are shown in Fig. 6.

(*ii*) *Example 2.* The positions of the bearings and the disks are considered as extra design variables, except for those in the first example. The initial and optimum design data for single objective optimization are shown in Table 5. It can be found that the transmitted forces at the No. 2 and No. 3 bearings are considerably larger than that at the No. 1 bearing. Comparison between Tables 3 and 5 shows that the added design variables, i.e., disk and bearing positions, lead to better final objectives as well as time saving. Note that the times for

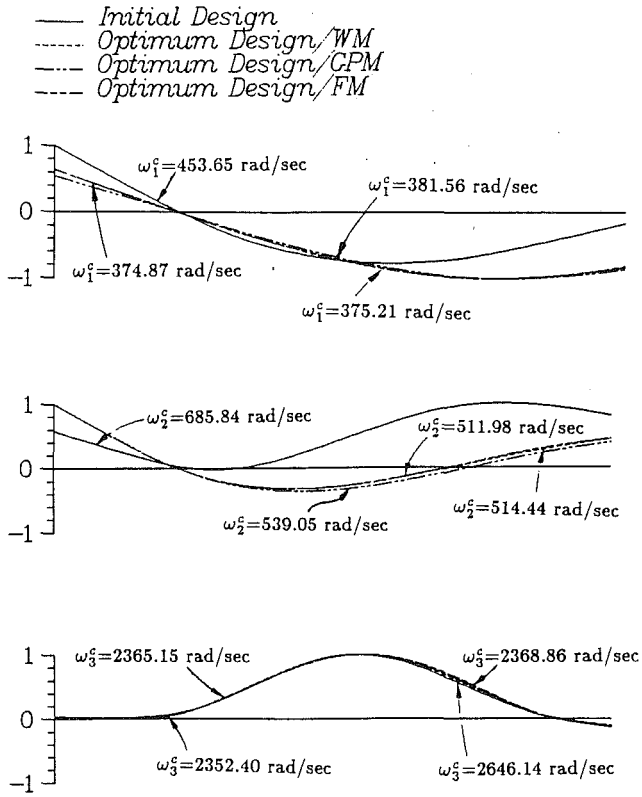

Fig. 6 Mode shapes of initial and optimum design of example 1 (multi-objective case)

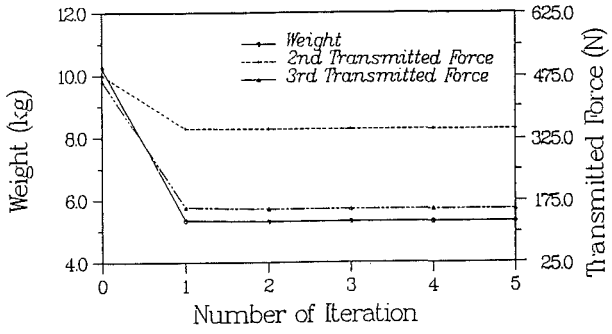

(7a)

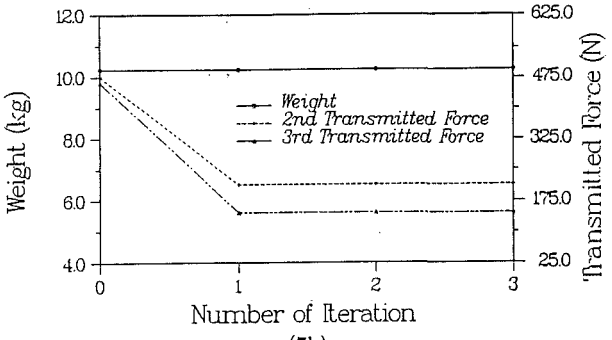

(7b)

the calculation of the sensitivity of these added variables are negligible compared to the case in the first example. The histories of single objective optimization are shown in Fig. 7.

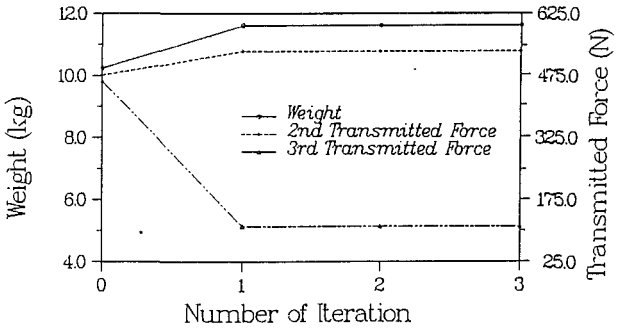

(7c)

Fig. 7 Histories of optimum design of: (7*a*) the total shaft weight; (7*b*) the second transmitted force; (7*c*) the third transmitted force

Table 5 Initial and final design of example 2 for single objective optimization: (5*a*) inner radius of shaft element, bearing stiffness, bearing position, and disk position; (5*b*) critical speed, shaft weight, transmitted forces, and CPU time

	Initial	Final		
Shaft		W*	F_2^{b*}	F_3^{b*}
Element	Inner Radius (cm)			
1	1.882	2.690	1.882	1.882
2	1.940	2.690	1.940	1.944
3	1.466	2.690	1.446	1.447
4	1.660	2.690	1.660	1.667
5	2.151	2.603	2.151	2.157
6	2.690	2.690	2.690	2.686
7	2.690	2.690	2.690	2.689
8	2.690	2.690	2.690	2.686
9	2.690	2.690	2.690	2.577
10	2.690	2.690	2.690	2.082
11	1.420	2.634	1.420	1.421
12	1.880	2.690	1.880	1.880
Bearing	Bearing Stiffness (N/m)			
1	3.50×10^6	3.50×10^6	3.50×10^6	3.50×10^6
2	1.27×10^8	1.27×10^8	1.31×10^8	1.27×10^8
3	1.20×10^7	3.51×10^6	3.50×10^6	3.50×10^6
Bearing	Bearing Position (cm)			
1	8.890	8.924	9.000	8.890
2	27.690	27.719	35.000	27.740
3	127.940	127.940	125.000	127.940
Disk	Disk Position (cm)			
1	0.000	0.000	0.000	0.000
2	10.490	10.476	10.000	10.490
3	20.170	20.170	18.338	20.170
4	120.140	120.111	117.000	120.127

(5a)

	Initial	Final		
		W*	F_2^{b*}	F_3^{b*}
	Critical Speed (rad/sec)			
ω_2^c	685.84	521.22	453.89	521.20
ω_3^c	2646.14	2303.45	3188.46	2305.61
	Shaft Weight (kg)			
W	10.235	5.034	10.235	11.615
	Transmitted Force (N)			
F_1^b	13.562	9.335	4.521	14.858
F_2^o	475.599	345.391	213.866	533.601
F_3^o	461.366	153.285	145.958	110.323
VAX-8600 CPU (sec)		11.85	10.17	8.34

* Single objective

(5b)

Table 6 Initial and final design of example 2: (6*a*) inner radius of shaft element, bearing stiffness, bearing position, and disk position; (6*b*) critical speed, shaft weight, transmitted forces, and CPU time

Multiobjective : W, F_2^b, and F_3^b				
	Initial	Final		
Shaft		WM	GPM	FM
Element	Inner Radius (cm)			
1	1.882	1.882	1.882	2.118
2	1.940	2.690	2.003	2.193
3	1.466	1.446	1.446	1.642
4	1.660	1.660	1.660	2.690
5	2.151	2.151	2.151	2.364
6	2.690	2.690	2.690	2.690
7	2.690	2.690	2.690	2.690
8	2.690	2.690	2.690	2.690
9	2.690	2.690	2.690	2.498
10	2.690	2.690	2.690	2.563
11	1.420	1.420	1.420	2.355
12	1.880	1.880	1.880	2.292
Bearing	Bearing Stiffness (N/m)			
1	3.50×10^6	3.50×10^6	3.50×10^6	3.50×10^6
2	1.27×10^8	1.51×10^8	1.27×10^8	1.26×10^8
3	1.20×10^7	3.50×10^6	3.50×10^6	3.50×10^6
Bearing	Bearing Position (cm)			
1	8.890	9.000	8.923	8.891
2	27.690	29.694	27.888	27.669
3	127.940	125.000	125.000	127.940
Disk	Disk Position (cm)			
1	0.000	0.000	0.000	0.000
2	10.490	10.000	10.473	10.489
3	20.170	20.132	20.168	20.170
4	120.140	118.383	120.100	117.000

(6a)

	Initial	Final		
		WM	GPM	FM
	Critical Speed (rad/sec)			
ω_2^c	685.84	494.68	508.95	532.08
ω_3^c	2646.14	2842.89	2633.19	2447.11
	Shaft Weight (kg)			
W	10.235	9.826	10.208	7.628
	Transmitted Force (N)			
F_1^b	13.562	7.346	9.641	10.352
F_2^b	475.599	284.444	272.090	386.303
F_3^b	461.366	142.345	132.283	134.816
VAX-8600 CPU (sec)		14.54	10.87	20.64

(6b)

Table 6 shows the initial and final design data for multi-objective optimization. The objectives are the shaft weight and the transmitted forces at the No. 2 and No. 3 bearings. The results show that the stiffness and the transmitted force at the No. 3 bearing are reduced about three times. However, the optimum weight is not greatly reduced except for the case of FM. On the contrary, the optimum design transmitted force at the No. 2 bearing of FM case results in higher value than those of WM and GPM cases. The optimum histories of using these methods are shown in Fig. 8.

Conclusions

1 For the single objective optimization, the weight of the shaft can be considerably reduced with high transmitted forces. However, the transmitted forces can be minimized with a slight increase of the shaft weight.

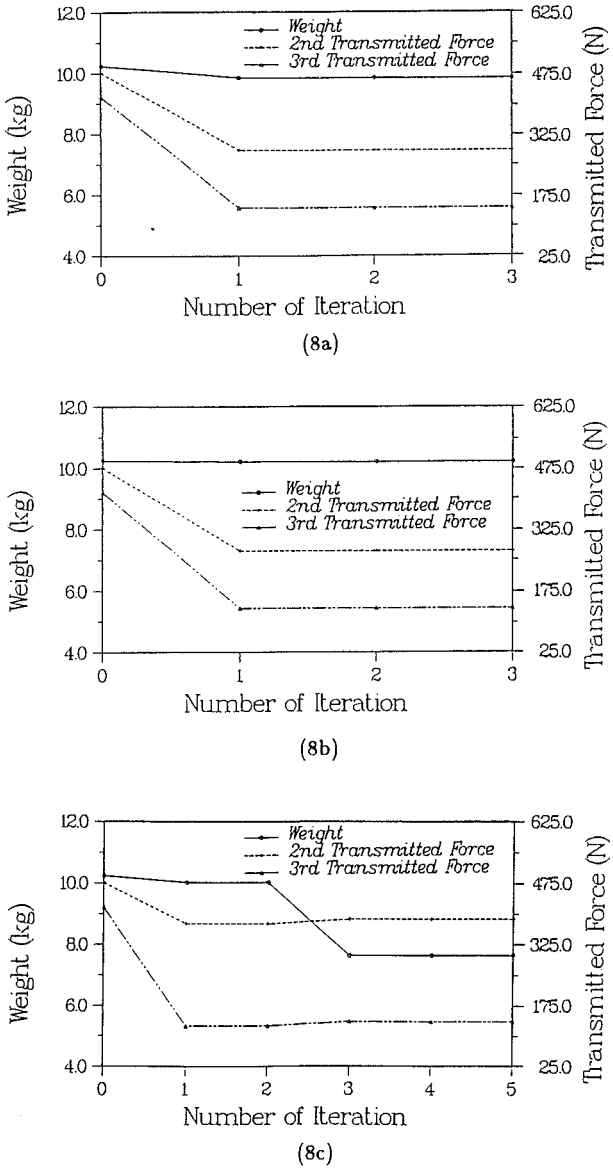

Fig. 8 Histories of optimum design of weight and second and third transmitted forces with: (8*a*) Weighting Method; (8*b*) Goal Programming Method; (8*c*) Fuzzy Method

2 If the weight is the only objective to be minimized, the inclusion of the positions of disks with unbalance and of bearings as the design variables, except the cross-sectional area of shaft elements and bearing stiffnesses, leads to good reduction of transmitted forces as well as of shaft weight.

3 In comparison to the single objective optimization, the optimum design weight of multi-objective optimization is smaller than that of the optimum transmitted force case but larger than that of the optimum weight case.

4 The multi-objective optimization techniques are applied to reduce the shaft weight and the transmitted forces simultaneously. The results show that a compromised optimum design can always be achieved.

5 The comparison of the results between multi-objective optimization techniques, i.e., WM, GPM, and FM, shows that the choice of the technique is case dependent. More studies of rotor bearing systems are needed.

References

Adams, M. L., 1980, "Nonlinear Dynamics of Flexible Multi-bearing Rotors," *Journal of Sound and Vibration*, Vol. 71(1), pp. 129–144.

Chankong, V., and Haimes, Y. Y., 1983, *Multiobjective Decision Making: Theory and Methodology*, North-Horland.

Childs, D. W., 1978, "The Space Shuttle Main Engine High-Pressure Fuel Turbopump Rotor Dynamic Instability Problem," ASME JOURNAL OF ENGINEERING FOR POWER, Vol. 100, pp. 48–57.

Childs, D. W., and Graviss, K., 1982, "A Note on Critical-Speed Solutions for Finite-Element-Based Rotor Models," ASME *Journal of Mechanical Design*, Vol. 104, pp. 412–415.

Duckstein, L., 1984, *Multiobjective Optimization in Structural Design: The Model Choice Problem*, Wiley, New York.

Feitzen, C. P., and Nordman, R., 1982, "Influence of Parameter Changes to Stability Behavior of Rotor," *Rotor-Dynamic Instability Problems in High-Performance Turbomachinery*, NASA Conference Publication 2250, Texas A&M Univ., College Station, pp. 284–297.

Gunter, E. J., 1970, "Influence of Flexibility Mounted Rolling Element Bearings on Rotor Response, Part 1: Linear Analysis," ASME *Journal of Lubrication Technology*, Vol. 92, pp. 59–75.

Kaplan, R. L., and Rao, S. S., 1987, "Nonlinear Goal Programming Techniques in the Synthesis of Mechanism," *Proceeding of the ASME Design Automation Conference*, pp. 173–180.

Lund, J. W., 1974, "Stability and Damped Critical Speeds of a Flexible Rotor in Fluid-Film Bearings," ASME *Journal of Engineering for Industry*, Vol. 96, pp. 509–517.

Lund, J. W., 1979, "Sensitivity of the Critical Speeds of a Rotor to Changes in Design," ASME *Journal of Mechanical Design*, Vol. 102, pp. 115–121.

Myklestad, N. O., 1944, "A New Method of Calculating Natural Modes of Uncoupled Bending Vibration of Airplane Wings and Other Types of Beams," *Journal of Aeronautical Science*, pp. 153–162.

Nelson, H. D., 1980, "A Finite Rotating Shaft Element Using Timoshenko Beam Theory," ASME *Journal of Mechanical Design*, Vol. 102, pp. 793–803.

Prohl, M. A., 1945, "A General Method for Calculating Critical Speeds of Flexible Rotors," ASME *Journal of Applied Mechanics*, Vol. 12, pp. A-142–A-148.

Rajan, M., Nelson, H. D., and Chen, W. J., 1986, "Parameter Sensitivity in Dynamics of Rotor-Bearing Systems," ASME *Journal of Vibration, Acoustics, Stress, and Reliability in Design*, Vol. 108, pp. 197–206.

Rao, S. S., 1984, "Multiobjective Optimization in Structural Design With Uncertain Parameters and Stochastic Process," *AIAA Journal*, Vol. 22, No. 11, pp. 1670–1678.

Rao, S. S., 1987, "Multiobjective Optimization of Fuzzy Structure Systems," *Int. J. for Num. Methods in Engineering*, Vol. 24, pp. 1157–1171.

Shiau, T. N., and Hwang, J. L., 1988, "Minimum Weight Design of a Rotor Bearing System With Multiple Frequency Constraints," ASME JOURNAL OF ENGINEERING FOR GAS TURBINES AND POWER, Vol. 110, pp. 592–599.

Shiau, T. N., and Hwang, J. L., 1989, "A New Approach to the Dynamic Characteristic of Undamped Rotor-Bearing Systems," ASME *Journal of Vibration, Acoustics, Stress, and Reliability in Design*, Vol. 111, pp. 379–385.

Shiau, T. N., and Hwang, J. L., 1990, "Optimum Weight Design of a Rotor Bearing System With Dynamic Behavior Constraints," ASME JOURNAL OF ENGINEERING FOR GAS TURBINES AND POWER, Vol. 112, pp. 454–462.

Shiau, T. N., and Hwang, J. L., 1993, "Generalized Polynomial Expansion Method for the Dynamic Analysis of Rotor-Bearing Systems," ASME JOURNAL OF ENGINEERING FOR GAS TURBINES AND POWER, Vol. 115, this issue, pp. 209–217.

Zoutendijk, M., 1960, *Methods of Feasible Directions*, Elsevier Publishing Co., Amsterdam, The Netherlands.

APPENDIX

$$M_{(m,n)} = \int_0^l A\rho x^{n+m-2}dx + \int_0^l (n-1)(m-1)I_D x^{n+m-4}dx + \sum_{i=1}^{N_d} [m_i^d (x_i^d)^{n+m-2} + (n-1)(m-1)I_{Di}^d (x_i^d)^{n+m-4}] \quad \text{(A1)}$$

$$G_{(m,n)} = \int_0^l (n-1)(m-1)I_P x^{n+m-4}dx + \sum_{i=1}^{N_d} [(n-1)(m-1)I_{Pi}^d (x_i^d)^{n+m-4}] \quad \text{(A2)}$$

$$K_{s(m,n)} = \int_0^l (n-1)(m-1)(n-2)(m-2) \cdot EIx^{n+m-6}dx \quad \text{(A3)}$$

$$K_{(m,n)} = \sum_{j=1}^{N_b} k_j^b (x_j^b)^{n+m-2} \quad \text{(A4)}$$

$$R_{a(j)} = \int_0^l eA\rho\Omega^2 \cos(\Omega t + \phi) x^{j-1}dx + \sum_{i=1}^{N_d} e_i^d m_i^d \Omega^2 \cos(\Omega t + \phi_i) x^{j-1} \quad \text{(A5)}$$

$$R_{b(j)} = \int_0^l eA\rho\Omega^2 \sin(\Omega t + \phi) x^{j-1}dx + \sum_{i=1}^{N_d} e_i^d m_i^d \Omega^2 \sin(\Omega t + \phi_i) x^{j-1} \quad \text{(A6)}$$

$$R_{(j)} = \sum_{i=1}^{N_d} e_i^d m_i^d \Omega^2 e^{i\phi_i} x_i^{j-1} \quad \text{(A7)}$$

$$\frac{\partial M_{(m,n)}}{\partial A_i} = \int_{l_j}^{l_{j+1}} \rho x^{n+m-2}dx \quad \text{(A8)}$$

$$\frac{\partial M_{(m,n)}}{\partial I_i} = \int_{l_j}^{l_{j+1}} (n-1)(m-1)\rho x^{n+m-4}dx \quad \text{(A9)}$$

$$\frac{\partial M_{(m,n)}}{\partial k_i^b} = 0 \quad \text{(A10)}$$

$$\frac{\partial M_{(m,n)}}{\partial x_i^b} = 0 \quad \text{(A11)}$$

$$\frac{\partial M_{(m,n)}}{\partial x_i^d} = (n+m-2)m_i^d (x_i^d)^{n+m-3} + (n-1)(m-1)(n+m-4)I_{Di}^d (x_i^d)^{n+m-5} \quad \text{(A12)}$$

$$\frac{\partial G_{(m,n)}}{\partial A_i} = 0 \quad \text{(A13)}$$

$$\frac{\partial G_{(m,n)}}{\partial I_i} = 2\int_{l_j}^{l_{j+1}} (n-1)(m-1)\rho x^{n+m-4}dx \quad \text{(A14)}$$

$$\frac{\partial G_{(m,n)}}{\partial k_i^b} = 0 \quad \text{(A15)}$$

$$\frac{\partial G_{(m,n)}}{\partial x_i^b} = 0 \quad \text{(A16)}$$

$$\frac{\partial G_{(m,n)}}{\partial x_i^d} = (n-1)(m-1)(n+m-4)I_{Pi}(x_i^d)^{n+m-5} \quad \text{(A17)}$$

$$\frac{\partial K_{(m,n)}^*}{\partial A_i} = 0 \quad \text{(A18)}$$

$$\frac{\partial K_{(m,n)}^*}{\partial I_i} = 0 \quad \text{(A19)}$$

$$\frac{\partial K_{(m,n)}^*}{\partial k_i^b} = (x_i^b)^{n+m-2} \quad \text{(A20)}$$

$$\frac{\partial K_{(m,n)}^*}{\partial x_i^b} = (n+m-2)k_i^b (x_i^b)^{n+m-3} \quad \text{(A21)}$$

$$\frac{\partial K_{(m,n)}^*}{\partial x_i^d} = 0 \quad \text{(A22)}$$

$$\frac{\partial M_{(m,n)}^*}{\partial z_i} = \frac{\partial M_{(m,n)}}{\partial z_i} - \lambda \frac{\partial G_{(m,n)}^*}{\partial z_i} \quad \text{(A23)}$$

Optimum Design of Rotor-Bearing Systems With Eigenvalue Constraints

T.-Y. Chen
Department of Mechanical Engineering,
National Chung-Hsing University,
Taichung, Taiwan 40227

B. P. Wang
Department of Mechanical Engineering,
The University of Texas at Arlington,
Arlington, TX 76019

The analysis and design of rotor-bearing systems with gyroscopic effects are discussed in this paper. The original problem of this nonproportionally damped mechanism is transformed into the state space form so that the transformed problem is similar to the eigenvalue problem for an undamped system. It can be easily solved by widely available eigensolvers and the eigenvalue sensitivities needed for the design optimization can also be obtained conveniently using the transformed form. The sequential linear programming technique is employed to solve the design optimization problem. The easy implementation of this proposed approach with a general purpose finite element program is shown in the solution algorithm.

Introduction

Rotating machines represent some of the most common designs in mechanical engineering. Rotating shafts supported by bearings are usually loaded with mechanical components such as gears, pulleys, turbine rotors, etc. Since this type of mechanism is broadly used in mechanical engineering design, the correct analysis of its dynamic behavior is essential. Based on various beam theories, the finite element method is the most often employed tool to do the analysis job [1, 2]. However, using a finite element method to analyze the eigenvalues of the rotor-bearing system will sometimes cause serious errors provided the rotational effects are neglected.

The rotational effects that influence the structural frequencies come from two major sources. One is the centrifugal forces, which are proportional to the square of the spinning speed. The centrifugal forces tend to strengthen the stiffness of some mechanical components on the rotating shaft. Therefore, the natural frequencies are actually found to be higher than expected. The effects due to centrifugal forces can be taken care of by incorporating the geometric stiffness matrix into the finite element analysis.

The other rotational effects are caused by the gyroscopic forces. This force couples motion in one plane with motion in another plane. The gyroscopic effect also depends on the spinning speed. The greater the spinning speed, the greater the coupling effect. The gyroscopic effect was derived to be a skew-symmetric damping matrix [3]. Therefore, if the structural system does not have other damping sources, the eigenvalues of the rotor-bearing system with gyroscopic effects are purely imaginary due to the nature of the skew-symmetric damping matrix.

The rotor-bearing system analyses considering these effects have attracted many researchers for a long time. Several useful approaches have been produced [3, 4]. However, the applications of these analysis methods in optimal designs of rotor-bearing systems are not addressed very often.

It is the purpose of this paper to design a minimum weight rotor-bearing mechanism with damped eigenvalue constraints. The supporting bearing stiffness and damping are also included in the design considerations. The gyroscopic effect is considered in the finite element analysis of the structure. The centrifugal force is neglected assuming the rotors are compactly lumped masses.

Theoretical Formulation

The finite element modeling of a beam considering two transverse displacements and corresponding rotational degrees of freedom forms an 8×8 stiffness matrix as follows:

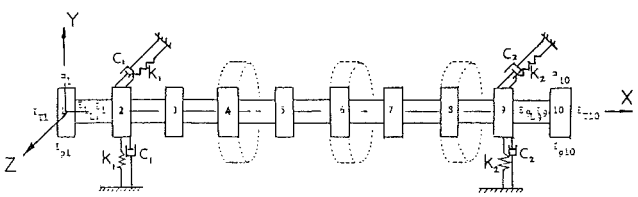

Fig. 1 Rotor-bearing system

Contributed by the International Gas Turbine Institute and presented at the 37th International Gas Turbine and Aeroengine Congress and Exposition, Cologne, Germany, June 1–4, 1992. Manuscript received by the International Gas Turbine Institute February 24, 1992. Paper No. 92-GT-307. Associate Technical Editor: L. S. Langston.

$$[K_i] = \begin{bmatrix} \frac{12EI_z}{L^3} & 0 & 0 & \frac{6EI_z}{L^2} & \frac{-12EI_z}{L^3} & 0 & 0 & \frac{6EI_z}{L^2} \\ 0 & \frac{12EI_y}{L^3} & \frac{-6EI_y}{L^2} & 0 & 0 & \frac{-12EI_y}{L^3} & \frac{-6EI_y}{L^2} & 0 \\ 0 & \frac{-6EI_y}{L^2} & \frac{4EI_y}{L} & 0 & 0 & \frac{6EI_y}{L^2} & \frac{2EI_y}{L} & 0 \\ \frac{6EI_z}{L^2} & 0 & 0 & \frac{4EI_z}{L} & \frac{-6EI_z}{L^2} & 0 & 0 & \frac{2EI_z}{L} \\ \frac{-12EI_z}{L^3} & 0 & 0 & \frac{-6EI_z}{L^2} & \frac{12EI_z}{L^3} & 0 & 0 & \frac{-6EI_z}{L^2} \\ 0 & \frac{-12EI_y}{L^3} & \frac{6EI_y}{L^2} & 0 & 0 & \frac{12EI_y}{L^3} & \frac{6EI_y}{L^2} & 0 \\ 0 & \frac{-6EI_y}{L^2} & \frac{2EI_y}{L} & 0 & 0 & \frac{6EI_y}{L^2} & \frac{4EI_y}{L} & 0 \\ \frac{6EI_z}{L^2} & 0 & 0 & \frac{2EI_z}{L} & \frac{-6EI_z}{L^2} & 0 & 0 & \frac{4EI_z}{L} \end{bmatrix} \quad (1)$$

The gyroscopic effects can be modeled by a 4×4 skew-symmetric damping matrix at each node on the rotating shaft:

$$[C_G] = \begin{bmatrix} 0 & 0 & 0 & 0 \\ 0 & 0 & 0 & 0 \\ 0 & 0 & 0 & \omega I_p \\ 0 & 0 & -\omega I_p & 0 \end{bmatrix} \quad (2)$$

where I_p is the mass moment of inertia about the rotating axis at the specific node; ω is the spinning speed of the shaft.

The lumped mass matrix used in this analysis produces a global diagonal mass matrix. The rotating shaft is assumed to be supported by bearings. The stiffnesses and the damping effects of the bearing supports are simulated by springs and viscous dampers in the two transverse directions. The damping matrix contains two parts. One is from the gyroscopic effects and the other one is due to the damping of supports. The free vibration motion equation of this problem is expressed as

$$[M]\{\ddot{U}\} + ([C_V] + [C_G])\{\dot{U}\} + [K]\{U\} = \{0\} \quad (3)$$

where $[M]$ is the mass matrix of the system; $[C_V]$ is the damping matrix due to support damping; $[C_G]$ is the skew-symmetric matrix representing the gyroscopic effects; $[K]$ is the stiffness matrix of the structure; and $\{U\}$ is the displacement vector.

Solving this equation yields an eigenproblem of the following form:

$$(\lambda_i^2[M] + \lambda_i([C_V] + [C_G]) + [K])\{\psi_i\} = \{0\} \quad (4)$$

where λ_i is the ith complex eigenvalue of the system and $\{\psi_i\}$ is the complex eigenvector associated with λ_i.

Considering the necessity of computing eigenvalue sensitivities and the availability of standard eigen-solvers, the eigenvalue problem is not solved directly from Eq. (4). Instead, the motion Eq. (3) is appended by an identity equation to constitute the state space equation as follows [5].

The identity equation added is

$$[M]\{\dot{U}\} - [M]\{\dot{U}\} = \{0\} \quad (5)$$

Combining Eqs. (3) and (5) gives

$$\begin{bmatrix} C & M \\ M & 0 \end{bmatrix} \begin{Bmatrix} \dot{U} \\ \ddot{U} \end{Bmatrix} + \begin{bmatrix} K & 0 \\ 0 & -M \end{bmatrix} \begin{Bmatrix} U \\ \dot{U} \end{Bmatrix} = \begin{Bmatrix} 0 \\ 0 \end{Bmatrix} \quad (6)$$

where

$$[C] = [C_V] + [C_G] \quad (7)$$

Nomenclature

A_k = cross-sectional area of kth shaft element
$[A]$ = the equivalent mass matrix of the transformed system
$[B]$ = the equivalent stiffness matrix of the transformed system
$[C]$ = total damping matrix including $[C_v]$ and $[C_G]$
$[C_G]$ = skew symmetric matrix representing the gyroscopic effect
$[C_v]$ = viscous damping matrix due to support damping
$[I]$ = unit matrix
$[I_p]$ = mass moment of inertia about the rotating axis
$[K]$ = stiffness matrix of the structure
L_k = length of the kth shaft element
$[M]$ = mass matrix of the structure
$[Q_s]$ = sth set of eigenvectors associated with the same repeated eigenvalue
$\{U\}$ = displacement vector for free vibration
W = weight of all design variables
$\{a_i\}$ = vector containing weighting coefficients to form $\{\bar{q}_i\}$
b_j = weight associated with per unit damping coefficient of the support
c_j = damping coefficient of the support
k_j = stiffness of the support
l = number of supports
m = number of eigenvalue constraints
n = number of design variables for the shaft elements
$\{q_i\}$ = eigenvector of the transformed system
$\{\bar{q}_i\}$ = eigenvector for repeated modes
w_j = weight associated with per unit stiffness constant of the support
α_k = kth design variable
λ_i = ith complex eigenvalue of the structure
$\bar{\lambda}_i$ = desired constraint target
λ_{i0} = eigenvalue of current design
ρ_k = weight density of kth shaft element
ψ_i = complex eigenvector associated with λ_i
ω = shaft rotating speed

Subscripts and Superscripts

L = constraint lower limit
T = transpose
U = constraint upper limit
j = design variable number for supports
k = design variable number for shaft element
s = set number for the repeated modes

Let

$$\{q\} = \begin{Bmatrix} U \\ \dot{U} \end{Bmatrix} \tag{8}$$

$$[A] = \begin{bmatrix} C & M \\ M & 0 \end{bmatrix} \tag{9}$$

and

$$[B] = \begin{bmatrix} -K & 0 \\ 0 & M \end{bmatrix} \tag{10}$$

Substituting Eqs. (8)–(10) into Eq. (6) results in

$$[A]\{\dot{q}\} - [B]\{q\} = \{0\} \tag{11}$$

or

$$[A]\{\dot{q}\} = [B]\{q\} \tag{12}$$

Assuming

$$\{q\} = e^{\lambda t}\{y\} \tag{13}$$

then

$$\begin{aligned} \{\dot{q}\} &= \lambda e^{\lambda t}\{y\} \\ &= \lambda\{q\} \end{aligned} \tag{14}$$

Plugging Eq. (14) into Eq. (11) yields

$$\lambda_i[A]\{q_i\} = [B]\{q_i\} \tag{15}$$

Equation (15) is apparently an eigenvalue problem with λ_i the eigenvalue and $\{q_i\}$ the eigenvector.

The dimension of Eq. (15) is twice the original system. The complex eigenvalues are always accompanied by their complex conjugates. The eigenvectors contain the data for both displacements and velocities. Although the dimension of the problem is increased, using this familiar form is justified by two major reasons. One is that a lot of commercially available computer software can solve the eigenvalue problem of Eq. (15). The other one is that the calculation of eigenvalue sensitivities for the similar undamped system is directly derived from the real eigenvalue problem similar to Eq. (15). Therefore, the algorithm for solving the optimization problem with real eigenvalue constraints can be easily modified to attack this damped system. Subroutine DGVCRG from the IMSL package is used to solve the eigensystem of Eq. (15).

The eigenvalue sensitivity using the Fox and Kapoor [6] formulation is

$$\frac{\partial \lambda_i}{\partial \alpha_k} = \{q_i\}^T \left(\frac{\partial [B]}{\partial \alpha_k} - \lambda_i \frac{\partial [A]}{\partial \alpha_k} \right) \{q_i\} \tag{16}$$

where α_k is the kth design variable and $\{q_i\}$ is normalized such that $\{q_i\}^T[A]\{q_i\} = 1$.

For the rotor-bearing system, if the cross-sectional area of the rotating shaft is circular, the bending stiffness in the two transverse directions is the same. Due to this equal stiffness in the two directions, repeated eigenvalues may appear in the eigensolution of Eq. (15). If the constrained eigenvalues happen to be one of the repeated sets of eigenvalues, then Eq. (16) sometimes does not give correct sensitivity informations. The reason is that the eigenvector associated with the repeated eigenvalue is not unique. In fact, it can be a linear combination of all the eigenvectors associated with the repeated eigenvalues. The determination of the proper eigenvector from these infinite choices is summarized below.

Assuming

$$\{\bar{q}_i\} = [Q_s]\{a_i\} \tag{17}$$

where $\{\bar{q}_i\}$ is the eigenvector that should be used in Eq. (16) for the repeated eigenvalue λ_i. $[Q_s]$ contains the eigenvectors associated with repeated λ_i; $\{a_i\}$ is the weighting vector for the linear combination.

Substituting $\{\bar{q}_i\}$ for $\{q_i\}$ in Eq. (15) for repeated modes results in

$$\lambda_i[A][Q_s]\{a_i\} = [B][Q_s]\{a_i\} \tag{18}$$

Taking the derivative of Eq. (18) with respect to α_k and premultiplying Eq. (18) by $[Q_s]^T$ gives

$$[Q_s]^T \frac{\partial(\lambda_i[A] - [B])}{\partial \alpha_k} [Q_s]\{a_i\} + [Q_s]^T(\lambda_i[A] - [B]) \frac{\partial\{\bar{q}_i\}}{\partial \alpha_k} = 0$$

or

$$[Q_s]^T \left(-\frac{\partial \lambda_i}{\partial \alpha_k}[A] - \lambda_i \frac{\partial [A]}{\partial \alpha_k} + \frac{\partial [B]}{\partial \alpha_k} \right) [Q_s]\{a_i\} = 0 \tag{19}$$

Equation (19) can be further simplified as

$$\left([Q_s]^T \left(\frac{\partial [B]}{\partial \alpha_k} - \lambda_i \frac{\partial [A]}{\partial \alpha_k} \right) [Q_s] - \frac{\partial \lambda_i}{\partial \alpha_k}[I] \right) \{a_i\} = \{0\} \tag{20}$$

where $[I]$ is the diagonal unit matrix.

Equation (20) is found to be another eigenvalue problem with its eigenvalues the sensitivities of the repeated modes of the original system. If the eigenvalues of Eq. (20) are not repeated, the eigenvectors $\{a_i\}$ are uniquely determined. The eigenvector $\{\bar{q}_i\}$ associated with the repeated eigenvalues in the original system is then recovered by Eq. (17). Using this proper $\{\bar{q}_i\}$ in Eq. (16), the correct eigenvalue sensitivities for the repeated eigenvalues are obtained. However, provided the eigenvalues obtained from Eq. (20) are again repeated, then the unique $\{\bar{q}_i\}$ cannot be found. But the eigenvalue sensitivities for the repeated eigenvalues of the original system have already been obtained as the eigenvalues of Eq. (20).

The optimum design problem is defined to be:

Minimize

$$W = \sum_{k=1}^{n} \rho_k A_k L_k + \sum_{j=1}^{l} (w_j k_j + b_j c_j) \tag{21}$$

subject to

$$\text{Real}(\lambda_i) > \text{Real}(\bar{\lambda}_i) \tag{22}$$

$$\text{Imag}(\lambda_i) > \text{Imag}(\bar{\lambda}_i) \tag{23}$$

$$i = 1, 2, \ldots, m$$

$$A_k^L < A_k < A_k^U \qquad k = 1, 2, \ldots, n \tag{24}$$

$$k_j^L < k_j < k_j^U \qquad j = 1, 2, \ldots, l \tag{25}$$

$$c_j^L < c_j < c_j^U \qquad j = 1, 2, \ldots, l \tag{26}$$

where W is the weight of the structure; ρ_i, A_i, and L_i are the weight density, the cross-sectional area, and the length of the ith design variable respectively. w_j and b_j are the weights associated with per unit bearing support stiffness and per unit damping coefficient respectively. n is the number of shaft design variables; l is the number of supporting design variables. Equations (22) and (23) are the eigenvalue constraints and m is the number of these behavior constraints. Equation (24) is the side constraint for the shaft cross-sectional area. Equations (25) and (26) are the side constraints for the bearing support stiffness and damping variables, respectively. $\text{Real}(\lambda_i)$ represents the real part of the constrained ith eigenvalue; $\text{Imag}(\lambda_i)$ stands for the imaginary part of the ith eigenvalue; $\bar{\lambda}_i$ is the constrained target of the ith constrained eigenvalue. The constraint equation can be generalized to be one of less than, greater than, equal to, and a range type constraint. The separation of the complex eigenvalue constraint into the real and the imaginary parts avoids the complex manipulations in the design process.

Equations (22) and (23) can be approximated by first-order Taylor's series as

Table 1 Eigenvalue constraints

Mode No.	Constraint type (real part)	Desired value (real part)	Constraint type (imag. part)	Desired value (imag.part)
1	<	-6	>	260
2	<	-8	<	300
3	<	-100	>	590

Table 2 Final and initial designs

	A_1	A_2	A_3	A_4	A_5	A_6	A_7	A_8	A_9
Initial(cm^2)	126.71	126.71	126.71	126.71	126.71	126.71	126.71	126.71	126.71
Final(cm^2)	64.52	82.32	146.77	168.13	176.13	168.45	133.94	83.03	64.52

	$k_1(KN/cm)$	$k_2(KN/cm)$	$c_1(N-s/cm)$	$c_2(N-s/cm)$
Initial	262.69	262.69	175.13	175.13
Final	262.72	262.72	152.19	142.22

Table 3 Histories of eigenvalues

Iteration	λ_1	λ_2	λ_3	Feasibility
0	-5.24+241.28i	-7.14+254.03i	-90.16+520.01i	no
1	-6.29+249.30i	-7.69+258.42i	-89.07+554.21i	no
2	-7.74+258.23i	-8.86+264.64i	-103.46+583.08i	no
3	-7.96+259.72i	-9.11+266.18i	-104.66+590.29i	no
4	-7.66+258.90i	-8.87+265.89i	-104.66+596.41i	no
5	-7.77+259.61i	-8.91+266.12i	-104.13+598.12i	no
6	-7.57+259.06i	-8.78+266.00i	-103.01+596.94i	no
7	-7.74+260.12i	-8.92+266.72i	-102.67+597.66i	yes
8	-7.59+259.59i	-8.86+266.81i	-102.18+594.81i	no
9	-7.74+260.44i	-8.94+267.06i	-101.65+596.74i	yes
10	-7.57+259.81i	-8.84+266.93i	-101.40+595.39i	no
11	-7.68+260.43i	-8.90+267.13i	-101.04+596.74i	yes
12	-7.58+260.03i	-8.79+266.78i	-100.42+597.38i	yes
13	-7.54+260.01i	-8.77+266.86i	-100.44+598.14i	yes
14	-7.58+260.21i	-8.78+266.78i	-100.15+600.73i	yes
15	-7.54+259.80i	-8.76+266.44i	-99.85+601.00i	no
16	-7.51+259.81i	-8.71+266.40i	-99.91+601.01i	no

Iteration 0 represents the initial design.

$$\text{Real}(\lambda_{i0}) + \text{Real}\left(\sum_{j=1}^{n} \frac{\partial \lambda_i}{\partial A_j}\Delta A_j + \sum_{j=1}^{l} \frac{\partial \lambda_i}{\partial k_j}\Delta k_j + \sum_{j=1}^{l} \frac{\partial \lambda_i}{\partial c_j}\Delta c_j\right) > \text{Real}(\bar{\lambda}_i) \quad (27)$$

and

$$\text{Imag}(\lambda_{i0}) + \text{Imag}\left(\sum_{j=1}^{n} \frac{\partial \lambda_i}{\partial A_j}\Delta A_j + \sum_{j=1}^{l} \frac{\partial \lambda_i}{\partial k_j}\Delta k_j + \sum_{j=1}^{l} \frac{\partial \lambda_i}{\partial c_j}\Delta c_j\right) > \text{Imag}(\bar{\lambda}_i) \quad (28)$$

where λ_{i0} is the ith eigenvalue of current design.

The sequential linear programming (SLP) technique is used to solve this optimization problem. The subroutine DDLPRS from IMSL package is called to solve the linear programming problem. Because of the linearized nature of the constraint equations, an iterative procedure is established as follows to get the optimum solution:

1 Solve Eq. (15) for eigenvalues and eigenvectors of current design.
2 Check convergence and feasibilities of the constraints. If satisfied, stop. Otherwise, go to Step 3.
3 Use Eq. (16) or (20) to evaluate the eigenvalue sensitivities for the constrained modes.
4 Form the optimization problem using Eqs. (21) and (24)–(28).
5 Solve the optimization problem using SLP and go to Step 1.

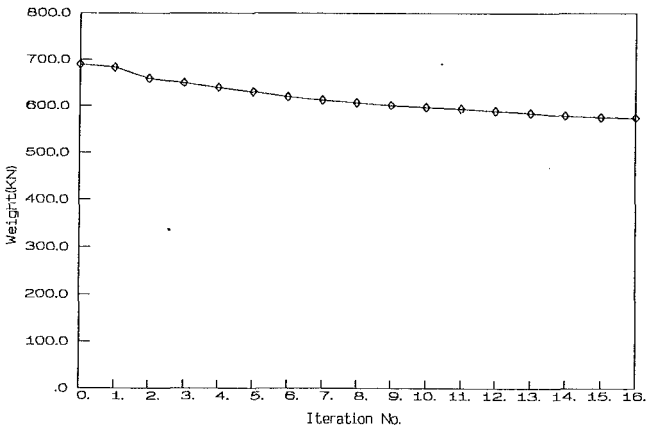

Fig. 2 Weight history

Numerical Examples

The example illustrated is a rotating shaft loaded with three big disks shown in Fig. 1.

The shaft is modeled by nine beam elements with eight degrees of freedom in each element. The initial design of the shaft has uniform circular cross-sectional area of 126.68 cm^2. The corresponding bending moment of inertia in the two transverse directions is 1277 cm^4. The length of each shaft element is 30.48 cm. Young's modulus is taken to be 206.84 GPa. The mass density of the shaft material equals 0.00024353 kg/cm^3. The transverse rotational moment of inertia for each shaft element is computed using the formula $m_i[(1/4)r_i^2 + (L_i^2/12)]$ and equally lumped at the two nodes of the beam element. The mass polar moment of inertia of each shaft element is obtained using the formula $(1/2)m_i r_i^2$ and also equally lumped at the two nodes of each shaft element. The bearing supports are located at nodes 2 and 9 as shown in the figure. The supporting stiffness in the y and z directions for both of the supports is 262.69 KN/cm. The viscous damping coefficient of bearing supports is 175.13 N-s/cm. Three identical big disks are loaded at nodes 4, 6, and 8. The mass of these disks is 0.7585 kg. The transverse rotational moment of inertia of these disks is 148.12 kg-cm^2. The mass polar moment of inertia of these disks is 296.24 kg-cm^2.

The shaft is assumed to be rotating at 1200 rad/s (11459.16 rpm). The weight constants associated with the supporting spring constant and the damping coefficients are 4.448×10^{-8} cm for w_j and 4.448 cm/s for b_j, respectively. Nine design variables, which are the cross-sectional areas of each shaft element, are used for the shaft. The side constraints that define the lower and upper bounds of the cross-sectional areas for all these nine design variables are set at 64.52 cm^2 and 258.06 cm^2. One design variable represents all four support stiffnesses. The limits set on this design variable are 131.345 KN/cm and 525.380 KN/cm. The last design variable is for the four support damping coefficients. The lower and the upper bounds for the damping coefficient are 87.56 N-s/cm and 350.25 N-s/cm, respectively.

The imposed eigenvalue constraints are shown in Table 1.

After 16 iterations, the design problem converges. The weight history is shown in Fig. 2. The final design is listed in Table 2. The variations of the three constrained eigenvalues in the iteration process are recorded in Table 3.

Concluding Remarks

A simple structure has been illustrated to demonstrate the possibility of optimum design of a rotor-bearing system with gyroscopic effects. In this paper the constraints are imposed on the complex eigenvalues only. For practical design considerations, the constraints may need to be extended to include

stress, deflection, and assembly constraints. The algorithm developed in this paper can be readily adjusted to include these constraints.

Acknowledgments

The authors deeply appreciate one anonymous reviewer's comments, which help to correct a programming error in the analysis program.

References

1 Ruhl, R. L., and Booker, J. L., "A Finite Element Model for Distributed Parameter Turborotor Systems," ASME *Journal of Engineering for Industry*, Vol. 94, No. 1, 1972, pp. 126–132.

2 Nelson, H. D., and McVaugh, J. M., "The Dynamics of Rotor-Bearing Systems Using Finite Elements," ASME *Journal of Engineering for Industry*, Vol. 98, No. 2, 1976, pp. 593–600.

3 Gmur, T. C., and Rodrigues, J. D., "Shaft Finite Elements for Rotor Dynamics Analysis," ASME *Journal of Vibration and Acoustics*, Vol. 113, 1991, pp. 482–493.

4 Gans, H. D., and Anderson, W. J., "Structural Optimization Incorporating Centrifugal and Coriolis Effects," *AIAA Journal*, Vol. 29, No. 10, 1991, pp. 1743–1750.

5 Clough, R. W., and Penaien, J., *Dynamics of Structures*, McGraw-Hill, Inc., New York, 1975, pp. 195–198.

6 Fox, R. L., and Kapoor, M. P., "Rates of Change of Eigenvalues and Eigenvectors," *AIAA Journal*, Vol. 6, 1968, pp. 2426–2429.

J. S. Rao
BHEL Chair,
Professor of Mechanical Engineering,
Indian Institute of Technology,
New Delhi 110016 India

Quality Factors of Rotors With Hydrodynamic Bearings

The quality factor of a system is a measure of the maximum amplitude of vibration that occurs at resonance when the frequency of excitation is equal to the undamped natural frequency. This factor can be easily determined for a given mode of vibration, given its equivalent viscous damping ratio, as $Q = 1/2\xi$. Such a definition becomes complicated for a rotor mounted on hydrodynamic bearings. This note discusses some factors involved in estimating the quality factor of a rotor.

1 Introduction

For a single degree of freedom system with a harmonic excitation or with rotating unbalance, it is well known that the amplitude of vibration is very large when the frequency of excitation is equal to its natural frequency. It is of obvious interest to have an idea of this amplitude of vibration, since maximum stresses occur at this point. This amplitude of vibration is limited only by the amount of damping present in the system. For systems with small values of damping, resonance occurs very close to the natural frequency, p, and therefore the quality factor representing maximum amplitude of vibration is determined at a forced frequency ω equal to the natural frequency. This value is given by (see Rao, 1983)

$$Q=\frac{1}{2\xi} \tag{1}$$

where $\xi = 2mp$ is the viscous damping ratio of the system and m is its mass. The maximum amplitude of vibration occurring at resonance can be reduced by increasing the damping as much as possible.

For symmetric rotors mounted on rigid bearings, the critical speeds are the same as natural frequencies of the stationary shaft in lateral bending. As the stiffness is the same in all directions, the rotor has circular whirl orbit, and there is a critical speed for each mode of vibration of the stationary shaft. When the rotor is mounted on hydrodynamic bearings, each stationary shaft mode is split into two, one a minor and the other a major natural frequency, and correspondingly there are two critical speeds for the rotor for each of its lateral modes of vibration. This is because the support stiffness offered by the bearing is not the same in all directions. The hydrodynamic bearings are asymmetric and cross coupled in nature. Moreover, the damping in hydrodynamic bearings can be significant in comparison to the shaft material damping. Further, all the stiffness and damping properties of the bearings are speed dependent, and hence a simple definition of the natural frequency is also not so easy. The problem becomes more complicated if one of the cross-coupled stiffnesses is negative and instabilities can occur very close to resonance itself. For this reason it is a general practice to determine the unbalance response of the rotors and find the critical speeds by locating maximum amplitudes of whirl. Hence the definition of quality factor is not so simple in the case of rotors mounted on hydrodynamic bearings. Some factors involved in the behavior of rotors mounted on hydrodynamic bearings are discussed in this paper.

2 A Simple Rotor in Hydrodynamic Bearings

Figure 1 shows a simple rotor in fluid film bearings. The parameters of the rotor, mass M and stiffness K, can be representative of modal parameters of a rotor in a given mode obtained from a numerical procedure like transfer matrix method. The bearings are assumed to be simple linear eight-coefficient bearings and the equations of motion are

$$\begin{aligned} M\ddot{z}+K_1^*z+\ +K_{12}^*y &= Ma\omega^2\cos\omega t \\ M\ddot{y}+K_2^*y+K_{21}^*z &= Ma\omega^2\sin\omega t \end{aligned} \tag{2}$$

where

$$K_1^*=\frac{K^*\{2K_{zz}^*(2K_{yy}^*+K^*)-4K_{zy}^*K_{yz}^*\}}{(2K_{zz}^*+K^*)(2K_{yy}^*+K^*)-4K_{zy}^*K_{yz}^*}$$

$$K_2^*=\frac{K^*\{2K_{yy}^*(2K_{zz}^*+K^*)-4K_{zy}^*K_{yz}^*\}}{(2K_{zz}^*+K^*)(2K_{yy}^*+K^*)-4K_{zy}^*K_{yz}^*}$$

$$K_{12}^*=\frac{2K_{zy}^*K^{*2}}{(2K_{zz}^*+K^*)(2K_{yy}^*+K^*)-4K_{zy}^*K_{yz}^*}$$

$$K_{21}^*=\frac{2K_{yz}^*K^{*2}}{(2K_{zz}^*+K^*)(2K_{yy}^*+K^*)-4K_{zy}^*K_{yz}^*}$$

$$K^*=K+i\omega C \quad K_{zz}^*=K_{zz}+i\omega C_{zz}, \text{ etc.} \tag{3}$$

The solution of Eq. (2) for the unbalance response can be obtained as

$$R=\frac{\omega^2(\omega_1^{*2}+\omega_2^{*2}-2\omega^2)-i(\mu_2^*\omega_2^{*2}\text{ms}\mu_1^*\omega_1^{*2})}{2(\omega_1^{*2}-\omega^2)(\omega_2^{*2}-\omega^2)-\mu_1^*\mu_2^*\omega_1^{*2}\omega_2^{*2}}\,e^{i\omega t}$$

$$-\frac{\omega^2}{2}\,\frac{(\omega_1^{*2}-\omega_2^{*2})+i(\mu_2^*\omega_2^{*2}+\mu_1^*\omega_1^{*2})}{(\omega_1^{*2}-\omega^2)(\omega_2^{*2}-\omega^2)-\mu_1^*\mu_2^*\omega_1^{*2}\omega_2^{*2}}\,e^{-i\omega t} \tag{4}$$

Contributed by the Power Division for publication in the JOURNAL OF ENGINEERING FOR GAS TURBINES AND POWER. Manuscript received by the Power Division July 13, 1990. Associate Technical Editor: R. W. Porter.

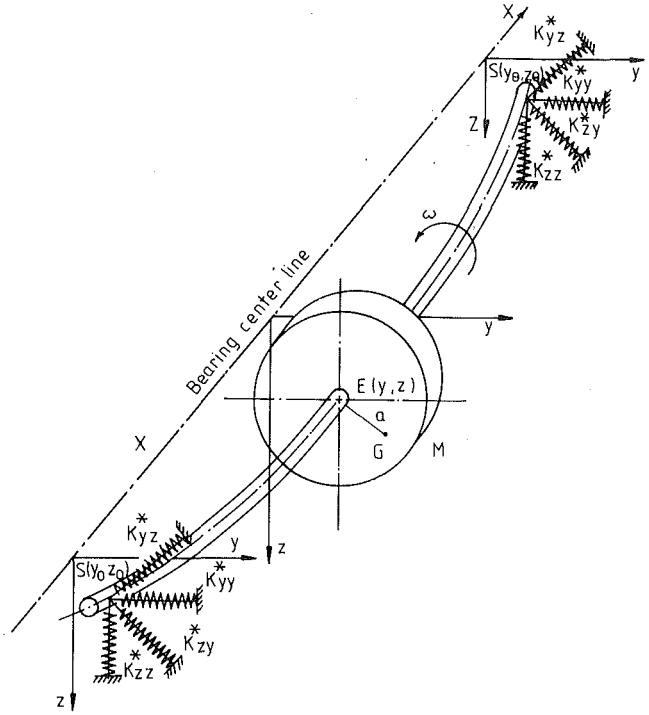

Fig. 1 A simple rotor on fluid film bearings

where

$$\omega_1^{*2} = \frac{K_1^*}{M} \qquad \omega_2^{*2} = \frac{K_2^*}{M}$$

$$\mu_1^* = \frac{K_{12}^*}{K_1^*} \qquad \mu_2^* = \frac{K_{21}^*}{K_2^*} \tag{5}$$

The unbalance response from the above equation for simple rotors has been discussed before (Rao, 1982; Rao et al., 1981). For rotors carrying several masses, the unbalance response can be determined using numerical methods such as transfer matrices and finite elements, e.g., Lund and Orcutt (1967), Kramer (1977), Rao and Sarma (1984), and Lalanne and Queau (1979).

Equations (2) are coupled equations and it is not simple to obtain an expression for the quality factor. In such cases the solution given by Eq. (4) can be used to determine the unbalance response as a function of speed and obtain the maximum whirl amplitudes. To obtain an idea of the quality factor, one can consider a system without cross-coupled stiffness and damping terms. In such a case the governing Eqs. (2) get decoupled as

$$M\ddot{z} + \bar{C}_z\dot{z} + \bar{K}_1 z = Ma\omega^2 \cos \omega t$$

$$M\ddot{y} + \bar{C}_y\dot{y} + \bar{K}_2 y = Ma\omega^2 \sin \omega t \tag{6}$$

where

$$\bar{C}_z = \frac{2(2CK_{zz}^2 + 2C\omega^2 C_{zz}^2 + \omega^2 C^2 C_{zz} + K^2 C_{zz})}{(2K_{zz} + K)^2 + \omega^2(2C_{zz} + C)^2}$$

$$\bar{C}_y = \frac{2(2CK_{yy}^2 + 2C\omega^2 C_{yy}^2 + \omega^2 C^2 C_{yy} + K^2 C_{yy})}{(2K_{yy} + K)^2 + \omega^2(2C_{yy} + C)^2}$$

$$K_z = \frac{2(KK_{zz} - \omega^2 CC_{zz})(2K_{zz} + K) + 2\omega^2(CK_{zz} + KC_{zz})(2C_{zz} + C)}{(2K_{zz} + K)^2 + \omega^2(2C_{zz} + C)^2}$$

$$K_y = \frac{2(KK_{yy} - \omega^2 CC_{yy})(2K_{yy} + K) + 2\omega^2(CK_{yy} + KC_{yy})(2C_{yy} + C)}{(2K_{yy} + K)^2 + \omega^2(2C_{yy} + C)^2} \tag{7}$$

Since Eqs. (6) are single degree of freedom vibrating system equations, we can easily determine the damping ratios for both z and y directions:

$$\xi_z = \frac{\bar{C}_z}{2\sqrt{\bar{K}_z M}}$$

$$\xi_y = \frac{\bar{C}_y}{2\sqrt{\bar{K}_y M}} \tag{8}$$

Equations (7) can be simplified further by assuming the shaft damping to be zero. This is quite often justified as the fluid

Nomenclature

a = eccentricity of the rotor
A = amplification factor
C = shaft damping coefficient
C_{yy} = direct damping coefficient for y direction
C_{yz} = cross-coupled damping coefficient for y direction
C_{zz} = direct damping coefficient for z direction
C_{zy} = cross-coupled damping coefficient for z direction
K = modal stiffness
K_1 = equivalent direct complex stiffness in z direction
K_2 = equivalent direct complex stiffness in y direction
K_{12} = equivalent cross complex stiffness in z direction
K_{21} = equivalent cross complex stiffness in y direction
K_{yy} = direct stiffness coefficient for y direction
K_{yz} = cross-coupled stiffness coefficient for y direction
K_{zz} = direct stiffness coefficient for z direction
K_{zy} = cross-coupled stiffness coefficient for z direction
m = system mass
M = modal mass of the rotor
n = X_r/X_c
p = natural frequency
Q_y = quality factor for y motion
Q_z = quality factor for z motion
R = unbalance response
r = frequency ratio
t = time
X = amplitude
X_c = amplitude at two frequencies
X_r = amplitude at frequency ratio r
X_{res} = amplitude at resonance
X_{st} = static deflection
y = horizontal displacement of the rotor center
z = vertical displacement of the rotor center
μ_1, μ_2 = cross-coupled stiffness ratios; see Eq. (5)
ξ_y = equivalent viscous damping ratio for y motion
ξ_z = equivalent viscous damping ratio for z motion
ω = forcing frequency, rotational speed, rad/s
ω_n = rigid bearing critical speed, rad/s
ω_{pk} = frequency where peak amplitude occurs
ω_1, ω_2 = uncoupled natural frequencies; also, two frequencies where the amplitude is same
* = complex quantities
$(\ )^i$ = ith iteration quantity
$(\bar{\ })$ = uncoupled quantities of equivalent stiffness and damping, with cross-coupled terms set to zero
$(\_)$ = uncoupled quantities of equivalent stiffness and damping, with zero cross-coupled terms and shaft damping

film damping is generally much larger compared with the shaft material damping. Then

$$\underline{C}_z = \frac{2K^2 C_{zz}}{(2K_{zz}+K)^2+\omega^2(2C_{zz})^2}$$

$$\underline{C}_y = \frac{2K^2 C_{yy}}{(2K_{yy}+K)^2+\omega^2(2C_{yy})^2}$$

$$\underline{K}_z = \frac{K\{2K_{zz}(2K_{zz}+K)+\omega^2(2C_{zz})^2\}}{(2K_{zz}+K)^2+\omega^2(2C_{zz}+C)^2}$$

$$\underline{K}_y = \frac{K\{2K_{yy}(2K_{yy}+K)+\omega^2(2C_{yy})^2\}}{(2K_{yy}+K)^2+\omega^2(2C_{yy}+C)^2} \tag{7a}$$

The corresponding damping ratios are

$$\xi_z = \frac{\underline{C}_z}{2\sqrt{\underline{K}_z M}}$$

$$\xi_y = \frac{\underline{C}_y}{2\sqrt{\underline{K}_y M}} \tag{8a}$$

Equations (7) and (8) give the effective stiffness and damping coefficients and the corresponding damping ratios. It may be noted the effective stiffness of the system is dependent on not only stiffness of the shaft and bearings but also on the shaft and bearing damping values. Similarly the effective damping is dependent on both the stiffness and damping properties of the shaft and bearings. The corresponding quality factors are

$$\overline{Q}_z = \frac{1}{2\overline{\xi}_z}$$

$$\overline{Q}_y = \frac{1}{2\overline{\xi}_y} \tag{9}$$

$$\underline{Q}_z = \frac{1}{2\underline{\xi}_z}$$

$$\underline{Q}_y = \frac{1}{2\underline{\xi}_y} \tag{9a}$$

3 Case Studies

3.1 Lightly Damped Rotor. Consider a rotor of mass 54.432 kg, with its rigid bearing critical speed equal to 4820 rpm, mounted on two 4 axial groove bearings 2.54 cm in diameter and 1.27 cm long with a radial clearance of 0.00254 cm and viscosity at operating temperature, 0.0242 Ns/m^2. The shaft stiffness for the fundamental rigid bearing critical speed is

$$K = M\omega_n^2 = 1.387 \times 10^7 \text{ N/m}$$

The stiffness and damping coefficients of the bearing can be obtained from Lund (1965), in the form of graphs, or from Rao (1985), as polynomial curves as a function of rotor speed. Let us assume for simplicity that the stiffness and damping coefficients can be taken to be constant in the range of resonance and evaluate them at 4500 rpm. Considering only the direct stiffness and damping coefficients, these values are

$K_{zz} = 4.16 \times 10^7$ N/m $C_{zz} = 70000$ Ns/m

$K_{yy} = 1.01 \times 10^7$ N/m $C_{yy} = 1930$ Ns/m

From Eqs. (7a)

$\overline{C}_z = 1955.2$ Ns/m

$\overline{K}_z = 1.25 \times 10^7$ N/m

$\overline{C}_y = 637.9$ Ns/m

$\overline{K}_y = 0.824 \times 10^7$ N/m

The uncoupled equations of motion are

$$\ddot{z} + 35.92\dot{z} + 229644.33z = a\omega^2 \cos \omega t$$

$$\ddot{y} + 11.7192\dot{y} + 151381.54y = a\omega^2 \sin \omega t$$

z direction:

$p_z = 479.212$ rad/s 4576.14 rpm

$C_{cz} = 52{,}220$ Ns/m $\xi_z = 0.0375$

$Q_z = 13.3333$

It may be noted that the quality factor is not exactly the peak value of response. The peak response, which may be called amplification factor, occurs at a frequency ratio given by (see Rao and Gupta, 1984)

$$r = \frac{1}{\sqrt{1-2\xi^2}} \tag{10}$$

The response of the uncoupled equation is given by

$$\frac{Z}{a} = \frac{r^2}{\sqrt{(1-r^2)^2+(2\xi_z r)^2}} \tag{11}$$

Substituting Eq. (10) into the above, the amplification factor is obtained as

$$A_z = \frac{1}{2\xi_z\sqrt{1-2\xi_z^2}} \tag{12}$$

The peak response occurs at 4582.55 rpm with

$$A_z = 13.3427$$

Since the damping is small, this value is not very much different from the quality factor.

y direction:

$p_y = 389.078$ rad/s 3715.42 rpm

$C_{cy} = 42355$ Ns/m $\xi_y = 0.015$

$Q_y = 33.333$

The peak response occurs at a frequency ratio 1.00023, i.e., at 3716.257 rpm, with

$$A_y = 33.337$$

3.2 Heavily Damped Rotor. Consider now a rotor of mass 453.6 kg, with its rigid bearing critical speed equal to 8600 rpm, mounted on two plain cylindrical bearings 10.16 cm in diameter and 5.08 cm long with a diametrical clearance 0.01016 cm and viscosity at operating temperature, 0.00568 Ns/m^2. The shaft stiffness for the fundamental rigid bearing critical speed is

$$K = M\omega_n^2 = 3.68 \times 10^8 \text{ N/m}$$

At 8600 rpm, the direct stiffness and damping coefficients can be evaluated. It is assumed that these are constant in the operating region for the purpose of evaluation of quality factors in z and y directions. Following calculations similar to the previous case, we obtain

$\overline{K}_z = 3.13 \times 10^8$ N/m $\overline{K}_y = 2.86 \times 10^8$ N/m

$\overline{C}_z = 135000$ Ns/m $\overline{C}_y = 133000$ Ns/m

The uncoupled equations of motion are

$$\ddot{z} + 297.619\dot{z} + 690035.27z = a\omega^2 \cos \omega t$$

$$\ddot{y} + 293.210\dot{y} + 630511.46y = a\omega^2 \sin \omega t$$

z direction:

$p_z = 830.6836$ rad/s $= 7932.444$ rpm

$C_{cz} = 753520$ Ns/m

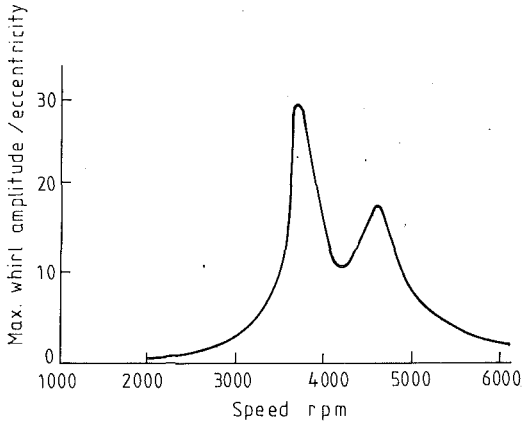

Fig. 2 Unbalance response of coupled system

$$\xi_z = 0.179$$

$$Q_z = 2.79$$

The peak amplitude occurs at 8199.5 rpm, given by

$$A_z = 2.839$$

y direction:

$$p_y = 794.1 \text{ rad/s} = 7583 \text{ rpm}$$

$$C_{cy} = 720408 \text{ Ns/m}$$

$$\xi_y = 0.185$$

$$Q_y = 2.7$$

The peak amplitude occurs at 7856.24 rpm, given by

$$A_y = 2.750$$

This rotor is heavily damped and therefore the quality factors are very low. The peak amplitudes, amplification factors, occur at speeds higher than the resonant speeds.

3.3 Coupled Systems. Consider the lightly damped rotor of section 3.1. Let us take into account all the direct and cross-coupled stiffness and damping coefficients of the bearing as functions of the rotational speed. The response of the system given by Eq. (4) is plotted in Fig. 2. The damping ratios of the system for the two criticals cannot be easily determined. To determine the damping ratio for the 3700 rpm critical, we follow the procedure outlined below.

The natural frequency as a first approximation can be written as

$$p^{(0)} = \omega_{pk}\sqrt{1-2\xi^{(0)2}}$$

We know that

$$\frac{X_{\text{res}}}{X_{st}} = \frac{1}{2\xi}$$

$$\frac{X_{pk}}{X_{st}} = \frac{1}{2\xi\sqrt{1-\xi^2}}$$

Hence

$$X_r^{(0)} = X_{pk}\sqrt{1-\xi^{(0)2}}$$

Let us pick up two frequencies, where the response has the same value, then

$$\frac{\omega_1}{p^{(0)}} = r_1^{(0)}$$

$$\frac{\omega_2}{p^{(0)}} = r_2^{(0)}$$

$$n^{(0)} = \frac{X_r^{(0)}}{X_c}$$

We can then write

$$\frac{X_c}{X_{st}} = \frac{1}{2\xi_1 n^{(0)}} = \frac{r_1^{(0)2}}{\sqrt{(1-r_1^{(0)2})^2 + (2\xi_1 r_1^{(0)})^2}}$$

$$\frac{X_c}{X_{st}} = \frac{1}{2\xi_2 n^{(0)}} = \frac{r_2^{(0)2}}{\sqrt{(1-r_2^{(0)2})^2 + (2\xi_2 r_2^{(0)})^2}}$$

From the above we obtain

$$\xi_1 = \frac{(1-r_1^{(0)2})}{2\sqrt{r_1^{(0)4} n^{(0)2} - r_1^{(0)2}}}$$

$$\xi_2 = \frac{(1-r_2^{(0)2})}{2\sqrt{r_2^{(0)4} n^{(0)2} - r_2^{(0)2}}}$$

The second approximation for the damping ratio is taken as

$$\xi^{(1)} = \frac{\xi_1 + \xi_2}{2}$$

The above iteration for the first step can be repeated until the damping ratio agrees with the previous iteration.

The peak amplitude ratio for the 3700 rpm critical in Fig. 2 is given by 29.333. For an amplitude ratio of 20, the two frequencies are 3600 and 3865 rpm. For the rotor in section 3.1, with no cross-coupled stiffness and damping, the damping ratio is found to be 0.015. Starting from this value, we obtain the final damping ratio for this mode to be 0.032.

The corresponding quality factor is 15.625 and the amplification factor is 15.633. With the inclusion of the cross-coupled terms, we note that the damping ratio is more than doubled, and the quality factor correspondingly is reduced by half. This shows that the cross-coupled stiffness and damping terms have a significant influence on the quality factor of a rotor.

The peak amplitude ratio for the 4600 rpm critical is 17.0. For an amplitude ratio of 12, the frequencies from Fig. 2 are 4365 and 4835 rpm. The damping ratio following the above procedure is found to be 0.051. The corresponding quality and amplification factors are 9.8 and 9.82, respectively. It can be seen that this mode is heavily damped compared with the earlier one. This corresponds to the uncoupled z mode of section 3.1.

4 Discussion

The designer of a rotor is generally interested in knowing the maximum amplitude of whirl at a critical speed. A simple way of expressing this quantity is by the quality factor. The term "quality factor" itself originates from electrical engineering, where increased resonant response of a system is often considered a measure of quality. A more appropriate term in mechanical engineering practice would be "amplification factor." Nevertheless, the term "quality factor" is more commonly used in mechanical engineering.

The behavior of a structure under resonance is generally well understood. The amplification factor depends on the modal damping and is given by $1/2\xi$ for small values of damping. When the damping is large enough, peak amplitudes occur at frequencies slightly lower than natural frequency. The amplification factor, that is, the peak amplitude, is then given by

$$A = \frac{1}{2\xi\sqrt{1-\xi^2}}$$

A rotor mounted on rigid bearings behaves in a similar manner to a structure, insofar as its dynamic behavior is centered around a critical speed. The shaft damping controls the amplitude of whirl. The peak amplitudes, however, occur at speeds slightly higher than the critical speed. The amplification factor, however, is the same as given above.

For rotors mounted on fluid film bearings, the picture is very much different from that of static structures or rotors mounted on rigid bearings. The main reason for this is due to the bearing stiffness and damping properties. Fluid film bearings offer different stiffness and damping properties in the vertical and horizontal directions. Moreover, the fluid film bearings are not direct in their action, that is, a force applied in a given direction not only produces displacement in the same direction, but also in a direction perpendicular to this. The difference in direct stiffness coefficients in the vertical and horizontal directions splits a rigid bearing critical speed into two. In addition, the cross-coupled bearing properties have a significant influence on the dynamic behavior of the rotor.

The objective of this paper is to show that the bearing properties have a significant influence on the maximum whirl amplitudes. A procedure to estimate the quality factor or amplification factor for such rotors is demonstrated. Some salient points of interest are noted below.

1 The modal system of a rotor can be obtained from a suitable numerical procedure to obtain the modal mass and stiffness based on rigid bearing conditions.

2 For the case of similar bearings on both sides of the rotor, the out-of-balance response can be determined using simple one degree of freedom system accounting for all stiffness and damping coefficients. Otherwise a computer code for a general rotor with bearings can be used to determine the response. From these response calculations, maximum whirl amplitudes can be determined, which give the quality factors.

3 For rotors mounted on similar bearings on both sides, the system can be reduced to two coupled second-order differential equations, taking into account both the direct and cross-coupled stiffness and damping coefficients.

4 These equations can be decoupled by neglecting the cross-coupled terms and further simplified by neglecting the shaft damping.

5 The decoupled equations give effective stiffness and damping values for both the z and y directions of motion. The corresponding major and minor critical speeds and critical damping values can be obtained from these terms.

6 It may be noted that the effective stiffness is a function of not only the shaft and bearing stiffnesses but also the shaft and bearing damping terms.

7 Similarly, the effective damping values of the system depend not only on damping terms but also on stiffness terms.

8 These effective stiffness and damping terms are also dependent on rotor speed.

9 From the effective damping and critical damping values, the quality factors can be easily determined.

10 When coupling is taken into account, it is not easy to determine the damping ratios, and hence the quality factors. It is necessary for these cases to plot the unbalance response and determine the damping ratios by an iteration procedure.

The above factors explain why some rotors are lightly damped and others are heavily damped.

References

Kramer, E., 1977, "Computation of Unbalance Vibrations of Turborotors," ASME Paper No. 77-DET-13.

Lalanne, M., and Queau, J. P., 1979, "Calcul par Elements Finis du Comportement Dynamique des Chaines Cinematiques de Reducteur," Societe Nationale des Industries Aerospatiales, France.

Lund, J. W., 1965, "Rotor Bearings Dynamic Design Technology, Part III, Design Handbook for Fluid Film Bearings," MTI, AFAPL-Tr-65-45.

Lund, J. W., and Orcutt, F. K., 1967, "Calculations and Experiments on the Unbalance Response of a Flexible Rotor," ASME *Journal of Engineering for Industry*, Vol. 87, p. 785.

Rao, J. S., 1982, "Synchronous Whirl of a Flexible Rotor in Hydrodynamic Bearings," *Mechanism and Machine Theory*, Vol. 17, No. 2, p. 143.

Rao, J. S., 1983, *Rotor Dynamics*, Wiley, New York.

Rao, J. S., 1985, "Instability of Rotors Mounted in Fluid Film Bearings With a Negative Cross-Coupled Stiffness Coefficient," *Mechanism and Machine Theory*, Vol. 20, p. 181.

Rao, J. S., Bhat, B. R., and Sankar, T. S., 1981, "Effect of Damping on the Synchronous Whirl of a Rotor on Hydrodynamic Bearings," *Trans. CSME*, Vol. 6, No. 3, p. 155.

Rao, J. S., and Gupta, K., 1984, *Introductory Course on Theory and Practice of Mechanical Vibrations*, Wiley, New York.

Rao, J. S., and Sarma, K. V. B., 1984, "Simulation of Multishaft Rotors Mounted on Fluid Film Bearings to Determine Unbalance Response," *Proc. Intl. Conf. Power Plant Simulation*, Mexico, p. 85.

Applications of Sweep Frequency Rotating Force Perturbation Methodology in Rotating Machinery for Dynamic Stiffness Identification

A. Muszynska

D. E. Bently

W. D. Franklin

J. W. Grant

P. Goldman

Bently Rotor Dynamics Research Corporation, Minden, NV 89423

This paper outlines the sweep frequency rotating force perturbation method for identifying the dynamic stiffness characteristics of rotor/bearing/seal systems. Emphasis is placed on nonsynchronous perturbation of rotating shafts in a sequence of constant rotative speeds. In particular, results of the identification of flexible rotor multimode parameters and identification of fluid forces in seals and bearings are given. These results, presented in the direct and quadrature dynamic stiffness formats, permit the separation of components for easy identification. Another example of the perturbation method application is the identification of the lateral-torsional coupling due to shaft anisotropy. Results of laboratory rig experiments, the identification algorithm, and data processing techniques are discussed.

Introduction

Modal testing is routinely used for identifying the dynamic characteristic of mechanical structures. The application of such "classical" modal testing to rotating machines usually results in a broad spectrum of natural frequencies and a rich variety of corresponding modes. Since all the modes are treated equally, the accuracy of the lowest, most important modal characteristics is often insufficient. In particular, poor sensitivity is achieved in the low-frequency ranges when accelerometers are used, as is often the case.

The low-order modes of rotating machines are usually the rotor or rotor/bearing modes. Shaft rotation often considerably modifies these modes, so modal testing should always be performed on shafts that are rotating, and under load, with other operational conditions maintained. Impulse testing routinely used on passive (nonrotating) structures may lead to underdetermination of input forces when applied radially to a rotating shaft as a result of the generation of a friction-related tangential force component. Furthermore, nonlinearities from the dynamics of fluid-lubricated bearings and close spacing of rotor two orthogonal lateral modes create additional problems in interpretation of modal testing results.

For most rotating machines, the shaft rotates in a fluid environment, and the fluid involved in the dynamic motion becomes an important part of the system. Fluid/solid interaction causes the appearance of additional, usually low-frequency modes of vibration, unknown in passive structures.

A survey of the rotating machine modal testing problems and solutions has been given in the papers by Muszynska (1986), Muszynska et al. (1989), and Muszynska and Bently (1990). The present paper outlines the use of nonsynchronous sweep frequency forward and backward rotating force perturbation method for identification of the dynamic stiffness characteristics of the low-order lateral modes of the rotor/bearing/seal systems.

Nonsynchronous Sweep Frequency Perturbation Testing of Rotor/Bearing/Seal Systems

According to the authors' experience, the most meaningful study, with excellent signal-to-noise ratio data for identification of the rotor system parameters, is achieved by *nonsynchronous rotating force* excitation. Different excitations have been used by other investigators, such as synchronous forces (Zhang et al., 1987), unidirectional impulses (Morton, 1975; Nordmann and Massmann, 1984; Nordmann et al., 1986; Nordmann and Dietzen, 1988; Massmann and Nordmann, 1985; Kanki et al., 1986a; Diewald and Nordmann, 1988), random inputs (Yasuda et al., 1986), or forced orbital motion/measured response forces (Iwatsubo, 1980; Iwatsubo et al., 1988; Ohashi, 1984; Ohashi et al., 1988; Jery et al., 1984; Adkins and Brennen, 1986; Childs, 1986; Childs et al., 1988; Adams et al., 1988; Brennen et al., 1988). For linear systems, all perturbation methods should lead to the same results. How-

Contributed by the International Gas Turbine Institute and presented at the 37th International Gas Turbine and Aeroengine Congress and Exposition, Cologne, Germany, June 1-4, 1992. Manuscript received by the International Gas Turbine Institute February 11, 1992, Paper No. 92-GT-176. Associate Technical Editor: L. S. Langston.

ever, in practice, each method has its own strong and weak features, which lead to different levels of accuracy in specific applications. The perturbation method discussed in this paper has several advantages over the other methods. For example, most other methods do not distinguish between the rotor forward and backward lateral modes, so that the interpretation of the results becomes incorrect. Also, in most other methods, the phase measurements are quite inaccurate, thus sine and cosine-related components are severely adversely affected, causing the final result error to be even higher than the range of the phase inaccuracy. In the current perturbation method presented here, the phase readings have an error lower than ± 0.3 percent, which is ten times better than most other methods. Furthermore, most other modal methods are based on pure linearity of the system; thus the existence of nonlinear effects produces additional errors. The approach discussed in this paper not only takes account of nonlinearities, but permits identification of individual nonlinear terms.

Some special auxiliary devices are needed for the application of the nonsynchronous perturbation method. These devices could include aerodynamically driven free spinners, electromagnetic actuators, auxiliary-driven unbalanced shafts, connected to the machine rotor end through a pivoting bearing, unbalanced or eccentric disks mounted on rotors through rolling element bearings and driven by an auxiliary motor. These devices generate rotating input forces at frequencies that are entirely independent from the rotative speed. The rotor lateral responses are measured by displacement transducers mounted in XY configuration at several locations along the rotor (Fig. 1). The phases of the responses filtered to the perturbation frequency are measured relative to a one-per-revolution mark, such as Keyphasor®. The response data recorded by a computerized acquisition system are then processed and presented in dynamic stiffness formats.

Nonsynchronous Sweep Frequency Perturbation Testing and Dynamic Stiffness Identification Algorithm

Consider a model of a nonsymmetric (laterally anisotropic), anisotropically supported, flexible $2n$ degree of freedom rotor rotating at a constant speed Ω:

$$\begin{vmatrix} [M_1] & [M_{12}] \\ [M_{21}] & [M_2] \end{vmatrix} [\ddot{Z}] + \begin{vmatrix} [D_1] & [D_{12}] \\ [D_{21}] & [D_2] \end{vmatrix} [\dot{Z}] + \begin{vmatrix} [K_1] & [K_{12}] \\ [K_{21}] & [K_2] \end{vmatrix} [Z] = [F] \quad (1)$$

where $Z = \text{col}[x_1,\ldots,x_p,\ldots,x_n, y_1,\ldots,y_p,\ldots,y_n]$ represents rotor deflections at its $p = 1,\ldots,n$ axial locations in two orthogonal directions x and y. The system parameters are represented by the matrices:

$$[M_q],\ [M_{q,3-q}],\ [D_q],\ [D_{q,3-q}],\ [K_q],\ [K_{q,3-q}],\ q = 1,\ 2,$$

which are inertia, damping, and stiffness matrices correspondingly. The matrices $[D_{q,\,3-q}]$ contain "cross" damping terms,

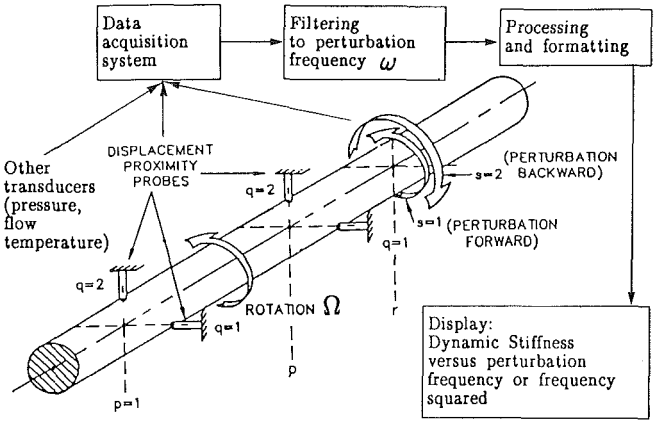

Fig. 1 Nonsynchronous perturbation testing of a rotating shaft using circular perturbation forces as inputs and displacement transducers for measuring output responses

and the matrices $[K_{q,\,3-q}]$ contain elements of the "cross" stiffness type. Both these matrices usually depend on the rotative speed Ω. The vector $[F]$ contains controlled excitation forces. For identification of the system parameters, a controlled rotating perturbation (excitation) force is applied consecutively at r $(r = 1,\ldots,n)$ axial locations of the rotor in either the forward $(s = 1)$ or backward $(s = 2)$ direction. The n pairs of displacement transducers in an XY configuration are mounted at p $(p = 1,\ldots,n)$ axial locations of the rotor (Fig. 1). When the force is applied at the rth location, the excitation vector used in nonsynchronous perturbation is, therefore,

$$[F] = \text{col}[0,\ldots,0,\ F_{sr}\cos(\omega t + \delta_{sr}),\ 0,\ldots,0,\ (-1)^{s+1}F_{sr}\sin(\omega t + \delta_{sr}),\ 0,\ldots,0],\ s = 1,\ 2. \quad (2)$$

where ω is perturbation frequency, F_{sr} and δ_{sr} are the perturbation force amplitude and phase, respectively. Note that the perturbation frequency ω is entirely independent of the rotative speed Ω.

The forced response of the model, Eq. (1), to exciting force, Eq. (2), is as follows:

$$[Z] = \text{col}[A_{1s1r}\cos(\omega t + \alpha_{1s1r}),\ldots,A_{1snr}\cos(\omega t + \alpha_{1snr}),\ A_{2s1r}\sin(\omega t + \alpha_{2s1r}),\ldots,A_{2snr}\sin(\omega t + \alpha_{2snr})] \quad (3)$$

where A_{qspr}, α_{qspr} are amplitudes and phases of the responses narrow-band filtered to the perturbation frequency. The phases are measured from the same once-per-rotation marker. By substituting Eq. (3) into Eqs. (1), reducing time-related functions, and using Euler's complex number transformation, the algebraic set of $2n$ equations is obtained:

$$[\kappa] \begin{bmatrix} [A_{1spr}e^{j\alpha_{1spr}}] \\ [A_{2spr}e^{j\alpha_{2spr}}] \end{bmatrix} = F_{sr}e^{j\delta_{sr}}\{\text{col}[0,\ldots,0,\ 1,\ 0,\ldots,0,\ (-1)^{s+1},\ 0,\ldots,0]\} \quad (4)$$

where $j = \sqrt{-1}$ and

Nomenclature

A = rotor response amplitude
D = damping
F, δ = perturbation exciting force amplitude and phase
j = $\sqrt{-1}$
K, M = stiffness and mass, respectively
M_f = fluid inertia effect
t = time
x, y = rotor deflections in two lateral directions
Z = vector of rotor deflections
α = rotor response phase
κ = dynamic stiffness
λ = fluid circumferential average velocity ratio
ν_t = torsional natural frequency
ω = perturbation frequency
Ω = rotative speed

Subscripts

n = number of measurement planes and number of experiments
p = measurement axial location, $p = 1,\ldots,n$
q = displacement in x direction $(q = 1)$, or y direction $(q = 2)$
r = perturbation force axial location, $r = 1,\ldots,n$
s = perturbation forward $(s = 1)$ or backward $(s = 2)$

$$[\kappa] = \begin{bmatrix} [K_1]+j\omega[D_1]-\omega^2[M_1] & -j([K_{12}]+j\omega[D_{12}]-\omega^2[M_{12}]) \\ j([K_{21}]+j\omega[D_{21}]-\omega^2[M_{21}]) & [K_2]+j\omega[D_2]-\omega^2[M_2] \end{bmatrix}$$

is the system complex dynamic stiffness matrix. The nonzero components at the right-hand side of Eq. (4) are at the rth and $(n+r)$th rows.

For the sequence of n experiments in which the force is applied consecutively at $r=1, 2,\ldots,n$ locations either in the forward ($s=1$) or backward ($s=2$) directions, the set of $2n$ equations is obtained:

$$[\kappa]\begin{bmatrix} [A_{11}] & [A_{12}] \\ [A_{21}] & [A_{22}] \end{bmatrix} = \begin{bmatrix} [F_1] & [F_2] \\ [F_1] & [-F_2] \end{bmatrix} \tag{5}$$

where

$$[A_{qs}] = \begin{bmatrix} \overline{A}_{qs11}\ldots\overline{A}_{qs1n} \\ \vdots \quad\quad \vdots \\ \overline{A}_{qsn1}\ldots\overline{A}_{qsnn} \end{bmatrix} \equiv [A_{qspr}e^{j\alpha_{qspr}}]$$

$$F_s = \text{diag}[F_{s1}e^{j\delta_{s1}},\ldots,F_{sn}e^{j\delta_{sn}}], \quad q,\ s=1,\ 2.$$

$\overline{A}_{qspr} \equiv A_{qspr}e^{j\alpha_{qspr}}$ represent response vectors (in the complex number sense), components of the response nonsingular matrix. Equation (5) represents the main equation for identification of the system parameters:

$$[\kappa] = \begin{bmatrix} [F_1] & [F_2] \\ [F_1] & [-F_2] \end{bmatrix}\begin{bmatrix} [A_{11}] & [A_{12}] \\ [A_{21}] & [A_{22}] \end{bmatrix}^{-1}$$

The identification procedure is reduced to the following expressions, representing the rotor dynamic stiffness components:

$$[K_q]-\omega^2[M_q] = -\text{Re}\{[(-1)^q[F_2]+[H_1]][H_2]\} \tag{6}$$

$$\omega[D_q] = -\text{Im}\{[(-1)^q[F_2]+[H_1]][H_2]\} \tag{7}$$

$$\omega[D_{3-q,q}] = \text{Re}\{[(-1)^q[F_2]-[H_1]][H_2]\} \tag{8}$$

$$[K_{3-q,q}]-\omega^2[M_{3-q,q}] = \text{Im}\{[(-1)^q[F_2]-[H_1]][H_2]\}, \quad q=1,\ 2 \tag{9}$$

where

$$[H_1] = [F_1][A_{3-q,1}]^{-1}[A_{3-q,2}]$$

$$[H_2] = [[A_{q,2}]-[A_{q,1}][A_{3-q,1}]^{-1}[A_{3-q,2}]]^{-1}$$

With the frequency sweep excitation (ω variable from zero to a selected value covering the range of n natural frequencies of the system) the results, Eqs. (6)–(9), are eventually graphically presented versus ω or ω^2 for the easiest curve fitting of straight lines.

Note that the model, Eq. (1), takes into consideration $2n$ rotor/bearing/seal system coupled modes. The vector Z contains *multimode modal coordinates*. Using this approach, the identification provides parameters of the coupled system, not only modal parameters of decoupled modes. The method works very well for systems with a low number of modes, and is extremely useful if the knowledge on all connecting masses and stiffnesses in the system is required. If the number of modes in the chosen frequency range is not known ahead of time, the additional measurements may serve for modal correction factor calculations, as discussed by Muszynska et al. (1989).

Synchronous perturbation testing using controlled unbalances as excitation and rotative speed as perturbation frequency ($\omega=\Omega$) is a simpler, but useful, technique, providing identification of parameters weakly depending on rotative speed. An example is presented in Fig. 2. The perturbation method applied in the frequency span of two rotor isotropic modes provides identification of not only the first and second mode modal masses and stiffnesses (four values), but the *multimode modal coordinates*, which include masses M_1, M_2 and stiffnesses K_1, K_2, K_3, where K_1 and K_3 include the supporting bearing radial stiffnesses. From the mathematical point of view, the identifying procedure applied to rotors provides *tridiagonal* matrices, as opposed to diagonal ones using classical approaches. Tridiagonal matrices can similarly be obtained from reduced and appropriately transformed FEM models (the transformation can be found in the book by Golub and Van Loan, 1983). The *multimode modal coordinates* represent the system much better because they can physically be attached to system elements.

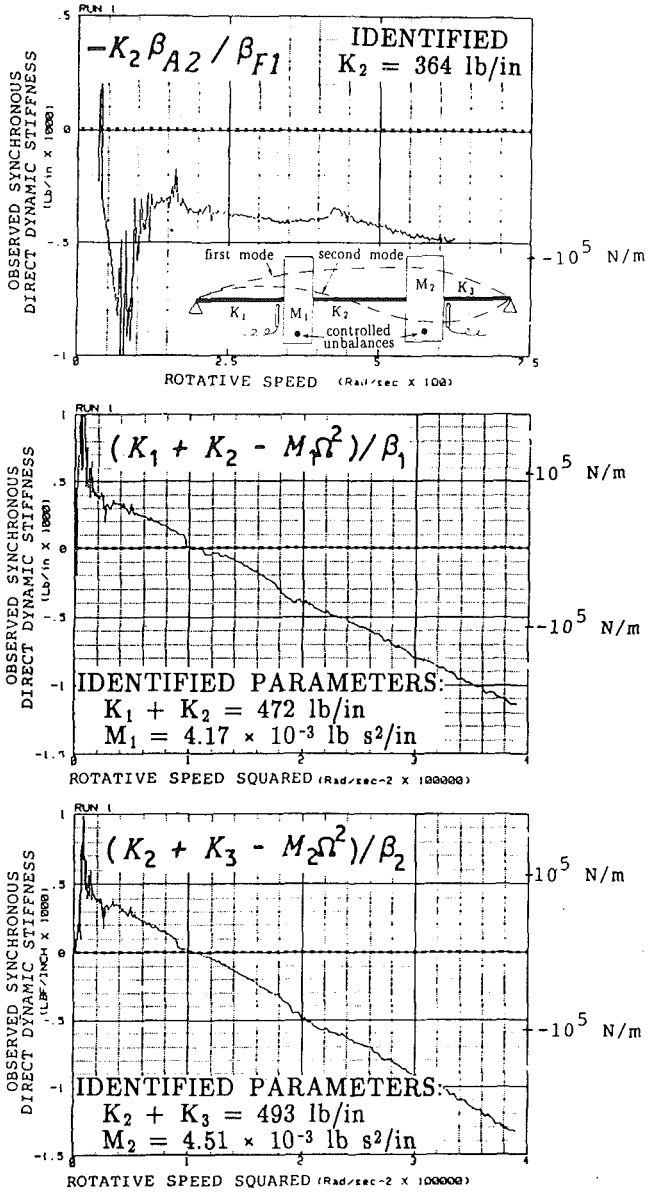

Fig. 2 Identification of two-mode modal masses and stiffnesses of a rotor using synchronous perturbation. β are modal correction factors (Muszynska et al., 1989).

The perturbation technique was successfully applied for parameter identification of several rotor systems (Muszynska, 1986; Muszynska et al., 1989; Muszynska and Bently, 1990). The results of application to rotor/bearing and rotor/seal systems have led to identification of a fluid force model for lightly radially loaded bearings and seals (Muszynska, 1988). The perturbation technique is also always routinely used for identification of rotor rigs designed for any experiment, which would further involve system modifications with possible nonlinear effects (such as rubbing or loose parts). This perturbation technique should also become a routine during rotating machine prototype testing.

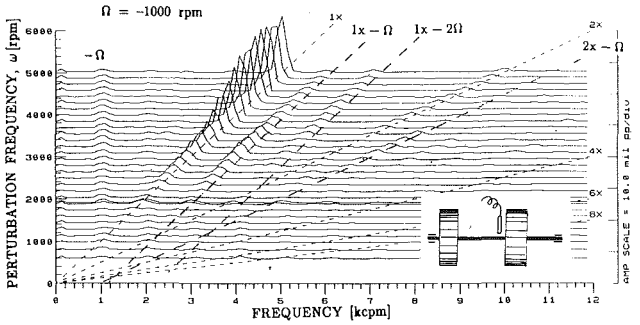

Fig. 3 Spectrum cascade of the rotor vertical response to lateral backward rotating force nonsynchronous perturbation (Bently et al., 1991)

Some more specific applications are described in the next two sections of this paper.

Lateral-Torsional Cross Coupling

The nonsynchronous sweep frequency lateral perturbation technique has been used to investigate the lateral-torsional cross coupling due to shaft anisotropy (Bently et al., 1991). The rotor of the experimental rig was driven by a synchronous electric motor, connected through a laterally flexible, torsionally rigid coupling. In order to simulate anisotropy of the shaft, a part of the shaft at midspan area was machined to produce two flats. There were two disks fixed on the shaft with 36 precisely manufactured gear teeth on each of them. The optical pickups observe the disk gear tooth passing frequencies. The data were then processed through a torsional signal conditioner to obtain the dynamic twist (torsional vibrations) of the shaft between two disks. The shaft lateral vibrations were observed by two sets of proximity probes in an XY configuration. The nonsynchronous perturbation unbalanced disk driven by a separate motor was attached through a rolling element bearing at the shaft midspan.

The lateral responses of the shaft to the nonsynchronous perturbation, presented in a form of the spectrum cascade plot (Fig. 3), exhibit significant amounts of the frequency difference components: $\omega - \Omega$, $\omega - 2\Omega$, and $2\omega - \Omega$. The existence of these components is due to the shaft anisotropy, and can be used for its identification. The rotor torsional responses are presented in the form of overall vibration amplitude versus perturbation frequency (Fig. 4). They exhibit high amplitudes at the excitation frequency equal to the first torsional natural frequency ν_t. This is related to the torsional/lateral coupling through rotor residual unbalance. The other peaks of the torsional vibrations occur when the linear combinations of frequencies ω and Ω are equal to the torsional natural frequency ν_t and half of it ($\nu_t/2$). These effects are due to the asymmetry of the shaft plus radial sideload, and could also be further used for identification of the shaft anisotropy, such as generated by a propagating transverse crack on the shaft.

Antiswirl Seal Testing

The sweep frequency rotating force nonsynchronous perturbation method was applied to identify the fluid force parameters in antiswirl seals equipped with radial and tangential inlet ports (Grant, 1991). The results provide clear effects of the input flow pattern on fluid force components. Water was used for series of experiments. Figure 5 illustrates an example of the obtained data presented in terms of dynamic stiffness components for the seal input flow through radial or antiswirl ports, and for three rotating speeds. Based on this type of data, the identified fluid force parameters, namely circumferential average velocity ratio λ, radial stiffness, and damping reduced from approximately 70 runs covering the range from 3 to 80 psi water pressure are presented in Fig. 6. While the

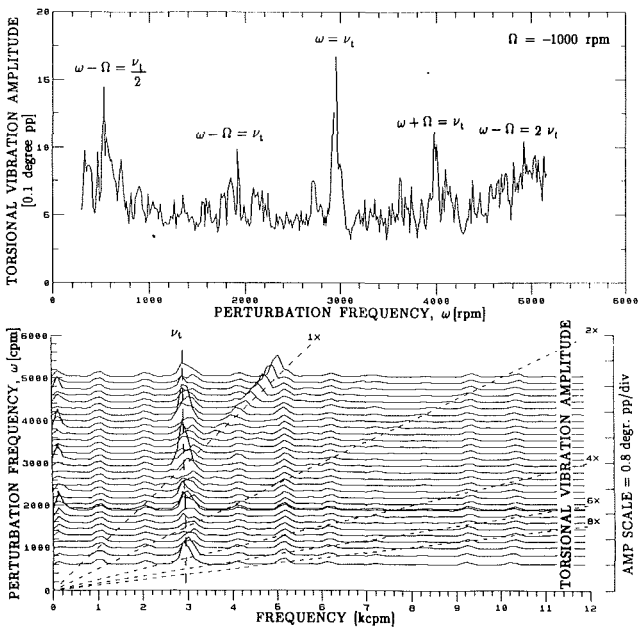

Fig. 4 Overall amplitude versus perturbation frequency and spectrum cascade of the anisotropic rotor torsional response to lateral backward nonsynchronous perturbation (Bently et al., 1991)

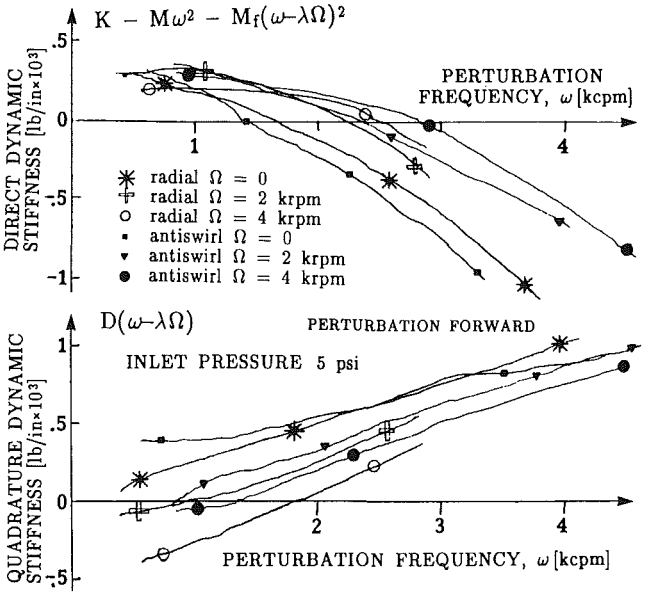

Fig. 5 Direct and quadrature dynamic stiffnesses versus perturbation frequency of the seal with either radial or antiswirl inlet ports

flow rate may not be the best factor to illustrate fluid force parameters for a variety of tested cases, the graphs clearly show general trends of these parameters for radial and antiswirl inlets.

As can be seen in Fig. 6, the antiswirl input fluid injection in the direction opposite to the shaft rotation makes dramatic change in the fluid circumferential average velocity ratio values, by considerably lowering them and improving stability features.

Parameter Identification Using Perturbation Techniques in Conjunction With Optimization Theory

Current data processing techniques used in parameter identification are based on algebraic manipulation of the forced response data in order to obtain values for the system param-

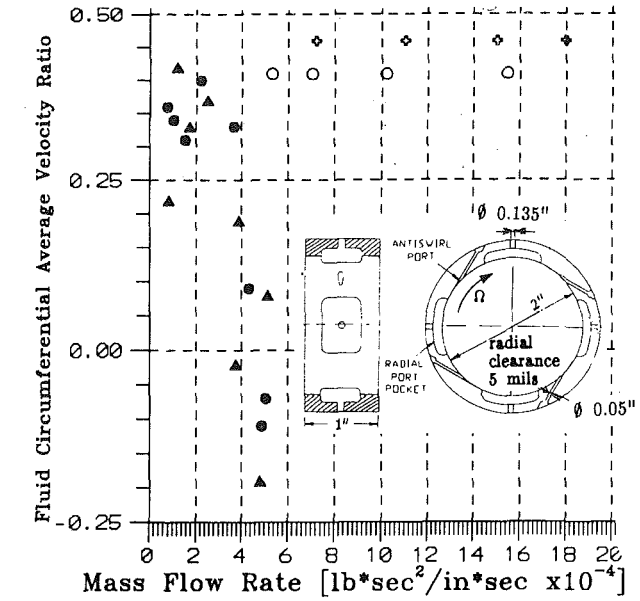

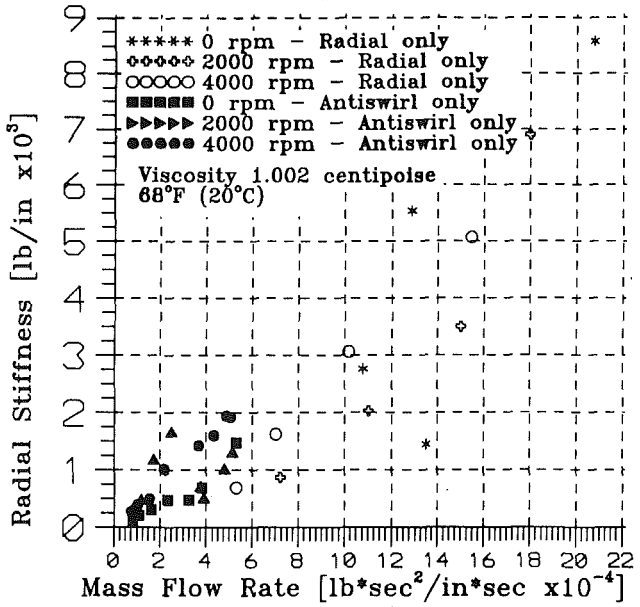

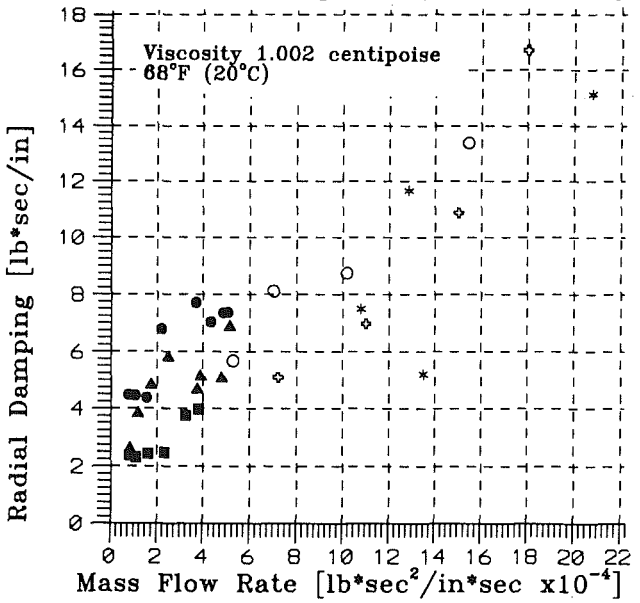

Fig. 6 Identified fluid circumferential average velocity ratio (λ), fluid radial stiffness (K), and damping (D) of the seal versus measured mass flow rate

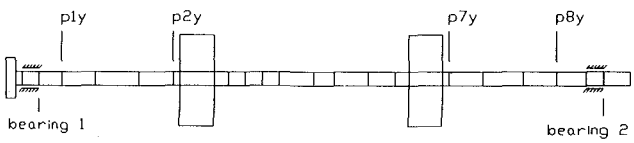

Fig. 7 Finite element model of a rotor showing element structures, bearings, and simulated measurement locations for synchronous testing

eters. These techniques provide accurate, easily interpretable results for systems in which the application of the perturbation force and the measurement of the associated response can be precisely controlled. As the system becomes more complex, requiring larger amounts of data for accurate analysis, or the location of the applied force or measurement transducers must be compromised, resulting in less than optimum databases, other data processing techniques must be developed for the perturbation technique to be effective. The alternative technique under consideration has been explored in references by Nordmann and Diewald (1990), and Mottershead (1991), and is based on the error minimization between a system measured response and one calculated from a mathematical model. The process consists of modifying the mathematical model parameters, computing a new response, generating the error value, and then using this information along with past computations to determine new values for the parameters, which will reduce the error value below an acceptable tolerance. To achieve this, adaptations of the bracketing routine, Brent's line minimization routine, and Powell's method of discarding the direction of largest decrease routine (as given by Press et al., 1986) are used in the optimization section of the program.

Since the target computing system for the analysis is a personal computer, computational complexity must be limited to produce solutions within a reasonable time. Toward this end, the rotor system is modeled using a simple finite element approach consisting of beam elements, bearings, and mass unbalance forces, which are input to the program through a mouse-driven graphic user interface. Following Al-Khafaji and Tooley (1986), a system of linear equations generated from the model is solved using the square root method, which is a form of LU decomposition adapted to symmetric equations.

In order to reduce the computational burden, the extent of the optimization can be limited by selection of the system parameters to be varied during the optimization process. This is accomplished using the graphic interface to select which elements are to be varied. Within each selected element, the variable could be stiffness (Young modulus), bearing stiffness (both direct and quadrature components), or unbalance force. For example, if only bearing stiffnesses of a two-bearing rotor system are desired, the problem is reduced to a four-dimensional optimization problem by selecting these stiffnesses as the only modifiable parameters; all other parameters are fixed during the solution process.

Preliminary results are encouraging. The forced response section of the program was used to calculated responses of the rotor-bearing system (Fig. 7) due to an unbalance force in the left-hand disk. This response was then used as a simulated measured response with infinite signal-to-noise ratio to estimate the bearing stiffnesses at each bearing location using the optimization portion of the program. As in the example above, all system parameters were fixed except for the bearing parameters at each bearing location. The results are shown in Fig. 8. The bearing radial stiffness value used in the original calculation was 1250 lb/in. and radial damping was 0.35 lb-sec/in. The corresponding direct and quadrature stiffnesses are shown in the figures as broken lines. As can be seen from the figures, there is almost perfect agreement between actual bearing parameters and those obtained through the optimization process. The slight deviations between actual and predicted parameter values at 3000 rpm correspond to the

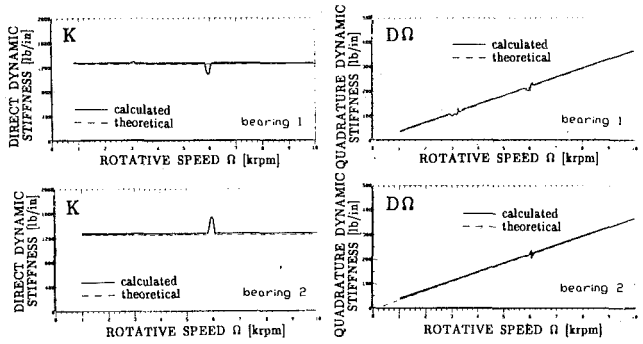

Fig. 8 Direct and quadrature dynamic stiffnesses versus rotative speed at bearings using simulated measured responses at *p1y*, *p2y*, *p7y*, *p8y* (Fig. 7)

frequency range in which the vibration levels at points "*p1y*" and "*p2y*" are very small, while those at 6000 rpm coincide with the second natural frequency. The most probable cause for both errors is selection of tolerances for various portions of the optimization subprograms. Further research to isolate these errors is currently being conducted. Research is continuing for this technique using measured data contaminated with noise, different locations of applied force and measurement transducers, and measured data taken from real rotating machines.

References

Adams, M. L., Yang, T., and Pace, S. E., 1988, "A Seal Test Facility for the Measurement of Isotropic and Anisotropic Linear Rotordynamic Characteristics," *Rotordynamic Instability Problems in High-Performance Turbomachinery*, NASA CP 3026, College Station, TX, pp. 253–268.

Adkins, D. R., and Brennen, C. E., 1986, "Origins of Hydrodynamic Forces on Centrifugal Pump Impellers," *Rotordynamic Instability Problems in High-Performance Turbomachinery*, NASA CP 2443, College Station, TX, pp. 467–492.

Al-Khafaji, A. W., and Tooley, J. R., 1986, *Numerical Methods in Engineering Practice*, CBS College Publishing, pp. 103–105.

Bently, D. E., Muszynska, A., and Goldman, P., 1991, "Torsional/Lateral Vibration Cross Coupling Due to Shaft Asymmetry," BRDRC Report No. 1, pp. 1–45.

Brennen, C. E., Franz, R., and Arndt, N., 1988, "Effects of Cavitation on Rotordynamic Force Matrices," *Conference on Advanced Earth-to-Orbit Propulsion Technology*, NASA, Huntsville, AL, pp. 227–239.

Childs, D. W., 1986, "Force and Moment Rotordynamic Coefficients for Pump-Impellor Shroud Surfaces," *Rotordynamic Instability Problems in High-Performance Turbomachinery*, NASA CP 2443, College Station, TX, pp. 503–530.

Childs, D. W., Elrod, D., and Hale, K., 1988, "Annular Honeycomb Seals: Test Results for Leakage and Rotordynamic Coefficients, Comparison to Labyrinth and Smooth Configurations," *Rotordynamic Instability Problems in High-Performance Turbomachinery*, NASA CP 3026, College Station, TX, pp. 143–160.

Diewald, W., and Nordmann, R., 1988, "Influence of Different Types of Seals on the Stability Behavior of Turbopumps," *Rotordynamic Instability Problems in High-Performance Turbomachinery*, NASA CP 3026, College Station, TX pp. 197–210.

Golub, G. H., and Van Loan, C. F., 1983, *Matrix Computation*, Johns Hopkins University Press, pp. 276–330.

Grant, J. W., 1991, "Modelling and Stabilization of a Rotor Supported in a Fluid Bearing," MSci Dissertation, University of Nevada, Reno, NV.

Iwatsubo, T., 1980, "Evaluation of Instability Forces of Labyrinth Seals in Turbines or Compressors," *Rotordynamic Instability Problems in High-Performance Turbomachinery*, NASA CP 2133, College Station, TX, pp. 139–168.

Iwatsubo, T., Sheng, B., and Matsumoto, T., 1988, "An Experimental Study on the Static and Dynamic Characteristics of Pump Annular Seals," *Rotordynamic Instability Problems in High-Performance Turbomachinery*, NASA CP 3026, College Station, TX, pp. 229–252.

Jery, B., Acosta, A. J., Brennen, C. E., and Caughey, T. K., 1984, "Hydrodynamic Impeller Stiffness, Damping, and Inertia," *Rotordynamic Instability Problems in High-Performance Turbomachinery*, NASA CP 2338, College Station, TX, pp. 137–160.

Kanki, H., Mori, S., and Hizume, A., 1986a, "Theoretical and Experimental Study on the Destabilizing Force by Labyrinth Seal," *The International Conference on Rotordynamics*, Tokyo, Japan, pp. 603–608.

Kanki, H., Fujii, H., Hizume, A., Ichimura, T., and Yamamoto, T., 1986b, "Solving Nonsynchronous Vibration Problems of Large Rotating Machineries by Exciting Test in Actual Operating Conditions," *The International Conference on Rotordynamics*, Tokyo, Japan, pp. 221–226.

Massmann, H., and Nordmann, R., 1985, "Some New Results Concerning the Dynamic Behavior of Annular Turbulent Seals," *Instability in Rotating Machinery*, NASA CP 2409, Carson City, NV, pp. 179–194.

Morton, P. G., 1975, "The Derivation of Bearing Characteristics by Means of Transient Excitation Applied Directly to a Rotating Shaft," *Dynamics of Rotors*, Springer-Verlag, Berlin–Heidelberg–New York, pp. 350–379.

Mottershead, J. E., 1991, "On the Optimal Correction of Structural Dynamic Models," *Modal Analysis, Modeling Diagnostics and Control*, ASME 13th Biennial Conference on Mechanical Vibration and Noise, Technical Conferences, Miami, FL, pp. 107–112.

Muszynska, A., 1986, "Modal Testing of Rotor/Bearing Systems," *International Journal of Analytical and Experimental Modal Analysis*, Vol. 1, No. 3, pp. 15–34.

Muszynska, A., 1988, "Improvements in Lightly Loaded Rotor/Bearing and Rotor/Seal Models," ASME *Journal of Vibration and Acoustics*, Vol. 110, pp. 129–136.

Muszynska, A., Bently, D. E., Franklin, W. D., and Hayashida, R. D., 1989, "Identification of Modal Parameters of Rotating Systems Using Perturbation Techniques, Parts 1 and 2," *Rotating Machinery Dynamics*, ASME DE-Vol. 18-1, pp. 107–118.

Muszynska, A., and Bently, D. E., 1990, "Frequency Swept Rotating Input Perturbation Techniques and Identification of Fluid Force Models in Rotor/Bearing/Seal Systems and Fluid Handling Machines," ASME *Journal of Vibration and Acoustics*, Vol. 143, No. 1, pp. 103–124.

Nordmann, R., and Massmann, H., 1984, "Identification of Dynamic Coefficients of Annular Turbulent Seals," *Rotordynamic Instability Problems in High-Performance Turbomachinery*, NASA CP 2338, College Station, TX, pp. 295–311.

Nordmann, R., Dietzen, F. J., Janson, W., Frei, A., and Florjancic, S., 1986, "Rotordynamic Coefficients and Leakage Flow for Smooth and Grooved Seals in Turbopumps," *The International Conference on Rotordynamics*, Tokyo, Japan, pp. 619–628.

Nordmann, R., and Diewald, W., 1988, "Influence of Different Types of Seals on the Stability Behavior of Turbopumps," *Dynamics and Design of Rotating Machinery*, The Second International Symposium on Transport Phenomena, Honolulu, HI, pp. 351–361.

Nordmann, R., and Diewald, W., 1990, "Parameter Optimization for the Dynamics of Rotating Machinery," *3rd International Conference on Rotordynamics*, IFToMM, Lyon, France, pp. 51–55.

Ohashi, H., 1984, "Lateral Fluid Forces Acting on a Whirling Centrifugal Impeller in Vaneless and Vaned Diffuser," *Rotordynamic Instability Problems in High-Performance Turbomachinery*, NASA CP 2338, College Station, TX, pp. 109–122.

Ohashi, H., Sakurai, A., and Nishihama, J., 1988, "Influence of Impeller and Diffuser Geometries on the Lateral Fluid Forces of Whirling Centrifugal Impeller," *Rotordynamic Instability Problems in High Performance Turbomachinery*, NASA CP 3026, College Station, TX, pp. 285–306.

Press, W. H., Flannery, B. P., Teukolsky, S. A., and Vetterling, W. T., 1986, *Numerical Recipes, the Art of Scientific Computing*, Cambridge University Press, pp. 277–301.

Yasuda, C., Kanki, H., Ozawa, T., and Kawakami, T., 1986, "Application of Random Excitation Technique to Dynamic Characteristics Measurement of Bearing," *The International Conference of Rotordynamics*, Tokyo, Japan, pp. 61–68.

Zhang, Q., Lallement, G., and Fillod, R., 1987, "Identification of the Dynamic Characteristics of Oil-Film Bearings," *Rotating Machinery Dynamics*, DE-Vol. 2, H0400A, Boston, MA, pp. 57–62.

The Effects of Friction in Axial Splines on Rotor System Stability

A. F. Artiles
Mechanical Technology Inc.,
Latham, NY 12110

An in-depth parametric evaluation of the effects of Coulomb friction in an axial spline joint on the stability of the rotor-bearing system was conducted through time transient integration of the equations of motion. The effects of spin speed, friction coefficient, spline torque, external damping, imbalance, and side load as well as asymmetric bearing stiffnesses were investigated. A subsynchronous instability is present at the bending critical speed when the spin speed is above this critical. The limit cycle orbit is circular, proportional to the product of the friction coefficient and spline torque (μT), inversely proportional to the external damping, and independent of spin speed. When imbalance is applied to the rotor, beating between the subsynchronous natural frequency and the synchronous (spin speed) frequency occurs. The subsynchronous component of the orbit is proportional to μT, while the synchronous component is proportional to the imbalance. When a static side load is applied, the unstable node at the center of the orbitally stable limit cycle grows into an ellitpical orbitally unstable limit cycle, separating stable from unstable regions of the phase plane. Below a threshold value of side load, the transient motion approaches one of two asymptotic solutions depending on the initial conditions: the larger stable limit cycle or a point at the center of the smaller unstable limit cycle. Beyond the threshold value of side load, the rotor-bearing is stable and all motions decay to a point. Asymmetry in the bearing stiffnesses reduces the size of the subsynchronous whirl orbit.

1.0 Introduction

Stability of rotor-bearing systems has been studied by numerous authors, such as Gunter [1], Black [2], Glasgow [3], and more recently, Lund [4]. Internal rotor friction has been demonstrated [5], both analytically and experimentally, to cause instability in rotors operating above their first bending critical. Turbopumps such as the Space Shuttle Main Engine (SSME) High-Pressure Oxidizer Turbopump (HPOTP) contain friction joints such as interference fits and splines. These rotors may operate above flexible bending criticals and have relatively light external damping, both of which are potential conditions for instability.

This paper is concerned with the evaluation of the effects of the system parameters on the stability of a rotor that contains two spline joints. The parameters investigated were spin speed, friction coefficient, spline torque, external damping, imbalance, side load, and asymmetry in bearing stiffnesses.

2.0 Rotor Model, Numerical Approach, and Initial Conditions

Figure 1 shows the rotor-bearing model used to exercise the spline. It consists of a shaft mounted on ball bearings at the ends with a spline sleeve in the middle. Spline couplings at the ends of the sleeve connect it to the rotor. External damping to ground is applied at the sleeve. The spline configuration is the same as that in the the SSME HPOTP rotor. This same spline was tested in a rotor-dynamic test rig, similar to the model in Fig. 1, which showed a very strong subsynchronous whirl at the first critical, as reported in [1]. The first undamped natural frequency of the system corresponds to a bending critical at 1247 rpm. Figure 2 is a plot of the corresponding mode shape, showing the relatively large bending of the shaft at the sleeve ends and the relatively small deflection at the bearings.

A Coulomb friction model that describes analytically the behavior of a spline coupling was developed in [1], showing that the moment transmitted across the spline joint is given by:

$$-M = K_a \Delta\theta + \frac{2\mu T}{\pi \cos\psi} \frac{\Delta\dot{\alpha}}{|\Delta\dot{\alpha}|}$$

$$M = \begin{Bmatrix} M_x \\ M_y \end{Bmatrix} \quad \Delta\theta = \begin{Bmatrix} \Delta\theta \\ \Delta\phi \end{Bmatrix} \quad \Delta\dot{\alpha} = \begin{Bmatrix} \Delta\dot{\theta} + \Omega\Delta\phi \\ \delta\dot{\phi} - \Omega\Delta\theta \end{Bmatrix} \quad (1)$$

where $\Delta\theta$ and $\Delta\alpha$ are the differences in angular displacements across the spline measured in coordinate systems fixed on the ground and on the rotor, respectively. K_a is the angular stiffness of the spline, T is the spline torque, μ is the coefficient of friction, and Ψ is the pressure angle.

When conditions are such that the relative angular velocity across the spline joint approaches zero, the joint will stick. However, the spline model is assumed to be slipping. The

Contributed by the International Gas Turbine Institute and presented at the 36th International Gas Turbine and Aeroengine Congress and Exposition, Orlando, Florida, June 3–6, 1991. Manuscript received at ASME Headquarters March 4, 1991. Paper No. 91-GT-251. Associate Technical Editor: L. A. Riekert.

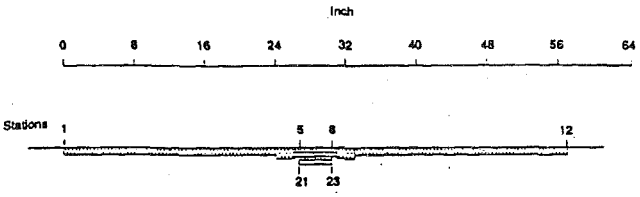

Fig. 1 Rotor model consisting of shaft and spline sleeve

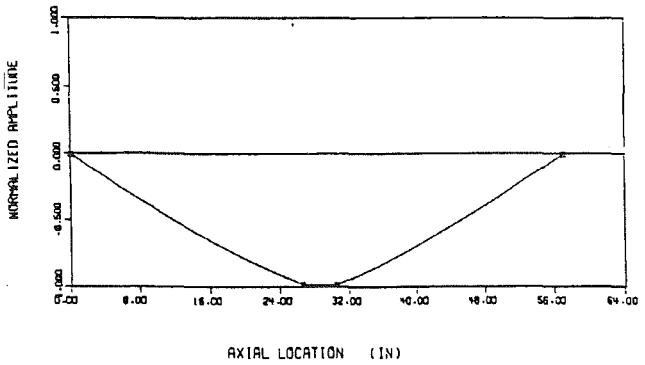

Fig. 2 Mode shape for first natural frequency

phenomenon of the transition from a slipping to a sticking interface was not found to be relevant to the stability question. The equations of motion were integrated versus time using a fourth-order Runge–Kutta method. The time step was made small enough to avoid numerical instability and assure accuracy of solution.

Different initial conditions were used to start the rotor transient motion. Either an imbalance force or a static side force of 1780 N [400 lb] was applied to the rotor at rest for 1 second, and then released. Figure 3 shows the transient response orbits for these two initial conditions. In both cases, the rotor motion approaches the same circular orbit from the outside. Another simulation where the displacements and velocities after the imbalance was removed were scaled down by a factor of 0.6 is shown in Fig. 4. In this case, the rotor motion approaches the same circular orbit from the inside. The parametric study is mostly concerned with the final motion of the system and not the intermediate transient. The set of displacements and velocities corresponding to the above circular limit cycle orbit was found to be the most appropriate choice of initial conditions. However, since under nonsymmetric operation there were two different solutions to the final motion, a scale factor (SI) was used to scale the set of displacements and velocities used for initial conditions.

3.0 Parametric Study

3.1 Symmetric Conditions. Under symmetric conditions (no side force and isotropic bearing coefficients), when the rotor is spinning at frequency Ω and whirling in a circular motion at frequency ω, the energy added in one cycle to the rotor-bearing system by the spline joint can be calculated to be:

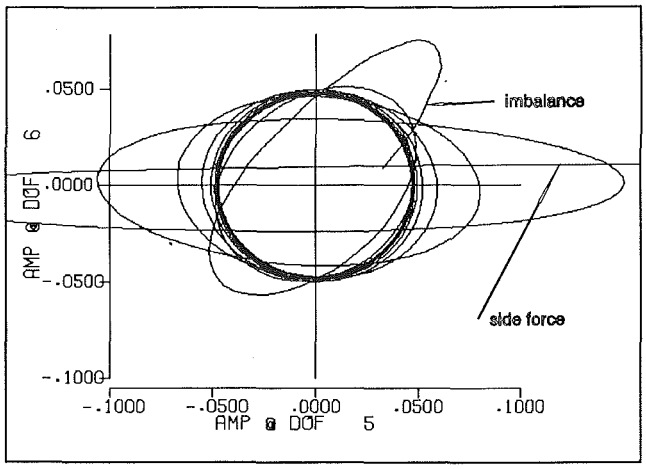

Fig. 3 Transient response orbit to different initial conditions

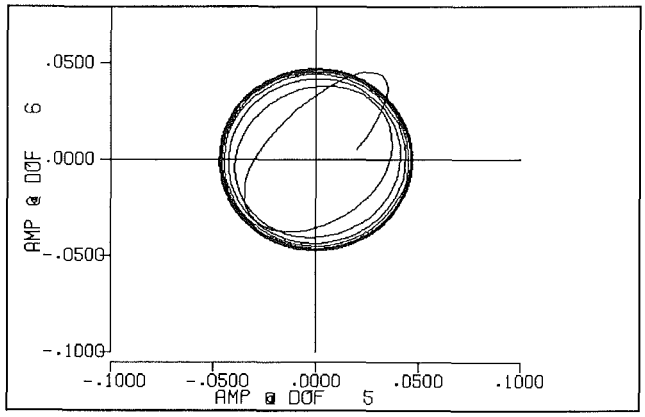

Fig. 4 Orbit for initial conditions scaled by *SI* = 0.6

$$U_f = \operatorname{sgn}(\omega - \Omega)\,\frac{4\mu T r_1}{\cos\Psi} \tag{2}$$

where r_1 is the amplitude of the relative angular displacement across the joint. On the other hand, the energy contribution from a viscous damper is given by:

$$U_v = -2\pi\omega B r_2^2 \tag{3}$$

where r_2 is the radius of the circular whirl orbit at the damper location. The negative sign indicates that energy is being dissipated.

When the motion reaches its limit cycle, the net energy added to the system is zero. Setting the sum of the above two equations to zero yields the amplitude of the motion:

$$r_1 = \begin{cases} 0, & \text{if } \Omega < \omega \\ \dfrac{2\mu T}{\pi\omega B\cos\Psi}\left(\dfrac{r_1}{r_2}\right)^2, & \text{if } \Omega > \omega \end{cases} \tag{4}$$

Nomenclature

$\Delta\theta$, $\Delta\alpha$ = difference in angular displacements across the spline measured in coordinate systems fixed on the ground and fixed on the rotor, respectively
K_a = angular stiffness of the spline
T = steady torque transmitted by spline
U_f, U_v = energy contributions per cycle due to spline friction and external damper, respectively
μ = coefficient of friction
Ψ = spline teeth pressure angle
Ω = spin speed of rotor

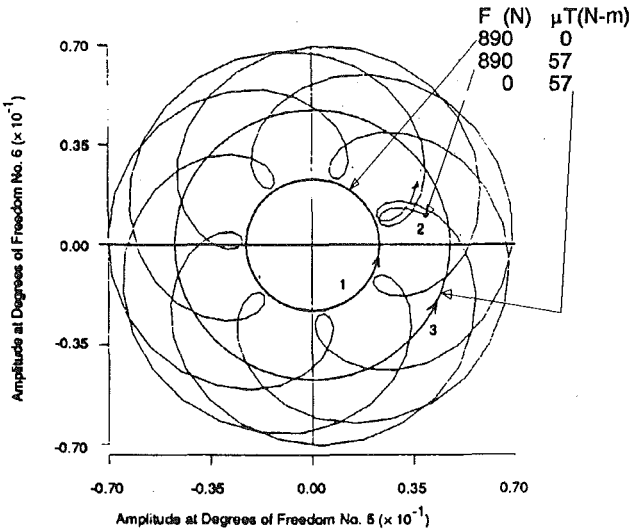

Fig. 5 Limit cycle orbits for different combinations of imbalance and friction torque product

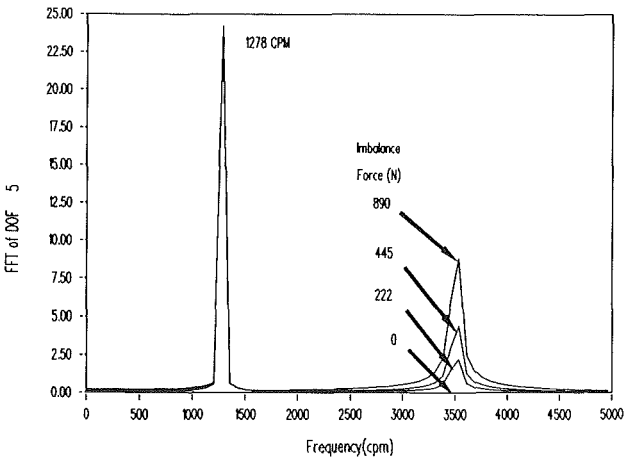

Fig. 6 FFT of lateral motion for different amounts of imbalance

where the ratio (r_1/r_2) is obtained from the mode shape of the motion. Below the first bending natural frequency, both energy contributions are negative, resulting in zero motion. Above the first bending natural frequency, the radius of the limit cycle orbit is proportional to the product of the friction coefficient and the spline torque (μT) and inversely proportional to the external viscous damping (B). Of course, when the rotor motion is such that the moment acting through the spline joint does not exceed that required to overcome slip $(2\mu T/\pi\cos\Psi)$ the joint connection will be elastic and the rotor will be stable without subsynchronous motion, in spite of operation above the first bending critical.

3.2 Imbalance. Figure 5 is a plot of three different limit cycle orbits showing the combined effects of friction and imbalance: (1) an imbalance of 890 N [200 lb] and zero friction; (2) an imbalance of 890 N and $\mu T = 56.5$ N-m [500 lb-in.]; and (3) zero imbalance and $\mu T = 56.5$ N-m. The case with imbalance only has purely synchronous motion while the case with only friction has motion purely at the first natural frequency. For both of these cases the orbit is circular.

The case with both imbalance and friction shows a combined motion beating between the two frequencies and contained within an annular region. Figure 6 shows the FFT of the lateral displacement as the imbalance force is increased from zero to 890 N. Clearly, the synchronous component of motion increases in proportion to the imbalance force while the subsynchronous component is unaffected. Thus, there are two components of motion, uncoupled from each other, at two frequencies:

1 a subsynchronous component (at the first bending critical), proportional to $\mu T/B$. This component is responsible for the mean radius of the annular region.
2 a synchronous component (at the spin speed), proportional to the imbalance force. This component is responsible for the width of the annular region.

3.3 Side Load. A static side load applied to the rotor will cause a moment to be transmitted through the spline connections between the sleeve and the rotor. There exists a threshold for this side load beyond which the rotor-bearing system is stable and all motions decay to a point. Below the threshold, the transient motion will approach one of two solutions as $t \to \infty$, depending on the initial conditions, as discussed below.

In the theory of the stability of nonlinear systems, a limit cycle is defined as an isolated closed phase path[1] that corresponds to a periodic mode of operation in the system. If all neighboring phase paths approach this cycle, from both the inside and outside, asymptotically as $t \to \infty$, it is called a stable limit cycle. On the other hand, if there exists at least one neighboring phase path that does not approach this cycle as $t \to \infty$; it is called an unstable limit cycle. Similarly, a stable or unstable node is a singular point toward which or away from which all neighboring phase paths move as $t \to \infty$. For more information on this subject, see [6].

When the rotor is operating above the first bending critical and at zero side load there is an orbitally stable circular limit cycle for the motion at a whirl frequency equal to the first bending critical, regardless of the initial conditions. The center of this circle is an unstable node.

As the side load is applied, the center of the orbitally stable limit cycle moves in the direction of the load. This unstable node grows into an orbitally unstable limit cycle. Figure 7 is a comparative plot of the two limit cycles as the side load is progressively increased from zero to 1780 N. The arrows indicate the stability status of the different cycles and nodes. The unstable limit cycle is elliptical in shape and has its major axis inclined a few degrees from the direction of the applied load, as can be determined by looking in more detail at the case of the 890 N side load at different initial conditions. Figure 8 shows part of the orbit of the rotor near this cycle for three values of initial conditions ($SI = 3.5$, 3.875, and 4.25) between $t = 0.55$ and $t = 0.60$ seconds. Figure 9 shows the complete orbits (from $t = 0$ to 1 sec) for these three conditions. As seen, the orbit decays to a point for $SI = 3.5$, whereas it grows to the stable limit cycle for $SI = 4.25$. For $SI = 3.875$ on the other hand, the orbit does not depart drastically from the cycle in Fig. 8 even after time has reached a full second. The criterian that determines the final orbit is not simply whether the initial rotor displacement is inside or outside this unstable limit cycle but is a complex function of all the initial displacements and velocities of the system.

Thus, the unstable limit cycle represents a threshold for the initial conditions of the rotor-bearing system eventually to reach the nonzero orbitally stable limit cycle, which is manifested as a subsynchronous vibration. For small initial conditions, the transient orbit will decay in an elliptically shaped spiral toward a point at its center, which is now a stable node. Figure 10 illustrates the transient orbits for three different values of small initial conditions ($SI = 3.5$, 2, and 1). On the

[1] "Phase path" is the term given to the path of a representative point in the phase plane, while "phase" is used to describe the state of the system, i.e., the set of displacements and velocities of the system at a given time.

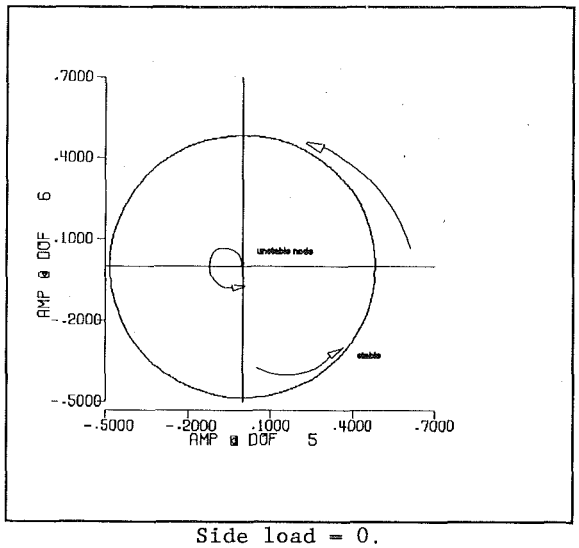

Side load = 0.

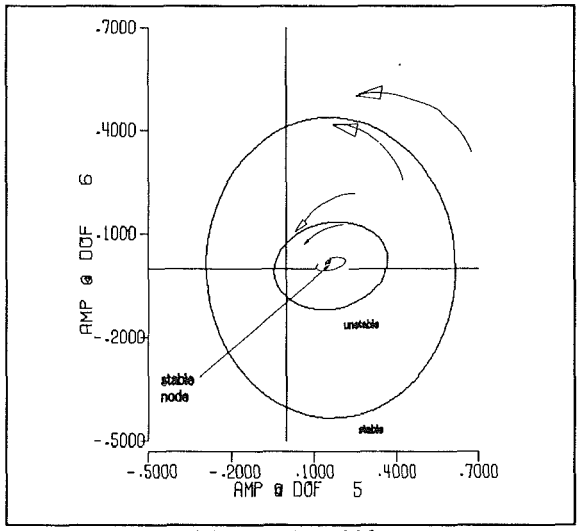

Side Load = 890 N

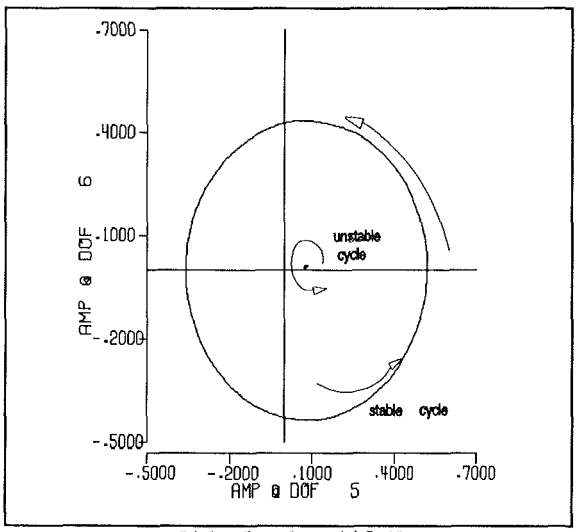

Side load = 445 N

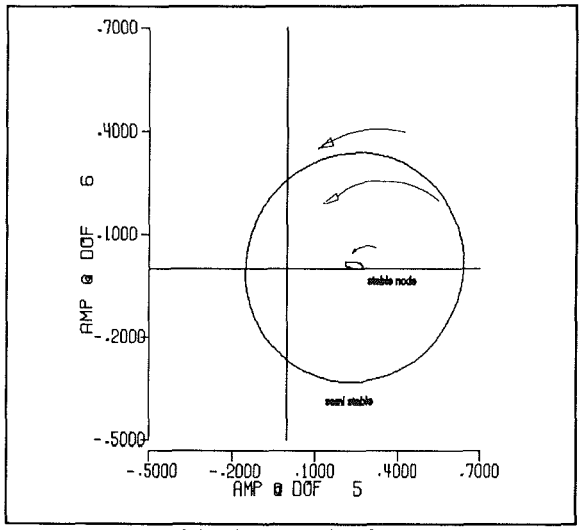

Side load = 1330 N.

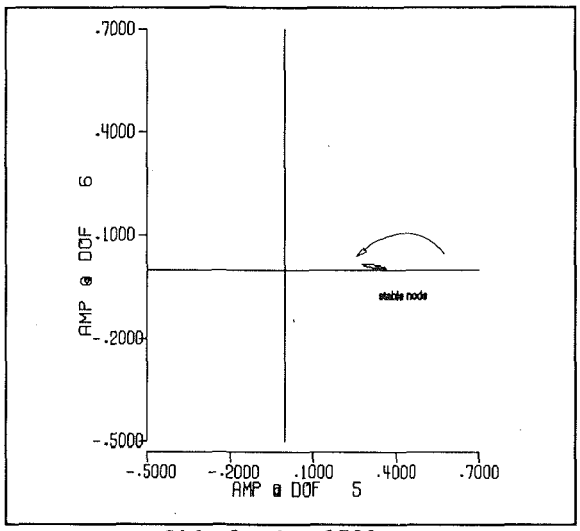

Side load = 1780 N.

Fig. 7 Comparison of orbitally stable (larger) and orbitally unstable (smaller) limit cycles at different side loads

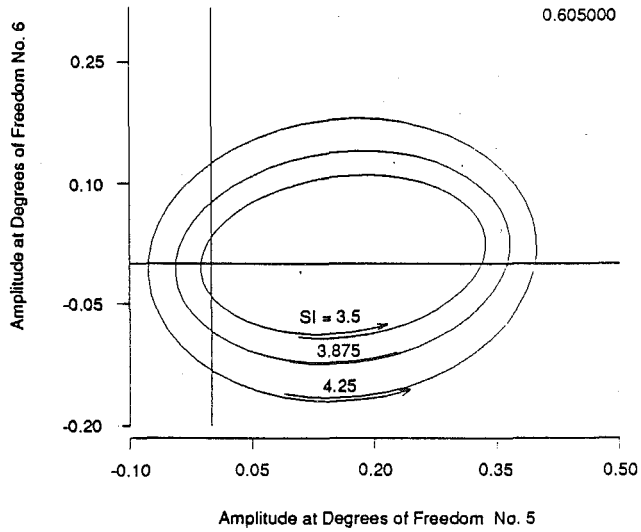

Fig. 8 Transient orbit for three different initial conditions near the unstable limit cycle between t = 0.55 and 0.65 s

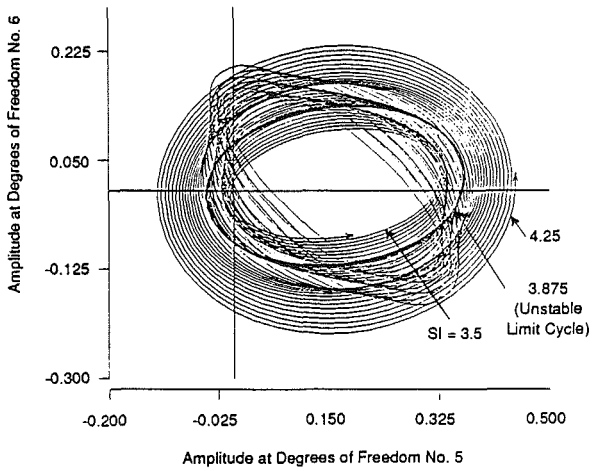

Fig. 9 Transient orbit for three different initial conditions near the unstable limit cycle between t = 0 and 1 s

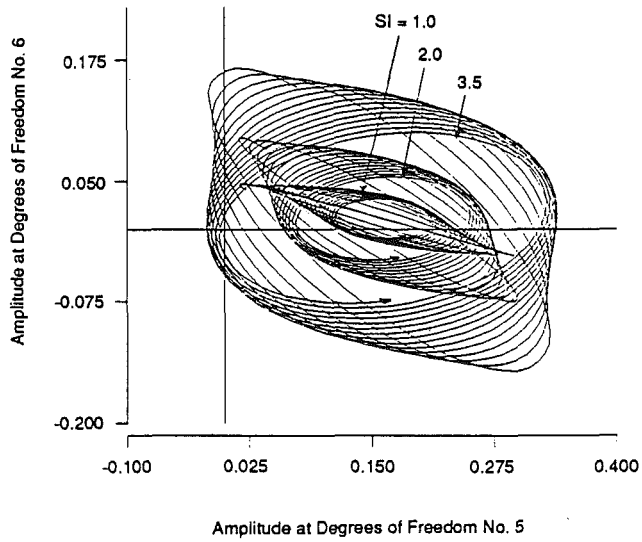

Fig. 10 Transient orbit for small initial conditions showing decay to a stable node

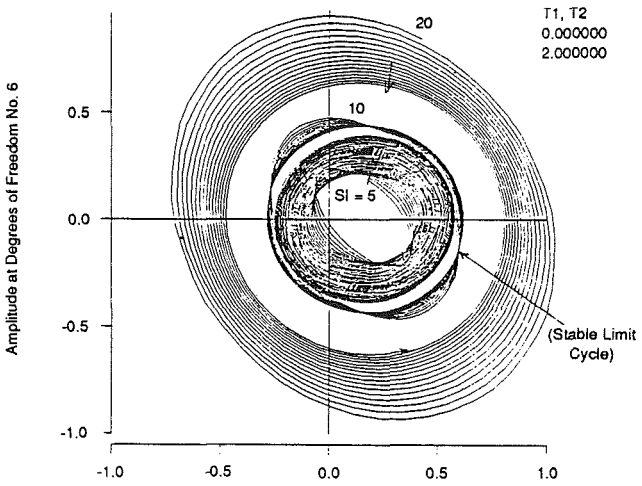

Fig. 11 Transient orbit for large initial conditions showing approach to stable limit cycle

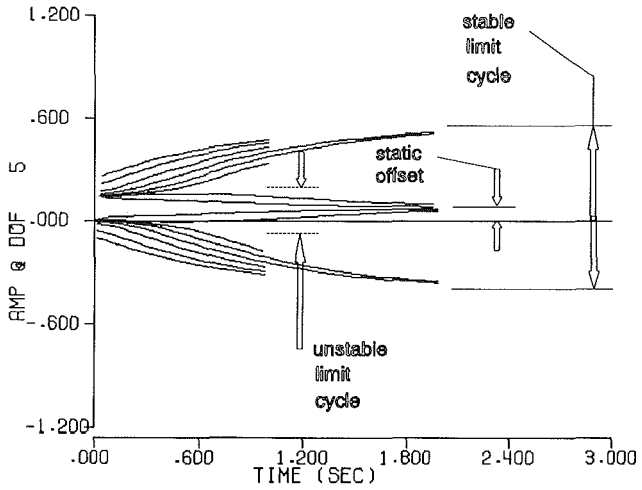

Fig. 12 Envelopes of lateral motion versus time for different initial conditions at 445 N side load

other hand, for large enough initial conditions, the orbit grows toward the larger, more circular stable limit cycle, from either the inside or the outside. Figure 11 illustrates the transient orbits for three different values of large initial conditions (*SI* = 5, 10, and 20).

As the side load is increased, the orbitally unstable limit cycle grows very rapidly toward the larger limit cycle. This larger cycle, on the other hand, decreases and becomes elliptical very gradually with increasing side load. The principal axis of this larger cycle is along the direction of load. Both limit cycles merge into one another at the threshold of side load (about 1330 N for this case) to form what is called a "semi-stable" or double cycle [2]. Although motions with large initial conditions approach this cycle asymptotically from the outside, any disturbance will cause the motion to decay toward the stable node at its center.

Figure 12 contains superimposed plots of the envelopes of the lateral component of motion versus time for numerous values of the initial condition scale factor (*SI*) and a side load of 100 lb. Figures 13, 14, and 15 are similar plots for side loads of 890, 1330, and 1780 N, respectively, except for a factor of 2 in the scale of the abscissa. At large orbit amplitudes (near the limit cycles) the decay rate with time is fairly slow, while as the orbit size decreases the decay rate rapidly increases.

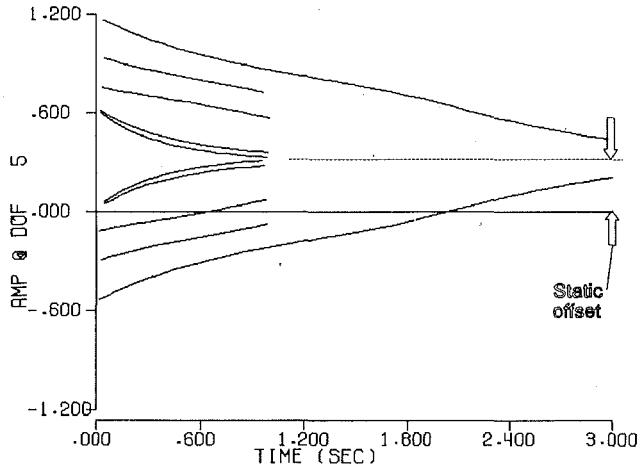

Fig. 13 Envelopes of lateral motion versus time for different initial conditions at 1780 N side load

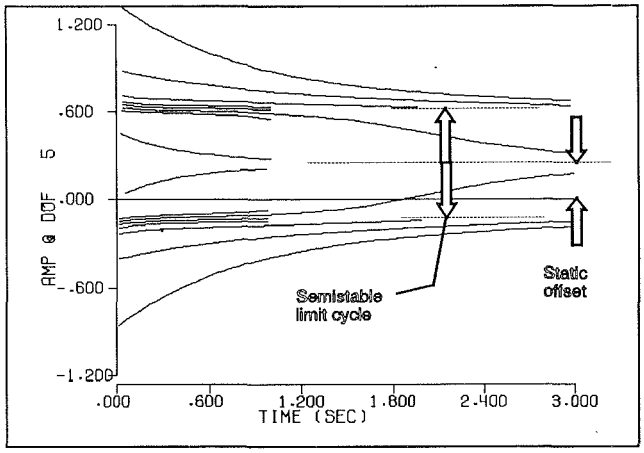

Fig. 15 Envelopes of lateral motion versus time for different initial conditions at 1330 N side load

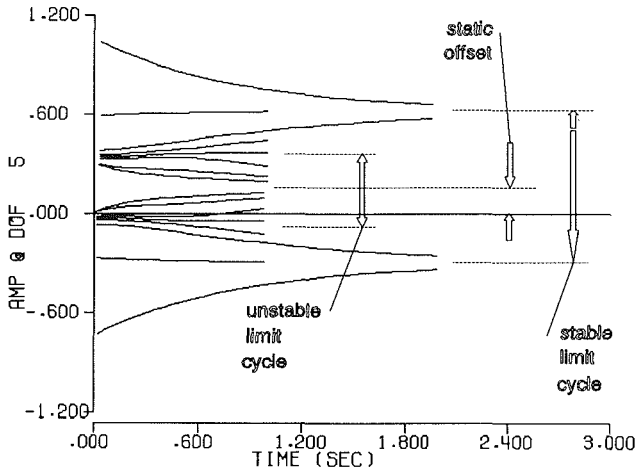

Fig. 14 Envelopes of lateral motion versus time for different initial conditions at 890 N side load

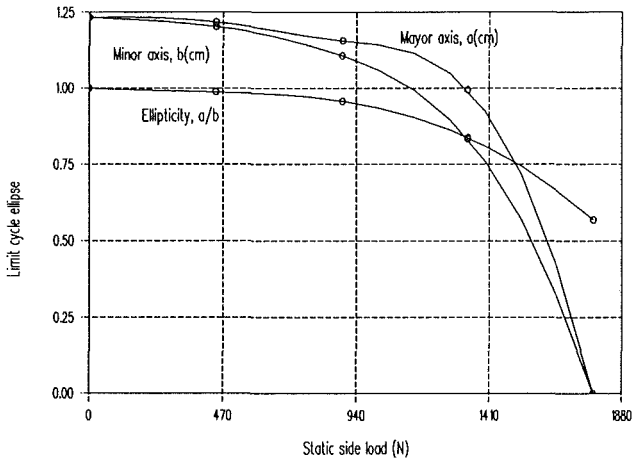

Fig. 16 Effect of side load on limit cycle

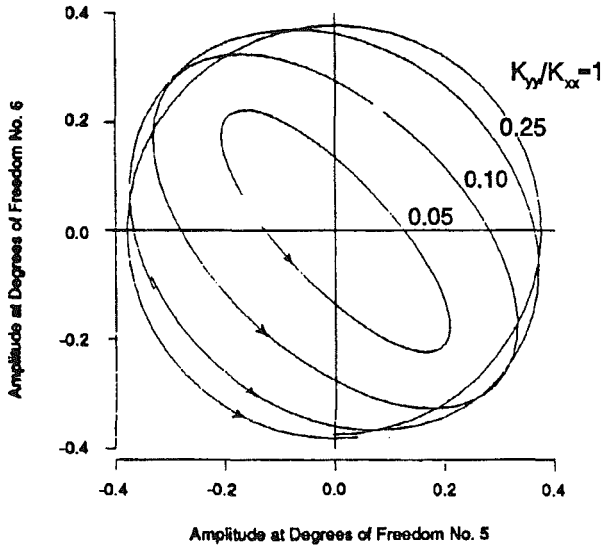

Fig. 17 Limit cycle orbits versus increasing bearing stiffness asymmetry

Further increases in side load beyond the threshold increase the rate of decay of the motion toward the stable node at the static offset. This is shown in the plots of the envelopes for the case of a side load of 1780 N (Fig. 15), which do not show any evidence of a limit cycle.

Figure 16 plots the size and ellipticity of the stable limit-cycle orbit as the side load is increased. The orbit starts out as a large circle, which becomes elliptical and shrinks in size, very slowly for small side load and then very rapidly as the threshold (1780 N) is approached.

3.4 Asymmetric Bearing Coefficients. Figure 17 shows the effect of decreasing one of the components of direct bearing stiffness (K_{yy}) on the limit cycle orbit. As K_{yy} is decreased from 100,000 to 10,000 lb/in., the orbit becomes elliptical with the major axis inclined about 135 deg from the x axis and increasing to about 110 percent of the radius of the original circular orbit. Further decrease in K_{yy} decreases the size of the orbit without much further effect on its ellipticity. Figure 17 is a plot of the major and minor axes of the limit cycle ellipse. In the case of this rotor model, no reduction in the major axis is noticed until K_{yy}/K_{xx} is less than 10 percent. However, as shown by the mode shape in Fig. 2, the rotor model utilized here to exercise the joint is fairly flexible compared to the bearing stiffness. A stiffer rotor would involve more participation of the bearings in the first bending mode. Therefore, it is expected that for relatively stiffer rotors, asymmetry in the bearing coefficients should have a more beneficial effect in controlling rotor instability.

3.5 Rotating Speed. The rotor will be stable or unstable depending on whether the rotating speed is lower or higher than the first bending critical speed is lower or higher than the first bending critical sped of the rotor-bearing system. Several simulations performed with and without side load showed no effect of speed. Other than determining the stability status, the spin speed has no noticeable effect on the size of the orbit or on the transient motion to reach it. (The only effect is through the small influence that the gyroscopic effects have on the first bending critical speed and mode shape.)

4.0 Conclusions

For symmetric operation:

1 There is only one asymptotic solution (as $t \rightarrow \infty$) independent of the initial conditions. If the spin speed is less that the first bending critical speed, the energy contribution from the friction in the spline is negative, resulting in zero subsynchronous motion and a stable rotor. If the spin speed is greater than the first bending critical speed, the rotor is unstable and its motion is a circular limit cycle whirling at a frequency equal to the first rotor bending critical. The radius of this limit cycle orbit is proportional to the product of the friction coefficient and the spline torque, and is inversely proportional to the external viscous damping. Transient motions proceed in spiral paths, from either the inside or the outside, toward the limit cycle circle. The center of the circle is an unstable node.

2 Other than determining whether instability is present, there is very little effect of spin speed on the size of the subsynchronous motion, only the small influence that the gyroscopic effects have on the first bending critical speed and mode shape.

3 With rotor imbalance the limits of the rotor orbit widen from a circle to an annulus. The motion within this annulus contains two components at two frequencies: a subsynchronous component (at the first bending critical) and the synchronous component. The subsynchronous component is proportional to the product of the friction coefficient and the spline torque. The synchronous component is proportional to the imbalance force and is responsible for the width of the annular region. Both components are uncoupled from each other.

Bearing asymmetry:

4 Asymmetry in rotor bearing stiffness coefficients reduces the size of the subsynchronous whirl orbit brought about by internal friction.

Static side load:

5 There exists a threshold for the side load beyond which the rotor-bearing system is stable and all motions decay to a point. Below the threshold, the transient motion will approach one of two asymptotic solutions depending on the initial conditions.

6 As the side load is applied, the unstable node at the center of the orbitally stable limit cycle moves in the direction of the load and grows into an orbitally unstable limit cycle. For small initial conditions, the transient orbit will decay in an elliptically shaped spiral toward a point at its center, which is now a stable node. On the other hand, for large enough initial conditions, the orbit grows toward the larger, more circular stable limit cycle, from either the inside or the outside. As the side load is increased, the orbitally unstable limit cycle grows very rapidly toward the larger limit cycle. This larger cycle, on the other hand, decreases and becomes slightly elliptical.

7 Both limit cycles merge into one another at the threshold of side load to form a "semi-stable" or double cycle. Although motions with large initial conditions approach this cycle asymptotically from the outside, any disturbance will cause the motion to decay toward the stable node at its center. Further increases in side load beyond the threshold increase the rate of decay of the motion toward the stable node at the static offset.

References

1 Gunter, E. J., "Dynamic Stability of Rotor-Bearing Systems," NASA SP-113, Office of Technical Utilization, U.S. Government Printing Office, 1966.

2 Black, H. F., "The Stabilizing Capacity of Bearing of Flexible Rotors With Hysteresis," ASME *Journal of Engineering for Industry*, Vol. 98, 1976, pp. 87–91.

3 Glasgow, D. A., and Nelson, H. D., "The Stability of Rotor-Bearing Systems Using Component Mode Synthesis," ASME *Journal of Mechanical Design*, Vol. 102, 1980.

4 Lund, J. W., "Destabilization of Rotors From Friction in Internal Joints With Micro-slip," presented at the JSME International Conference on Rotordynamics, Sept. 14–17, 1986.

5 Mechanical Technology Inc., "Internal Rotor Friction Instability," Technical Report 88TR39, prepared for NASA Marshall Space Flight Center, under contract No. NAS8-35601, Feb. 1990.

6 Andronov, A. A., Vitt, A. A., and Khaikin, S. E., *Theory of Oscillators*, Dover Publications, New York, 1966, p. 289.

A Study of the Influence of Bearing Clearance on Lateral Coupled Shaft/Disk Rotordynamics

G. T. Flowers

Fang Sheng Wu

Department of Mechanical Engineering,
Auburn University,
Auburn University, AL 36849-5341

This study examines the influence of bearing clearance on the dynamic behavior of a rotating, flexible disk/shaft system. Most previous work in nonlinear rotordynamics has tended to concentrate separately on shaft vibration or on bladed disk vibration, neglecting the coupling dynamics between them. The current work examines the important rotordynamic behavior of coupled disk/shaft dynamics. A simplified nonlinear model is developed for lateral vibration of a rotor system with a bearing clearance nonlinearity. The steady-state dynamic behavior of this system is explored using numerical simulation and limit cycle analysis. It is demonstrated that bearing clearance effects can produce superharmonic vibration that may serve to excite high-amplitude disk vibration. Such vibration could lead to significantly increased bearing loads and catastrophic failure of blades and disks. In addition, multivalued responses and aperiodic behavior were observed.

Introduction

Rotors for high-speed turbomachinery are designed to minimize disk and blade vibratory failure. This is usually accomplished by designing the disk and blades to be sufficiently rigid so that their natural frequencies are significantly above the operating speed. Such an approach is adequate when the primary concern is synchronous excitation of resonant vibrations. However, there are excitation frequencies that are multiples of the rotor speed (from blade passages, for example) that may serve to excite high-amplitude disk vibration if they correspond with a resonant frequency of the disk. In addition, nonlinear structural effects are inherent in all turbomachinery. Bearing stiffnesses are typically modeled as bilinear springs, often with a deadband (zero restoring force for a finite displacement). Damper seals and bearings provide inherently nonlinear damping and stiffness effects due to fluid compression. Nonlinear inertial terms (restoring forces proportional to acceleration) are also possible. Rubbing contact between rotor and housing is another source of nonlinearity. The contact is intermittent and frictional forces provide energy dissipation. Such nonlinear dynamics may excite dynamic responses not predicted by linear analyses and result in unexpected, high-amplitude vibration and structural failure. The objective of the current work is to develop a better understanding of the complex interaction between flexible bladed-disk/shaft dynamics and nonlinear interconnection forces. This research effort investigates the influence of bearing clearances (resulting in nonlinear rotor support forces) on the steady-state dynamic responses of a simplified rotor system. A simplified model is developed to simulate the lateral dynamics of a rotor system with a flexible disk and support clearances. The rotordynamic behavior of this model is studied using nonlinear analysis techniques and numerical simulation.

Background and Motivation

Rotordynamic analyses are typically performed using models with rigid disks and blades. If excitations are of sufficiently high frequency so as to excite disk and blade vibration, such models are not adequate to predict dynamic responses. In addition, linearized analyses are commonplace in turbomachinery design studies, as they are in many other fields of engineering. Linear analyses adequately predict the stability of responses for small perturbations about the nominal operating condition, but may be grossly inadequate for larger amplitude vibration and may completely ignore important dynamic behavior, such as limit cycling, that is dependent on nonlinearities.

There is a fairly large body of work documented in the literature concerning studies of disk flexibility on rotors and turbomachinery. A discussion of this previous work with regard to linear rotor systems is presented by Flowers and Ryan (1993). An excellent source for a comprehensive review of work in this area is presented by Davis (1989).

Nonlinearities can greatly affect rotordynamic responses. There has been considerable work in this area with regard to shaft dynamics. A few of the ones that have significantly influenced this work will be discussed. Black (1968) conducted an experimental investigation of the interaction of rotor whirling with stator vibrations. Loewy and Piarulli (1969) described a number of nonlinear effects that can significantly affect rotordynamic responses. This text serves as an excellent source of information on studies of nonlinear rotordynamics. Begg (1974) discusses the effects of friction on the whirl stability of

Contributed by the International Gas Turbine Institute and presented at the 37th International Gas Turbine and Aeroengine Congress and Exposition, Cologne, Germany, June 1-4, 1992. Manuscript received by the International Gas Turbine Institute February 11, 1992. Paper No. 92-GT-177. Associate Technical Editor: L. S. Langston.

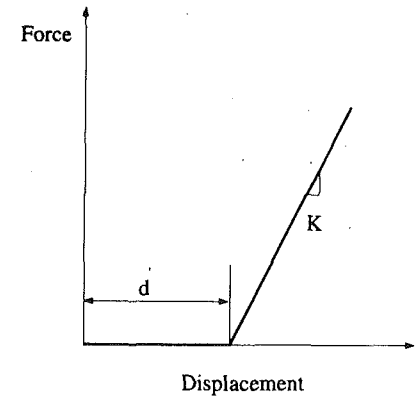

Fig. 1(*a*) Deadband nonlinearity

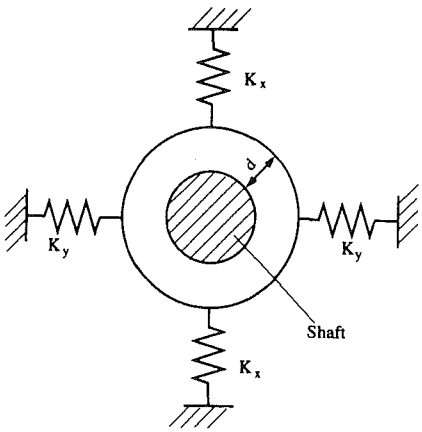

Fig. 1(*b*) Bearing model with deadband nonlinearity

a rotor system. Muszynska (1984) studied full annular rub due to rotor/seal contact and described the resulting synchronous self-excited excitations that occur. Muszynska (1968) investigated the nonlinear phenomena of oil whirl and oil whip in rotor bearing support systems and concluded that significant stability problems can occur due to the self-excited responses that result. She has also examined material nonlinearities, geometric nonlinearities, shaft/housing rub, nonlinear support stiffness, and nonlinear damping effects. Padovan and Choy (1987) investigated the nonlinear dynamic behavior excited by blade-casing rub interactions. They noted the lack of work in this area that addresses the complete global dynamics during rubbing.

A critical issue with regard to bearing supports is the presence of clearances in the bearings. Such clearances produce nonlinear bearing forces that can significantly influence rotordynamic behavior. A typical model for such behavior is shown in Fig. 1(*a*). The bearing force acts as a linear spring with a deadband region. For displacements below the deadband threshold, the restoring force is zero. A schematic diagram for the bearing model used in this study is shown in Fig. 1(*b*).

Much of the work in the field of nonlinear rotordynamics has concentrated on rotor models with rigid disks and blades. These studies have typically emphasized shaft dynamics and neglected coupling between the dynamics of the bladed disks and the shaft. Nonlinearities can serve to excite subharmonic and superharmonic responses that cannot be predicted by linear analyses. If the natural frequency associated with disk vibration is at or near a multiple of the rotor speed, such an excitation may result in severe oscillations and increased bearing loads. Such a concept agrees well with the work of other researchers in this field, most notably Chivens and Nelson (1975) and Klompas (1983). They noted that disk flexibility appears to have little influence on rotor critical speeds but that it may significantly impact system natural frequencies. So, it is important to assess under what conditions nonlinear effects are important and the best techniques for predicting such behavior.

Simulation Study

The present research effort is concerned with the dynamic responses of rotating, flexible disk/shaft systems. A simulation study was undertaken to evaluate the influence of bearing clearance on the steady-state vibration of coupled rotor shaft/disk systems. The results are confirmed at selected points by numerical integration of the governing differential equations.

Equations of Motion. Due to the complexity of a full-scale rotor model and the desire to vary the system parameters easily, a simplified model is used in this study. A model was developed that captures the essential dynamic characteristics of coupled rotor/disk vibration that are of interest in this study. This model is similar to the Jeffcott rotor model except that a model for lateral disk flexibility has been added to the structure. A schematic diagram of the simplified rotor-disk model is shown in Fig. 2. Models consisting of a rigid ring elastically coupled to a rigid hub have often been used to study disk flexibility effects. The fundamental dynamics of the present model are quite similar and it lends itself more readily to increased disk

Nomenclature

A_i, B_i, C_i, D_i = matrices for nonlinear analysis
d = Δ/e
e = imbalance eccentricity
F_y, F_z = nonlinear bearing forces
F_e = $m/2m_1$
I_{nd} = inertia of rotor hub
k_y, k_z = support stiffnesses
k_i = multiple of synchronous frequency
L = rotor shaft length
m = one-fourth mass of disk
m_1 = $I_{nd}/L^2 + 2mr^2/L^2$
m_2 = mr/L
m_3 = $8mr^2/L^2$
m_{20} = m_2/m
m_{21} = m_2/m_1
m_{31} = m_3/m_1
N = number of harmonics
r = disk radius
x_1, x_2 = shaft degrees of freedom
x_3, x_4 = disk degrees of freedom
z_1, z_2, z_3, z_4 = physical displacements for disk mass elements
Δ = bearing clearance
$\zeta_1, \zeta_2, \zeta_3, \zeta_4$ = damping ratios for x_1, x_2, x_3, x_4 degrees of freedom, respectively
Λ_1 = Ω/ω_{r1}
Λ_2 = Ω/ω_{r2}
Λ_3 = Ω/ω_d
τ = Ωt
ψ_i = azimuth angle for ith rotor mass
Ω = rotor speed
ω_d = natural frequency of nonrotating disk
ω_{r1} = natural frequency of rotor support x_1 direction
ω_{r2} = natural frequency of rotor support x_2 direction
$(')$ = $d/d\tau$
$(\dot{})$ = d/dt

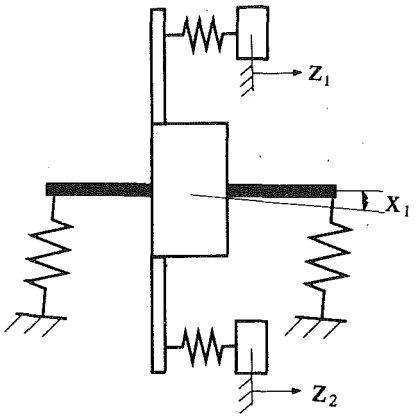

Fig. 2 Simplified flexible disk rotor model

complexity for future work. The equation development for this model is based upon the following considerations:

1 The disk is modeled as a collection of four equally spaced mass elements connected to a central hub by linear springs (see Fig. 2). The rigid central hub simulates the shaft/disk interconnection.
2 The hub is restricted to rotational motion.
3 The motion of the central hub is restrained by rotational springs, which represents the bearing forces.
4 The rotor speed is constant.
5 The disk motion is assumed to be asymmetric around the circumference of the disk. For this development, this assumption means that $z_1 = -z_3$ and $z_2 = -z_4$. This type of motion results in responses that transmit a moment to the shaft through the disk/shaft interconnections and thereby assures that the disk motion and shaft motion are coupled.

The rotor system is allowed to rotate about the z axis. The other degrees of freedom, x_1, x_2, x_3, and x_4 will be considered to be infinitesimal quantities of order 1. In the equations of motion, the length dimensions for this development are scaled by e, the imbalance eccentricity. Time is scaled by the rotor speed, Ω.

The equations of motion that result are:

$$x_1'' - \frac{1}{2} m_{21} x_3'' + \frac{1}{2} m_{31} x_2' - m_{21} x_4' + 2\zeta_1 \frac{\omega_{r1}}{\Omega} x_1' - F_y = F_e \cos(\Omega t) \quad (1a)$$

$$x_2'' - \frac{1}{2} m_{21} x_4'' - \frac{1}{2} m_{31} x_1' + m_{21} x_3' + 2\zeta_2 \frac{\omega_{r2}}{\Omega} x_2' - F_z = F_e \sin(\Omega t) \quad (1b)$$

$$-4m_{20} x_1'' + x_3'' - 8m_{20} x_2' + 2x_4' - x_3 + 2\zeta_3 \frac{\omega_d}{\Omega} x_3' + \frac{\omega_d^2}{\Omega^2} x_3 = 0 \quad (1c)$$

$$-4m_{20} x_2'' + x_4'' + 8m_{20} x_1' - 2x_3' - x_4 + 2\zeta_4 \frac{\omega_d}{\Omega} x_4' + \frac{\omega_d^2}{\Omega^2} x_4 = 0 \quad (1d)$$

where

$$F_e = \frac{m}{2m_1}$$

$$F_y = -\frac{\phi}{\Lambda_1^2}\left(1 - \frac{d}{\sqrt{x_1^2 + x_2^2}}\right) x_1$$

$$F_z = -\frac{\phi}{\Lambda_2^2}\left(1 - \frac{d}{\sqrt{x_1^2 + x_2^2}}\right) x_2$$

$$\phi = 1 \text{ if } \sqrt{x_1^2 + x_2^2} > d$$

$$0 \text{ otherwise}$$

$$x_3 = \sum_{i=1}^{N} z_i \cos(\Omega t + \psi_i)$$

$$x_4 = \sum_{i=1}^{N} z_i \sin(\Omega t + \psi_i)$$

It is important to note that the influence of bearing clearance in producing subsynchronous or supersynchronous responses is canceled for rotors with isotropic supports and no gravitational effects and with response amplitudes greater than the bearing clearance. This can be clearly seen by examining the equations for bearing support forces, F_y and F_z, shown above. First, assume that $x_1 = a_1 \cos(\Omega t)$ and $x_2 = a_1 \sin(\Omega t)$ as would be expected for a rotor with isotropic supports ($\Lambda_1 = \Lambda_2$). Also, assume that $a_1 > d$ so that $\phi = 1$. Substitution of these expressions into the equations for F_y and F_z results in

$$F_y = -\frac{1}{\Lambda_1^2}(a_1 - d)\cos(\Omega t)$$

and

$$F_z = -\frac{1}{\Lambda_1^2}(a_1 - d)\sin(\Omega t)$$

These expressions are now linear in terms of cos (Ωt) and sin (Ωt). So, no subharmonic or superharmonic components are produced.

Analysis Technique. Of interest in this study is the investigation of steady-state responses for the above system of equations. This work will be concerned primarily with periodic motions. An appropriate analysis technique in this regard is the harmonic balance method (HB). To apply the harmonic balance method, the steady-state responses associated with Eqs. (1) and the nonlinear bearing forces, F_y and F_z, are assumed to have the form:

$$x_j = \sum_{i=1}^{N} (a_{ji} \cos(k_i \Omega t) + b_{ji} \sin(k_i \Omega t) \quad (2a)$$

$$(j = 1, 2, 3, 4)$$

$$F_y = \sum_{i=1}^{N} (g_{1i} \cos(k_i \Omega t) + h_{1i} \sin(k_i \Omega t) \quad (2b)$$

$$F_z = \sum_{i=1}^{N} (g_{2i} \cos(k_i \Omega t) + h_{2i} \sin(k_i \Omega t) \quad (2c)$$

Substitution of Eqs. (2) into the equations of motion, Eqs. (1), and equating all the trigonometric terms leads to the following nonlinear algebraic equations in matrix form:

$$A_i P_{1i} + B_i P_{2i} - Q_i - F_i = 0 \quad (3a)$$

$$C_i P_{1i} + D_i P_{2i} = 0 \quad (3b)$$

where:

$$A_i = \begin{bmatrix} -k_i^2 & 2\frac{\zeta_1}{\Lambda_1} k_i & 0 & \frac{1}{2} m_{31} k_i \\ -2\frac{\zeta_1}{\Lambda_1} k_i & -k_i^2 & -\frac{1}{2} m_{31} k_i & 0 \\ 0 & -\frac{1}{2} m_{31} k_i & -k_i^2 & 2\frac{\zeta_2}{\Lambda_2} k_i \\ \frac{1}{2} m_{31} k_i & 0 & -2\frac{\zeta_2}{\Lambda} k_i & k_i^2 \end{bmatrix}$$

$$B_i = \begin{bmatrix} \frac{1}{2} m_{21} k_i^2 & 0 & 0 & -m_{21} k_i \\ 0 & \frac{1}{2} m_{21} k_i^2 & m_{21} k_i & 0 \\ 0 & m_{21} k_i & \frac{1}{2} m_{21} k_i^2 & 0 \\ -m_{21} k_i & 0 & 0 & \frac{1}{2} m_{21} k_i^2 \end{bmatrix}$$

$$C_i = \begin{bmatrix} 4m_{20} k_i^2 & 0 & 0 & -8m_{20} k_i \\ 0 & 4m_{20} k_i^2 & 8m_{20} k_i & 0 \\ 0 & 8m_{20} k_i & 4m_{20} k_i^2 & 0 \\ -8m_{20} k_i & 0 & 0 & 4m_{20} k_i^2 \end{bmatrix}$$

$$D_i = \begin{bmatrix} \frac{1}{\Lambda_3^2} - 1 - k_i^2 & 2\frac{\zeta_3}{\Lambda_3} k_i & 0 & 2k_i \\ -2\frac{\zeta_3}{\Lambda_3} k_i & \frac{1}{\Lambda_3^2} - 1 - k_i^2 & -2k_i & 0 \\ 0 & -2k_i & \frac{1}{\Lambda_3^2} - 1 - k_i^2 & 2\frac{\zeta_4}{\Lambda_3} k_i \\ 2k_i & 0 & -2\frac{\zeta_4}{\Lambda_3} k_i & \frac{1}{\Lambda_3^2} - 1 - k_i^2 \end{bmatrix}$$

$$P_{1i} = \begin{pmatrix} a_{1i} \\ b_{1i} \\ a_{2i} \\ b_{2i} \end{pmatrix} \qquad P_{2i} = \begin{pmatrix} a_{3i} \\ b_{3i} \\ a_{4i} \\ b_{4i} \end{pmatrix}$$

$$Q_{1i} = \begin{pmatrix} q_{1i} \\ h_{1i} \\ q_{2i} \\ h_{2i} \end{pmatrix} \qquad F_i = \begin{pmatrix} \delta_1 F_e \\ 0 \\ 0 \\ \delta_1 F_e \end{pmatrix}$$

where

$$\delta_1 = 1 \text{ if } k_i = 1$$
$$0 \text{ if } k_i \neq 1$$

Rearrangement of Eq. (3*b*) yields:

$$P_{2i} = -D_i^{-1} C_i P_{1i} \tag{4}$$

Substituting the above expression for P_{2i} into Eq. (3*a*) results in the following expression:

$$(A_i - B_i D_i^{-1} C_i) P_{1i} - Q_i - F_i = 0 \quad (i = 1, \ldots, N) \tag{5}$$

Equation (5) is a nonlinear algebraic equation in terms of the unknown constants associated with the assumed responses. Q is a nonlinear function of P_1. In this study, a Newton-Raphson algorithm is used to solve Eq. (5) for the unknown constants.

Parameter Variation Studies. A number of computer simulation studies were performed using the model described above. Parameter variation studies were performed for varied disk stiffnesses and for varied bearing clearances. In order to avoid excessive cluttering of the figures with parametric plots, typical results from each study will be presented and discussed. The nominal parametric configuration that was selected for the model is shown in Table 1. The parameters selected for the example cases are thought to be representative values that are practical for turbomachinery. In particular, the ratio of disk frequency to rotor frequency is 5.0 for the results presented herein. The ratio is a quite reasonable value for a practical rotor system.

Table 1 Nominal parameter values for simulation studies

Parameter	Value
ω_1	1.0
ω_2	2.0
ω_3	5.0
m_{20}	0.2
m_{21}	0.1
m_{31}	0.16
ζ_1	0.01
ζ_2	0.01
ζ_3, ζ_4	0.01
d	0.0, 0.5, 1.0
F_e	0.25

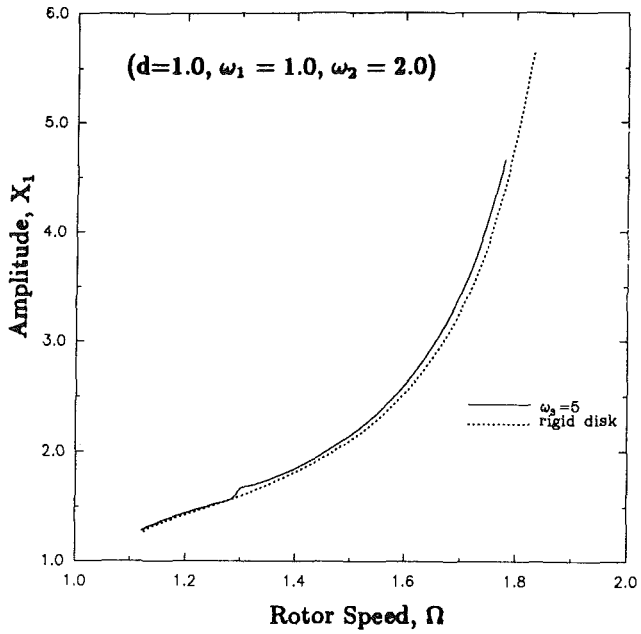

Fig. 3(*a*) 1/2Ω component of rotor response

Figures 3(*a*)-3(*c*) show the predicted responses for the x_1 body motion for the rotor model with a rigid disk ($\omega_3 = \infty$) and with a flexible disk ($\omega_3 = 5.0$) from the harmonic balance analyses for $d = 1.0$. Figures 4(*a*)-4(*c*) and 5(*a*)-5(*c*) show the predicted responses for the x_1 and x_3 motion for three values of bearing clearance ($d = 0.0$, 0.5, and 1.0). For all cases, similar behavior is observed for the x_2 body motion (to the x_1 motion) and for the x_4 disk motion (to the x_3 motion), except that the response amplitudes are different due to the nonisotropic supports. For all the cases presented here, the frequency content is assumed to consist of 1/2Ω, 1Ω, 3Ω, and 5Ω components. The 5Ω components are small for all cases and will not be discussed further.

Examination of Figs. 3, 4, and 5 indicates that dual-valued responses exist for much of the operating range for rotor speeds below about 1.6. It should be emphasized that, for the 1/2Ω

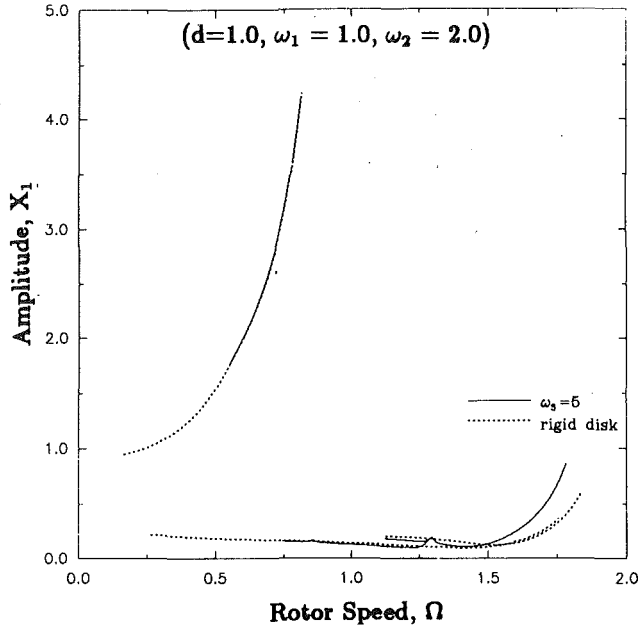

Fig. 3(*b*) 1Ω component of rotor response

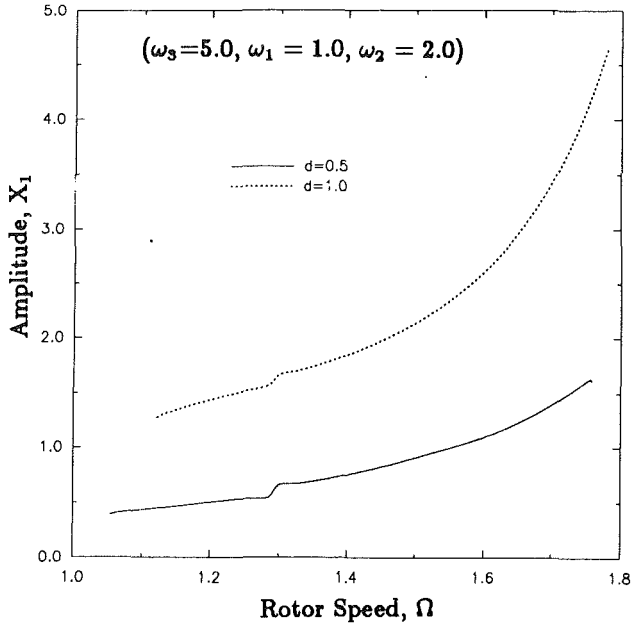

Fig. 4(*a*) 1/2Ω component of rotor response

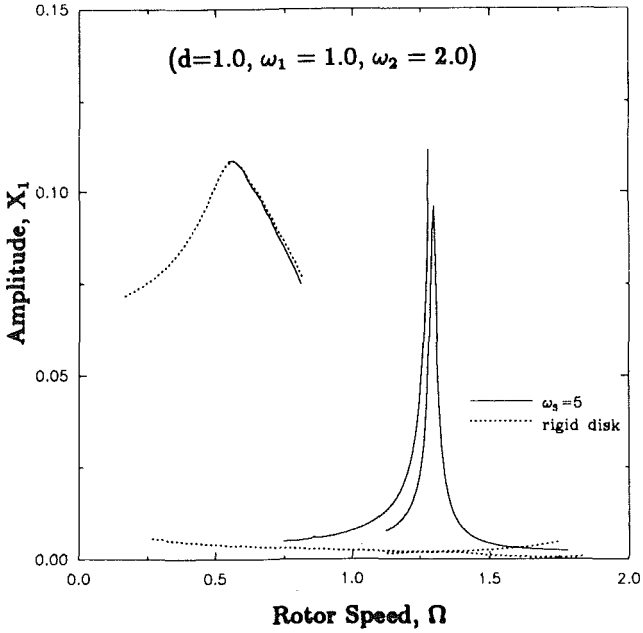

Fig. 3(*c*) 3Ω component of rotor response

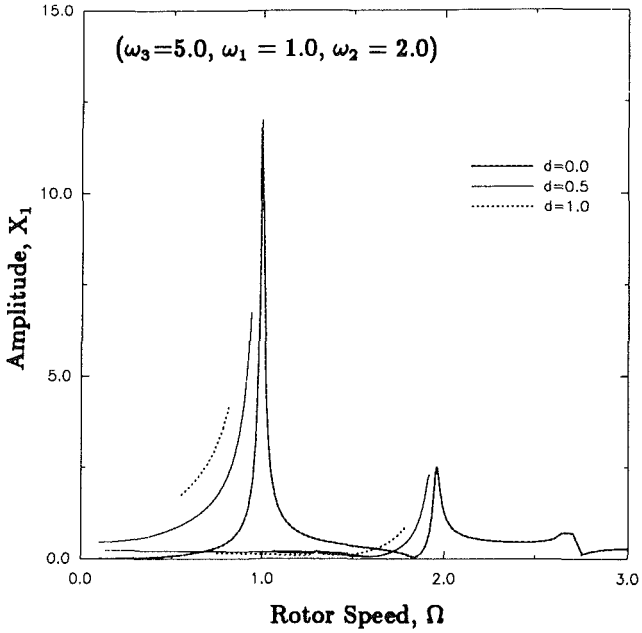

Fig. 4(*b*) 1Ω component of rotor response

plots, a zero component comprises the corresponding dual response curve for Figs. 3(*a*), 4(*a*), and 5(*a*).

This research effort is concerned with both coupling between disk and shaft motion and with the influence of bearing clearance. A relevant question in this regard concerns discerning between which motion is due primarily to disk flexibility, which is due primarily to nonlinear effects, and which is significantly influenced by both effects. Examination of Figs. 3(*a*, *b*), 4(*a*, *b*), and 5(*a*, *b*) indicates that the 1/2Ω and 1Ω components are primarily influenced by nonlinear effects. Figures 3(*a*, *b*) indicate that lateral disk flexibility has little effect on the 1/2Ω and Ω components of the rotor responses. Only at high rotor speeds are any significant variations observed between the curves for rigid and flexible disk responses. In addition, the 1/2Ω disk component (from Fig. 5*a*) is an order of magnitude less than the corresponding rotor component. However, significant variation in response amplitude is observed as the bearing clearance, d, is varied for Figs. 4(*a*, *b*) and 5(*a*, *b*). The case $d = 0.0$ represents the fully linear case, for which only 1Ω responses occur.

Figures 3(*c*), 4(*c*), and 5(*c*) are a bit more interesting. Examination of these figures indicates that the 3Ω component responses consist of two types. The first type of motion occurs for rotor speeds less than about 1.0 and is represented by the upper curves for this speed range in Figs. 3(*c*) and 4(*c*). These responses are primarily influenced by nonlinear effects, with disk flexibility having little impact. Indeed, little disk vibration occurs in this region, as seen from Fig. 5(*c*). The second type of motion is a combined motion of disk and rotor and is represented by the curves that peak sharply at $\Omega \approx 1.3$. This motion consists of severe disk vibration and relatively moderate amplitude rotor vibration. Note that such supersynchronous motion would not occur without the presence of the nonlinear bearing effect. Physical understanding of this behavior is quite

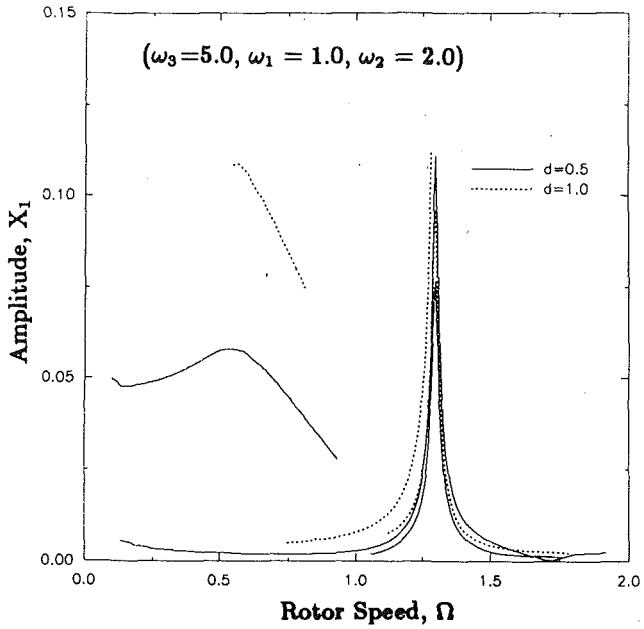

Fig. 4(*c*) 3Ω component of rotor response

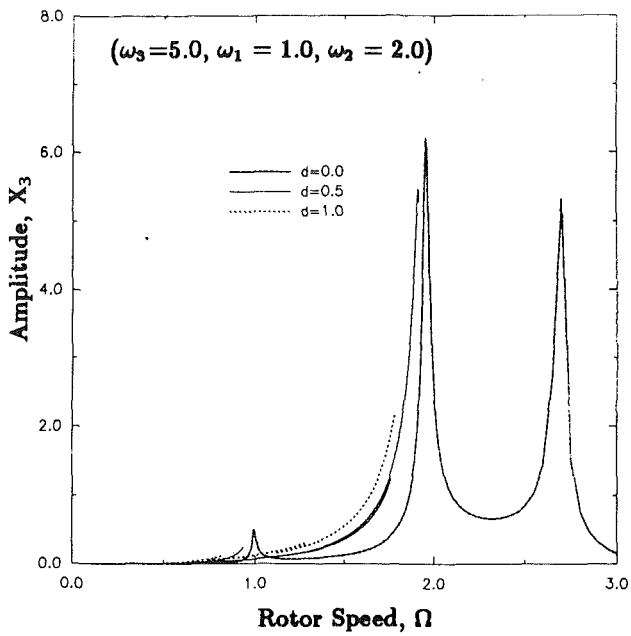

Fig. 5(*b*) 1Ω component of disk response

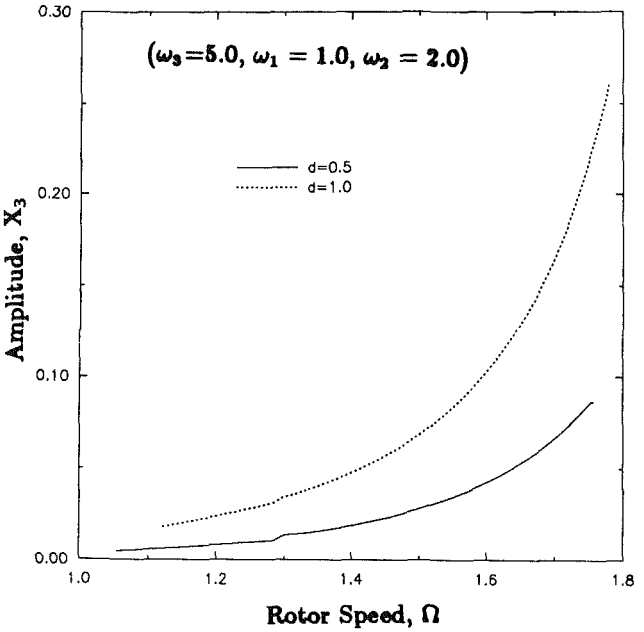

Fig. 5(*a*) 1/2Ω component of disk response

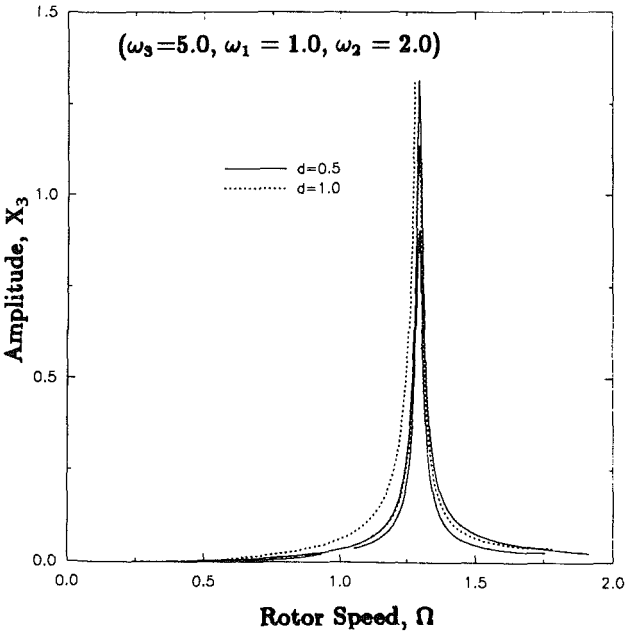

Fig. 5(*c*) 3Ω component of disk response

straightforward. The parametric configuration is such that the 3Ω responses serve to excite the disk resonance at a rotor speed of about 1.3, which in turn excites significant rotor vibration.

A first interpretation of the dynamic behavior of the simplified model might lead one to conclude that disk flexibility does not have a practical impact on rotordynamical responses. After all, the amplitude of the 3Ω component is, in general, an order of magnitude less than the 1/2Ω and Ω components. For certain rotor speeds, it is indeed true that the contribution to the total response of the supersynchronous components is completely overshadowed by the contributions of the synchronous and subsynchronous components. This type of behavior occurs for rotor speeds below 1.0. However, for other rotor speeds, the supersynchronous components can play a very important role. For example, interesting responses occur at $\Omega \approx 1.3$. The responses consist of two possible limit cycles. Time traces for the x_1 motion are given in Figs. 6(*a*) and 6(*b*). Both limit cycle responses are stable (as shown by numerical simulation) and are excited by different initial conditions. Figure 6(*a*) shows a high-amplitude limit cycle (for x_1) associated with a frequency of 1/2Ω. The disk interaction for this response is relatively small. A second limit cycle of lower amplitude is associated with the frequencies of Ω and 3Ω. This response shows quite a bit of disk/shaft interaction and is very dependent on the disk flexibility. The importance of disk flexibility in this particular response can be seen by comparing Figs. 6(*b*) and 6(*c*). Figure 6(*c*) represents the rigid disk rotor response corresponding to the flexible disk rotor response shown in Fig. 6(*b*). The response amplitude for the rigid disk model is approximately 50 percent of that of the flexible disk rotor model.

In addition to the periodic motion discussed above, aperiodic motion has been observed by other investigators in the field

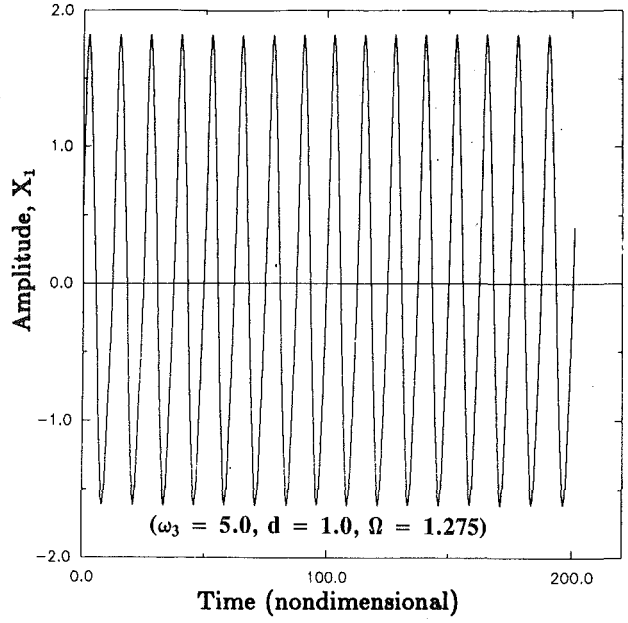

Fig. 6(*a*) Rotor limit cycle responses (predominant frequency is 1/2Ω)

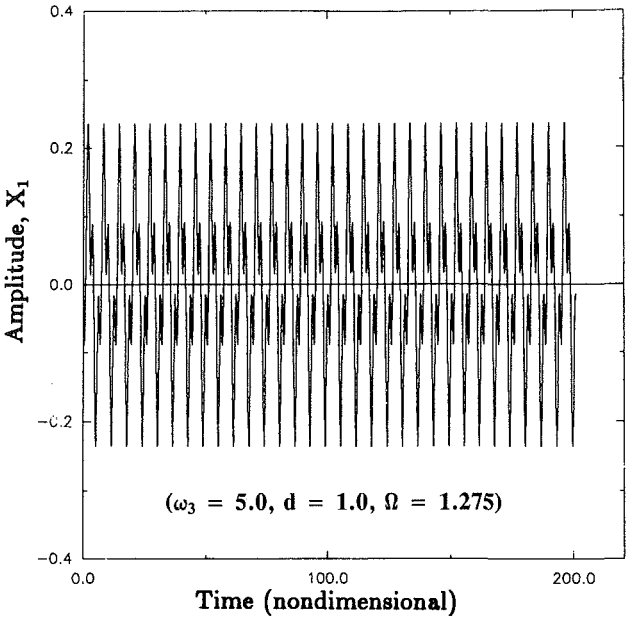

Fig. 6(*b*) Rotor limit cycle responses (predominant frequencies are 1Ω and 3Ω)

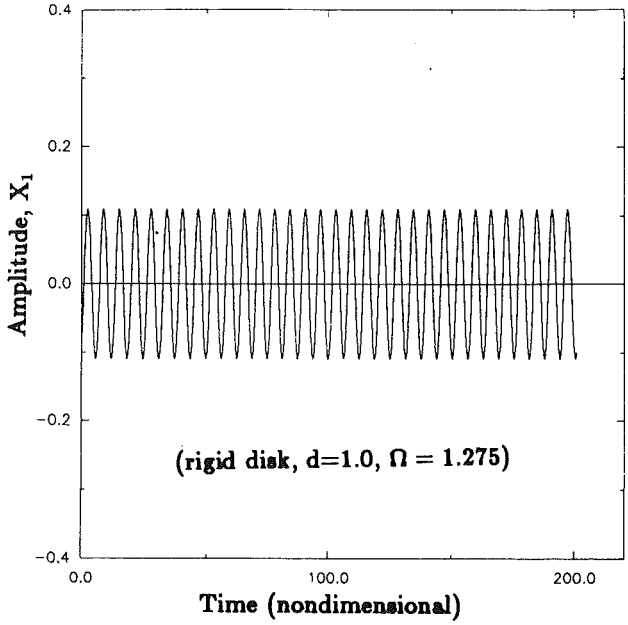

Fig. 6(*c*) Rotor limit cycle responses (predominant frequency is 1Ω)

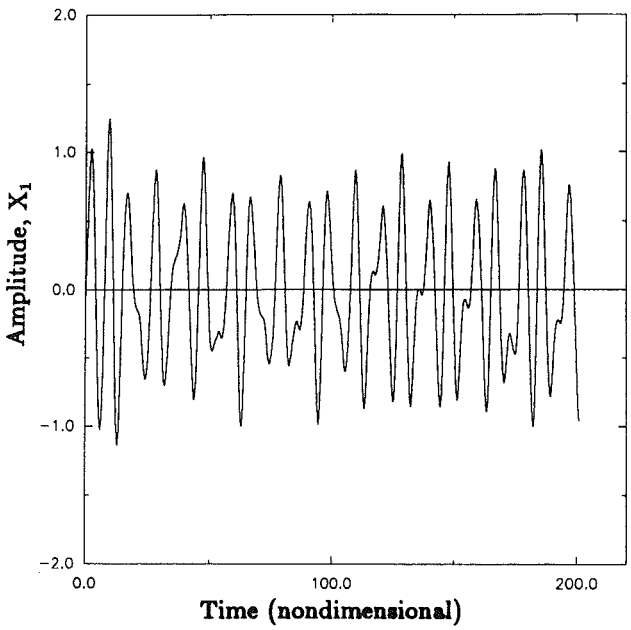

Fig. 7(*a*) Aperiodic rotor response ($d = 0.5$, $\omega_3 = 5.0$, $\Omega = 0.9$)

of nonlinear rotordynamics, most particularly by Kim and Noah (1990). The harmonic balance analyses are based on the assumption that the frequencies of the steady-state responses are integer multiples of the rotor speed. In general, this assumption appears to be quite accurate, with close agreement between the predicted behavior and numerical simulation results. However, it is well known that nonlinear dynamic systems may exhibit multiple responses for identical parametric configurations (as discussed above for the dual-valued responses). Which response actually occurs depends on the initial conditions of the system. The rotor model used in this study exhibits aperiodic behavior in addition to the periodic responses discussed earlier. Figure 7(*a*) show a typical aperiodic response associated with the x_1 motion and Fig. 7(*b*) displays the frequency content for this behavior. The frequency content has a strong component at 1Ω, but it also is a near continuum for frequencies between 0 and about 2.0.

Conclusion

This study has investigated the influence of bearing clearance on coupled shafe/disk lateral vibration for a simplified rotor model. Of primary concern in this study were responses that have frequencies that are integer multiples or divisors of the rotor speed. Synchronous responses, subsynchronous responses of 1/2Ω, and supersynchronous responses of 3Ω and 5Ω were all observed. In addition, some responses were observed in numerical simulation that are aperiodic and appear to verge on chaotic behavior.

This study has served to demonstrate that disk flexibility can contribute significantly to rotordynamic vibration for systems in which there is clearance in the rotor supports. Of particular importance is the demonstrated possibility of increased bearing loads due to flexible disk/shaft lateral interaction.

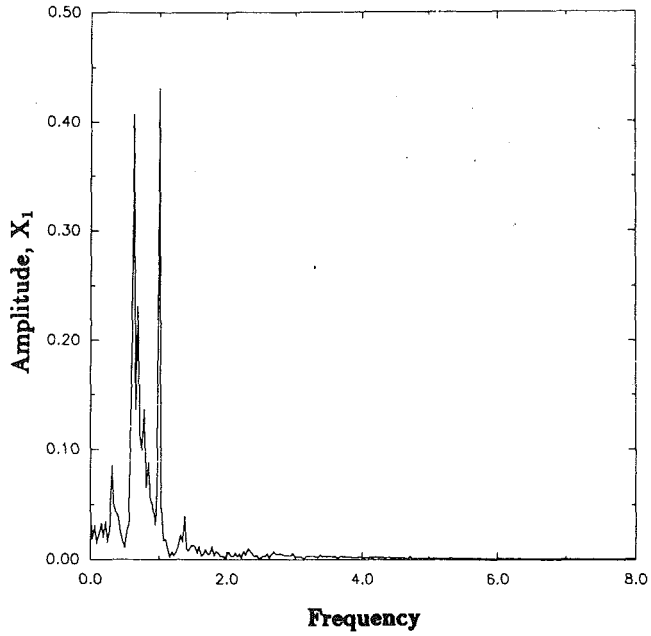

Fig. 7(*b*) Frequency content of aperiodic rotor response ($d = 0.5$, $\omega_3 = 5.0$, $\Omega = 0.9$)

The following results were observed:

1 It was demonstrated that bearing clearance effects can produce superharmonic vibration that may serve to excite high-amplitude disk vibration. Such vibration could lead to significantly increased bearing loads and catastrophic failure of blades and disks.

2 Multivalued responses were observed. Thus, several types of responses may be possible for identical parametric configurations.

3 Responses with frequencies of $1/2\Omega$ and Ω were observed for both the rigid disk rotor model and the flexible disk rotor model for the complete rotor speed range.

4 Responses with frequencies of 3Ω were observed for the flexible disk rotor model for the complete rotor speed range. Significant 3Ω responses were observed for the rigid disk rotor model only for rotor speeds less than about 1.0.

Acknowledgments

This material is based upon work supported by the National Science Foundation under Grant No. MSS-9110051. The government has certain rights in this material.

References

Begg, I. C., 1974, "Friction Induced Rotor Whirl—A Study in Stability," ASME *Journal of Engineering for Industry*, Vol. 96, pp. 450–454.

Black, H. F., 1968, "Forced Subrotative Speed Dynamic Action of Rotating Machines," *Journal of Mechanical Engineering Science*, Vol. 10, No. 4, pp. 1–12.

Chivens, D. R., and Nelson, H. D., 1975, "The Natural Frequencies and Critical Speed of a Rotating, Flexible Shaft-Disk System," ASME *Journal of Engineering for Industry*, Vol. 97, 1989, pp. 881–886.

Davis, R. R., 1989, "Practical Nonlinear Simulation of Rotating Machinery Dynamics With Application to Turbine Blade Rubbing," Ph.D. Dissertation, Department of Mechanical Engineering, University of California, Davis, June.

Flowers, G. T., and Ryan, S. G., 1993, "Development of a Set of Equations for Incorporating Disk Flexibility Effects in Rotordynamic Analyses," ASME JOURNAL OF ENGINEERING FOR GAS TURBINES AND POWER, Vol. 115, this issue, pp. 227–233.

Kim, B. Y., and Noah, S. T., 1990, "Stability and Bifurcation Analysis for a Nonlinear MDOF Rotor System," presented at Third Conference on Nonlinear Vibrations, Stability, and Dynamics of Structures and Mechanisms, Virginia Polytechnic Institute and State University, June 25–27.

Klompas, N., 1983, "Unbalance Response Analysis of a Complete Turbomachine," ASME JOURNAL OF ENGINEERING FOR POWER, Vol. 105, pp. 184–191.

Lamb, H., and Southwell, R. V., 1921, "The Vibrations of a Spinning Disk," *Proceedings of the Royal Society of London*, Series A, Vol. 99, pp. 272–280.

Loewy, R. G., and Piarulli, V. J., 1969, *Dynamics of Rotating Shafts*, The Shock and Vibration Information Center, United States Department of Defense, pp. 31–39.

Muszynska, A., 1984, "Synchronous and Self-Excited Vibrations Caused by Full Annular Rub," presented at Eighth Machinery Dynamics Seminar, Halifax, Nova Scotia, Canada, Oct. 1-2.

Muszynska, A., 1986, "Whirl and Whip—Rotor/Bearing Stability Problems," *Journal of Sound and Vibration*, Vol. 110, No. 3, pp. 443–462.

Padovan, J., and Choy, F. K., 1987, "Nonlinear Dynamics of Rotor/Blade/Casing Rub Interactions," ASME *Journal of Turbomachinery*, Vol. 109, pp. 527–534.

Vance, J. C., 1988, *Rotordynamics of Turbomachinery*, Wiley, New York, pp. 137–170.

A. Guinzburg

C. E. Brennen

A. J. Acosta

T. K. Caughey

California Institute of Technology,
Division of Engineering and Applied Science,
Pasadena, CA 91125

The Effect of Inlet Swirl on the Rotordynamic Shroud Forces in a Centrifugal Pump

The role played by fluid forces in determining the rotordynamic stability of a centrifugal pump is gaining increasing attention. The present research investigates the contributions to the rotordynamic forces from the discharge-to-suction leakage flows between the front shroud of the rotating impeller and the stationary pump casing. In particular, the dependency of the rotordynamic characteristics of leakage flows on the swirl at the inlet to the leakage path was examined. An inlet guide vane was designed for the experiment so that swirl could be introduced at the leakage flow inlet. The data demonstrate substantial rotordynamic effects and a destabilizing tangential force for small positive whirl ratios; this force decreased with increasing flow rate. The effect of swirl on the rotordynamic forces was found to be destabilizing.

1 Introduction

In turbomachinery, the trend toward higher speeds and higher power densities has led to an increase in the number and variety of fluid–structure interaction problems in pumps, compressors, turbines, and other machines. This occurs because the typical fluid forces scale like the square of the speed and thus become increasingly important relative to the structural strength. This becomes particularly acute in rocket engine turbopumps where demands to minimize the turbopump mass may also lead to reductions in the structural strength. Consequently designers and manufacturers are concerned with the fluid-induced rotordynamic forces on impellers in turbomachines. Knowledge of the steady and unsteady forces and the associated rotordynamic coefficients is required to model the rotordynamics of high-speed turbomachines effectively.

2 Background

Rotordynamic forces imposed on a centrifugal pump by the fluid flow through it were first measured by Domm and Hergt (1970), Hergt and Krieger (1969–70), Chamieh et al. (1985), and Jery et al. (1985). In the Rotor Force Test Facility (RFTF) at Caltech (Jery et al., 1985; Adkins and Brennen, 1988; Franz et al., 1989) known whirl motions over a full range of frequencies (subsynchronous, supersynchronous as well as reverse whirl) are superimposed on the normal motion of an impeller.

The hydrodynamic force on a rotating shroud or impeller (see Fig. 1) that is whirling can be expressed in the stationary laboratory frame in linear form as:

$$\begin{bmatrix} F_x^*(t) \\ F_y^*(t) \end{bmatrix} = \begin{bmatrix} F_{ox}^* \\ F_{oy}^* \end{bmatrix} + [A^*] \begin{bmatrix} x^*(t) \\ y^*(t) \end{bmatrix} \quad (1)$$

The first term on the right-hand side represents the radial force in the absence of whirl motion, so that F_{ox}^*, F_{oy}^* are the steady, time-averaged forces in a stationary frame, which result from flow asymmetries in the volute or the inlet duct. These steady radial forces are discussed in detail elsewhere (Iverson et al., 1960; Domm and Hergt, 1970; Chamieh, 1983; Chamieh et al., 1985; Adkins, 1986). The matrix $[A^*]$ is the rotordynamic matrix that operates on the instantaneous displacement $[x^*]$ of the rotor center. Note that $[A^*]$ will in general be a function not only of the mean flow conditions and pump geometry but also of the frequency of whirl, Ω. Outside the linear range, it

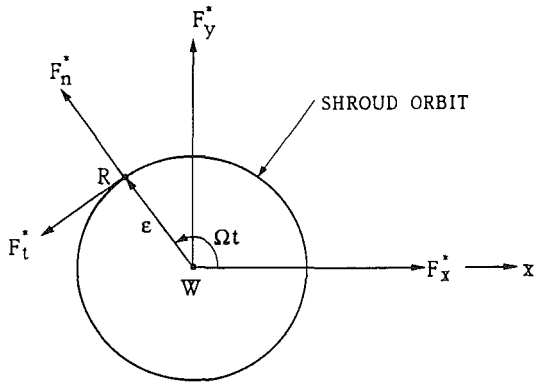

Fig. 1 Schematic of the fluid-induced radial forces acting on an impeller whirling in a circular orbit. F_x^* and F_y^* represent the instantaneous forces in the stationary laboratory frame. F_n^* and F_t^* are the forces normal and tangential to the whirl orbit where Ω is the whirl frequency.

Contributed by the International Gas Turbine Institute and presented at the 37th International Gas Turbine and Aeroengine Congress and Exposition, Cologne, Germany, June 1–4, 1992. Manuscript received by the International Gas Turbine Institute February 11, 1992. Paper No. 92-GT-126. Associate Technical Editor: L. S. Langston.

may also be a function of the amplitude of the whirl motion, ϵ. At small, linear amplitudes $[A^*]$ should be independent of ϵ and presented as a function of the whirl ratio Ω/ω, where ω is the impeller rotation frequency. In the case of a circular whirl orbit $x^* = \epsilon \cos \Omega t$, $y^* = \epsilon \sin \Omega t$. Then the forces normal and tangential to the imposed circular whirl orbit are related to the matrix elements as follows:

$$F_n^*(t) = \frac{1}{2}(A_{xx}^* + A_{yy}^*)\epsilon$$

$$F_t^*(t) = \frac{1}{2}(-A_{xy}^* + A_{yx}^*)\epsilon \tag{2}$$

The reader is referred to Jery et al. (1985) and Franz et al. (1989) for details. In the analysis that follows, the above equations will be expressed in nondimensional terms. If in addition, $[A]$ is to be rotationally invariant, then

$$A_{xx} = A_{yy} = F_n$$

$$A_{xy} = -A_{yx} = F_t \tag{3}$$

When it became apparent that leakage flows could contribute significantly to the rotordynamics of a pump, Childs (1989) adapted the bulk-flow model that was developed for the analysis of fluid-induced forces in seals to evaluate the rotordynamic forces, F_n and F_t, due to these leakage flows. The magnitude and overall form of the model predictions are consistent with the experimental data. In the context of the present paper, Childs' theory yielded some unusual results, including peaks in the rotordynamic forces at particular positive whirl ratios. This phenomenon was tentatively described as a "resonance" of the leakage flow. Childs suggested that this unexpected phenomenon develops at small positive whirl ratios when the inlet swirl velocity ratio exceeds about 0.5. It remains to be seen whether such "resonances" occur in practice. Childs (1986) points out that a typical swirl velocity ratio at inlet (pump discharge) would be about 0.5 and may not therefore be large enough for the resonance to be manifest. There have been reports that SSME impellers fitted with antiswirl vanes in the leakage flow annulus have had noticeably different rotordynamic characteristics (Childs et al., 1990a, 1990b). These results were partly responsible for motivating the present investigations of the dependency of the normal and tangential forces on the swirl at the inlet to the leakage path.

3 Leakage Flow Test Apparatus

A detailed description of the test facility can be found in many of the references (Chamieh 1983; Adkins, 1986; Jery, 1986; Franz et al., 1989), so only a brief description will be given here. The experiments were conducted in the Rotor Force Test Facility (RFTF), which was constructed to study fluid-induced forces on an impeller whirling around the machine axis of rotation. The experimental objective was to impose well-controlled rotations and whirl motions on a very stiff impeller/shaft system and to measure directly the resulting force on the impeller. This is accomplished by the eccentric drive mechanism, which superposes a circular orbit on the basic rotation. The shroud is mounted on a spindle attached to the rotating force balance (Jery et al., 1985; Franz et al., 1989), which measures the forces directly on the shroud. The rotating dynamometer permits measurements of the rotordynamic force matrix due to the shroud fluid forces. The experimental apparatus sketched in Fig. 2 was designed and constructed to simulate the leakage flow along the shroud from the impeller discharge to the impeller inlet (Zhuang, 1989; Guinzburg et al., 1990a; Guinzburg et al., 1992). The clearance between the rotating shroud and the stationary casing can be varied by both axial and radial adjustment of the stationary casing. For the present experiment, the initial geometric configuration consists of a straight annular gap inclined at an angle of 45 deg to the axis of rotation. The schematic in Fig. 3 shows the clearance in the centered position when the centers of the shroud and the casing both coincide. In order to model losses in the flow, an adjustable seal ring was used (refer to Fig. 2). The face seal clearance in this experiment permits the pressure drop to be adjusted separately from the flow.

Nomenclature

$[A^*]$ = rotordynamic matrix
$[A]$ = rotordynamic matrix, normalized by $\rho\pi\omega^2 R_2^3 L$
B = depth of inlet guide vane
C, c = rotordynamic damping coefficients, normalized by $\rho\pi\omega R_2^3 L$
$F^*(t)$ = hydrodynamic forces
$F(t)$ = hydrodynamic forces, normalized by $\rho\pi\omega^2 R_2^3 L\epsilon/R_2$
$F_x^*(t), F_y^*(t)$ = lateral forces on the rotating shroud in the stationary laboratory frame
$F_x(t), F_y(t)$ = lateral forces on the rotating shroud in the stationary laboratory frame, normalized by $\rho\pi\omega^2 R_2^3 L\epsilon/R_2$
F_{ox}^*, F_{oy}^* = steady hydrodynamic forces
F_{ox}, F_{oy} = steady hydrodynamic forces, normalized by $\rho\pi\omega^2 R_2^3 L$
$F_n^*(t), F_t^*(t)$ = unsteady hydrodynamic forces
$F_n(t), F_t(t)$ = unsteady hydrodynamic forces, normalized by $\rho\pi\omega^2 R_2^3 L\epsilon/R_2$
H = shroud clearance between rotor and casing
K, k = rotordynamic stiffness coefficients, normalized by $\rho\pi\omega^2 R_2^3 L$
L = axial length of the shroud
M, m = rotordynamic inertial coefficients, normalized by $\rho\pi R_2^3 L$
Q = volume flow rate
R = shroud radius
Re_φ = axial flow Reynolds number based on axial flow $= 2HU_s/\nu$
Re_ω = rotational Reynolds number based on tip speed $= \omega R_2^2/\nu$
t = time
u_s = mean inlet meridional velocity of the fluid
u_θ = mean inlet swirl velocity of the fluid
$x^*(t)$ = instantaneous displacement in the x direction
$y^*(t)$ = instantaneous displacement in the y direction
α = turning angle of the flow
Γ = swirl ratio of fluid tangential velocity to rotor tip velocity $= u_\theta/\omega R_2$
δ = offset or distance between the center of the whirl orbit and the center of the stationary casing
ϵ = eccentricity or radius of the whirl motion
ν = dynamic viscosity of the fluid
ρ = density of the fluid
ϕ = flow coefficient $= Q/2\pi R_2^2 H\omega$
ω = rotor frequency
Ω = whirl frequency

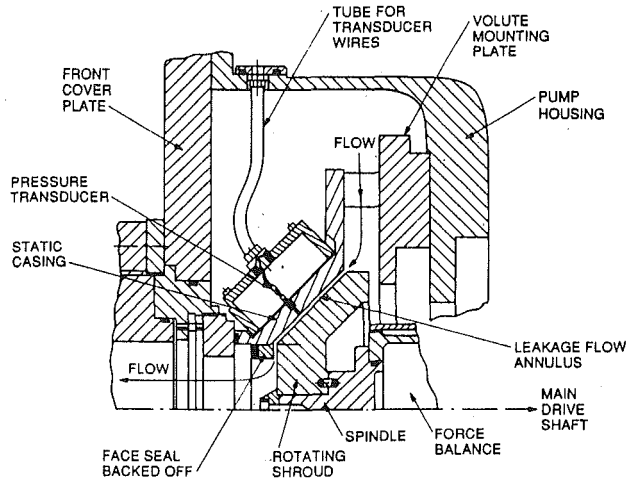

Fig. 2 Layout of the leakage flow test apparatus for installation in the RFTF (Zhuang, 1989)

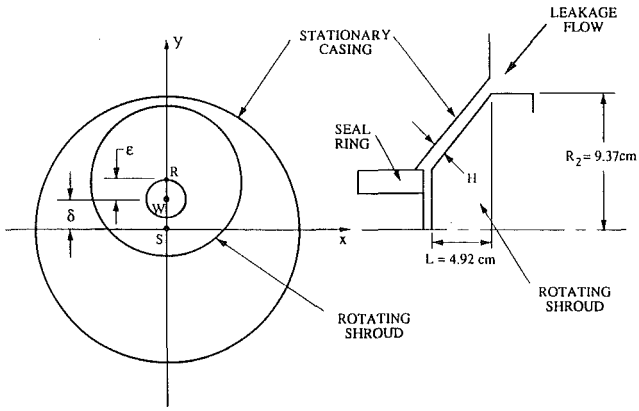

Fig. 3 Schematic of the whirling shroud where *S* is the center of the stationary casing, *R* is the center of the rotating shroud, *W* is the center of the whirl orbit along which *R* travels, *WR* = ϵ is the eccentricity, and *WS* = δ is the offset

The flow through the leakage path is generated by an auxiliary pump and the selection of flow rates through the leakage path was based on performance characteristics of a typical centrifugal pump. The shroud can be driven at speeds up to 3500 rpm and a circular whirl motion with a frequency up to 1800 rpm can be superimposed on the basic rotation. The eccentric drive mechanism permits testing with the amplitude of the whirl motion or eccentricity, ϵ, adjustable from 0.000 cm to 0.152 cm. Further details on the experimental equipment can be found in Guinzburg (1992). The results from these experiments will be presented nondimensionally by dividing the forces by $\rho\pi\omega^2 R_2^3 L\epsilon/R_2$.

As was mentioned previously, the inlet tangential velocity to the leakage path was shown by Childs (1989) to have an effect on the rotordynamic forces. Consequently, the effect of swirl was investigated by installing a device that was used to introduce prerotated fluid, in the direction of shaft rotation, at the shroud inlet. This was accomplished by constraining the flow in a logarithmic spiral channel. The inlet swirl vane was designed with sufficient solidity to create an isotropic inlet flow. The turning angle was chosen to be 2 deg and this allowed a range of swirl ratios, defined as the ratio of the inlet tangential velocity to the rotor velocity. Thus, as the leakage flow rate and therefore tangential velocity was increased, the swirl ratio could be increased for a fixed rotor speed. Various views of the device are shown Fig. 4.

Assuming conservation of circulation and using a continuity relation, the swirl ratio, Γ, of the inlet swirl velocity, u_θ, to

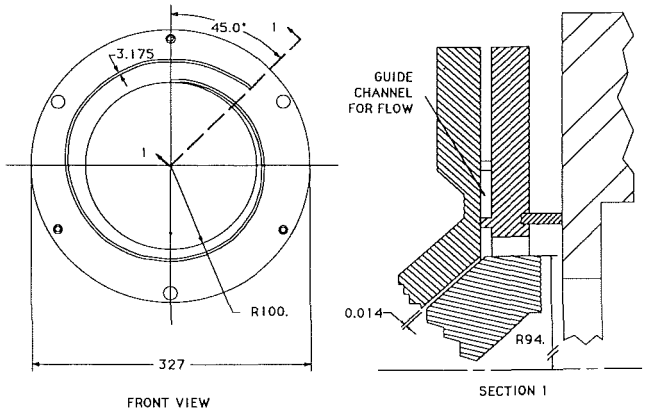

Fig. 4 Installation of the inlet swirl vane in the leakage flow test apparatus

the rotor speed, ωR_2, which resulted from the installed vane, was estimated to be given by

$$\Gamma = \frac{u_\theta}{\omega R_2} = \frac{Q}{B}\frac{1}{2\pi R_2^2 \omega}\frac{1}{\tan\alpha} \tag{5}$$

The above relation implies that the flow discharging from the inlet swirl vane is parallel with that vane. However, we need to note that this was not confirmed by measurement of the inlet swirl velocity. It is also important to observe that the inlet swirl could not be varied arbitrarily as it depends on the leakage flow rate. Recalling that the flow coefficient, ϕ, is given by

$$\phi = Q/2\pi R_2^2 H\omega \tag{6}$$

it follows that

$$\frac{\Gamma}{\phi} = \frac{H}{B\tan\alpha} \tag{7}$$

Therefore the only way to vary the inlet swirl independently of the flow coefficient would be to vary the geometry of the inlet swirl vane.

4 Experimental Results for Rotordynamic Forces

Typical experimental measurements of the dimensionless normal and tangential forces, F_n and F_t, will be presented in this section. The fluid medium in which the experiments were conducted was water. The rotordynamic results from the force balance measurements were obtained for different rotating speeds of 500, 1000, 2000 rpm, different rotating speeds of 500, 1000, 2000 rpm, different leakage flow rates (zero to 50 gpm), three different clearances, H, and two eccentricities, ϵ. The range of rotational Reynolds numbers was 462×10^3–1851×10^3 and the range of axial flow Reynolds numbers was 2136–8546. While the rotational Reynolds numbers for the experimental flows are clearly in the developed turbulent regime, it is possible that the axial flow Reynolds numbers were too slow for the kind of resonances predicted by Childs to be manifest. Data have already been presented for experiments performed without the inlet swirl vane so that the inlet swirl ratios are close to zero. They will be summarized here, but the reader is referred to Guinzburg et al. (1992) for greater detail. The effect of inlet swirl is the primary subject of this paper.

The components of the generalized hydrodynamic force matrix that result when the impeller whirls in an eccentric orbit of 0.118 cm, at 1000 rpm, and a clearance of 0.140 cm are shown in Fig. 5. Note that the general form and magnitude of the data is very similar to that obtained for impellers by Jery (1986) and Adkins (1986) and to that from Childs' model in the absence of "resonance." One of the most significant features of these results is the range of positive whirl ratios

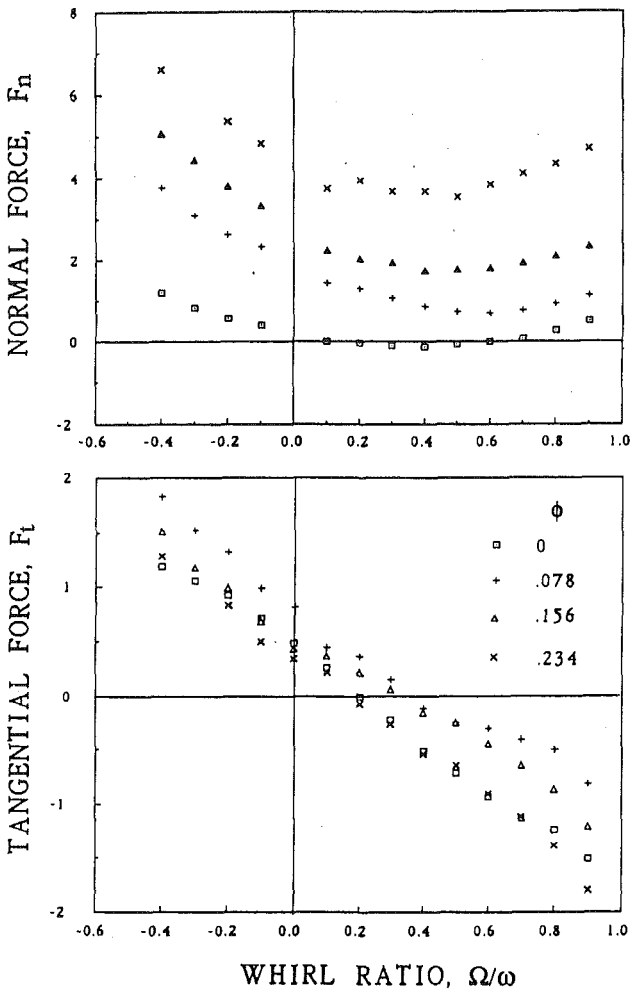

Fig. 5 Dimensionless normal and tangential forces for zero inlet swirl at 1000 rpm, for an eccentricity ϵ = 0.118 cm, a clearance H = 0.140 cm, offset δ = 0, and various flow rates as follows: 0 ℓ/s, 0.631 ℓ/s, 1.262 ℓ/s, 1.893 ℓ/s

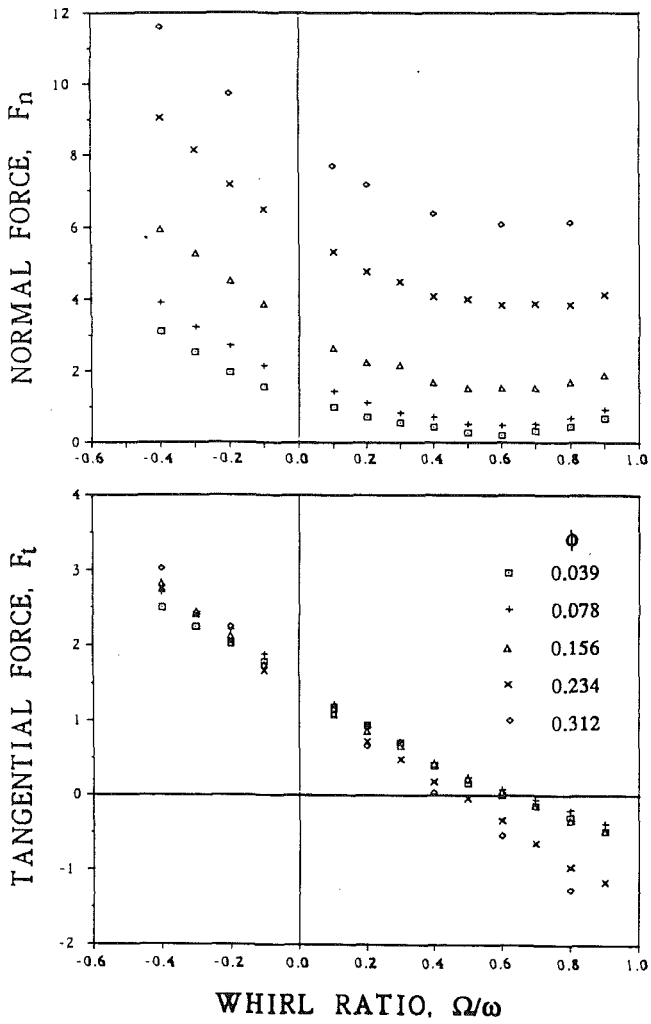

Fig. 6 Dimensionless normal and tangential forces with swirl at 1000 rpm, eccentricity ϵ = 0.118 cm, clearance H = 0.140 cm, offset δ = 0, and various flow rates as follows: 0.315 ℓ/s (Γ = 0.5), 0.631 ℓ/s (Γ = 1.0), 1.262 ℓ/s (Γ = 2.0), 1.892 ℓ/s (Γ = 3.0). The inlet swirl changes as the flow coefficient changes.

within which the tangential force is positive and therefore potentially destabilizing rotordynamically.

From other experiments, the data were determined to lie within the linear regime of small eccentricities (note that the assumption of linearity was implicit in Eq. (1)). The Bernoulli effect on the normal force increases with increasing flow at both positive and negative whirl ratios. It would also appear that the positive tangential forces at small positive whirl ratios are smallest at the highest flow rate and therefore increasing the flow is marginally stabilizing. It seems that all the forces are roughly inversely proportional to the clearance, H. For the same eccentricity and two different clearances, the smaller clearance generates larger perturbations in the flow, which accentuate the acceleration in the fluid and increase the pressure differences.

Figure 6 shows data taken for a wide range of swirl conditions. This set could be compared with the data obtained for Fig. 5, noting that increasing the flow coefficient in Fig. 6 also increases the swirl ratio. Figure 7 compares data without swirl at a flow coefficient of ϕ = 0.078 to data with swirl (Γ = 1.0). It can be seen that the effect of swirl is to increase the tangential force, thereby also increasing the range of whirl ratios for which there is a potentially destabilizing force. As the flow coefficient increases, the tangential force decreases. However, it should be noted that the flow coefficient is coupled to the swirl; therefore the swirl also increases. For the normal force, a decrease occurs with swirl for high positive whirl ratios. So the effects of flow and swirl seem to act in competition. Clearly it would be interesting to examine the case where flow is increasing and the swirl is fixed, which would require construction of additional inlet guides.

5 Rotordynamic Coefficients

Conventionally, rotordynamicists represent the force matrix by subdividing into components that depend on the orbit position (x, y), the orbit velocity $(\dot{x}, \dot{y})$ and the orbit acceleration $(\ddot{x}, \ddot{y})$. It is convenient for analytical purposes to evaluate these components by fitting quadratics to the experimental data. Athough the functional dependence of F_n on the whirl ratio is not necessarily quadratic nor is F_t linear, it is nevertheless of value to the rotordynamicists to fit the data of the figures from the previous section to the following expressions:

$$F_n = M\left(\frac{\Omega}{\omega}\right)^2 - c\left(\frac{\Omega}{\omega}\right) - K$$

$$F_t = +m\left(\frac{\Omega}{\omega}\right)^2 - C\left(\frac{\Omega}{\omega}\right) + k \tag{8}$$

where M, C, c, K, k are the dimensionless direct added mass (M), direct damping (C), cross-coupled damping (c), direct

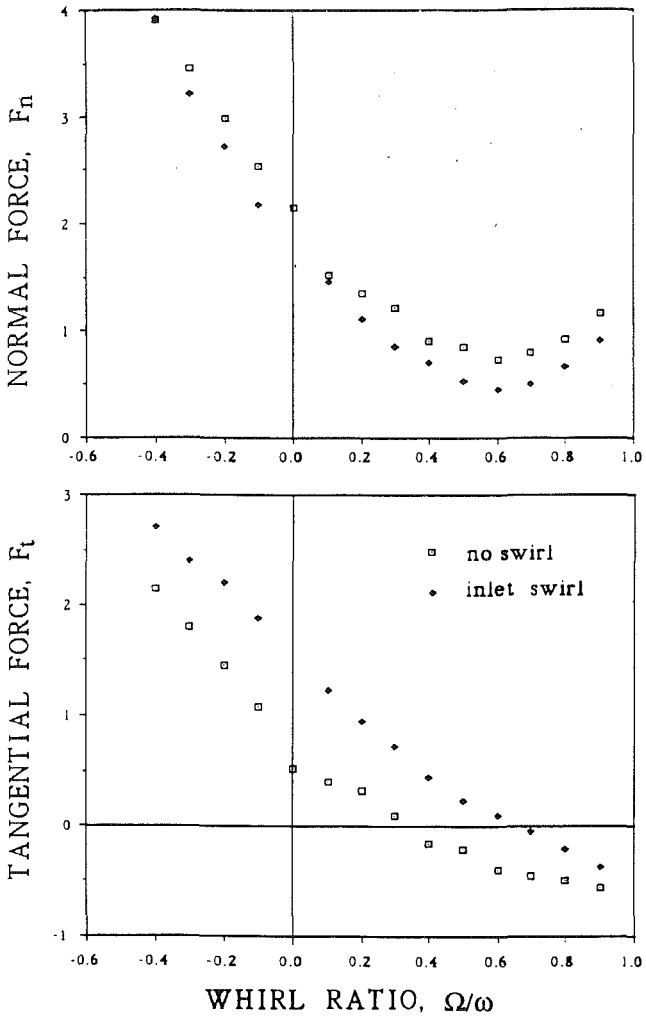

Fig. 7 Comparison of the dimensionless normal and tangential forces with and without inlet swirl at 1000 rpm, an eccentricity ϵ = 0.118 cm, clearance H = 0.140 cm, offset δ = 0, and flow rate of 0.631 ℓ/s. The inlet swirl is Γ = 1.0.

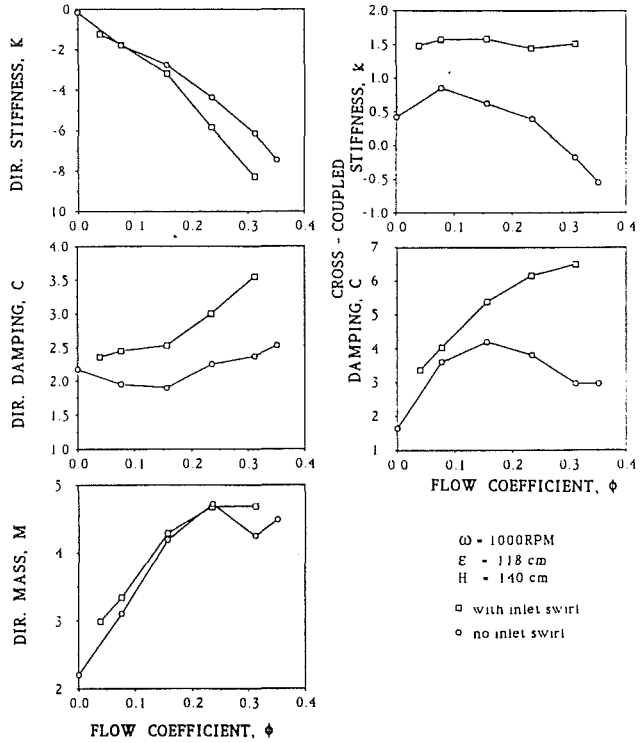

Fig. 8 Rotordynamic coefficients showing the effect of inlet swirl as a function of flow coefficient for 1000 rpm and an eccentricity of 0.118 cm

stiffness (K), and cross-coupled stiffness (k). The cross-coupled added mass (m) will be omitted for simplicity, since a linear fit for F_t is adequate. From a stability point of view, the tangential force is most interesting; a positive cross-coupled stiffness is destabilizing because it drives the forward orbital motion of the rotor. Positive direct damping and negative cross-coupled stiffness are stabilizing because they oppose orbital motion.

Various effects such as speed, eccentricity, shroud clearance, and seal clearance have already been discussed in a separate paper (Guinzburg et al., 1992). To summarize, a large negative stiffness results in a positive normal force, which would tend to increase the radius of the orbital motion; increasing the leakage flow increases this force. On the other hand, a positive cross-coupled stiffness is destabilizing because it drives the forward orbital motion of the rotor so as to encourage whirl. Increased leakage flow is stabilizing in that the tangential force decreases with leakage flow. Direct damping decreases slightly with flow and would therefore be less stabilizing since the tangential force increases. Below a flow coefficient of 0.7, direct damping is negative, so it would seem to encourage whirl. At higher flow rates, direct damping begins to increase, which would decrease the tangential force. However, these flow rates are not particularly meaningful as far as leakage flow rates in real pumps are concerned. The cross-coupled damping decreases slightly and the added mass term increases with flow, thus contributing to a larger normal force. In other words, inertial motion would discourage orbital motion of the impeller but drive the impeller in the direction for displacement. It is interesting to note that at higher flow rates, the trend of the added mass also changes.

The results were obtained for a range of shaft speeds from 500 rpm to 2000 rpm and shown to be independent of speed. Also, the effect of eccentricity has little effect on the normalized rotordynamic coefficients. The effect of the clearance between the rotating shroud and the stationary casing on the rotordynamic coefficients for three clearances was also explored and the normalized coefficients were shown to be roughly inversely proportional. Rotordynamically speaking, a smaller force is generated with a larger clearance. The effect of increasing the seal clearance indicated that wear of the seal is rotordynamically destabilizing.

6 Inlet Swirl Effects

The effects of inlet swirl velocity are presented in Fig. 8. Neither the direct stiffness nor the direct damping change substantially with the addition of swirl. However, the cross-coupled damping and hence the magnitude of the normal force increase with the addition of swirl. The cross-coupled stiffness and therefore the tangential force also increase. Thus, reducing the swirl to the flow would be stabilizing.

The data obtained in the present study show that the effect of inlet swirl is to increase the tangential force, thereby also increasing the range of whirl ratios for which there is a potentially destabilizing force. However, inlet swirl seems to decrease the normal force at high positive whirl ratios. The effects of swirl are in contrast to the effects of increasing the leakage flow, which cause a decrease in the normal force and an increase in the tangential force. Clearly it would be interesting to examine the case where flow is increasing and the swirl is fixed. This would require construction of additional inlet swirl vanes.

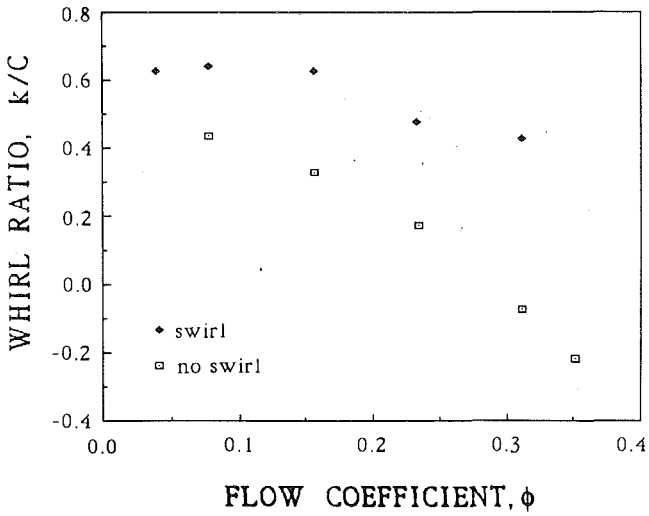

Fig. 9 Whirl ratio with and without the inlet swirl vane for eccentricity, ϵ = 0.118 cm, speed 1000 rpm, clearance, H = 0.140 cm, and offset, δ = 0, as a function of flow coefficient

The test results of Childs et al. (1990a, 1990b) also demonstrated the favorable influence that a swirl brake has in reducing the seal destabilizing forces. Benckert and Wachter (1980) originally showed that a swirl brake, which reduces the inlet tangential velocity, would also reduce the cross-coupled stiffness. In earlier experiments on smooth seals by Childs et al. (1988), the direct damping was shown to be relatively insensitive to changes in inlet swirl, while the cross-coupled stiffness was shown to increase with swirl. The only result that is different is for the direct stiffness of smooth seals, which shows a slight increase with swirl.

7 Rotordynamic Stability

The cross-coupled coefficient, k, and the direct damping coefficient, C, are important considerations with regard to rotordynamic stability; k and C oppose each other in trying to destabilize/stabilize the rotor. A convenient measure of the stability is the ratio of cross-coupled stiffness to direct damping k/C, which would estimate the whirl ratio at which the force would no longer be destabilizing. For circular synchronous orbits, it provides a ratio between the destabilizing force due to k and the stabilizing force due to C. Thus, reducing the ratio of k/C improves the stability of the rotor system.

Figure 9 shows the effect of swirl on the whirl ratio. The tangential velocity of the bulk flow will clearly decrease as the flow increases. It can be seen that as the flow increases, the whirl ratio decreases. This trend agrees with Childs et al. (1988) wherein the whirl frequency ratio decreases as the swirl decreases. While the present experiment involves a different geometry from the bearing model, the whirl frequency ratio k/C is of the same order of magnitude as the heuristic proposal that Crandall (1982) applied to the Sommerfeld bearing model.

8 Conclusions

A review of the existing experimental and analytical results shows that the discharge-to-suction leakage flow in a centrifugal pump can contribute substantially to the fluid-induced rotordynamic forces for that turbomachine. This motivated the current experimental study of leakage flows between the shroud and the stationary casing of a centrifugal pump and their rotordynamic effects. The focus was to investigate the dependency of the normal and tangential forces on the swirl at the inlet to the leakage path. Experimental results for simulated leakage flows of rather simple geometry have been presented for different whirl frequencies and flow rates. As with previous results for impellers, the forces scaled with the square of the rotor speed. The functional dependence on whirl frequency to rotating frequency ratio (termed the whirl ratio) is very similar to that measured in experiments and to that predicted in the theoretical work of Childs.

The effect of swirl is to increase the tangential force, thereby also increasing the range of whirl ratios for which there is a potentially destabilizing force. Thus reducing the swirl to the flow would be stabilizing. As for the normal force, swirl seems to decrease the force at higher positive whirl ratios. The effects of swirl are in contrast to the effects of increasing the leakage flow, which cause a decrease in the normal force and an increase in the tangential force. Clearly it would be interesting to examine the case where flow is increased while the swirl remains fixed. This would, however, require the construction of additional inlet guides. Finally, experiments that included the addition of a wide range of prescribed inlet swirl ratios showed none of the "resonances" predicted by Childs.

Acknowledgments

The assistance provided by F. Zhuang, A. Bhattacharyya, F. Rahman, and Sandor Nagy with the experimental program is greatly appreciated. We would also like to thank NASA George Marshall Space Flight Center for support under Grant No. NAG8-118.

References

Adkins, D. E., 1986, "Analyses of Hydrodynamic Forces on Centrifugal Pump Impellers," Ph.D. Thesis, California Institute of Technology, Pasadena, CA.

Adkins, D. R., and Brennen, C. E., 1988, "Analyses of Hydrodynamic Radial Forces on Centrifugal Pump Impellers," ASME *Journal of Fluids Engineering*, Vol. 110, pp. 20–28.

Benckert, H., and Wachter, J., 1980, "Flow Induced Spring Coefficients of Labyrinth Seals for Application in Rotor Dynamics," *Workshop on Rotordynamic Instability Problems in High Performance Turbomachinery*, pp. 189–212.

Bolleter, U., Wyss, A., Welte, I., and Stürchler, R., 1987, "Measurement of Hydrodynamic Interaction Matrices of Boiler Feed Pump Impellers," ASME *Journal of Vibration, Acoustics, Stress, and Reliability in Design*, Vol. 109, pp. 144–151.

Bolleter, U., Leibundgut, E., and Sturchler, R., 1989, "Hydraulic Interaction and Excitation Forces of High Head Pump Impeller," *Pumping Machinery—1989*, Vol. 81, 3rd Joint ASCE/ASME Mechanics Conference, UCSD, July 9–12, 1989, pp. 187–193.

Chamieh, D. S., 1983, "Forces on a Whirling Centrifugal Pump-Impeller," Ph.D. Thesis, Division of Engineering and Applied Science, California Institute of Technology, Pasadena, CA.

Chamieh, D. S., Acosta, A. J., Brennen, C. E., and Caughey, T. K., 1985, "Experimental Measurements of Hydrodynamic Radial Forces and Stiffness Matrices for a Centrifugal Pump-Impeller," ASME *Journal of Fluids Engineering*, Vol. 107, pp. 307–315.

Childs, D. W., 1986, "Force and Moment Rotordynamic Coefficients for Pump-Impeller Shroud Surfaces," *Proceedings of Advanced Earth-to-Orbit Propulsion Technology Conference*, Huntsville, AL, May, NASA Conf. Publ. 2436, pp. 296–326.

Childs, D. W., Elrod, D., and Hale, K., 1988, "Annular Honeycomb Seals: Test Results for Leakage and Rotordynamic Coefficients: Comparisons to Labyrinth and Smooth Configurations," *3rd Conference on Advanced Earth-to-Orbit Propulsion Technology*, Huntsville, AL, May, pp. 79–94.

Childs, D. W., 1989, "Fluid Structure Interaction Forces at Pump-Impeller-Shroud Surfaces for Rotordynamic Calculations," ASME *Journal of Vibration, Acoustics, Stress, and Reliability in Design*, Vol. 111, pp. 216–225.

Childs, D. W., and Ramsey, C., 1990a, "Seal-Rotordynamic-Coefficient Test Results for a Model SSME ATD-HPFTP Turbine Interstage Seal With and Without Swirl Brake," ASME Paper No. 90-Trib-12.

Childs, D. W., Baskharone, E., and Ramsey, C., 1990b, "Test Results for Rotordynamic Coefficients of the SSME HPOTP Turbine Interstage Seal With Two Swirl Brakes," ASME Paper No. 90-Trib-45.

Crandall, S. H., 1982, "Heuristic Explanation of Journal Bearing Instability," *Rotordynamic Instability Problems of High Performance Turbomachinery*, NASA Conference Publication 2250, pp. 274–283.

Domm, U., and Hergt, P., 1970, "Radial Forces on Impeller of Volute Casing Pumps," *Flow Research on Blading*, L. S. Dzung, ed., Elsevier Publ. Co., Netherlands, pp. 305–321.

Franz, R., Acosta, A. J., Brennen, C. E., and Caughey, T. K., 1989, "The Rotordynamic Forces on a Centrifugal Pump Impeller in the Presence of Cavitation," *Proceedings of 3rd Joint ASCE/ASME Mechanics Conference*, Vol. 81, Pumping Machinery, UCSD, July, pp. 205–212.

Guinzburg, A., Brennen, C. E., Acosta, A. J., and Caughey, T. K., 1990a, "Rotordynamic Forces Generated by Discharge-to-Suction Leakage Flows in Centrifugal Pumps," NASA CP-3092.

Guinzburg, A., Brennen, C. E., Acosta, A. J., and Caughey, T. K., 1990b, "Measurements of the Rotordynamic Shroud Forces for Centrifugal Pumps," presented at the ASME Turbomachinery Forum, Toronto, Canada, June 1990.

Guinzburg, A., 1992, "Rotordynamic Forces Generated by Discharge-to-Suction Leakage Flows in Centrifugal Pumps," Ph.D. Thesis, Division of Engineering and Applied Science, California Institute of Technology, Pasadena, CA.

Guinzburg, A., Brennen, C. E., Acosta, A. J., and Caughey, T. K., 1992, "The Rotordynamic Characteristics of Leakage Flows in Centrifugal Pumps," to be presented at the 1992 NFDC.

Hawkins, L., and Childs, D. W., 1988, "Experimental Results for Labyrinth Gas Seals With Honeycomb Stators: Comparisons to Smooth-Stator Seals and Theoretical Predictions," *3rd Conference on Advanced Earth-to-Orbit Propulsion Technology*, Huntsville, AL, May, pp. 94–111.

Hergt, P., and Krieger, P., 1969–70, "Radial Forces in Centrifugal Pumps With Guide Vanes," *Proc. Inst. Mech. Eng.*, Vol. 184, Part 3N, pp. 101–107.

Iversen, H. W., Rolling, R. E., and Carlson, J. J., 1960, "Volute Pressure Distribution, Radial Force on the Impeller and Volute Mixing Losses of a Radial Flow Centrifugal Pump," ASME JOURNAL OF ENGINEERING FOR POWER, Vol. 82, pp. 136–44.

Jery, B., Acosta, A. J., Brennen, C. E., and Caughey, T. K., 1985, "Forces on Centrifugal Pump Impellers," presented at the Second International Pump Symposium, Houston, TX, April 29–May 2.

Jery, B., 1986, "Experimental Study of Unsteady Hydrodynamic Force Matrices on Whirling Centrifugal Pump Impellers," Ph.D Thesis, California Institute of Technology, Pasadena, CA.

Zhuang, F., 1989, "Experimental Investigation of the Hydrodynamic Forces on the Shroud of a Centrifugal Pump Impeller," Division of Engineering and Applied Science, California Institute of Technology, Pasadena, CA, Report No. E249.9.

Investigation of the Vibration of a Blade With Friction Damper by HBM

J. H. Wang
Professor.

W. K. Chen
Graduate Student.

Department of Power Mechanical Engineering, National Tsing Hua University, Hsinchu, Taiwan

The friction damper has been widely used to reduce the resonant vibration of blades. The most commonly used methods for studying the dynamic behavior of a blade with a friction damper are direct integration methods. Although the harmonic balance method (HBM) is a well-known method for studying nonlinear vibration problems, generally only a one-term approximation has been proposed to study the nonlinear vibration of a frictionally damped blade. In this work, a HMB procedure with a multiterm approximation is proposed. The results show that the steady-state response and other related behavior of a frictionally damped blade can be predicted accurately and quickly by an HBM with a multiterm approximation.

Introduction

The friction damper has been widely used to reduce the resonant vibration of blades. In the past, many works have been done to investigate the dynamic behavior of a blade with a friction damper either by the macroslip approach (Griffin, 1980; Srinivasan and Gutts, 1986; Wang and Yau, 1990) or by the microslip approach (Menq et al., 1986a, 1986b). Generally, the steady-state nonlinear forced vibration of a blade was investigated by direct time-step integration with iterative process. It is very time consuming because the decay of the transient vibration generally is very slow. Although the harmonic balance method (HBM) is a well-known method to study the nonlinear vibration problems, usually only the HBM with one-term harmonic was used to investigate the harmonic forced vibration of a blade with a friction damper (Menq and Griffin, 1985). This is due to the difficulty that the nonlinear friction force is dependent on the stepwise stick-slip motion, which is not known in advance. As a consequence, the number of simultaneous algebraic equations found from the HBM is less than the number of unknowns if the response is assumed to consist of many harmonic terms. The slowly varying parameter method has also been used to study the harmonic response of a blade with a friction damper (Sinha and Griffin, 1984). However, only one term of harmonic has been considered in that work. A modified HBM with a multiharmonic approximation has been proposed by Pierre et al. (1985) to investigate a dry friction damped system. The method is also known as incremental harmonic balance (IHM). However, the IHB method is no more efficient than direct numerical integration when the number of harmonics is increased. Besides the IHB, an alternating frequency/time (AFT) method (Cameron and Griffin, 1989) can also accommodate multiple harmonics for the study of a dry friction problem. However, the method has to switch the calculation alternately in frequency and time domains. Besides, the aliasing and leakage problems also must be handled carefully.

The traditional HBM due to its simplicity has been widely accepted in the past. However, as mentioned, it is difficult to apply the traditional HBM with multiple harmonics to investigate the vibration of a dry friction damped blade. In this work, a method was developed to overcome the difficulty when the HBM with many harmonic terms was used. Some extra constraint equations were found to supplement the algebraic equations found from the traditional harmonic balance method. The accuracy and the computational time from the multiterm HBM were compared with the results from the direct time integration.

Analysis

As mentioned, two different friction models, i.e., macroslip and microslip approaches, have been proposed in the past. Generally speaking, the microslip approach can provide more accurate results only when the normal preload of the damper is high, and at the expense of higher computational effort, as discussed by Menq et al. (1986a) and Wang and Shieh (1991). Therefore, the macroslip approach was adopted in this work.

A typical single blade with a massless, flexible, blade-to-ground friction damper is shown in Fig. 1. If the blade is discretized by the finite element method, then the equation of motion of the blade can be written as:

$$[M]\{\ddot{X}\} + [C]\{\dot{X}\} + [K]\{X\} = \{F\} + \{F_n\} \qquad (1)$$

where $\{X\}$ is the generalized displacement vector; $[M]$, $[C]$, and $[K]$ are the mass, damping, and stiffness matrices; $\{F\}$ and $\{F_n\}$ are the linear external force and the nonlinear friction force vectors. If only a one-mode approximation is used to investigate the response of the blade near a resonance frequency, then the blade of Fig. 1 can be approximated by a

Contributed by the International Gas Turbine Institute and presented at the 37th International Gas Turbine and Aeroengine Congress and Exposition, Cologne, Germany, June 1-4, 1992. Manuscript received by the International Gas Turbine Institute January 16, 1992. Paper No. 92-GT-8. Associate Technical Editor: L. S. Langston.

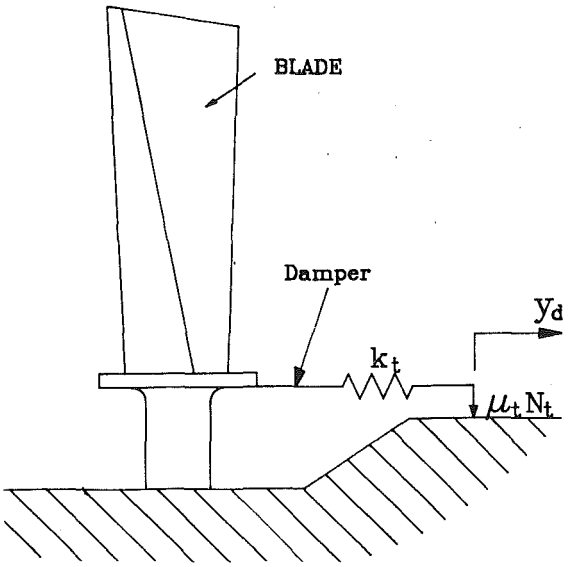

Fig. 1 Schematic of a single blade with a friction damper

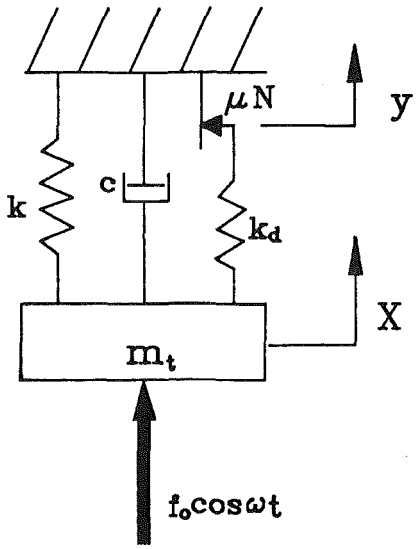

Fig. 2 Model of one-degree-of-freedom system

single degree of freedom system, as shown in Fig. 2. The equation of motion of the single-mode model can be written as

$$m\ddot{x} + c\dot{x} + kx = f - f_n \tag{2}$$

where f is the external excitation force and f_n is the friction force due to the friction damper. N, μ, and k_d in Fig. 2 represent the normal preload, the friction coefficient of the friction damper, and the stiffness of the damper in the direction of relative motion, respectively. According to the macroslip approach, the friction force, f_n, can be expressed as

$$f_n = \begin{cases} +k_d(x-y) & \text{when } k_d|x-y| \le \mu N \\ +\mu N \text{sign}(\dot{y}) & \text{when } k_d|x-y| \ge \mu N \end{cases} \tag{3}$$

where y is the displacement of the friction damper, as shown in Fig. 2. If the external excitation force is a simple harmonic force $f = f_0 \times \cos wt$, the steady-state solution of Eq. (2) can then be found by the harmonic balance method (HBM). In the following section, the one-term, two-term, and multi-term approximations will be discussed separately.

One-Term Approximation. According to the HBM the steady-state solution of Eq. (2) can be expressed as a Fourier expansion,

$$x = \sum_{i=1}^{\infty} [A_i \cos(iwt) + B_i \sin(iwt)] \tag{4}$$

In this section, only a one-term approximation will be used, i.e.,

$$\begin{aligned} x &= A_1 \cos wt + B_1 \sin wt \\ &= A_1 \cos\underline{\theta} + B_1 \sin\underline{\theta} \equiv R \cos\theta \end{aligned} \tag{5}$$

where $\underline{\theta} = wt$ and $\theta = wt - \phi$. The angle ϕ is the phase difference between the external excitation force and the response. According to Eq. (5) the angle θ should be equal to zero when the response is maximum, R. A typical relationship between the response and the friction force is shown in Fig. 3. The damper is in stick and slip conditions during the AB and BC sections, respectively. Then the velocity of the damper, $\dot{y}$ (indicated in Fig. 2), should be:

$$\dot{y} = \begin{cases} 0 & \text{when } 0 \le \theta \le \theta^* \\ \dot{x} & \text{when } \theta^* \le \theta \le \pi \end{cases} \tag{6}$$

From Eq. (6), one has

$$y = \begin{cases} c_1 & \text{when } 0 \le \theta \le \theta^* \\ x + c_2 & \text{when } \theta^* \le \theta \le \pi \end{cases} \tag{7}$$

The two constants c_1 and c_2 can be determined by the analysis in what follows. During the stick section, the friction force is equal to zero when x is equal to y. According to Fig. 3, $f_n = 0$ (the middle point of line AB), when x is equal to $R - \mu N/k_d$. In other words, one finds that $c_1 = R - \mu N/k_d$. During the slip section, the difference between x and y is held constant, i.e., c_2 which is the horizontal distance between point B and the middle point of line AB in Fig. 3. Then one can find that $c_2 = \mu N/k_d$. From Eq. (3), the friction force can then be expressed as:

$$\begin{aligned} f_n &= k_d(x-y) \\ &= k_d(x-R) + \mu N, \quad \text{when } 0 \le \theta \le \theta^* \end{aligned} \tag{8a}$$

$$\begin{aligned} f_n &= \mu N \text{sign}(\dot{y}) \\ &= \mu N \text{sign}(\dot{x}) = -\mu N, \quad \text{when } \theta^* \le \theta \le \pi \end{aligned} \tag{8b}$$

Equation (8a) should be equal to Eq. (8b) when $\theta = \theta^*$, then one has

$$\theta^* = \cos^{-1}[1 - 2\mu N/(k_d R)] \tag{9}$$

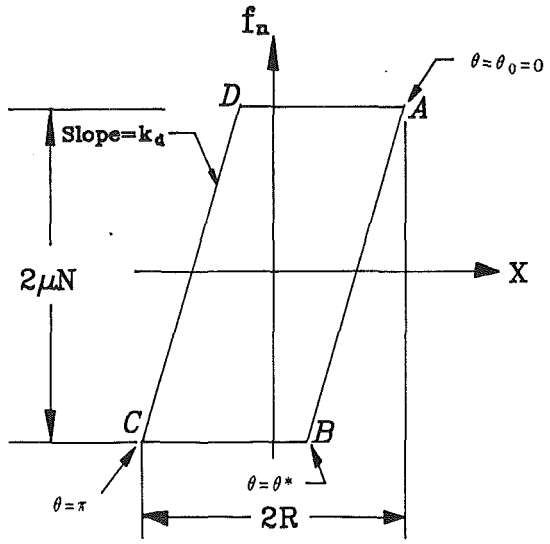

Fig. 3 Frictional damping loop, friction force versus the response (one-term approximation)

Because the response is assumed to be a simple harmonic form, the response cycle can be divided into two symmetric half cycles, i.e., the half cycle ABC is equal to the other half cycle CDA in Fig. 3. So, one can find that

$$f_n(\theta+\pi) = -f_n(\theta), \quad 0 \le \theta \le \pi \tag{10}$$

With Eqs. (8) and (10), the friction force can be expanded by Fourier series, and only the first harmonic term is kept,

$$f_n(\theta) = F_c \cos\theta + F_s \sin\theta \tag{11}$$

with

$$F_c = (-k_d R/\pi)[\theta^* - 0.5\sin(2\theta^*)]$$
$$F_s = (-4\mu N/\pi)[1 - \mu N/(k_d R)]$$

Substituting Eqs. (5) and (11) into Eq. (2) and separate the coefficients of $\cos\theta$ and $\sin\theta$, one has:

$$(k - mw^2)R + F_c = f_0 \cos\phi \tag{12a}$$
$$cwR - F_s = f_0 \sin\phi \tag{12b}$$

or

$$[(k - mw^2)R + F_c]^2 + [cwR - F_s]^2 = f_0^2 \tag{12c}$$
$$\phi = \sin^{-1}[(cwR - F_s)/f_0] \tag{12d}$$

Equations (12c) and (12d) are nonlinear equations with two unknowns R and ϕ, which can be solved by the traditional Newton-Raphson method. In practice, only the unknown R needs to be found by iteration; the angle ϕ can be obtained directly from Eq. (12d) providing the R is known. The response is then known from Eq. (5). The one term approximation is not the target of the present work; however, it may provide valuable information for multiterm approximation.

Two-Term Approximation. From the result of the direct time integration, it is known that the steady-state response of the system in Fig. 2 contains only the odd harmonic components of the external excitation force. Therefore, if a two-term approximation is assumed, according to Eq. (4), the response can be written as

$$\begin{aligned} x &= A_1 \cos wt + B_1 \sin wt + A_3 \cos 3wt + B_3 \sin 3wt \\ &= A_1 \cos\underline{\theta} + B_1 \sin\underline{\theta} + A_3 \cos 3\underline{\theta} + B_3 \sin 3\underline{\theta} \end{aligned} \tag{13}$$

Let the maximum value of x be denoted by A_m and the corresponding $\underline{\theta}$ be denoted by $\underline{\theta}_0$, as shown in Fig. 4. Point B in Fig. 4 is the slip impending point, and the value of $\underline{\theta}$ at this point is indicated by $\underline{\theta}^*$. In a manner similar to the one-term approximation, the friction force during the stick portion (line AB) can be expressed as

$$\begin{aligned} f_n &= k_d(x - A_m) + \mu N \\ &= k_d[A_1(\cos\underline{\theta} - \cos\underline{\theta}_0) + B_1(\sin\underline{\theta} - \sin\underline{\theta}_0) + A_3(\cos 3\underline{\theta} - \cos 3\underline{\theta}_0) \\ &\quad + B_3(\sin 3\underline{\theta} - \sin 3\underline{\theta}_0)] + \mu N, \quad \text{when } \underline{\theta}_0 \le \underline{\theta} \le \underline{\theta}^* \end{aligned} \tag{14}$$

During the slip portion, the friction force is

$$f_n = -\mu N, \quad \text{when } \underline{\theta}^* \le \underline{\theta} \le \pi + \underline{\theta}_0 \tag{15}$$

So far, $\underline{\theta}_0$ and $\underline{\theta}^*$ are unknown. This is the main difference between the one-term and the multiterm approximations. How to determine these unknowns will be discussed later. With Eqs. (14) and (15), the friction force can be expanded as a Fourier series; however, only the first two terms are kept,

$$f_n = F_{c1} \cos\underline{\theta} + F_{s1} \sin\underline{\theta} + F_{c3} \cos 3\underline{\theta} + F_{s3} \sin 3\underline{\theta} \tag{16}$$

The coefficients F_{c1}, F_{s1}, F_{c3}, and F_{s3} can be found in the appendix. By substituting Eqs. (13) and (16) into Eq. (2), and setting the coefficients of $\cos\underline{\theta}$, $\sin\underline{\theta}$, $\cos 3\underline{\theta}$, and $\sin 3\underline{\theta}$ equal to zero, one has

$$(k - mw^2)A_1 + wcB_1 - f_0 + F_{c1} = 0 \tag{17}$$
$$(k - 9mw^2)A_3 + 3wcB_3 + F_{c3} = 0 \tag{18}$$
$$(k - mw^2)B_1 - wcA_1 + F_{s1} = 0 \tag{19}$$

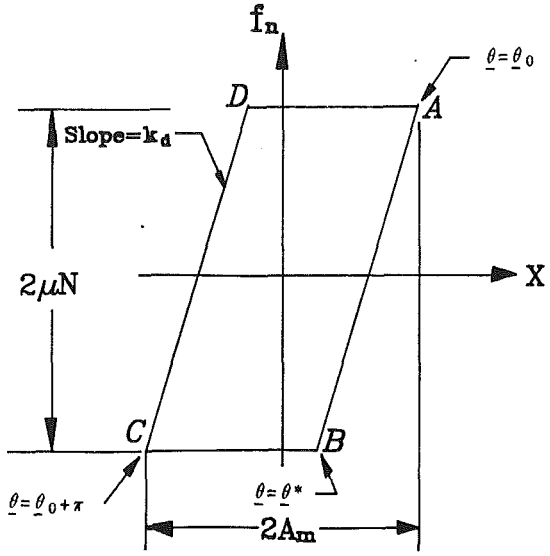

Fig. 4 Frictional damping loop, multiterm approximation

$$(k - 9mw^2)B_3 - 3wcA_3 + F_{s3} = 0 \tag{20}$$

Because the F_{c1}, F_{s1}, F_{c3}, and F_{s3} are functions of $\underline{\theta}_0$ and $\underline{\theta}^*$ which are unknown, the four equations Eqs. (17)–(20) have six unknowns, i.e., A_1, B_1, A_3, B_3, $\underline{\theta}_0$ and $\underline{\theta}^*$. So, one must find other equations to supplement Eqs. (17)–(20). The response x is maximum (with value A_m) when $\underline{\theta} = \underline{\theta}_0$. Thus, the following equations should be satisfied:

$$\left.\frac{\partial x}{\partial t}\right|_{\underline{\theta}=\underline{\theta}_0} = -A_1 \sin\underline{\theta}_0 + B_1 \cos\underline{\theta}_0 - 3A_3 \sin 3\underline{\theta}_0 + 3B_3 \cos 3\underline{\theta}_0 = 0 \tag{21}$$

$$\left.\frac{\partial^2 x}{\partial t^2}\right|_{\underline{\theta}=\underline{\theta}_0} = -A_1 \cos\underline{\theta}_0 - B_1 \sin\underline{\theta}_0 - 9A_3 \cos 3\underline{\theta}_0 - 9B_3 \sin 3\underline{\theta}_0 < 0 \tag{22}$$

It is also known that the friction forces in Eqs. (14) and (15) should be equal when $\underline{\theta} = \underline{\theta}^*$. Thus,

$$\begin{aligned} &k_d[A_1(\cos\underline{\theta}^* - \cos\underline{\theta}_0) + B_1(\sin\underline{\theta}^* - \sin\underline{\theta}_0) \\ &\quad + A_3(\cos 3\underline{\theta}^* - \cos 3\underline{\theta}_0) + B_3(\sin 3\underline{\theta}^* - \sin 3\underline{\theta}_0)] + \mu N = -\mu N \end{aligned} \tag{23}$$

or in a compact functional form,

$$G(\underline{\theta}^*, \underline{\theta}_0) = 0 \tag{24}$$

If $\underline{\theta}_0$ and $\underline{\theta}^*$ are known, then Eqs. (17)–(20) are linear equations with A_1, A_3, B_1, B_3 as unknowns, which can be solved easily. The values of $\underline{\theta}_0$ and $\underline{\theta}^*$ can be determined by Eqs. (21)–(23), which are nonlinear. In summary, Eqs. (17)–(23) can be used to determined the unknowns A_1, A_3, B_1, B_3, $\underline{\theta}_0$, $\underline{\theta}^*$. The procedure is summarized as follows:

1 Give proper initial guess values of $\underline{\theta}_0$ and $\underline{\theta}^*$ and then F_{c1}, F_{c3}, F_{s1}, and F_{s3} can be found (see appendix).

2 The unknowns A_1, A_3, B_1, B_3 can be determined from the linear equations Eqs. (17)–(20) by direct matrix inversion.

3 With A_1, A_3, B_1, and B_3, the condition of Eq. (22) is then checked:

(a) If Eq. (22) is satisfied, then go to step (4).

(b) If Eq. (22) is not satisfied, then the initial guess values of $\underline{\theta}_0$ and $\underline{\theta}^*$ are modified as: new $\underline{\theta}_0$ = old $\underline{\theta}_0 + \pi$, new $\underline{\theta}^*$ = old $\underline{\theta}^* + \pi$. After the modification, then go back to step (1).

4 With A_1, A_3, B_1, and B_3, Eqs. (21) and (23) are then used to find the exact values of $\underline{\theta}_0$ and $\underline{\theta}^*$ by the Newton–Raphson iteration method. The flow chart of the procedure is given in Fig. 5.

The modification in step (3) can be understood easily be-

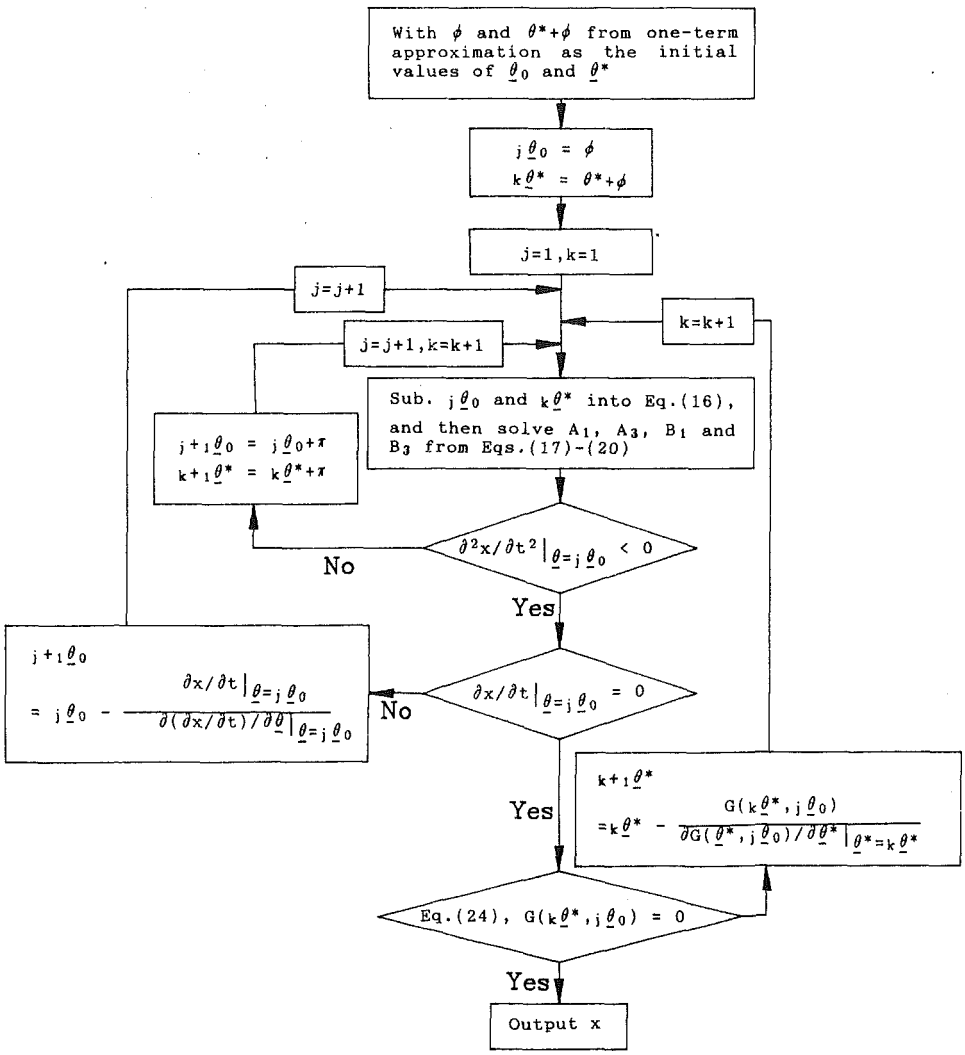

Fig. 5 Flow chart of the proposed iteration procedure

cause, according to Fig. 4, the response is symmetric, i.e., $x(\underline{\theta}) = -x(\underline{\theta}+\pi)$.

It is known that the most important step in using the Newton-Raphson iteration method is the guess of the initial values. How to guess proper initial values of $\underline{\theta}_0$ and $\underline{\theta}^*$ will be discussed in the next section.

The above derivation and solution procedure can easily be extended to the multiterm approximation. If an n-term approximation is used, then one can find $2n$ linear equations like Eqs. (17)–(20) and two nonlinear equations like Eqs. (21) and (23).

Results and Discussion

In this section, three main topics will be discussed, i.e., the accuracy of the HBM, the computation time, and the effect of the initial guess values. Before the discussion, the system parameters of Fig. 2 are given here: $m=1.24$, $k=17890$, $c=3$, and $k_d=3500$.

Accuracy of the HBM. As mentioned, generally only one-term HBM was used to investigate the vibration of a blade with a friction damper. In some cases, for instance, in fully stuck or fully slipping conditions, the one-term approximation is accurate enough to predict the response. However, the one-term approximation generally may cause significant error. Here, an example is given to show this situation. Figure 6 shows a response found by the direct time integration, one-term HBM, two-term HBM and three-term HBM, respectively. The vertical axis is the normalized response A/A_m, where A_m is the maximum amplitude found by the direct time integration. In this case the excitation frequency w is set to be 1/3 w_0, where w_0 is the natural frequency of the system of Fig. 2 without the friction damper. It is known that if the excitation frequency w and the amplitude of excitation force f_0 are determined, then

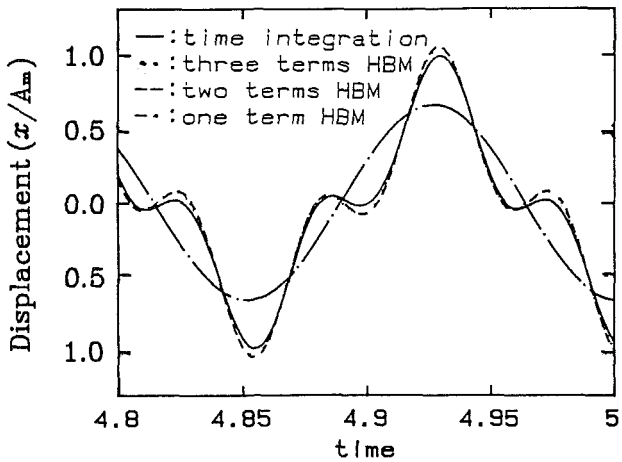

Fig. 6 Steady-state forced response, $w/w_0 = 0.334$, $\mu N/f_0 = 0.145$

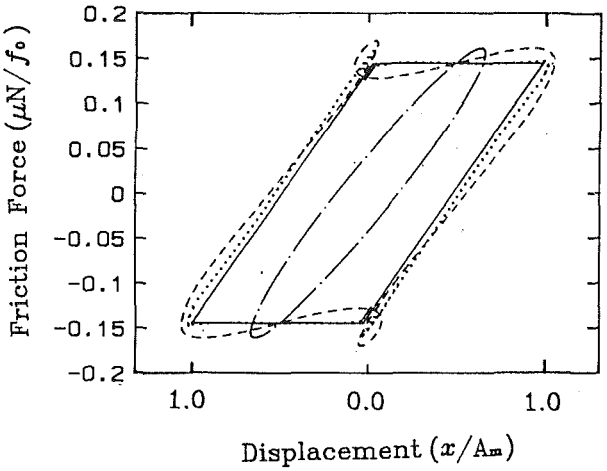

Fig. 7 Frictional damping loop; the legend is the same as Fig. 6

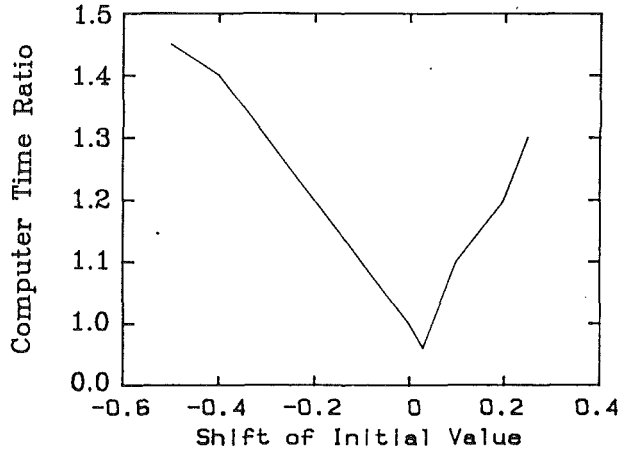

Fig. 8 Effect of initial guess values on computer time

an optimal normal load N, which results in minimum response, can be found. The normalized normal load $\mu N/f_0$ in Fig. 6 is set to the optimal value $\mu N/f_0 = 0.145$. One can find that the one-term approximation results in significant error. In this case, the three-term approximation can accurately predict the response, and its result is difficult to distinguish from the result of the direct integration in the figure. The corresponding frictional damping loop is shown in Fig. 7. One can find that the frictional damping cannot be simulated accurately by the one-term approximation. The above result indicates that only the multiterm HBM can accurately predict the response of a blade with a friction damper. The result also demonstrates that the multiterm HBM proposed in this work is feasible. Theoretically, the HBM with more terms will result in a more accurate solution. In practice, according to our experience, it needs no more than three terms. The question of the computational time will be discussed in the next section.

Computer Time. No matter how many terms, say n terms, are kept in the HBM, only two nonlinear equations (i.e., Eqs. (21) and (23)) and $2n$ simultaneous linear equations (i.e., Eqs. (17)–(20) are needed to find all the unknowns. As shown in Fig. 5, the two nonlinear equations are solved by the iteration method, and the $2n$ linear equations must be solved once for each iteration. In other words, if m iterations are needed until convergence is reached, then the $2n$ linear equations must be solved m times. Therefore, how to reduce the number of iteration is very important. It is known that the initial guess values are very important for the iteration process. An improper initial guess value may drastically increase the number of iterations or cause divergence. Thus, to discuss the computational time, the effect of the number of terms should be considered together with the effect of the initial guess values. First, the effect of the initial guess values will be discussed.

The nonlinearity of the vibratory blade comes only from that nonlinear friction force. It is known that the friction force can be expanded by Fourier series with the fundamental frequency equal to the external excitation frequency w. In other words, the vibration of the blade is mainly caused by a harmonic force with a frequency equal to w. Thus, the solution obtained from the one-term approximation should be a good initial guess value for the multiterm approximation. For the multiterm approximation, one should give the initial guess values of $\underline{\theta}_0$ and $\underline{\theta}^*$. In this work, it is suggested that the θ_0 and θ^* obtained from the one-term approximation can be used as the initial guess values of $\underline{\theta}_0$ and $\underline{\theta}^*$ for the multiterm approximation. According to Eq. (5), one has the relations: $\underline{\theta}_0 = \theta_0 + \phi$ and $\underline{\theta}^* = \theta^* + \phi$. As pointed out in the one-term approximation, θ_0 is zero, while θ^* and ϕ can be obtained from Eq. (9) and Eq. (12), respectively. To understand the effect of the initial guess values on the computer time, different guess values are assumed and the necessary computer time is recorded. The result is shown in Fig. 8. The horizontal axis "shift of initial value" means the amount the initial guess values of $\underline{\theta}_0$ and $\underline{\theta}^*$ are shifted from the suggested initial values, i.e., $\underline{\theta}_0 = \phi$ and $\underline{\theta}^* = \theta^* + \phi$. For instance, "$-0.2$" indicates that initial guess values are given as: $\underline{\theta}_0 = (1-0.2)\phi$, $\underline{\theta}^* = (1-0.2)(\theta^* + \phi)$. One can find that if the shift of the initial value is between -0.5 and 0.3, one can find a converged solution corresponding to the solution found from the direct integration. If the initial guess values are beyond this range, one may find another converged solution or the solution is diverged. Here "another converged solution" means a solution different from the solution found from the direct time integration. So far, it is not certain that this "another solution" exist in practice. The result of Fig. 8 indicates that the θ^* and ϕ found from one-term approximation are the proper initial guess values of $\underline{\theta}_0$ and $\underline{\theta}^*$ for the multiterm approximation.

If the initial guess values are selected properly, the ratios of the computer time are 1:2.4:5.5:61 for one-term, two-term, three-term approximations and the direct time integration, respectively. Note that the computer time for the two-term and three-term approximations includes the portion to find the proper initial guess values, i.e., θ^* and ϕ. As mentioned, the HBM requires no more than three terms in order to obtain an accurate result. That is to say the HBM needs a computer time about one order of magnitude smaller than that of the direct integration. The above result is concluded not only from the above example, but also from many other calculated examples.

The advantage of the proposed HBM is especially significant when the response must be recalculated many times, for instance, to find the optimal normal load or the frequency response curve. It is well known that there exists an optimal normal load N with which the blade will experience minimum forced vibration. The optimal normal load is an important design parameter of the friction damper. Generally, the optimal normal load cannot be found directly except when the response is a pure simple harmonic function. The optimal normal load generally is found by observing the response for many different normal load values. In other words, a curve indicating the responses versus the normal load N should be created, and the minimum response corresponds to the optimal normal load. For each value of N, a new calculation must be executed. It is very time consuming if the direct integration method is used. For the proposed method, the answer can be found very quickly, because the solution for normal load N can be used as a very good initial guess value for finding the solution at $N + \Delta N$; ΔN is a small increment. Because the initial guess values are very close to the exact values, the iteration converges very quickly. The frequency, response curve, i.e.,

the response versus the excitation frequency, can also be found quickly by the proposed method. The response at a certain excitation frequency w can be used as a very good initial guess value for finding the response at frequency $w+\Delta w$.

In summary, there are two important features of the proposed method: (1) There are only two nonlinear equations no matter how many terms are kept in the HBM; (2) a proper initial guess value for the iteration generally can be found easily. Due to these features, the proposed method is very efficient for the steady-state response and related analyses.

Conclusion

The dynamic behavior of a blade with a friction damper has been intensively investigated in the past. Although the harmonic balance method (HBM) is a well-known method, usually only the HBM with a one-term (or one harmonic component) approximation was used to investigate the harmonic forced vibration of a blade with a friction damper. Generally, the HBM with an n-term approximation will result in $2n$ simultaneous nonlinear algebraic equations in terms of $2n$ unknown Fourier coefficients for a system with one degree of freedom. However, this is not the case in the proposed method. The main step of the proposed procedure is to find the impending time points (i.e., $\underline{\theta}_0$ and $\underline{\theta}^*$) of stick and slip of the friction damper. Because the $\underline{\theta}_0$ and $\underline{\theta}^*$ are found from two nonlinear algebraic equations, the problem of the initial guess values of the $\underline{\theta}_0$ and $\underline{\theta}^*$ has also been discussed in this work. The results show that the HBM needs no more than three terms in order to obtain an accurate result. The main advantage of the HBM is the computational efficiency; it needs only about one-tenth of the computer time in comparison with the direct integration. Due to the drastic reduction of the computer time, it becomes possible to investigate many important characteristics of a frictionally damped blade in a very short time.

References

Cameron, T. M., and Griffin, J. H., 1989, "An Alternating Frequency/Time Domain Method for Calculating the Steady-State Response on Nonlinear Dynamic Systems," ASME *Journal of Applied Mechanics*, Vol. 56, pp. 149–154.

Griffin, J. H., 1980, "Friction Damping of Resonant Stress in Gas Turbine Engine Airfoil," ASME JOURNAL OF ENGINEERING FOR GAS TURBINES AND POWER, Vol. 102, pp. 329–333.

Menq, C. M., and Griffin, J. H., 1985, "A Comparison of Transient and Steady State Finite Element of Forced Response of a Frictionally Damped Beam," ASME *Journal of Vibration, Acoustics, Stress, and Reliability in Design*, Vol. 107, pp. 19–25.

Menq, C. M., Bielak, J., and Griffin, J. H., 1986a, "The Influence of Microslip on Vibration Response," *Journal of Sound and Vibration*, Vol. 107, pp. 279–293.

Menq, C. M., Griffin, J. H., and Bielak, J., 1986b, "The Forced Response of Shrouded Fan Stage," ASME *Journal of Vibration, Acoustics, Stress, and Reliability in Design*, Vol. 108, pp. 50–55.

Pierre, C., Feri, A. A., and Dowell, E. H., 1985, "Multi-harmonic Analysis of Dry Friction Damped Systems Using an Incremental Harmonic Balance Method," ASME *Journal of Applied Mechanics*, Vol. 52, pp. 958–964.

Sinha, A., and Griffin, J. H., 1984, "Effects of Static Friction on the Forced Response of Frictionally Damped Turbine Blades," ASME JOURNAL OF ENGINEERING FOR GAS TURBINES AND POWER, Vol. 106, pp. 65–69.

Srinivasan, A. V., and Gutts, D. G., 1986, "Dry Friction Damping Mechanisms in Engine Blades," ASME JOURNAL OF ENGINEERING FOR GAS TURBINES AND POWER, Vol. 105, pp. 525–530.

Wang, J. H., and Yau, H. L., 1990, "Design of Shroud Interface—Angle to Minimize the Forced Vibration of Blades," ASME Paper No. 90-GT-247.

Wang, J. H., and Shieh, W. L., 1991, "The Influence of a Variable Friction Coefficient on the Dynamic Behavior of a Blade With a Friction Damper," *Journal of Sound and Vibration*, Vol. 149, pp. 137–145.

APPENDIX

The coefficient of the Fourier series in Eq. (16) is derived in this appendix.

$$F_{c1}=(2/\pi)\left\{\int_{\underline{\theta}_0}^{\underline{\theta}^*}[k_d(x-A_m)+\mu N]\cos\underline{\theta}\,d\underline{\theta}-\int_{\underline{\theta}^*}^{\underline{\theta}_0+\pi}\mu N\cos\underline{\theta}\,d\underline{\theta}\right\}$$

$$=(2/\pi)\left\{\int_{\underline{\theta}_0}^{\underline{\theta}^*}k_d[A_1(\cos\underline{\theta}-\cos\underline{\theta}_0)+A_3(\cos 3\underline{\theta}-\cos 3\underline{\theta}_0)+B_1(\sin\underline{\theta}-\sin\underline{\theta}_0)+B_3(\sin 3\underline{\theta}-\sin 3\underline{\theta}_0)]\cos\underline{\theta}\,d\underline{\theta}\right.$$

$$\left.+\int_{\underline{\theta}_0}^{\underline{\theta}^*}\mu N\cos\underline{\theta}\,d\underline{\theta}-\int_{\underline{\theta}^*}^{\underline{\theta}_0+\pi}\mu N\cos\underline{\theta}\,d\underline{\theta}\right\}$$

$$=(2/\pi)\{k_d[A_1S_1+A_3S_2+B_1S_3+B_3S_4]+k_d[A_1\cos\underline{\theta}_0+A_3\cos 3\underline{\theta}_0+B_1\sin\underline{\theta}_0+B_3\sin 3\underline{\theta}_0](\sin\underline{\theta}_0+\sin\theta^*)+2\mu N\sin\underline{\theta}^*\}$$

$$F_{c3}=(2/\pi)\left\{\int_{\underline{\theta}_0}^{\underline{\theta}^*}[k_d(x-A_m)+\mu N]\cos 3\underline{\theta}\,d\underline{\theta}-\int_{\underline{\theta}^*}^{\underline{\theta}_0+\pi}\mu N\cos 3\underline{\theta}\,d\underline{\theta}\right\}$$

$$=(2/\pi)\{k_d[A_1S_2+A_3S_5+B_1S_6+B_3S_7]+(k_d/3)]A_1\cos\underline{\theta}_0+A_3\cos 3\underline{\theta}_0+B_1\sin\underline{\theta}_0+B_3\sin 3\underline{\theta}_0](\sin 3\underline{\theta}_0-\sin 3\underline{\theta}^*)+(2\mu N/3)\sin 3\underline{\theta}^*\}$$

$$F_{s1}=(2/\pi)\left\{\int_{\underline{\theta}_0}^{\underline{\theta}^*}[k_d(x-A_m)+\mu N]\sin\underline{\theta}\,d\underline{\theta}-\int_{\underline{\theta}^*}^{\underline{\theta}_0+\pi}\mu N\sin\underline{\theta}\,d\underline{\theta}\right\}$$

$$=(2/\pi)\{k_d[A_1S_3+A_3S_6+B_1S_8+B_3S_9]-k_d[A_1\cos\underline{\theta}_0+A_3\cos 3\underline{\theta}_0+B_1\sin\underline{\theta}_0+B_3\sin 3\underline{\theta}_0](\cos\underline{\theta}_0-\cos\underline{\theta}^*)-2\mu N\cos\underline{\theta}^*\}$$

$$F_{s3}=(2/\pi)\left\{\int_{\underline{\theta}_0}^{\underline{\theta}^*}[k_d(x-A_m)+\mu N]\sin 3\underline{\theta}\,d\underline{\theta}-\int_{\underline{\theta}^*}^{\underline{\theta}_0+\pi}\mu N\sin\underline{\theta}\,d\underline{\theta}\right\}$$

$$=(2/\pi)\{k_d[A_1S_4+A_3S_7+B_1S_9+B_3S_{10}]-(k_d/3)[A_1\cos\underline{\theta}_0+A_3\cos 3\underline{\theta}_0+B_1\sin\underline{\theta}_0+B_3\sin 3\underline{\theta}_0](\cos 3\underline{\theta}_0-\cos 3\underline{\theta}^*)-(2\mu N/3)\cos 3\underline{\theta}^*\}$$

where

$$S_1=(\underline{\theta}^*-\underline{\theta}_0)/2+(\sin 2\underline{\theta}^*-\sin 2\underline{\theta}_0)/4$$

$$S_2=(\sin 2\underline{\theta}^*-\sin 2\underline{\theta}_0)/4+(\sin 4\underline{\theta}^*-\sin 4\underline{\theta}_0)/8$$

$$S_3=(\cos 2\underline{\theta}_0-\cos 2\underline{\theta}^*)/4$$

$$S_4=(\cos^4\underline{\theta}_0-\cos^4\underline{\theta}^*)+(\cos 2\underline{\theta}^*-\cos 2\underline{\theta}_0)$$

$$S_5=(\underline{\theta}^*-\underline{\theta}_0)/2+(\sin 6\underline{\theta}^*-\sin 6\underline{\theta}_0)/12$$

$$S_6=(\cos^4\underline{\theta}_0-\cos^4\underline{\theta}^*)+(3/4)(\cos 2\underline{\theta}^*-\cos 2\underline{\theta}_0)$$

$$S_7=(\cos 6\underline{\theta}_0-\cos 6\underline{\theta}^*)/12$$

$$S_8=(\underline{\theta}^*-\underline{\theta}_0)/2-(\sin 2\underline{\theta}^*-\sin 2\underline{\theta}_0)/4$$

$$S_9=(\sin 2\underline{\theta}^*-\sin 2\underline{\theta}_0)/4-(\sin 4\underline{\theta}^*-\sin 4\underline{\theta}_0)$$

$$S_{10}=(\underline{\theta}^*-\underline{\theta}_0)/2-(\sin 6\underline{\theta}^*-\sin 6\underline{\theta}_0)/12$$

Coupled Multidisciplinary Simulation of Composite Engine Structures in Propulsion Environment

C. C. Chamis
NASA Lewis Research Center,
Cleveland, OH 44135

S. N. Singhal
Sverdrup Technology, Inc.,
Cleveland, OH 44135

A computational simulation procedure is described for the coupled response of multilayered multimaterial composite engine structural components that are subjected to simultaneous multidisciplinary thermal, structural, vibration, and acoustic loading including the effect of hostile environments. The simulation is based on a three-dimensional finite element analysis technique in conjunction with structural mechanics codes and with the acoustic analysis methods. The composite material behavior is assessed at the various composite scales, i.e., the laminate/ply/fiber and matrix constituents, via a nonlinear material characterization model. Sample cases exhibiting nonlinear geometric, material, loading, and environmental behavior of aircraft engine fan blades are presented. Results for deformed shape, vibration frequencies, mode shapes, and acoustic noise emitted from the fan blade are discussed for their coupled effect in hot and humid environments. Results such as acoustic noise for coupled composite-mechanics/heat transfer/structural/vibration/acoustic analyses demonstrate the effectiveness of coupled multidisciplinary computational simulation and the various advantages of composite materials compared to metals.

Introduction

The unquenchable thirst of the human race for better and newer technology keeps imposing bigger challenges. One key human endeavor successfully materialized was the ability to fly. The oncoming challenge is to fly faster than ever before. Fulfillment of this challenge is going to require new materials and new simulation approaches to designing aircraft that can survive hostile environments at speeds that are multiples of the speed of sound. The new breed of materials, known as elevated temperature composites, which are light in weight, high in strength and durability, and can be tailored for required performance, are already finding applications and acceptance in aircraft frame and engine structures. There are already many competing requirements such as minimum temperature gradient versus maximum pressure tolerance, as well as equally important considerations such as minimum noise. Designing with composite materials poses additional challenges in the areas of material selection, fabrication, durability, and failure mechanisms. Further complexities such as the influence of hostile environments, nonlinear material/structural behavior, and coupling between responses induced by various discipline-specific loads, require complex analysis methods. Clearly, coupled multidisciplinary analysis methods capable of simulating the many discipline-specific loads and their interaction with each other are needed. Additionally, newly evolving materials, which may respond to the various multidisciplinary loads and environments in an as yet unknown manner, have no pre-existing data base. Since the acquisition of even a minimum necessary new database may not be possible within the oncoming twenty-first century's short design-cycle time limits and within competitive cost constraints, computational simulation methods must be developed for the coupled multidisciplinary analysis of engine structures.

Some recently evolving multidisciplinary analysis codes were discussed in a recent article in *Mechanical Engineering* magazine [1]. The need for developing coupled multidisciplinary analysis methods/codes has been recognized for quite some time. For example, a multifaceted research program aimed at simulating coupled multidisciplinary behavior of aircraft engine/frame structures made of advanced composite materials is described in [2]. A significant amount of research conducted for simulating the characteristics/performance of elevated temperature composite materials/structures has been embedded in user-friendly computer codes. This effort continues to evolve and contains a multitude of discipline-specific as well as integrated codes covering a vast spectrum of consistent, compatible, and interactive analysis methods [3]. More recently, a stand-alone multidisciplinary simulation procedure code was developed by integrating the three-dimensional finite element analysis method with several single-discipline (thermal, acoustic [4]) codes including those for integrated composite mechanics [5].

Contributed by the International Gas Turbine Institute and presented at the 37th International Gas Turbine and Aeroengine Congress and Exposition, Cologne, Germany, June 1–4, 1992. Manuscript received by the International Gas Turbine Institute January 13, 1992. Paper No. 92-GT-6. Associate Technical Editor: L. S. Langston.

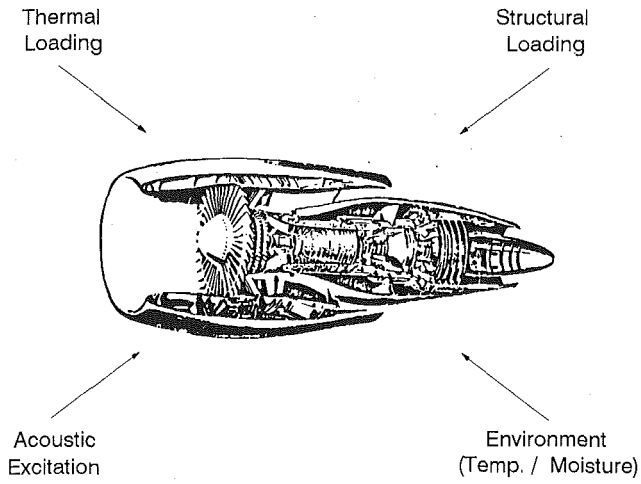

Fig. 1 Engine components under multidisciplinary loadings

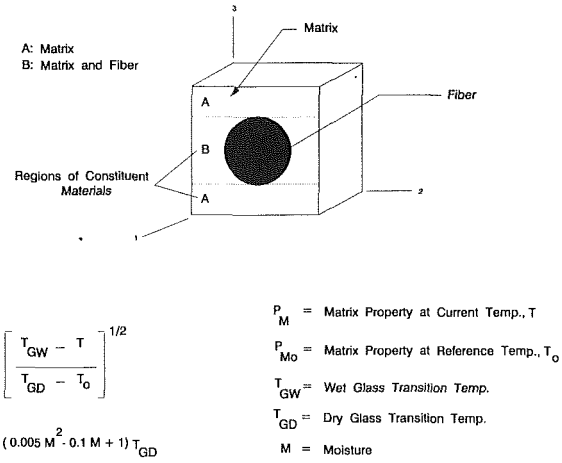

$$\frac{P_M}{P_{Mo}} = \left[\frac{T_{GW} - T}{T_{GD} - T_o}\right]^{1/2}$$

$$T_{GW} = (0.005\,M^2 - 0.1\,M + 1)\,T_{GD}$$

P_M = Matrix Property at Current Temp., T
P_{Mo} = Matrix Property at Reference Temp., T_o
T_{GW} = Wet Glass Transition Temp.
T_{GD} = Dry Glass Transition Temp.
M = Moisture

Fig. 3 Regions of constituent materials an nonlinear material characterization model

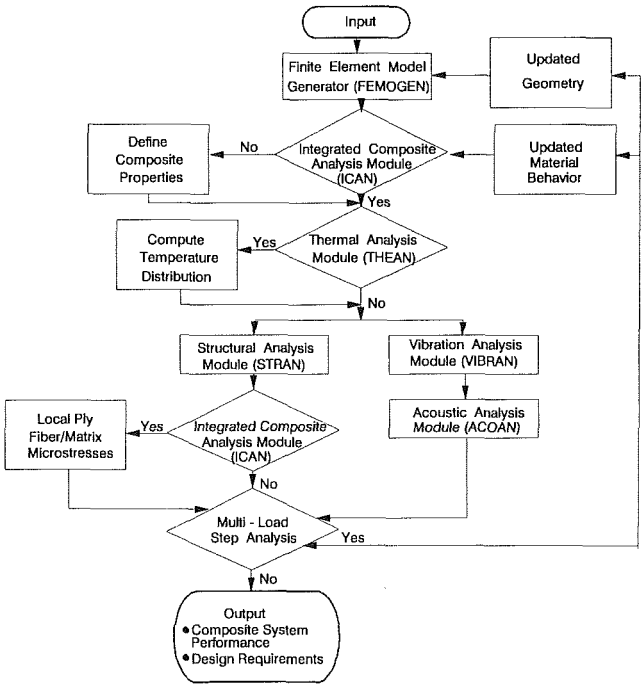

Fig. 2 Multidisciplinary simulation procedure

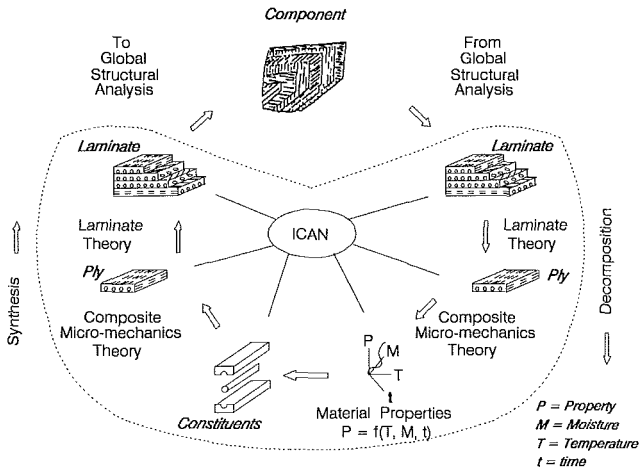

Fig. 4 Integrated composite mechanics—ICAN

The objective of the present paper is to demonstrate the computational simulation of the coupled multidisciplinary behavior of multilayered multimaterial elevated temperature aircraft engine composite structures under simultaneous thermal, structural, and acoustic loadings in propulsion environment, typified in Fig. 1.

Brief Description of Simulation Procedure

A general-purpose procedure was developed to simulate computationally the coupled multidisciplinary heat transfer, structural, vibration, and acoustic analysis of high-temperature composite structures in propulsion environment. All the disciplines are coupled for nonlinear geometric, material, loading, and environmental effects.

A schematic of the procedure is shown in Fig. 2. First, the model definition module generates the finite element model of the structure geometry, composite configuration, boundary conditions, and loading. The resident mesh generator is capable of generating solids of revolution such as cylinders, cones,and general double-curved surfaces of up to 360 deg rotation, with minimum input parameters needed to define the complicated geometries. In the case of combined different types of solids of revolution/flat surfaces, duplicate nodes are automatically checked and only one of each coincident node is kept. The Integrated Composite Analysis module, ICAN [5] is then used for determining the thermal and mechanical properties at various scales (fiber/matrix constitutes, ply, and laminate) of the composite structure, based on composite micromechanics and laminate theories, starting from the room temperature properties of the constituents. A nonlinear material characterization model [6], shown in Fig. 3, is used a the matrix level to simulate the degradation in material properties due to applied temperature, time, and environmental effects, etc., via an iterative approach, as shown on the left-hand side of Fig. 4. The ICAN module thus makes it possible automatically to compute the multiscale composite properties of the virgin arbitrary combinations of multilayered multimaterial composite configurations, as well as for the degraded configurations at various stages of the composite structure life-cycle. The room temperature properties of fiber/matrix constituents for typical aircraft structure materials are automatically extracted from the ICAN resident data bank, which can be augmented for properties of new materials. This feature results in a considerable saving of time required for searching the inputting the composite material property data. The ICAN module simulates the material behavior of polymer matrix composites. Similar codes (METCAN [7] and CEMCAN [8]) for simulating the material behavior of other types of elevated temperature composites such as metal matrix and ceramic matrix composites,

respectively, are available. The simulation procedure can be adopted for these types of composites with minimal effort.

The computational procedure for couple heat transfer, structural, vibration, and acoustic analysis is based on the three dimensional finite element formulation. Each element can be modeled as consisting of several layers of the composite material. Each layer can be arbitrarily oriented and be of different material. The heat transfer response is computed first via the Thermal Analysis module, THEAN. Four types of heat transfer analyses: (1) linear steady state, (2) nonlinear steady state, (3) linear transient, and (4) nonlinear transient, can be performed, with thermal properties computed and updated via the ICAN module. All types of thermal loadings including prescribed temperatures, surface heat fluxes, convection, radiation, and internal heat generation can be applied. Upon completion of the heat transfer analysis, the temperature at each node of the structure is defined.

The same finite element mesh that was used for the heat transfer analysis is also used for the structural and vibration analyses. This minimizes the data preparation time and eliminates the errors incurred in transforming the temperatures from one finite element mesh to another. Two types of structural analyses: (1) static and (2) buckling, can performed at the end of any heat transfer analysis step. All types of loadings including displacements, forces, accelerations, centrifugal, and pressure can be applied. The pressure can vary across the element face. Several coordinate systems including global, skew, local, material, and for micromechanics, are used to allow maximum flexibility in inputting data at any orientation for complex structures. For example, a skew coordinate system allows input of skew boundary conditions. The vibration analysis computes the free vibration frequencies and mode shapes. Free vibration frequencies and mode shapes can be calculated using the "determinant search" or the "subspace iteration" method. The effect of environment (temperature and moisture) on the structural and vibration response of the material is accounted for via the ICAN module. Nonlinear geometric effects such as large deformation/centrifugal stiffening are accounted for via updated Lagrange analysis. In such cases: (1) The pressure can be computed for either the original or the updated deformed geometry and (2) free vibration frequencies and mode shapes are calculated including the effect of updated geometry on the stiffness and mass matrices. Buckling eigenvalues also use modified stiffness for large deformation. The local structural response at ply and fiber/matrix scales of the composite structure can be computed via ICAN, as shown on the right-hand side of Fig. 4.

The acoustic analysis module, ACOAN, computes the acoustic noise emitted from the composite structure, due to (1) free vibration, or (2) forced vibration induced by applying a force at a point of the structure to excite the vibration modes of interest selectively. The acoustic noise is computed by first calculating radiation efficiencies of the structure for each natural vibration mode as a function of forced vibration frequency. The total sound power for each forced vibration frequency is then calculated by summing the contribution from each free vibration mode. The computation of acoustic noise includes: (1) the effect of updata geometry due to large deformation via (*a*) updated structure stiffness and mass, and (*b*) updated geometry of the structure affecting the location and direction of the acoustic excitation force, (2) the effect of environment on thermal and mechanical properties via updated structure stiffness, and (3) the effect of natural vibration frequency on the modal loss factor (damping). A part of the structure can be masked from emitting the noise.

Finally, the multiload step analysis feature allows multidirectional coupling among all the participating disciplines by passing the updated geometry and updated material behavior back to any one or all analysis disciplines via a nonlinear iterative procedure.

The coupling between the various disciplines due to geometric, material, loading, and environmental complexities descibed above, allows many combinations of coupled multidisciplinary analyses, as will be demonstrated in the next section for a fan blade. There are several other advanced features in this computational simulation procedure. They are not discussed here as they are beyond the scope of the demonstration cases presented in this paper. An example is the two-way coupling of the updated geometry due to large deformation and the heat transfer analysis via multiload increment analysis capability.

Sample Cases—Fan Blade

A multimaterial, multilayered aircraft engine fan blade was simulated for a coupled multidisciplinary thermal, structural, vibration, and acoustic response. The geometry, boundary conditions, material, composite configuration, environment, and thermal/structural/acoustic loadings are shown in Fig. 5. A summary of the various analysis disciplines, and coupling effects demonstrated for the fan blade, is provided in Table 1. The design requirements may include other considerations such as aerodynamics of the blade. These are beyond the scope of this paper and have been and are being addressed via other integrated codes [3]. A description of the loadings, boundary conditions, environmental effects, and of the single-discipline or coupled multidiscipline analyses performed for the fan blade follows the description of the blade structure, material, and the finite element model.

Blade Structure, Material, and Finite Element Model. The blade consists of a twisted aerofoil shape with varying thickness along the span and the chord. The maximum span of the blade is 10.19 in. and the maximum chord is 3.43 in. The thickness varies from 0.20 at the leading edge tip to 1.35 in. at the trailing

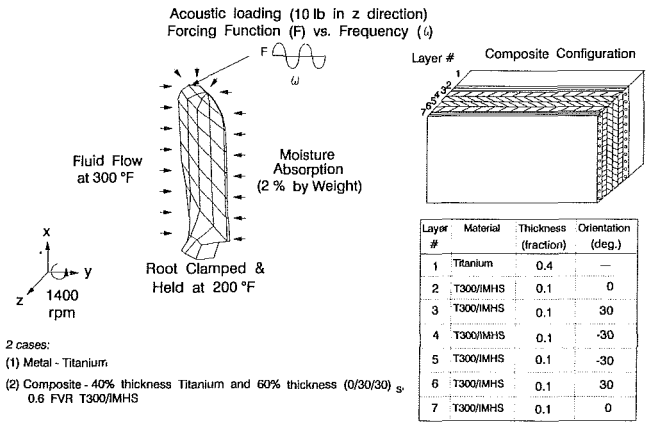

Fig. 5 Fan blade under multidisciplinary loading

Table 1 Coupled multidisciplinary analysis demonstrated for fan blade

Analysis Discipline	Loading	Coupled with
Heat Transfer * Steady State - Nonlinear	- Prescribed Temperature - Convection	● Composite Mechanics
Structural * Static	- Centrifugal Loading	● Composite Mechanics ● Heat Transfer Analysis
Vibration * Vibration Frequencies/ Mode Shapes		● Composite Mechanics ● Heat Transfer Analysis ● Structural Analysis via Geometric Stiffening
Acoustic * Forced Excitation Noise	- Point Load	● Composite Mechanics ● Heat Transfer Analysis ● Structural Analysis via Geometric Stiffening ● Vibration

Table 2 Constituent (fiber/matrix) material properties at unstressed reference temperature (70°F)

T300 Fiber		IMHS Matrix	
Filament Equivalent Diameter	= 0.0003 inch	Weight Density	= 0.044 lb/in^3
Weight Density	= 0.064 lb/in^3	Elastic Modulus	= 0.5x10^{6}psi
Modulus in Longitudinal Direction	= 32x10^{6}psi	Poisson's Ratio	= 0.35
Modulus in Transverse Direction	= 2x10^6 psi	Thermal Expansion Coefficient	= 36x10^{-6}in/in - °F
In-plane Poisson's Ratio	= 0.2	Heat Conductivity	= 1.25 Btu/hr-ft - °F
Out-of-plane Posson's Ratio	= 0.25	Tensile Strength	= 15,000 psi
In-plane Shear Modulus	= 1.3x10^{6}psi	Compressive Strength	= 35,000 psi
Out-of-plane Shear Modulus	= 0.7 x10^{6}psi	Shear Strength	= 13,000 psi
Thermal Expansion Coefficient in Longitudinal Direction	= -0.55x10^{-6}in/in - °F	Void Fraction	= 0.225
Thermal Expansion Coefficient in Transverse Direction	= 5.6x10^{-6} in/in - °F	Glass Transition Temp.	= 420 °F
Thermal Conductivity in Longitudinal Direction	= 48.3 Btu/hr-ft - °F		
Thermal Conductivity in Transverse Direction	= 4.83 Btu/hr-ft - °F		
Tensile Strength	= 35,000 psi		
Compressive Strength	= 30,000 psi		

Conversion Factors for SI Units: 1 in = 0.0254 m; 1lb/in^3 = 0.2714x10^{6}N/m^3 ; 1 psi = 6.895x10^{3}N/m^2
°F = 1.8 °C+32; 1 Btu/hr-ft - °F = 1.73 watts/meter - °K

edge tip. As noted in Fig. 5, the blade is analyzed for two materials: (1) metal–titanium, and (2) multilayered multimaterial composite: 40 percent thickness of titanium and 60 percent thickness of six-layered T300/IMHS material with $(0/30/-30)_s$ ply orientations and 0.6 fiber volume ratio. The T300 stands for the graphite fibers and IMHS for intermediate high-strength epoxy matrix. The thermal and mechanical properties of the T300 fibers and IMHS matrix at room temperature are shown in Table 2. The finite element model consisted of 40 20–noded brick elements with 110 nodes.

Heat Transfer. The root of the blade was held at a constant temperature of 200°F and the blade surfrace was subjected to fluid flow at 300°F. The thermal material properties, thermal conductivity and coefficient of heat convection, were considered temperature dependent via (*a*) direct input of temperature-dependent properties for the metal, and (*b*) ICAN for the composite. A nonlinear steady-state heat transfer analysis coupled with composite mechanics was conducted for both materials.

Structural Analysis. The root of the blade was fixed and a centrifugal loading of 1400 rpm was applied. The effect of propulsion environments was simulated for several cases: (1) room temperature (70°F) with no moisture absorption, (2) uniform temperature rise from 70 to 300°F with no moisture absorption, (3) nonuniform temperature distribution as computed by the heat transfer analysis with no moisture absorption, and (4) nonuniform temperature distribution computed by the heat transfer analysis with 2 percent absorption of moisture in the composite, by weight. Notice that cases (3) and (4) with nuniform temperature distribution require coupled composite-mechanics/heat transfer/structural analysis. A fifth case (5) was simulated for the effect of geometric stiffening at room temperature and no moisture. The thermal and mechanical properties, coefficient of thermal expansion, stiffness, and strength, were considered temperature dependent via (*a*) direct input of temperature-dependent properties for the metal, and (2) ICAN for the composite. A static structural analysis was conducted for both materials.

Vibration. The root of the blade was fixed. Five vibration analysis cases similar to those described above for the "Structural Analysis" were simulated. Again, cases (3) and (4) with nonuniform temperature distribution computed via heat transfer analysis require a coupled composite-mechanics/heat transfer/vibration analysis. Case (5) with geometric stiffening requires a coupled composite-mechanics/structural/vibration analysis to account for the effect of updated geometry due to geometric stiffening. The thermal and mechanical properties were also treated similar to those described above for the "Structural Analysis." Three natural vibration frequencies and mode shapes were computed for all five cases for both materials.

Acoustic Excitation. The root of the blade was fixed and sinusoidal force vibrations of 10 lb amplitude were applied at the leading edge tip in the blade thickness direction, at several forcing frequencies ranging from 100 to 1000 cps. Again, five cases with thermomechanical properties as discussed above were simulated. Cases (1) and (2) with room temperature and uniform temperature distribution, respectively, require coupled composite-mechanics/vibration/acoustic analysis. Cases (3) and (4) with nonuniform temperature distribution computed via heat transfer and analysis, require coupled composite-mechanics/heat transfer/vibration/acoustic analysis, and case (5) with geometric stiffening, requires a coupled composite-mechanics/structural/vibration/acoustic analysis. A special variation of case (3) with frequency-dependent model loss damping factor was also run. This is just one of many special features of the computational simulation procedure demonstrated in the present paper. The modal loss factors used for this evaluation are only estimates. The computational simulation of damping in composite materials is described in [9].

Results and Discussions

The results of several cases of the fan blade with varying degree of complexity/coupling among various disciplines are discussed below in the same order in which the sample cases are described above. The effect of coupling among different disciplines is explained, as appropriate.

Heat Transfer. The heat transfer results in terms of temperature contours for both the metal and composite blades are shown in Fig. 6. Notice that the computed temperatures vary from 200 to 285°F for the metal and from 200 to 275°F for the composite blade.

Structural Analysis. Only a representative result, i.e., the deformed shape of the blade for the case with nonuniform temperature distribution computed via heat transfer analysis and with no moisture absorption and no effect of geometric

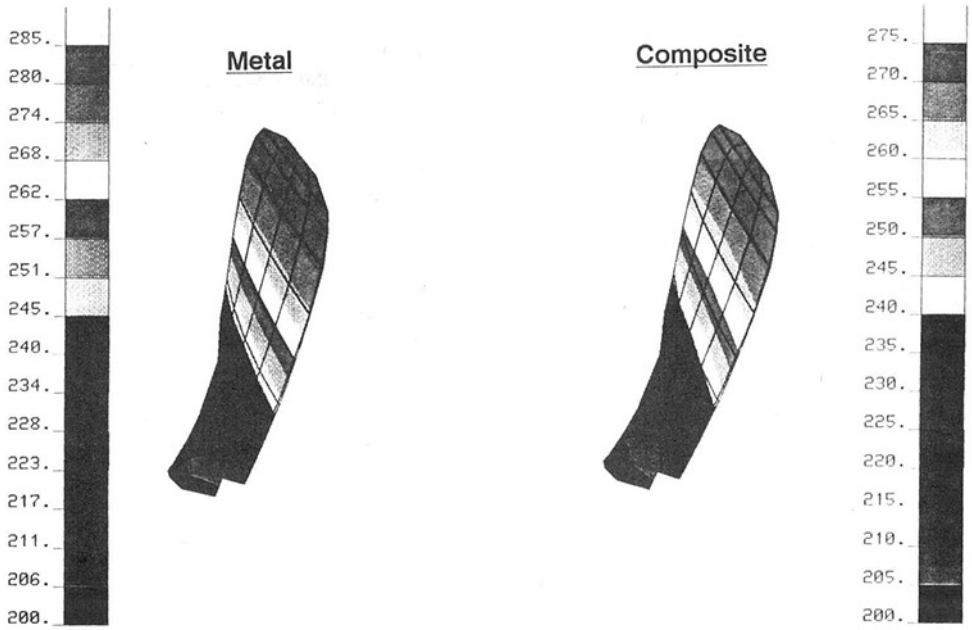

Fig. 6 Thermal response of fan blade; °F = 1.8°C + 32

Deformed Shape via Coupled Composite-Mechanics/Heat-Transfer/Structural Analysis (Centrifugal Loading at 1400 rpm; Root @ 200 °F; Fluid Flow @ 300 °F)

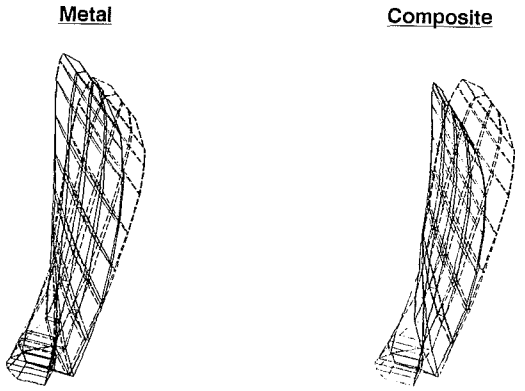

Fig. 7 Structural response of fan blade; °F = 1.8°C + 32

Vibration Frequencies via Coupled Composite-Mechanics/Heat-Transfer/ Vibration Analysis (Root @ 200 °F; Fluid Flow @ 300 °F)

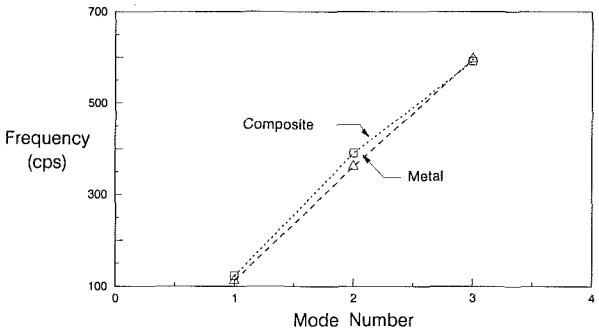

Fig. 8 Vibration response of fan blade—frequencies

stiffening is shown in Fig. 7 for both the metal and composite blades. The metal blade shows more radial deformation than the composite blade. The blade deforms less at the room temperature and more at 300°F uniform temperature. The geometric stiffening reduces the blade deformation. These results are not shown in figure form in the present paper. The results for global and local stresses at ply and fiber/matrix constituents scales are also available, but not presented here.

Vibration. The first three natural vibration frequencies for the case with nonuniform temperature distribution computed via heat transfer analysis and with no moisture absorption and no geometric stiffening are shown in Fig. 8. The corresponding mode shapes are shown in Fig. 9. These are about the same. The effects of various environmental conditions (temperature/moisture) and geometric stiffening on the fundamental vibration frequency are shown in Fig. 10. The vibration frequency decreases with increasing temperature and moisture and the material degrades. The moisture does not affect their vibration frequency of the metallic blade. Geometric stiffening increases the vibration frequency by about 6 percent in the metal and about 5 percent in the composite as would be expected from the heavier metal density.

Acoustic Excitation. The acoustic noise emitted from the fan blade is shown in Fig. 11, in watts as well as in decibles. To put the decibel values in perspective, a human whisper is at 50 decibles, a truck horn is at 110 decibles, and an airplane engine propeller is at 120 decibles. Increasing damping decreases the noise level. The noise is much less for the composite material than for metal. Figure 12 shows the acoustic noise for various cases of environmental conditions and geometric stiffening. The acoustic noise decreases or increases depending on if the forcing frequency is farther away from or closer to the natural vibration frequency, respcetively. The effect of environment on the acoustic noise from the metallic fan blade is negligible. At temperature higher than those used here, it may not be so. For the composite blade, increasing temperature and moisture increase the acoustic noise at the forcing frequency of 119 cps. These results are consistent with the results for the natural vibration frequencies shown in Fig. 10, which become closer to 119 cps as temperature and moisture increase. The effect of geometric stiffening is to decrease the acoustic noise as the forcing frequency moves away from the natural vibration frequency. Another effect, that the frequency dependence of the modal loss factors, is shown in Fig. 13 for

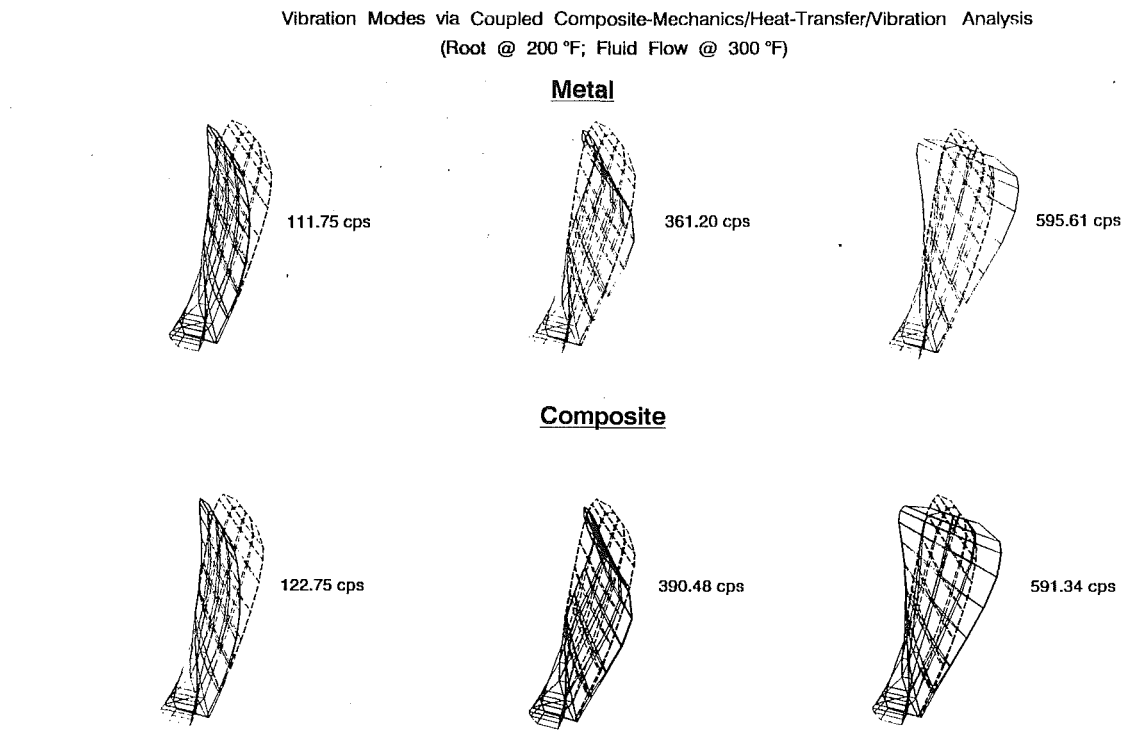

Fig. 9 Vibration response of fan blade—mode shapes

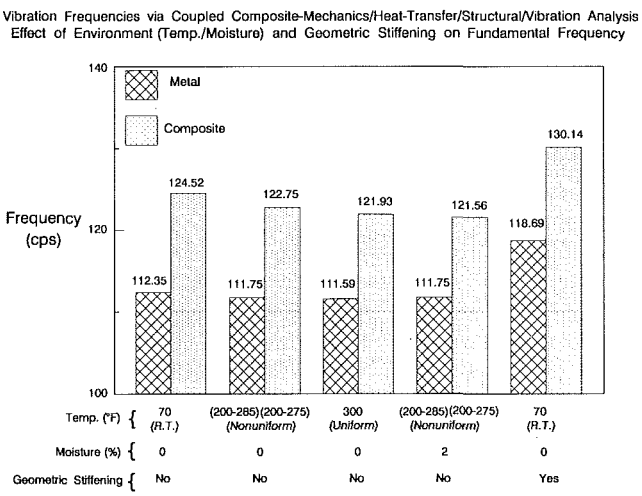

Fig. 10 Vibration response of fan blade—fundamental frequency

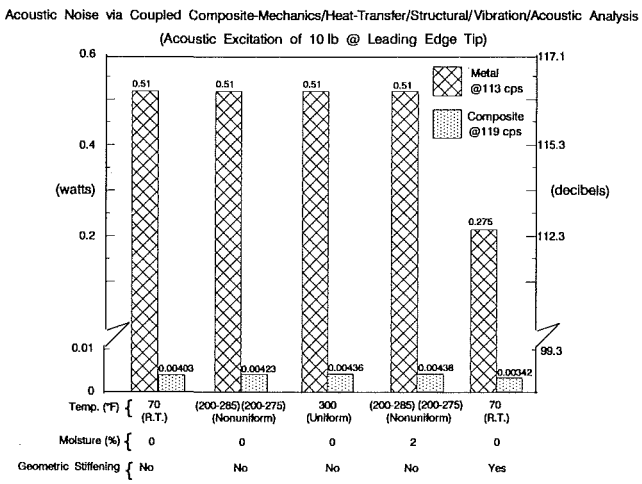

Fig. 12 Acoustic noise emitted from fan blade @ specified forcing frequency

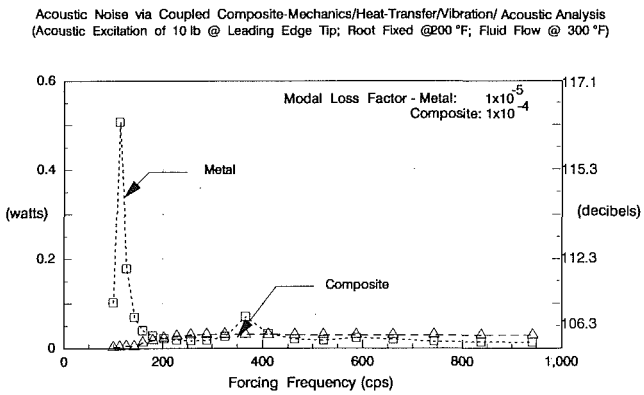

Fig. 11 Acoustic noise emitted from fan blade

both the metal and composite blades. The modal loss factor decreases with the vibration frequency, as tabulated in Fig. 13. The acoustic noise increases, only slightly, by accounting for frequency dependence of the modal loss factors both for the metal and composite blades.

The significant observation is that the acoustic noise from the composite fan blade is negligible compared to that from the metal blade, Fig. 11. The effect of frequency dependence of the modal loss factors is practically the same of the two blades, Fig. 13.

General Remarks

A stand-alone computational simulation procedure has been demonstrated for coupled response of an aricraft engine fan blade under multidisciplinary thermal/structural/vibrations/ acoustic loading in propulsion environments. The procedure

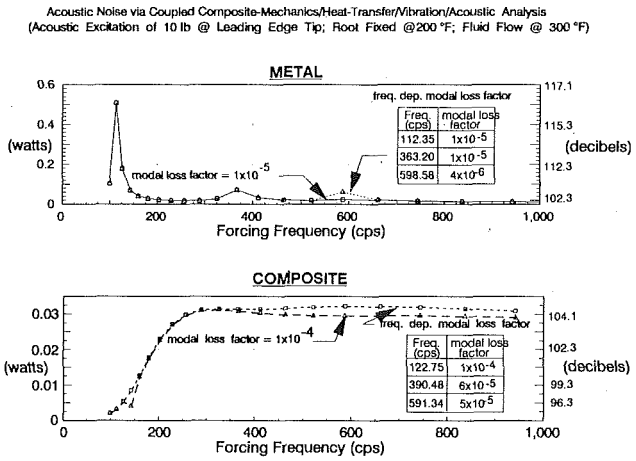

Fig. 13 Acoustic noise emitted from fan blade—frequency-dependent modal loss factor

was developed via integrating the three dimensional finite element technique with in-house single-discipline codes coupled with acoustic analysis methods. The simulation procedure is of general purpose in nature and can be used for designing/analyzing multilayered multimaterial composite structures. The results, such as the decrease in acoustic noise level by accounting for structural/acoustic coupling due to geometric stiffening, demonstrate the significance of coupled multidisciplinary simulation of the blade. Results such as these can be generated via a single coupled multidisciplinary code in a very short time. In an effort to satisfy the competing requirements imposed by individual discipline-specific behavior, many design variation/parameters will need to be considered. Multidisciplinary computational simulation is the approach that will provide a realistic assessment of the various competing design requirements of advanced composite materials/structures. Unlike experimental data generation that may be untimely and costly, computational simulation is able to produce rapid reasonable results for specific designs.

The environmental effects discussed herein include temperature and moisture. Other environmental effects such as chemical interactions can be incorporated in the same way. The effect of chemical interaction on the degradation of material resistance can be simulated via the Integrated Composite Analyzer Code, ICAN, by adding respective terms in the nonlinear material characterization model, shown in Fig. 3 [6]. The modified form of the nonlinear material characterization model will consist of a product of nonlinear factors for each environmental effect. Such nonlinear multifactor interaction models (MFIM) for factors such as cyclic effect have been implemented in metal matrix composite analysis codes [7]. The effect of chemical interaction on changes in the geometry, if any, can be addressed in the finite element models by suitable changes in the dimensions. These effects can then be passed on to the multidisciplinary analysis via the geometry update module.

Summary

A general-purpose computational simulation procedure is presented for coupled multidisciplinary thermal, structural, vibration, and acoustic analysis of elevated temperature composite structures in propulsion environments. All the disciplines are coupled for nonlinear geometric, material, loading, and environmental effects. The procedure is embedded in a stand-alone state-of-the-art computer code, enabled by integrating the three-dimensional finite element technique with in-house codes for integrated composite mechanics, thermal, and acoustic analysis methods. A nonlinear material characterization model is used to simulate the degradation in material properties due to applied temperature, time, and environmental effects. Sample cases exhibiting various combinations of coupled multidisciplinary analysis of an aircraft engine fan blade are presented. Results indicate lower temperatures, higher vibration frequencies, and substantially lower acoustic noise levels for the T300/IMHS composite versus that for titanium.

References

1 Puttré, M., "FEA Programs Band Together," *Mechanical Engineering*, Vol. 113, No. 9, Sept. 1991, pp. 77–82.

2 Chamis, C. C., "Computer Code for the Analysis of Mulitlayered Fiber Composite—User's Manual," NASA TN D-7013, 1971.

3 "A Guide to NASA Lewis Structural Mechanics Codes," NASA Report (under preparation), 1991.

4 Hayes, P. E., "Determining Vibration, Radiation Efficiency, and Noise Characteristics of Structural Designs Using Analytical Techniques," *Proceedings Society of Automotive Engineers*, p. 106, SAE, Warrendale, PA, 1982, pp. 236–270.

5 Murthy, P. L. N., and Chamis, C. C., "Integrated Composite Analyzer (ICAN)—User's and Programmer's Manual," NASA TP 2515, Mar. 1986.

6 Chamis, C. C., "Simplified Composite Micro-mechanics Equations for Hygral, Thermal, and Mechanical Properties," NASA TM-83320, 1987.

7 Murthy, P. L. N., and Hopkins, D. A., "Metal Matrix Composites Analyzer: METCAN User's Guide," NASA Report (in draft form), 1988.

8 Murthy, P. L. N., et al., "Ceramic Matrix Composite Analyzer: CEMCAN," NASA Report (under preparation), 1991.

9 Saravanos, D. A., and Chamis, C. C., "Mechanics of Damping for Fiber Composite Laminates Including Hydrothermal Effects," *AIAA Journal*, Vol. 28, No. 10, 1990, pp. 1813–1819.

Optimal Output Feedback Control of Asymmetric Systems Using Complex Modes

G. W. Fan
Chief Engineer,
3-I Scientific Development Inc.,
Tempe, AZ 85282

H. D. Nelson
Professor and Chair,
Department of Engineering,
Texas Christian University,
Fort Worth, TX 76129

M. P. Mignolet
Assistant Professor,
Department of Mechanical and
Aerospace Engineering,
Arizona State University,
Tempe, AZ 85287

A Linear Quadratic Regulator (LQR)-based least-squares output feedback control procedure using a complex mode procedure is developed for the optimal vibration control of high-order asymmetric discrete system. An LQ Regulator is designed for a reduced-order model obtained by neglecting high-frequency complex modes of the original system. The matrix transformations between physical coordinates and complex mode coordinates are derived. The complex mode approach appears to provide more accurate reduced-order models than the normal mode approach for asymmetric discrete systems. The proposed least-squares output feedback control procedure takes advantage of the fact that a full-state feedback control is possible without using an observer. In addition, the lateral vibration of a high-order rotor system can be effectively controlled by monitoring one single location along the rotor shaft, i.e., the number of measured states can be much less than the number of eigenvectors retained in producing the reduced-order model while acceptable performance of the controller is maintained. The procedure is illustrated by means of a 52 degree-of-freedom finite element based rotordynamic system. Simulation results show that LQ regulators based on a reduced-order model with 12 retained eigenvalues can be accurately approximated by using feedback of four measured states from one location along the rotor shaft. The controlled and uncontrolled transient responses, using various numbers of measured states, of the original high-order system are shown. Comparisons of reduced-order model results using normal modes and complex modes are presented. The spillover problem is discussed for both collocated and noncollocated cases based on this same example.

Introduction

The design of a control system for an asymmetric rotordynamic system initially requires the development of a discrete mathematical model. For most realistic rotor systems these models are typically several tens of degrees of freedom. Active control of lateral vibrations in rotordynamic systems has been studied by many researchers in the last several years. Several of these researchers have successfully used the normal mode approach to obtain reduced-order systems. These normal modes do not include gyroscopic and/or circulation effects and as a result they do not decouple the asymmetric system equations. This work utilizes a complex mode approach to deal with such systems in the process of LQR design.

A full-state feedback control system does not require an observer. This is a primary motivation for using an optimal feedback technique. In addition, the use of an observer has the following disadvantages: (*a*) very high-speed computation is required for on-line state estimation, and this is especially difficult to implement for many rotor systems; (*b*) the cost is much higher for fabrication of an observer for implementation of an optimal output feedback procedure. The concept of optimal output feedback control has been used recently by several of the researchers cited below.

Salm and Schweitzer (1984) discussed the modeling and control of a flexible rotor using magnetic bearings. They also used a normal mode approach to obtain a reduced-order system, and, based on this system, designed an output feedback controller that guarantees closed-loop stability for the original high-order system despite some spillover effects. Ulsoy (1984) investigated an optimal active control scheme by pole assignment and the effects of observation and control spillover in an translating elastic system. His method was verified by using simulation results of two examples based on both physical and normal mode coordinates.

Cannon and Schmitz (1984) studied the precise control of a one-arm flexible manipulator without gyroscopic effects. They used a normal mode reduced-order model, and then designed an optimal controller based on this model. The system modal parameters in their work were measured and they were successful in experimentally verifying the validity of the proposed approach.

Palazzolo et al. (1989) experimentally demonstrated the success of this procedure with the limitation that the number of measured states must be equal to the number of retained ei-

Contributed by the International Gas Turbine Institute for publication in the JOURNAL OF ENGINEERING FOR GAS TURBINES AND POWER. Manuscript received by the International Gas Turbine Institute February 15, 1992. Associate Technical Editor: L. S. Langston.

genvalues in the reduced-order model. He studied the active control of transient lateral rotor vibrations due to a sudden change in imbalance, such as caused by blade loss, by utilizing optimal control methods. A seven-mass rotor system was considered and a normal model approach was used to obtain a reduced-order model. Comparisons of responses were made for various configurations of sensors and actuators. The spillover effect was examined by comparing results from collocated and noncollocated sensor configurations. A spillover filter was used in the experiments to prevent spillover effects for the noncollocated case.

In this present work, an LQ regulator is designed based on a reduced-order model utilizing complex modes. The least-squares output feedback procedure is essentially a modification of Palazzolo's strategy, requiring fewer measured states, while providing comparable performance. The performance index is chosen so that the difference between the designed control input (from the LQ regulator) and the control input from the output feedback procedure is small. Controlled responses associated with several choices of the performance index are shown for comparison purposes. A 52 degree-of-freedom finite element based model for a rotordynamic system is used as an example to illustrate the proposed procedure.

System Equations

The general linear matrix equation of motion of an nth-order rotordynamic system, in terms of physical coordinates, is of the form

$$M_q\ddot{q} + D_q\dot{q} + K_q q = f + Pu \tag{1}$$

The M_q, D_q, and K_q arrays represent the mass, dissipation/gyroscopic, and stiffness/circulation properties of the rotor system. The M_q array is usually symmetric and positive definite while the D_q and K_q arrays are generally asymmetric. These asymmetric arrays can be written as the sum of a symmetric and skew-symmetric component. The symmetric part of the D_q array is referred to as the dissipation matrix while the skew-symmetric part is the gyroscopic matrix. The symmetric part of the K_q array is the system stiffness matrix while the skew-symmetric part is referred to as the circulation matrix. In addition, D_q and K_q are generally a function of the rotor spin speeds. The excitation force f is usually dominated by harmonic terms associated with the synchronous rotating unbalance of the rotating assembly. The P array identifies the physical location of the external forces included in the control vector u. The speed dependency of the unbalance forces, gyroscopic moments, and the bearing forces requires spin speed dependency as well for the control action. In first-order state form, Eq. (1) is written as

$$\dot{x} = A_x x + B_x u + W_x f \tag{2}$$

where $x = [\dot{q}^t \; q^t]^t$ is the system state and $B_x = W_x P$ is the control matrix with

$$A_x = \begin{bmatrix} -M_q^{-1}D_q & -M_q^{-1}K_q \\ I & 0 \end{bmatrix}, \text{ and } W_x = \begin{bmatrix} M_q^{-1} \\ 0 \end{bmatrix} \tag{3}$$

The partial state measurements represented by the vector r are expressed by an output equation of the form

$$r = C_x x \tag{4}$$

Modal Reduction

Normal Mode Approach. A modal transformation

$$q \doteq \Phi\xi = \sum_{j=1}^{\hat{n}<n} \phi_j \xi_j \tag{5}$$

is defined where the columns of the modal matrix Φ are the M_q-normalized real eigenvectors $\phi_j (j = 1, 2, \ldots, \hat{n})$ of the undamped symmetric system associated with Eq. (1). The ξ_j are normal mode coordinates associated with the ϕ_j, respectively. The modal matrix satisfies the orthogonality conditions $\Phi^t M_q \Phi = I$ and $\Phi^t K_q \Phi = \Omega$, and the diagonal elements of Ω are squared natural frequencies of the undamped symmetric problem. The introduction of the transformation of Eq. (5) into Eq. (1), premultiplication by Φ^t, and of the orthogonality conditions yields the reduced-order ($\hat{n} < n$) model

$$\ddot{\xi} + D_\xi\dot{\xi} + K_\xi\xi = \Phi^t f + \Phi^t P u \tag{6}$$

Nomenclature

A = system matrix ($2n \times 2n$)
B = control distribution matrix ($2n \times r$)
c = bearing damping coefficient
C = output matrix ($m \times 2n$)
D = dissipation/gyro matrix ($n \times n$)
E = elastic modulus
f = unbalance force vector ($n \times 1$)
G = optimal gain matrices ($r \times 2n$)
I = identity matrices ($n \times n$)
J = performance index
k = bearing stiffness
K = stiffness/circulation matrix ($n \times n$)
m = number of outputs
M = mass matrix ($n \times n$)
n = system order
P = control distribution matrix ($n \times r$)
q = physical coordinate vector ($n \times 1$)
r = measurement vector ($m \times 1$), number of control forces
R = solution to Ricatti equations ($2n \times 2n$)
S = state weighting matrix ($2n \times 2n$)
T = time, transformation matrix ($4n \times 2n$)
U = control weighting matrix ($r \times r$)
u = control force vector ($r \times 1$)
V, W = Y, Z translations
x = state vector ($2n \times 1$)
X, Y, Z = fixed reference
y = right eigenvector
Y = system right eigenvectors (modal matrix)
z = left eigenvector
Z = system left eigenvectors (modal matrix)
α = state vector (subset of ζ)
B, Γ = Y, Z rotations
ζ = complex mode coordinate vector
η = state vector associated with ξ
λ = eigenvalue
ξ = normal mode coordinate vector
Φ = normal mode transformation matrix
ϕ = eigenvector
Ψ = complex mode transformation matrix

Subscripts

1, 2, 3 = bearing indices
j = station indices
L = left inverse
o = original high-order systems
α = terms associated with α
ξ, η, ζ = terms associated with ξ, η, ζ coordinates

Superscripts

-1 = inverse
i = imaginary part
r = real part
t = transpose
$\cdot$ = d/dt
$\hat{}$ = retained coordinates

where $D_\xi = \Phi^t D_q \Phi$ and $K_\xi = \Phi^t K_q \Phi$. If D_q is symmetric and also proportional, the D_ξ array is diagonal. Similarly, a symmetric K_q array leads to $K_\xi = \Omega$. Thus, the presence of gyroscopic and/or circulation terms in the q-coordinates results in ξ coordinate coupling.

The high-frequency modes are normally truncated in the transformation of Eq. (5) based on the assumption that most of the system's energy is contained in the lower few modes. Engineering judgment must, of course, be utilized in the process of selecting those modes to be retained. This choice is strongly dependent on the frequency content of the system excitation. For harmonic excitation, as considered here, the retention of a relatively small number of the lower frequency modes is usually adequate for an accurate reduced-order model. Modes with natural frequencies much higher than the excitation frequency are not strongly excited.

The reduced-order model of Eq. (6), written in first-order form, is

$$\dot{\eta} = A_\eta + B_\eta u + W_\eta f \tag{7}$$

where

$$A_\eta = \begin{bmatrix} -D_\xi & -K_\xi \\ I & 0 \end{bmatrix}, \; B_\eta = \begin{bmatrix} \Phi^t P \\ 0 \end{bmatrix}, \; W_\eta = \begin{bmatrix} \Phi^t \\ 0 \end{bmatrix}, \text{ and } \eta = \begin{bmatrix} \dot{\xi} \\ \xi \end{bmatrix} \tag{8}$$

Complex Mode Approach. A modal transformation, based on the physical coordinate state form of the system equations,

$$x \doteq Y\zeta = \sum_{j=1}^{2\hat{n}<2n} y_j \zeta_j \tag{9}$$

is defined where the columns of Y contain the complex right eigenvectors y_j ($j = 1, 2, \ldots, 2\hat{n}$) of the system. These vectors are obtained from the eigenvalue problem associated with the homogeneous form of Eq. (2), i.e.,

$$(A_x - \lambda_j I) y_j = 0 \tag{10}$$

where λ_j is the jth eigenvalue of the system associated with the right eigenvector y_j. Let Z represent a matrix of complex left eigenvectors z_j ($j = 1, 2, \ldots, 2\hat{n}$), which are obtained from the adjoint eigenvalue problem

$$(A_x^t - \lambda_j^* I) z_j = 0 \tag{11}$$

where λ_j^* is the conjugate to λ_j. It is convenient to binormalize the dual set of right and left eigenvectors so that $Z^t Y = I$, then this set also satisfies a second biorthogonality condition

$$Z^t A_x Y = A_\zeta \tag{12}$$

where A_ζ is a diagonal array of the system eigenvalues, λ_j.

The eigenvalues from Eq. (10) appear as complex conjugate pairs for underdamped modes and are purely real for overdamped modes. For stable linear systems, the real parts of all eigenvalues are nonpositive. The selection of the modes to be retained in the transformation of Eq. (9) requires careful consideration. The underdamped right eigenvectors appear in complex conjugate pairs and the superposition of the corresponding eigensolutions provides a real precessional mode solution. Thus, the transformation of Eq. (9) would generally contain the complex conjugate pairs of right eigenvectors associated with the lower frequency precession modes. In addition, any purely real modes with relatively large time constants would also be retained. A verification of the accuracy of a particular choice, however, can only be obtained by comparison with other choices and experience with particular types of applications.

The substitution of the transformation of Eq. (9) into the state equations, Eq. (2), and premultiplication by Z^t, and use of the biorthogonality conditions gives the reduce-order ($2\hat{n} < 2n$) state model

$$\begin{aligned} \dot{\zeta} &= A_\zeta \xi + u + W_\zeta f \\ r &= CY\zeta \end{aligned} \tag{13}$$

where $A_\zeta = Z^t A_X Y$, $B_\zeta = Z^t B_X$, $W_\zeta = Z^t W_X$. The control u and excitation f are real, while the other elements of this state equation are in terms of complex quantities. Since most readily available computational procedures are written in real form, it is convenient to separate Eq. (13) into real and imaginary parts as

$$\begin{bmatrix} \dot{\zeta}^r \\ \dot{\zeta}^i \end{bmatrix} = \begin{bmatrix} A_\zeta^r & -A_\zeta^i \\ A_\zeta^i & A_\zeta^r \end{bmatrix} \begin{bmatrix} \zeta^r \\ \zeta^i \end{bmatrix} + \begin{bmatrix} B_\zeta^r \\ B_\zeta^i \end{bmatrix} u + \begin{bmatrix} W_\zeta^r \\ W_\zeta^i \end{bmatrix} f$$

$$r = C\,[Y^r - Y^i] \begin{bmatrix} \zeta^r \\ \zeta^i \end{bmatrix}$$

or

$$\begin{aligned} \dot{\zeta}' &= A_{\zeta'} \zeta' + B_{\zeta'} u + W_{\zeta'} f \\ r &= CY_{\zeta'} \zeta' \end{aligned} \tag{14}$$

where the order has been increased to $4\hat{n}$.

At this point, the analysis is restricted to only underdamped systems. In these cases the modes appear only on complex conjugate pairs and it is possible to reduce the $4\hat{n}$ order of Eq. (14) back to $2\hat{n}$. This is accomplished by noting the relation

$$\zeta' = \begin{bmatrix} \zeta^r \\ \zeta^i \end{bmatrix} = \begin{bmatrix} T^r & 0 \\ 0 & T^i \end{bmatrix} \begin{bmatrix} \alpha^r \\ \alpha^i \end{bmatrix} = T\alpha \tag{15}$$

Both T^r and T^i arrays consist of $2\hat{n}$ rows and $\hat{n}$ columns of zero elements except for

$$T^r_{(2j-1,j)} = 1 = T^r_{(2j,j)} \text{ for } j = 1, 2, 3, \ldots, \hat{n},$$

and

$$T^i_{(2j-1,j)} = 1 = -T^i_{(2j,j)} \text{ for } j = 1, 2, 3, \ldots, \hat{n}.$$

The elements of ζ^r and ζ^i consist of the real an imaginary parts of the elements ζ for the odd j integers (i.e., $j = 1, 3, \ldots, (2\hat{n} - 1)$). Thus, the relation of Eq. (15) provides a simple method for retaining only one of the modal coordinates associated with each retained complex conjugate pair. In this application, the modal coordinates with a positive imaginary part are retained. The introduction of relation (15) into Eq. (14) and premulitplication by the left inverse of T (see Noble and Daniel, 1977, pp. 15–17) gives

$$\begin{aligned} \dot{\alpha} &= A_\alpha \alpha + B_\alpha u + W_\alpha f \\ r &= C_\alpha \alpha \end{aligned} \tag{16}$$

where $A_\alpha = T_L^{-1} A_{\zeta'} T$, $B_\alpha = T_L^{-1} B_{\zeta'}$, $W_\alpha = T_L^{-1} W_{\zeta'}$, and $C_\alpha = CY_{\zeta'} T$. It is useful here to note the identity $2T_L^{-1} = T^t$.

Optimal Output Feedback Controller Design

Basic Concepts. The following explanation of the procedure used in designing the control system is presented in terms of physical coordinates. The same procedure, however, can also be developed in terms of complex mode coordinates through the modal transformation defined by Eq. (9). Equation (2), without the unbalance forcing term $W_x f$, is

$$\dot{x} = A_x x + B_x u \tag{17}$$

For a full-state linear feedback control, the control input, associated with the physical state x, can be written as

$$u_x = -K_x x \tag{18}$$

where K_x is a state feedback gain matrix obtained based on minimization of the selected performance index. One can either measure all required states or use an observer to reconstruct the required states; however, the former involves a larger number of sensors for larger-order systems and the latter requires high-speed computation for on-line state estimation. The following provides a procedure to avoid the above practical prob-

lems. The objective here is to obtain a control input, associated with the system output r,

$$u_r = -K_r r \tag{19}$$

such that $u_r = u_x$. An error vector $e = u_x - u_r$ is defined and the introduction of relations from Eqs. (4), (18), and (19) with the assumption that the C_x is properly selected such that the output of the least-squares controller approaches that of the full-state feedback controller, then provides

$$e \doteq (K_x - K_r C_x)x \tag{20}$$

For the special case when

$$K_r C_x = K_x \tag{21}$$

the error vector e is obviously null. Unfortunately Eq. (21) does not hold unless C_x is an identity matrix (or equivalently $r = x$), and K_r and K_x are of the same size. Generally, the size of K_r is much smaller than that of K_x. The number of accessible sensor locations is usually severely limited. A least-squares solution based on minimizing the quadratic error $(K_r C_x - K_x)(K_r C_x - K_x)^t$ can be obtained (Noble, 1988, p.69), however, and is shown below that

$$K_r = K_x C_x^t (C_x C_x^t)^{-1}. \tag{22}$$

It is possible to arrange the order of the elements of the state vector x such that the observation matrix C_x has the form

$$C_x = [I_m \; 0] \tag{23}$$

where m is the number of measured states. Substituting Eqs. (22) and (23) into Eq. (21), and utilizing the fact that $C_x C_x^t = m$, yields

$$e^t e = \frac{1}{m^2} x^t \begin{bmatrix} 0_m & 0 \\ 0 & -I_{(2n-m)} \end{bmatrix} K_x^t K_x \begin{bmatrix} 0_m & 0 \\ 0 & -I_{(2n-m)} \end{bmatrix} x \tag{24}$$

Equation (24) provides two ways to reduce the error e. The first is to increase the number of measured states m. As m increases toward $2n$ the error e decreases, and the case of $m = 2n$ corresponds to all states being measured with $e = 0$. The second method is to design K_x such that the elements associated with the measured states are much larger in magnitude tan those associated with the unmeasured states while the desired performance is maintained. The latter can be achieved by minimizing the following performance index, which includes the system outputs, r, instead of the system states, x.

$$J = \lim_{T \to \infty} \frac{1}{2T} \int_0^T (r^t S_r r + u_w U u)\, dt \tag{25}$$

In Eq. (25), S_r is a positive semidefinite state weighting matrix, U a positive definite control weighting matrix, u_w a weighting constant, and r is the system output as defined in Eq. (4).

Linear Quadratic Regulator Design. The physical state is related to the modal state through the transformation of Eq. (9). This relation may be separated into the real and imaginary components and written equivalently, using Eq. (15), as

$$x = \Psi_o \alpha_o \doteq \Psi_\alpha \alpha \tag{26}$$

where $\Psi_\alpha = [Y^r \; -Y^i]$ T and α are associated with the reduced-order model, and Ψ_o and α_o are associated with the full-order model. In addition, the relation between α_o and α as

$$\alpha = T_\alpha \alpha_o \tag{27}$$

With this relation, the performance index from Eq. (25) may be rewritten as

$$J = \lim_{T \to \infty} \frac{1}{2T} \int_0^T (\alpha^t S_{\alpha r} \alpha + u_w u^t U u)\, dt \tag{28}$$

where $S_{\alpha r} = \Psi_\alpha^t C^t S_r C \Psi_\alpha$ is a weighing matrix associated with the retained complex coordinates. The steady-state Ricatti equation associated with Eq. (28) is

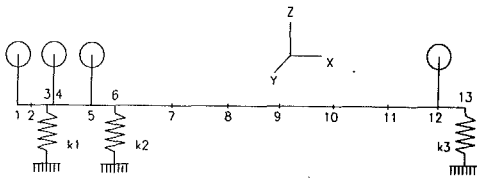

Fig. 1 Rotor schematic of three-bearing system

$$R_\alpha A_\alpha + A_\alpha^t R_\alpha - \frac{1}{u_w} R_\alpha B_\alpha U^{-1} B_\alpha^t R_\alpha + S_{\alpha r} = 0 \tag{29}$$

and the optimal control law is

$$u = -G_\alpha \alpha \tag{30}$$

where

$$G_\alpha = U^{-1} B_\alpha^t R_\alpha.$$

Introducing Eq. (27) into Eq. (30) provides

$$u = -G_\alpha T_\alpha \alpha_o \tag{31}$$

Using Eqs. (4) and (26), Eq. (19) can be written as

$$u_r = -K_r C \Psi_\alpha \alpha_o \tag{32}$$

or

$$u_r = -K_r C_\alpha \alpha_o \tag{33}$$

where $C_\alpha = C\Psi_\alpha$. Similar to the procedure used to obtain Eq. (22), the objective here is to determine K_r such that u_r in Eq. (33) is a good approximation of u in Eq. (31) for any selected observation matrix C. The least-square solution associated with Eq. (31) and (33) is

$$K_r = G_\alpha T_\alpha C_\alpha^t (C_\alpha C_\alpha^t)^{-1} \tag{34}$$

The number of measured states of matrix C in Eq. (32) should generally be equal to the number of rows in matrix C as defined in Eq. (28) for best performance. One can use less measured states, however, than the output r to be minimized in the performance index, Eq. (25), but a price of degrading the controller performance. In the next section, an example is given for demonstration of the proposed procedure. Several possible choices for the perfomance index are also tested with this example for comparison purposes.

Example

Simulations are performed on a large-order rotordynamic system so as to test the optimal active control procedures presented above. The test rotor configuration is shown in Fig. 1 and it consists of four rigid disks, three isotropic bearings, and twelve rotating shafts elements. The discrete model of this system is a finite element based model (Nelson and McVaugh, 1976), and it utilizes 13 stations and 2 translation (V_j, W_j) and 2 rotation (B_j, Γ_j) coordinates at each station j ($j = 1, 2, \ldots, 13$) for a total of 52 degrees of freedom. The geometric and material properties are listed in Tables 1 and 2. The mass unbalance for this system is assumed to be localized at each disk and is arbitrarily chosen in phase and of equal cg eccentricity. A plot of the natural frequencies of whirl versus the rotor spin speed is presented in Fig. 2. The first three forward critical speeds are 649, 872, 1320 rad/s and the first three backward critical speeds are 479, 718, 949 rad/s.

The control inputs are taken as translation forces at station 7 in the perpendicular Y, Z directions. The modal displacement of station 7 is relatively large for each of the first several modes. In the simulations presented here, a spin speed of 649 rad/s is chosen such that it coincides with the first forward critical speed. The professional modes are circular here since the bearings are isotropic and the first three forward modes are shown in Fig. 3(a) corresponding to the spin speed of 649 rad/s. The right eigenvectors associated with these precessional modes are

Table 1 Mass properties of rigid disks

Station No.	Mass (Kg)	Polar Inertia (Kg-m^2)	Transverse Inertia (Kg-m^2)	cg Eccentricity (μm)
1	11.38	19.53	9.82	25.4
4	7.88	16.70	8.35	25.4
5	7.70	17.61	8.80	25.4
12	21.70	44.48	22.24	25.4

Table 2 Shaft and bearing information

Station No.	Axial Distance to Station (cm)	Other Properties
1	0.0	shaft : Inner Radius = 1.68 cm
2	4.29	Outer Radius = 2.95 cm
3	8.89	Elastic modulus = 2.069x10^{11} N/m^2
4	10.49	Density = 8193.0 Kg/m^3
5	20.17	bearing :
6	27.69	$k_1 = k_2 = k_3 = 175 \times 10^5$ N/m
7	44.20	$c_1 = c_2 = c_3 = 900$ N-Sec/m
8	59.44	
9	74.68	
10	89.92	
11	105.16	
12	120.14	
13	127.94	

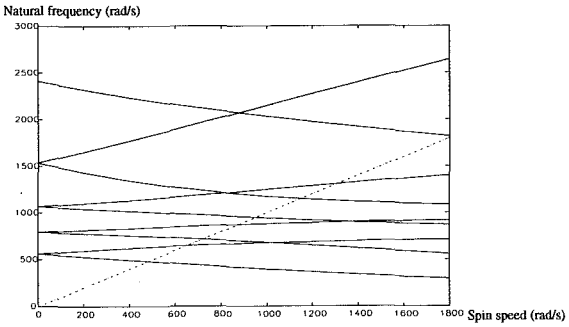

Fig. 2 Whirl speed map

used in designing the controller for the complex mode approach. The normal modes are independent of the rotor spin speed and are obtained from the undamped symmetric eigenvalue problem related to Eq. (1). The first three planar modes are also displayed in Fig. 3(*b*) and provide a graphic comparison with the gyroscopic influenced precessional modes. It should be noted that the superposition of two planar normal modes of the same frequency and amplitude can form a forward or backward whirling mode of the same frequency depending on the phasing. The three planar normal modes in Fig. (3*b*) are retained for both the horizontal and vertical planes for the controller design using normal modes. This is equivalent to retaining three forward and three backward precessional modes where the forward-backward pair are of the same frequency.

The frequency response functions of the *Y*-direction displacement at station 12 due to the *Y*-direction force input at station 7, associated with the reduced-order model (12 states), are plotted in Fig. 4 for both the complex and normal model approaches. The corresponding frequency response function for the original 52 degree-of-freedom system is also included in these graphs. The reduced-order frequency response functions are both quite accurate at the low-frequency range with slightly better accuracy when using complex modes. As the frequency increases above the highest retained frequency mode,

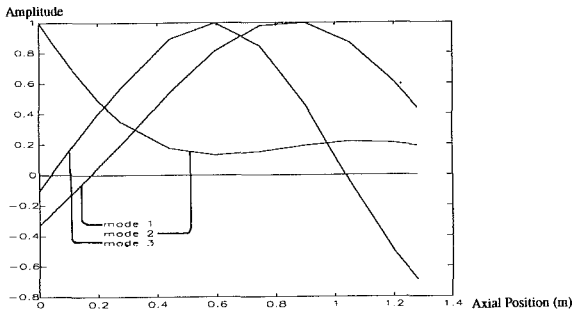

Fig. 3(*a*) Forward precessional modes (first three modes at 649, 854, and 1177 rad/s)

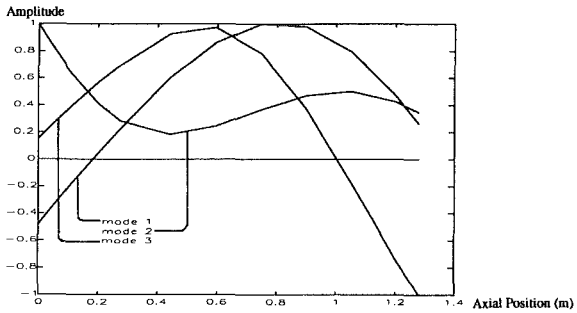

Fig. 3(*b*) Normal modes (first three modes at 561, 796, and 1070 rad/s)

Fig. 3 System mode shapes

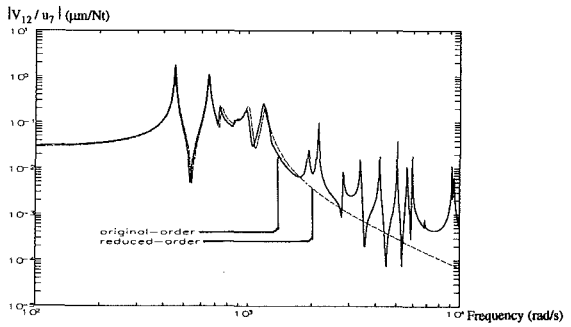

Fig. 4(*a*) Normal mode reduced model (twelve eigenvalues retained)

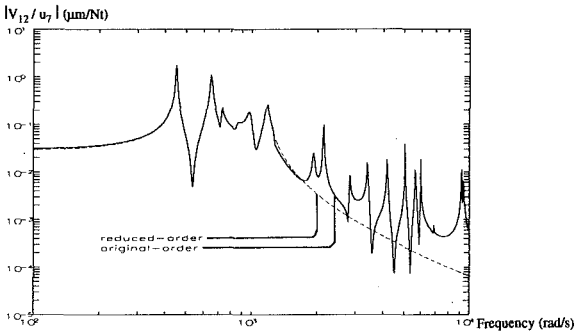

Fig. 4(*b*) Complex mode reduced model (twelve eigenvalues retained)

Fig. 4 Frequency response functions of reduced models

both reduced-order functions deteriorate as expected. Note that the complex modes are eigenmodes of the asymmetric system while the normal modes are assumed modes.

The controlled and uncontrolled time responses, which are associated with Eq. (25), from stations 1, 7, and 12, and the control input forces (*Y* and *Z* directions) from station 7 of the original systems, Eq. (2), for measurements from different numbers of stations are shown in Fig. 5. In this work, four

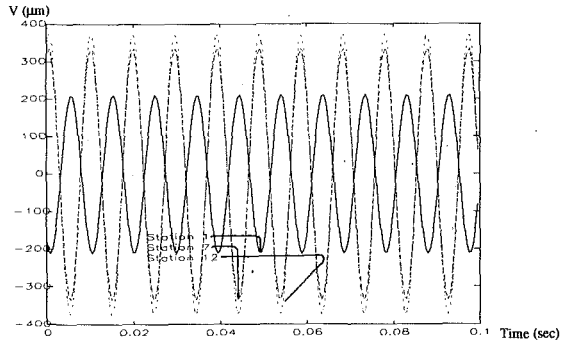

Fig. 5(*a*) Uncontrolled responses at stations 1, 7, and 12

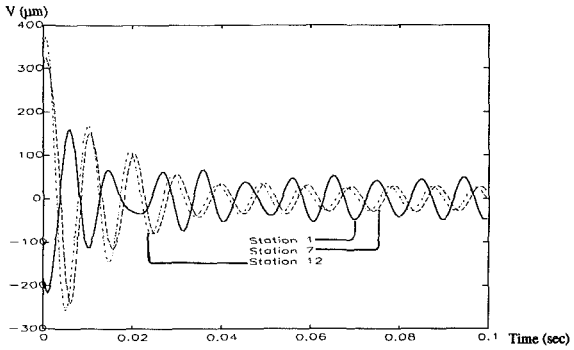

Fig. 5(*b*) Controlled responses: full-state measurements

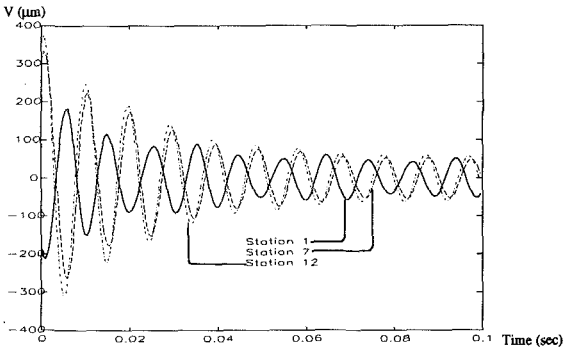

Fig. 5(*c*) Controlled responses: four measured states from station 7

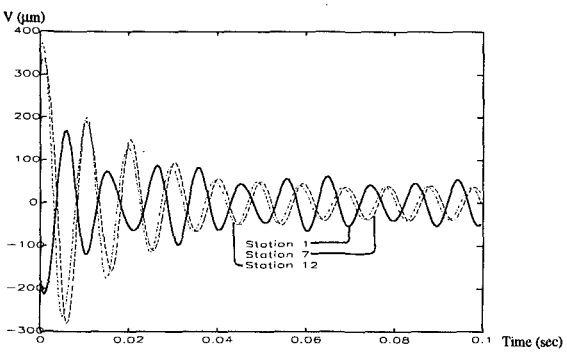

Fig. 5(*d*) Controlled responses: eight measured states from station 7 and 12

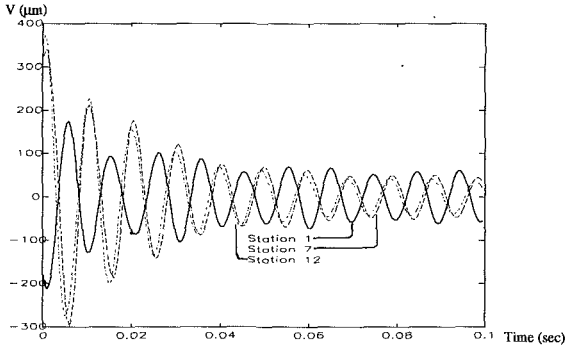

Fig. 5(*e*) Controlled responses: twelve measured states from stations 1, 7, and 12

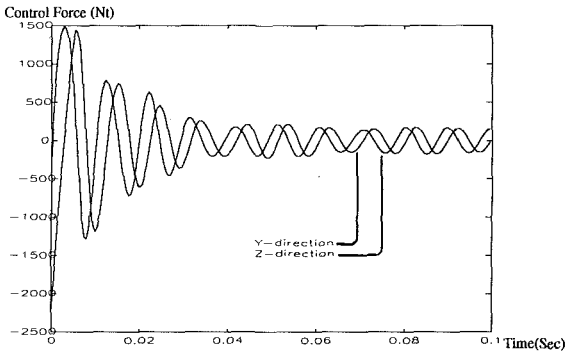

Fig. 5(*f*) Control forces: full-state measurements

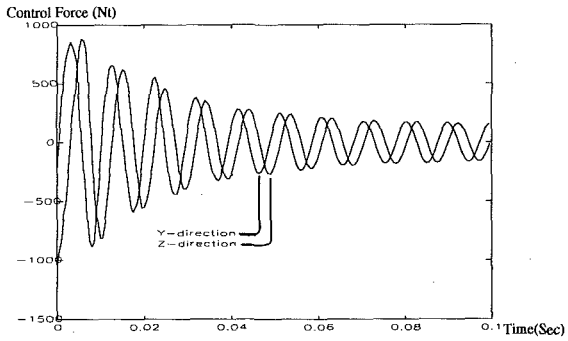

Fig. 5(*g*) Control forces: four measured states from station 7

Fig. 5 Responses of the original system

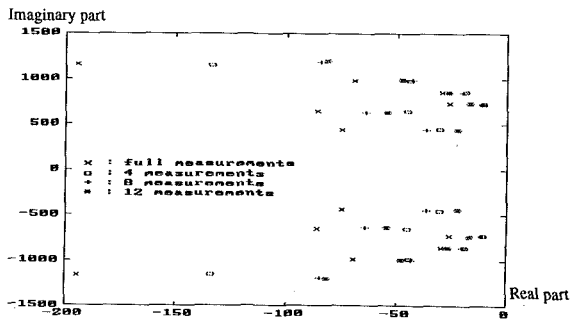

Fig. 6 Eigenvalues of closed-loop system: various numbers of measured states

measured states are made per selected station, and they are the two translational displacements and two translational velocities in Y, Z directions. S_{or} is chosen to be an identity matrix and u_w is selected as 10^{-7} in this example. Figure 5 shows that the controller performance associated with eight measured states (stations 7 and 12) are almost the same as those from twelve measured states (stations 1, 7, and 12), while the controller performance from four measured states (station 7) shows only slight degradation. Figure 6 shows the eigenvalues of the closed-loop systems for different numbers of measured states. In addition to slight degradation of the performance, using smaller number of measured states also causes a less stable

closed-loop system based on the set of eigenvalues closest to the imaginary axis in Fig. 6.

Simulation of the time response for the controller system using a design based on minimizing the performance index Eq. (35) and Eq. (36) was performed; however, the results are stated below without showing the responses due to the limitation of paper length. For both performance indexes, Eqs. (35) and (36), the magnitude of the weighting matrices is selected such that the control input magnitude is limited. The performance of these two controllers is about the same as the associated with a controller designed by minimizing Eq. (25); however, the controller associated with Eq. (36) provides slightly better results:

$$J_x = \lim_{T\to\infty} \frac{1}{2T} \int_0^T (x^t S_x x + u_w u^t U u)\, dt \tag{35}$$

$$J_\sigma = \lim_{T\to\infty} \frac{1}{2T} (\alpha^t S_\alpha \alpha + u_w u^t U u)\, dt \tag{36}$$

Note that all of the LQ regulators are solved in complex mode coordinates, Eq. (16), through a modal transformation, and only the lowest twelve eigenvalues are retained. Also, the state weighting matrices S_r, S_x, and S_α are selected to be identity matrices, and S_r and S_x are then transformed into complex mode coordinates. S_α is associated with modal coordinates throughout the analysis, and u_w is selected to be 10^{-7} for both cases.

No spillover problems were found for all the collocated configurations simulated, and this was also true for simulations at spin speeds of 600, 800, and 1000 rad/s. However, the following noncollocated configurations were tested and resulted in spillover instability: twelve measured states from stations 1, 5, and 12; eight measured states from stations 1 and 12; four measured states from station 12 each with two control forces at station 7. Spin speeds of 649 and 900 rad/s were utilized in these noncollocated configurations.

Conclusions

This work introduces a systematic complex-mode procedure for coordinate reduction of high-order asymmetric dynamic systems, and for their optimal control system design. The coordinate transformation matrices are derived so that an LQ regulator can be designed. For asymmetric dynamic systems, the normal mode approach for reduction of the equation order does not decouple the system equations, while the complex mode approach provides full coordinate decoupling. The complex mode approach is computationally more involved than the normal mode approach; however, the procedures are still straightforward, and result in improved accuracy.

Full-state measurement for high-order systems is usually not possible. In order to utilize full-state feedback control realistically, either an observer or an "optimal output feedback" procedure can be used. The advantage of using an observer is that the control system only requires the measurement of a small number of system responses so long as the open-loop system is observable. This is desirable for physical systems with limited sensor accessibility. A disadvantage, however, is that the closed-loop system might be quite sensitive to certain system parameter variations (Ridgy and Banda, 1986), and the process of obtaining the estimation of all the states requires particularly fast computational equipment. This is especially difficult for high-speed rotor systems.

The "output feedback" procedure as presented by Palazzolo (1989) provides the advantage that on-line state estimation (an observer) is not required; however, the number of sensors must be at least as large as the number of eigenvectors retained in the reduced order model, i.e., three locations along the shaft were monitored for a reduced model with twelve eigenvalues to control the vibration. The proposed LQR-based least-squares output feedback procedure eliminates the limitation on the number of sensors while providing acceptable performance. The lateral vibrations of a rotor system can be effectively controlled, based on the simulation results, by monitoring one single location along the shaft for a given spin speed. One disadvantage is that the required accuracy cannot be considered before performing the design procedure, and improper selection of the measured responses may destabilize the closed-loop system. The use of either an observer or an "optimal output feedback" method may introduce additional stability problems, such as the stability robustness for the closed-loop control system, which need to be considered in the optimal control design of a particular problem.

References

Bryson, A. E., Jr., and Ho, Y. C., 1975, *Applied Optimal Control*, Hemisphere Publishing Corp. New York.

Burrow, C. R., and Sahinkaya, M. N., 1983, "Vibration Control of Multimode Rotor-Bearing Systems," *Proc. R. Soc. Lond.*, Vol. A386, pp. 77–94.

Cannon, R. H., and Schmitz, E., 1984, "Precise Control of Flexible Manipulators," Robotics Research, The 1st Int. Symp., M. Brady and R. Paul, eds., MIT Press, Cambridge, MA, pp. 841–861.

Kirk, D. E., 1970, *Optimal Control Theory: An Introduction*, Prentice-Hall, Englewood Cliffs, N.J.

Kwakernaak, H., and Sivan, R., 1972, *Linear Optimal Control Systems*, Wiley-Interscience, New York.

Nelson, H. D., and McVaugh, J. M., 1976, "The Dynamics of Rotor-Bearing Systems Using Finite Elements," ASME *Journal of Engineering for Industry*, Vol. 98, pp. 593–600.

Noble, B., and Daniel, J. W., 1977, *Applied Linear Algebra*, Prentice-Hall, Englewood Cliffs, NJ.

Palazzolo, A. B., Lin, R. R., Kascak, A. F., and Alexander, R. M., 1989, "Active Control of Transient Rotordynamic Vibration by Optimal Control Methods," ASME *Journal of Engineering for Gas Turbines and Power*, Vol. 111, pp. 264–270.

Ridgy, A., and Banda, C., 1986, "Introduction to Robust Multivariable Control," USAF, Technical Report, AFWAL-TR-85-3102.

Salm, J., and Schweitzer, G., 1984, "Modeling and Control of a Flexible Rotor With Magnetic Bearings," *Proceedings of Conference on Vibrations in Rotating Machinery*, York, United Kingdom, Paper No. C277.

Skelton, R. E., 1988, *Dynamic Systems Control: Linear System Analysis and Synthesis*, Wiley, New York.

Stanway, R., and Burrows, C. R., 1981, "Active Vibration Control of a Flexible Rotor on Flexibly-Mounted Journal Bearings," ASME *Journal of Dynamic Systems, Measurement, and Control*, Vol. 103, pp. 383–388.

Stanway, R., and O'Reilly, J., 1984, "State-Variable Feedback Control of Rotor-Bearing Suspension Systems," *Proceedings of Conference of Vibrations in Rotating Machinery*, York, United Kingdom, Paper No. C274.

Ulsoy, A. G., 1984, "Vibration Control in Rotating or Translating Elastic Systems," ASME *Journal of Dynamic Systems, Measurement, and Control*, Vol. 106, pp. 6–14.

G. W. Fan
Chief Engineer,
3-I Scientific Development Inc.,
Tempe, AZ 85282

H. D. Nelson
Professor,
Department of Engineering,
Texas Christian University,
Fort Worth, TX 76129

P. E. Crouch
Professor,
Center for Systems Science
and Engineering.

M. P. Mignolet
Assistant Professor,
Department of Mechanical and
Aerospace Engineering.

Arizona State University,
Tempe, AZ 85287-6106

LQR-Based Least-Squares Output Feedback Control of Rotor Vibrations Using the Complex Mode and Balanced Realization Methods

The complex mode and balanced realization methods are used separately to obtain reduced-order models for general linear asymmetric rotor systems. The methods are outlined and then applied to a typical rotor system represented by a 52 degree-of-freedom finite element model. The accuracy of the two methods is compared for this model and the complex model method is found to be more accurate than the balanced realization method for the desired frequency bandwidth and for models of the same reduced order. However, with some limitations, it is also shown that the balanced realization method can be applied to the reduced-order complex mode model to obtain further order reduction without loss of model accuracy. A "Linear-Quadratic-Regulator-based least-squares output feedback control" procedure is developed for the vibration control of rotor systems. This output feedback procedure eliminates the requirement of an observer for the use of an LQ regulator, and provides the advantage that the rotor vibration can be effectively controlled by monitoring only one single location along the rotor shaft while maintaining an acceptable performance. The procedures presented are quite general and may be applied to a large class of vibration problems including rotordynamics.

Introduction

The control system design for asymmetric rotordynamic system initially requires the development of a discrete mathematical model. For most realistic rotor systems these models are typically tens of degrees of freedom. Active control of lateral vibrations in rotordynamic systems has been studied by many researchers within the last several years. Several researchers have successfully used the normal mode approach to obtain a reduced-order system from an original high-order model. These normal modes do not include gyroscopic and/or circulation effects and as a result they do not decouple the asymmetric system equations. This work introduces a consecutive application approach of the complex mode procedure (Fan and Nelson, 1991) and the balanced truncation method (Moore, 1981) to deal with such systems in the process of LQR design.

A full-state feedback control system does not require an observer and this is a primary motivation for using an optimal output feedback technique. In addition, the use of an observer has the following disadvantages: (*a*) Very high-speed computation is needed for on-line state estimation, and this is especially difficult to implement for high-speed rotor systems. (*b*) The cost is much higher for fabrication of an observer than for implementation of an optimal output feedback procedure. (*c*) Many more components are required for an observer than for an output feedback controller, and this results in less accuracy and less reliability. This work introduces an "LQR-based least-squares output feedback control" procedure for the vibration control of rotor systems to eliminate the requirement of an observer while using the LQR control.

Moore (1981) has shown that every system can be brought to a balanced form via a balancing transformation, and then a reduced-order model can be obtained by truncating the states associated with the smaller controllability (or observability) grammians. This balancing procedure was tested on two example systems that possess real eigenvalues, and was proved to produce accurate reduced-order models. Laub et al. (1987) presented an algorithm for computing the balancing transformation matrix directly from any given state space realization. Safonov and Chiang (1988) introduced another algorithm for implementing the balancing and truncation model reduction procedure presented by Moore (1981), but unlike Moore's original algorithm, these algorithms bypass the numerically delicate preliminary step of computing a balanced realization of the

Contributed by the International Gas Turbine Institute and presented at the 37th International Gas Turbine and Aeroengine Congress and Exposition, Cologne, Germany, June 1-4, 1992. Manuscript received by the International Gas Turbine Institute January 16, 1992. Paper No. 92-GT-9. Associate Technical Editor: L. S. Langston.

system. In other words, a not-necessarily-balanced state-space realization of Moore's reduced model can be computed directly without balancing the system first.

Palazzolo et al. (1989) experimentally demonstrated the success of an output feedback procedure with the limitation that the number of measured states has to be equal to the number of eigenvalues retained in the reduced-order model. He studied the active control of transient lateral rotor vibrations due to a sudden change in imbalance, such as caused by loss of a blade, by utilizing optimal control methods. A seven-mass rotor system was considered and a normal mode approach was used to obtain a reduced-order model. Comparisons of responses were made for various configurations of sensors and actuators. The spillover effect was examined by comparing results from collocated and noncollocated sensor configurations. Results were verified by experimental work. A filter was used in the experiments to prevent spillover effects for the noncollocated case. In the particular example used in his work, the number of measured states is 12, which is equal to the number of eigenvalues in the reduced-order rotor model. The least-squares output feedback procedure presented in this work requires only 4 measured states (instead of 12) from one single location while providing an acceptable performance.

Salm and Schweitzer (1984) discussed the modeling and control of a flexible rotor using magnetic bearings. They used a normal mode approach to obtain a reduced-order system, and, based on this system, designed an output feedback controller that guarantees the closed-loop stability for the original high-order system despite some spillover effects. Ulsoy (1984) investigated an optimal active control scheme by pole assignment and the effects of observation and control spillover in a translating elastic system. His method was verified by using simulation results of two examples based on both physical coordinates and normal mode coordinates, respectively.

Cannon and Schmitz (1984) studied the precise control of a one-armed flexible manipulator without gyroscopic effects. They used a normal mode transformation to obtain a reduced-order model, and then designed an optimal controller based on this model. The system modal parameters in their work were measured and they were successful in experimentally verifying the validity of the proposed approach.

In this present work, the LQR-based least-squares output feedback controllers are designed based on the reduced-order model by using the complex mode and balanced realization methods. Controlled responses of the original high-order system with the reduced-order controllers are shown for comparison purposes. A 52 degree-of-freedom finite element based model for a rotordynamic system is used as an example to illustrate the proposed procedure.

System Equations

The general linear matrix equation of motion of an nth order rotordynamic system, in terms of physical coordinates, is of the form

$$M_q\ddot{q} + D_q\dot{q} + K_q q = f + Pu \tag{1}$$

The M_q, D_q, and K_q arrays represent the mass, dissipation/gyroscopic, and stiffness/circulation properties of the rotor system. The M_q array is usually symmetric and positive definite while the D_q and K_q arrays are generally asymmetric. These asymmetric arrays can be written as the sum of a symmetric and skew-symmetric component. The symmetric part of the D_q array is referred to as the dissipation matrix while the skew-symmetric part is the gyroscopic matrix. The symmetric part of the K_q array is the system stiffness matrix while the skew-symmetric part is referred to as the circulation matrix. In addition, D_q and K_q are generally a function of the rotor spin speeds. The excitation force f is usually dominated by harmonic terms associated with the synchronous rotating unbalance of

Nomenclature

A = system matrix ($2n \times 2n$)
B = control distribution matrix ($2n \times r$)
c = bearing damping coefficient
C = output matrix ($m \times 2n$)
D = dissipation/gyro matrix ($n \times n$)
E = elastic modulus
f = unbalance force vector ($n \times 1$)
G = optimal gain matrices ($r \times 2n$), system transfer function
I = identity matrices ($n \times n$)
J = performance index
k = bearing stiffness
K = stiffness/circulation matrix ($n \times n$)
m = number of outputs
M = mass matrix ($n \times n$)
n = system order
P = control distribution matrix ($n \times r$)
q = physical coordinate vector ($n \times 1$)
r = measurement vector ($m \times 1$), number of control forces
R = solution to Ricatti equations ($2n \times 2n$)
S = state weighting matrix ($2n \times 2n$)
T = time, transformation matrix ($4n \times 2n$)
U = control weighting matrix ($r \times r$)
u = control force vector ($r \times 1$), weighting constant
V, W = Y, Z translations
W = controllability and observability grammiam
x = state vector ($2n \times 1$)
X, Y, Z = fixed reference
y = right eigenvector
Y = system right eigenvectors (modal matrix)
z = left eigenvector
Z = system left eigenvectors (modal matrix)
α = state vector (subset of ζ)
B, Γ = Y, Z rotations
ζ = complex mode coordinate vector
λ = eigenvalue
Ξ = controllability and observability grammiam
σ = singular value
ϕ = eigenvector
Ψ = complex mode transformation matrix

Subscripts

1, 2, 3 = bearing indices
b = balanced system
c = controllability
j = station indices
o = observability
r = balanced reduced-order system
L = left inverse
α = corresponding terms associated with α
ζ = corresponding terms associated with complex mode coordinate

Superscripts

-1 = inverse
i = imaginary part
r = real part
t = transpose
$\cdot$ = d/dt
$\hat{}$ = number of coordinates retained in complex mode method
$\tilde{}$ = number of coordinates retained in balanced truncation method

the rotating assembly. The P array identifies the physical location of the external forces included in the control vector u. The speed dependency of the unbalance forces, gyroscopic moments, and the bearing forces also requires spin speed dependency for the control action. In first-order state form, Eq. (1) is written as

$$\dot{x} = A_x x + B_x u + W_x f \tag{2}$$

where $x = [\dot{q}^t \ q^t]^t$ is the system state and $B_x = W_x P$ is the control matrix with

$$A_x = \begin{bmatrix} -M_q^{-1} D_q & -M_q^{-1} K_q \\ I & 0 \end{bmatrix}, \text{ and } W_x = \begin{bmatrix} M_q^{-1} \\ 0 \end{bmatrix} \tag{3}$$

The partial state measurements represented by the vector r are expressed by an output equation of the form

$$r = C_x x \tag{4}$$

Modal Reduction

Complex Mode Approach. A mode transformation, based on the physical coordinate state form of the system equations,

$$x \doteq Y\zeta = \sum_{j=1}^{2\hat{n}<2n} y_j \zeta_j \tag{5}$$

is defined where the columns of Y contain the complex right eigenvectos y_j ($j = 1, 2, \ldots, 2\hat{n}$) of the system. These vectors are obtained from the eigenvalue problem associated with the homogeneous form of Eq. (2), i.e.,

$$(A_x - \lambda_j I) y_j = 0 \tag{6}$$

where λ_j is the jth eigenvalue of the system associated with the right eigenvector y_j. Let Z represent a matrix of complex left eigenvectors z_j ($j = 1, 2, \ldots, 2\hat{n}$), which are obtained from the adjoint eigenvalue problem

$$(A_x^t - \lambda_j^* I) z_j = 0 \tag{7}$$

where λ_j^* is the conjugate of λ_j. It is convenient to binormalize the dual set of right and left eigenvectors so that $Z^t Y = I$, then this set also satisfies another biorthogonality condition

$$Z^t A_x Y = A_\zeta \tag{8}$$

where A_ζ is a diagonal array of the system eigenvalues, λ_j.

The eigenvalues from Eq. (6) appear as complex conjugate pairs for underdamped modes and are purely real for overdamped modes. For stable linear systems, the real parts of all eigenvalues are nonpositive. The selection of the modes to be retained in the transformation of Eq. (5) requires careful consideration. The underdamped right eigenvectors appear in complex conjugate pairs and the superposition of the corresponding eigensolutions provides a real precessional mode solution. Thus, the transformation of Eq. (5) would generally contain the complex conjugate pair right eigenvectors associated with the lower frequency precession modes. In addition, any purely real modes with relatively large time constants would also be retained. A verification of the accuracy of a particular choice, however, can only be obtained by comparison with other choices and experience with particular types of applications.

The substitution of the transformation of Eq. (5) into the state equations, Eq. (2), and premultiplication by Z^t, and use of the biorthogonality conditions gives the reduced-order ($2\hat{n} < 2n$) state model

$$\begin{aligned} \dot{\zeta} &= A_\zeta \zeta + B_\zeta u + W_\zeta f \\ r &= C Y \zeta \end{aligned} \tag{9}$$

where $A_\zeta = Z^t A_x Y$, $B_\zeta = Z^t B_x$, $W_\zeta = Z^t W_x$. The control u and excitation f are real while the other elements of this state equation are in terms of complex quantities. Since most readily available computational procedures are written in real form, it is convenient to separate Eq. (9) into real and imaginary parts. Equation (9) may then be written as

$$\begin{bmatrix} \dot{\zeta}^r \\ \dot{\zeta}^i \end{bmatrix} = \begin{bmatrix} A_\zeta^r & -A_\zeta^i \\ A_\zeta^i & A_\zeta^r \end{bmatrix} \begin{bmatrix} \zeta^r \\ \zeta^i \end{bmatrix} + \begin{bmatrix} B_\zeta^r \\ B_\zeta^i \end{bmatrix} u + \begin{bmatrix} W_\zeta^r \\ W_\zeta^i \end{bmatrix} f$$

$$r = C[Y^r - Y^i] \begin{bmatrix} \zeta^r \\ \zeta^i \end{bmatrix}$$

or

$$\begin{aligned} \dot{\zeta}' &= A_{\zeta'} \zeta' + B_{\zeta'} u + W_{\zeta'} f \\ r &= C Y_{\zeta'} \zeta' \end{aligned} \tag{10}$$

where the order has been increased to $4\hat{n}$.

At this point, the analysis is restricted to only those systems that possess solely underdamped modes. In this case the modes appear only in complex conjugate pairs and it is possible to reduce the $4\hat{n}$ order of Eq. (10) back to $2\hat{n}$. This is accomplished by noting the following relation:

$$\begin{bmatrix} \zeta^r \\ \zeta^i \end{bmatrix} = \begin{bmatrix} T^r & 0 \\ 0 & T^i \end{bmatrix} \begin{bmatrix} \alpha^r \\ \alpha^i \end{bmatrix}$$

or

$$\zeta' = T\alpha \tag{11}$$

Both T^r and T^i arrays consist of $2\hat{n}$ rows and $\hat{n}$ columns of zero elements except for

$$T^r_{(2j-1,j)} = 1 = T^r_{(2j,j)} \quad \text{for} \quad j = 1, 2, 3, \ldots, \hat{n},$$

and

$$T^i_{(2j-1,j)} = 1 = -T^i_{(2j,j)} \quad \text{for} \quad j = 1, 2, 3, \ldots, \hat{n}.$$

The elements of ζ^r and ζ^i consist of the real and imaginary parts of the elements ζ for the odd j integers (i.e., $j = 1, 3, \ldots, (2\hat{n} - 1)$). Thus, the relation of Eq. (1) is simply a method of retaining only one of the modal coordinates associated with each retained complex conjugate pair. In this application, the modal coordinates with a positive imaginary part are retained. The introduction of relation (11) into Eq. (10) and premultiplication by the left inverse of T (see Noble and Daniel, 1977, pp. 15–17) gives

$$\begin{aligned} \dot{\alpha} &= A_\alpha \alpha + B_\alpha u + W_\alpha f \\ r &= C_\alpha \alpha \end{aligned} \tag{12}$$

where $A_\alpha = T_L^{-1} A_{\zeta'} T$, $B_\alpha = T_L^{-1} B_{\zeta'}$, $W_\alpha = T_L^{-1} W_{\zeta'}$, and $C_\alpha = C Y_{\zeta'} T$.

It is useful here to also note the identity $2T_L^{-1} = T^t$.

Balanced Realization Method. The model reduction procedure outlined below is summarized from the papers by Moore (1981), Laub et al. (1987), and Safonov and Chiang (1988). Consider the physical state form of the equations of motion, Eq. (2), without including the unbalance forces,

$$\dot{x} = A_x x + B_x u \tag{13}$$

$$r = C_x x \tag{14}$$

Assume that the system is asymptotically stable and define the controllability grammian as

$$W_c = \lim_{T \to \infty} \int_0^T (e^{A\tau} B B^t e^{A^t \tau}) d\tau \tag{15}$$

and the observability grammian as

$$W_o = \lim_{T \to \infty} \int_0^T (e^{A^t \tau} C^t C e^{A\tau}) d\tau \tag{16}$$

Also, W_c and W_o satisfy, respectively, the following algebraic Lyapunov equations:

$$A_x W_c + W_c A_x^t + B_x B_x^t = 0 \tag{17}$$

$$A_x^t W_o + W_o A_x + C_x^t C_x = 0 \tag{18}$$

The state space representation is said to be balanced over the interval [0, ∞] if $W_c = W_o = \Xi$ for some diagonal matrix Ξ. Moore (1981) has shown that every system can be brought to a balanced form via a matrix transformation. In other words, Eqs. (13) and (14) can be rewritten, by introducing $x = T_b x_b$, as

$$\dot{x}_b = A_b x_b + B_b u \tag{19}$$

$$r = C_b x_b \tag{20}$$

where x_b is the balanced state, $A_b = T_b^{-1} A_x T_b$, $B_b = T_b^{-1} B_x$, $C_b = C_x T_b$, and T_b is the balanced transformation matrix from the balanced states x_b to the physical states x, and is obtained by using the procedure proposed by Laub et al. (1987). Furthermore, the following model reduction scheme is proposed. Assume that the diagonal entries of Ξ are ordered as $\sigma_1 \geq \sigma_2 \geq \sigma_3 \geq \cdots \geq \sigma_{2n}$ and that is is possible to partition Ξ as $\Xi = \text{diag}(\Xi_1, \Xi_2)$, where the dimension of Ξ_1 is $2(n-\tilde{n})$, Ξ_2 is $2\tilde{n}$, and $\sigma_{2(n-\tilde{n})}$ is much larger than $\sigma_{2(n-\tilde{n})+1}$. Let the balanced system matrices in Eqs. (19) and (20) be partitioned as

$$A_b = \begin{bmatrix} A_{b11} & A_{b12} \\ A_{b21} & A_{b22} \end{bmatrix}, \quad B_b = \begin{bmatrix} B_{b1} \\ B_{b2} \end{bmatrix}, \quad \text{and } C_b = [C_{b1} \; C_{b2}] \tag{21}$$

The balanced reduced-order model, by neglecting all the states associated with $\sigma_{2(n-\tilde{n})+1} \ldots \sigma_{2n}$, is defined as below:

$$\dot{x}_{br} = A_{br} x_{br} + B_{br} u \tag{22}$$

$$r = C_{br} x_{br} \tag{23}$$

where $A_{br} = A_{b11}$, $B_{br} = B_{b1}$, and $C_{br} = C_{b1}$. Physically, this procedure neglects the $2\tilde{n}$ weakly controllable/observable states in the system. Moore (1981) proved that the reduced-order model is minimal and balanced with both controllability and observability grammians equal to Ξ_1. Glover (1984) proved that the reduced-order model $G_{br}(s)$ satisfies the frequency domain infinity-norm (Noble and Daniel, 1977) error bound

$$\| G_x(s) - G_{br}(s) \|_\infty \leq 2 \sum_{j=2\tilde{n}+1}^{2n} \sigma_i \quad \text{for all } s \; (= j\omega) \tag{24}$$

where $G_x(s) = C_x (sI - A_x)^{-1} B_x$, $G_{br}(s) = C_{br}(sI - A_{br})^{-1} B_{br}$, σ_j are the diagonal elements of Ξ and are equal to

$$\sigma_j = [\lambda_j \{ \Xi^t \Xi \}]^{1/2}$$

where $\lambda_j\{\Xi^t \Xi\}$ denotes the jth eigenvalues of $(\Xi^t \Xi)$. Note that Eq. (24) implies that the infinity norm of the error of the impulse responses between the reduced-order and original-order models is limited to the trace of Ξ; in other words, the reduced-order model has an impulse response that approximates the impulse response of the original-order model under the condition defined in Eq. (24).

Unfortunately, the balanced model reduction procedure is, in general, not a good choice for high-order lightly damped mechanical systems. The simulation result of this method on a 52 degree-of-freedom rotor system shows that the resulting reduced-order model is not accurate within the operating frequency range at all. However, the balancing method can be applied to a complex mode (or normal mode) reduced-order model to obtain a further model reduction without loss of model accuracy if the complex mode reduced-order model possesses weakly controllable/observable states. The following section outlines the formulation for this consecutive application of the complex mode and balanced realization methods. The "combined method" will be used to represent this type of procedure in the rest of this work. The consecutive application of normal mode and balanced realization methods can be done in a similar process, and will not be presented here.

Combined Method. We start with a complex mode reduced-order model as defined in Eq. (12), without the unbalance force term included, and introducing

$$\alpha = T_{b\alpha} x_{b\alpha} \tag{25}$$

where $T_{b\alpha}$ is the balanced transformation from the balanced states to the complex modal states. Then, the balanced system based on the complex mode reduced-order model can be written as

$$\dot{x}_{b\alpha} = A_{b\alpha} x_{b\alpha} + B_{b\alpha} u \tag{26}$$

$$r = C_{b\alpha} x_{b\alpha} \tag{27}$$

where $A_{b\alpha} = T_{b\alpha}^{-1} A_\alpha T_{b\alpha}$, $B_{b\alpha} = T_{b\alpha}^{-1} B_\alpha$, and $C_{b\alpha} = C_\alpha T_{b\alpha}$. By neglecting the $2\tilde{n}$ weakly controllable/observable states, the further reduced model of order $(2\hat{n} - 2\tilde{n})$ can be obtained in a similar process as Eqs. (22) and (23), and can be written as

$$\dot{x}_r = A_r X_r + B_r u \tag{28}$$

$$r = C_r x_r \tag{29}$$

where A_r, B_r, and C_r are the retained parts in $A_{b\alpha}$, $B_{b\alpha}$, and $C_{b\alpha}$, respectively, and are associated with the retained states in $x_{b\alpha}$.

The physical state, x, is related to the complex modal state through the transformation of Eqs. (5) and (11). Equation (5) may be separated into the real part and imaginary components and written equivalently, using Eq. (11), as

$$x \doteq \Psi_\alpha \alpha \tag{30}$$

where

$$\Psi_\alpha = [Y^r - Y^i] T \tag{31}$$

The transformation between x_r defined in Eq. (28) and the original physical state x can be obtained from Eqs. (25) and (30), and can be written as

$$x \doteq T_{xr} x_{b\alpha} \doteq T_{xr} \begin{bmatrix} x_r \\ 0 \end{bmatrix}_{2\hat{n} \times 1} = \mathrm{T}_r \mathrm{x}_r \tag{32}$$

where $T_{xr} = \Psi_\alpha T_{b\alpha}^{-1}$, and T_r consists of the first $(2\hat{n} - 2\tilde{n})$ columns of T_{xr}.

Optimal Output Feedback Controller Design

Basic Concept. The following explanation of the procedure used in designing the control system is presented in terms of physical coordinates. The same procedures, however, can also be developed in terms of the complex mode coordinates and balanced coordinates. Equation (2), without the unbalance forcing term $W_x f$, is

$$\dot{x} = A_x x + B_x u \tag{33}$$

For a full-state linear feedback control, the control input, associated with the physical state x, can be written as

$$u_x = -K_x x \tag{34}$$

where K_x is a state feedback gain matrix, which is obtained based on minimization of the selected performance index to provide a desired performance. Practically, we can either measure all required states or use an observer to reconstruct the required states; however, the former involves a large number of sensors for large-order systems and the latter requires high-speed computation for on-line state estimation. The following provides a procedure to avoid the above practical problems. The objective here is to obtain a control input, associated with the system output r,

$$u_r = -K_r r \tag{35}$$

such that $u_r = u_x$. An error vector $e = u_x - u_r$ is defined and the introduction of relations from Eqs. (4), (34), and (35) with the assumption that the C_x is properly selected such that the output of the least-squares controller approaches that of the full-state feedback controller, then provides

$$e \doteq (K_x - K_r C_x) x \tag{36}$$

It is seen here that for the case when

$$K_r C_x = K_x \tag{37}$$

the error vector e is null. Unfortunately Eq. (37) does not hold unless C_x is an identity matrix (or equivalently $r=x$), and K_r and K_x are of the same size. Practically, the size of K_r is much smaller than that of K_x, because the number of sensor locations is usually severely limited. A least-squares solution based on minimizing the quadratic error $(K_r C_x - K_x)(K_r C_x - K_x)^t$ can be obtained (Noble and Daniel, 1977, p. 69); however, as shown below

$$K_r = K_x C_x^t (C_x C_x^t)^{-1}. \tag{38}$$

It is possible to arrange the order of the elements of the state vector x such that the observation matrix C_x has the following form:

$$C_x = [I_m \ \ 0] \tag{39}$$

where m is the number of independent measured states. Substituting Eqs. (38) and (39) into Eq. (36), and utilizing the fact that $C_x C_x^t = m$, we have

$$e^t e \doteq \frac{1}{m^2} x^t \begin{bmatrix} 0_m & 0 \\ 0 & -I_{(2n-m)} \end{bmatrix} K_x^t K_x \begin{bmatrix} 0_m & 0 \\ 0 & -I_{(2n-m)} \end{bmatrix} x \tag{40}$$

Equation (40) provides two ways to reduce the error e. The first is to increase the number of measurements m. As m increases toward $2n$ the error e decreases, and the case of $m=2n$ corresponds to all states being measured with $e=0$. The second method is to design K_x such that the elements associated with the measured states are much larger in magnitude than those associated with the unmeasured states while the desired performance is maintained. The latter can be achieved by minimizing the following performance index, which includes the system measurements, r, instead of system states, x, for certain areas such as rotor systems

$$J = \lim_{T\to\infty} \frac{1}{2T} \int_0^T (r^t S_r r + u_w u^t U u)\, dt \tag{41}$$

where S_r is a positive semidefinite state weighting matrix, U is a positive definite control weighting matrix, u_w is the weighting constant, and system output r is defined in Eq. (4).

Least-Squares Output Feedback Design

1 Complex Mode Method. The physical state is related to the modal state through the transformation of Eq. (5). Equation (5) may be separated into the real part and imaginary components and written equivalently, using Eq. (11), as

$$x \doteq \Psi_\alpha \alpha \tag{42}$$

where

$$\Psi_\alpha = [Y^r - Y^i]T \tag{43}$$

With this relation, the performance index from Eq. (41) may be rewritten as

$$J = \lim_{T\to\infty} \frac{1}{2T} \int_0^T (\alpha^T S_{\alpha r} \alpha + u_w u^t U u)\, dt$$

where $S_{\alpha r} = \Psi_\alpha^t C^t S_r C \Psi_\alpha$ is a weighting matrix associated with the retained complex coordinates. The steady-state Ricatti equation associated with Eq. (44) is

$$R_\alpha A_\alpha + A_\alpha^t R_\alpha - \frac{1}{u_w} R_\alpha B_\alpha U^{-1} B_\alpha^t R_\alpha + S_{\alpha r} = 0 \tag{45}$$

and the optimal control law can be written as

$$u = -G_\alpha \alpha \tag{46}$$

where

$$G_\alpha = U^{-1} B_\alpha^t R_\alpha$$

Introducing Eq. (42) into Eq. (46), we have

$$u = -G_\alpha \alpha \tag{47}$$

Using Eqs. (4) and (42), we can rewrite Eq. (35) as

$$u_r = -K_r C_x \Psi_\alpha \alpha \tag{48}$$

or

$$u_r = -K_r C_\alpha \alpha \tag{49}$$

where $C_\alpha = C_x \Psi_\alpha$. Similar to the procedure used to obtain Eq. (38), the objective here is to determine K_r such that u_r in Eq. (49) is a good approximation of u in Eq. (47) for any selected observation matrix C. The least-square solution associated with Eqs. (47) and (49) is

$$K_r = G_\alpha C_\alpha^t (C_\alpha \ C_\alpha^t)^{-1} \tag{50}$$

Note that the number of measured states associated with matrix C_x in Eq. (32) should generally be equal to that of matrix C in Eq. (44) for best performance; however, one can use less measured states than the output r to be minimized in the performance index, Eq. (41), but at a price of degrading the controller performance.

2 Combined Method. The physical state x is related to the balanced reduced model state x_1 through the transformation of Eq. (32). With this relation, the performance index from Eq. (41) may be rewritten as

$$J = \lim_{T\to\infty} \frac{1}{2T} \int_0^T \left(x_r^t S_{xr} x_r + \frac{1}{u_w} u^t U u \right) dt \tag{51}$$

where $S_{xr} = T_r^t C^t S_r C T_r$ is a weighting matrix associated with the retained complex coordinates. The steady-state Ricatti equation associated with Eq. (51) is

$$R_r A_r + A_r^t R_r - \frac{1}{u_w} R_r B_r U^{-1} B_r^t R_r + S_{xr} = 0 \tag{52}$$

and the optimal control law can be written as

$$u = -G_{xr} x_r \tag{53}$$

where $G_{xr} = U^{-1} B_r^t R_r$. Using Eqs. (4) and (32), we can rewrite Eq. (35) as

$$u_r = -K_{xr} r \doteq -K_{xr} C_x T_r x_r \tag{54}$$

or

$$u_r \doteq -K_{xr} C_{xr} x_r \tag{55}$$

where $C_{xr} = C_x T_r$. Similar to the procedure used to obtain Eq. (38), the objective here is to determine K_{xr} such that u_r in Eq. (55) is a good approximation of u in Eq. (53) for any selected observation matrix C_x. The least-squares solution associated with Eqs. (53) and (55) is

$$K_{xr} = G_{xr} C_{xr}^t (C_{xr} C_{xr}^t)^{-1} \tag{56}$$

Similar to the complex mode procedure, the number of measured states of matrix C_x in Eq. (54) should generally be equal to that of matrix C in Eq. (51) for best performance; however, one can use less measured states than the output r to be minimized in the performance index, Eq. (44) or (51), but at a price of degrading the controller performance. In the next section, an example is given for demonstration of the proposed procedure.

Example

Simulations are performed on a large-order rotordynamic system so as to test the optimal active control procedures presented above. The test rotor configuration is shown in Fig. 1 and it consists of 4 rigid disks, 3 isotropic bearings, and 12 rotating shaft elements. The discrete model of this system is a finite element based model (Nelson and McVaugh, 1976), and it utilizes 13 stations with 2 translation (V_i, W_i) and 2

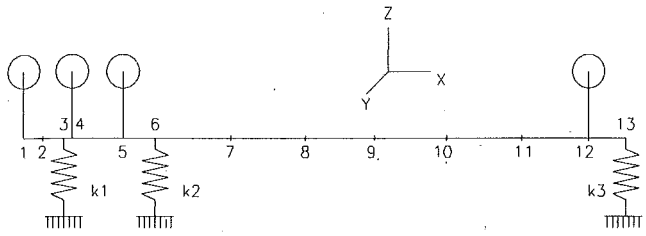

Fig. 1 Rotor schematic of three bearing system

Table 1 Mass properties of rigid disks

Station No.	Mass (Kg)	Polar Inertia (Kg-m^2)	Transverse Inertia (Kg-m^2)	cg Eccentricity (μm)
1	11.38	19.53	9.82	25.4
4	7.88	16.70	8.35	25.4
5	7.70	17.61	8.80	25.4
12	21.70	44.48	22.24	25.4

Table 2 Shaft and bearing information

Station No.	Axial Distance to Station (cm)	Other Properties
1	0.0	shaft : Inner Radius = 1.68 cm
2	4.29	Outer Radius = 2.95 cm
3	8.89	Elastic modulus = 2.069x10^{11} N/m^2
4	10.49	Density = 8193.0 Kg/m^3
5	20.17	bearing :
6	27.69	$k_1 = k_2 = k_3 = 175 \times 10^5$ N/m
7	44.20	$c_1 = c_2 = c_3 = 900$ N-Sec/m
8	59.44	
9	74.68	
10	89.92	
11	105.16	
12	120.14	
13	127.94	

rotation (B_j, Γ_1) coordinates at station j ($j = 1, 2, \ldots, 13$) for a total of 52 degrees of freedom. The geometric and material properties are listed in Tables 1 and 2. The mass unbalance for this system is assumed to be localized at each disk and is chosen in phase and of equal cg eccentricity. A plot of the natural frequencies of whirl versus the rotor spin speed is presented in Fig. 2. The first three forward critical speeds are 649, 872, 1320 rad/s and the first three backward critical speeds are 479, 718, and 949 rad/s.

The control inputs are taken as translational forces at station 7 in the perpendicular Y, Z directions. The modal displacement of station 7 is relatively large for each of the first several modes. In the simulations presented here, a spin speed of 649 rad/s is chosen such that it coincides with the first forward critical speed. The precessional modes are circular here since the bearings are isotropic and the first three backward and forward modes are illustrated in Fig. 3 corresponding to the spin speed of 649 rad/s. The right eigenvectors associated with these precessional modes are used in designing the controller for the complex mode approach. The normal modes are independent of the rotor pin speed and are obtained from the undamped symmetric eigenvalue problem related to Eq. (1). The first three planar modes are illustrated in Fig. 3 and provide a graphic comparison with the gyroscopic influenced precessional modes. It should be noted that the superposition of two planar normal

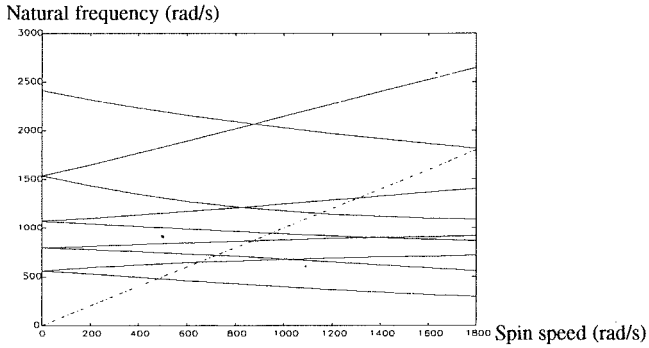

Fig. 2 Whirl speed map

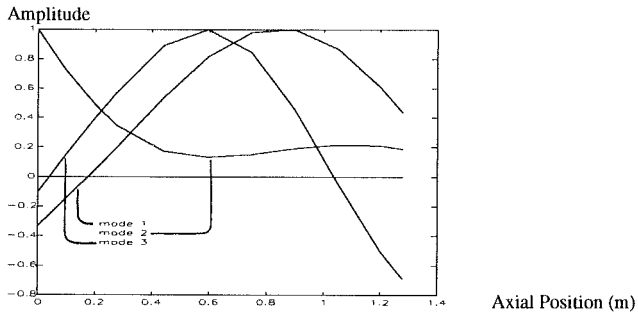

***a.* First 3 forward precessional modes (at 649, 854, and 1177 rad/s)**

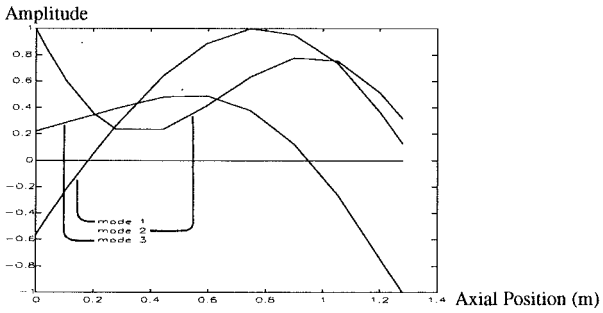

***b.* First 3 backward precessional modes (at 450, 728, and 985 rad/s)**

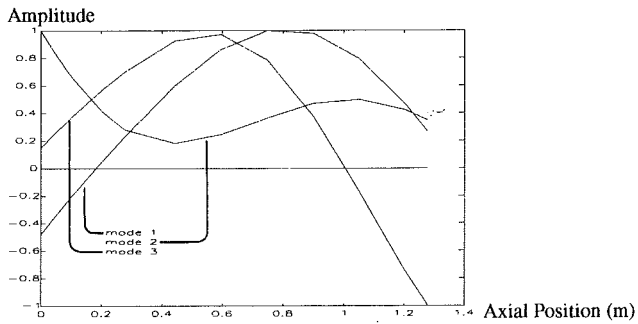

***c.* First 3 normal modes (at 561, 796, and 1070 rad/s)**

Fig. 3 System mode shapes

modes of the same frequency and amplitude can form a forward or backward whirling mode of the same frequency depending on the phasing. The three planar normal modes in Fig. 3 are retained for both the horizontal and vertical planes for the controller design using normal modes. This is equivalent to retaining three forward and three backward precessional modes where the forward-backward pair are of the same frequency.

The frequency response functions of the Y-direction dis-

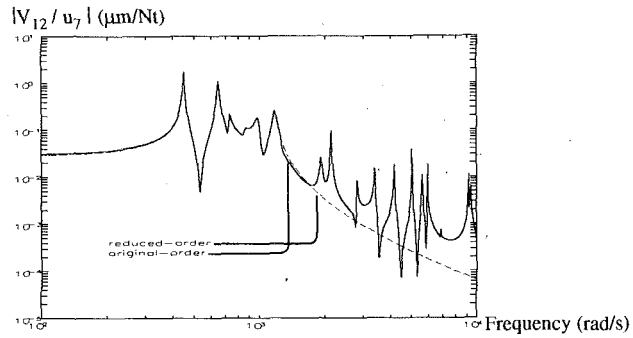

a. **Complex mode reduced model (with 12 eigenvalues retained)**

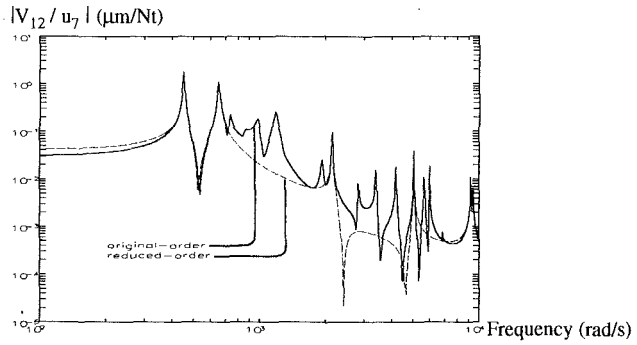

b. **Balanced reduced model (with 12 eigenvalues retained)**

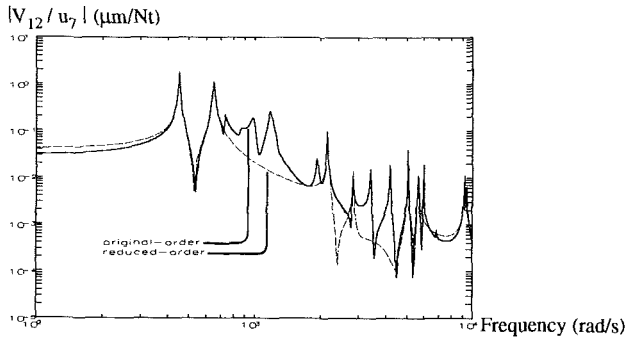

c. **Balanced reduced model (with 16 eigenvalues retained)**

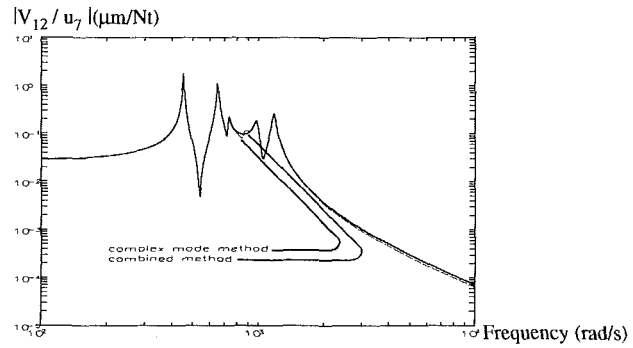

d. **Combined reduced model (with 10 eigenvalues retained)**

Fig. 4 Frequency response functions of reduced models

placement at station 12 due to the Y-direction force input at station 7, associated with the reduced-order models, are plotted in Fig. 4 for the complex mode (12 states retained), the balanced realization (12 and 16 states retained), and the combined approaches (10 states retained). The corresponding frequency response function for the original 52 degree-of-freedom system is also included in the graph. Figure 4(a) shows that the mode associated with natural frequency at 852 rad/s has a zero very close to the pole, i.e., the zero tends to cancel the pole. Under this condition, the balanced truncation method seems to be a reasonable choice to eliminate that pairs of pole and zero to obtain a further order reduction from a complex mode reduced-order model. Figure 4(d) shows the combined reduced-order frequency response function versus the complex mode reduced-order transfer function. The reduced-order frequency response functions are both quite accurate at the low-frequency range for the complex mode and the combined methods. As the frequency increases above the highest retained frequency mode, both reduced-order functions deteriorate as expected. The reduced-order transfer functions associated with the balanced method along are not good, in general, even at the low-frequency range for both cases of 12 and 16 retained states. This is because the balanced truncation method neglects the weaker controllable/observable states first, and tends to give a reduced-order model with an approximating impulse response to the impulse response of the original high-order model over the entire frequency.

The controlled and uncontrolled time responses of the original-order system from stations 1, 7, and 12, and the control input forces (Y direction) from station 7, for measurements from different number of stations are shown in Figs. 5 and 6 for the complex mode and the combined methods, respectively. In this work, four measurements are made per selected station, and they are two translational displacements and two translational velocities in the Y–Z directions. The weighting matrices S_x and U are chosen to be an identity matrix and u_w is 10^{-6} in this example. Figures 5 and 6 show that the controller performance associated with 8 measured states (stations 7 and 12) are almost the same as those from 12 measured states (stations 1, 7, and 12), while the controller performance from 4 measurements (station 7) shows only slight degradation for both the complex mode and the combined methods. Also, the performance of the combined reduced-order controller. Figure 7 shows the eigenvalues of the closed-loop systems for different numbers of measurements. Apparently, the "LQR-based least-squares output feedback control" can be considered as an alternative way of implementing a full-state feedback control for a general high-order system without using an observer, in other words, Figs. 7(a) and 7(b) demonstrate that a desirable closed-loop response may be obtained by using this least-squares output feedback procedure without having to use a full-state feedback, which is important for high-order systems.

Conclusions

This work introduces a coordinate reduction procedure by consecutively applying the complex mode method and the balanced truncation method for high-order asymmetric dynamic systems, and for their optimal control system design. Whether the balancing method should be applied to a complex mode reduced-order model will depend on the number of weak controllable/observable states in the reduced model and on the desired reduced-model accuracy. The coordinate transformation matrices are derived so that an LQ regulator can be designed.

The balanced truncation method alone is not a good choice for a reduced-order model in this particular application of a high-order under damped mechanical systems due to the fact that it produces an approximating model over the entire frequency range. However, it can be applied to a complex mode reduced-order model to obtain a further order reduction.

An LQR-based least-squares output feedback control procedure is presented and is shown to be effective based on the simulation results; however, one disadvantage is that the required accuracy cannot be taken into consideration before performing the design procedure, and improper selection of the measurements may destabilize the closed-loop system.

Full-state measurement for high-order systems is usually not

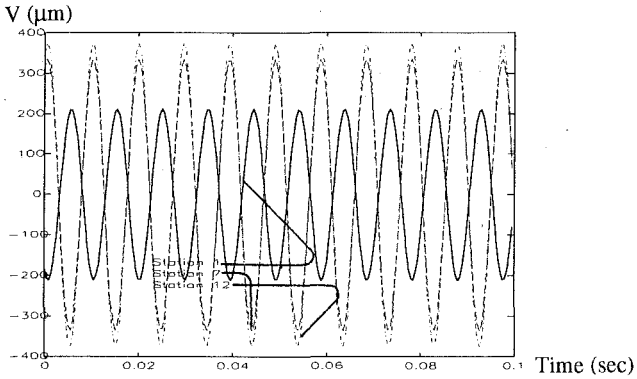

a. Uncontrolled responses at stations 1, 7, and 12

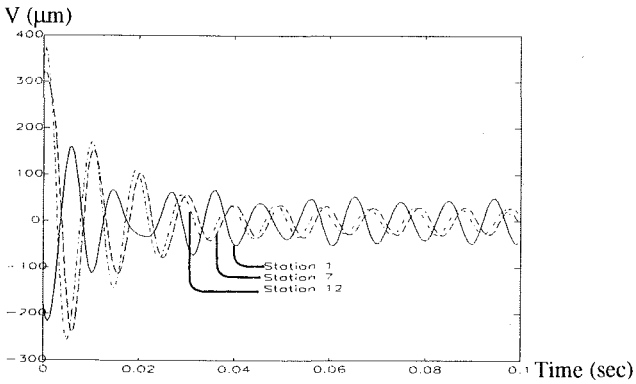

b. Controlled responses of full measurements

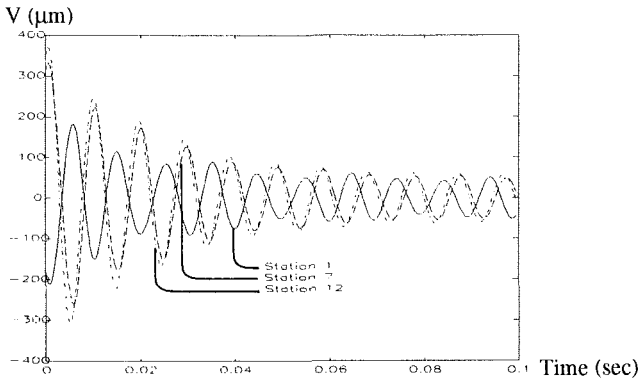

c. Controlled responses of 4 measurements (station 7)

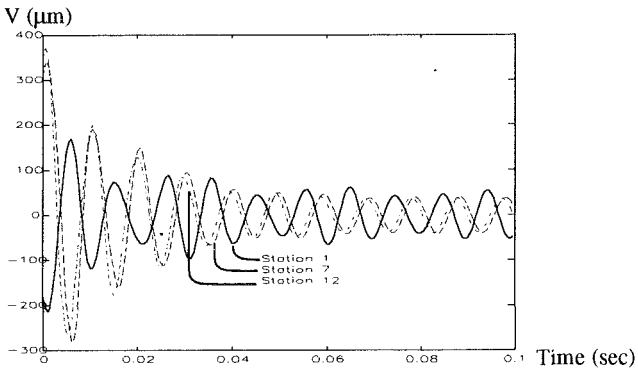

d. Controlled responses of 8 measurements (stations 7 and 12)

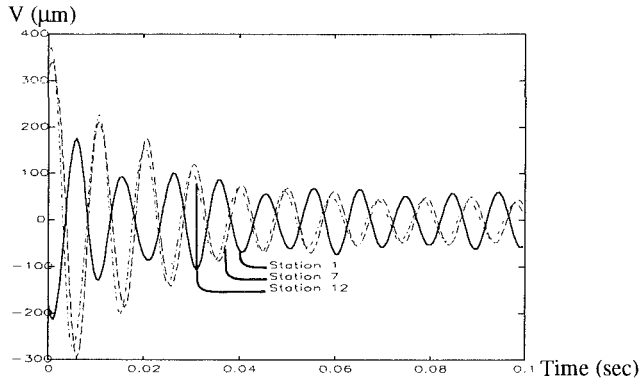

e. Controlled responses of 12 measurements (stations 1, 7, and 12)

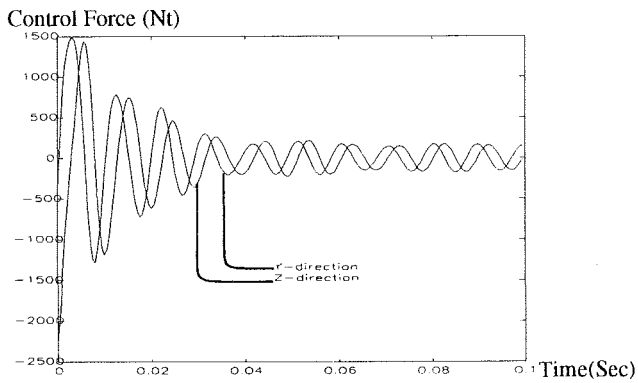

f. Control forces associated with full measurements

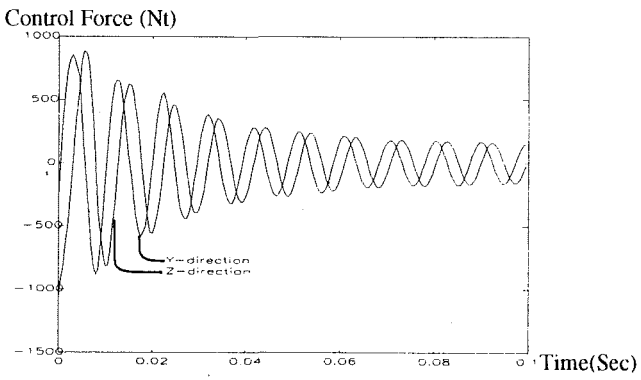

g. Control forces associated with 4 measurements (station 7)

Fig. 5 Responses of the original system with complex mode reduced- order controller

possible. In order to utilize full-state feedback control realistically either an observer or an "optimal output feedback" procedure can be used. The advantage of using an observer is that the control system only requires the measurement of a small number of system responses so long as the open-loop system is observable. This is desirable for physical systems with limited sensor accessibility. A disadvantage, however, is that the closed-loop system might be quite sensitive to certain system parameter variations (Ridgy and Banda, 1986), and the process of obtaining the estimation of all the states requires particularly fast computational equipment. This is especially difficult for high-speed rotor systems. An LQR-based least-squares output feedback procedure presented here makes a full-state feedback of a high-order system possible without using an observer, and eliminates the limitation of sensor number (Palazzolo et al., 1989). Either the use of an observer or an "optimal output feedback" method may introduce additional stability problems, such as stability robustness for the closed-loop control system, which need to be considered in the optimal control design of a particular problem.

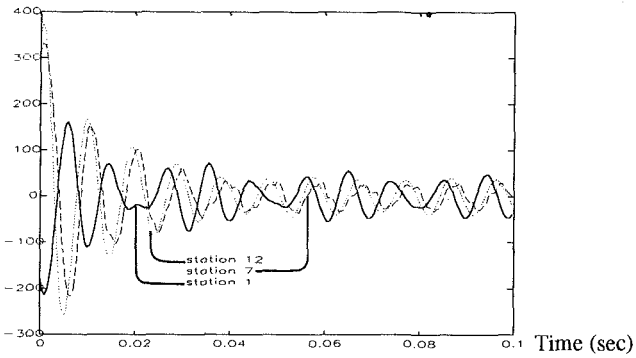

a. Controlled responses of full measurements

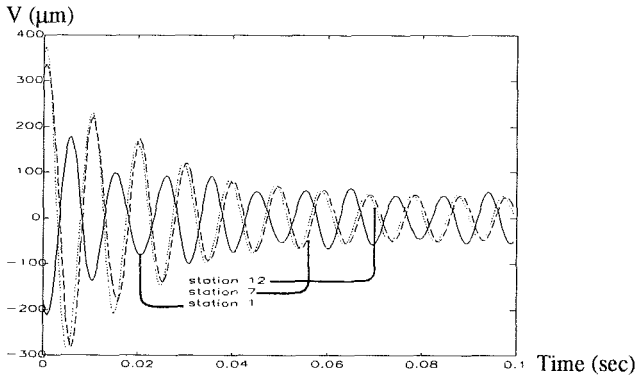

c. Controlled responses of 8 measurements (stations 7 and 12)

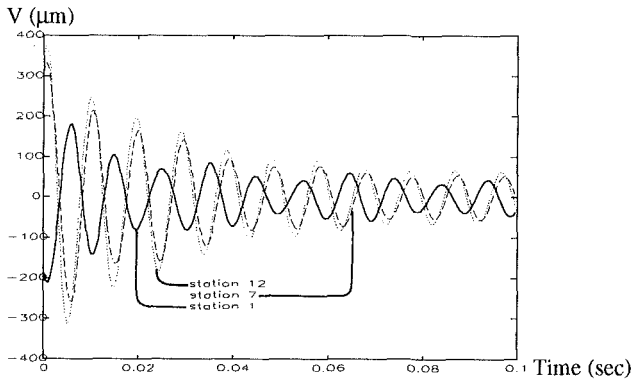

b. Controlled responses of 4 measurements (station 7)

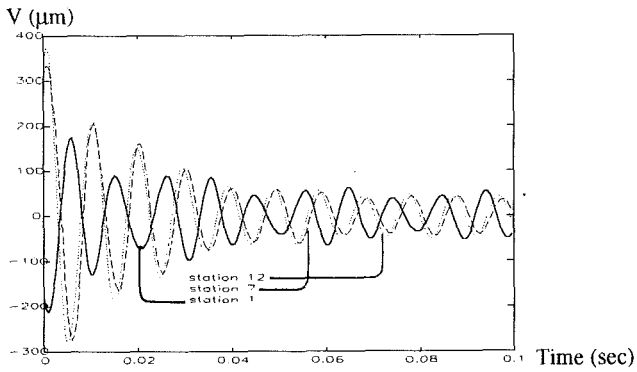

d. Controlled responses of 12 measurements (stations 1, 7, and 12)

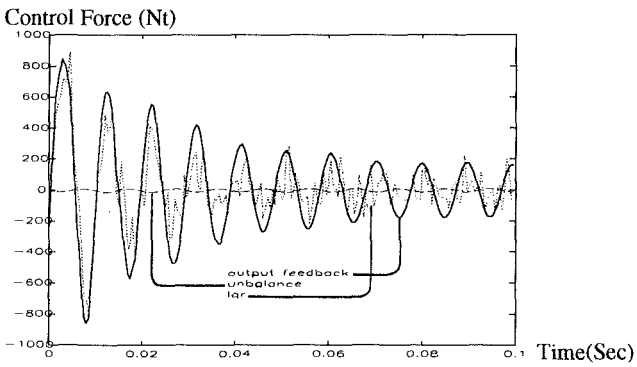

e. Y-control forces at station 7 (LQR: full measurement, output feedback: 4 measurements)

Fig. 6 Responses of the original system with combined reduced-order controller

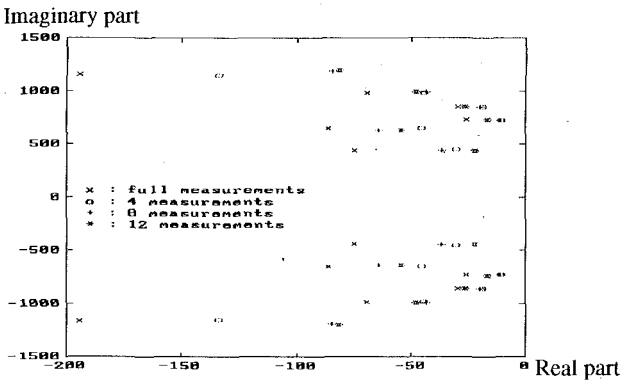

a. Complex mode method

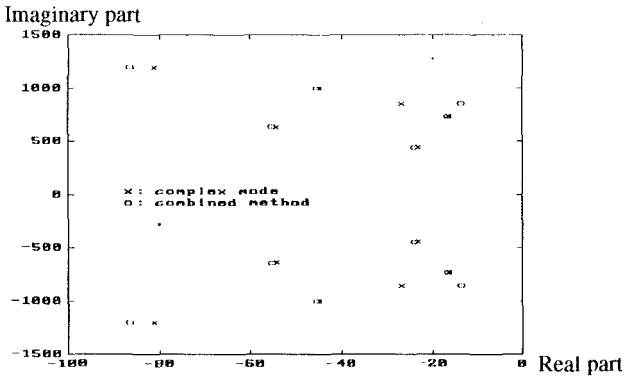

c. Complex mode versus combined method: 12 measurements

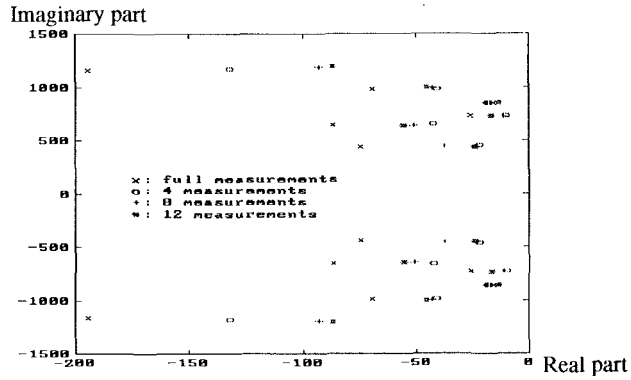

b. Combined method

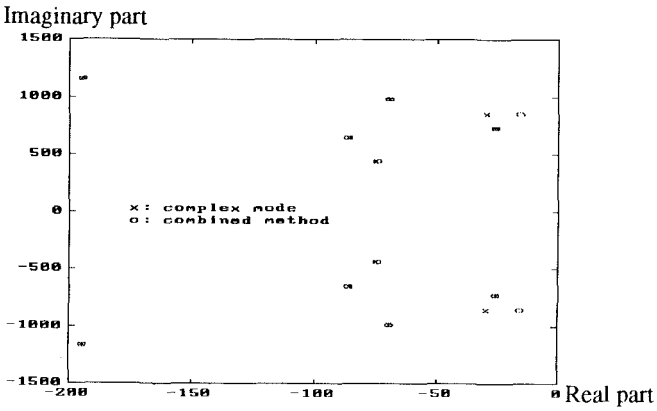

d. Complex mode versus combined method: full measurements

Fig. 7 Eigenvalues of closed-loop system associated with various numbers of measurements

References

Bryson, A. E., Jr., and Ho, Y. C., 1975, *Applied Optimal Control*, Hemisphere Publishing Corp., New York.

Cannon, R. H., and Schmitz, E., 1984, "Precise Control of Flexible Manipulators," *Robotics Research, The 1st Int. Symp.*, M. Brady and R. Paul, eds., MIT Press, Cambridge, MA, pp. 841–861.

Fan, G. W., and Nelson, H. D., 1991, "Control of Asymmetric Systems Using Complex Modes," *The 13th Biennial Conference on Mechanical Vibration and Noise*, DE-Vol. 38, pp. 195–201.

Glover, K., 1984, "All Optimal Hankel Norm Approximations of Linear Multivariable Systems and Their L-Error Bounds," *Int. Journal of Control*, Vol. 39, No. 6, pp. 1115–1193.

Kirk, D. E., 1970, *Optimal Control Theory: An Introduction*, Prentice-Hall, Englewood Cliffs, NJ.

Kwakernaak, H., and Sivan, R., 1972, *Linear Optimal Control Systems*, Wiley-Interscience, New York.

Laub, A. J., Heath, M. T., Page, C. C., and Ward, R. C., 1987, "Computation of Balanced Transformations and Other Applications of Simultaneous Diagonalization Algorithms," *IEEE Transactions on Automatic Control*, Vol. AC-32, pp. 115–122.

Moore, B. C., 1981, "Principal Component Analysis in Linear Systems: Controllability, Observability, and Model Reduction," *IEEE Transactions on Automatic Control*, Vol. AC-26, No. 1, pp. 17–32.

Nelson, H. D., and McVaugh, J. M., 1976, "The Dynamics of Rotor-Bearing Systems Using Finite Elements," ASME *Journal of Engineering for Industry*, Vol. 98, pp. 593–600.

Noble, B., and Daniel, J. W., 1977, *Applied Linear Algebra*, Prentice-Hall, Englewood Cliffs, NJ.

Palazzolo, A. B., Lin, R. R., Kascak, A. F., and Alexander, R. M., 1989, "Active Control of Transient Rotordynamic Vibration by Optimal Control Methods," ASME *Journal of Engineering for Gas Turbines and Power*, Vol. 111, pp. 264–270.

Ridgy, A., and Banda, C., 1986, "Introduction to Robust Multivariable Control," USAF Technical Report, AFWAL-TR-85-3102.

Safonov, M. G., and Chiang, R. Y., 1988, "Schur Balanced Model Reduction," *Proceedings of American Control Conference*, June 15–17; also, *IEEE Transactions on Automatic Control*, 1988.

Salm, J., and Schweitzer, G., 1984, "Modelling and Control of a Flexible Rotor With Magnetic Bearings," *Proceedings of Conference on Vibrations in Rotating Machinery*, York, UK, C277.

Ulsoy, A. G., 1984, "Vibration Control in Rotating or Translating Elastic Systems," ASME *Journal of Dynamic Systems, Measurement, and Control*, Vol. 106, pp.6–14.

Reng Rong Lin[1]

A. B. Palazzolo

Texas A&M University,
College Station, TX 77843

A. F. Kascak
U.S. Army at NASA Lewis,
Cleveland, OH 44135

G. T. Montague
Sverdrup at NASA Lewis,
Cleveland, OH 44135

Electromechanical Simulation and Testing of Actively Controlled Rotordynamic Systems With Piezoelectric Actuators

Past research on this subject has treated piezoelectric actuators as ideal devices that have tip displacements proportional to their input voltages, at any instant in time. This assumption neglected phase lag and amplitude change at high frequencies. This characteristic of any actuator may lead to coupled control system–structural system instability that limits the amount of active stiffness or active damping that can be obtained. The paper presents a method for simulating the coupled "electromechanical" system to predict rotordynamic stability and unbalance response along with control system stability. The piezoelectric actuators and their amplifiers are represented as equivalent linear electrical circuits. The electromechanical system modeling approach is utilized to correlate test results from a double overhung rotor rig at NASA Lewis. The test results also show the effectiveness of the control system for suppressing the unbalance response of two modes using active stiffness and active damping.

Introduction

There are two major strategies in rotordynamic vibration control: passive control and active control. Passive control is achieved by changing system parameters via passive damping components or devices. Some of these devices are Lanchester dampers, impact dampers, and squeeze-film dampers. Active control uses sensor-actuator systems to produce control forces that act directly upon the rotor in response to measured vibrations.

Active vibration control has become an area of intense research in rotorbearing system dynamics. Research has been focused on developing effective active vibration control algorithms for machine tools, large space structures, and in robots. Significant efforts are being made to apply active vibration control (AVC) devices to rotating machinery in the petrochemical, aerospace, and power utility industries. The advantages of active control over passive, i.e., absorbers and dampers, is the versatility of active control in adjusting to a myriad of load conditions and machinery configurations. This is clearly illustrated when one considers the very narrow bandwidth over which a tuned spring mass absorber is effective. Other possible advantages of AVC include compact size, light weight, no lubrication systems needed in the control components, and operation in high or low-temperature environments.

Literature Review

Electromagnetic shakers and magnetic bearings have been used for actuators in the majority of the active vibration control research mentioned in the literature. Magnetic bearings force the rotor without contact while electromagnetic actuators apply forces to the rotor indirectly through the bearings. Schweitzer (1985) examined the stability and observability of rotorbearing systems with active vibration control, and presented an analysis that related force and stiffness to electrical and geometric properties of electromagnetic bearings.

Nikolajsen et al. (1979) examined the application of magnetic dampers to a 3.2 m simulated marine propulsion system. Gondhalekar and Holmes (1984) suggested that electromagnetic bearings be employed to shift critical speeds by altering the suspension stiffness. Weise (1985) discussed proportional, integral, derivative (PID) control of rotor vibrations and illustrated how magnetic bearings could be used to balance a rotor by forcing it to spin about its inertial axis. Humphris et al. (1986) compared predicted and measured stiffness and damping coefficients for a magnetic journal bearing.

Several papers describe active vibration control utilizing other types of actuators such as pneumatic, hydraulic, electrohydraulic, and eddy current force generators. Ulbrich and Althaus (1989) discussed the advantages and disadvantages of different types of actuators, and examined controlled hydraulic chambers as force actuators. This compact system could develop very large forces and thereby influence even large turbines weighing several tons; however, the difficulty of hydraulic control lies in high-frequency (over 100 Hz) response. This was essentially limited by the servovalve implemented and fluid losses. Feng and Xin (1986) developed an active vibration control scheme with actuator forces resulting from varying bearing

[1]Current address: A. C. Compressor, Appleton, WI.

Contributed by the International Gas Turbine Institute and presented at the 36th International Gas Turbine and Aeroengine Congress and Exposition, Orlando, Florida, June 3-6, 1991. Manuscript received at ASME Headquarters March 4, 1991. Paper No. 91-GT-245. Associate Editor: L. A. Riekert.

oil pressure. Heinzmann et al. (1980) employed loud speaker coils linked to the shaft via ball bearings to control vibrations.

Crawley and de Luis (1983, 1985) used piezoceramics, bonded on the surface of cantilever beams, as actuators either to excite vibrations or to suppress the vibrations by introducing damping to the system. Furthermore, they developed a theoretical background for predicting the amplitude of the vibration induced by piezoceramics. Stjernstrom (1987) bonded piezoceramics on cantilever beams as actuators and sensors to induce the first and second vibration modes.

Matsubara et al. (1989) employed piezoelectric dampers to suppress chatter vibration during a boring process. These piezoelectric dampers were driven so as to generate damping forces corresponding to the vibration velocity of the boring bar. Tzou (1987) demonstrated the control of bending vibration in nonrotating beams by using layered piezoelectric materials.

Palazzolo et al. (1989a, 1989b) and Lin (1990) derived simulation models and demonstrated test results of active vibration control of rotorbearing systems utilizing piezoelectric pushers as actuators. The correlation for unbalance response and transient response between the predicted and test results was very good. This paper extends these theories from a soft-mounted single pusher configuration to a soft-mounted opposing pusher one and considers the effects on the system stability due to nonideal characteristics (e.g., phase lag) of the piezoelectric pushers and other electrical components in the control loop. The piezoelectric actuators are represented by equivalent, linear electric circuits with components selected so as to match the frequency response function of the circuit to that of the actuator. The differential equations for the circuits are assembled into the structural matrices to form an electromechanical model of the system. This model may then be employed to predict instability onset feedback gains, total system stability, and total system forced response.

Electromechanical Simulation With Ideal Control Model

The governing differential equations for the combined rotorbearing-control system may be derived assuming ideal actuators and control circuits. By "ideal" it is meant that the piezoelectric actuators do not have any phase lag or amplitude rolloff at high frequencies. Similarly electrical components such as differentiators and filters are assumed to experience no phase lag or amplitude rolloff. This simplifies the analysis significantly since the piezoelectric actuator and electrical components can be represented merely in terms of scale (conversion) factors in the feedback loop. The drawback to this simplified model is its inability to predict the feedback gains (active stiffness and damping levels) at which the electromechanical system will go unstable.

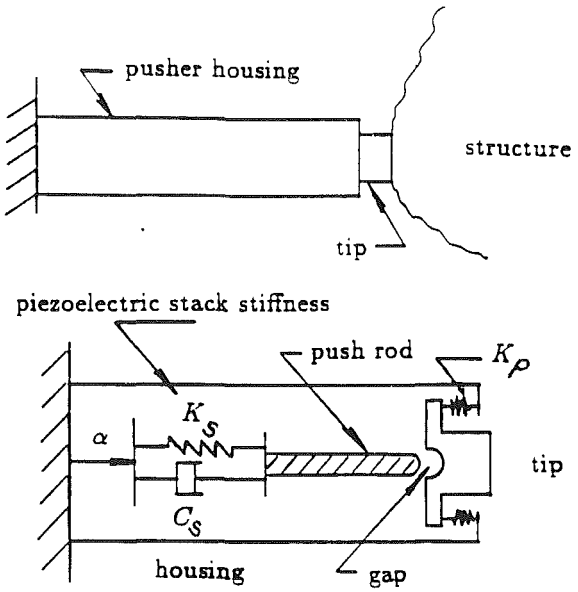

Fig. 1 Sketch of piezoelectric pusher (top) and corresponding analysis model (bottom).

The piezoelectric pusher consists of a stack of piezoelectric ceramic disks, which are arranged on top of one another and connected in parallel electrically. The stack expands in response to an applied voltage, which causes the electric field to point in the direction of polarization for each disk. The extension of the pusher under zero load depends on the number and thickness of the disks and the force for zero extension depends on the cross-sectional area of the disks. Figure 1 shows a sketch

Nomenclature

ADFT = active damping feedback theory
ADSFT = active damping and stiffness feedback theory
ASFT = active stiffness feedback theory
AVC = active vibration control
$[C]$ = damping matrix
C_{A_j} = viscous damping between pusher and ground
C_{c_i} = viscous damping coefficient for the series combination of the ith piezo pusher and the absorber pad between the pusher tip and bearing housing
C_{D_i} = capacitors used in differentiator
C_i = capacitors used in second-order noninverting LPF
C_s = damping coefficient of the piezoelectric stack
$\{F_D(t)\}$ = external forces (disturbance)
$F_j(S)$ = jth input of the transfer function
$G_{ij}(S)$ = transfer function between the ith output and the jth input
K = feedback gain in amplifier
$[K]$ = stiffness matrix
K_{A_j} = same as C_{A_j} but for stiffness
K_{c_i} = same as C_{c_i} but for stiffness
K_p = preload spring inside the pusher
K_{PA} = stiffness of pusher A
K_{PB} = stiffness of pusher B
K_{RA} = absorber stiffness at pusher A
K_{RB} = absorber stiffness at pusher B
K_s = stiffness of the stack of piezoelectric disks
LPF = low pass filter
M = number of actuators
$[M]$ = mass matrix
$[M_p]$ = lumped mass matrix of piezoelectric pushers
N = number of degrees of freedom
R_{D_i} = resistors used in differentiator
R_i = resistors used in second-order noninverting LPF
R_F = feedback resistor used in amplifier
R_I = resistor used in amplifier
$T.F.$ = transfer function
V_p = probe voltage
Z_i^* = pusher tip displacement
$\{\alpha\}$ = prescribed internal displacement of the pushers
β_i = scale factors used in transfer function match
ζ_i = ith modal damping
$[\Omega_i]$ = ith natural frequency
4NILPF = fourth-order noninverting low-pass filter

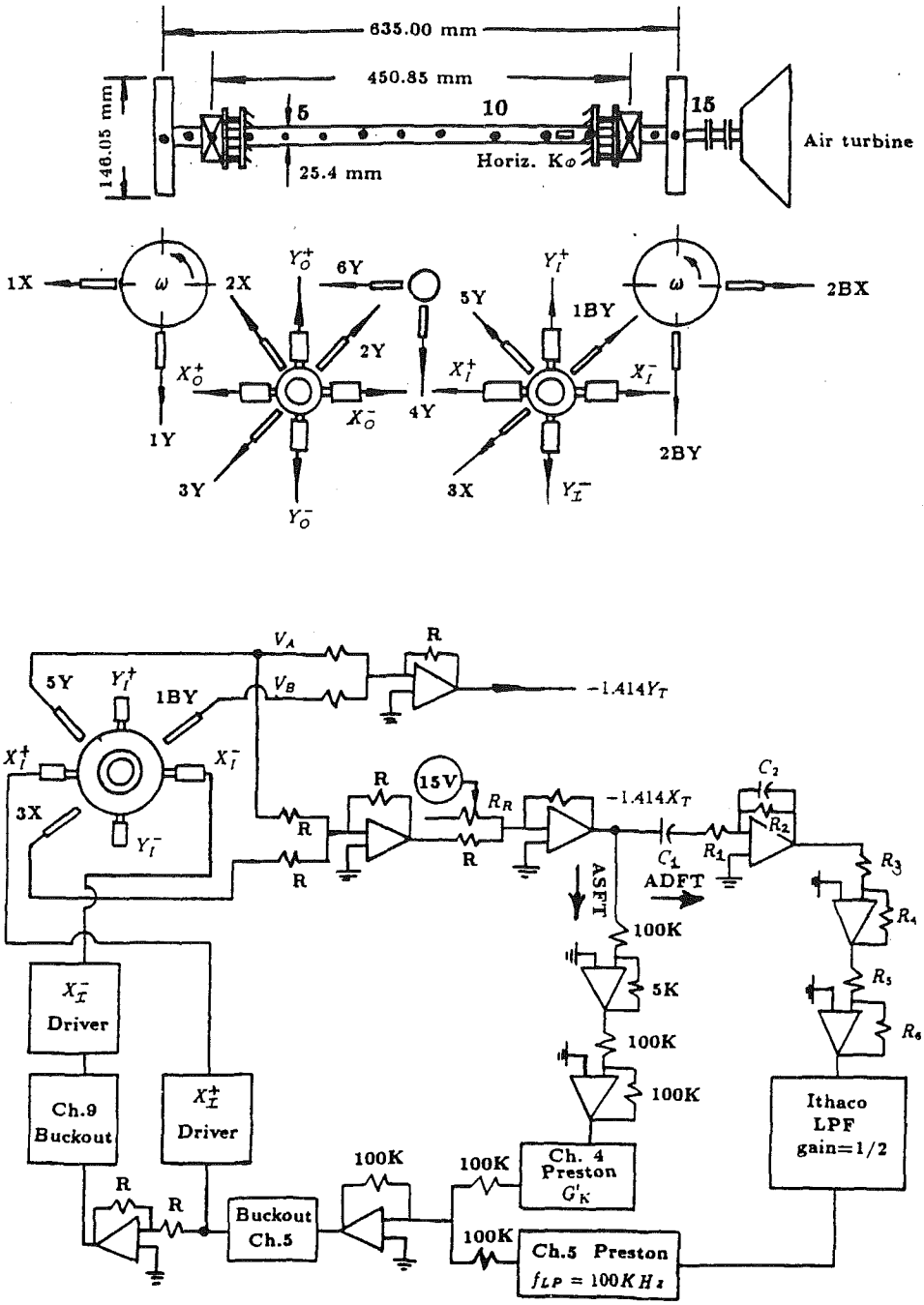

Fig. 2 Schematic diagram of sensors, actuators, and control circuit of NASA test rig

of a pusher and the corresponding ideal model. The model consists of a prescribed displacement (α), which is proportional to the input voltage and a spring (K_s) representing the stiffness of the stack of piezoelectric disks. The displacement (α) is the "internal" displacement of the pusher in Fig. 1, which will equal the tip displacement only when the tip is free and the mass of the push rod in Fig. 1 is neglected. The stiffness K_p is a preload spring, which is typically 0.001 to 0.01 times the stiffness K_s. The effect of the preload is to minimize any excess compliance at adhesive layers or mechanical interfaces and thereby improve the stability of the pusher (Burleigh, 1988). The figure shows that the device has a bilinear spring unless the tip is sufficiently preloaded to maintain a zero gap at all times.

Two opposing pushers are positioned at each controlled dof in order to prevent the loss of contact between the pusher tips and bearings, which may result in an unstable system. Figure 2 shows the schematic diagram of the soft-mounted opposing pushers with absorbers. X_I^- and X_I^+ represent the pair of pushers installed in the X direction and $1BY$, $5Y$, $3X$, $2Y$, $2X$, and $3Y$ are the displacement sensors located at the bearings. The active damping feedback theory (ADFT) and the active stiffness feedback theory (ASFT) loops are connected by a summer. The ADFT loop contains a differentiator, two inverting amplifiers, one low-pass filter, and one externally adjustable amplifier. The ASFT loop contains two inverting amplifiers and one externally adjustable amplifier. The two inverting amplifiers share the total gain required to avoid circuit oscillation problems.

If M pairs of opposing pushers are forcing the rotorbearing system at the degrees of freedom $j_1, j_2, \ldots, j_M$, the matrix differential equation for the entire system can be expressed as:

$$\begin{pmatrix} [\mathbf{M}] & \vdots & [0] \\ \cdots & \cdots & \cdots \\ [0] & \vdots & [\mathbf{M}_p] \end{pmatrix} \begin{pmatrix} \{\ddot{\mathbf{Z}}\} \\ \cdots \\ \{\ddot{\mathbf{Z}}_p\} \end{pmatrix} + \begin{pmatrix} [\mathbf{C}'] & \vdots & [\mathbf{C}''] \\ \cdots & \cdots & \cdots \\ [\mathbf{C}'']^T & \vdots & [\hat{\mathbf{C}}] \end{pmatrix} \begin{pmatrix} \{\dot{\mathbf{Z}}\} \\ \cdots \\ \{\dot{\mathbf{Z}}_p\} \end{pmatrix}$$

$$+ \begin{pmatrix} [\mathbf{K}'] & \vdots & [\mathbf{K}''] \\ \cdots & \cdots & \cdots \\ [\mathbf{K}'']^T & \vdots & [\hat{\mathbf{K}}] \end{pmatrix} \begin{pmatrix} \{\mathbf{Z}\} \\ \cdots \\ \{\mathbf{Z}_p\} \end{pmatrix} = \begin{pmatrix} \{\mathbf{F}_D\} \\ \cdots \\ [0] \end{pmatrix}$$

$$+ \begin{pmatrix} [-\mathbf{K}''] & \vdots & [-\mathbf{C}''] \\ \cdots & \cdots & \cdots \\ -[\mathbf{K}_c] & \vdots & [-\mathbf{C}_c] \end{pmatrix} \begin{pmatrix} \{\alpha\} \\ \cdots \\ \{\dot{\alpha}\} \end{pmatrix} \quad (1)$$

$$[\mathbf{M}_p]_{(2M\times 2M)} = [\mathrm{diag}(M_{p_j})], \quad j = 1, \ldots, 2M \quad (2)$$

$$\{\alpha\} = \begin{pmatrix} \alpha_1 \\ \alpha_2 \\ \alpha_3 \\ \alpha_4 \\ \vdots \\ \alpha_{2m-1} \\ \alpha_{2m} \end{pmatrix} \quad (11)$$

where N and $2M$ are the number of degrees of freedom of the rotor and the number of piezoelectric pushers, respectively; the $[M]$, $[C]$, and $[K]$ matrices are the rotor bearing system mass, damping, and stiffness, and $\{F_D\}$ represents the external forces exerted on the system. Note that vector $\{Z\}$ is $N \times 1$

$$[\mathbf{C}']_{(N\times N)} = [\mathbf{C}]_{(N\times N)} + \begin{array}{c} \\ j_1 \\ j_2 \\ \\ j_m \\ \end{array} \begin{array}{c} \begin{array}{cccccc} & j_1 & \cdots & j_2 & \cdots & j_m \end{array} \\ \begin{pmatrix} \cdots & \vdots & \cdots & \vdots & \cdots & \vdots & \cdots \\ \cdots & C_{c_1}+C_{c_2} & \cdots & \vdots & \cdots & \vdots & \cdots \\ \cdots & \vdots & \cdots & C_{c_3}+C_{c_4} & \cdots & \vdots & \cdots \\ \cdots & \vdots & \cdots & \vdots & \ddots & \vdots & \cdots \\ \cdots & \vdots & \cdots & \vdots & \cdots & C_{c_{2m-1}}+C_{c_{2m}} & \cdots \\ \cdots & \vdots & \cdots & \vdots & \cdots & \vdots & \cdots \end{pmatrix} \end{array} \quad (3)$$

$$[\mathbf{C}'']_{(N\times 2M)} = \begin{array}{c} \\ j_1 \\ j_2 \\ \\ j_m \\ \end{array} \begin{array}{c} \begin{array}{ccccccc} 1 & 2 & 3 & 4 & \cdots & 2M-1 & 2M \end{array} \\ \begin{pmatrix} \cdots & \cdots & \cdots & \cdots & \cdots & \cdots & \\ -C_{c_1} & -C_{c_2} & \cdots & \cdots & \cdots & \cdots & \cdots \\ \cdots & \cdots & -C_{c_3} & -C_{c_4} & \cdots & \cdots & \cdots \\ \cdots & \cdots & \cdots & \cdots & \ddots & \cdots & \cdots \\ \cdots & \cdots & \cdots & \cdots & \cdots & -C_{c_{2m-1}} & -C_{c_{2m}} \\ \cdots & \cdots & \cdots & \cdots & \cdots & \cdots & \cdots \end{pmatrix} \end{array} \quad (4)$$

$$[\hat{\mathbf{C}}]_{(2M\times 2M)} = [\mathrm{diag}(C_{A_j} + C_{c_j})], \quad j = 1, \ldots, 2M \quad (5)$$

$$[\mathbf{K}']_{(N\times N)} = [\mathbf{K}]_{(N\times N)} + \begin{array}{c} \\ j_1 \\ j_2 \\ \\ j_m \\ \end{array} \begin{array}{c} \begin{array}{cccccc} & j_1 & \cdots & j_2 & \cdots & j_m \end{array} \\ \begin{pmatrix} \cdots & \vdots & \cdots & \vdots & \cdots & \vdots & \cdots \\ \cdots & K_{c_1}+K_{c_2} & \cdots & \vdots & \cdots & \vdots & \cdots \\ \cdots & \vdots & \cdots & K_{c_3}+K_{c_4} & \cdots & \vdots & \cdots \\ \cdots & \vdots & \cdots & \vdots & \ddots & \vdots & \cdots \\ \cdots & \vdots & \cdots & \vdots & \cdots & K_{c_{2m-1}}+K_{c_{2m}} & \cdots \\ \cdots & \vdots & \cdots & \vdots & \cdots & \vdots & \cdots \end{pmatrix} \end{array} \quad (6)$$

$$[\mathbf{K}'']_{(N\times 2M)} = \begin{array}{c} \\ j_1 \\ j_2 \\ \\ j_m \\ \end{array} \begin{array}{c} \begin{array}{ccccccc} 1 & 2 & 3 & 4 & \cdots & 2M-1 & 2M \end{array} \\ \begin{pmatrix} \cdots & \cdots & \cdots & \cdots & \cdots & \cdots & \\ -K_{c_1} & -K_{c_2} & \cdots & \cdots & \cdots & \cdots & \cdots \\ \cdots & \cdots & -K_{c_3} & -K_{c_4} & \cdots & \cdots & \cdots \\ \cdots & \cdots & \cdots & \cdots & \ddots & \cdots & \cdots \\ \cdots & \cdots & \cdots & \cdots & \cdots & -K_{c_{2m-1}} & -K_{c_{2m}} \\ \cdots & \cdots & \cdots & \cdots & \cdots & \cdots & \cdots \end{pmatrix} \end{array} \quad (7)$$

$$[\hat{\mathbf{K}}]_{(2M\times 2M)} = [\mathrm{diag}(K_{A_j} + K_{c_j})], \quad j = 1, \ldots, 2M \quad (8)$$

$$[\mathbf{C}_c]_{(2M\times 2M)} = [\mathrm{diag}(C_{c_j})], \quad j = 1, \ldots, 2M \quad (9)$$

$$[\mathbf{K}_c]_{(2M\times 2M)} = [\mathrm{diag}(K_{c_j})], \quad j = 1, \ldots, 2M \quad (10)$$

and

and vector $\{Z_p\}$ is $2M \times 1$. The coefficients K_{C_i}, C_{C_i}, K_{A_j}, and C_{A_j} are explained in the nomenclature and (Palazzolo et al., 1989a).

Active Damping Feedback Theory (ADFT). Let the feedback law be defined as

$$\{\alpha\}_{(2M\times 1)} = -[\mathbf{G}]_{(2M\times N)}\{\dot{\mathbf{Z}}\}_{(N\times 1)} \quad (12)$$

where

$$[\mathbf{G}]_{(2\mathbf{M}\times\mathbf{N})} = \begin{array}{c} \\ 1 \\ 2 \\ 3 \\ 4 \\ \vdots \\ 2M-1 \\ 2M \end{array} \begin{pmatrix} & j_1 & j_2 & \cdots & j_m & \\ \cdots & G_1 & \cdots & \cdots & \cdots & \cdots \\ \cdots & G_2 & \cdots & \cdots & \cdots & \cdots \\ \cdots & \cdots & G_3 & \cdots & \cdots & \cdots \\ \cdots & \cdots & G_4 & \cdots & \cdots & \cdots \\ \cdots & \cdots & \cdots & \vdots & \cdots & \cdots \\ \cdots & \cdots & \cdots & \cdots & G_{2M-1} & \cdots \\ \cdots & \cdots & \cdots & \cdots & G_{2M} & \cdots \end{pmatrix} \tag{13}$$

Substituting Eqs. (12) and (13) into Eq. (1) gives the closed loop equation of the system:

$$\begin{pmatrix} [\tilde{\mathbf{M}}] & \vdots & [\mathbf{0}] \\ \cdots & \cdots & \cdots \\ [\tilde{\tilde{\mathbf{M}}}] & \vdots & [\mathbf{M_p}] \end{pmatrix} \begin{pmatrix} \{\ddot{\mathbf{Z}}\} \\ \cdots \\ \{\ddot{\mathbf{Z}}_\mathbf{p}\} \end{pmatrix} + \begin{pmatrix} [\tilde{\mathbf{C}}_\mathbf{c}] & \vdots & [\mathbf{C}'] \\ \cdots & \cdots & \cdots \\ [\tilde{\tilde{\mathbf{C}}}_\mathbf{c}] & \vdots & [\hat{\mathbf{C}}] \end{pmatrix} \begin{pmatrix} \{\dot{\mathbf{Z}}\} \\ \cdots \\ \{\dot{\mathbf{Z}}_\mathbf{p}\} \end{pmatrix}$$

$$+ \begin{pmatrix} [\mathbf{K}'] & \vdots & [\mathbf{K}''] \\ \cdots & \cdots & \cdots \\ [\mathbf{K}'']^\mathbf{T} & \vdots & [\hat{\mathbf{K}}] \end{pmatrix} \begin{pmatrix} \{\mathbf{Z}\} \\ \cdots \\ \{\mathbf{Z}_\mathbf{p}\} \end{pmatrix} = \begin{pmatrix} \{\mathbf{F}_D\} \\ \cdots \\ [\mathbf{0}] \end{pmatrix} \tag{14}$$

where

$$[\tilde{M}]_{(N\times N)} = [M]_{(N\times N)} - [C'']_{(N\times 2M)}[G]_{(2M\times N)} = [M]$$

$$\begin{array}{c} \\ j_1 \\ +j_2 \\ \vdots \\ j_m \\ \vdots \end{array} \begin{pmatrix} \cdots & j_1 & \cdots & j_2 & \cdots & j_m & \cdots \\ \cdots & \vdots & \cdots & \vdots & \cdots & \vdots & \cdots \\ \cdots & \tilde{M}_{j_1} & \cdots & \vdots & \cdots & \vdots & \cdots \\ \cdots & \vdots & \cdots & \tilde{M}_{j_2} & \cdots & \vdots & \cdots \\ \cdots & \vdots & \cdots & \vdots & \ddots & \vdots & \cdots \\ \cdots & \vdots & \cdots & \vdots & \cdots & \tilde{M}_{j_m} & \cdots \\ \cdots & \vdots & \cdots & \vdots & \cdots & \vdots & \cdots \end{pmatrix} \tag{15}$$

where

$$\tilde{M}_{j_i} = C_{c_{2i-1}}G_{2i-1} + C_{c_{2i}}G_{2i}; \quad i = 1, \ldots, M \tag{16}$$

$$[\tilde{\tilde{\mathbf{M}}}]_{(2\mathbf{M}\times\mathbf{N})} = -[\mathbf{C_c}]_{(2\mathbf{M}\times 2\mathbf{M})}[\mathbf{G}]_{(2\mathbf{M}\times\mathbf{N})}$$

$$= \begin{array}{c} \\ 1 \\ 2 \\ 3 \\ 4 \\ \vdots \\ 2M-1 \\ 2M \end{array} \begin{pmatrix} & j_1 & j_2 & \cdots & j_m & \\ \cdots & -C_{c_1}G_1 & \cdots & \cdots & \cdots & \cdots \\ \cdots & -C_{c_2}G_2 & \cdots & \cdots & \cdots & \cdots \\ \cdots & \cdots & -C_{c_3}G_3 & \cdots & \cdots & \cdots \\ \cdots & \cdots & -C_{c_4}G_4 & \cdots & \cdots & \cdots \\ \cdots & \cdots & \cdots & \ddots & \cdots & \cdots \\ \cdots & \cdots & \cdots & \cdots & -C_{c_{2m-1}}G_{2M-1} & \cdots \\ \cdots & \cdots & \cdots & \cdots & -C_{c_{2m}}G_{2M} & \cdots \end{pmatrix} \tag{17}$$

$$[\tilde{C}]_{(N\times N)} = [C']_{(N\times N)} - [K'']_{(N\times 2M)}[G]_{(2M\times N)} = [C]$$

$$\begin{array}{c} \\ j_1 \\ +j_2 \\ \vdots \\ j_m \\ \vdots \end{array} \begin{pmatrix} \cdots & j_1 & \cdots & j_2 & \cdots & j_m & \cdots \\ \cdots & \vdots & \cdots & \vdots & \cdots & \vdots & \cdots \\ \cdots & \tilde{C}_{cj_1} & \cdots & \vdots & \cdots & \vdots & \cdots \\ \cdots & \vdots & \cdots & \tilde{C}_{cj_2} & \cdots & \vdots & \cdots \\ \cdots & \vdots & \cdots & \vdots & \ddots & \vdots & \cdots \\ \cdots & \vdots & \cdots & \vdots & \cdots & \tilde{C}_{cj_m} & \cdots \\ \cdots & \vdots & \cdots & \vdots & \cdots & \vdots & \cdots \end{pmatrix} \tag{18}$$

where

$$\tilde{C}_{cj_i} = C_{c_{2i-1}} + C_{c_{2i}} + K_{c_{2i-1}}G_{2i-1} + K_{c_{2i}}G_{2i}; \quad i = 1, \ldots, M \tag{19}$$

$$[\tilde{\tilde{C}}_c]_{(2M\times N)} = [C'']^T_{(2M\times N)} - [K_c]_{(2M\times 2M)}[G]_{(2M\times N)}$$

$$= \begin{array}{c} \\ 1 \\ 2 \\ 3 \\ 4 \\ \vdots \\ 2M-1 \\ 2M \end{array} \begin{pmatrix} & j_1 & j_2 & \cdots & j_m & \\ \cdots & \tilde{\tilde{C}}_{1,j_1} & \cdots & \cdots & \cdots & \cdots \\ \cdots & \tilde{\tilde{C}}_{2,j_1} & \cdots & \cdots & \cdots & \cdots \\ \cdots & \cdots & \tilde{\tilde{C}}_{3,j_2} & \cdots & \cdots & \cdots \\ \cdots & \cdots & \tilde{\tilde{C}}_{4,j_2} & \cdots & \cdots & \cdots \\ \cdots & \cdots & \cdots & \vdots & \cdots & \cdots \\ \cdots & \cdots & \cdots & \cdots & \tilde{\tilde{C}}_{2M-1,j_m} & \cdots \\ \cdots & \cdots & \cdots & \cdots & \tilde{\tilde{C}}_{2M,j_m} & \cdots \end{pmatrix} \tag{20}$$

where

$$\begin{cases} \tilde{\tilde{C}}_{2i-1,j_i} = -(K_{c_{2i-1}}G_{2i-1} + C_{c_{2i-1}}) \\ \tilde{\tilde{C}}_{2i,j_i} = -(K_{c_{2i}}G_{2i} + C_{c_{2i}}) \end{cases} \quad i = 1, \ldots, M \tag{21}$$

Note that the "active" damping coefficients in Eqs. (18) and (19) are composed of products of feedback gain and pusher equivalent stiffness, i.e., $K * G$.

Active Stiffness Feedback Theory (ASFT). In this section, the pusher internal displacements are proportional to the bearing housing displacements rather than to their velocities. The feedback control law is

$$\{\alpha\}_{(2\mathbf{M}\times\mathbf{1})} = -[\mathbf{H}]_{(2\mathbf{M}\times\mathbf{N})}\{\mathbf{Z}\}_{(\mathbf{N}\times\mathbf{1})} \tag{22}$$

Note that the feedback gain matrix [H] has the same form as defined in Eq. (13). Substituting Eqs. (13) and (22) into Eq. (1) gives the closed-loop system equation as

$$\begin{pmatrix} [\mathbf{M}] & \vdots & [\mathbf{0}] \\ \cdots & \cdots & \cdots \\ [\mathbf{0}] & \vdots & [\mathbf{M_p}] \end{pmatrix} \begin{pmatrix} \{\ddot{\mathbf{Z}}\} \\ \cdots \\ \{\ddot{\mathbf{Z}}_\mathbf{p}\} \end{pmatrix} + \begin{pmatrix} [\tilde{\mathbf{C}}_\mathbf{K}] & \vdots & [\mathbf{C}''] \\ \cdots & \cdots & \cdots \\ [\tilde{\tilde{\mathbf{C}}}_\mathbf{K}] & \vdots & [\hat{\mathbf{C}}] \end{pmatrix} \begin{pmatrix} \{\dot{\mathbf{Z}}\} \\ \cdots \\ \{\dot{\mathbf{Z}}_\mathbf{p}\} \end{pmatrix}$$

$$+ \begin{pmatrix} [\tilde{\mathbf{K}}] & \vdots & [\mathbf{K}''] \\ \cdots & \cdots & \cdots \\ [\tilde{\tilde{\mathbf{K}}}] & \vdots & [\hat{\mathbf{K}}] \end{pmatrix} \begin{pmatrix} \{\mathbf{Z}\} \\ \cdots \\ \{\mathbf{Z}_\mathbf{p}\} \end{pmatrix} = \begin{pmatrix} \{\mathbf{F}_\mathbf{D}\} \\ \cdots \\ [\mathbf{0}] \end{pmatrix} \tag{23}$$

where

$$[\tilde{C}_K]_{(N\times N)} = [C']_{(N\times N)} - [C'']_{(N\times 2M)}[H]_{(2M\times N)} = [C]$$

$$\begin{array}{c} \\ j_1 \\ +j_2 \\ \vdots \\ j_m \\ \vdots \end{array} \begin{pmatrix} & j_1 & \cdots & j_2 & \cdots & j_m & \cdots \\ \cdots & \vdots & \cdots & \vdots & \cdots & \vdots & \cdots \\ \cdots & \tilde{C}_{kj_1} & \cdots & \vdots & \cdots & \vdots & \cdots \\ \cdots & \vdots & \cdots & \tilde{C}_{kj_2} & \cdots & \vdots & \cdots \\ \cdots & \vdots & \cdots & \vdots & \ddots & \vdots & \cdots \\ \cdots & \vdots & \cdots & \vdots & \cdots & \tilde{C}_{kj_m} & \cdots \\ \cdots & \vdots & \cdots & \vdots & \cdots & \vdots & \cdots \end{pmatrix} \tag{24}$$

where

$$\tilde{C}_{kj_i} = (1 + H_{2i-1}) C_{c_{2i-1}} + (1 + H_{2i}) C_{c_{2i}}; \quad i = 1, \ldots, M \tag{25}$$

$$[\tilde{\tilde{C}}_K]_{(2M \times N)} = [C'']^T_{(2M \times N)} - [C_c]_{(2M \times 2M)} [H]_{(2M \times N)}$$

$$= \begin{array}{c} \\ 1 \\ 2 \\ 3 \\ 4 \\ \vdots \\ 2M-1 \\ 2M \end{array} \begin{pmatrix} & j_1 & j_2 & \cdots & j_m & \\ \cdots & \tilde{\tilde{C}}_{k_1,j_1} & \cdots & \cdots & \cdots & \cdots \\ \cdots & \tilde{\tilde{C}}_{k_2,j_1} & \cdots & \cdots & \cdots & \cdots \\ \cdots & \cdots & \tilde{\tilde{C}}_{k_3,j_2} & \cdots & \cdots & \cdots \\ \cdots & \cdots & \tilde{\tilde{C}}_{k_4,j_2} & \cdots & \cdots & \cdots \\ \cdots & \cdots & \cdots & \ddots & \cdots & \cdots \\ \cdots & \cdots & \cdots & \cdots & \tilde{\tilde{C}}_{k_{2M-1},j_m} & \cdots \\ \cdots & \cdots & \cdots & \cdots & \tilde{\tilde{C}}_{k_{2M},j_m} & \cdots \end{pmatrix} \tag{26}$$

where

$$\begin{cases} \tilde{\tilde{C}}_{k_{2i-1},j_i} = -(1 + H_{2i-1}) C_{c_{2i-1}} \\ \tilde{\tilde{C}}_{k_{2i},j_i} = -(1 + H_{2i}) C_{c_{2i}} \end{cases} \quad i = 1, \ldots, j_M \tag{27}$$

Note that $[C']$, $[C'']$, and $[C_c]$ are defined in Eqs. (3), (4), and (9), respectively.

$$[\tilde{K}]_{(N \times N)} = [K']_{(N \times N)} - [K'']_{(N \times 2M)} [H]_{(2M \times N)} = [K]$$

$$\begin{array}{c} \\ j_1 \\ +\, j_2 \\ \\ j_m \end{array} \begin{pmatrix} & j_1 & \cdots & j_2 & \cdots & j_m & \cdots \\ \cdots & \vdots & \cdots & \vdots & \cdots & \vdots & \cdots \\ \cdots & \tilde{K}_{j_1} & \cdots & \vdots & \cdots & \vdots & \cdots \\ \cdots & \vdots & \cdots & \tilde{K}_{j_2} & \cdots & \vdots & \cdots \\ \cdots & \vdots & \cdots & \vdots & \ddots & \vdots & \cdots \\ \cdots & \vdots & \cdots & \vdots & \cdots & \tilde{K}_{j_m} & \cdots \\ \cdots & \vdots & \cdots & \vdots & \cdots & \vdots & \cdots \end{pmatrix} \tag{28}$$

where

$$\tilde{K}_{j_i} = (1 + H_{2i-1}) K_{c_{2i-1}} + (1 + H_{2i}) K_{c_{2i}}; \quad i = 1, \ldots, M$$

$$[\tilde{\tilde{K}}]_{(2M \times N)} = [K'']^T_{(2M \times N)} - [K_c]_{(2M \times 2M)} [H]_{(2M \times N)}$$

$$= \begin{array}{c} \\ 1 \\ 2 \\ 3 \\ 4 \\ \vdots \\ 2M-1 \\ 2M \end{array} \begin{pmatrix} & j_1 & j_2 & \cdots & j_m & \\ \cdots & \tilde{\tilde{K}}_{1,j_1} & \cdots & \cdots & \cdots & \cdots \\ \cdots & \tilde{\tilde{K}}_{2,j_1} & \cdots & \cdots & \cdots & \cdots \\ \cdots & \cdots & \tilde{\tilde{K}}_{3,j_2} & \cdots & \cdots & \cdots \\ \cdots & \cdots & \tilde{\tilde{K}}_{4,j_2} & \cdots & \cdots & \cdots \\ \cdots & \cdots & \cdots & \ddots & \cdots & \cdots \\ \cdots & \cdots & \cdots & \cdots & \tilde{\tilde{K}}_{2M-1,j_m} & \cdots \\ \cdots & \cdots & \cdots & \cdots & \tilde{\tilde{K}}^{\text{last}}_{2M,j_m} & \cdots \end{pmatrix} \tag{30}$$

where

$$\begin{cases} \tilde{\tilde{K}}_{2i-1,j_i} = -(1 + H_{2i-1}) K_{c_{2i-1}}; \\ \tilde{\tilde{K}}_{2i,j_i} = -(1 + H_{2i}) K_{c_{2i}} \end{cases} \quad i = 1, \ldots, M \tag{31}$$

Note that $[K']$, $[K'']$, and $[K_c]$ are defined in Eqs. (6), (7), and (10), respectively. The "active" stiffness coefficients in Eqs. (28) and (29) are composed of products of feedback gain and pusher equivalent stiffness, i.e., $K * H$.

Active Damping and Stiffness Feedback Theory (ADSFT). In this case the feedback control law of pusher internal displacement is defined to be proportional to the combination of rotor velocity and rotor displacement as:

$$\{\alpha\}_{(2M \times 1)} = -[\mathbf{G}]_{(2M \times N)} \{\dot{\mathbf{Z}}\}_{(N \times 1)} - [\mathbf{H}]_{(2M \times N)} \{\mathbf{Z}\}_{(N \times 1)} \tag{32}$$

Differentiating Eq. (32) gives

$$\{\dot{\alpha}\}_{(2M \times 1)} = -[\mathbf{G}]_{(2M \times N)} \{\ddot{\mathbf{Z}}\}_{(N \times 1)} - [\mathbf{H}]_{(2M \times N)} \{\dot{\mathbf{Z}}\}_{(N \times 1)} \tag{33}$$

Substituting Eqs. (11), (32), and (33) into Eq. (1) gives the matrix differential equation of the closed-loop system as:

$$\begin{pmatrix} [\tilde{M}] & \vdots & [0] \\ \cdots & \cdots & \cdots \\ [\tilde{\tilde{M}}] & \vdots & [M_p] \end{pmatrix} \begin{pmatrix} \{\ddot{\mathbf{Z}}\} \\ \cdots \\ \{\ddot{\mathbf{Z}}_p\} \end{pmatrix} + \begin{pmatrix} [\tilde{C}^*] & \vdots & [\mathbf{C}''] \\ \cdots & \cdots & \cdots \\ [\tilde{\tilde{C}}^*] & \vdots & [\hat{\mathbf{C}}] \end{pmatrix} \begin{pmatrix} \{\dot{\mathbf{Z}}\} \\ \cdots \\ \{\dot{\mathbf{Z}}_p\} \end{pmatrix}$$

$$+ \begin{pmatrix} [\tilde{\mathbf{K}}] & \vdots & [\mathbf{K}''] \\ \cdots & \cdots & \cdots \\ [\tilde{\tilde{\mathbf{K}}}] & \vdots & [\hat{\mathbf{K}}] \end{pmatrix} \begin{pmatrix} \{\mathbf{Z}\} \\ \cdots \\ \{\mathbf{Z}_p\} \end{pmatrix} = \begin{pmatrix} \{\mathbf{F}_D\} \\ \cdots \\ [\mathbf{0}] \end{pmatrix} \tag{34}$$

where $[M_p]$, $[\tilde{M}]$, $[\tilde{\tilde{M}}]$, $[C'']$, $[\hat{C}]$, $[K'']$, $[\hat{K}]$, $[\tilde{K}]$, $[\tilde{\tilde{K}}]$, and are defined in Eqs. (2), (15), (17), (4), (5), (7), (8), (28), and (30), respectively, and

$$[\tilde{C}^*]_{(N \times N)} = [C']_{(N \times N)} - [K'']_{(N \times 2M)} [G]_{(2M \times N)}$$
$$- [C'']_{(N \times 2M)} [H]_{(2M \times N)} = [C]$$

$$\begin{array}{c} \\ j_1 \\ +\, j_2 \\ \\ j_m \end{array} \begin{pmatrix} & j_1 & \cdots & j_2 & \cdots & j_m & \cdots \\ \cdots & \vdots & \cdots & \vdots & \cdots & \vdots & \cdots \\ \cdots & \tilde{C}^*_{j_1} & \cdots & \vdots & \cdots & \vdots & \cdots \\ \cdots & \vdots & \cdots & \tilde{C}^*_{j_2} & \cdots & \vdots & \cdots \\ \cdots & \vdots & \cdots & \vdots & \ddots & \vdots & \cdots \\ \cdots & \vdots & \cdots & \vdots & \cdots & \tilde{C}^*_{j_m} & \cdots \\ \cdots & \vdots & \cdots & \vdots & \cdots & \vdots & \cdots \end{pmatrix} \tag{35}$$

where

$$\tilde{C}^*_{j_i} = K_{c_{2i-1}} G_{2i-1} + (1 + H_{2i-1}) C_{c_{2i-1}} + (1 + H_{2i}) C_{c_{2i}}$$
$$i = 1, \ldots, M \tag{36}$$

and

$$[\tilde{\tilde{C}}^*]_{(2M \times N)} = [C'']^T_{(2M \times N)} - [K_c]_{(2M \times 2M)} [G]_{(2M \times N)}$$
$$- [C_c]_{(2M \times 2M)} [H]_{(2M \times N)}$$

$$= \begin{array}{c} \\ 1 \\ 2 \\ 3 \\ 4 \\ \vdots \\ 2M-1 \\ 2M \end{array} \begin{pmatrix} & j_1 & j_2 & \cdots & j_m & \\ \cdots & \tilde{\tilde{C}}^*_{1,j_1} & \cdots & \cdots & \cdots & \cdots \\ \cdots & \tilde{\tilde{C}}^*_{2,j_1} & \cdots & \cdots & \cdots & \cdots \\ \cdots & \cdots & \tilde{\tilde{C}}^*_{3,j_2} & \cdots & \cdots & \cdots \\ \cdots & \cdots & \tilde{\tilde{C}}^*_{4,j_2} & \cdots & \cdots & \cdots \\ \cdots & \cdots & \cdots & \ddots & \cdots & \cdots \\ \cdots & \cdots & \cdots & \cdots & \tilde{\tilde{C}}^*_{2M-1,j_m} & \cdots \\ \cdots & \cdots & \cdots & \cdots & \tilde{\tilde{C}}^*_{2M,j_m} & \cdots \end{pmatrix} \tag{37}$$

where

$$\begin{cases} \tilde{\tilde{C}}^*_{2i-1,j_i} = -[K_{c_{2i-1}} G_{2i-1} + (1 + H_{2i-1}) C_{c_{2i-1}}] \\ \tilde{\tilde{C}}^*_{2i,j_i} = -[K_{c_{2i}} G_{2i} + (1 + H_{2i}) C_{c_{2i}}] \end{cases}$$
$$i = 1, \ldots, M \tag{38}$$

Note that the matrix $[G]$ has the same form for both ADFT and ASFT, but the units are different. In ADFT, the unit of $[G]$ is seconds while the $[H]$ in ASFT is dimensionless.

Electromechanical Simulation With Nonideal Control Model

In the previous section and in previous references (Palazzolo et al., 1989a, 1989b) the free tip response of a piezoelectric pusher is assumed to be approximately equal to the internal prescribed displacement, which is assumed to vary in proportion to input voltage at all frequencies. This assumption is

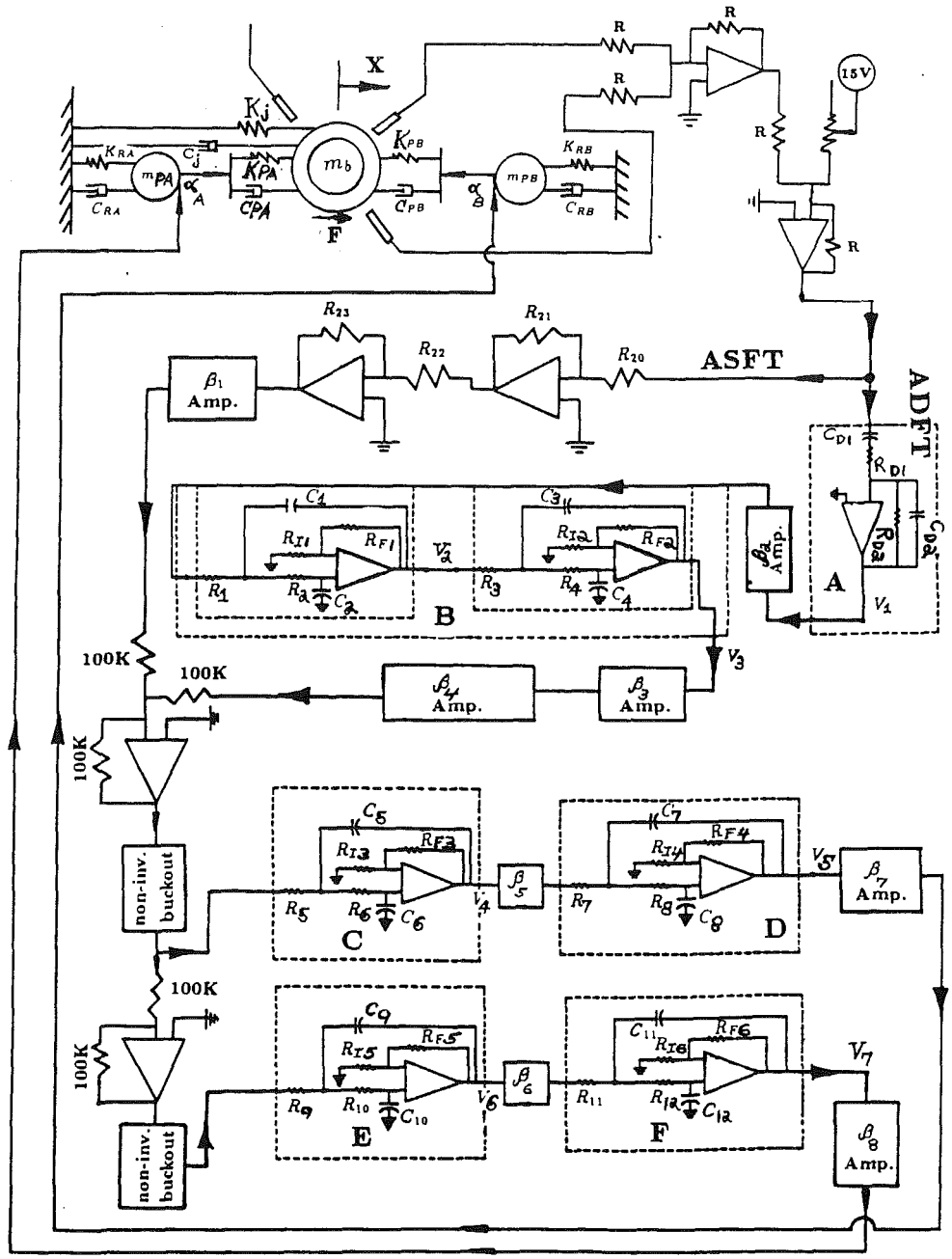

Fig. 3 Electromechanical model with two opposing soft-mounted pushers

valid only at frequencies well below the resonant frequency of the pusher. The phase lag of the piezoelectric pusher increases with frequency and may even cause negative active damping to occur if the phase lag is greater than 90 deg. Phase lag is also introduced by the pusher drivers and other electronic components in the control loop, such as filters and differentiators.

A linear time-invariant system with input $f(t)$ and with output $r(t)$ can be characterized by its impulse response $g(t)$, which is the response when subjected to an unit impulse input $\delta(t)$. Once the impulse response of the linear system is known, the output of the system $r(t)$, with any input $f(t)$, may be found from the transfer function of the system.

The transfer function of a linear time-invariant system is defined as the Laplace transform of the impulse response with zero initial conditions (Kuo, 1987). In general, if a linear system has p inputs and q outputs, the transfer function between the ith output and the jth input is defined as

$$G_{ij}(S) = \frac{R_i(S)}{F_j(S)} \tag{39}$$

where $F_j(S) = 0, j = 1, 2, \ldots, p, j \neq i$.

Equivalent electrical circuits are constructed to reproduce the measured transfer (frequency response) functions of the piezoelectric actuators and their amplifier drivers. The linear differential equations of these circuits may then be assembled with the structural system equations to form a coupled electromechanical model.

An electromechanical representation of an AVC system, consisting of soft-mounted pushers, isolation pads, probes, and control devices, is shown in Fig. 3. In this figure the buckout circuit removes d-c bias from the eddy current displacement sensor; the low pass filter (B) (L.P.F.) is utilized to reduce high-frequency noise and improve stability. The figure also shows how the piezoelectric actuator (D) and its amplifier driver (C) are both represented by equivalent second-order

noninverting low pass filters. With this model, the nonideal characteristics of the overall system due to phase lag and frequency dependency can be included.

The differential equation for the differentiator (A) in Fig. 3 is

$$-\dot{V}_{in} = R_{D1}C_{D2}\ddot{V}_{\text{out}} + \left(\frac{R_{D1}}{R_{D2}} + \frac{C_{D2}}{C_{D1}}\right)\dot{V}_{\text{out}} + \frac{1}{R_{D2}C_{D1}}V_{\text{out}} \quad (40)$$

The corresponding transfer function is then

$$T.F. = \frac{V_{\text{out}}(S)}{V_{in}(S)} = \frac{-R_{D2}C_{D1}S}{[R_{D1}R_{D2}C_{D1}C_{D2}S^2 + (R_{D1}C_{D1} + R_{D2}C_{D2})S + 1]} \quad (41)$$

If the variable S in Eq. (41) is replaced by the variable jw, then Eq. (41) represents the frequency response function of the differentiator in the frequency domain.

The differential equation for the second-order noninverting low pass filter is

$$V_1 = \frac{R_1R_2C_1C_2}{K}\ddot{V}_2 + \left(-R_1C_1 + \frac{R_1C_2}{K} + \frac{R_1C_1}{K} + \frac{R_2C_2}{K}\right)\dot{V}_2 + \frac{1}{K}V_2 \quad (42)$$

The corresponding transfer function is then

$$T.F. = \frac{V_2(S)}{V_1(S)} = \frac{\dfrac{K}{(R_1R_2C_1C_2)}}{S^2 + \left[\dfrac{1}{C_1}\left(\dfrac{1}{R_1} + \dfrac{1}{R_2}\right) + \dfrac{1}{R_2C_2}(1-K)\right]S + \dfrac{1}{R_1R_2C_1C_2}} \quad (43)$$

Again, if the variable S is replaced by the variable jw in the above equation, Eq. (43) represents the frequency response function in the frequency domain and is shown below:

$$T.F. = \frac{V_2(jw)}{V_1(jw)} = \frac{K}{(1 - R_1R_2C_1C_2\omega^2) + jw[C_2(R_1 + R_2) + (1-K)R_1C_1]} \quad (44)$$

The electrically undamped natural frequency, ω_n, of this circuit is defined by

$$\omega_n^2 = \frac{1}{R_1R_2C_1C_2} \quad (45)$$

and the phase lag angle is

$$\phi = \tan^{-1}\frac{\omega[C_2(R_1 + R_2) + (1-K)R_1C_1]}{1 - \left(\dfrac{\omega}{\omega_n}\right)} \quad (46)$$

The following steps summarize a simple procedure to identify the resistances and capacitances of an equivalent second-order noninverting low pass filter:

(a) Make a frequency response plot of the physical system (pusher or pusher driver).

(b) Locate the cutoff frequency, ω_n, from this plot.

(c) Assume $R_1 = R_2$ and $C_1 = C_2$.

(d) Select C_1 arbitrarily and then calculate R_1 by

$$R_1 = \frac{1}{\omega_n C_1}$$

(e) Use $K = 3$ for an undamped electrical system and $K < 3$ for damped electrical system.

(f) Construct the electrical circuit using the calculated R and C values.

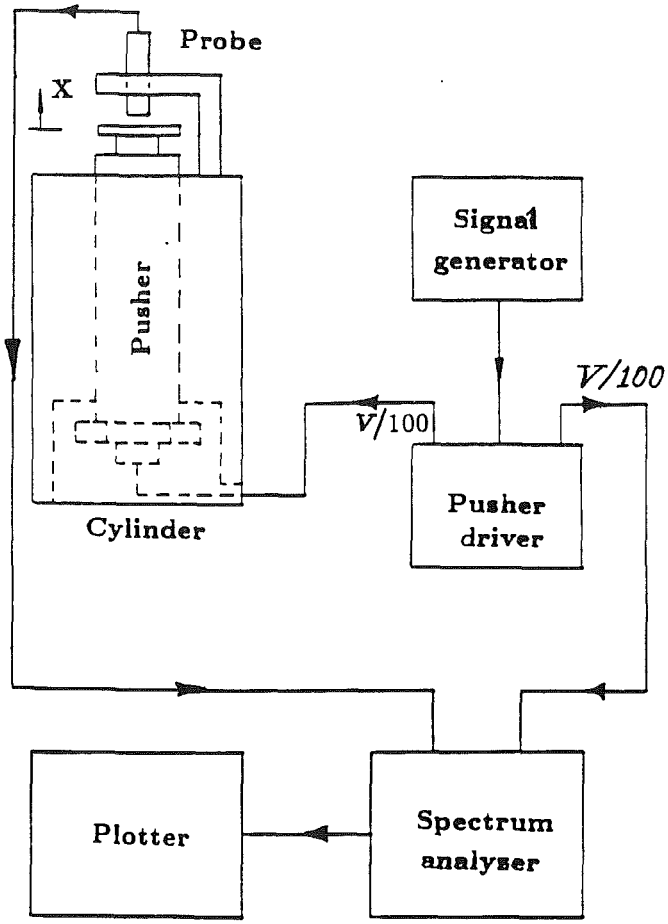

Fig. 4 Schematic diagram for measuring the pusher frequency response function

(g) Adjust the damping factor in the equivalent electrical circuit by varying the K value to match the peak magnitude at the cutoff frequency location.

(h) Multiply this realized frequency response function by a proper scale factor, which represents the magnitude ratio between the known and the realized frequency response functions at $\omega = 0$.

Figure 4 shows the schematic diagram for measuring the frequency response function of a pusher. The pusher is secured inside a vertical steel cylinder and excited by a signal generator through the pusher driver. The displacement of the free tip of the pusher, the output for the frequency response function, is measured by an eddy current probe. The exciting signal is the input for the frequency response function. Both input and output are connected to a spectrum analyzer and the results of the frequency response function are sent to a printer.

Figure 5 shows the frequency response function of a typical pusher while Fig. 6 shows the corresponding frequency response function of the equivalent second-order noninverting low pass filter circuit with identified R and C values. This simulation shows a very good correlation between the two transfer functions when the frequency is below 4000 Hz. Note that a jet aircraft engine, depending on the size, normally operates at speeds from 5000 rpm (83.3 Hz) up to 25000 rpm (416.6 Hz). Furthermore, electromechanical instability frequencies have always occurred below 4000 Hz, in our testing.

The stability of the active vibration control system is affected by both the characteristics of the mechanical system (e.g., rotor) and those of the electrical devices (e.g., actuators) used in the control feedback loop. The characteristics, i.e., phase lag, of the electrical devices are incorporated in the mechanical system model by including their frequency response function

behavior represented by equivalent electrical circuits. Incorporation of an opposing piezoelectric pusher assembly acting on a bearing housing into the simulation model is discussed next.

Let two opposing, soft-mounted pushers be installed at the jth bearing of the rotor system (see Fig. 3) where m_b, c_j, and k_j are the mass, damping, and stiffness of the jth bearing, and k_{PA} and k_{PB} are the stiffnesses of pushers A and B. The dashed blocks represent the following components:

Block A: Inverting differentiator
Block B: Fourth-order noninverting low pass filter to simulate the Ithaco filter
Block C: Second-order noninverting low pass filter to simulate pusher driver B
Block D: Second-order noninverting low pass filter to simulate pusher B
Block E: Second-order noninverting low pass filter to simulate pusher driver A
Block F: Second-order noninverting low pass filter to simulate pusher A

Combining the mechanical and electrical differential equations for the model in Fig. 3 yields

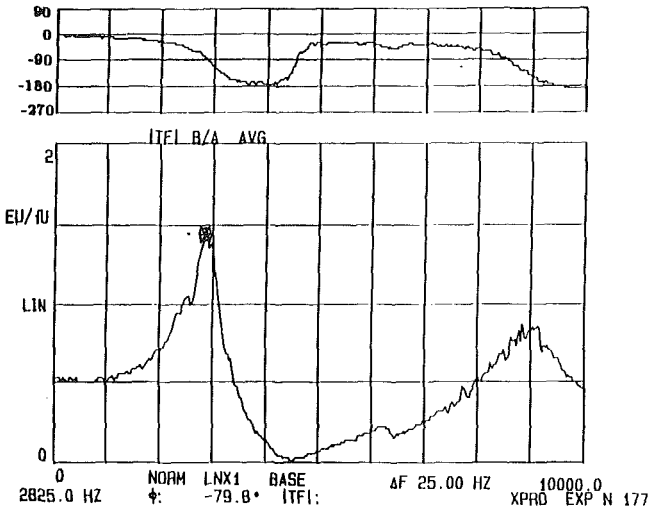

Fig. 5 Transfer function plot of a typical pusher

$$
\begin{pmatrix}
m_b & 0 & 0 & 0 & 0 & 0 & 0 & 0 & 0 & 0 \\
0 & m_{PA} & 0 & 0 & 0 & 0 & 0 & 0 & 0 & 0 \\
0 & 0 & m_{PB} & 0 & 0 & 0 & 0 & 0 & 0 & 0 \\
0 & 0 & 0 & R_{D1}C_{D2} & 0 & 0 & 0 & 0 & 0 & 0 \\
0 & 0 & 0 & 0 & 1 & 0 & 0 & 0 & 0 & 0 \\
0 & 0 & 0 & 0 & 0 & 1 & 0 & 0 & 0 & 0 \\
0 & 0 & 0 & 0 & 0 & 0 & 1 & 0 & 0 & 0 \\
0 & 0 & 0 & 0 & 0 & 0 & 0 & 1 & 0 & 0 \\
0 & 0 & 0 & 0 & 0 & 0 & 0 & 0 & 1 & 0 \\
0 & 0 & 0 & 0 & 0 & 0 & 0 & 0 & 0 & 1
\end{pmatrix}
\times
\begin{pmatrix}
\ddot{x} \\ \ddot{x}_A \\ \ddot{x}_B \\ \ddot{V}_1 \\ \ddot{V}_2 \\ \ddot{V}_3 \\ \ddot{V}_4 \\ \ddot{V}_5 \\ \ddot{V}_6 \\ \ddot{V}_7
\end{pmatrix}
+
\begin{pmatrix}
c_j & 0 & 0 & 0 & 0 & 0 & 0 & 0 & 0 & 0 \\
0 & C_{RA} & 0 & 0 & 0 & 0 & 0 & 0 & 0 & 0 \\
0 & 0 & C_{RB} & 0 & 0 & 0 & 0 & 0 & 0 & 0 \\
\zeta_1 & 0 & 0 & \left(\frac{R_{D1}}{R_{D2}}+\frac{C_{D2}}{C_{D1}}\right) & 0 & 0 & 0 & 0 & 0 & 0 \\
0 & 0 & 0 & 0 & A_1 & 0 & 0 & 0 & 0 & 0 \\
0 & 0 & 0 & 0 & 0 & A_2 & 0 & 0 & 0 & 0 \\
0 & 0 & 0 & 0 & 0 & 0 & A_3 & 0 & 0 & 0 \\
0 & 0 & 0 & 0 & 0 & 0 & 0 & A_4 & 0 & 0 \\
0 & 0 & 0 & 0 & 0 & 0 & 0 & 0 & A_5 & 0 \\
0 & 0 & 0 & 0 & 0 & 0 & 0 & 0 & 0 & A_6
\end{pmatrix}
\times
\begin{pmatrix}
\dot{x} \\ \dot{x}_A \\ \dot{x}_B \\ \dot{V}_1 \\ \dot{V}_2 \\ \dot{V}_3 \\ \dot{V}_4 \\ \dot{V}_5 \\ \dot{V}_6 \\ \dot{V}_7
\end{pmatrix}
+
\begin{pmatrix}
k_{11} & k_{12} & k_{13} & 0 & 0 & 0 & 0 & k_{18} & 0 & k_{110} \\
k_{21} & k_{22} & 0 & 0 & 0 & 0 & 0 & 0 & 0 & k_{210} \\
k_{31} & 0 & k_{33} & 0 & 0 & 0 & 0 & k_{38} & 0 & 0 \\
0 & 0 & 0 & k_{44} & 0 & 0 & 0 & 0 & 0 & 0 \\
0 & 0 & 0 & k_{45} & k_{55} & 0 & 0 & 0 & 0 & 0 \\
0 & 0 & 0 & 0 & k_{65} & k_{66} & 0 & 0 & 0 & 0 \\
k_{71} & 0 & 0 & 0 & 0 & k_{76} & k_{77} & 0 & 0 & 0 \\
0 & 0 & 0 & 0 & 0 & 0 & k_{87} & k_{88} & 0 & 0 \\
k_{91} & 0 & 0 & 0 & 0 & k_{96} & 0 & 0 & k_{99} & 0 \\
0 & 0 & 0 & 0 & 0 & 0 & 0 & 0 & k_{109} & k_{1010}
\end{pmatrix}
\times
\begin{pmatrix}
x \\ x_A \\ x_B \\ V_1 \\ V_2 \\ V_3 \\ V_4 \\ V_5 \\ V_6 \\ V_7
\end{pmatrix}
=
\begin{pmatrix}
F(t) \\ 0 \\ 0 \\ 0 \\ 0 \\ 0 \\ 0 \\ 0 \\ 0 \\ 0
\end{pmatrix}
\tag{47}
$$

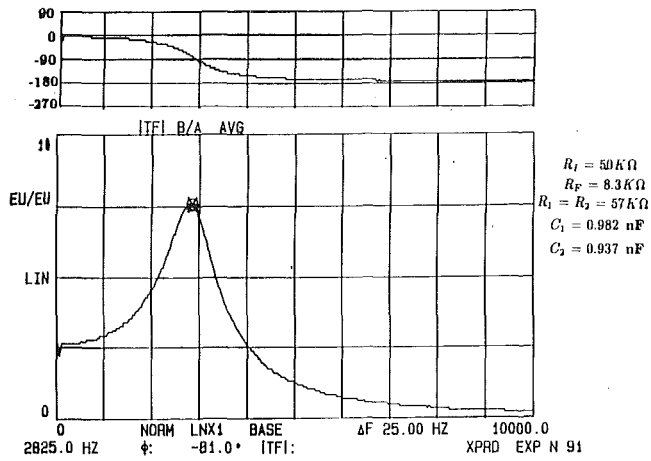

Fig. 6 Transfer function plot of realized electrical circuit of pusher *A*

where

$$
\begin{aligned}
k_{11} &= k_j + k_{PA} + k_{PB} & k_{12} &= -k_{PA} \\
k_{13} &= -k_{PB} & k_{18} &= k_{PB}\beta_7 \\
k_{1,10} &= -k_{PA}\beta_8 & k_{21} &= -k_{PA} \\
k_{22} &= k_{RA} + k_{PA} & k_{2,10} &= k_{PA}\beta_8 \\
k_{31} &= -k_{PB} & k_{33} &= k_{RB} + k_{PB} \\
k_{38} &= -k_{PB}\beta_7 & k_{44} &= \frac{1}{C_{D1}R_{D2}} \\
k_{54} &= -\omega_1^2 K_1\beta_2 & k_{55} &= \omega_1^2 \\
k_{65} &= -\omega_2^2 K_2 & k_{66} &= \omega_2^2 \\
k_{71} &= \omega_3^2 K_3\beta_1\zeta_1 & k_{76} &= \omega_3^2 K_3\beta_3\beta_4 \\
k_{77} &= \omega_3^2 & k_{87} &= -\omega_4^2 K_4\beta_5 \\
k_{88} &= \omega_4^2 & k_{91} &= -\omega_5^2 K_5\beta_1\zeta_1 \\
k_{96} &= -\omega_5^2 K_5\beta_3\beta_4 & k_{99} &= \omega_5^2 \\
k_{10,9} &= -\omega_6^2 K_6\beta_6 & k_{10,10} &= \omega_6^2
\end{aligned} \tag{48}
$$

and where K_i is the internal zero frequency gain of the individual filter and is defined as

$$K_i = \frac{R_{I_i} + R_{F_i}}{R_{I_i}}, \quad i = 1, 2 \tag{49}$$

and

$$\omega_i^2 = \frac{1}{R_{2i-1}R_{2i}C_{2i-1}C_{2i}}, \quad i = 1, 2 \tag{50}$$

$$A_i = \left[\frac{1}{C_{2i-1}}\left(\frac{1}{R_{2i-1}} + \frac{1}{R_{2i}}\right) + \frac{1-K_i}{R_{2i}C_{2i}}\right], \quad i = 1, 2 \tag{51}$$

$$\alpha_A = \beta_8 V_7 \tag{52}$$

$$\alpha_B = \beta_7 V_5 \tag{53}$$

$$V_p = \zeta_1 x \tag{54}$$

Finally β_5 and β_7 are the scale factors used to match the amplitudes (to those of the equivalent electrical circuit) of the frequency response functions of the pusher driver B and pusher B, respectively.

The "electromechanical" element matrices in Eq. (47) are next assembled into the structural finite element model of the rotor bearing system. The total system model can then be employed for free or forced vibration response simulation.

Test Result Correlation

A diagram representing the actively controlled rotor bearing test rig at NASA Lewis is shown in Fig. 2. Each bearing has a control circuit as shown in this figure. Unbalance response was obtained by measuring the influence coefficients for an

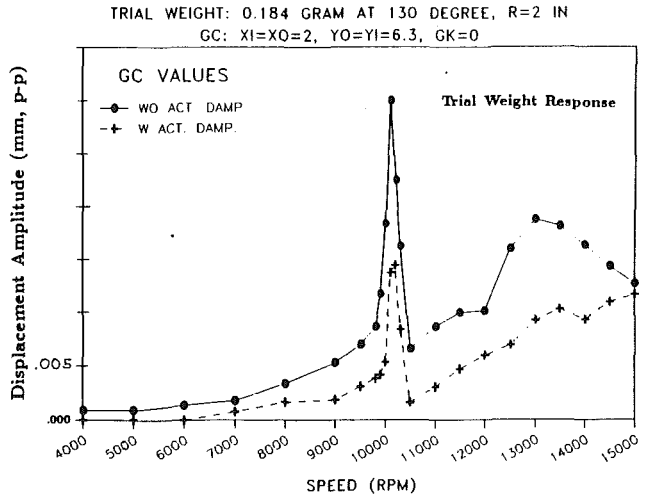

Fig. 7 Measured unbalance responses at YO^{+}_{BRG} with and without ADFT

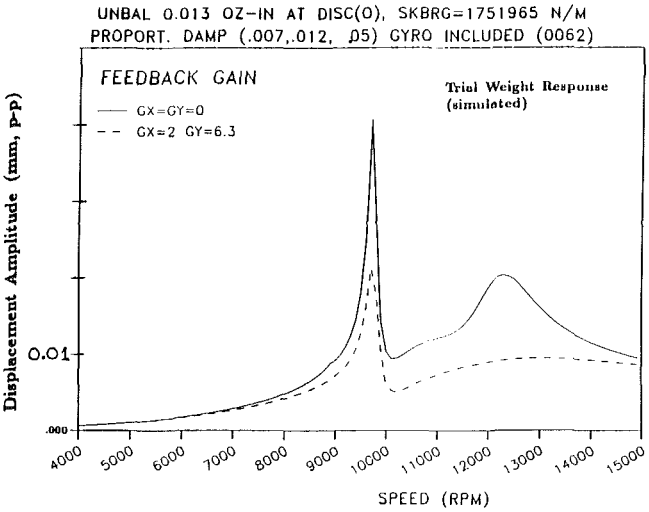

Fig. 8 Simulated unbalance responses at YO^{+}_{BRG} with and without ADFT, with three-mode proportional damping method

imbalance attached on the outboard disk. Figure 7 shows the measured influence coefficient at the outboard bearing for the controlled and uncontrolled cases. Figure 8 shows that the predicted influence coefficient as obtained from the electromechanical simulation model is in good agreement with the test results. The simulation model employed a proportional damping assumption for the uncontrolled (tare) system. The predicted response in Fig. 8 was identical for both the "ideal" and "nonideal" simulation models discussed in the preceding section. The similarity of the predicted and measured results lends credibility to the accuracy of the representation of the pusher model presented in Fig. 1.

The Y_O velocity feedback gain was increased in Fig. 2 until the system became unstable at zero rpm. The unstable mode shape was measured with a transient analyzer and appears in Fig. 9. Figure 10 shows that the corresponding unstable mode predicted by the "nonideal" electromechanical simulation model is very similar in form and frequency. The instability onset-feedback gain was very sensitive to the amount of passive damping of the unstable mode. The measured passive damping ratios for this mode ranged between 0.001 and 0.01. The measured instability onset feedback gain (β_4) was 5. The predicted value was 7 with an unstable mode passive damping of 0.001.

The "nonideal" electromechanical simulation model can be very useful for determining changes to either the electrical (control) or structural (rotorbearing) systems to improve sta-

bility or forced response. To illustrate this Fig. 11 shows the simulation model's predicted real part of the unstable mode (Fig. 9 or 10) versus cutoff frequency of the low pass filter (B) in Fig. 3. The cutoff frequency is in turn a direct function of the resistors and capacitors in that filter. Figure 11 was generated with a tare (passive) damping factor of $G = 0.0011$ for the unstable mode.

Figure 12 shows the measured unbalance response amplitude at the rotor's midspan location, with and without active vibration control. In this test case active stiffness was applied below 10,500 rpm and both active stiffness and damping were applied above 10,500 rpm.

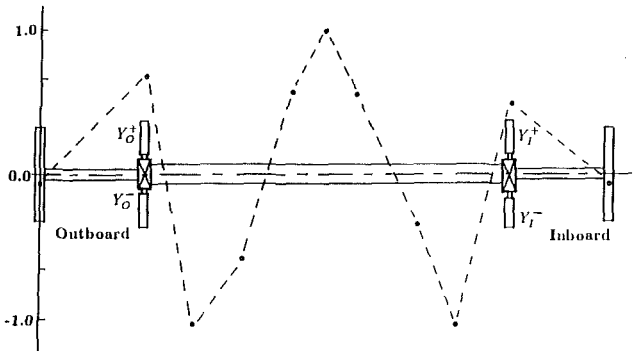

Fig. 9 Measured mode shape of unstable mode at a frequency of 2100 Hz

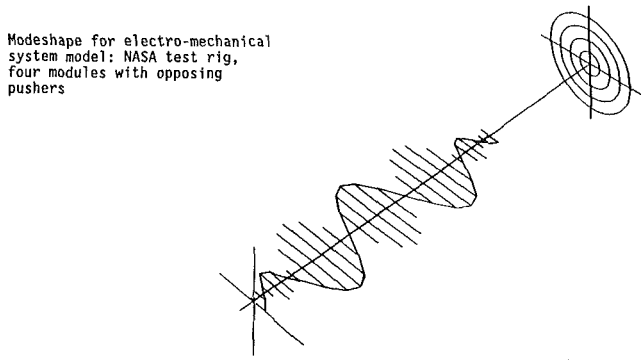

Fig. 10 Predicted mode shape of unstable mode at 2400 Hz

Summary

This paper summarizes theoretical developments for the simulation of an actively controlled rotorbearing system with piezoelectric type actuators. Two simulation models were derived; the first assumes that the actuators and other electrical components in the feedback system operate at all frequencies without phase lag or rolloff; the second model includes the nonideal behavior of these components, which are modeled with linear electric circuits. The two models predict identical unbalance response at low frequencies and the nonideal model also predicts instability-onset feedback gains. The agreement between the measured and predicted results for unbalance response and instability onset gain is very good. The predicted instability-onset feedback gain for active damping was found to be very sensitive to the tare (uncontrolled) damping in the unstable mode.

A PD type controller was utilized in this research to suppress vibration. The differentiator circuit employed in this controller has a rolloff characteristic, which eliminates high frequency noise amplification. The basic method of control utilized is to feedback velocity and displacement to a "displacement-based" actuator to obtain active stiffness and damping. Since no tracking type target signal is employed and the vibration is steady-state harmonic, it was not necessary to use a PDI type controller. Some control systems employ observers to obtain non-measured state variables. The authors did not utilize this approach since they felt it would be impractical at the relatively high frequencies of vibration encountered.

Future research in this area will include installation of the piezoelectric actuator AVC in a gas turbine driven transmission line at Lewis and incorporation of casing flexibility effects into the simulation model.

Acknowledgments

The authors gratefully acknowledge the funding for this research provided by NASA Lewis, the Texas A&M Turbomachinery Consortium, and the U.S. Army. Sincere appreciation is also extended to the following people for their technical assistance: John Ropchock, Dr. Gerald Brown, and Tom Lokatos.

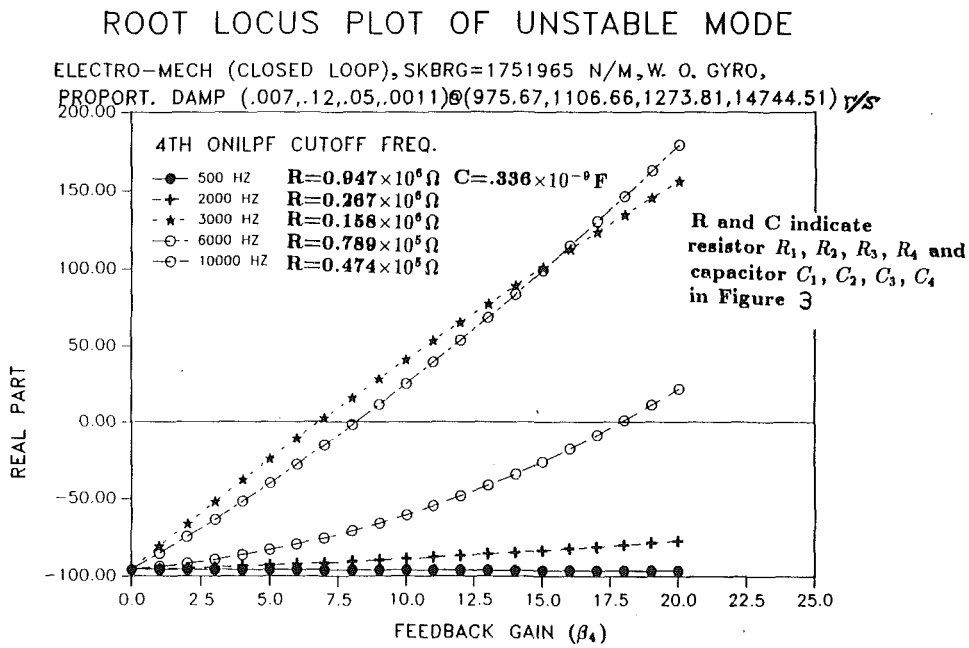

Fig. 11 Effects of cutoff frequency of 4NILPF on the system instability onset gain

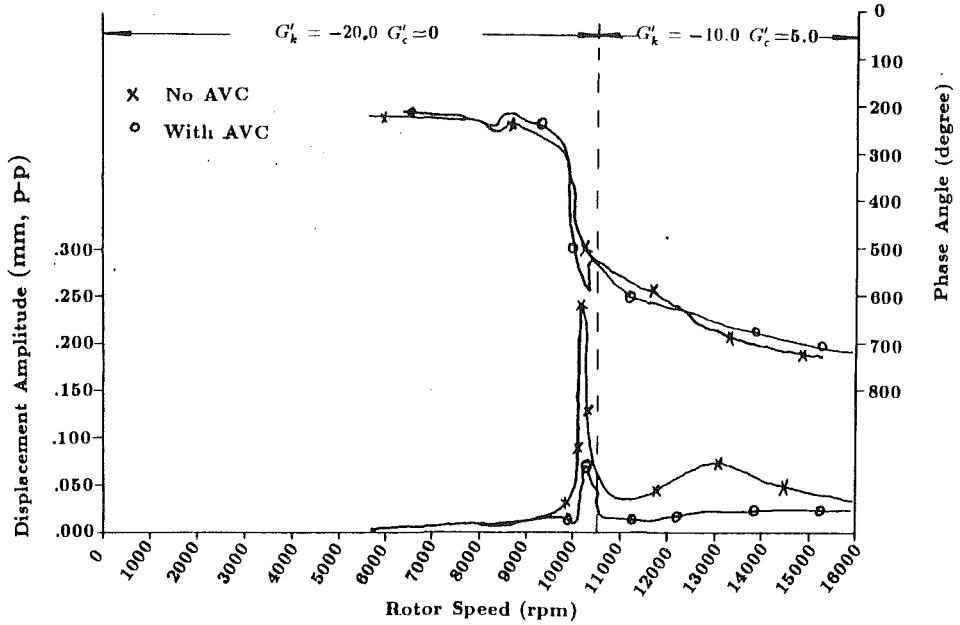

Fig. 12 Midspan vibration with and without active damping and stiffness

References

Burleigh, 1988, "The Piezo Book," 330-288-51683-0, Burleigh Park, Fishers, NY.

Crawley, E. F., and de Luis, J., 1983, "Experimental Verification of Piezoelectric Actuators for Use in Precision Space Structures," AIAA Paper No. 83-0878.

Crawley, E. F., and de Luis, J., 1985, "Use of Piezoceramics as Distributed Actuators in Large Space Structures," *Proceedings of the 26th Structures, Structural Dynamics, and Materials Conference, Part 2*, AIAA-ASME-ASCE, Orlando, FL, Apr., pp. 126-133.

Feng, G., and Xin, N., 1986, "Automatic Control of the Vibration of the Flexible Rotor With Microcomputer," *Int. Conf. on Rotordynamics*, IFTOMM and JSME, Tokyo, Sept., pp. 14-17.

Gondholekar, V., and Holmes, R., 1984, "Design of Electromagnetic Bearing for Vibration Control of Flexible Transmission Shaft," *Rotor Dynamic Instability Problem in High Performance Turbomachinery*, Texas A&M Univ., May.

Heinzmann, J. D., Flack, R., and Lewis, D., 1980, "The Implementation of Automatic Vibration Control in High Speed Rotating Test Facility," Univ. of Virginia Report UVA/464761/MAE80/160.

Hermann, E., 1988, personal communications, Hartford Insurance, Houston, TX.

Humphris, R., et al., 1986, "Effect of Control Algorithms on Magnetic Journal Bearing Properties," ASME JOURNAL OF ENGINEERING FOR GAS TURBINES AND POWER, Vol. 108, pp. 624-632.

Kuo, B. C., 1987, "Automatic Control Systems," 5th ed., Prentice-Hall, Inc., Englewood Cliffs, NJ.

Lin, Reng R., 1990, "Active Vibration Control of Rotor-bearing Systems Utilizing Piezoelectric Pushers," Texas A&M University Dissertation, Mechanical Engineering Department, Aug.

Matsubara, T., Yamamoto, H., and Mizumoto, H., 1989, "Chatter Suppression by Using Piezoelectric Active Dampers," *Rotatory Machinery Dynamics*, ASME DE-Vol. 18-1, 12th Biennial Conference on Mechanical Vibration and Noise, Montreal, Quebec, Canada, Sept., pp. 79-83.

Nikolajsen, J., Holmes, R., and Gondholekar, V., 1979, "Investigation of an Electromagnetic Damper for Vibration Control of a Transmission Shaft," *Proc. Instn. Mech. Engr.*, Vol. 193, pp. 331-336.

Palazzolo, A. B., 1981, "Vibrations of Locally Modified Mechanical and Structural Systems," University of Virginia Dissertation, Mechanical Engineering, Jan.

Palazzolo, A. B., Lin, R. R., Kascak, A. F., Montague, J., and Alexander, R. M., 1989a, "Test and Theory for Piezoelectric Actuator—Active Vibration Control of Rotating Machinery," submitted to ASME *Journal of Vibration, Acoustics, Stress, and Reliability in Design*.

Palazzolo, A. B., Lin, R. R., Kascak, A. F., Montague, J., and Alexander, R. M., 1989b, "Piezoelectric Pushers for Active Vibration Control of Rotating Machinery," ASME *Journal of Vibration, Acoustics, Stress, and Reliability in Design*, Vol. 111, pp. 298-305.

Schweitzer, G., 1985, "Magnetic Bearings for Vibration Control," Bently Nevada Instability Seminar, Minden, NV.

Stjernstrom, S. C., 1987, "Active Vibration Control Using Piezoceramic Transducers," Texas A&M University Thesis, Mechanical Engineering Department, Dec.

Tzou, H. S., 1987, "Active Vibration Control of Flexible Structures Via Converse Piezoelectricity," presented at the 20th Midwestern Mechanics Conference, 8/31-9/2; *Developments in Mechanics*, pp. 1201-1206, Vol. 14-c.

Ulbrich, H., and Althaus, J., 1989, "Actuator Design for Rotor Control," *Machinery Dynamics—Applications and Vibration Control Problems*, ASME DE-Vol. 18-2, pp. 17-22.

Weise, D., 1985, "Active Magnetic Bearings Provide Closed Loop Servo Control for Enhanced Dynamic Response," *Proc. 27th IEEE Machine Tool Conf.*, Oct.

Design of a Hydraulic Actuator for Active Control of Rotating Machinery

M. Rashidi
Assistant Professor,
Mechanical Engineering Department,
Cleveland State University,
Cleveland, OH 44135

E. Dirusso
Aerospace Engineer,
Structural Dynamics Branch,
NASA Lewis Research Center,
Cleveland, OH 44135

A hydraulic actuator was designed and is described herein. This actuator consists of: a pump, which generates the nominal pressure, a hydraulic servovalve, and a thin elastic plate, which transduces the generated pressure variations into forces acting on a mass, which simulates the bearing of a rotor system. An actuator characteristic number is defined to provide a base for an optimum design of force actuators with combined weight, frequency, and force considerations. This characteristic number may also be used to compare hydraulic and electromagnetic force actuators. In tests this actuator generated 182.3 N force at a frequency of 100. Hz. and a displacement amplitude of 5.8×10^{-5} *m.*

Introduction

Demands for higher frequencies, improved reliability, reduced noise, higher longevity, and safety require an effectively controlled rotor dynamics system. Using only passive damping elements often does not meet the desired requirements; further improvements can be achieved only with the aid of active elements. In the growing field of vibration control of rotating machinery, many different kinds of concepts have already been applied. In general, the controlled forces may be applied to the rotor system directly (magnetic bearings) or indirectly (via the existing contact or journal bearings).

The key to success in improving the dynamic behavior of rotor systems by active elements lies in the availability of suitable actuators. For industrial applications, the actuators have to be compact, capable of generating high forces at frequencies as high as needed (up to 500 Hz), and able to generate required displacements in the range of the vibration amplitudes to be influenced. The usefulness of electromagnetic actuators has been proven for many special applications, but electromagnetic actuators require a relatively large amount of space, corresponding to the attainable forces. Employing these actuators on rotating shafts often demands a considerable design alteration of an existing machine. This deficiency may be avoided by the use of hydraulically controlled actuators acting via the bearings on the rotor.

Conventional cylinder-piston hydraulic actuators possess moving elements (the piston) with high inertia, which are not desirable; in addition, sealing problems and friction forces may arise. These are unfavorable characteristics of the dynamic behavior of a conventional hydraulic actuator, especially at higher frequencies.

Generating high magnitudes of force at high frequencies with large displacement amplitudes is a fundamental performance characteristic of a force actuator. If the overall weight of a force actuator is included as a constraint in its design optimization process, a unified design criterion may be defined as follows:

$$\text{ODAN} = \frac{F_\omega X_L}{W} \tag{1}$$

where ODAN = Optimally Designed Actuator Number; F = magnitude of the force generated; ω = frequency of the force generated; X_L = displacement of the force generated; W = overall weight of the actuator.

Using the above criterion, hydraulic and electromagnetic force actuators can be compared with each other in terms of their suitability for a particular application. Depending upon the specific application site of the actuator (aerospace or earth-bound machines) the expression given in (1) can be modified as:

$$\text{ODAN} = \frac{\alpha_1 F \alpha_2 \omega \alpha_3 X_L}{\alpha_4 W} \tag{2}$$

where α_1, α_2, α_3, and α_4 are the scaling factors accounting for the importance of any of the four parameters appearing in Eq. (1) for the particular application of the actuator. For instance, in an aerospace application the weight, W, and frequency, ω, are the two important design parameters to be optimized.

Most of the previous theoretical research and applied work have been focused on either conventional cylinder-piston hydraulic actuators (Alekseyev and Chelyshev, 1987; Barkan et al., 1980; Martin and McCloy, 1979; Ulrich, 1971) or those operating upon electromagnetic principals; each category having some desirable as well as undesirable attributes as mentioned earlier. Introduced in this work is a hydraulic actuator designed to combine the desirable performance characteristics of the electromagnetic actuators (high frequencies) along with those of hydraulic actuators (high force magnitudes).

A hydraulic actuator was designed and is described herein; it rectifies to a considerable degree the undesirable characteristics of the conventional cylinder-piston hydraulic actuators. This actuator system consists mainly of a pump, which gen-

Contributed by the International Gas Turbine Institute and presented at the 36th International Gas Turbine and Aeroengine Congress and Exposition, Orlando, Florida, June 3-6, 1991. Manuscript received at ASME Headquarters March 4, 1991. Paper No. 91-GT-246. Associate Technical Editor: L. A. Riekert.

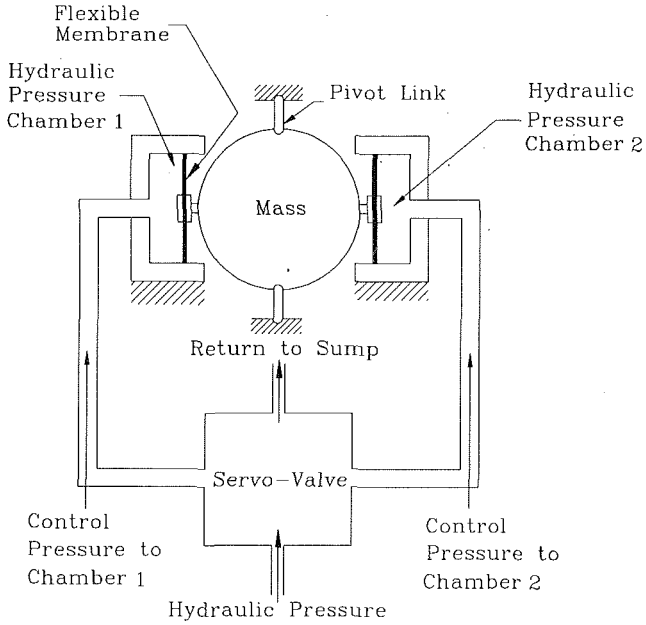

Fig. 1 Schematic of actively controlled hydraulic force actuator

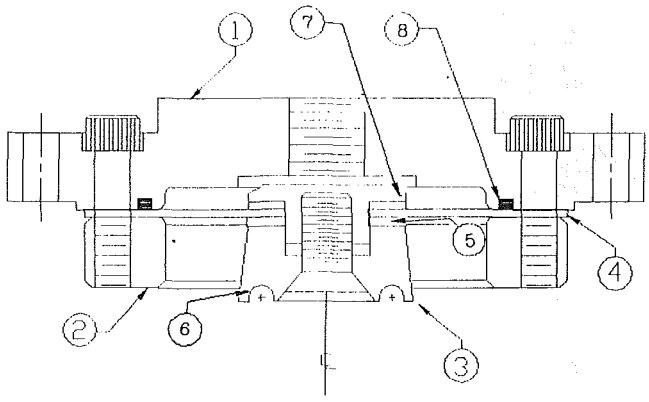

1	Base
2	Bottom Retainer
3	Sub-Assembly
4	Membrane (Elastic Plate)
5	Spacer
6	Lower Fixture
7	Upper Fixture
8	O-Ring

Fig. 2 Hydraulic actuator assembly

erates the nominal pressure, hydraulic servovalves, and a thin elastic plate(s), which transduces the generated pressure variations into forces acting on the bearing housing.

Design Description of the Actuator

Figure 1 shows a schematic of the hydraulic force actuator system presented in this work. The cross section of the actuator itself is depicted in Fig. 2. The actuator consists of a circular elastic steel plate (membrane), which deflects in response to a pressure induced by a pump and controlled by a servovalve. The circular membrane is sandwiched between two pieces of aluminum ring, leading to clamped-clamped boundary conditions. Hydraulic pressure introduced to the pressure chamber causes membrane deflection, thereby transmitting a force to the mass shown in Fig. 1.

The servovalve is in a closed-loop control system and controls the pressure difference in the chamber in response to electrical signal inputs. The control system can adjust either the amplitude of the motion of the mass or the magnitudes of the generated force. Figures 3(*a*) and 3(*b*) show photographs of the test rig employed in this work.

Mathematical Modeling

Dynamics of the Actuator System. The overall dynamic behavior of the system shown in Fig. 1 can be derived from the behavior of the subsystems associated with the following components:

- Membrane (circular elastic plate)
- Servovalve characteristics
- Hydraulic fluid characteristics (fluid compressibility)

The combination of the dynamic behavior of the above components determines the characteristics of the actuator system and the overall input-output relationships of the system.

Membrane Characteristics

The fluid flow, generated by the pump and controlled by the servovalve, induces membrane deflection; factors involved in this part are:

- Membrane stiffness
- Hydraulic fluid compressibility

The continuity equation for the flow requires:

$$Q = A^* \dot{X}_L + C^* \Delta \dot{P}_v \tag{3}$$

Nomenclature

A^* = characteristic area of membrane
C^* = hydraulic fluid compressibility effects and plate deformation under a stationary boundary condition
C_K = hydraulic fluid compressibility and servovalve spool leakage effects
C_M = plate geometry factor
F = generated force by the actuator
G_1 = displacement transfer function
G_2 = pressure transfer function
G_{valve} = servovalve transfer function
K_L = membrane (plate) stiffness
K_{pq} = servovalve spool leakage factor
K_v = servovalve gain
m = mass
ODAN = actuator characteristic number
P_v = hydraulic fluid pressure
Q = total fluid flow
Q_v = valve flow rate
U_v = applied input voltage to the servovalve
W = weight of the actuator
X_L = displacement induced by the actuator
α_1 = force scaling factor
α_2 = frequency scaling factor
α_3 = displacement scaling factor
α_4 = weight scaling factor
β_K = bulk modulus of fluid
ζ = damping ratio of the servovalve
ω = frequency of the force generated by the actuator
ω_n = natural frequency of the servovalve

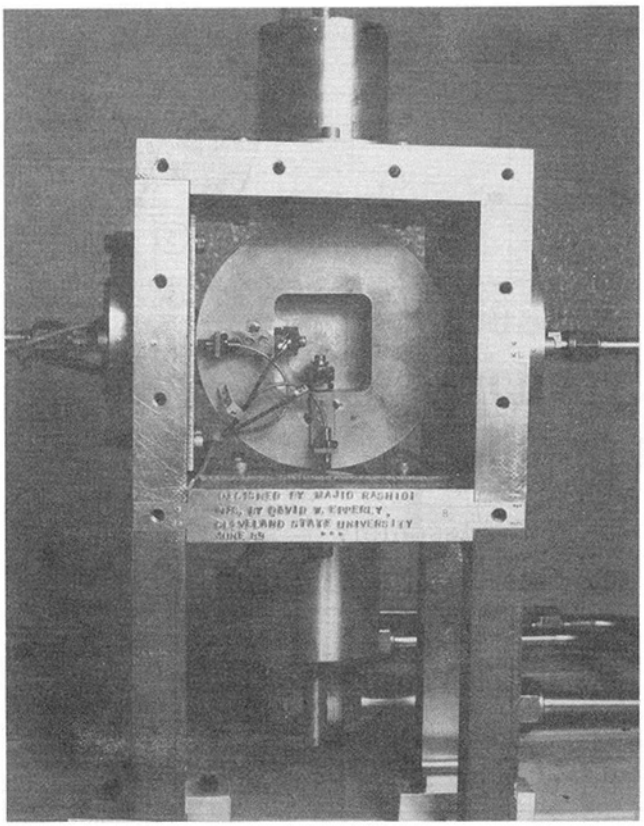

Fig. 3(*a*) Front view of the test rig

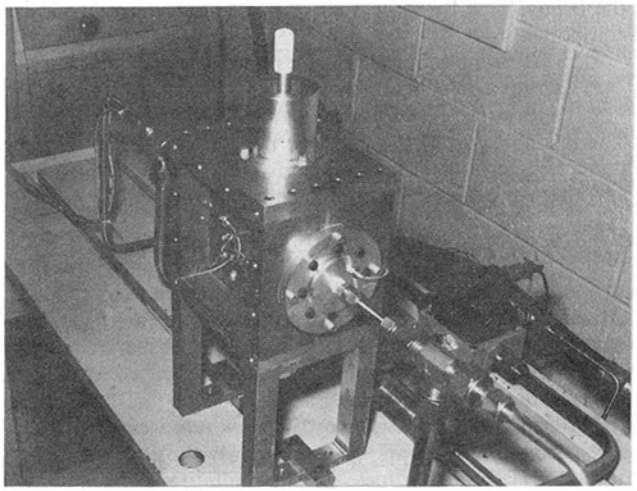

Fig. 3(*b*) Oblique view of the test rig

where Q = fluid flow; A^* = the characteristic area of the membrane; X_L = velocity at which the load is applied; P_v = pressure induced by the load; C^* = fluid compressibility effects and plate deformation under a stationary load condition.

Figure 4 helps to understand C^* and its relation with plate deformation under pressure with a stationary load condition. Here the boundary conditions of the circular plate are set to be rigid and stationary (inner and outer boundaries). The C^* factor can be represented as:

$$C^* = \frac{V}{4\beta_K} + C_M \tag{4}$$

where V = fluid volume; β_K = bulk modulus of fluid; C_M = plate geometry factor.

The force equilibrium equation is written as:

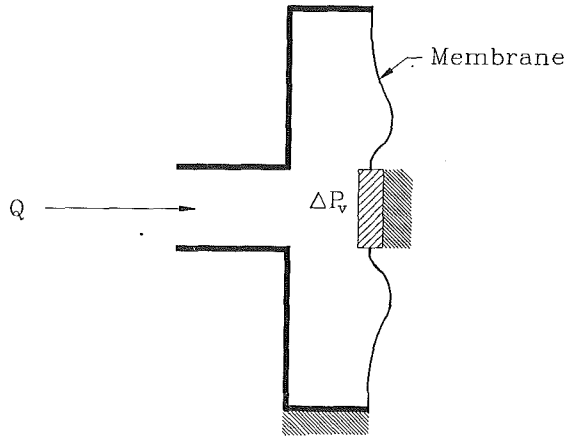

Fig. 4 Membrane deflection under stationary boundary conditions

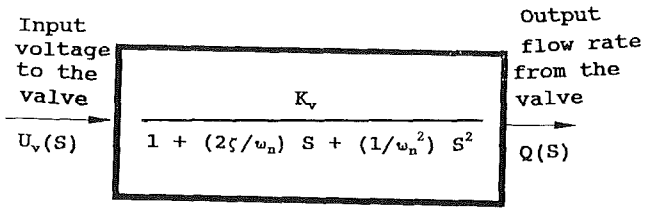

Fig. 5 Transfer function of the servovalve

$$F = A^* \Delta P_v - K_L X_L \tag{5}$$

where F = generated (exerted) force; K_L = stiffness of the membrane.

Servovalve Characteristics

The dynamic characteristics of the servovalve can be represented by the block diagram shown in Fig. 5 and the following formula in the Laplace domain:

$$Q_v = K_v G_{\text{valve}} U_v \tag{6}$$

where Q_v = valve flow rate (unloaded valve) (output); K_v = valve's proportional gain; G_{valve} = transfer function of the valve (second-order system); U_v = applied voltage to the valve (input).

Here K_v is influenced by the supply pressure and the geometry of the valve. ω_n and ζ are the natural frequency and the damping ratio of the second-order system describing the valve dynamics.

The total fluid flow, Q, is:

$$Q = Q_v - K_{pq} \Delta P_v \tag{7}$$

where K_{pq} is a leakage factor around the spool of the servovalve.

Total System Characteristics

The overall dependence of the generated output force, F, the input voltage applied to the servovalve, U_v, and the load displacement, X_L can be summarized in the Laplace domain as:

$$F = G_v U_v - G_L X_L \tag{8}$$

where G_v and G_L are the transfer functions as given below:

$$G_v = \frac{G_{\text{valve}}(A^* K_L / K_{pq})}{1 + C_K S}$$

$$G_L = \frac{(A^{*2}/K_{pq})S}{1 + C_K S} + K_L \tag{9}$$

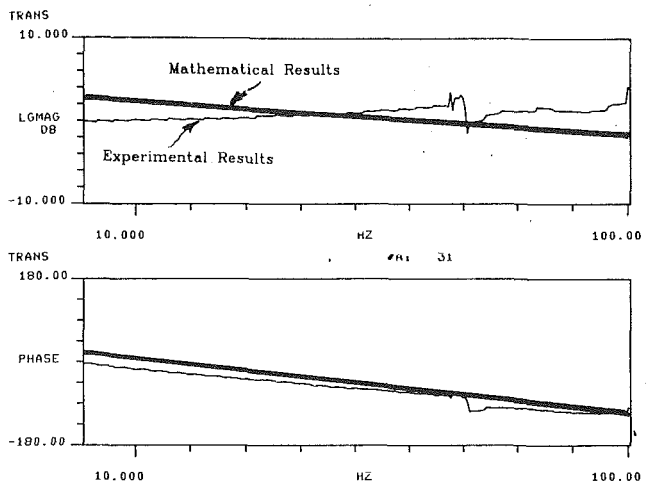

Fig. 6 Frequency response and phase shift of the mass

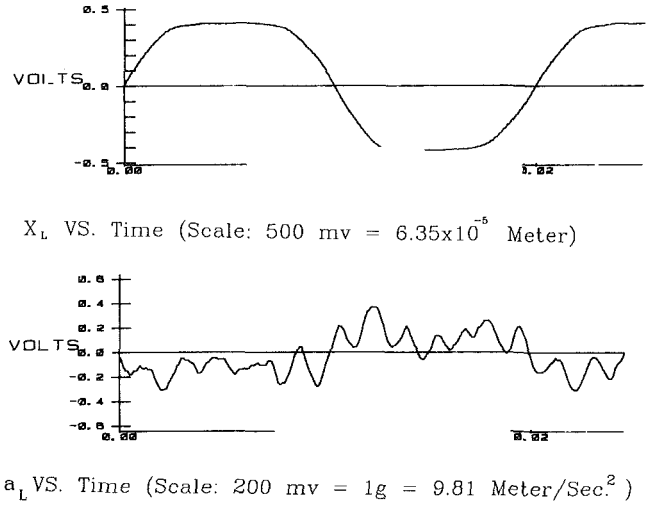

Fig. 7 Displacement and acceleration of the mass versus time: supply pressure = 6.89 x 10^6 Pa; frequency = 50 Hz

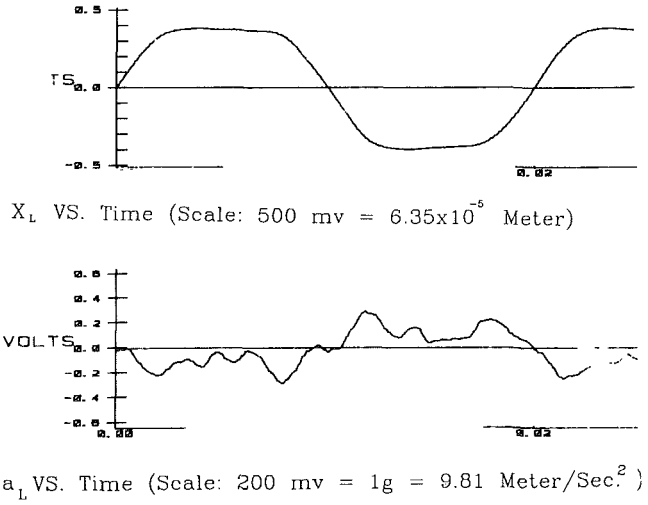

Fig. 8 Displacement and acceleration of the mass versus time; supply pressure = 3.45 x 10^6 Pa; Frequency = 50 Hz

The C_K in Eq. (9) represents the hydraulic fluid compressibility, servovalve spool leakage factor K_{pq}, and C^* (see Eq. (4)).

The C_K factor can be expressed as:

$$C_K = \frac{C^*}{K_{pq}} \tag{10}$$

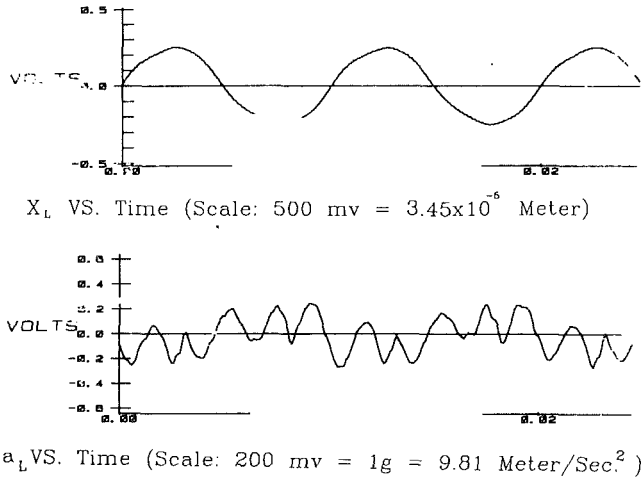

Fig. 9 Displacement and acceleration of the mass versus time; supply pressure = 3.45 x 10^6 Pa; frequency = 100 Hz

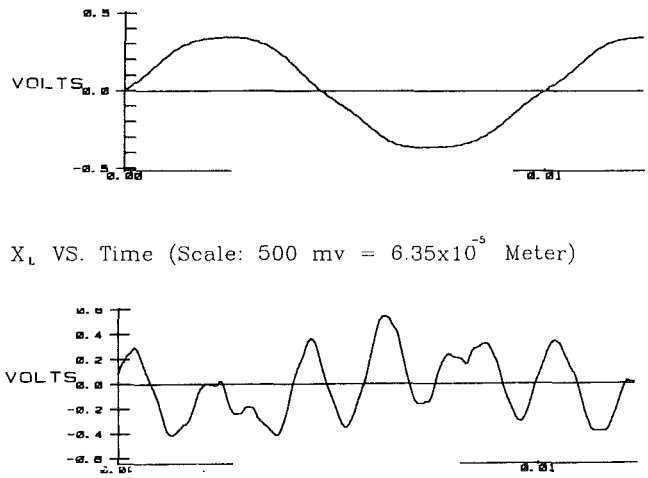

Fig. 10 Displacement and acceleration of the mass versus time; supply pressure = 6.89 x 10^6 Pa; frequency = 100 Hz

At this point the reader should be reminded that the goal of this mathematical analysis is to interrelate the input voltage applied to the servovalve, U_v, the output force, F, and the load displacement X_L.

The second law of Newton can be applied to the motion of the mass shown in Fig. 1, in the time domain, as:

$$F = m\ddot{X}_L \tag{11}$$

Equation (11) can be written in the Laplace domain as:

$$F = mX_L S^2 \tag{12}$$

If the X_L is considered as the output (response) to the input voltage, U_v, then:

$$X_L = G_1 U_v \tag{13}$$

where

$$G_1 = \frac{bG_{\text{valve}}}{C_K m S^3 + mS^2 + d_L S + K_L} \tag{14}$$

Here

$$b = \frac{A^* K_v}{K_{pq}} \text{ and } d_L = (A^{*2}/K_{pq}) + C_K K_l$$

If the pressure fluctuation behind the membrane, ΔP_v, is

Table 1 Performance characteristics of the actuator

Supply Pressure MPa	Frequency Hz	Generated Force N	Mass Accl. M/S^2	Mass Disp. M
6.89	50	200	22.1	4.5×10^{-5}
6.89	100	182.3	20.1	5.8×10^{-5}
3.45	50	164.5	18.2	5.8×10^{-5}
3.45	100	97.8	10.8	3.6×10^{-5}

considered as the output (response) and the applied voltage to the servovalve, U_v, as the input, then:

$$\Delta P_v = G_2 U_v \tag{15}$$

where

$$G_2 = [(mS^2 + K_L)/A^*]G_1 \tag{16}$$

Small values of C_K expressed in Eq. (10) amount to the actuator system acting similar to a passive stiffness and passive damper unit. Later, it will be mentioned that this could be realized as an advantage of this system over the electromagnetic actuator system, should the control system fail to operate.

The mathematical formulation presented in this section can be utilized to group the design parameters involved in this system. These parameters can be categorized in the following groups:

- Membrane characteristics (A^*, K_L, C^*)
- Valve characteristics (fK_v, K_{pq}, ω_n, ζ)
- Flow parameters (V, ΔP_s)

The frequency response of this actuator system is shown in Fig. 6 along with the experimental test results.

Experimental Results

The actuator system shown in Fig. 1 was run with a sinusoidal input voltage applied to the servovalve. The supply pressure produced by the pump was 6.89×10^6 Pa. The frequency response characteristics of the system (magnitude and phase angle) were recorded for a spectrum of the input voltage frequencies. The results are shown in Fig. 6. The peaks observed around 68 Hz (see Fig. 6) turned out to be a resonance frequency of the legs supporting the actuators. These peaks are not inherent in the dynamics of the actuators. Figures 7, 8, 9, and 10 show the displacement, X_L, and the acceleration, a_L of the mass shown in Fig. 1. Table 1 summarizes the force and displacement characteristics of the designed actuator system presented in this work.

Conclusions and Remarks

This work presents the results of the design of a hydraulic actuator system to be utilized in implementing the already developed active vibration control strategies and algorithms for rotating machinery. The design combines and offers the advantages of the electromagnetic force actuators (frequency characteristics) and those of conventional hydraulic force actuators (force magnitudes). Three of the main benefits of this system are:

1 This hydraulic force actuator is well suited to control rotor vibration actively in aircraft engines because it can use hydraulic power already available on aircraft vehicles.

2 This actuator provides higher forces for a given size and weight than electromagnetic actuators, resulting in a lighter and more efficient system.

The ODAN of this actuator (actuator characteristic number), introduced in the beginning, is six times greater than that of a typical electromagnetic actuator if the force amplitudes and the frequencies of both actuators are to be the same (182.3 N and 100 Hz). The actuator characteristic number of the actuator described in this work will be favorably higher if the weight factor α_4 (see Eq. (2)) is a critical design consideration.

3 Upon the loss of the control pressure or input voltage to the servovalve, this actuator functions as a passive stiffness and damper.

Acknowledgments

The authors wish to express their gratitude to the Structural Dynamics Branch at NASA Lewis Research Center, Cleveland, OH, for providing the experimental facilities utilized in this work. Thanks are also due to Mr. David W. Epperly for his excellent work on the manufacturing of the actuators and the test rig.

References

Alekseyev, A. P., and Chelyshev, V. A., 1987, "Analysis of the Dynamics of a Hydraulic Actuator-Servomotor System Taking Into Account Nonlinearity and Interference of the Two Working Chambers," *Fluid Mechanics, Soviet Research*, Vol. 7, No. 5, pp. 114–126.

Barkan, P., Imam, I., and Premerlani, W., 1980, "New Rapid-Response Hydraulic Actuator—Design, Analysis Test Results," ASME *Journal of Mechanical Design*, Vol. 102, pp. 3–13.

Martin, H. A., and McCloy, D., 1979, "Pressure Transient Generated During the Rapid Braking of Asymmetric Hydraulic Actuators," *Journal of Mechanical Engineering Science*, Vol. 21, No. 2, pp. 93–103.

Ulrich, H. J., 1971, "Some Factors Influencing the Natural Frequency of Linear Hydraulic Actuators," *International Journal of Machine Tool Design & Research*, Vol. 11, No. 2, pp. 199–207.

Dynamic Force Response of an Open-Ended Squeeze Film Damper

L. A. San Andres

G. Meng

S. Yoon

Mechanical Engineering Department,
Texas A&M University,
College Station, TX 77843

The effects of whirl frequency and lubricant viscosity on the experimental pressure field and film forces in an open-ended squeeze film damper test rig are presented. The measurements refer to circular centered journal motion of amplitude equal to one half the damper clearance ($\epsilon = 0.5$). The whirl frequency varied between 16 Hz and 85 Hz, while the lubricant temperature increased from 25°C to 45°C. The damper operated with levels of external pressurization that supressed lubricant cavitation. The experimental results show conclusively that the radial film force is purely an inertial effect, i.e., it depends solely on the fluid density and the second power of the whirl frequency. The tangential film force shows a variation that depends on the viscous and inertial flow conditions in the squeeze film region. Correlation of experimental forces with conventional SFD models shows the radial force to be π times larger than the theoretical prediction, while the tangential force correlates well for low whirl frequencies and large lubricant viscosities.

Introduction

Lightweight, high-performance engines exhibit a trend toward increased flexibility and sensitivity to unbalance, leading to higher than desired vibration levels and reduced reliability. One method to control this sensitivity is by the use of squeeze film dampers (SFD). However, experience has shown that damper performance ranges from erratic to nonfunctioning despite analytical predictions to the contrary. It is recognized that implementing a damper in practice introduces features that have an adverse impact on the oil film pressure distribution to the point where the oil film is destroyed and the damper dynamic force performance significantly reduced. There is need for experimental analyses of SFD film pressures and forces to help in the design of actual damper applications and also to assess their actual benefits or pitfalls. Effects requiring careful and planned study are related to fluid inertia, liquid cavitation and compressibility, two-phase fluid structure, and the impact of external restrictions such as inlet holes and efficient end seals.

The importance of fluid inertia and liquid cavitation in the performance of squeeze film dampers has been demonstrated by numerous theoretical and experimental investigations. The relevance of fluid inertia is related to the squeeze film Reynolds number ($\mathrm{Re}_s = \rho\omega c^2/\mu$), which ranges from 1 to 50 in most practical applications. Theoretical advances have been made by Tichy and Modest (1978), Szeri et al. (1983), and San Andres and Vance (1986, 1987a). Important contributions to the understanding of SFD performance are given by the experimental analyses of Vance and Kirton (1975), Feder et al. (1978), Tichy (1984), San Andres and Vance (1978b), Ramli et al. (1986), Roberts and Ellis (1989), Kinsale and Tichy (1989), and Jung et al. (1990a, 1990b). Correlation of measurements with analytical force and dynamic force coefficients has ranged from poor to satisfactory and depended strongly on the test damper geometry and actual operating conditions. In general, it has been found that fluid inertia has a larger effect on the damper force response than predictions obtained from analyses based on sound inertia-viscous models. Results from these investigations have been accepted slowly by the interested engineering community due to the improper comparison made most times between squeeze film flows and shear flows dominant in cylindrical journal bearings. The experimental work of Zeidan and Vance (1989a, b, c) has brought to attention the issue of cavitation in a controlled SFD orbit test apparatus. The significance of these investigations can not be overlooked. Most importantly, it has already prompted significant changes in the current philosophy of damper design. Finally, the urgent call issued by Roberts and Ellis (1989) to improve our present understanding of squeeze film flow behavior cannot be left unnoticed.

The SFD research work at Texas A&M University has been directed to measure damper performance characteristics in test apparatus closely reproducing conditions found in actual practice. The experimental program has focused on the effects of fluid inertia, cavitation, and end seals, and has provided meaningful information for dampers with constrained circular motions. Past experimental analyses have presented measurements for a constant whirl frequency while the lubricant temperature rose in the film flow region. The present paper describes and analyzes experiments conducted to measure the effect of whirl frequency and film temperature on the pressure field and film forces in an open end damper configuration. The experimental results presented herein complement and extend those given by Jung et al. (1990a, b).

Contributed by the International Gas Turbine Institute and presented at the 36th International Gas Turbine and Aeroengine Congress and Exposition, Orlando, Florida, June 3-6, 1991. Manuscript received at ASME Headquarters March 4, 1991. Paper No. 91-GT-247. Associate Technical Editor: L. A. Riekert.

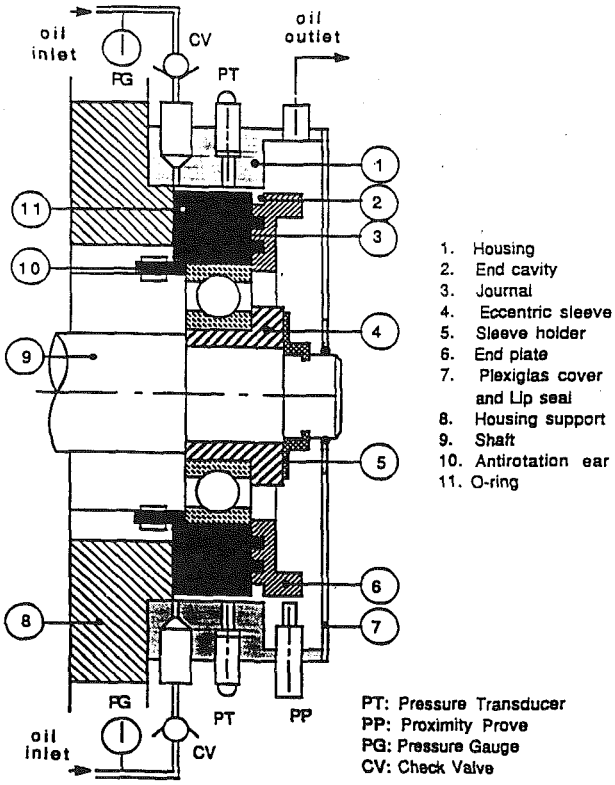

Fig. 1 Section of variable speed, squeeze film damper test rig

Experimental Facility and Procedure

Figure 1 shows the major components of the squeeze film damper (SFD) test apparatus. The damper journal (3) with an outer diameter (D) of 12.7 cm (5 in.) and axial length (L) of 2.4 cm (0.94 in.) is press fitted on the outer race of a ball bearing. An 0-ring (11) installed at the left end face of the damper journal prevents leakage to the space enclosed between the housing and rotating shaft. At the damper right end, a large end cavity is present so that the test configuration is essentially open ended to ambient conditions. The damper slenderness ratio (L/D) is 0.188 and simulates a short bearing configuration typical of an engine application. The nominal damper film clearance (c) at room temperature is equal to 1.55 mm (0.0625 in.). The larger than usual clearance tested gives large squeeze film Reynolds numbers at low whirling frequencies so that significant effects of fluid inertia are produced. In the test apparatus, the journal is mounted eccentric relative to the rotor shaft, and thus, it is constrained to describe circular centered orbits about the damper bearing center. The present investigation refers to experimental results for a nominal dimensionless orbit radius equal to one half the damper clearance ($\epsilon = e/c = 0.50$).

Table 1 Viscosity and density for SAE 30 oil

Temperature, °C	Viscosity Pa-s	Density, kg/m^3
25.0	0.1895	899.8
30.0	0.1480	888.6
35.0	0.1130	882.5
40.0	0.0872	878.8
45.0	0.0693	875.2
50.0	0.0553	871.6

A detailed description of the squeeze film damper test apparatus and instrumentation has been given by Jung et al. (1990a). Experimental results for open-ended and partially sealed damper configurations were obtained at a fixed rotational speed equal to 1770 rpm (29.5 Hz.). Presently, the drive motor to the test rig has been replaced by a variable speed motor. This modification has enabled us to increase the range of testing for frequencies up to 120 Hz.

The lubricant used for the experiments is SAE 30 engine oil. Prior to experimental tests, oil viscosity is measured for a range of temperatures using a Synchroelectric viscometer. For data analysis and reduction, oil viscosity formulae are obtained in terms of temperature using an algebraic relationship formulated in the ASTM D-341. Table 1 presents a collection of the measured oil viscosity and density for a range of temperatures typical of the experimental conditions.

Piezoelectric pressure transducers are used to measure the dynamic pressure field. The transducers are located around the bearing circumference at equal angles and at two axial positions, z_1 and z_2, 0.56 cm and 1.67 cm apart from the damper lubricant inlet, respectively. The dynamic journal center motion and whirl frequency (equal to shaft rotational speed) are also measured with noncontacting eddy current sensors and an optical sensor, respectively. Fluid film temperature is measured with a thermocouple directly embedded on the squeeze film region.

The experiments were carried out with supply pressures ranging from 0.137 to 0.275 MPa (20 to 40 psig) while lubricant flow rates varied from 0.945 to 1.7 liter/min. The levels of external pressures used prevented lubricant cavitation in the squeeze film region. The restriction at the inlet check valves constrained the amount of flow through the damper test rig and this was not sufficient to remove all the heat generated by fluid friction in the squeeze film land and on the ball bearings. Thus, the oil temperature increased while testing and the lubricant viscosity varied accordingly.

For a *rotationally symmetric* SFD and circular centered orbits, the time variations in circumferential pressure measured at any location on the damper annulus are identical for any one cycle of journal orbiting. Thus, the dynamic pressure field is measured with only one pressure transducer at a fixed angular location. Subsequently, the circumferential pressure field is directly inferred with the use of simple kinematical relationships. Then, fluid film forces are calculated by numerical in-

Nomenclature

c, e = damper radial clearance, journal orbit radius, m
D = $2\times R$ = damper journal diameter, m
Fr, Ft = fluid film radial and tangential forces, N
F_{rs}, F_{ts} = open-ended short SFD radial and tangential forces given in Table 2
f_r, f_t = $F_r/F_{rs}, F_t/F_{ts}$ = dimensionless fluid film forces
L = damper journal axial length, m
P = fluid pressure, Pa
Re_s = $\rho\omega c^2/\mu$ = squeeze film Reynolds number
Z_i = axial location of pressure transducers, m
ϵ = e/c = dimensionless orbit radius
γ = $\sqrt{(1-\epsilon^2)}$
θ, z = circumferential and axial coordinates
μ = fluid viscosity, Pa-s
ρ = fluid density, kg/m^3
ω = damper whirl frequency = $\Omega/60$, Hz
Ω = rotor shaft speed, rpm

tegration of the dynamic pressure waves around the journal circumference at two axial locations (z_i). The equations used to evaluate the fluid radial and tangential forces are given as

$$\begin{Bmatrix} Fr \\ Ft \end{Bmatrix} = \int\int_{0\ 0}^{L2\pi} P(\omega t, z) \begin{Bmatrix} \cos\theta \\ \sin\theta \end{Bmatrix} Rd\theta dz \simeq \sum_{i=1}^{2} \int_0^{2\pi} P(z_i) \begin{Bmatrix} \cos\theta \\ \sin\theta \end{Bmatrix} Rd\theta\Delta z \quad (1)$$

Experimental Results and Discussion

Preliminary film pressure measurements at six equally spaced circumferential locations confirmed that the dynamic pressure fields were identical regardless of the imposed external supply pressure level (maximum tested 0.275 MPa). These results are due to the inlet check valves used to prevent oil back flow. *Fluid film cavitation was observed to occur for tests at high shaft speeds (over 6000 rpm) and/or low lubricant temperatures.* In these experiments, the dynamic pressure waves showed high-frequency transient components in the region of positive squeeze action. The chaotic film pressure spikes were due to collapsing of air bubbles on the region of minimum film thickness. At the onset of cavitation, the lubricant at the damper outlet transformed from a uniform structure, through a liquid with minute bubbles, to a foamy composition when the flow rate was not sufficient (low supply pressures). The experiments also made it evident that the cavitated damper produced fewer frictional forces than a (full film) uncavitated damper. Detailed information on the force response of a cavitated damper can be found from Zeidan and Vance (1989a, 1989b, 1989c) and also Jung et al. (1990a, 1990b).

Shaft and housing growth due to temperature rise were measured. Most important was the increase in orbit radius as the whirl frequency increased. With no shaft rotation, the orbit radius is equal to $e = 0.77$ mm (0.0305 in.). In dimensionless form, this amounts to an orbit radius $\epsilon = e/c = 0.50$. At the highest frequency tested (95 Hz), the measured orbit radius was equal to $e = 0.91$ mm (0.036 in.), or based on the cold clearance, a dimensionless value of $\epsilon = 0.59$. The increment in orbit size is due to centrifugal and rotordynamics effects as the shaft speed increases. It is important to note that the orbit measured was circular and no test rig critical speeds were ever found within the speed range tested.

The experimental procedure followed a test schedule for the following test classes:

- (*a*) Tests for fixed rotational speed while fluid temperature increased.
- (*b*.1) Tests for increasing speed and increasing fluid temperature
- (*b*.2) Tests for decreasing speed and increasing fluid temperature.

Test results for class (*b*.1) have been presented by the author (San Andres, 1990). The experimental results show that the radial fluid film force is due to a pure inertial effect while the tangential force depends on both the viscous and inertial flow conditions in the damper test rig. Here we refer to tests in classes (*a*) and (*b*.2), respectively. The results obtained from tests (*b*.1) and (*b*.2) are considered identical, and thus, experimental measurements from class (*b*.1) are omitted here for brevity. On the other hand, due to the poor controllability of fluid temperature in the damper rig, tests for a natural class (*c*), i.e., fixed lubricant temperature while speed varied, could not be performed satisfactorily.

The results from the experimental measurements are compared to the film forces obtained from the short open-ended squeeze film damper model. Due to the perfect seal at the left end of the damper, the pressure field is a maximum at this point and then drops parabolically to ambient pressure at the end cavity. Thus, the theoretical film forces are calculated as

Table 2 Film forces for short open ended squeeze film damper from San Andres and Vance (1986)

$Fr = \frac{2\pi}{3}\rho R L^3\omega^2 \frac{(1-\gamma)}{\epsilon\gamma}\left\{\frac{6}{5}+\frac{102}{35}(\gamma-1)\right\}$	Radial force
$Ft = \frac{4\pi\mu R L^3 \epsilon\omega}{c^2\gamma^3};\ \gamma = \sqrt{(1-\epsilon^3)}$	Tangential force

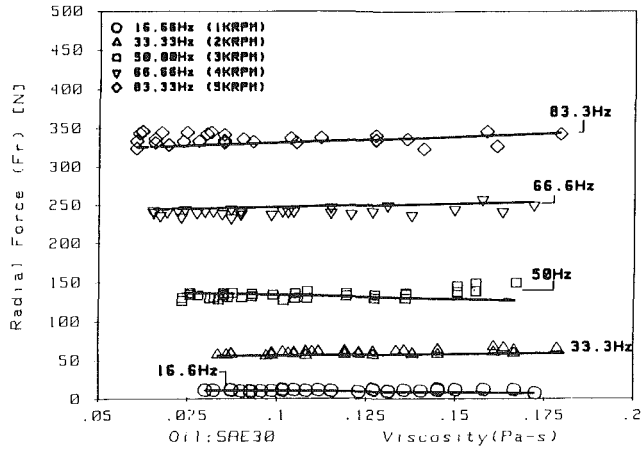

Fig. 2 Experimental SFD radial force (*Fr*) versus lubricant viscosity for increasing whirl frequencies: class (*a*) tests

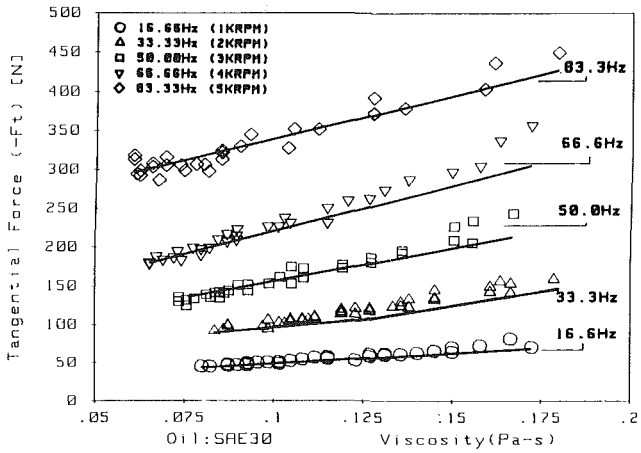

Fig. 3 Experimental SFD tangential force (– *Ft*) versus lubricant viscosity for increasing whirl frequencies: class (*a*) tests

half those obtained from a damper with a total length equal to $2\times L$. Table 2 presents the analytical full film, radial, and tangential forces for circular centered orbits. The theoretical results given by San Andres and Vance (1986) are valid for low to moderate values of the squeeze film Reynolds number $\mathrm{Re}_s(\rho\omega c^2/\mu)$. Note that the analytical radial and tangential forces are due to inertial and viscous effects, respectively.

For constant whirl speeds and film temperature increasing (lubricant viscosity decreasing), Figs. 2 and 3 show the film radial and tangential forces calculated by numerical integration of the measured dynamic pressure field. The experimental results (symbols) are shown for five different whirl frequencies ranging from 16.6 Hz (1000 rpm) to 83.3 Hz (5000) rpm). Lines in the figures represent the linear least-square fit to the test results. Measurements were taken at each speed while the temperature in the fluid film increased from 28°C to 49°C. The lowest squeeze film Reynolds number is equal to 1.43 at a speed of 1000 rpm and a temperature equal to 28°C, while the highest test Reynolds number is equal to 18.4 at 5000 rpm and 48°C.

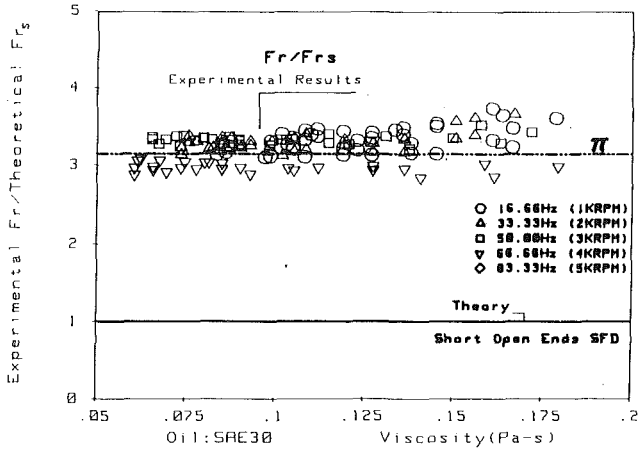

Fig. 4 Ratio of experimental radial force to short-SFD theory radial force for increasing whirl frequencies and lubricant viscosity

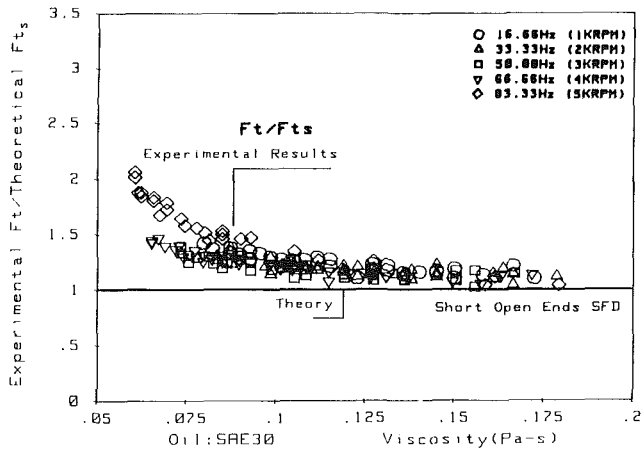

Fig. 5 Ratio of experimental tangential force to short-SFD theory tangential force for increasing whirl frequencies and lubricant viscosity

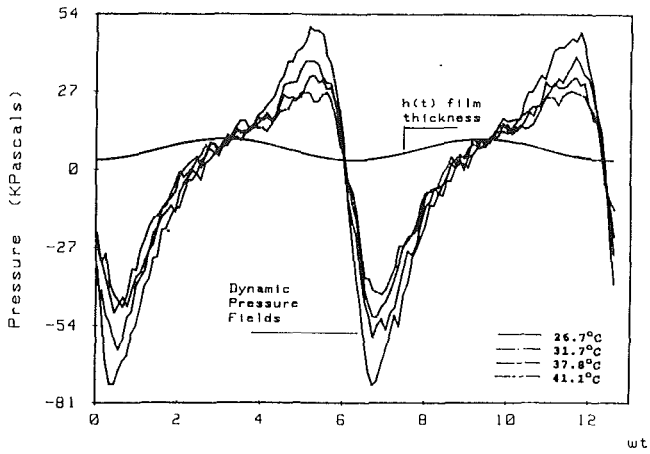

Fig. 6 Measured dynamic film thickness and pressure waves at axial location z_1 for various film temperatures at a frequency ω = 33.3 Hz

Figure 2 shows the radial force to be independent of fluid viscosity and increasing approximately with the second power of the whirl frequency. Thus, in the absence of oil cavitation, this radial force is entirely due to a pure fluid inertial effect. The tangential force depicted in Fig. 3 presents an approximate linear behavior with both fluid viscosity and whirl frequency. It should be observed that the radial force at the highest test frequencies and lower viscosities (largest Reynolds numbers) is greater than the tangential force.

Figures 4 and 5 show the ratio of the experimental film forces (F_r, F_t) to those predicted by the short open-ended theory (F_{rs}, F_{ts}). A value of one (1) in the figures indicates a perfect match between measurements and theory. The analytical forces are calculated with the actual values of orbit radius ϵ and fluid properties measured for each test. Figure 4 shows that the experimental radial force is approximately π times larger than the theoretical predictions. Past references, namely San Andres and Vance (1987a), Jung et al. (1990a, 1990b), and Ramli et al. (1989), have presented a similar correlation of current theories with experimental results. An explanation for the large discrepancy found is not yet available and urges the development of improved viscous-inertial SFD theories. A sound theory needs to include the effect of entrance and discharge conditions (i.e., Bernoulli effects), which seem to be most disturbing and greatly influence the inertia pressure field (Rhim and Tichy, 1987).

Figure 5 shows the analytical predictions to correlate best with the experimental tangential force for the highest fluid viscosities. For this condition, essentially very low of vanishing Reynolds numbers, the tangential force is proportional to viscosity and whirl speed. As the viscosity in the oil decreases (squeeze film Reynolds number increasing) the discrepancies with the short SFD theory results increase. Note that for 66 Hz and 83.3 Hz, the experimental tangential force is 1.5 and 2.0 times larger than the theoretical predictions. The rationale for this behavior is due again to fluid inertia affecting the effective viscous wall shear stresses. Current inertia models, based on no influence of fluid inertia on velocity profiles, neglect the important effect of inertia on shear stresses. San Andres and Vance (1987a) have shown that for small amplitude circular centered orbits, $\epsilon \rightarrow 0$, this effect is pronounced for Reynolds numbers larger than 50. However, at large orbit radii and accounting for entrance and discharge effects, fluid inertia seems to play a more important role at lower values of the squeeze film Reynolds number (Kinsale and Tichy, 1989).

Figure 6 shows the measured film thickness and dynamic pressure waves at a whirl frequency of 33.3 Hz (2000 rpm) and for four film temperatures. The results refer to measurements taken at axial location z_1 closest to the lubricant inlet. As expected, the largest pressures occur for the lowest lubricant temperature (highest viscosity). Observe that the pressure fields are not symmetric about the maximum film thickness, showing then a characteristic effect of fluid inertia.

Experimental measurements for class (*b.2*) tests, decreasing whirl speed and increasing oil temperature, were performed at two different supply pressures equal to 207 kPa (30 psig) and 276 kPa (40 psig). With the damper test rig at room temperature, the rotor speed was increased rapidly to a top speed. This maximum speed was determined for no cavitation inception on the damper fluid film. Then, while the lubricant temperature increased, measurements were taken as the rotor speed was steadily reduce to zero. In these transient tests, whirl frequency (ω), lubricant temperature and material properties (ρ, μ), and orbit radius (e) varied. The values for all these variables are presented in Fig. 7 as a function of shaft speed.

Figure 8 shows the experimental radial and tangential film forces as the whirl frequency decreases. These results also show the effect of varying viscosity and orbit radius on the damper force response. For the largest speeds, both film forces are essentially equal, while as speed decreases there is a region where the radial force is larger than the tangential force. The opposite effect is observed to occur at the lowest speeds. The most important conclusion derived from these experiments is that the film forces are independent of the level of external pressurization. Further experiments with pressure supplies to 0.550 MPa (80 psig) confirm this assertion.

Figure 9 shows the ratio of measured forces to those given by the short open-ended SFD theory. The experimental radial

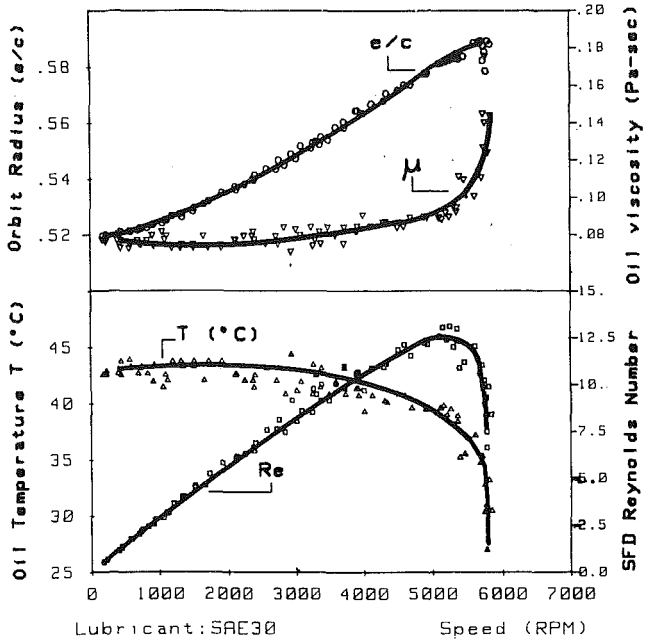

Fig. 7 Class (*b.2*) test: variation of lubricant temperature and viscosity, orbit radius (ϵ), and Reynolds number (Re_s) as shaft speed decreases

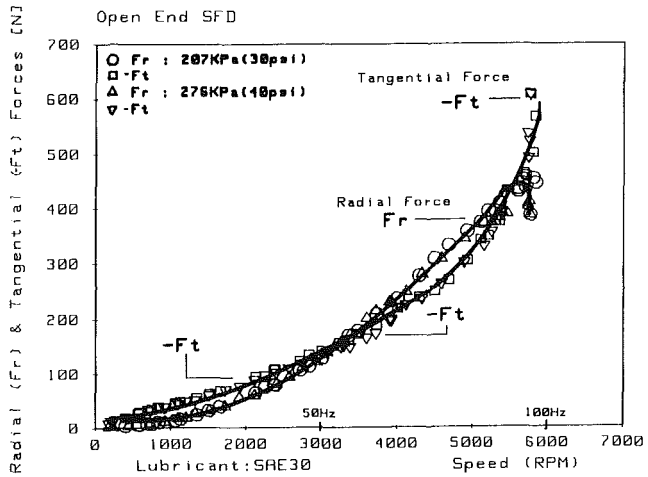

Fig. 8 Experimental radial and tangential film forces a shaft speed decreases for two values of supply pressure, P_s = 0.207 MPa and 0.276 MPa

force is consistently larger than the analytical predictions, while the tangential force shows correlation close to 1. The scatter of data at the lowest speeds ($\omega \rightarrow 0$) is due to the small pressures measured and larger noise-to-signal ratios. The experimental results show that the radial force is purely inertial, while the tangential force is essentially due to viscous effects. The correlation of experimental and theoretical forces is consistent with the results presented in Figs. 4 and 5 for class (*a*) tests.

Conclusions

An experimental analysis has determined the effect of whirl frequency and lubricant viscosity on the dynamic force response of a squeeze film damper test rig. The damper tested corresponds to an open-ended configuration with a constrained circular motion of *nominal* amplitude equal to one half the bearing radial clearance (ϵ = 0.5). The SFD test rig operated with levels of external pressurization, which suppressed lubricant cavitation. The supply pressure and flow rate were approximately constant and equal to 0.276 MPa and 1.5 liters/

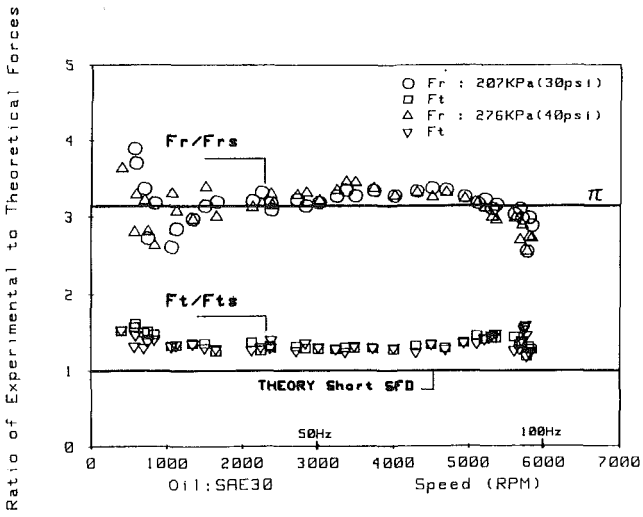

Fig. 9 Ratio of experimental forces to analytical predictions from short SFD theory: P_s = 0.207, 0.276 MPa; class (*b.2*) test

min, respectively. The whirl frequency of the damper journal varied between 16.6 Hz (1000 rpm) to 83.3 Hz (5000 rpm).

The experimental analysis shows that the radial fluid film force is solely due to fluid inertia effects, while the tangential force shows a variation that depends on both the viscous and inertial flow conditions in the damper test rig. Comparison of results with existing theoretical inertial-viscous SFD analyses shows that the experimental radial force is approximately π times larger than the analytical predictions, while the tangential force correlates one to one with theory at low frequencies and large viscosities. For the largest squeeze film Reynolds numbers tested, the experimental tangential force is two times the corresponding theoretical prediction. The experimental work has provided further evidence that fluid inertia effects are significant in the dynamic force response of squeeze film dampers.

Acknowledgments

The generous support of the Turbomachinery Research Consortium at Texas A&M University is gratefully acknowledged. The authors also thank Professor John M. Vance for providing them with a unique environment to produce the present research work.

References

Feder, E., Bansal, P. N., and Blanco, A., 1978, "Investigation of Squeeze Film Damper Forces Produced by Circular Centered Orbits," ASME JOURNAL OF ENGINEERING FOR POWER, Vol. 100, pp. 15–21.

Jung, S. Y., San Andres, L., and Vance, J. M., 1990a, "Measurements of Pressure Distribution and Force Coefficients in a Squeeze Film Damper, Part I: Fully Open Ended Configuration," *STLE Transactions*, Preprint No. 90-TC-1E-1.

Jung, S. Y., San Andres, L., and Vance, J. M., 1990b, "Measurements of Pressure Distribution and Force Coefficients in a Squeeze Film Damper, Part II: Partially Sealed Configuration," *STLE Transactions*, Preprint No. 90-TC-1E-2.

Kinsale, I., and Tichy, J., 1989, "Numerical and Experimental Study of a Finite Submerged Squeeze Film Damper," *Proceedings of the 1989 ASME Vibrations Conference, Machinery Dynamics: Applications and Vibration Control Problems*, ASME DE-Vol. 18-2.

Ramli, M. D., Roberts, J. B., and Ellis, J., 1986, "Determination of Squeeze Film Dynamic Coefficients from Experimental Transient Data," ASME Paper No. 86-Trib-17.

Rhim, Y., and Tichy, J., 1987, "Entry Flow of a Lubricant Into a Slider Bearing—Analysis and Experiment," *Tribology Transactions*, Vol. 31, No. 3, pp. 350–358.

Roberts, J. B., and Ellis, J., 1989, "The Determination of Squeeze Film Dynamic Coefficients From Transient Two-Dimensional Experimental Data," presented at the ASME-STLE Joint Tribology Conference, Fort Lauderdale, FL, Oct.

San Andres, L., and Vance, J. M., 1986, "Effects of Fluid Inertia and Turbulence on the Force Coefficients for Squeeze Film Dampers," ASME JOURNAL OF ENGINEERING FOR GAS TURBINES AND POWER, Vol. 108, pp. 332–339.

San Andres, L., and Vance, J., 1987a, "Effect of Fluid Inertia on Squeeze Film Damper Forces for Small Amplitude Circular Centered Motions," *ASLE Transactions*, Vol. 30(1), pp. 69–76.

San Andres, L., and Vance, J. M., 1987b, "Experimental Measurement of the Dynamic Pressure Distribution in a Squeeze Film Damper Executing Circular Centered Orbits," *ASLE Transactions*, Vol. 30(3), pp. 373–383.

San Andres, L., 1990, "Experimental Results for Variable Speed TRC Squeeze Film Damper Test Rig," TRC-SFD-3-90, #117, Turbomachinery Laboratories, Texas A&M University, College Station, TX.

Szeri, A., Raimonid, A. A., and Giron Duarte, A., 1983, "Linear Force Coefficients for Squeeze Film Dampers," ASME *Journal of Lubrication Technology*, Vol. 105, pp. 326–334.

Tichy, J. A., and Modest, M., 1978, "Squeeze-Film in Arbitrary Shaped Journal Bearings Subject to Oscillations," ASME *Journal of Lubrication Technology*, Vol. 100, pp. 323–330.

Tichy, J. A., 1984, "Measurements of Squeeze Film Bearing Forces to Demonstrate the Effect of Fluid Inertia," ASME Paper No. 84-GT-11.

Vance, J. M., and Kirton, A., 1975, "Experimental Measurement of the Dynamic Force Response of a Squeeze Film Bearing Damper," ASME *Journal of Engineering for Industry*, Vol. 97, pp. 1282–1290.

Zeidan, F. Y., and Vance, J. M., 1989a, "Cavitation Leading to a Two Phase Fluid in a Squeeze Film Damper," *STLE Tribology Transactions*, Vol. 32 No. 1, pp. 100–104.

Zeidan, F. Y., and Vance, J. M., 1989b, "Experimental Investigation of Cavitation Effects on the Squeeze Film Force Coefficients," presented at the 1989 ASME Design Technology Conference, Rotating Machinery Dynamics, Montreal, Canada.

Zeidan, F. Y., and Vance, J. M., 1989c, "Cavitation Regimes in Squeeze Film Dampers and Their Effect on the Pressure Distribution," presented at the STLE Annual Meeting, Atlanta, GA, STLE No. 89-AM-4B-1.

Rotordynamic Evaluation of an Advanced Multisqueeze Film Damper—Imbalance Response and Blade-Loss Simulation

J. F. Walton II

H. Heshmat

Mechanical Technology Inc.,
Latham, NY 12110

In this paper results of rotordynamic response and transient tests of a novel, high load squeeze film damper design are presented. The spiral foil multisqueeze film damper has been previously shown to provide two to fourfold or larger increases in damping levels without resorting to significantly decreased damper clearances or increased lengths. By operating with a total clearance of approximately twice conventional designs, the nonlinearities associated with high-eccentricity operation are avoided. Rotordynamic tests with a dual squeeze film configuration were completed. As a part of the overall testing program, a flexible rotor system was subjected to high steady-state imbalance levels and transient simulated blade-loss events for up to 0.254 mm (0.01 in.) mass c. g. offset or 180 g-cm (2.5 oz-in.) imbalance. The spiral foil multisqueeze film damper demonstrated that the steady-state imbalance and simulated blade-loss transient response of a flexible rotor operating above its first bending critical speed could be readily controlled. Rotor system imbalance sensitivity and logarithmic decrement are presented showing the characteristics of the system with the damper installed. The ability to accommodate high steady-state and transient imbalance conditions make this damper well suited to a wide range of rotating machinery, including aircraft gas turbine engines.

Introduction

The design trend for high-performance rotating machinery has been toward reduced machine size, increased output, and higher efficiency. This has been especially true for gas turbine engines, which have experienced consistent increases in thrust-to-weight ratios and reductions in specific fuel consumption. The impact of this trend on the rotating elements of these machines has been the design of rotors that are smaller in size and that spin more rapidly. Furthermore, design refinements such as integrally bladed disks greatly increase the difficulty of field repair of damaged blades, so that rotor imbalance may reach higher levels than in previous designs.

Rotor-bearing systems have become more complicated and increasingly flexible behavior is being seen. Bending critical speeds and natural frequencies occur more frequently below maximum operating speeds. The result is increased sensitivity to imbalance due to the dynamic amplification seen at resonant frequencies. An increasing amount of attention is being paid to control rotor system dynamic behavior, and one of the most important means for this is the addition of external damping to the system.

Squeeze film dampers are commonly used in gas turbines to provide for such dynamic control. When properly designed, these dampers have been extremely effective in reducing system dynamic sensitivity, as documented by Bhat et al. (1981), Lund et al. (1983), Pinkus and Bupara (1980), San Andres and Vance (1986), Tecza et al. (1982, 1983), Tichy (1983, 1984), and Walton et al. (1987). The reduction in dynamic sensitivity achieved with squeeze film dampers results in lower transmitted forces (hence longer bearing life and less mount fatigue), lower rotor amplitudes at critical clearance locations, and the need for less frequent balancing. However, squeeze film dampers are limited in their ability to control the effects of abusive imbalance levels. The behavior of a squeeze film is such that, at large eccentricity ratios, damping becomes highly nonlinear. A cross-coupled damping force also arises, which effectively acts to stiffen the rotor mount. This combination of effects can both shift the direct damping coefficient away from optimum levels and cause a previously traversed natural frequency to shift upward close to operating speed, with potentially disastrous consequences. Squeeze film damper-supported rotors may also exhibit bistability, a nonlinear phenomenon whereby the system has two orbit states (low and high) for a given imbalance level. A simple "cure" where abusive imbalance is expected might be simply to increase the radial clearance. However, this frequently entails an unacceptably large increase in damper diameter and/or length.

This paper is a continuation of work completed by Heshmat and Walton (1990) in which a new multisqueeze film damper concept, well suited to both normal and abusive rotor vibration

Contributed by the International Gas Turbine Institute and presented at the 36th International Gas Turbine and Aeroengine Congress and Exposition, Orlando, Florida, June 3–6, 1991. Manuscript received at ASME Headquarters March 4, 1991. Paper No. 91-GT-242. Associate Technical Editor: L. A. Riekert.

levels, was presented. Based on the demonstrated performance of the multisqueeze film damper in controlled orbit testing, rotordynamic response testing was conducted. Results of the imbalance response and simulated blade loss testing through and above the first flexible/bending critical speed are presented in this paper as further demonstration of the suitability of this damper concept for application to high-speed rotating machinery.

Multisqueeze Film Damper Description

The spiral foil multisqueeze film damper (MSFD) concept presented herein incorporates a thin foil material to provide multiple squeeze films in series in one single large clearance, as well as self-centering, self-alignment, and high load capabilities. The damper conceptual design has already been presented by Heshmat and Walton (1990) and thus is not be reviewed in detail here. Rather, a brief concept description and results from rotordynamic testing of a radial spiral foil multisqueeze film damper are presented.

Figures 1 and 2 schematically illustrate the concept of the

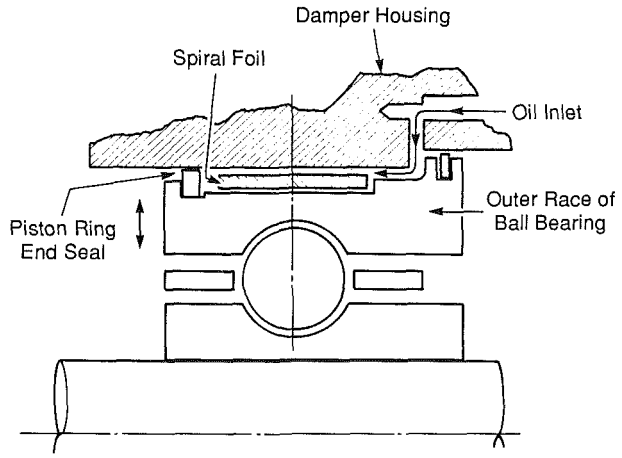

Fig. 1 Schematic configuration of multisqueeze film damper concept

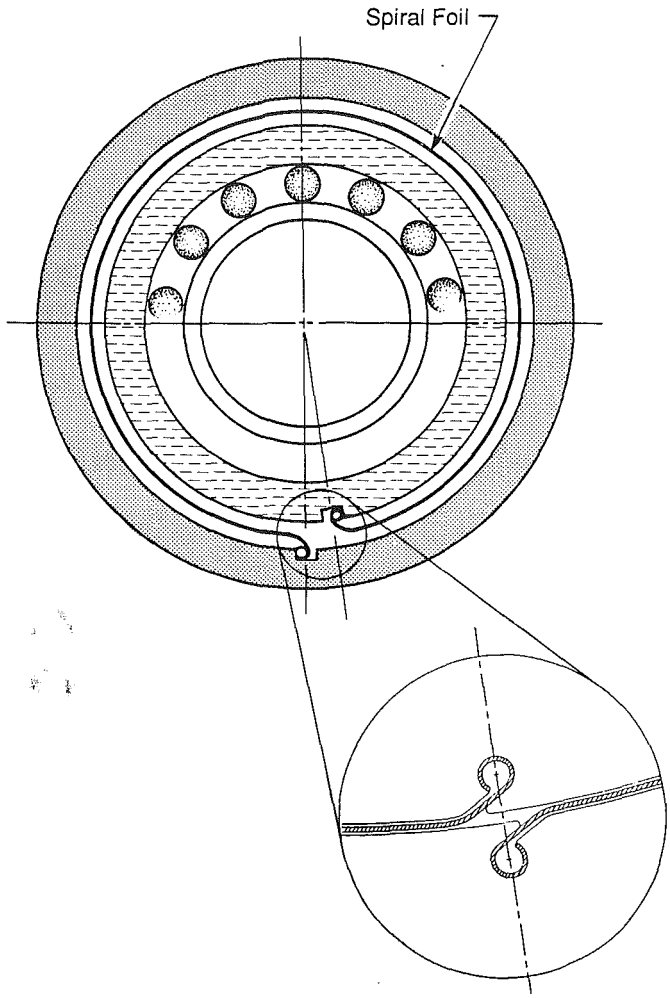

Fig. 2 Cross-sectional view of a single wrap multisqueeze film damper including foil anchoring joint design

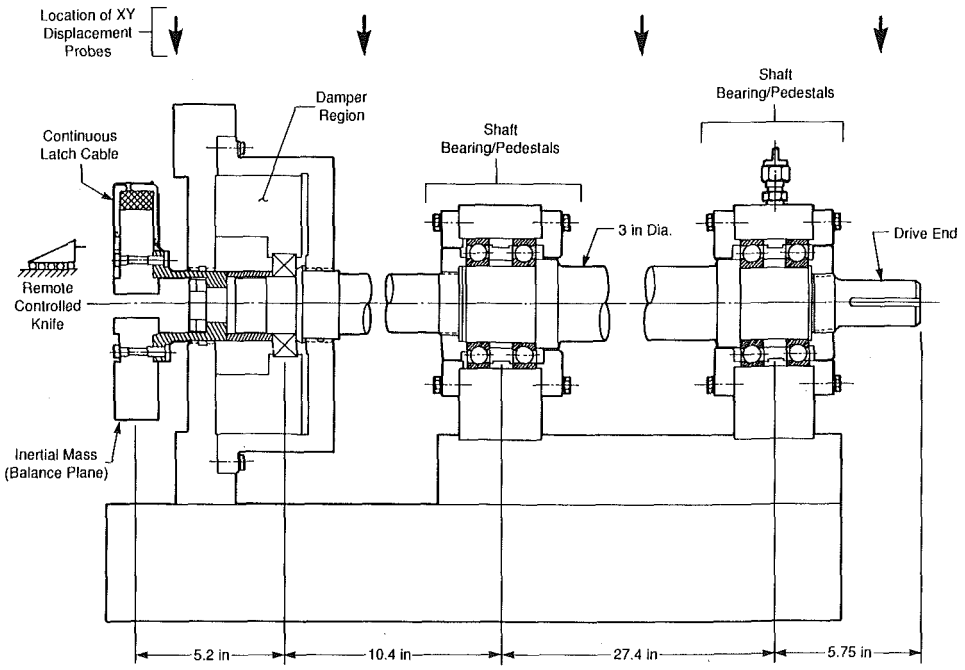

Fig. 3 Schematic of rotordynamic test rig showing instrumentation and key mechanical elements

Table 1 MSFD design values

Foil Width	24.90 mm	(0.98 in)
Foil Thickness	0.29 mm	(0.012 in)
Damper Mean Diameter	141.00 mm	(5.50 in)
Clearance (per film)	0.19 mm	(0.0075 in)
Damper Length	25.40 mm	(1.00 in)
Foil material	Inconel X-750	

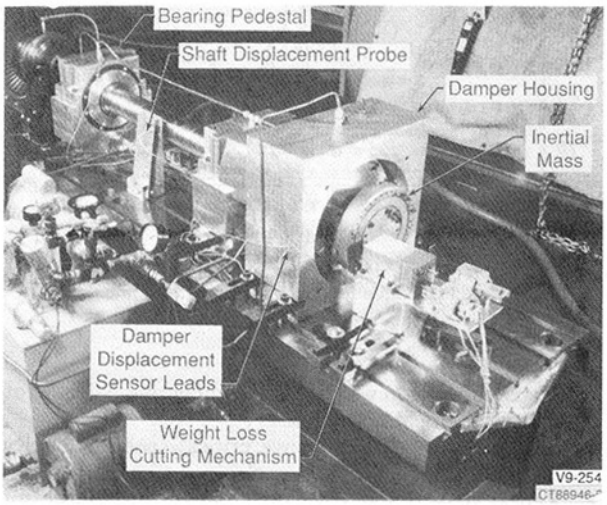

Fig. 4 Assembled rotordynamic simulator with simulated blade-loss capability

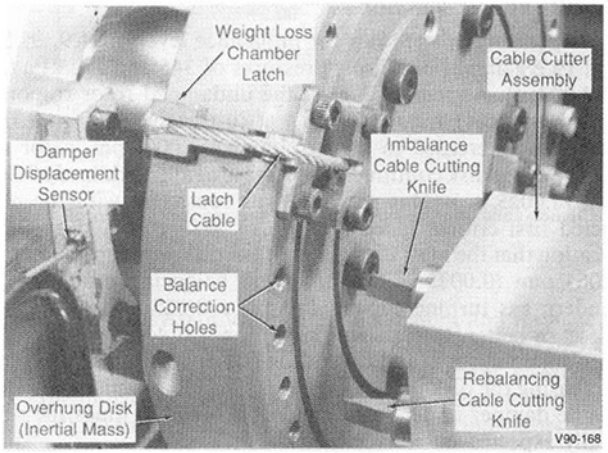

Fig. 5 Close up view of test disk with weight loss chamber and cable cutting assembly

radial MSFD configuration. The oil film is separated into several squeeze films via a spirally formed thin foil whose ends are attached to the damper journal and housing. With this concept, the spiral foil wraps may be used to provide two or more squeeze film dampers in series. With this arrangement the available damping for a given film clearance may be increased without resorting to the use of clearances that would result in the nonlinear damper operation for large vibration orbits. Since the MSFD operates in series, the bearing load is transmitted first through the inner film, through the spiral foil, to the intermediate film(s) and foils and finally through the outer film to the bearing/damper support structure. At any given angular position the fluid film pressures will be maintained equal across the film since there is little or no rigidity provided by the thin foil. As such the local film thicknesses tend to equalize to accommodate any film pressure imbalances as illustrated in Fig. 3.

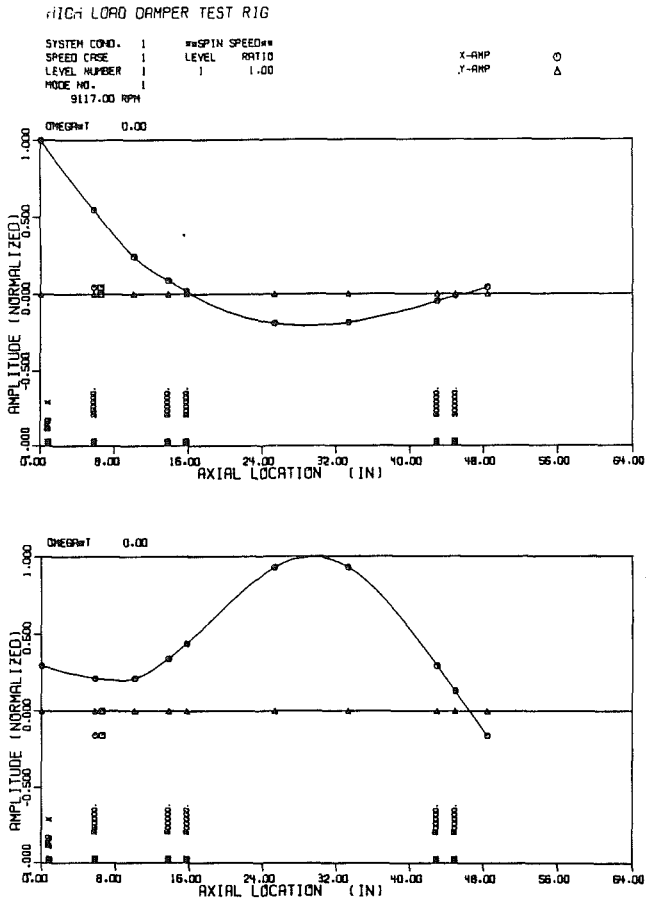

Fig. 6 Normalized mode shapes for rotordynamic blade-loss simulator first critical speed at 9117 rpm, and second critical speed at 18,000 rpm

Based on the demonstrated feasibility of the spiral foil damper in controlled orbit tests, the single wrap MSFD design presented in Table 1 was used for rotordynamic imbalance response and transient weight loss tests.

Experimental Apparatus and Procedures

The rotordynamic test rig shown in Figs. 3–5 consists of four major components: a high-speed shaft, an overhung inertial mass, a damper assembly, and a weight loss cutting mechanism. This rig was developed to evaluate the performance of dampers and their ability to control the dynamic behavior of a large flexible rotor. The maximum test rig speed is approximately 14,000 rpm with predicted first and second critical speeds nominally at 9100 rpm and 18,000 rpm. Figure 6 presents the first two critical speed mode shapes for the rotordynamic test rig, showing that the damper location (approximately 5 in. from the weight loss disk) should experience considerable motion during testing and thereby exercise the damper. The steel shaft is 76 mm (3 in.) in diameter and 1.29 m (48 in.) long, is supported on two sets of 75 mm duplex ball bearings, and is driven by a flat belt coupling that is interfaced through a drive pulley to a 25-hp, d-c drive motor capable of 2500 rpm. The overhung disk, which weighs approximately 75.6 N (17 lb), is attached to the end of the shaft, has 36 tapped holes for the rotor steady-state imbalance response studies, and has two latched chambers 180 deg apart for simulating blade loss events. Two chambers were installed to provide for a degree of safety. Should the damper fail, the weight in the second chamber could be released and the rotor partially rebalanced for deceleration through the first bending critical

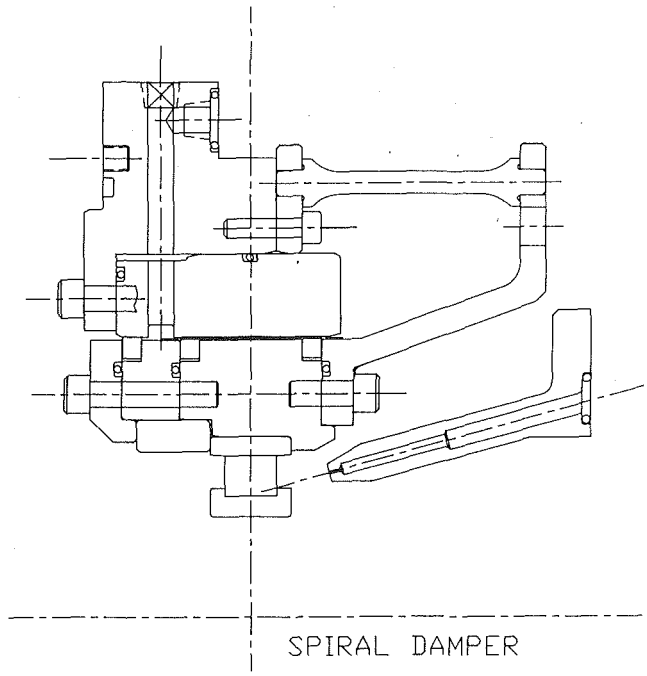

Fig. 7 Cross-sectional view of rotordynamic simulator damper cartridge and rotor support structure

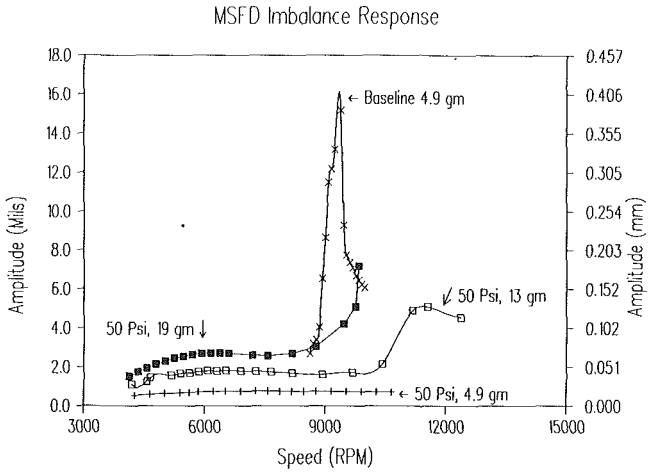

Fig. 8 Comparison of undamped and damped (50 psi oil supply pressure) steady-state imbalance response for up to 19 g imbalance

speed of the rotor. To secure the latched chambers, 3.18 mm (0.125 in.) diameter aircraft-quality cable with steel ball ends is used. Releasing the weight at the desired speed and time is accomplished by remotely activating the solenoid operated knife and plunger assembly. As seen in Fig. 5, two separate knives are provided in the cutting assembly. Each knife is located at a different radius so that the cable for the two separate weight loss chambers can be cut independently.

The damper cartridge, shown in Fig. 7, is installed in the damper housing, which is located between the inertial mass and the shaft support bearings to permit easy access to the damper. This damper cartridge was previously installed in the MTI Controlled Orbit Rig and characterized by Heshmat and Walton (1990) prior to the rotordynamic response and transient weight loss studies reported here.

Instrumentation included in the test rig setup is shown in Fig. 3, and consists mainly of horizontal and vertical eddy current displacement sensors to assess the rotordynamic behavior of the test rig. The damper region was the primary rotor location monitored during testing, though other shaft orbits were also monitored for safety considerations and to assess rotor mode shapes. A tachometer probe was also used to permit speed measurement and to establish a phase reference for the measured displacement data. Instrumentation for measuring damper oil supply pressure and temperature was also included.

Once the damper assembly was installed in the test rig, the following series of tests were conducted:

1 Balance the test rig with the damper inactive (no oil supplied to the damper).
2 Install a known imbalance in the weight loss disk and run the test rig to full speed with the damper inactive to establish the baseline response.
3 Activate the damper with 345 kPa (50 psi) oil supply pressure and operate the test rig to the maximum attainable speed, then repeat with 552 kPa (80 psi) oil supply pressure.
4 Repeat step 3 for increasing imbalance weights until orbits approach 0.38 mm (0.015 in.).
5 Rebalance rotor.
6 Place lead shot in weight loss chamber and balance rotor for supercritical operation.
7 Operate rig at speeds above critical speed and release weight.
8 Repeat steps 6 and 7 for different oil supply pressures and weight loss levels.

Results and Discussion

Response tests were run for imbalance levels of 4.9, 9, 13, and 19.2 g and at oil supply pressures of 345 and 552 kPa (50 and 80 psi). As seen in Fig. 8, the undamped rotor response approaches 0.41 mm (0.016 in.) at just above 9000 rpm. As speed was increased to approximately 13,000 rpm, rotor response at the disk continued to decrease to approximately 0.064 mm (0.0025 in.). This response was consistent with the predicted first critical speed location of 9117 rpm and gave indication that the mass c.g. offset of the disk was approximately 0.064 mm (0.0025 in.). Since good balancing practices for modern gas turbine engines call for a 0.025 mm (0.001 in.) offset or better, this baseline condition was considered a valid starting point for evaluation of the high load damper. Further, increasing the disk imbalance to 19 g would permit evaluation of the damper under rotor conditions with 10 times the normally expected imbalance levels.

Introducing oil at 345 kPa (50 psi) into the damper reduced rotor response for the 4.9 g imbalance condition to less than 0.025 mm (0.001 in.) throughout the entire speed range evaluated up to 11,000 rpm. Increasing the imbalance level at the disk to 13 g resulted in a maximum disk vibration amplitude of 0.046 mm (0.0018 in.) at approximately 6520 rpm. The subsequent increase in vibration that began to appear above 10,000 rpm resulted in a maximum amplitude of 0.127 mm (0.005 in.) at 11,550 rpm. This increase in vibrations was also observed when the 19 g imbalance run was conducted. It is believed that the most likely cause for the change in rotor system response was due to a combination of a loss of preload on the shaft duplex ball bearings located next to the damper bearing assembly and the onset of cavitation in the damper. As seen in Fig. 9, an increase in damper oil supply pressure from 345 kPa (50 psi) to 552 kPa (80 psi) virtually eliminated the increase in rotor response above 10,000 rpm for the 13 g imbalance test case. Regardless, it is evident from these tests that the multisqueeze film damper provides significant control over rotor system response even to levels of imbalance 10 times greater than would normally be expected.

A further review of the experimental data was conducted to

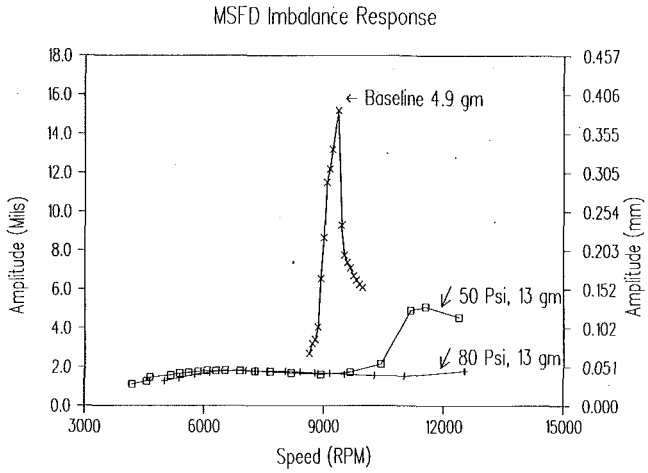

Fig. 9 Comparison of rotor system undamped to damped steady-state response at 345 and 552 kPa (50 and 80 psi) oil supply pressure

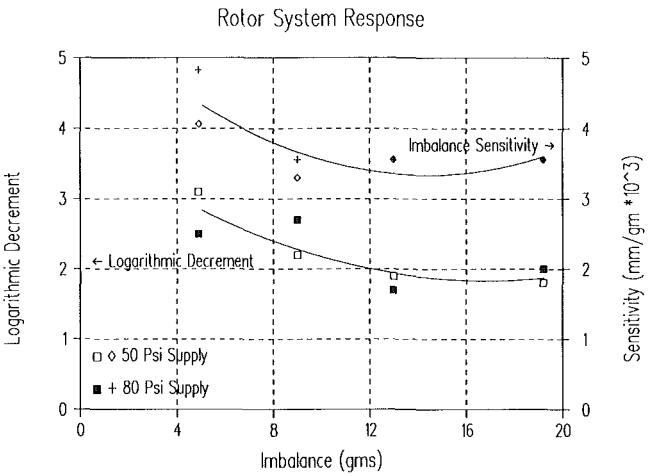

Fig. 10 Rotor system logarithmic decrement and imbalance sensitivity as a function of steady-state imbalance

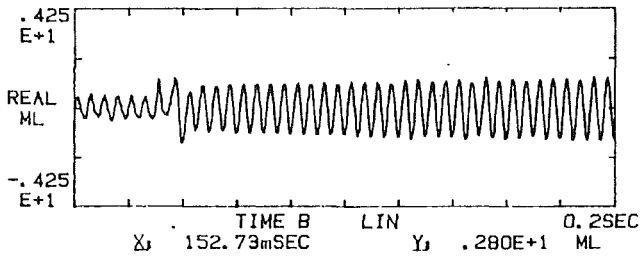

Fig. 11 Rotor system transient response resulting from 10.2 g weight loss at 345 kPa (50 psi) oil supply pressure; displacement measured in mils between multifilm damper and overhung disk

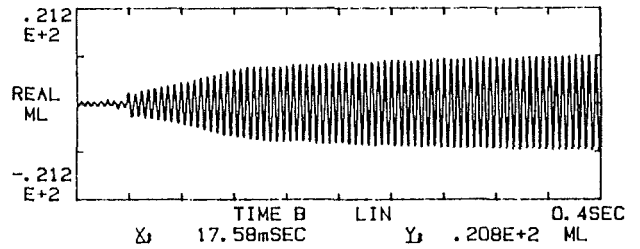

Fig. 12 Rotor system transient response resulting from 17.7 g weight loss at 345 kPa (50 psi) oil supply pressure; displacement measured in mils between multifilm damper and overhung disk

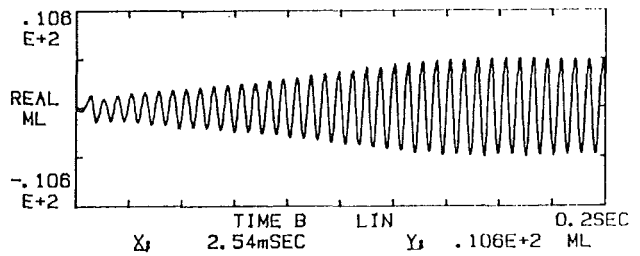

Fig. 13 Rotor system transient response resulting from 10.3 g weight loss at 345 kPa (50 psi) oil supply pressure; displacement measured in mils between squeeze film damper and overhung disk

assess the rotor system logarithmic decrement and imbalance response sensitivity. As seen from Fig. 10 the system Log Dec was consistently around 2 or higher for all cases evaluated, while the imbalance sensitivity ranged from 3.2 to 4.8 $\times$ 10^{-3} mm/g (0.13 to 0.19 mil/g). Both values are indicators of a well-controlled rotor system.

Having characterized the rotor system response due to imbalance, simulated blade loss tests were conducted. In each test the rotor was balanced, the damper was activated, and the rotor was run through the critical speed up to approximately 12,000 rpm and the weight released. As seen in Figs. 11 and 12, the system appears to be critically damped, as would be expected from the calculated logarithmic decrements shown in Fig. 10. After the initial overshoot, the rotor orbits for the 10.2 g weight loss test settled out at approximately 0.076 mm (0.003 in.) peak-to-peak. An increase in the simulated blade loss weight to 17.2 g resulted in a steady-state peak-to-peak orbit of approximately 0.51 mm (0.021 in.).

To assess the performance of the MSFD, a comparative simulated blade loss test with a conventional squeeze film damper design was conducted. The conventional squeeze film damper was sized to provide the same damping as the MSFD or approximately 35 N-s/mm (200 lb-sec/in.) damping. The piston ring sealed damper design dimensions were as follows:

- 25.4 (1.0 in.) length
- 140 mm (5.5 in.) diameter
- 0.191 mm (0.0075 in.) clearance

As seen in Fig. 13, a 10.3 g transient weight loss results in behavior very similar to that observed for the MSFD, but with a resulting steady-state peak-to-peak orbit that eventually reached 0.28 mm (0.011 in.). The same test with the MSFD resulted in an orbit of only 0.076 mm (0.003 in.), a significantly lower orbit than achieved with a conventional squeeze film damper. From Fig. 14 it is evident that the MSFD provides performance superior to the conventional squeeze film damper. In addition to producing lower vibration amplitudes, the MSFD can sustain substantially higher weight losses. The larger overall clearance of the MSFD provides two benefits over a conventional squeeze film damper. First, the damper has a substantially larger linear operating region than a conventional damper for the same vibration amplitudes while still providing the desired damping. Second, the larger overall clearance of the MSFD can aid in minimizing the secondary damage that may occur during a partial blade-loss event. Typically, conventional squeeze film dampers begin to exhibit nonlinear performance at around 70 percent eccentricity, with further increases in vibration resulting in large increases in both direct and cross-coupled damping coefficients as well as increasing the potential for the onset of "jump." Increases in the cross-coupled damping result in an increase in the effective overall rotor system stiffness. Under a blade-loss event or partial blade-loss event, where rotor orbits increase rapidly, the increased system stiffness may severely restrict rotor motion such that

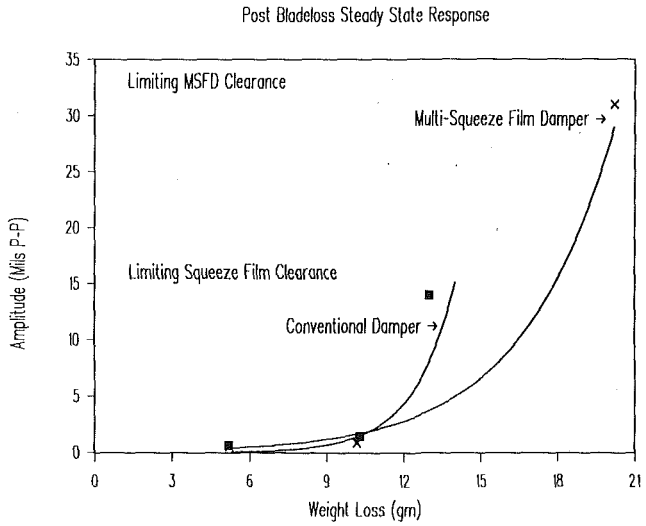

Fig. 14 Comparison of conventional and multisqueeze film damper post-blade-loss steady-state response

the direct damping may be almost totally eliminated and bearing transmitted loads increased to the point that the bearing is destroyed. In addition, the large imbalance levels experienced from a weight loss transient may cause a conventional squeeze film damper to experience bistable operation or a "jump" in vibration orbits. Further, where a conventional damper may bottom out after relatively small transient weight loss events, resulting in large loads being transmitted through the bearings and rotor support structure, the MSFD can permit, as a minimum, twice the range of motion without bottoming out. Increasing the clearance of a conventional squeeze film damper to accommodate the motions of abusive imbalance conditions, however, will result in a significant reduction in system damping for the same length damper. Thus, the MSFD provides the same level of damping as a conventional squeeze film damper, but with a larger total clearance for improved performance under both normal and abusive imbalance conditions.

In summary, a novel multisqueeze film damper was conceived, designed, and tested. This damper performed as expected and appears to be an excellent candidate for a wide range of rotor systems. With its large clearance and predictable performance, this damper is ideally suited to applications where high or abusive rotating loads may be encountered, such as may result from a partial blade-loss event in a gas turbine engine.

Acknowledgments

The work reported herein was performed under U.S. Air Force sponsorship (Contract F33615-C-85-2518). The authors would like to acknowledge the support of Capt. J. Griffin and Mr. T. Fecke of the Air Force Wight Aeronautical Laboratories, Aero Propulsion and Power Laboratory, and Messrs. M. Martin and P. Quantock of MTI for their contributions in completing this work.

References

Bhat, S. T., Buono, D. F., and Hibner, D. H., 1981, "Analysis of High Load Dampers," NASA CR165503.

Heshmat, H., and Walton, J., 1990, "Advanced Multisqueeze Film Dampers for Rotor Vibration Control," ASME/STLE 1990 Tribology Conference Preprint No. 90-TC-3E-1.

Lund, J. W., et al., 1983, "Squeeze Film Damper Technology: Part I—Prediction of Finite Length Damper Performance," ASME Paper No. 83-GT-247.

Pinkus, O., and Bupara, S. S., 1980, "Adiabatic Solutions for Finite Journal Bearings," ASME *Journal of Lubrication Technology*, Vol. 101, pp. 492–496.

San Andres, L., and Vance, J., 1986, "Effects of Fluid Inertia and Turbulence on the Force Coefficients for Squeeze Film Dampers," ASME JOURNAL OF ENGINEERING FOR GAS TURBINES AND POWER, Vol. 108, pp. 332–339.

Tecza, J. A., Zorzi, E. S., and Parker, W. H., 1982, "Squeeze Film Damper Technology Program First Interim Report: Damper Component Analysis and Integration With Rotordynamics Program," U.S. Air Force, Dayton, OH, AFWAL-TR-82-2112.

Tecza, J. A., et al., 1983, "Squeeze Film Dampers Technology: Part 2—Experimental Verification Using a Controlled-Orbit Test Rig," ASME Paper No. 83-GT-248.

Tichy, J. A., 1983, "The Effect of Fluid Inertia in Sequence Film Bearings: A Heuristic and Physical Description," ASME Paper No. 83-GT-177.

Tichy, J. A., 1984, "Measurements of Squeeze Film Bearing Forces and Pressures, Including Effects of Fluid Inertia," *ASLE Trans.*, Vol. 28, No. 4, pp. 520–526.

Walton, J., Pinkus, O., Walowit, J., Tecza, J., and Lee, C., 1986, "Squeeze Film Damper Technology: Part II—Extension of Analysis and Parametric Study," U.S. Air Force, Dayton, OH, AFWAL-TR-82-2112, Part II.

Walton, J., Walowit, J. A., Zorzi, E. S., and Schrand, J., 1987, "Experimental Observations of Cavitating Squeeze Film Dampers," ASME *Journal of Tribology*, Vol. 109, pp. 290–295.

Experimental and Analytical Investigation of Hybrid Squeeze Film Dampers

A. El-Shafei
Assistant Professor,
Department of Mechanical Design and Production,
Cairo University,
Giza, Egypt

A new concept for actively controlling high-speed rotating machinery is investigated both analyically and experimentally. The controlling mechanism consists of a hybrid squeeze film damper (patent pending) that can be adaptively controlled to change its characteristics according to the instructions of a controller. In an extreme case the hybrid damper can act as a long damper, which is shown to be effective in reducing the amplitude of vibration of rotating machinery. In the other extreme the hybrid damper acts as a short damper, which is shown to be effective in reducing the force transmitted to the support. In the long damper configuration the oil flow is circumferential, while in the short damper configuration the oil flow is predominantly axial. The hybrid damper is designed to operate in either the short or the long damper configuration by controlling the positions of two movable sealing rings. The hybrid damper was tested on a Bently Nevada Rotor Kit and it is shown experimentally that the long damper configuration is extremely efficient at controlling the amplitude of vibration and the short damper configuration reduces the force transmitted to the support.

Introduction

Magnetic bearings have been investigated for the last ten years or so for actively controlling the vibration of rotating machinery (Schweitzer and Ulbrich, 1980; Nonami et al., 1989). Yet, as far as aircraft engines are concerned, magnetic bearings are still at a developmental stage and have not been used in aircraft engines for several reasons, including: (1) the inability of magnetic bearings to withstand high temperatures, (2) the control algorithms for magnetic bearings are still under development, and most importantly (3) magnetic bearings have still to prove their reliability.

Squeeze film dampers (SFDs), on the other hand, have a proven track record. They have been used successfully for the last twenty years to passively damp rotating machinery, in particular aircraft engines (White, 1972; Gunter et al., 1977; Holmes and Dogan, 1985). They provide the primary source of damping in aircraft engines since the rolling element bearings on which these engines are mounted provide very little damping. Thus, because of their reliability, it seems natural to develop SFDs to control rotor vibrations actively. Burrows et al. (1983) investigated the possibility of controlling rotating machinery vibration by controlling the pressure in a SFD, and they point out that control of rotors using active SFDs is much cheaper than using magnetic bearings, and is more simple and reliable. Adams and Zahloul (1987) studied the control of rotors by controlling the pressure in hydrostatic SFDs.

In previous studies (El-Shafei, 1989a, b, 1990) it was shown that there are two distinct kinds of SFDs, namely short dampers and long dampers. In short dampers, the oil flow is primarily axial and thus the pressure gradient in the axial direction dominates and consequently the short bearing approximation to the Reynolds equation applies. In long dampers, on the other hand, the oil flow is primarily circumferential and thus the pressure gradient in the circumferential direction dominates and consequently the long bearing approximation to the Reynolds equation applies. Usually open-ended dampers are considered short dampers and tightly sealed dampers are considered long dampers regardless of the actual physical length of the damper (which is usually short with respect to the diameter of the damper).

Short dampers and long dampers have very different characteristics (El-Shafei, 1989a). In general, because of their larger damping capacity, long dampers are better at attenuating the amplitude response of the rotor, while short dampers are better at reducing the force transmitted to the support. In this study, we exploit the differences between the long and short dampers and develop a hybrid damper that can act as a long damper or as a short damper based on the instructions of a controller. The design of the hybrid damper is discussed and its performance is experimentally verified.

Squeeze Film Dampers

Figure 1 shows a SFD, and the coordinate systems used. The film thickness h at any given location is given by

$$h = c - e \cos \theta \tag{1}$$

where c is the clearance, e is the eccentricity of the journal, and θ is measured from the positive r axis of the whirling

Contributed by the International Gas Turbine Institute and presented at the 36th International Gas Turbine and Aeroengine Congress and Exposition, Orlando, Florida, June 3-6, 1991. Manuscript received at ASME Headquarters March 4, 1991. Paper No. 91-GT-250. Associate Technical Editor: L. A. Riekert.

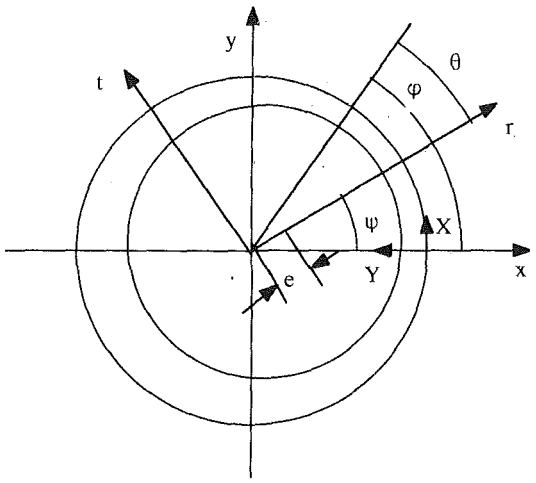

Fig. 1 Coordinate frames

coordinate system (r, t, z). The z axis is perpendicular to the plane of the paper.

The damping forces in SFDs are obtained by solving the Reynolds equation for fluid lubrication, which, for a SFD, reduces to

$$\frac{1}{R}\frac{\partial}{\partial\varphi}\left(\frac{h^3}{\mu R}\frac{\partial p}{\partial\varphi}\right)+\frac{\partial}{\partial z}\left(\frac{h^3}{\mu}\frac{\partial p}{\partial z}\right)=-12(e\dot{\psi}\sin\theta+\dot{e}\cos\theta) \quad (2)$$

where μ is the viscosity of the oil, R is the radius of the damper, p is the pressure, and $\dot{e}$ and $e\dot{\psi}$ are the radial and tangential velocities of the journal in the damper, respectively. There are two mathematical approximations to the Reynolds equation that have physical significance, namely, the short bearing approximation and the long bearing approximation. In the short bearing approximation to the Reynolds equation, which is justified if the damper is short in the axial direction, the flow in the damper is predominantly axial rather than circumferential, and thus the axial pressure gradient is much larger than the circumferential pressure gradient. On the other hand, in the long bearing approximation to the Reynolds equation, which is justified if the damper is long in the axial direction, the flow in the damper is circumferential, and thus the circumferential pressure gradient is much larger than the axial pressure gradient. In practice, if the damper is tightly sealed, then the flow is circumferential even if the dampers are physically short. In this case, the long bearing approximation would describe the conditions in the damper better than the short bearing approximation.

Thus for a short damper, $\partial p/\partial z >> \partial p/\partial\varphi$ and the Reynolds equation (2) can be solved for the pressure p, such that

$$p=\frac{6\mu}{h^3}\left(\frac{L^2}{4}-z^2\right)(e\dot{\psi}\sin\theta+\dot{e}\cos\theta)$$

and for a long damper, $\partial p/\partial\varphi >> \partial p/\partial z$ and the Reynolds equation (2) can then be solved for the pressure p, such that

$$p=\frac{6\mu R^2}{c^3}\left\{\left[\frac{1}{\epsilon(1-\epsilon\cos\theta)^2}-\frac{1}{\epsilon(1+\epsilon)^2}\right]\dot{e}+\left[\frac{2\sin\theta(2-\epsilon\cos\theta)}{(2+\epsilon^2)(1-\epsilon\cos\theta)^2}\right]e\dot{\psi}\right\}$$

Integrating the pressure obtained by the solution of the Reynolds equation, we obtain the damping forces in SFDs, which take the form

$$F_{rc}=-C_{rr}\dot{e}-C_{rt}e\dot{\psi} \quad (3)$$

$$F_{tc}=-C_{tr}\dot{e}-C_{tt}e\dot{\psi} \quad (4)$$

where F_{rc} and F_{tc} are the radial and tangential damping forces, respectively. The damping coefficients C_{rr}, C_{tt}, C_{tr}, and C_{rt} are in general nonlinear functions of the position and velocity of the journal in the damper. Figure 2 shows a plot of the damping coefficients C_{rr}, C_{tt}, C_{tr}, and C_{rt} versus the eccentricity ratio ϵ, which is defined as the ratio e/c, for a cavitated damper executing a nearly circular-centered whirl, using the π-film cavitation theory. It can be seen from Fig. 2 that the damping coefficients for the short and long bearing approximations are nonlinear functions of the position of the journal in the damper. In fact, the damping coefficients increase as the eccentricity increases, and this, in one sense, is a desirable characteristic, since the damper provides more damping as the amplitude of the whirl increases, which is obviously beneficial. Perhaps this is why squeeze film dampers are such effective damping devices. On the other hand, it is precisely this nonlinear characterisitic that may, for a badly designed damper, result in nonlinear behavior of the rotor-bearing system (such as jump resonance, subharmonic motion, etc.). A well-designed damper

Nomenclature

B = bearing parameter = $\mu R^3L/m\omega_n c^3$ for long dampers; = $\mu RL^3/m\omega_n c^3$ for short dampers
c = clearance, m
C = half damping coefficient at rotor center, Ns/m
C_{rr}, C_{tt}, C_{tr}, C_{rt} = damping coefficients, Ns/m
C^*_{rr}, C^*_{tt}, C^*_{tr}, C^*_{rt} = nondimensional damping coefficients
e = eccentricity, m
F_r = radial force, N
F_{rc} = radial damping force, N
F_t = tangential force, N
F_{tc} = tangential damping force, N
g = unbalance, m
h = film thickness, m
K = half rotor stiffness, N/m
K_r = retainer spring stiffness, N/m
L = damper length, m
m = half mass of disk, kg
m_r = radial inertia coefficient, kg
m_t = tangential inertial coefficient, kg
M = inertial parameter = $\rho R^3L/mc$ for long dampers; = $\rho RL^3/mc$ for short dampers
p = pressure, Pa
(r, t, z) = whirling frame (Fig. 1)
R = damper radius, m
R_k = K_r/K = stiffness ratio
Re = $\rho\Omega c^2/\mu$ = Reynolds number
Tr = transmissibility
U = g/c = nondimensional unbalance
(x, y, z) = stationary frame (Fig. 1)
(X, Y, Z) = stationary frame (Fig. 1)
ϵ = e/c = eccentricity ratio
η = $C/m\omega_n$ = damping loss factor
θ = angle (Fig. 1), rad
μ = fluid dynamic viscosity coefficient, Ns/m^2
π = 3.14159265.....
ρ = fluid density, kg/m^3
φ = angle (Fig. 1), rad
ψ = angle (Fig. 1), rad
ω_n = natural frequency of rotor-bearing system, Hz
Ω = rotor speed, Hz
Ω^* = Ω/ω_n = nondimensional rotor speed

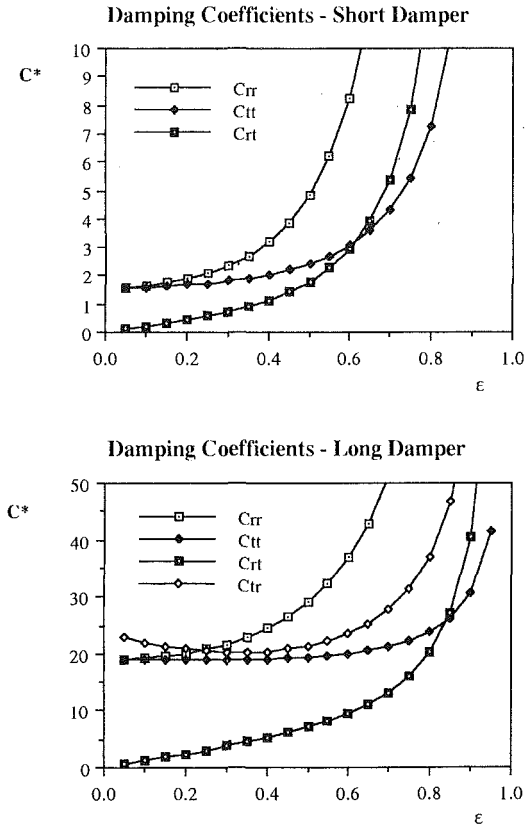

Fig. 2 Damping coefficients (nondimensional) versus ϵ

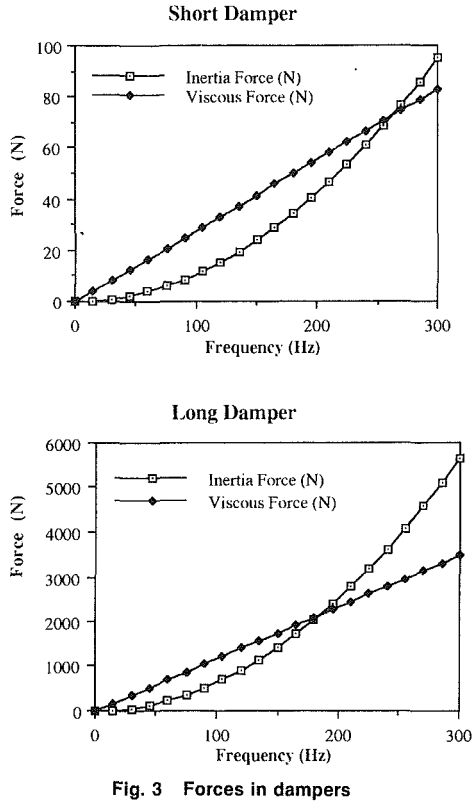

Fig. 3 Forces in dampers

will not experience this nonlinear behavior, while still taking advantage of the increasing damping coefficients with position. Note that, in Fig. 2, the damping coefficients C_{rt} and C_{tr} are equal for the short bearing. It also should be noted that in Fig. 2, the short damper coefficients are nondimensionalized by $\mu RL^3/c^3$, and long damper coefficients are nondimensionalized by $\mu R^3 L/c^3$.

The above model is valid for dampers with a very low squeeze Reynolds number (Re). For high Re (of the order of 10) the inertia of the fluid has to be taken into account. In fact, it can be shown (El-Shafei, 1989c) that at Re = 10 the inertia force is equal to the viscous force and is larger thereafter for small circular whirl of the journal in the damper. Also it can be shown, in this case, that the added mass to the journal for an uncavitated long damper is about 120 times the mass of the journal, while for an uncavitated short damper the added mass is about 10 times the mass of the journal (El-Shafei, 1989c), although there are only a few drops of fluid and the journal is made of steel. This is because the fluid is being squeezed at very high velocities and accelerations. The effect of fluid inertia on the dynamics of the rotor is to introduce additional resonances in the speed range of interest due to the added mass, with a consequent reduction in the region of good vibration isolation (El-Shafei, 1989b, 1990), but fluid inertia is beneficial in reducing the possibility of the jump resonance phenomenon.

To include fluid inertia in the damper model, we use the energy approximation of El-Shafei (1988). The velocity profiles of the fluid are assumed not to change much due to fluid inertia (El-Shafei, 1989c). Using the velocity profiles predicted from the classical lubrication theory, the kinetic coenergy of the fluid is calculated, and the inertia forces are obtained by Lagrange's equations in conjunction with the Reynolds transport theorem (El-Shafei, 1989c). The resulting forces in the damper (both viscous and inertial) for a circular-centered whirl are given by (El-Shafei, 1989b, 1990)

$$F_r = m_r e\dot{\psi}^2 - C_{rt} e\dot{\psi} \tag{5}$$

$$F_t = -m_t e\dot{\psi}^2 - C_{tt} e\dot{\psi} \tag{6}$$

where m_r and m_t are the damper's inertial coefficients.

To illustrate the importance of the fluid inertia forces, Fig. 3 shows plots of the magnitude of the inertial force and the viscous force versus frequency, for $\epsilon = 0.25$, for both the long and short dampers. The parameter values used to obtain these plots are: ρ = 773.07 kg/m^3 (1.5 slugs/ft^3), μ = 0.0048 Ns/m^2 (0.0001 lb sec/ft^2), R = 50.8 mm (2 in.), L = 25.4 mm (1 in.), c = 0.2032 mm (8 mils). It can be seen from Fig. 3 that, for the above damper parameters, the inertia force is equal to the viscous force at approximately 250 Hz (15,000 cpm), for the short dampers, and 200 Hz (12,000 cpm) for the long dampers; and is larger thereafter. It can also be seen that the inertia force cannot be neglected in the analysis of squeeze film dampers since it is of the same order of magnitude as the viscous force, nearly throughout the whole speed range.

An important observation from Fig. 3 is that the forces in the long damper are much higher than those for the short damper. In fact, for this case the forces in the long damper are approximately 50 times higher than those of the short damper. This can also be seen from Fig. 2, from which it can be seen that the nondimensional damping coefficients for the long damper are approximately twelve times higher than those of the short damper. Thus, for the same damper parameters, if the damper is designed as a long damper (i.e., a tightly sealed damper) it will exhibit larger forces than a damper designed as a short damper (i.e., an open-ended damper). This may be visualized physically, since for an open-ended damper the oil is squeezed out from the damper causing a relief in pressure, and consequently a smaller force in short dampers, while for a tightly sealed damper no relief of pressure occurs when the journal squeezes the oil, and thus the long damper exhibits an appreciably higher force.

Also from Figs. 2 and 3, it can be concluded that the long damper provides more damping than a short damper. Thus if it is required to stabilize a rotor, then the long damper will remove more energy than the short damper. Also, because of

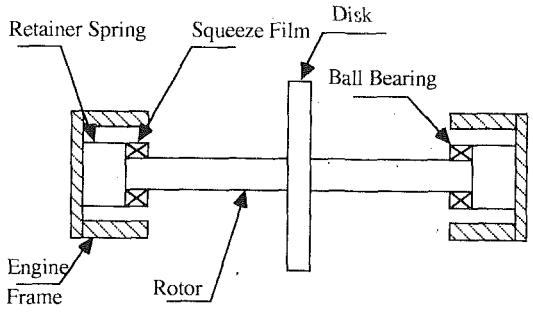

Fig. 4 Jeffcott rotor on squeeze film dampers

the larger forces that are transmitted through a long damper, the long damper can be considered as a high load damper, i.e., it will be able to sustain high loads without executing large orbits (El-Shafei, 1989c), and thus the possibility of jump resonance is reduced.

Jeffcott Rotor Incorporating SFDs

Figure 4 shows a Jeffcott rotor mounted on two identical ball bearings, each of which is surrounded by a squeeze film. The outer race of each ball bearing, which is assumed rigid and massless, is constrained from rotating by a retainer spring of stiffness K_r, which also acts to center the journal in the clearance of the oil film. The rotor is assumed massless with stiffness of $2K$, the disk is assumed rigid with mass $2m$, and the damping acting at the rotor center has a damping coefficient of $2C$.

The unbalance response of the Jeffcott rotor of Fig. 4 can be obtained by assuming circular-centered whirl of the journals in the dampers. This is justified because the rotor is symmetric. The circular-centered whirl assumption results in the reduction of the nonlinear differential equations of motion to nonlinear algebraic equations (El-Shafei, 1990). Further manipulation of the algebraic equations results in a single eighth-order polynomial in the speed of rotation, which is then solved by the IMSL routine ZPOLR. This permits all the solutions to be found without trial and error, and results in a hugh savings in computation time over numerical integration of the equations of motion, and permits parametric studies of the rotor damper system to be performed (El-Shafei, 1990).

Figures 5 and 6 show the unbalance response of the Jeffcott rotor of Fig. 4, with short and long dampers, respectively. The eccentricity ratio ϵ and the transmissibility Tr are plotted against the nondimensional frequency Ω^*, which is defined as the ratio of the rotor rotation speed Ω to the natural frequency of the system ω_n. The transmissibility Tr is defined as the ratio of the magnitude of the force transmitted to the engine frame with squeeze film damper support, to the magnitude of the force transmitted to the engine frame if the support was rigid. The damper is a successful support if $Tr < 1$. The parameters defining the system for Figs. 5 and 6 are: $B = 0.1$, $M = 0.2$, $U = 0.3$, $R_k = 0.1$, and $\eta = 0.01$.

For the short damper, Fig. 5, it can be seen that the rotor exhibits the jump resonance phenomenon and, for most of the speed range, has low transmissibility. On the other hand, for the long damper, Fig. 6, it can be seen that the rotor successfully attenuates the amplitude of the whirl at the critical speed of the Jeffcott rotor, but it exhibits an additional critical due to fluid inertia, which is not well attenuated. We have seen earlier that the added mass to the rotor is much higher in the case of the long dampers than in the case of the short dampers, which is the reason for the appearance of the second critical for the long damper supported rotor in the speed range under consideration. Also it can be seen from Fig. 6 that for long dampers the speed range of good vibration isolation ($Tr < 1$) is diminished compared to that of the short dampers.

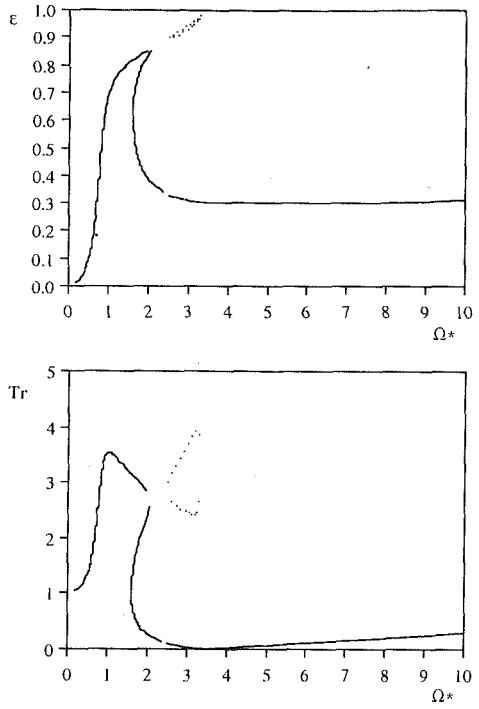

Fig. 5 Unbalance response using short dampers

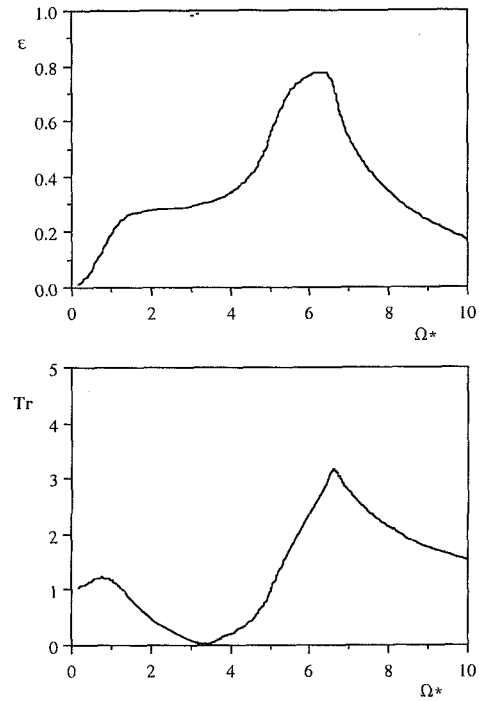

Fig. 6 Unbalance response using long dampers

Comparing Figs. 5 and 6, it can be seen that the short damper is better at decreasing the force transmitted to the engine frame above the critical speed, while the long damper is better at attenuating the amplitude of the whirl at the critical speed. Also the long damper does not exhibit the jump resonance phenomenon while the short damper does not exhibit the second critical due to fluid inertia in the speed range under consideration. In fact, for the rotor of Fig. 4, if it operated as a long damper up to a speed of about $\Omega^* = 4$, and is operated as a short damper thereafter, then the rotor will be operating with much better behavior as regards both the amplitude response and the transmissibility. Thus, if a squeeze film damper

is designed to operate as a short damper when a small force transmitted to the support is desired, and to operate as a long damper when a small amplitude of vibration is desired, this would lead to a more effective squeeze film damper, and would allow rotors to operate safely at higher speeds. This can be accomplished by actively controlling the squeeze film damper to change its characteristics to either the long damper or the short damper. The example of the rotor response in Figs. 5 and 6 implies that the control algorithm for such a hybrid damper would be as simple as just switching from long to short dampers and vice versa.

This suggests that it is possible to develop an actively controlled hybrid squeeze film damper that can operate as a long damper near critical speeds, such that it effectively attenuates the amplitude response of the engine and avoids the possibility of a jump resonance, and it also can operate as a short damper at the operating speed region, such that it effectively reduces the force transmitted to the engine frame. This is possible by designing the sealing on the damper, such that the damper becomes tightly sealed (i.e., long damper) or open-ended (i.e., short damper) according to the instructions of the controller.

Design of the Hybrid Damper

Tecza et al. (1983) examined two dampers, and the results of their experiments showed that the so-called globally sealed damper simulated a short damper and the locally sealed damper simulated a long damper. In the globally sealed damper they had two grooves: a feed groove and a drain groove at each end of the damper with no end seals. The only sealing was by quad rings on the journal face to prevent oil leakage. The locally sealed damper has two end holes: a feed hole and a drain hole. Piston rings were used to seal the ends of the damper. Thus, both the oil feed and drain and the sealing method affect the performance of the damper.

In the design of the hybrid damper, it was decided to feed the oil by three feed holes distributed circumferentially at the center of the damper. The three holes would ensure continuous oil feed to the damper and would have minimum effect on the flow pattern in the damper. The feed holes were provided with check valves to prevent back flow through the feed holes.

Several sealing methods were investigated for the hybrid damper. The sealing had to be both controllable and effective, i.e., it had to be an effective seal for the long damper mode, and it had to be controllable in order to have no end seal in the short damper mode. Inflatable seals were considered but were rejected because: (1) the performance is uncertain when subjected to high pressures, (2) there was concern the seals would become fatigued and rupture over time, (3) the seal had to be specially made to be tested, and (4) it may provide a centering force that may be of the same order of magnitude as the forces in the damper.

It was finally decided to use two movable sealing rings with sliding fit both to the end caps and to the housing, one on each end of the damper as shown in Fig. 7. The principle of the seals' operation is simple. The damper oil film and the hydraulically actuated seals are supplied from independently variable sources. In order for the damper to operate as a long damper, the pressure to the seal chambers is elevated above the internal pressure of the damper. The seal rings will move in axially and seal the oil film inside the damper clearance. In order to return to the short damper configuration, the seal chamber pressure is lowered until it is less than the internal pressure of the damper. This causes the seal rings to return to their original positions.

Testing

The hybrid damper was tested on a Bently Nevada rotor kit. The rotor kit has a maximum speed of 167 Hz (10,000 rpm)

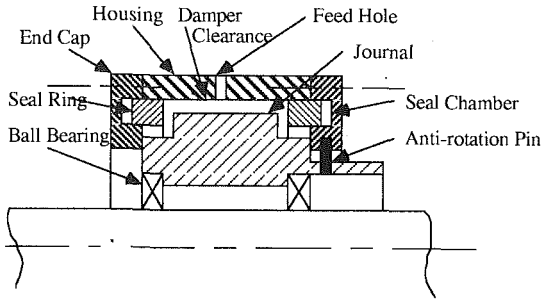

Fig. 7 Schematic of the hybrid damper

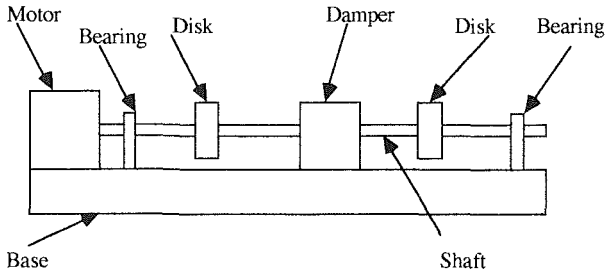

Fig. 8 Schematic of rotor kit including the hybrid damper as tested

and is provided with a speed control. It consists of a shaft with two massive disks as shown in Fig. 8. The damper was placed between the two disks, and its journal motion was monitored by two proximity probes provided with the rotor kit. The proximity probes have a sensitivity of 7.874 V/mm (200 mV/mil). The damper housing was mounted on a bracket that was allowed to move vertically on linear bearings. A Brüel & Kjaer 8200 force transducer was attached beneath the housing, between the housing and the rotor kit base, which was bolted to the test bench. The force transducer allowed measurement of the force transmitted through the damper to the support.

The damper had a radial clearance of 0.2794 mm (11 mils), and the damper journal had a diameter of 51.003 mm (2.008 in.), an active length of 25.4 mm (1 in.), and weighed 4.982 N (1.12 lb). The rotor kit shaft had a length of 0.635 m (25 in.) and a diameter of 9.525 mm (0.375 in.). The massive disks supplied with the rotor kit were provided with balancing holes. The heavier disk weighing 8.763 N (1.97 lb) was located 0.2032 m (8 in.) from the motor end, while the other disk was 0.5207 m (20.5 in.) from the motor end and weighted 6.583 N (1.48 lb). The bearings were located 3.81 cm (1.5 in.) and 0.603 m (23.75 in.) from the motor end, respectively. The damper, at its central plane, was located 0.394 m (15.5 in.) from the left end.

The force transducer was connected to a Brüel & Kjaer 2635 Charge Amplifier, which amplified and conditioned the output signal from the transducer. The signal was then displayed on the screen of a Tektronix 2235 oscilloscope, which had the Bently Nevada modifications. The proximity probes were powered through the proximitors provided with the rotor kit. The signals from the proximitors were displayed simultaneously on the oscilloscope screen in the XY mode to view the journal orbit. The rotor speed was monitored by a Brüel & Kjaer 4912 stroboscope, which was used as a tachometer. The stroboscope was triggered once per revolution by a signal from a proximity probe monitoring a key-way.

Oil was supplied from a hydraulic bench that was capable of supplying oil at pressures up to 20.68 MPa (3000 psi); however, supply oil pressure was limited to 5.515 MPa (800 psi) by way of a bypass valve. Oil from the supply of the test bench is routed through two loops, one of which supplies the damper while the other supplies the seal chambers as shown

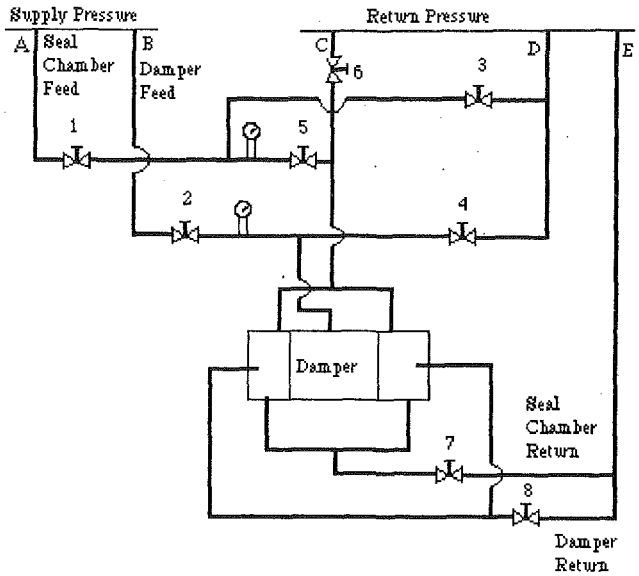

Fig. 9 Hydraulic circuit

in Fig. 9. The pressure in each loop is controlled manually by means of a bypass back to the low-pressure return side of the test bench. Needle valves 3 and 4 in each loop control the amount of flow through each bypass. In addition, needle valves 1 and 2 above the bypass in each loop provide a pressure drop if a lower pressure is required than can be attained by fully opening the bypass. The loop that supplies the seal rings also includes a bypass to the atmospheric pressure drain. Two shut-off valves 5 and 6 in this loop allow the seals to be alternately exposed to the loop pressure and atmospheric pressure, respectively. This change in pressure is what actuates the seals. Connections are also made from both of the seal chambers and the drain grooves in the damper to the drain, and are regulated by needle valves 7 and 8. These connections provide a means of expelling trapped air from the system, as well as an additional means of regulating the pressure inside the damper and behind the seals. It should be noted the redundancy was an objective in designing the hydraulic circuit shown in Fig. 9.

The objective of the testing was to demonstrate that the long damper is more effective than the short damper in reducing the amplitude of vibration at the critical speed, and the short damper was more effective than the long damper in reducing the force transmitted to the support at the operating speed.

First the rotor was balanced in two planes, without oil, then an unbalance was created by adding 0.25 g weight to the heavy disk. The speed range was then scanned and the rotor's first critical speed was determined to be 56.25 Hz (3375 rpm). The orbit size at the damper location was measured off the oscilloscope screen and was 0.254 mm (10 mils) peak-to-peak. While operating at this critical speed, oil was supplied to the damper and the damper was operated in the short damper mode. The supply pressure to the damper was varied to determine its effect on the orbit size at the damper location. Also, while operating at this speed, the damper was operated in the long damper mode, and also in this case the supply pressure was varied. The results are illustrated in Fig. 10.

In the long damper mode, the orbit at the damper location was nearly reduced to a point at a supply pressure of 2.068 MPa (300 psi) and above. It is not clear whether the journal was stationary, or there was motion at the journal and we could not see it because of the resolution of the oscilloscope. If the journal was stationary, there were two possibilities: Either the long damper mode was so effective that no motion occurred, or the seal rings were holding the journal stationary. It should be noted that when the pressures were reduced slightly

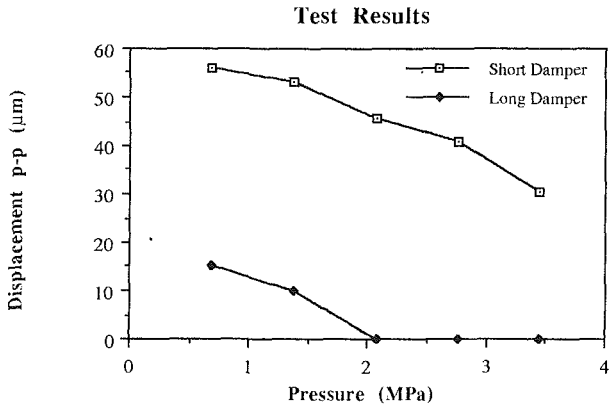

Fig. 10 Experimental results at 3375 rpm (first critical)

in the seal chambers, the journal orbit was minute, but could be viewed clearly on the oscilloscope screen. In general, the pressure in the seal chambers had to be nearly twice that in the damper to achieve the long damper configuration; for example, a pressure of 1.276 MPa (185 psi) was required to be supplied to the seal chambers when the damper was supplied with 0.689 MPa (100 psi). It should be noted that the experimental results of Holmes and Dogan (1985) have indicated that if the seal ring is at a distance equal to the clearance away from the damper end, then the damper is in the short damper mode, and if the seal ring moves closer then we approach the long damper mode.

Figure 10 illustrates that both the short and long dampers are effective damping devices, reducing the undamped orbit of 0.254 mm (10 mils) p-p appreciably. However, the long damper mode is much more effective than the short damper, reducing the orbit by at least a factor of 4 from that of the short damper. Also, Fig. 10 illustrates that controlling the supply pressure to the damper is not as effective in reducing the orbit as controlling the flow in the damper by changing from the short to the long damper modes. This suggests that the hybrid damper is a much more effective control device than the control schemes developed by Adams and Zahloul (1987) and Burrows et al. (1983).

While in the long damper mode with a damper supply pressure of 0.689 MPa (100 psi), the rotor speed was increased to 93.33 Hz (5600 rpm). The output from the force transducer at this speed was viewed on the oscilloscope screen and was determined to be 3.4 N zero-to-peak. Changing to the short damper mode the force was reduced to 1.8 N zero-to-peak. This confirmed that the short damper is a better vibration isolator than the long damper.

Discussion and Conclusion

In this paper, we have shown that the long and short dampers have very different characteristics. The long damper: (1) is better at attenuating the amplitude response at the critical speed; (2) is less susceptible to the jump resonance phenomenon; (3) removes more energy to stabilize a rotor; and (4) can be considered as a high load damper. However, the long damper is susceptible to the effects of fluid inertia and transmits a large force to the support. On the other hand, the short damper transmits a small force to the support and has negligible fluid inertia effect, but is susceptible to the jump resonance phenomenon.

We exploited the differences between the short and long dampers, and developed a hybrid damper that can act as a short damper or as a long damper based on the instructions of a controller. Experimentally, we controlled the hybrid damper manually, and we demonstrated that in the long damper mode the hybrid damper was extremely efficient at reducing the orbit size, and in the short damper mode the hybrid damper

was efficient at reducing the force transmitted to the support. Thus we have experimentally verified our theoretical findings, and have shown that the hybrid damper can be used effectively to control rotating machinery vibrations.

In effect, the hybrid damper changes the stiffness and damping characteristics of the support to provide better performance. We have demonstrated the hybrid damper's characteristics as an on-off controller; that is, it operates in either the long damper mode or the short damper mode, which may be sufficient. However, there are an infinite number of configurations of finite dampers that can be obtained by placing the sealing rings in intermediate positions. Thus, an adaptive controller needs to be developed to exploit these possibilities and continuously adapt the hybrid damper to the continuously varying operating conditions.

Acknowledgments

This work was done while the author was at the University of South Florida, in Tampa. The support of the USF President's Council Faculty Award and the College of Engineering Research Initiation Grant is acknowledged. Two undergraduate students, Matthew Smith and Keith Panick, helped in the design and testing of the hybrid damper, as part of their independent study work.

References

Adams, M. L., and Zahloul, H., 1987, "Attenuation of Rotor Vibration Using Controlled-Pressure Hydrostatic Squeeze-Film Dampers," presented at the Eleventh Biennial ASME Vibrations Conference, Boston, MA, Sept.

Burrows, C. R., Sahinkaya, M. N., and Turkay, O. S., 1983, "An Adaptive Squeeze-Film Bearing," ASME Paper No. 83-Lub-23.

El-Shafei, A., 1988, "Dynamics of Rotors Incorporating Squeeze Film Dampers," Ph.D. Thesis, Department of Mechanical Engineering, Massachusetts Institute of Technology, Cambridge, MA.

El-Shafei, A., 1989a, "Long and Short Bearing Approximations for Squeeze Film Dampers," *Proceedings of the Vibration Institute*, pp. 145–151.

El-Shafei, A., 1989b, "Unbalance Response of a Jeffcott Rotor Incorporating Long Squeeze Film Dampers," in: *Machinery Dynamics—Applications and Vibration Control Problems*, T. S. Sanker et al., eds., ASME DE-Vol. 18-2, pp. 149–158.

El-Shafei, A., 1989c, "Fluid Inertia Effects in Squeeze Film Dampers," *Proceeding of Damping '89*, U. S. Air Force Report WRDC-TR-89-3116, Vol. II, Nov., pp. GAA 1–15.

El-Shafei, A., 1990, Unbalance Response of a Jeffcott Rotor Incorporating Short Squeeze Film Dampers," ASME JOURNAL OF ENGINEERING FOR GAS TURBINES AND POWER, Vol. 112, pp. 445–453.

Gunter, E. J., Barrett, L. E., and Allaire, P. E., 1977, "Design of Nonlinear Squeeze Film Dampers for Aircraft Engines," ASME *Journal of Lubrication Technology*, Vol. 99, pp. 57–64.

Holmes, R., and Dogan, M., 1985, "The Performance of a Sealed Squeeze-Film Bearing in a Flexible Support Structure," *Proc. I. Mech. E.*, Vol. 199, No. C1.

Nonami, K., DiRusso, E., and Fleming, D. P., 1989, "Active Vibration Control for Flexible Rotor by Optimal Direct-Output Feedback Control," in: *Rotating Machinery Dynamics*, T. S. Sankar et al., eds., ASME DE-Vol. 18-1, pp. 327–334.

Schweitzer, G., and Ulbrich, H., 1980, "Magnetic Bearings—A Novel Type of Suspension," *Proceedings of the Second International Conference on Vibrations in Rotating Machinery*, I. Mech. E., pp. 151–156.

Tecza, J. A., Giordano, J. C., Zorzi, E. S., and Drake, S. K., 1983, "Squeeze Film Damper Technology: Part 2—Experimental Verification Using a Controlled Orbit Test Rig," ASME Paper No. 83-GT-248.

White, D. C., 1972, "The Dynamics of a Rigid Rotor Supported on Squeeze Film Bearings," *Conference on Vibrations in Rotating Machinery*, Proc. I. Mech. E., pp. 213–229.

A Chambered Porous Damper for Rotor Vibration Control: Part I—Concept Development

J. Tecza

J. Walton

Mechanical Technology Inc.,
Latham, NY 12110

In this paper a novel, high-load chambered porous damper design, supporting analysis, and experimental results are presented. It was demonstrated that significant damping can be generated from the viscous discharge losses of capillary tubes arranged in chambered segments with large radial clearances and that the resulting damping is predictable and fairly constant with speed and eccentricity ratio. This design avoids the nonlinearities associated with high-eccentricity operation of conventional squeeze film dampers. Controlled orbit tests with a porous chambered configuration were completed and favorably compared with theoretical predictions. The ability to accommodate high steady-state and transient imbalance conditions makes this damper well suited to a wide range of rotating machinery, including aircraft gas turbine engines.

Introduction

The design trend for high-performance rotating machinery has historically been toward reduced machine size, increased output, and higher efficiency. This has been especially true for gas turbine engines, which have experienced consistent increases in thrust-to-weight ratios and reductions in specific fuel consumption. The impact of this trend on the rotating elements of these machines has been the design of rotors that are smaller in size and spin more rapidly. Furthermore, design refinements such as integrally bladed disks greatly increase the difficulty of field repair of damaged blading, so that rotor imbalance may reach higher levels than in previous designs.

Rotor-bearing systems have become more complicated and increasingly flexible behavior is being seen. Bending critical speeds and natural frequencies occur more frequently below maximum operating speeds. The result is increased sensitivity to imbalance due to the dynamic amplification seen at resonant frequencies. An increasing amount of attention is being paid to control rotor system dynamic behavior, and one of the most important means for this is the addition of external damping to the system.

The dynamic behavior of gas turbines is controlled in a number of ways, one of the most important being the stiffness and damping of the bearing mounts. The stiffness, often provided through a "squirrel cage" or curved beam mount, is set by rotordynamic requirements and the need to handle loads such as those resulting from rotor weight and maneuver conditions. Damping is typically provided by squeeze film dampers. It is critical that the damping provided by these devices be as constant as possible in order to maintain the designed rotordynamic behavior.

When properly designed, squeeze film dampers have been extremely effective in reducing system dynamic sensitivity, as documented by Bhat et al. (1981), Lund et al. (1983), Pinkus and Bupara (1980), San Andres and Vance (1986), Tecza et al. (1982, 1983), Tichy (1983, 1984), and Walton et al. (1987). The reduction in dynamic sensitivity achieved with squeeze films results in lower transmitted forces (hence longer bearing life and less mount fatigue), lower rotor amplitudes at critical clearance locations, and the need for less frequent balancing. However, squeeze film dampers are limited in their ability to control the effects of abusive imbalance levels. The behavior of a squeeze film is such that, at large eccentricity ratios, damping becomes highly nonlinear and tends to rise sharply. A cross-coupled damping force also arises, which effectively acts to stiffen the rotor mount. This combination of effects can both shift the direct damping coefficient away from optimum levels and cause a previously traversed natural frequency to shift upward close to operating speed, with potentially disastrous consequences. Squeeze film damper-supported rotors may also exhibit bistability, a nonlinear phenomenon whereby the system has two orbit states (low and high) for a given imbalance level. A simple "cure" where abusive imbalance is expected might be simply to increase the radial clearance. However, this frequently entails an unacceptably large increase in damper diameter and/or length.

This paper describes a new hydraulic damper concept that can handle large orbit amplitudes and whose behavior remains very nearly linear, with no cross-coupling and minimal inertial effects. It involves the use of a porous element (a separator with many fine channels) between discrete chambers to absorb energy as a viscous loss, retaining linear damper behavior over a wide amplitude range. Described below are the overall design, its principle of operation, and the basic design analysis. Finally a hardware design using this concept is designed and results of testing in a controlled orbit damper test rig are presented.

Contributed by the International Gas Turbine Institute and presented at the 36th International Gas Turbine and Aeroengine Congress and Exposition, Orlando, Florida, June 3–6, 1991. Manuscript received at ASME Headquarters March 4, 1991. Paper No. 91-GT-244. Associate Technical Editor: L. A. Riekert.

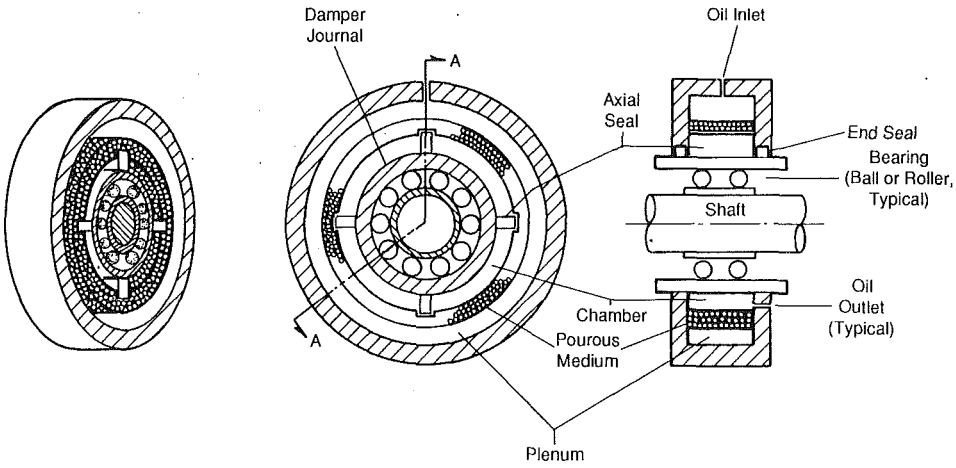

Fig. 1 Schematic of the chambered porous damper geometry

Concept Description

The chambered porous damper is a device in which energy is dissipated by forcing fluid from one chamber into another through small openings in a barrier between the two chambers. These passages are sized such that the desired pressure drop, and therefore damping force, is generated under nominal operating conditions. However, if these passages are too few in number, flow velocity through each one will be very large. The resulting pressure drop will be primarily through discharge losses and the damping coefficient will be directly proportional to amplitude and frequency.

One way to linearize this system is to use a very large "bias" flow through the orifices, but this is impractical. A better way is to connect the chambers with a very large number of small passages. As the length of each hole becomes much greater than its diameter, viscous flow resistance begins to dominate. The effects of discharge losses are further minimized by the large number of passages, which minimizes the velocity through any one passage. This is the principle of operation of the chambered porous damper. As shown in Fig. 1, a porous element is "wrapped" around a damper journal. Several individual chambers are formed by a series of axial seals around the circumference and a pair of end seals. A circumferential plenum surrounds the porous member and chambers. The assembly is filled with fluid and kept at a static pressure high enough to prevent cavitation. As the damper journal precesses, fluid is pumped out of one chamber through the porous member (see Fig. 2) and forced through the plenum into the opposite chamber by the static pressure. Damping force results from the pressure differential across the two opposing porous members. Any squeeze film effect is minimized or eliminated by the large radial clearance between the journal and the porous medium, the presence of axial flow barriers, and the short, radial flow path of the fluid into and out of each chamber. Damping is viscous, there is no cross-coupling, and fluid inertia effects are absent. If the damper is properly designed, the flow resistance across the porous member depends only on geometric parameters and fluid viscosity. The damping coefficient is linear and is insensitive to journal amplitude or frequency.

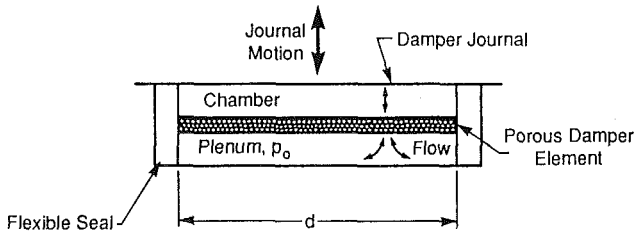

Fig. 2 Fluid flow between chambers and supply plenum

Damper Analysis

To analyze the feasibility of a porous damper, an individual element will be considered, as shown in Fig. 2. The span of this element, d, would be the projected length of a chamber of the type shown in Fig. 1. For the simplest case, a three-element damper, this would be:

$$d \sim D \sin 60 \text{ deg} \tag{1}$$

In general, the damping coefficient for a noncavitating damper will be approximately twice that of the single element treated here. In order to estimate the damping coefficient, the flow through the porous medium can be modeled as flow through a number of capillaries in parallel. The relationship

Nomenclature

A = projected damper segment area
B = damping coefficient
D = damper diameter
F^* = transmitted damper test rig force vector
Q = porous element flow rate
R = effective radius of porous capillary
$\dot{X}$ = Instanteous Tangential Velocity
a = vibration amplitude
d = projected circumferential length of damper
e^* = damper journal eccentricity vector
k = permeability
l = axial length of damper
n = number of porous capillaries
t = porous element radial length
p = fluid film pressure
p_0 = plenum oil supply pressure
Δp = pressure drop = $p - p_0$
Δp_d = discharge pressure drop
Δp_v = viscous pressure drop
μ = viscosity
ρ = density
ω = whirl frequency

between the pressure and the flow for laminar flow is given by

$$\Delta p = p - p_0 = \frac{8\mu t Q}{\pi R^4 n} + \frac{1}{2}\rho\left[\frac{Q}{\pi R^2 n}\right]^2 \tag{2}$$

The first term on the right-hand side of Eq. (2) represents the viscous loss, which is linear with flow. The second term represents an inertial discharge loss, which is nonlinear. The ratio of the discharge loss to the viscous loss is the ratio of these two terms:

$$\frac{\Delta p_d}{\Delta p_v} = \frac{\rho Q}{16\pi\mu t n} \tag{3}$$

Equation (3) provides a criterion for sizing the capillaries for linear damper behavior. Specifically, the damping coefficient, B, for a single element is found from the projected area, the pressure differential, and the journal velocity to be:

$$B = A\frac{\Delta p}{\dot{X}} \tag{4}$$

The flow rate out of the chamber, Q, is given by:

$$Q = A\dot{X} \tag{5}$$

Equation (3) is used to ensure that the nonlinear discharge is negligible by specifying a large enough number, n, of capillaries at the anticipated maximum flow conditions so that the discharge to viscous pressure ratio is a small number, for example, 0.1 or less. Given this condition, Eqs. (2), (4), and (5) may be combined to obtain:

$$B = \frac{8\mu t A^2}{\pi R^4 n} \tag{6}$$

This equation yields the damping coefficient for the single element of Fig. 2. As an example of how these equations are used to analyze a porous damper design, consider a three-chambered damper with a porous element diameter of 165 mm (6.5 in.), a length of 20.3 mm (0.8 in.), and a thickness of 50 mm (0.2 in.). The journal is assumed to be precessing at 10,000 rpm with an orbit radius of 0.127 mm (0.005 in.). The damper fluid is a typical gas turbine lubricant with a viscosity of 2.0E-7 lb-sec/in^2 and a density of 0.8E-4 lb-sec^2/in.^{4}. With these parameters, the maximum flow rate from Eq. (5) is:

$$Q_{\max} = A\ \omega\ a\ =\ 23.6\ \text{in.}^3/\text{sec} \tag{7}$$

When this value for flow is used in Eq. (3), the following result is obtained:

$$\frac{\Delta p_d}{\Delta p_v} = \frac{940}{n} \tag{8}$$

This requires approximately 10,000 capillaries in the damper element to ensure damping coefficient linearity. If a value of n = 10,000 is used in Eq. (6) and the required damping coefficient for the element is 50 lb-sec/in. (100 lb-sec/in. for the damper), then the maximum effective capillary radius, R, is calculated to be 0.036 mm (1.42E-3 in.), which corresponds to a diameter of 72 μm. This should be achievable with existing technology, either in porous filter materials or in assembling chamber partitions with built-in tubular capillaries. To relate this to terminology used in specifying porous materials, the above numbers would correspond to a permeability, k, of

$$k = \frac{\pi R^4 n}{8A} = \frac{\mu t A}{B} = 3.6 \times 10^{-9}\ \text{in.}^2 \tag{9}$$

which is equivalent to a permeability of 2.3 darcys. The peak pressure differential in each damper element may be calculated from Eq. (4) for this example damper to be 401 kPa (58.2 psi). The supply pressure must be maintained above this value to prevent cavitation. Thus, it can be seen the reasonably large damping coefficients are readily achievable with this design with the potential for higher values, as needed.

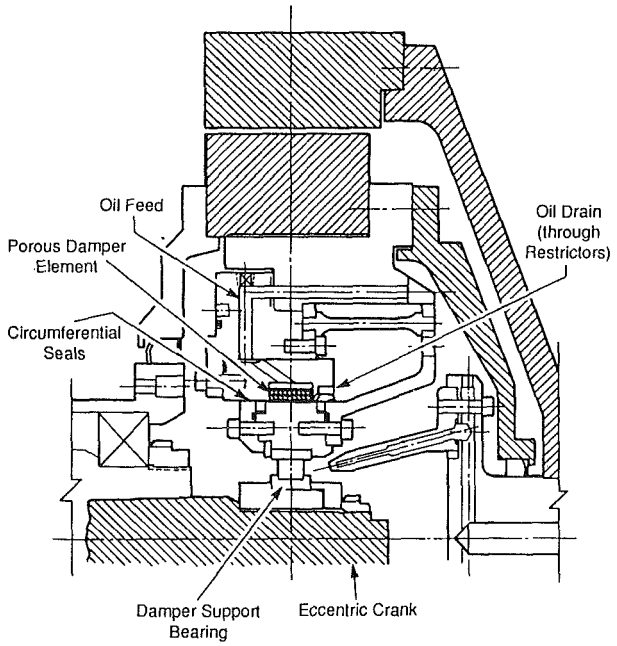

Fig. 3 Chambered porous damper installation in controlled orbit test rig

Test Damper Design

The chambered porous damper concept was tested by constructing a damper of this type and testing it in an existing controlled orbit damper test rig (COR). This rig had been used previously for squeeze film damper performance tests by Tecza et al. (1983) and Heshmat and Walton (1990) and also for measurements of squeeze film damper cavitated regions by Walton et al. (1987). The COR consists of a belt-driven spindle having a tapered bore. Several matching, tapered shafts fit into the spindle. Each of these "cranks" has a bearing journal, which is machined eccentric to the tapered fit. The COR is of overhung construction for easy access to install different damper geometries. The damper journal itself is mounted on the crank and the housing is mated to an adaptor, which in turn is mounted on load cells to measure transmitted force. Noncontacting displacement probes measure the damper orbit. Damper oil temperature and pressure are controllable. Speeds up to 20,000 rpm are possible, with damper transmitted loads to 4450 Newton (1,000 lb).

Figure 3 shows a cross section of the COR with the porous damper installed. The damper journal is mounted on the eccentric crank through a stiff roller bearing. A series of soft flexures prevents journal rotation and ensures cylindrical precession. The porous member lies just outside the journal, with a 0.635 mm (0.025 in.) radial clearance (this could have been larger, if desired). The oil supply plenum can be seen radially outboard of the porous member. This plenum is fed with a light spindle oil (Mobil Velocite #6) while the damper is drained through several 0.5 mm (0.020 in.) restrictor tubes, which are used to maintain a static pressure. Circumferential piston ring seals are located in the journal, while the axial seals (of an "x" cross section elastomeric material) are in the porous member.

The selected design approach for the porous damper ring is shown in Fig. 4. The initial design approaches were to employ a porous bronze or stainless steel filter element, or an assembly of several layers of sintered wire cloth. However, the filter material presented strength and predictability problems. The sintered wire cloth would be a custom fabrication with much

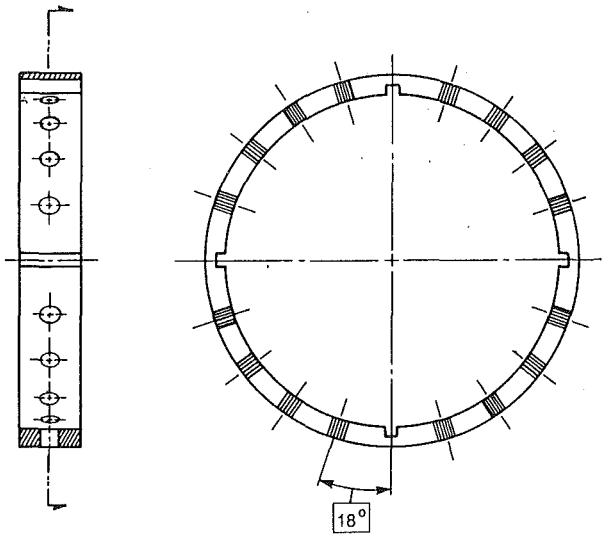

Fig. 4 Construction of porous damper ring

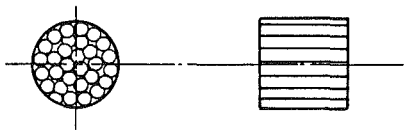

Fig. 5 Construction of porous damper elements

Table 1 Porous chambered damper design

Damper Diameter	141 mm	(5.5 in)
Clearance	0.64 mm	(0.025 in)
Chambers	4	
Pores/Chamber	1120	
Pore Diameter	0.203mm	(0.008 in)
Pore Length	8 mm	(0.3125 in)
Chamber Dividers	Elastomer Quad Rings	
Total Damping	170 lb-sec/in	

testing required to develop the correct porosity. Therefore an innovative, and ultimately simpler, approach was evolved for this proof-of-concept test. Shown in Fig. 5, this involves replacing the porous material with a series of inserts fabricated from bundles of stainless steel tubing. Each insert had a diameter of 7.94 mm (0.3125 in.) and a length of 7.94 mm (0.3125 in.), and was located in the middle of the damper ring axial length.

The porous damper was divided into four chambers, each having four porous element inserts. With this construction, the inserts were sized directly using the equations given in the previous section. The result was a damper designed to have a nominal damping coefficient of 170 lb-sec/in., assuming an oil viscosity of 14.3 Cp (2.083×10^{-6} lb-sec/in.^{2}). Final details of damper design are presented in Table 1.

Experimental Procedure

The porous damper was fabricated and installed in the controlled orbit rig (COR) to evaluate its performance and damping characteristics. Tests were run at speeds up to 18,000 rpm, oil supply pressures to 552 kPa (80 psi), eccentricities up to 0.15 mm (0.006 in.), and oil viscosities of 14.3 and 5.9 Cp (2.083×10^{-6} and 0.85×10^{-6} lb-sec/in.^{2}). During each test, damper transmitted forces, motion, and speed were recorded along with oil temperature and supply pressure. These recorded

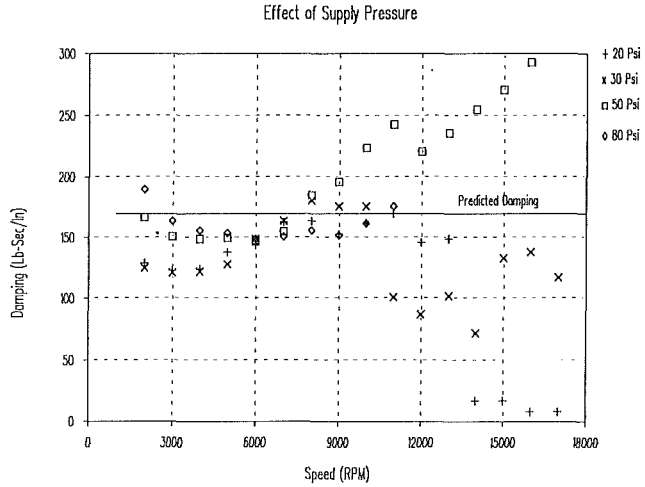

Fig. 6 Comparison of predicted and measured damping for a nominal 0.1 mm (0.004 in.) eccentricity orbit

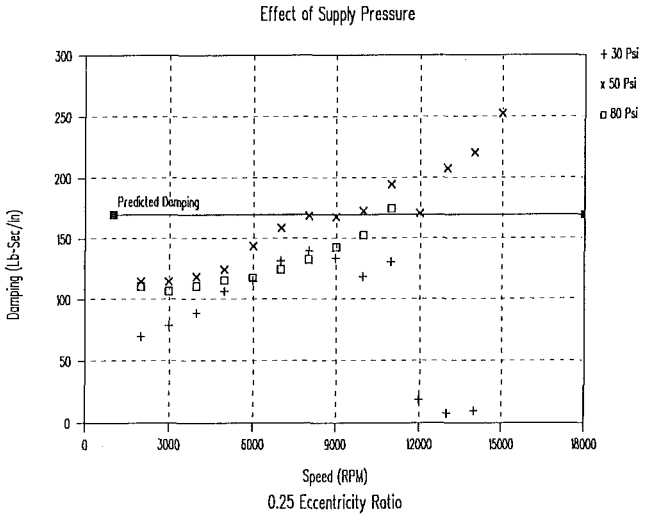

Fig. 7 Comparison of predicted and measured damping for a nominal 0.15 mm (0.006 in.) eccentricity orbit

data were then used to calculate the damping produced using the following data reduction approach:

$$B = \frac{F^*}{(e^*\Omega)} \tag{10}$$

where F^* and e^* are complex quantities including both amplitude and phase with respect to a common reference mark on the COR spindle.

Results and Discussion

As shown in Figs. 6 and 7, which present damping as a function of speed for 0.1 and 0.15 mm (0.004 and 0.006 in.) eccentricities, there is a fairly good agreement between the predicted and measured damping for speeds up to approximately 12,000 rpm for the range of supply pressures tested. The observed drop in measured damping around 12,000 rpm, for both the 0.1 and 0.15 mm (0.004 and 0.006 in.) eccentricities, is believed to be attributed to cavitation in the porous damper elements. Cavitation is suspected since no drop-off in measured damping was observed for oil supply pressures above 345 kPa (50 psi) and the pressure drop across the porous elements at a speed of 12,000 rpm was expected to approach 1380 kPa (200 psi). This large pressure drop would be expected

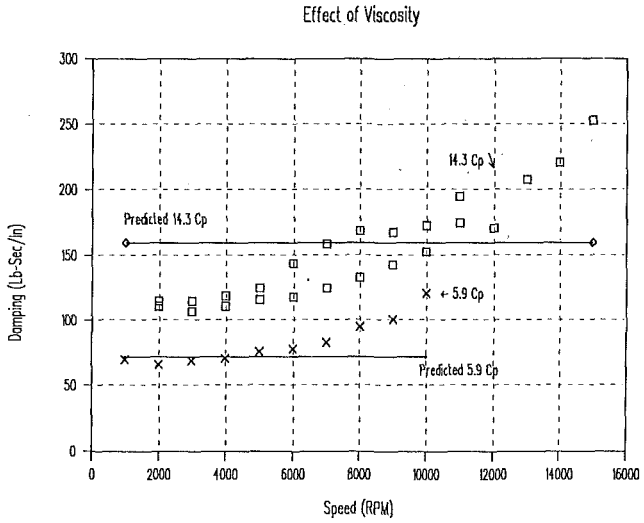

Fig. 8 Measured damping at oil viscosities of 14.3 Cp and 5.9 Cp

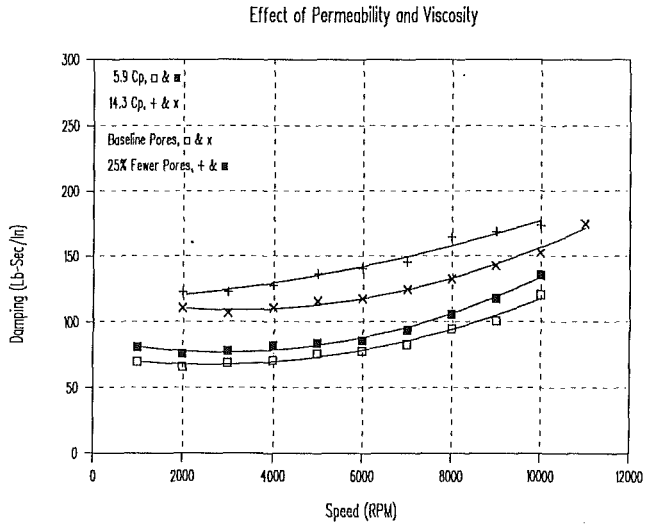

Fig. 9 Measured damping for reduced oil viscosity and damper porosity

to produce cavitation in the porous chambered damper when a supply pressure of only 207 kPa (30 psi) was applied. The absence of cavitation at the higher supply pressures may be due to pressurization of the oil plenum that completely surrounds the porous chambered ring. With no dividers in the plenum, its overall pressure may be affected by the positive pressures generated in the minimum film region of the damper. In addition, the oil was fed into the plenum through only one feed hole, thereby introducing a restriction to flow out of the damper assembly.

Data above 11,000 rpm for the 552 kPa (80 psi) oil supply pressure test case were not obtained due to transmitted loads, which exceeded the safety limit of the force transducers. Regardless, the trends observed in Figs. 6 and 7 indicate a damper yielding damping coefficients remarkably close to predictions for such a simple analysis as presented in this paper. The increasing level of damping with speed may be attributed to two sources: a squeeze film component within each of the four damper chambers, and an increase in the damping contribution of the elastomeric seals with frequency. The squeeze film component may be the result of the relatively small radial clearance of 0.64 mm (0.025 in.) present in the damper and the fact that the damper's porous elements were localized at four discrete locations within each chamber. Squeeze film effects could be eliminated in the future by enlarging the clearance (to 1.0 mm or greater) and by distributing the porous elements more uniformly. Any contributions of the elastomeric seals could be eliminated by substituting alternative spring-loaded metallic seal elements in their place.

To evaluate further the performance of the chambered porous damper, tests were conducted at a viscosity of 5.9 Cp (0.85×10^{-6} lb-sec/in.^{2}). The lower viscosity tests would be expected to produce lower damping levels and also less of a squeeze film effect. This effect can be seen in Fig. 8. Reducing the oil viscosity did reduce the measured damping, though not quite by the expected amount. A reduction in viscosity of approximately 60 percent, as tested, should have yielded a corresponding 60 percent reduction in damping. Measured damping however, was only reduced by approximately 50 percent. Again the discrepancy is probably due to some squeeze film effects present in the damper. Regardless, the fact that the trends are in the appropriate order of magnitude and appear fairly constant with speed, as is shown in Fig. 8, makes this a promising concept for the designer of modern gas turbine engines.

Since the design analysis indicates that a reduction in the number of porous capillary tubes should produce a corresponding increase in damping, tests with 25 percent of the pores blocked off were also conducted at both 14.3 and 6.9 Cp (2.083×10^{-6} and 0.85×10^{-6} lb-sec/in.^{2}). In each case, the measured damping values increased by approximately 12.5 to 18 percent as shown in Fig. 9 and appear both repeatable and fairly constant. The failure to increase by the expected 25 percent is most likely due to a failure of the shields that were used to block off one bundle of pores in each quadrant. Post-test examination revealed that several of the shields had come loose and were not completely blocking the oil flow through the pores.

In summary, a novel chambered porous damper was conceived, designed, and tested. This damper performed as expected and appears to be an excellent candidate for a wide range of rotor systems. With its independence of clearance and damper eccentricity, and predictable performance, this damper is ideally suited to applications where high or abusive rotating loads may be encountered, such as may result from a blade-loss event in a gas turbine engine. Further evaluations to assess the potential of this concept under high load and transient conditions are required to assess the potential of this concept fully and are the subject of a companion paper. In addition, improvements in the analysis to predict the performance of this concept should consider the effects of the flow path geometry in the chambers (including any squeeze film action) and the stiffness and damping characteristics of the chamber axial seals.

Acknowledgments

The work reported herein was performed under U.S. Air Force sponsorship (Contract No. F33615-C-85-2518). The authors would like to acknowledge the support of Capt. J. Griffin and Mr. T. Fecke of the Air Force Wright Aeronautical Laboratories, Aero Propulsion and Power Laboratory, and Messrs. M. Martin, P. Quantock, and M. Tomaszewski of MTI for their contributions in completing this work.

References

Bhat, S. T., Buono, D. F., and Hibner, D. H., 1981, "Analysis of High Load Dampers," NASA CR165503.

Heshmat, H., and Walton, J., 1990, "Advanced Multisqueeze Film Dampers for Rotor Vibration Control," ASME/STLE 1990 Tribology Conference Preprint No. 90-TC-3E-1.

Lund, J. W., et al., 1983, "Squeeze Film Damper Technology: Part I—Prediction of Finite Length Damper Performance," ASME Paper No. 83-GT-247.

Pinkus, O., and Bupara, S. S., 1980, "Adiabatic Solutions for Finite Journal Bearings," ASME *Journal of Lubrication Technology*, Vol. 101, pp. 492–496.

San Andres, L., and Vance, J., 1986, "Effects of Fluid Inertia and Turbulence on the Force Coefficients for Squeeze Film Dampers," ASME JOURNAL OF ENGINEERING FOR GAS TURBINES AND POWER, Vol. 108, pp. 332–339.

Tecza, J. A., Zorzi, E. S., and Parker, W. H., 1982, "Squeeze Film Damper Technology Program First Interim Report: Damper Component Analysis and Integration With Rotordynamics Program," U.S. Air Force, Dayton, OH, AFWAL-TR-82-2112.

Tecza, J. A., et al., 1983, "Squeeze Film Damper Technology: Part 2—Experimental Verification Using a Controlled-Orbit Test Rig," ASME Paper No. 83-GT-248.

Tichy, J. A., 1983, "The Effect of Fluid Inertia in Sequence Film Bearings: A Heuristic and Physical Description," ASME Paper No. 83-GT-177.

Tichy, J. A., 1984, "Measurements of Squeeze Film Bearing Forces and Pressures, Including Effects of Fluid Inertia," *ASLE Trans.*, Vol. 28, No. 4, pp. 520–526.

Walton, J., Pinkus, O., Walowit, J., Tecza, J., and Lee, C., 1986, "Squeeze Film Damper Technology: Part II—Extension of Analysis and Parametric Study," U.S. Air Force, Dayton, OH, AFWAL-TR-82-2112, Part II.

Walton, J., Walowit, J. A., Zorzi, E. S., and Schrand, J., 1987, "Experimental Observations of Cavitating Squeeze Film Dampers," ASME *Journal of Tribology*, Vol. 109, pp. 290–295.

A Chambered Porous Damper for Rotor Vibration Control: Part II—Imbalance Response and Blade-Loss Simulation

J. Walton

M. Martin

Mechanical Technology Inc.,
Latham, NY 12110

In this paper, results of experimental rotordynamic evaluations of a novel, high load chambered porous damper design are presented. The chambered porous damper concept was evaluated for gas turbine engine application since this concept avoids the nonlinearities associated with high-eccentricity operation of conventional squeeze film dampers. The rotordynamic testing was conducted under large steady-state imbalance and simulated transient bladeloss conditions for up to 0.254 mm (0.01 in.) mass c.g offset or 180 g-cm (2.5 oz-in.) imbalance. The chambered porous damper demonstrated that the steady-state imbalance and simulated blade-loss transient response of a flexible rotor operating above its first bneding critical speed could be readily controlled. Rotor system imbalance sensitivity and logarithmic decrement are presented showing the characteristics of the system with the damper installed. The ability to accommodate high steady-state and transient imbalance conditions makes this damper well suited to a wide range of rotating machinery, including aircraft gas turbine engines.

Introduction

The design trend for high-performance rotating machinery has historically been toward reduced machine size, increased output, and higher efficiency. This has been especially true for aircraft gas turbine engines, which have experienced consistent increases in thrust-to-weight ratios and reductions in specific fuel consumption. The impact of this trend on the rotating elements of these machines has been the design of rotors that are smaller in size and which spin more rapidly. The result is increased sensitivity to imbalance due to the dynamic amplification seen at resonant frequencies. Furthermore, design refinements such as integrally bladed disks greatly increase the difficulty of field repair of damaged blading, so that rotor imbalance may reach higher levels than in previous designs. As such, a significant amount of attention is being paid to means for adding external damping to rotor systems.

Squeeze film dampers are commonly used in gas turbines to provide for such dynamic control. When properly designed, these dampers have been extremely effective in reducing system dynamic sensitivity, as documented by Bhat et al. (1981), Lund et al. (1983), Pinkus and Bupara (1980), San Andres and Vance (1986), Tecza et al. (1982, 1983), Tichy (1983, 1984), and Walton et al. (1987). The reduction in dynamic sensitivity achieved with squeeze films results in lower transmitted forces (hence longer bearing life and less mount fatigue), lower rotor amplitudes at critical clearance locations, and the need for less frequent balancing. However, squeeze film dampers are limited in their ability to control the effects of abusive imbalance levels. The behavior of a squeeze film is such that, at large eccentricity ratios, damping becomes highly nonlinear. A cross-coupled damping force also arises, which effectively acts to stiffen the rotor mount. Squeeze film damper-supported rotors may also exhibit bistability, a nonlinear phenomenon whereby the system has two orbit states (low and high) for a given imbalance level. A simple "cure" where abusive imbalance is expected might be simply to increase the radial clearance. However, this frequently entails an unacceptably large increase in damper diameter and/or length to achieve the desired damping.

This paper is a continuation of work completed by Tecza and Walton (1993) in which a new hydraulic damper concept, well suited to both normal and abusive rotor vibration levels, was presented. Based on the demonstrated performance of the chambered porous damper in controlled orbit testing, rotordynamic response testing was conducted. Results of the imbalance response and simulated blade-loss testing through and above the first flexible/bending critical speed are presented in this paper as further demonstration of the suitability of this damper concept for application to high-speed rotating machinery.

Concept Description

The chambered porous damper is a device in which energy is dissipated by forcing fluid from one chamber into another through small capillaries in a barrier between the two cham-

Contributed by the International Gas Turbine Institute and presented at the 36th International Gas Turbine and Aeroengine Congress and Exposition, Orlando, Florida, June 3-6, 1991. Manuscript received at ASME Headquarters Paper No. 91-GT-243. Associate Technical Editor: L. A. Riekert.

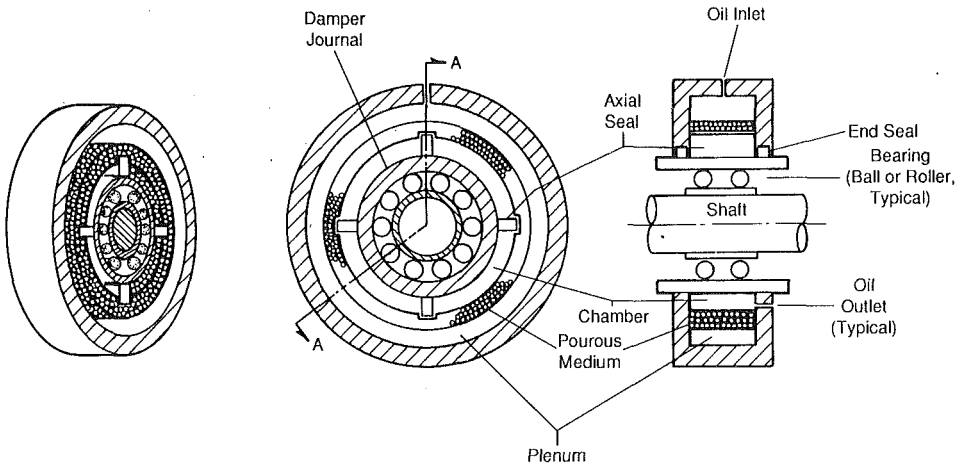

Fig. 1 Schematic of the chambered porous damper geometry

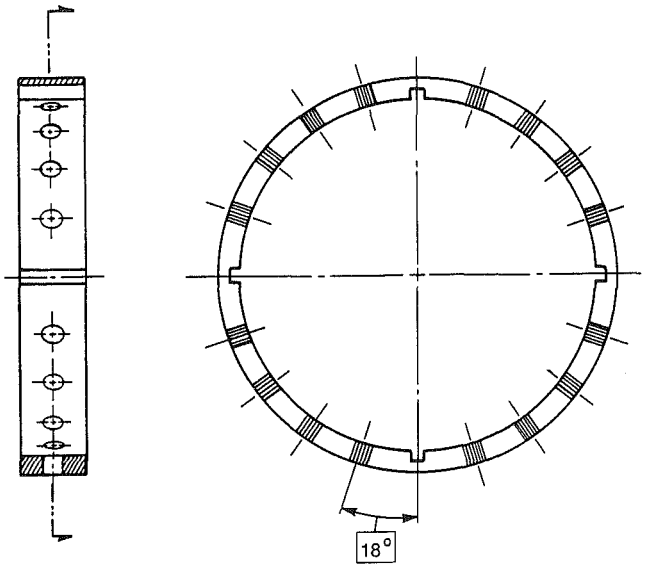

Fig. 2 Porous damper ring construction with four porous element bundles per quadrant

Table 1 Porous chambered damper design

Damper Diameter	141 mm	(5.5 in)
Clearance	0.64 mm	(0.025 in)
Chambers	4	
Pores/Chamber	1120	
Pore Diameter	0.203mm	(0.008 in)
Pore Length	8 mm	(0.3125 in)
Chamber Dividers	Elastomer Quad Rings	
Total Damping	170 lb-sec/in	

bers. The resulting pressure drop is primarily owing to discharge losses and the damping coefficient being proportional to amplitude and frequency.

As shown in Fig. 1, a porous ring surrounds a damper journal. Several individual chambers are formed by a series of axial seals around the circumference and a pair of end seals. The circumferential plenum surrounding the porous ring is filled with oil and pressurized to prevent cavitation. As the damper journal precesses, oil is either pumped out of or drawn into individual chambers through the porous media. The damping force results from the pressure drop across the porous media of the opposing chambers.

The tested porous damper was divided into four chambers, each having four porous element inserts as shown in Fig. 2. Using this construction approach, the inserts were sized using the analysis presented in the companion paper by Tecza and Walton (1993). The result was a damper designed to have a nominal damping coefficient of 170 lb-sec/in., assuming an oil viscosity of 14.3 Cp (2.083×10^{-6} lb-sec/in.^{2}). Final details of damper design are presented in Table 1.

Experimental Apparatus and Procedures

The rotordynamic test rig, shown in Figs. 3 and 4, consists of four major components: a high-speed shaft, an overhung inertial mass, a damper assembly, and a weight loss cutting mechanism. This rig was developed to evaluate the performance of dampers and their ability to control the dynamic behavior of a large flexible rotor. The maximum test rig speed is approximately 14,000 rpm with predicted first and second critical speeds nominally at 9100, and 18,000 rpm. Figure 5 presents the first test rig mode shape (at 9100 rpm), showing that the damper location (approximately 5 in. from the weight loss disk) should experience considerable motion during testing and thereby exercise the damper. The steel shaft is 76 mm (3 in.) in diameter, 1.29 m (48 in.) long, is supported on two sets of 75 mm duplex ball bearings, and is driven by a flat belt coupling that is interfaced through a drive pulley to a 25-hp, d-c drive motor capable of 2500 rpm. The overhung disk, which weighs approximately 75.62 N (17 lb) is attached to the end of the shaft, has 36 tapped holes for the rotor steady state imbalance response studies, and has two latched chambers 180 deg apart for simulating blade-loss events. Two chambers were installed to provide for a degree of safety. Should the damper fail, the weight in the second chamber could be released and the rotor partially rebalanced for deceleration through the first bending critical speed of the rotor. To secure the latched chambers, 3.18 mm (0.125 in.) diameter aircraft quality cable with steel ball ends is used. Releasing the weight at the desired speed and time is accomplished by remotely activating the solenoid-operated knife and plunger assembly. As seen in Fig. 4, two separate knives are provided in the cutting assembly. Each knife is located at a different radius so that the cable for the two separate weight loss chambers can be cut independently.

The damper cartridge is installed in the damper housing, which is located between the inertial mass and the shaft support bearings to permit easy access to the damper. This damper cartridge was previously installed in the MTI Controlled Orbit Rig and used in the damper characterization tests by Tecza and Walton (1993) prior to the rotordyanmic response and transient weight loss studied reported here.

The instrumentation shown in Fig. 3 consists mainly of eddy current displacement sensors to assess the rotordynamic behavior of the test rig. The damper region was the primary rotor location monitored during testing, though other shaft orbits

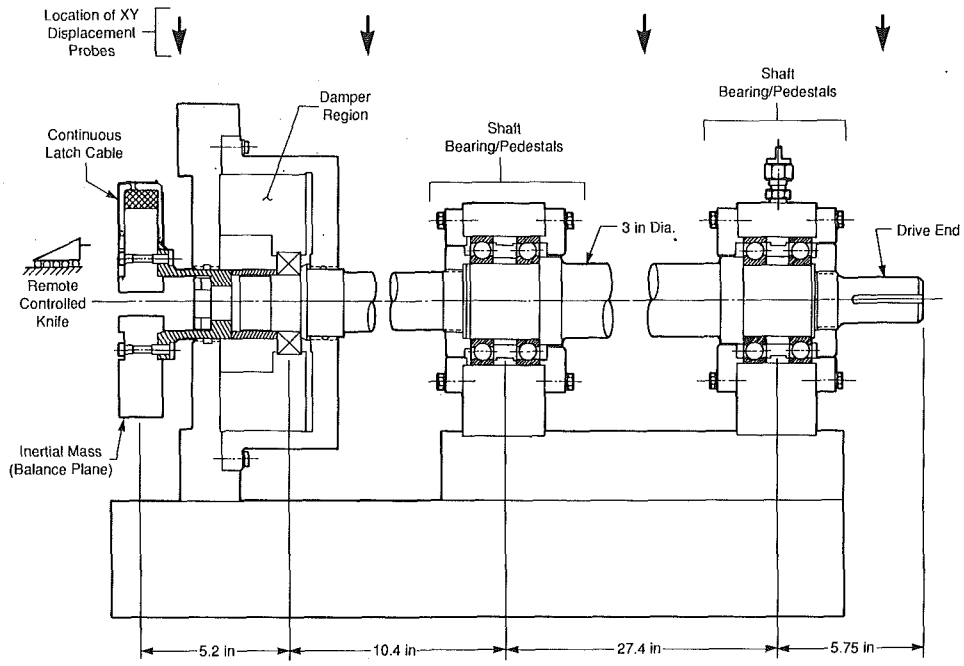

Fig. 3 Schematic of rotordynamic test rig showing instrumentation and key mechanical elements

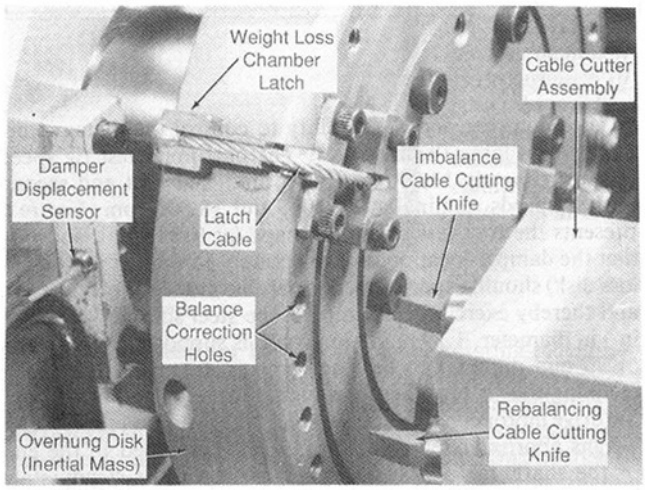

Fig. 4 View of test disk with weight loss chamber and cable cutting assembly

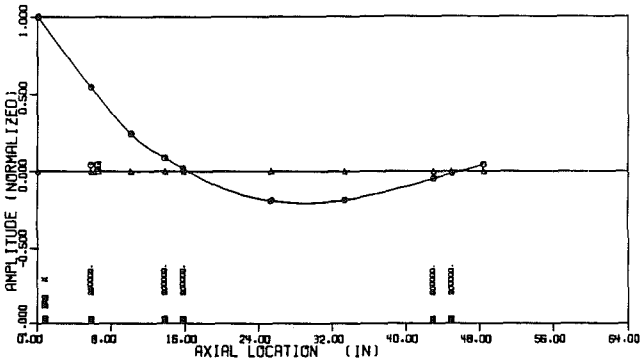

Fig. 5 Normalized mode shape for rotordynamic bladeloss simulator first critical speed at 9117 rpm

were also monitored for safety considerations and to assess rotor mode shapes. A tachometer probe was also used to measure speed and to establish a phase reference for the measured displacement data. Instrumentation for measuring damper oil supply pressure and temperature were also included.

Once the damper assembly was installed in the test rig the following series of tests were conducted:

1 Balance the test rig with the damper inactive (no oil supplied to the damper).
2 Install a known imbalance in the weight loss disk and run the test rig to full speed with the damper inactive to establish the baseline response.
3 Activate the damper with 345 kPa (50 psi) oil supply pressure and operate the test rig to the maximum attainable speed, then repeat with 552 kPa (80 psi) oil supply pressure.
4 Repeat step 3 for increasing imbalance weights until orbits approach 0.38 mm (0.015 in.).
5 Rebalance rotor.
6 Place lead shot in weight loss chamber and balance rotor for supercritical operation.
7 Operate rig at speeds above critical speed and release weight.
8 Repeat steps 6 and 7 for different oil supply pressures and weight loss levels.

Results and Discussion

Response tests were run for imbalance levels of 4.9, 9, 13, and 17.7 g and at oil supply pressures of 345 and 552 kPa (50 and 80 psi). As seen in Figs. 6 and 7, the undamped rotor response approaches 0.36 mm (0.014 in.) at just above 9300 rpm. As speed was increased to approximately 13000 rpm, rotor response at the disk continued to decrease to approximately 0.075 mm (0.003 in.). This response was consistent with the predicted first critical speed location of 9117 rpm and gave indication that the residual mass C.G. offset of the disk was approximately 0.75 mm (0.003 in.). Since good balancing practices for modern gas turbine engines call for a 0.25 mm (0.001 in.) offset or better, this baseline condition was considered a valid starting point for evaluation of the high load damper. Increases in the disk imbalance to 17.7 g (135 g-cm) were used to evaluate the damper under rotor conditions with approxi-

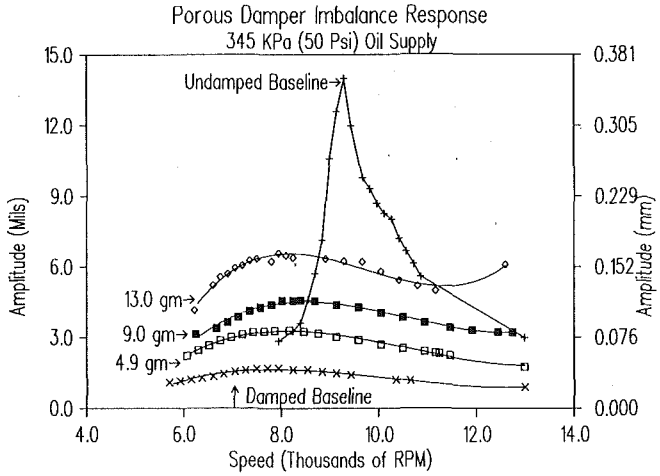

Fig. 6 Comparison of undamped test rig imbalance response with damped response at 345 kPa (50 psi) oil supply pressure and imbalance to 13.0 g

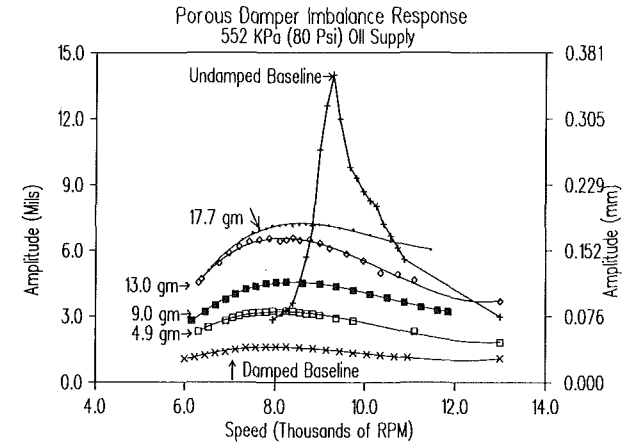

Fig. 7 Comparison of undamped test rig imbalance response with damped response at 552 kPa (80 psi) oil supply pressure and imbalance to 17.7 g

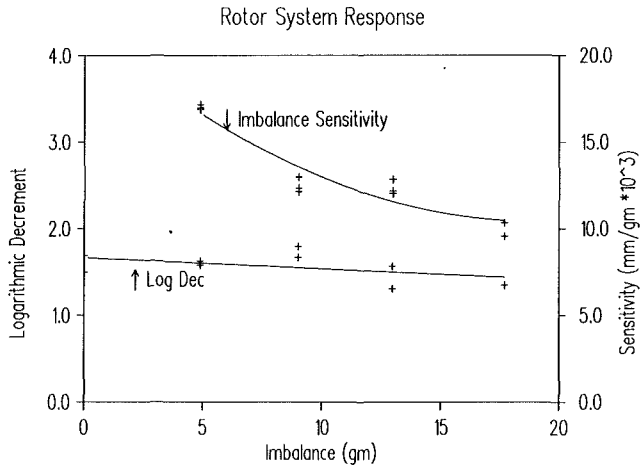

Fig. 8 Measured rotor system imbalance sensitivity and logarithmic decrement

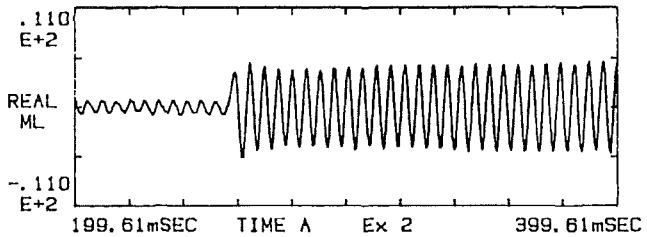

Fig. 9 Rotor system transient response for a 20 g weight loss at 345 kPa (50 psi) oil supply pressure; displacement measured in mils between porous damper and overhung disk

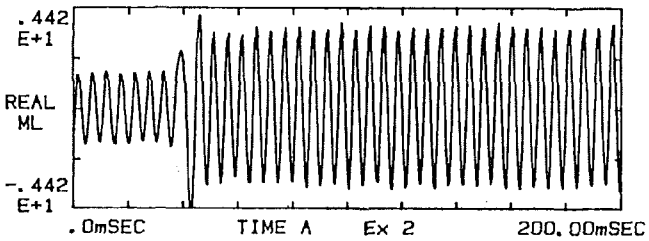

Fig. 10 Rotor system transient response for a 20 g weight loss at 552 kPa (80 psi) oil supply pressure; displacement measured in mils between porous damper and overhung disk

mately 10 times the normally expected imbalance levels. Efforts were made to have the baseline imbalance vector in line with the simulated blade loss chamber so that the weight release would increase the imbalance vibration with a minimal change in the imbalance vector direction.

Activating the damper with oil at 345 kPa (50 psi) reduced rotor response for the baseline case to approximately 0.043 mm (0.0017 in.), a peak amplitude reduction of over eight times. As seen in Fig. 6, increasing the imbalance level to 13 g (99 g-cm) at the disk while maintaining the oil supply pressure at 345 kPa (50 psi) resulted in a peak disk vibration amplitude of 0.167 mm (0.0066 in) at approximately 7950 rpm. The increase in vibration that began to appear above 11,500 rpm resulted in a maximum amplitude of 0.17 mm (0.0067 in) at 13,000 rpm. The most likely cause for the change in rotor system response above 11,500 rpm was due to a combination of a loss of preload on the shaft duplex ball bearings located next to the damper bearing assembly and the onset of cavitation in the damper. An increase in damper oil pressure to 552 kPa (80 psi) eliminated the increase in rotor vibrations above 11,500 rpm previously observed and permitted operation with an imbalance level of 17.7 g (135 g-cm) as shown in Fig. 7. Regardless, it is evident from these tests that the porous chambered damper provides significant control over rotor system response even to levels of imbalance that are ten times greater than would normally be expected.

A further review of the experimental data was conducted to assess the rotor system logarithimic decrement and imbalance response sensitivity. As seen from Fig. 8 the system Log Dec was consistently around 1.5 or higher for all cases evaluated, while the imbalance sensitivity ranged from 10 to 17 $\times$ 10^{-3} mm/g (0.38 to 0.67 mil/g). Both values are indicators of a well-controlled rotor system.

Having characterized the rotor system response due to imbalance, simulated blade loss tests were conducted. In each test the rotor was balanced, the damper was activated, and the rotor was run through the critical speed up to approximately 12,000 rpm and the weight released. As seen in Figs. 9 and 10, the system appears to be well controlled, as would be expected from the calculated logarithmic decrements presented in Fig. 8. After the initial overshoot, the rotor orbits for the 345 kPa (50 psi) oil supply, 20 g weight loss test settled out at approximately 0.254 mm (0.010 in.) peak-to-peak. When the oil supply pressure was set to 552 kPa (80 psi) for a second test with a 20 g weight loss, it resulted in a post-transient steady-state amplitude peak-to-peak orbit of approximately 0.19 mm (0.0075 in.) as shown in Fig. 10. The reduction in the steady-state vibration amplitude of approximately 25 percent is most

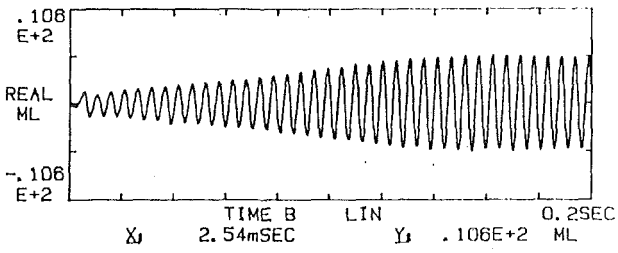

Fig. 11 Rotor system transient response for a 10.3 g weight loss at 345 kPa (50 psi) oil supply pressure; displacement measured in mils between squeeze film damper and overhung disk

likely due to the increased oil pressure and the resultant suppression of any cavitation that may occur in the damper under the high load conditions.

To further assess the performance of the porous chambered damper, a comparative simulated blade-loss test with a conventional squeeze film damper design was conducted. The conventional squeeze film damper provided approximately 35 N-sec/mm (200 lb-sec/in.) damping, approximately 50 percent more damping than the porous chambered damper. The piston ring sealed damper design dimensions were as follows:

- 25.4mm (1.0 in.) length
- 140 mm (5.5 in.) diameter
- 0.191 mm (0.0075 in.) clearance

This damper design was previously tested in a controlled orbit test rig with results reported by Walton et al. (1986a).

As seen in Fig. 11, a 10.3 g transient weight loss with a 345 kPa (50 psi) oil supply pressure resulted in a gradually increasing rotor orbit (indicative of a critically damped system) until a resulting steady-state peak-to-peak orbit of 0.28 mm (0.011 in.) was eventually reached. Duplicating the test with the supply pressure increased to 552 kPa (80 psi) resulted in a steady-state orbit of only 0.038 mm (0.0015 in.). From Fig. 12, it appears that the conventional squeeze film damper performs better than the porous chambered damper for low weight loss levels. However, it should be noted that the squeeze film damper provided almost 50 percent more damping than the porous chambered for the two designs tested. Thus it may be expected that an increase in the porous damper design for increased damping would improve the performance at low levels of weight loss. The significant impact of Fig. 12, however, is the ability of the porous damper to sustain substantially higher levels of weight loss than the squeeze film with very little increase in rotor orbit. As seen, the maximum rotor orbit for the porous damper only increases from 0.127 mm (0.005 in.) to 0.193 mm (0.0076 in.) for a fourfold increase in weight loss (5 to 20 g). The squeeze film damper on the other hand was limited to a maximum of 13 g weight loss due to the squeeze film damper clearance. Since the rotor orbit for the 13 g weight loss test approached 93 percent of the squeeze film damper 0.381 mm (0.015 in.) clearance, further weight losses were not attempted.

In addition to producing lower vibration amplitudes than a conventional squeeze film damper, the porous chambered damper can sustain substantially higher weight losses. The porous chambered damper provides two benefits over a conventional squeeze film damper. First, the damper has a substantially larger linear operating region than a conventional damper for the same vibration amplitudes while still providing the desired damping. Second, the larger overall clearance of the porous chambered damper can aid in minimizing the secondary damage that may occur during a transient such as might be expected from a partial blade-loss event. Typically, conventional squeeze film dampers begin to exhibit nonlinear performance at around 70 percent eccentricity, with further

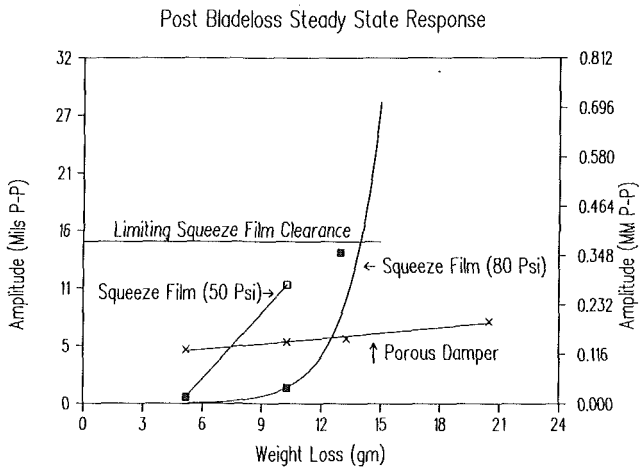

Fig. 12 Comparison of posttransient, steady-state orbit between squeeze film and porous chambered dampers

increases in vibration resulting in large increases in both direct and cross-coupled damping coefficients as well as increasing the potential for the onset of "jump." Increases in the cross-coupled damping result in an increase in the effective overall rotor system stiffness. Under a blade-loss or partial blade-loss event, where rotor orbits increase rapidly, the increased system stiffness may severely restrict rotor motion such that the direct damping may be almost totally eliminated and bearing transmitted loads increased to the point that the bearing is destroyed. In addition, the large imbalance levels experienced from a weight loss transient may cause a conventional squeeze film damper to experience bistable operation or a "jump" in vibration orbits. Further, where a conventional damper may bottom out after relatively small transient weight loss events, the porous chambered damper can permit, as a minimum, three times the range of motion without bottoming out. Stops or bumpers may of course be used to restrict rotor orbits for blade tip clearance control if needed. Increasing the clearance of a conventional squeeze film damper to accommodate the motions of abusive imbalance conditions or to eliminate the potential for bistable orbits, however, will result in a significant reduction in system damping for the same length damper. Thus, the porous chambered damper can provide the same level of damping as a conventional damper, but with improved performance under both normal and abusive imbalance conditions.

In summary, a novel porous chambered damper was conceived, designed, and tested. This damper performed as expected and appears to be an excellent candidate for a wide range of rotor systems. With its large clearance and superior performance, this damper is ideally suited to applications where high or abusive rotating loads may be encountered, such as may results from a partial blade-loss event in a gas turbine engine.

Acknowledgments

The work reported herein was performed under U. S. Air Force sponsorhip (Contract F33615-C-85-2518). The author would like to acknowledge the support of Capt. J. Griffin and Mr. T. Fecke of the Air Force Weight Aeronautical Laboratories, Aero Propulsion and Power Laboratory, and Mr. P. Quantock, of MTI for his contributions in completing this work.

References

Bhat, S. T., Buono, D. F., and Hibner, D. H., 1981, "Analysis of High Load Dampers," NASA CR165503.

Lund, J. W., et al., 1983, "Squeeze Film Damper Technology: Part I—Prediction of Finite Length Damper Performance," ASME Paper No. 83-GT-247.

Pinkus, O., and Bupara, S. S., 1980, "Adiabatic Solutions for Finite Journal Bearings," ASME *Journal of Lubrication Technology*, Vol. 102, pp. 492–496.

San Andres, L., and Vance, J., 1986, "Effects of Fluid Inertia and Turbulence on the Force Coefficients for Squeeze Film Dampers," ASME JOURNAL OF ENGINEERING FOR GAS TURBINES AND POWER, Vol. 108, pp. 332–339.

Tecza, J. A., Zorzi, E. S., and Parker, W. H., 1982, "Squeeze Film Damper Technology Program First Interim Report: Damper Component Analysis and Integration With Rotordynamics Program," U.S. Air Force, Dayton, OH, AFWAL-TR-82-2112.

Tecza, J. A., et al., 1983, "Squeeze Film Dampers Technology: Part 2—Experimental Verification Using a Controlled-Orbit Test Rig," ASME Paper No. 83-GT-248.

Tecza, J., and Walton, J., 1993, "A Chambered Porous Damper for Rotor Vibration Control: Part I—Concept Development," ASME JOURNAL OF ENGINEERING FOR GAS TURBINES AND POWER, Vol. 115, this issue, pp. 360-365.

Tichy, J. A., 1993, "The Effect of Fluid Inertia in Sequence Film Bearings: A Heuristic and Physical Description," ASME Paper No. 83-GT-177.

Tichy, J. A., 1984, "Measurements of Squeeze Film Bearing Forces and Pressures, Including Effects of Fluid Inertia," *ASLE Trans.*, Vol. 28, No. 4, pp. 520–526.

Walton, J., Pinkus, O., Walowit, J., Tecza, J., and Lee, C., 1986a, "Squeeze Film Damper Technology: Part II — Extension of Analysis and Parametric Study," U. S. Air Force, Dayton, OH, AFWAL-TR-82-2112, Part II.

Walton, J., Pinkus, O., Zorzi, E., Tecza, J., and Giordano, J., 1986b, "Squeeze Film Damper Technology: Part III—Experimental Investigation of Squeeze Film Dampers," U.S. Air Force, Dayton, OH AFWAL-TR-82-2112, Part III.

Walton, J., Walowit, J. A., Zorzi, E. S., and Schrand, J., 1987, "Experimental Observations of Cavitating Squeeze Film Dampers," ASME *Journal of Tribology*, Vol. 109, pp. 290–295.

The Basics of Powder Lubrication in High-Temperature Powder-Lubricated Dampers

H. Heshmat

J. F. Walton

Mechanical Technology Inc.,
Latham, NY 12110

The objective of this investigation is to develop a novel powder-lubricated rotor bearing system damper concept for use in high-temperature, high-speed rotating machinery such as advanced aircraft gas turbine engines. The approach discussed herein consists of replacing a conventional oil lubrication or frictional damper system with a powder lubrication system that uses the process particulates or externally fed powder lubricant. Unlike previous work in this field, this approach is based on the postulate of the quasi-hydrodynamic nature of powder lubrication. This postulate is deduced from past observation and present verification that there are a number of basic features of powder flow in narrow interfaces that have the characteristic behavior of fluid film lubrication. In addition to corroborating the basic mechanism of powder lubrication, the conceptual and experimental work performed in this program provides guidelines for selection of the proper geometries, materials, and powders suitable for this tribological process. The present investigation describes the fundamentals of quasi-hydrodynamic powder lubrication and defines the rationale underlying the design of the test facility. The performance and the results of the experimental program present conclusions reached regarding design requirements as well as the formulation of a proper model of quasi-hydrodynamic powder lubrication.

Background and Objectives

In many applications where solid-lubricated bearings are used, some form of solid-lubricated damper will be required. The need for solid lubricated bearing and damper technology has become increasingly evident with the Air Force High Performance Turbine Engine Technology (HPTET) initiative. A major goal of the HPTET initiative is to double the propulsive capabilities of advanced gas turbine engines; this will require increased engine operating temperatures and more stringent vibration control. In contrast with existing gas turbine engine designs, which routinely use squeeze film dampers with liquid-lubricated rolling element bearings, engine bearing environment temperatures are expected to exceed 540°C (1000°F) and approach 816°C (1500°F). The severity of the thermal environment will preclude the use of conventional and even high-performance high-temperature liquid lubricants. To address the need for high-temperature rotor support, considerable and intense effort has been directed at the development of solid-lubricated, including powder-lubricated, bearing development. However, with the exception of the pure Coulomb friction damper (Heshmat et al., 1982), little, if any, effort has yet addressed the need for dampers to complement and support high-temperature rotor bearing systems.

To overcome the problem of excessive wear associated with frictional damper devices, an approach beyond conventional palliatives was needed. A new tribosystem—powder lubrication—was introduced to generate a lubricating film persisting at all frequencies (speeds). Success in powder-lubricated systems may go beyond the therapeutic role of alleviating wear in damper components and actually make possible such technological breakthroughs as the bearings of aforementioned high-performance turbine engine, where high temperatures prohibit the use of liquid lubricants.

Powder lubrication is based on previous investigations and on experiments conducted by the authors and documented in the attached bibliography. It has been postulated that powder flow exhibits some of the basic features of hydrodynamic lubrication. However, such quasi-hydrodynamic behavior holds only for a certain range of particle size with respect to particular tribomaterial combinations.

Given the proper size and appropriate surface geometry, the particles exhibit a layerlike shearing reminiscent of genuine fluids. This shearing was responsible for the experimentally observed drop in wear when debris was present between the two contacting surfaces.

It has been postulated by Heshmat (1989a, 1990a), and is shown in the model of Fig. 1, that under powder lubrication conditions an intermediate film—a form of boundary layer—is created between the interacting surfaces and the lubricant film. An accommodation between the velocities of the two surfaces (V_1 and V_2) and the edge velocities of the lubricant

Contributed by the International Gas Turbine Institute and presented at the 36th International Gas Turbine and Aeroengine Congress and Exposition, Orlando, Florida, June 3-6, 1991. Manuscript received at ASME Headquarters March 4, 1991. Paper No. 91-GT-248. Associate Technical Editor: L. A. Riekert.

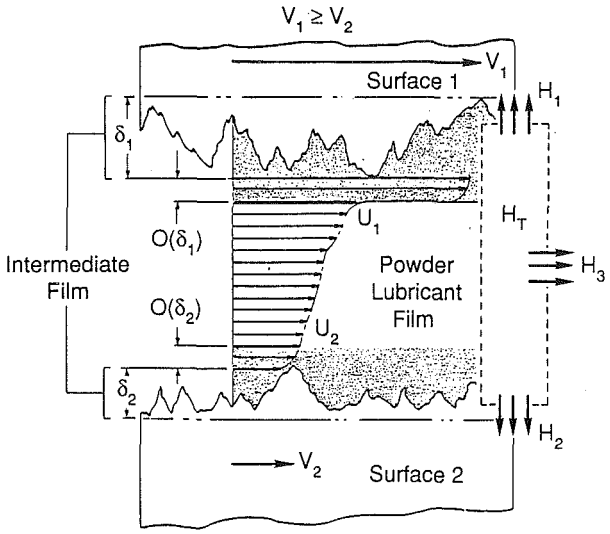

Fig. 1 Quasi-hydrodynamic model for powder lubrication

film (U_1 and U_2) occurs across this intermediate film. The thicknesses of the intermediate films are of the order of the surface roughness (δ_1 and δ_2) of the respective mating materials.

The tests conducted under this program clarify and amplify the mechanism of formation of these intermediate films. This adhesive film consists of the powder lubricant, or of one of its components, either in pure form or in some chemically altered state, very likely an oxide. The intermediate layer, made up of the adhered powder, has a flexibility of behaving either as a solid or as a semi-powder in which considerable creep occurs. This creep makes the accommodation of flow velocities from V_1 to U_1 and V_2 to U_2 possible, as shown in Fig. 1.

The total heat generated from the shearing of the powder film (H_T) is mainly convected (H_3) via powder lubricant film flow through the interface gap, as shown in Fig. 1. The intermediate film attaches to the surfaces; of these layers of thin powder only a fraction of the powder lubricant film continues to absorb the heat from the sheared film (conduction term: $H_1 + H_2$).

As shown in Fig. 1, H_T is equal to the sum of H_1, H_2, and H_3 for powder lubrication conditions. However, in a dry solid lubrication situation the chief heat transfer mode is conduction and all of the generated friction heat in the contact is dissipated to the tribosurfaces ($H_T = H_1 + H_2$), leading to a higher surface temperature, which has been proven to have a detrimental effect on the tribomaterials.

In practical terms, the above considerations call for a system approach to match the requirements of this quasi-hydrodynamic mode of lubrication with several important subelements, including

- Geometry of the components
- Surface properties of the materials
- Physical, mechanical, and chemical characteristics of the powder
- Lubricant delivery and scavenging system

The overall objective of this program was to deal with the development of powder-lubricated dampers. The feasibility of a recently conceived powder-lubricated damper concept (Heshmat, 1988) has been demonstrated in a series of experiments using a controlled orbit test rig to evaluate the concept at temperatures to 540°C (1000°F). Damping performance of suitable high-temperature materials lubricated with a powder has been evaluated in terms of load, temperature, and wear.

A theoretical model developed to predict damper performance is described in this paper. However, since the concept of particulate lubrication is new, there is no analytical base for estimating wear performance. Consequently, heavy reliance was placed on experimentation. For the present application, the tests performed had two basic goals: to test the feasibility of introducing particulate lubrication, and to quantify the behavior of the quasi-hydrodynamic film to obtain empirical correlations for calculating load capacity and other performance characteristics of the damper. Ultimately, using the rheo-

Nomenclature

B_{eq} = shear damping (theoretical)
$\tilde{B}_{eq}$ = $B_{eq}/(\rho R^2 e_r \omega/c)$
C = solid fraction of powder = ρ/ρ_s
C_{eq} = equivalent viscous damping
$\tilde{C}_{eq}$ = $C_{eq}/(\rho R^2 e_r \omega/C)$
d = mean average particle diameter
e_r = radial eccentricity
F_s = shear force
$\tilde{F}_{td}$ = transmitted dynamic force
h = film thickness
$\tilde{h}$ = h/h_o
h^* = 2 $(Q/u_o h_o)$ = nondimensional flow
h_o = film thickness scale factor
L = slider length
p = pressure, applied unit load = W_n/A
$\tilde{p}$ = $(h_o^2/\mu_o u_o L)p$
Q = flow per unit transverse length
R = damper radius
T = period
T_η = $F_{td}/(W_n \eta_x)$
u = velocity
u = u/u_o = dimensionless velocity
u_o, u_1 = surface velocities as shown in Fig. 1 with $u_1 < u_o$
u_{so}, u_{s1} = surface velocities of powder at $y = 0, h$
U = surface tangential velocity
W = load
W_n = normal load
x, y = position coordinates (Fig. 1)
α, γ = constants of rheological Eq. (2*a*)
$\tilde{\alpha}$ = $\alpha(h_o/U_o)(\mu_o U_o/h_o)^3$
$\tilde{\gamma}$ = $\gamma(h_o/U_o)(\mu_o U_o/h_o)^5$
η = y/h
η_x = reference η for K162B = 0.55
η_T = traction coefficient
η^* = equivalent powder viscosity = 1.0
Λ = apparent surface contact area
μ_o = effective viscosity defined by Eq. (19)
ξ = x/L, $\eta = y/n$, nondimensional x and y
ρ = powder lubricant density
ρ_s = solid density of lubricant
τ = shear stress
τ^* = apparent powder film shear stress
$\tilde{\tau}$ = $(h_o/\mu_o u_o)\tau$
τ_o, τ_y = yield shear stress
τ_l = limiting shear stress
$\tilde{\tau}_o$, $\tilde{\tau}_1$ = shear stress at $y = 0, h$
$\tilde{\tau}$, $\tilde{p}$, $\tilde{\xi}$, $\tilde{\eta}$, $\tilde{h}$, $\tilde{u}$, $\tilde{h}^*$, $\tilde{\phi}$ = dimensionless quantities
$\phi(\tau)$ = function relating shear rate to shear stress
$\tilde{\phi}(\tilde{\tau})$ = $h/h_o\, \phi((\mu_o u_o/h_o)\tilde{\tau})$
ω = rotational frequency, rad/s

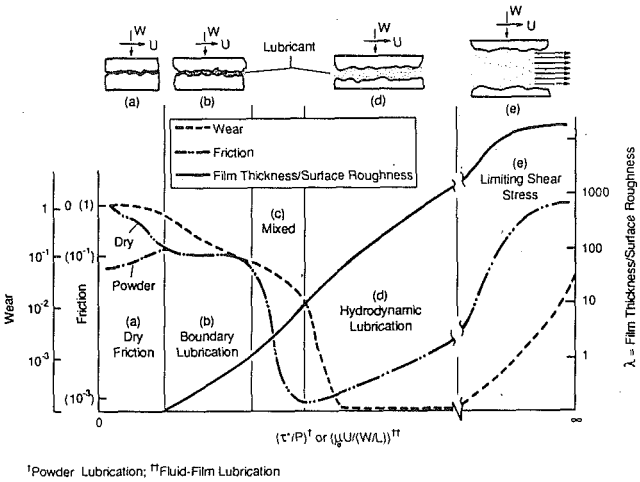

[I]Powder Lubrication; [II]Fluid-Film Lubrication

Fig. 2 Regimes of lubrication in a powder and fluid film lubricated system for a finite value of load

logical parameters determined (or verified) from the experimental data, an overall powder-lubricated damper assembly for the HPTET engine bearings will be developed.

The Quasi-Hydrodynamic Nature of Powder Lubrication

In studies of powder lubrication, it was found that, while a dry particulate film has no viscosity as it is understood in liquids, it exhibits a strain-stress relationship, μ_o, which represents a resistance to flow much as viscosity does in fluids (Heshmat, 1990b). The motion of the particles in this concept resembles molecules in a liquid. Thus, given an appropriate geometry, the dry particulate film will generate a lift. Using μ_o, the criteria of friction and film thickness, and consequently of wear, can be related to the group of variables $\mu_o * U/W/L$, much as the Sommerfeld number does in hydrodynamic lubrication, as shown in Fig. 2. The exact nature of this dependence will have to be extracted from the test data gathered in the program. One advantage of a powder film over liquids is that it can provide separation even when there is no relative motion. This is of particular relevance in dampers, where the velocity is related to the amplitude of vibration.

Figure 2 shows qualitatively the five operating regimes of lubrication: dry, boundary, mixed, hydrodynamic, and limiting shear. At low values of the speed parameter, the liquid or gas has virtually no effect; there is intimate contact between the surfaces; and the conditions are essentially the same as those with dry friction, which results in high friction and wear. As the speed increases a thin boundary layer film is formed with a thickness of the same order as the composite roughness of the two surfaces. With a further increase in speed, the system moves into the mixed regime where the lubricant film thickness increases progressively to the level typically regarded as hydrodynamic and boundary lubrication. As the film thickness increases, asperity contacts decline rapidly, giving a significant reduction in both friction and wear. When full hydrodynamic lubrication is achieved it is believed that the surfaces are completely separated by the lubricant film and that no wear due to asperity contacts occurs. In the full hydrodynamic region, friction increases with speed due to viscous drag. For a finite value of an applied load, W, with further increase in the relative sliding speed U, limiting shear stress may prevail; thus slip may occur at the boundary or near the contact surfaces. This phenomenon has been experimentally observed for powder, reported by Heshmat (1989b, 1990b), and for liquid, in particular in EHD lubrication, by Scott and Winer (1979a, 1979b),

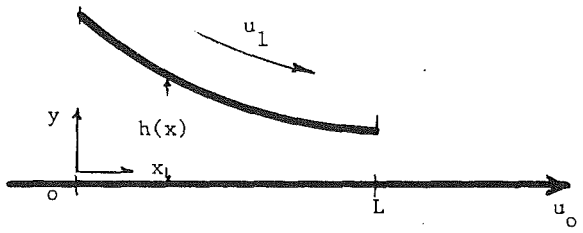

Fig. 3 Geometry and coordinate system

Tevaarwek and Johnson (1979), and recently by Kaneta et al. (1990). Consequently, wear will be predominant and lubricant film thickness along with friction values will approach its limiting value. Indeed in the latter region the wear of tribomaterial is due to the tribological action taking place between "lubricant" and tribosurfaces, rather than asperity or surface contact.

Generalized One-Dimensional Quasi-Hydrodynamic Equation

Considering the geometry and coordinate system given in Fig. 3, the governing momentum equation is

$$dp/dx = \partial\tau/\partial y \tag{1}$$

One possible rheological model of a quasi-hydrodynamic powder can be written in the form of a quintic equation (Heshmat, 1989a):

$$\partial u/\partial y = (1/\mu_o)\tau + \alpha\tau^3 + \gamma\tau^5, \tag{2a}$$

Thus the shear stress–shear rate relationship (constitutive) may be expressed as follows:

$$\dot{\epsilon} = \partial u/\partial y = \phi(\tau) \tag{2b}$$

As is typical with pseudoplastic material with a yield value, a powder is not likely to flow until the shear exceeds the yield strength of the powder film τ_y.

In addition to τ_y a powder film has a limiting shear strength τ_l, which is related to the bulk powder property, characteristics, and physical boundary conditions of tribosurfaces. An example of levels of τ_y and τ_l conditions for TiO_2, NiO, and others is given by Heshmat (1990c).

The form of $\phi(\tau)$ that will be considered is shown in Fig. 4. The function $\phi(\tau)$ shown in Fig. 4 may be expressed mathematically as follows:

$$\phi(\tau) = \text{sign}(\tau)\begin{cases} 0, \text{ if } 0 \le |\tau| \le \tau_y \\ \psi(|\tau - \tau_y|), \text{ if } \tau_y < |\tau| \le \tau_l \end{cases} \tag{3}$$

where

$$\text{sign}(\tau) = \begin{cases} -1, \text{ if } \tau < 0 \\ 1, \text{ if } \tau > 0 \end{cases} \tag{4}$$

Continuity Equation. For one-dimensional flow the integral of velocity, u, across the film will be independent of x:

$$\int_0^h u\, dy = Q \tag{5}$$

Boundary Conditions.

(*a*) *Velocity and Shear*

$$\text{At } y = 0,\ u = u_{so} \tag{6}$$

$$\text{at } y = h(x),\ u = u_{sl} \tag{7}$$

where the surface velocities of the powder u_{so} and u_{sl} will be equal to the velocity of the moving surfaces u_o and u. If the shear stress is less than the limiting value, τ_l, slip will occur at

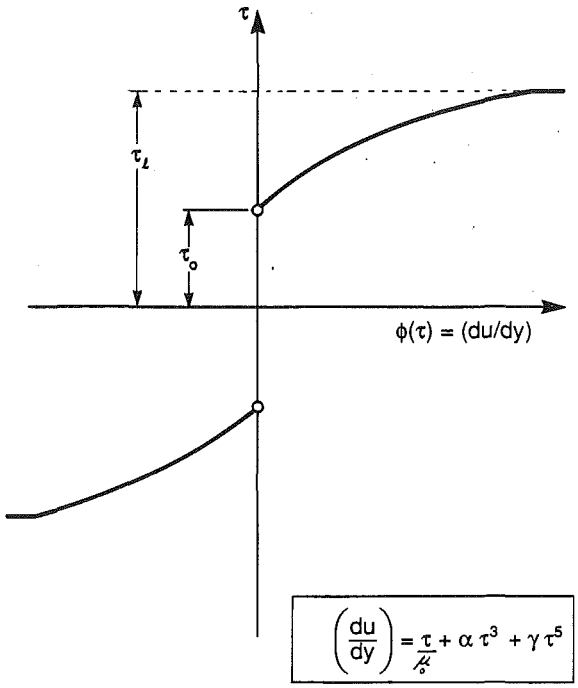

Fig. 4 Shear rate versus shear stress with the conditions of a yield shear and limiting shear stress

the limiting shear stress as necessary to prevent exceeding the limiting shear stress. The velocity boundary conditions may thus be written as

$$u_{so} = u_o, \text{ if } \tau_o < \tau_l \tag{8}$$

or

$$\tau_o = \tau_l \tag{9}$$

$$u_{s1} = u_1, \text{ if } \tau_1 < \tau_l \tag{10}$$

or

$$\tau_1 = \tau_l \tag{11}$$

(*b*) *Pressure.* The pressure is taken to be 0 at both ends of the bearing, thus

$$p = 0 \ @x = 0 \tag{12}$$

and

$$p = 0 \ @x = L \tag{13}$$

Method of Solution. Equations (1)–(13) provide a complete statement of the problem. For given values of u_1, u_o, L, $h(x)$, τ_y, τ_l, and $\phi(\tau)$ we need to solve for u_{so}, u_{s1}, $p(x)$, Q, and $\tau(x, y)$. The pressure and surface shear stress may then be used to determine the load and friction force.

To proceed, one may integrate Eq. (1) with respect to y to obtain

$$\tau(y) = dp/dx\ y + \tau_o. \tag{14}$$

The shear stress will always vary linearly across the film. The velocity distribution may be determined by integrating Eq. (2) with respect to y subject to Eq. (6) to obtain

$$u = u_{so} + \int_0^y \phi(\tau(y'))dy' \tag{15}$$

and applying Eq. (7) at $y = h$

$$\int_0^h \phi(\tau(y))dy = u_{s1} - u_{so} \tag{16}$$

Equation (5) (the continuity equation) may be integrated by parts to obtain

$$\int_0^h u\ dy = u_{s1}h - \int_0^h y \frac{\partial u}{\partial y}\ dy = Q \tag{17}$$

Hence from Eq. (2)

$$u_{s1}h - \int_0^h y\phi(\tau(y))dy = Q \tag{18}$$

where $\tau(y)$ is given by Eq. (14).

Computational Procedure. The problem is solved by using two primary levels of iteration. The inner level consists of solving Eqs. (14), (16), and (18) to determine dp/dx and τ_0 at each value of x on a discrete grid for a given value of Q. The outer level of iteration determines the value of Q needed to satisfy the pressure boundary conditions given in Eqs. (12) and (13).

A Mueller iteration procedure is used for the outer level. This requires two initial guesses, which must bracket the flow rate Q. In general the flow is bracketed by Couette at the mean and minimum film thicknesses assuming no slip:

$$(u_o + u_1)/2h_{\min} < Q < (u_o + u_1)/2h_{\text{avg}}$$

The inner level, which requires determining the values of dp/dx and τ_o that satisfy the two integrals in Eqs. (16) and (18), is carried out by means of a Newton–Raphson iteration with the two integrals evaluated by 10 point Gaussian quadratures. The interval $0 \le x \le L$ is subdivided into N equally spaced points starting at $x = 0$. The inner level solutions at each value of x are mutually independent.

Inner Level Iterations for $\tau < \tau_l$. Again it should be noted that the inner level solution corresponds to values of dp/dx and τ_o that satisfy Eqs. (16) and (18) for a given value of Q. At any point within an iteration the τ_o and dp/dx are assumed to be known.

Initially it is assumed that the limiting shear stress is not reached; hence the surface velocities of the powder are prescribed (u_1 and u_o). Since the shear stress varies linearly across the film it is straight-forward to determine the location of any points within the film where $\tau = \pm\tau_y$. As such, bands in which $\tau < \tau_y$ may be excluded from the integrals in Eqs. (16) and (18), thereby maintaining a high level of accuracy in the Gaussian integrations.

Inner Level Iterations When τ_l is Reached. An inner level solution is initially obtained in the manner described above assuming that no slip takes place. If the limiting shear is exceeded, Eqs. (16) and (18) must be resolved in the appropriate manner. Noting that $\tau_1 = \tau_o + h\ dp/dx$, we may consider Eqs. (16) and (18) to be functions of the four variables (τ_o, τ_1, $u_{so}u_{s1}$).

Two of the variables will be known and the other two must be determined. If τ_l is not exceeded then u_{so} and u_{s1} are known and τ_o and τ_1 must be determined. If $|\tau_o|$, based on this solution, exceeded τ_l, then the equations must be resolved for τ_1 and u_{so}, assuming that τ_o and τ_l and $u_{s1} = u_1$. If $|\tau_1|$ now exceeds τ_l, we must obtain a third solution for u_{so} and u_{s1}, assuming that τ_o and τ_1 are equal to $\pm\tau_l$.

Dimensionless Variables and Parameters. Although the problem has been described in the previous sections using dimensional variables, actual computations are carried out using nondimensional variables and parameters. These are based on quantities given above and a reference film thickness, h_o, usually taken as the minimum film thickness. They are given in the nomenclature section.

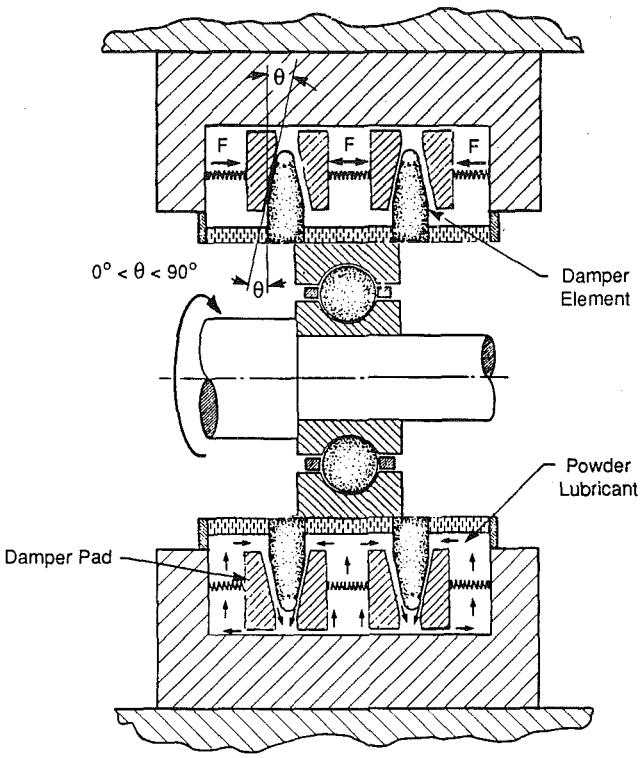

Fig. 5 Schematic of high-temperature dry powder-lubricated damper for a turbine engine bearing

Powder-Lubricated Damper Description

To overcome the negative aspects of the Coulomb friction damper, a dry powder-lubricated damper concept as depicted in the schematic of Fig. 5 was conceived. The concept is based on internally or externally fed triboparticulate matter, which acts as the lubricating agent, reducing wear and carrying heat away from the contact.

The ability of a powder lubricant film to carry away a large portion of the heat generated and separate the damper elements gives the powder-lubricated damper concept a distinct advantage over any system based on the direct contact of materials or surface coatings. Figure 5 illustrates one possible powder-lubricated damper concept with an associated self-contained powder lubrication scheme. In this concept, high levels of direct damping are possible with a minimum of material wear due to the shearing of the lubricious powders as they undergo relative sliding motion during damper nutation. Among the unique features of the powder-lubricated damper are the following:

- It can be decoupled from the bearing dynamic coefficients.
- It can be operated as an active vibration controller by varying the normal load.
- A wide range of damping can easily be achieved by expanding the powder-lubricated damper to include a greater or small number of shearing surfaces.
- The damping element materials and powders can be engineered to suit the system needs.
- The powders used to lubricate the bearing may also be used in the damper.

The cone or convergent wedge-shaped damper components provide self-lubrication and re-entry of the powder to the shearing zone. The frictional heat generated is removed from the contact zone via the powder flow, thus preventing many of the tribological problems associated with the pure frictional dampers. The powder-lubricated damper concept also provides some self-alignment capabilities in a compact design.

This concept consists of pairs of damper pads that are loaded axially against nutating damper elements. Powder in the case of internally fed conditions is agitated via nutating motion of the damper elements, making it accessible to the damper components. An alternative method of lubrication is a mixture of gas and powder to be transported to the damper entrance region at the inner diameter of the damper pads. The contacting surfaces of the damper pads are designed to have a radial converging wedge and a circumferential wave. The converging regions on the damper pads enhance the powder flow, causing the formation of a powder film that separates the mating surfaces. The damper pads are also wedge shaped in the radial direction to enhance the radially outward flow of the powder and assist in removing heat from the contact.

The bearing outer race is mounted to the damper element, which is in turn secured by an antirotation device to the engine static structure.

Theoretical Evaluation of Powder-Lubricated Damper (PLD)

The basic elements and operation of a powder-lubricated damper (PLD) are portrayed in Fig. 5. The powder film is sheared in the radial and circumferential directions between the mating surfaces. The shear force can be obtained from the following equations:

$$F_s = \tau A \qquad (a)$$

The relevant energy relationship for the PLD can be written

$$E = \int_0^T (B_{eq}X)X dt; \quad X = e_r\omega \cos \omega t \qquad (b)$$

From Eq. (*b*) we have

$$B_{eq} = E/\omega\pi x_o^2 \qquad (c)$$

where frictional energy per cycle can be written

$$E = 4\pi x_o F_s \qquad (d)$$

Solving for equivalent viscous damping B_{eq}, we obtain

$$B_{eq} = 4F_s/\omega x_o \quad \text{or} \quad = 4A\tau/\omega e_r \qquad (e)$$

The parameter τ, which is the shear stress generated in the powder film due to the relative motion of the damper surfaces, can be obtained from the solution of governing dimensionless momentum and constitutive Eqs. (1) and (2), respectively.

In order to demonstrate some of the salient features of the model, a parametric analysis was conducted to evaluate the curved slider geometries representative of the PLD. Equation (2*a*) was evaluated at constant values of $\alpha = 280$, $\gamma = 2900$, $\eta = 2 \times 10^{-4}$, and $\tilde{h}_l = 3$. Using existing experimental data for the TiO_2 powder, a segment of the PLD was analyzed. A sample velocity distribution along and across the film of the PLD, simulated as a slider configuration, is given in Fig. 9, with the pressure boundary conditions of $\tilde{p} = 0$ at $\xi = 0$ and 1.

As can be seen from Fig. 6, the model predicts the occurrence of powder lubricant slip relative to the surfaces of the slider. The generated slip velocity is due to the shear stresses τ_o and τ_l. The effect of τ_o dominates the leading end portion (i.e., near the stationary surface of the slider), while the effect of τ_l is more pronounced near the trailing ends of both surfaces.

Figure 7 shows the dimensionless load capacity (W) and traction coefficients (τ) as a function of the normalized surface velocity in a curved slider with dry TiO_2 powder lubricant, for an assumed constant film ratio of $h_1/h_2 = 3$. These parameters were nondimensionalized as follows:

$$\tilde{F}_s = F_s(h_o/\mu_o U_o) = A\tilde{\tau}_s; \quad \tilde{W} = Wh_o/\mu_o U_o L^2$$

where L is taken to be the length in the sliding direction and is equal to the damper eccentricity.

From the predicted data shown in Fig. 7, it appears that an increase in U_o beyond 1.5, unlike conventional fluid film sliders, has a degrading effect on the hydrodynamic component of load capacity and has a weak effect on the traction performance. In addition, the tractive force τ increases as a function of U_o and asymptotically approaches its limiting value, due to τ_l, while the load-carrying capacity of the powder film diminishes as slider velocity is increased. However, U_o beyond 4.0 has no effect on traction, which ultimately produces constant shear force. Experimental evidence confirmed this effect and it is therefore concluded that, once the shear force becomes constant, the damping possible from a single damper element will decrease with further increases in speed. Thus, if a higher velocity is expected or higher damping values are required, an alternative version of the PLD such as is shown in Fig. 5, where multiple dampers are configured in parallel, should be considered.

Experimental Facility. The program described herein, although based on a new concept in lubrication theory, is both practical and experimental. The program is aimed at determining the feasibility of lubricating surfaces with titanium dioxide (TiO_2, rutile form) powder; baseline data were obtained for unlubricated conditions. The results of tests correlated with theory and other available data for the conditions reported here and elsewhere (Heshmat and Walton, 1990).

A series of controlled orbit tests were conducted using square-shaped damper pads (25 mm × 25 mm × 13 mm thick) and a circular damper element as shown in Fig. 8.

To simulate the action of a full ring, each pad had a 12.7 μm (0.0005 in.) crown machined in the circumferential direction and chamfer machined in the radial direction. The radial chamfer provided a converging wedge region at the powder inlet to assist powder flow. The damper element and pads were made from titanium carbide cermet material (K162B). They were lapped to achieve a surface finish of $\leq$ 0.05 μm rms. The damper element's flatness was about two light bands. The K162B was selected because of its good wear resistance, mechanical properties, resistance to oxidation, and its ability to run against itself at temperatures to 760°C (1400°F).

Each test pad was instrumented with a thermocouple located 127 ± 5 μm (5.0 ± 0.2 mil) beneath the contact surface at the center of the pad to measure pad temperature rise during

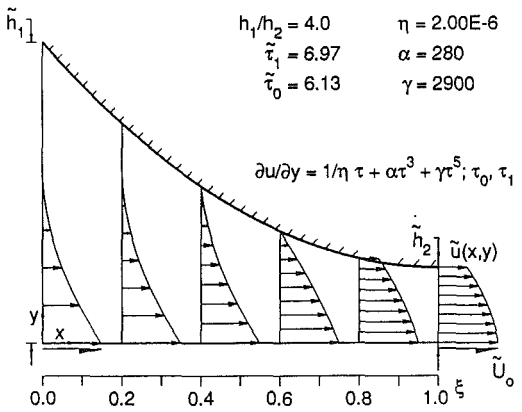

Fig. 6 Coordinate system and velocity profile of a powder film in a curved slider

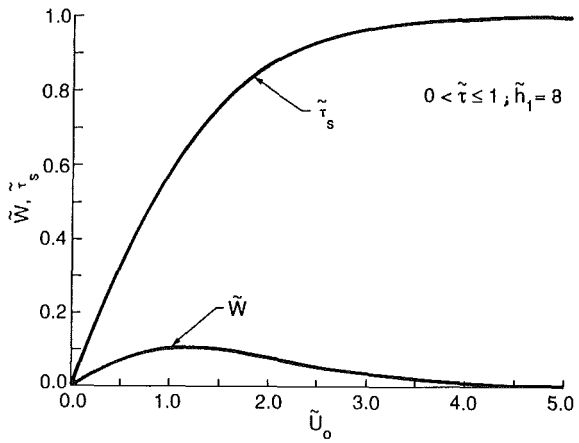

Fig. 7 Traction and load as a function of surface velocity in a curved slider

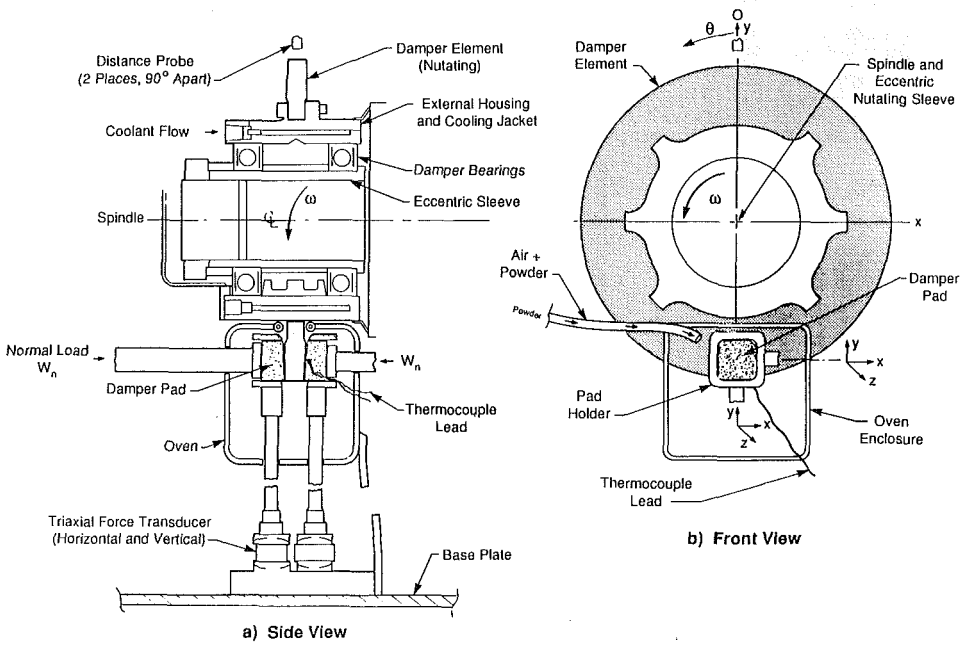

Fig. 8 Powder-lubricated damper controlled orbit test rig for extreme environment

testing. Two additional thermocouples were installed in the opposite corners of the pad holder to measure the ambient temperature. The damper pads were placed in a four-sided holder that had two radial arms 90 deg apart that mounted to the rig base plate through tri-axial quartz force transducers for dynamic force measurements. The pads were isolated from external vibrations by compliant mounts placed between the sides of the pads and the pneumatically operated normal load mechanism. The compliant elements provides a stiffness of about 67 MPa (10,000 lb/in./in.). The controlled orbit test rig consists of a high-speed spindle, stub shaft with an eccentric sleeve, and a drive motor that is capable of speeds to 20,000 rpm. The stub shaft accepts eccentric sleeves to which the damper element is attached so that prescribed test orbits may be evaluated. The damper element controlled circular orbit motions were recorded with two eddy current probes mounted 90 deg apart.

Displacement and transmitted force test data were taken in a parametric manner at various normal loads, temperatures, and speeds. Using the measured force and eccentricity, the direct damping of the damper pad was calculated using the following relation:

$$B = |F_{td}|/(\omega|e_x|)$$

At the start of elevated temperature testing the damper pads were heated by introducing 705°C ±8 (1300°F ±15) air into the oven compartment surrounding the damper pads. Once the pad reached the desired temperature, powder from the fluidized supply was sprayed directly to the pad/element.

The damper pads were weighed and the surface condition documented before and after selected tests to establish wear rates. For each test run, the eccentricity, normal load, and ambient test temperature were held constant while the rotor precessional speed was increased in 1000 rpm increments to a maximum speed of 10,000 rpm.

Properties of Powder Lubricant. Titanium dioxide powder (TiO_2, rutile form) with a boiling point of 2480–3000°C (4500–5400°F), a melting point of 3300–3330°F, and a molecular weight and density of 79.9 and 4.26 g/cc, respectively, was used to lubricate the damper. An analysis of the powder showed that it had a 50 percent accumulative particle size distribution of 5.95 micron, matches PDF 21-1276 Tetragonal, and was 99.5 percent pure. A fluidized bed powder delivery system and a high-temperature pressurized air system capable of 700°C (1300°F) were used to deliver the powder to the damper.

Description of Test Performed. Because of the large volume of data, only results that revealed aspects pertinent to the present investigation will be cited and, where necessary, discussed.

The PLD was first tested with dry powder TiO_2. The runs covered the entire range of loads from 22.3 to 223 N (5 to 50 lb) and speeds up to 10,000 rpm, and test temperatures from room temperature up to 427°C (800°F).

The lubricated damper pad and element specimens after a 35-min test at room temperature showed no signs of wear. After the test, a small weight gain could be measured for the pad; this gain was 1.5 mg. This gain was due to TiO_2 film formation. The appearance of the contact surfaces of the test specimens after the test is shown in Figs. 9(*a*) and 9(*b*).

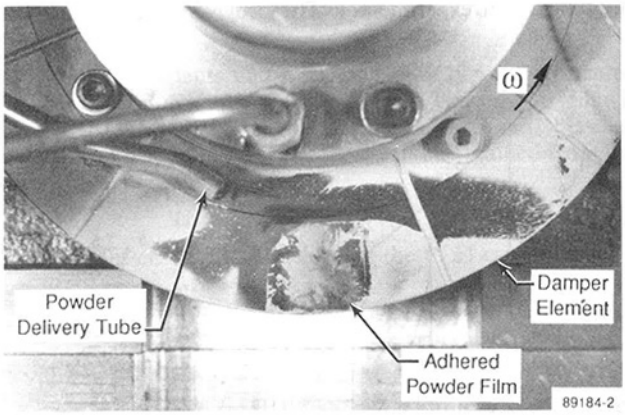

Fig. 9(*a*) Powder-lubricated damper element after 35-min test at room temperature (W_n = 22.24 to 222.4 N, speed to 10,000 rpm, e_r = 0.24 mm)

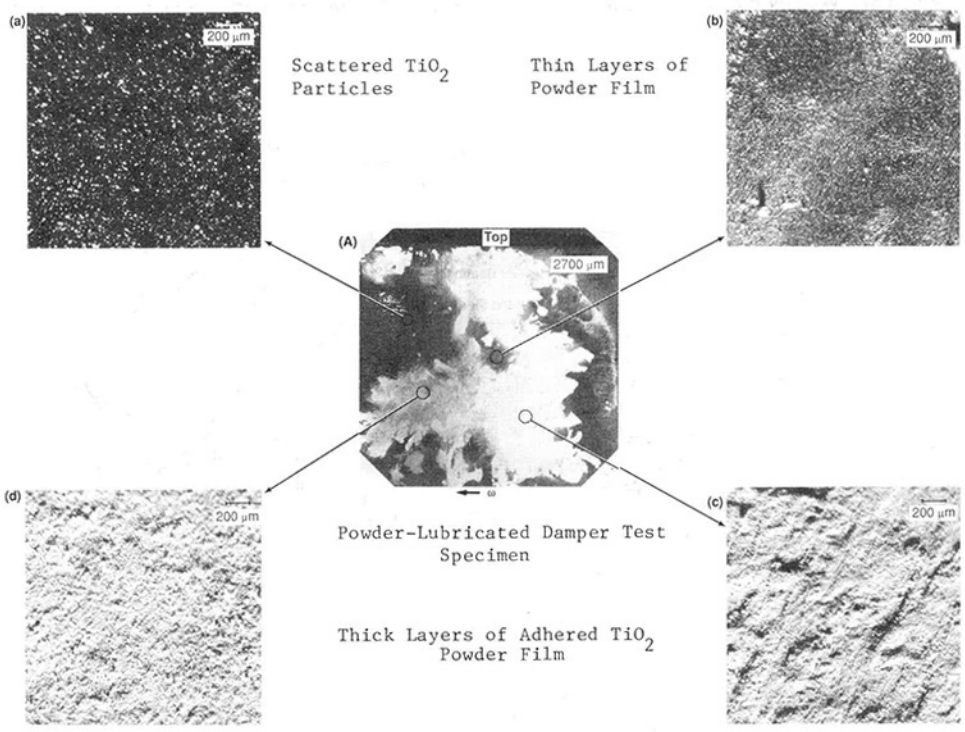

Fig. 9(*b*) Powder-lubricated damper pad after 35-min test at room temperature (W_n = 22.24 to 222.4 N, speed to 10,000 rpm, e_r = 0.24 mm)

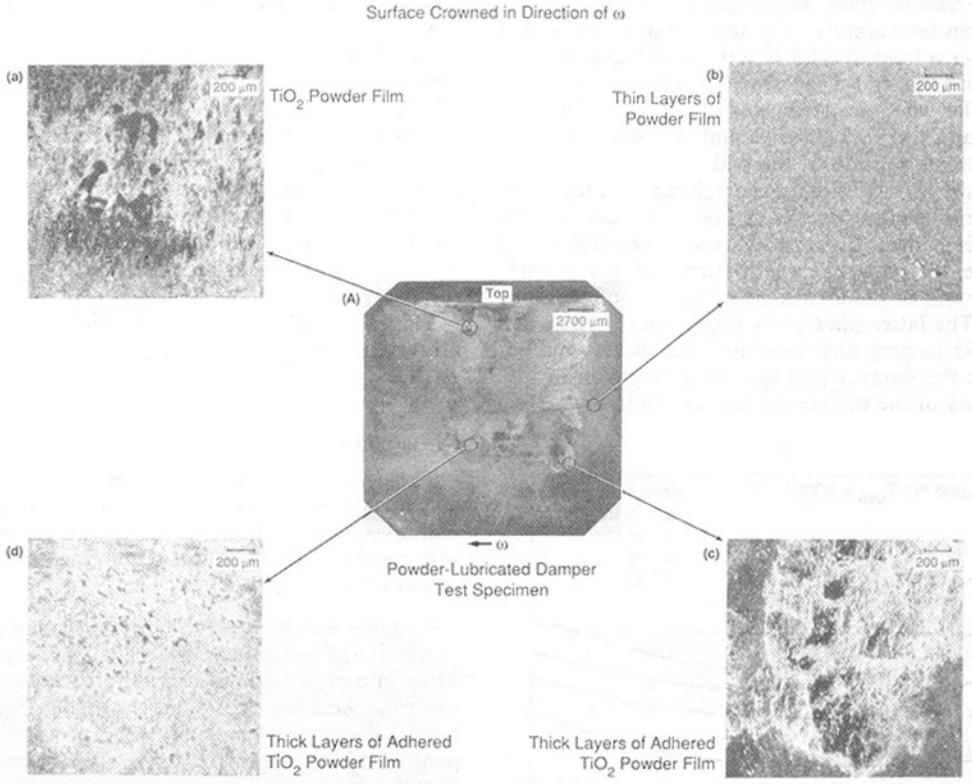

Fig. 10 Powder-lubricated damper pad after high-temperature test for 12 min (W_n = 22.3 to 89.0 N, speed to 6000 rpm, e_r = 0.24 mm, at 427°C)

In the same series of tests, the damper specimens were tested with TiO_2 powder and the runs covered the entire range of temperatures up to 426°C (800°F). After a 12-min test no wear had occurred in any of the test samples. Overall test results with the powder lubricant were excellent. The damper pad specimen showed a 2.5 μm thick, TiO_2-type buildup. The appearance of the damper pad after high-temperature testing is shown in Fig. 10.

The surfaces of the slider and counterface have been covered with thin adhered layers of extremely fine powder after a period of testing with powder lubricant. This adhered layer is believed to play a major role in terms of protecting the tribomaterial surfaces and dictating the magnitude of slip velocity at the boundaries. The presence of adhered and residual powder film is shown in the light micrographs of Figs. 9 and 10. This adhered powder film was considered intermediate film as shown in the model of Fig. 1 under powder lubrication conditions.

Figure 11 presents powder-lubricated damper performance, C_{eq}, as a function of speed and ambient temperature for a constant eccentricity of e_r = 0.152 mm (0.006 in.) and a constant load of 44.5 N. As can be seen from the plots of data in Fig. 11, the deviations in damping are small and they fall within a nearly constant data band.

As given in Table 1, there is a modest agreement between the predicted and measured damping as a function of speed. While the measured direct damping does not exactly match the theory, especially at lower speed, it is evident that the trends are similar. However, some of the discrepancy between the measurements and predictions may be due to the constants of the rheological model: μ_o, α, and γ. Indeed, physical properties of the powder such as density, yield, and limiting shear stresses are functions of local film pressure, strain rate and others. In this first-order analysis they were assumed to be constant throughout operation.

In reviewing equivalent damping as a function of load and speed, given in Fig. 12, the following characteristic behavior

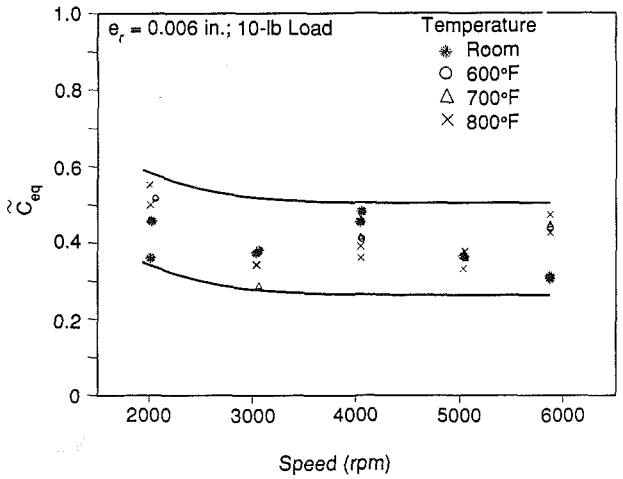

Fig. 11 Powder-lubricated damper performance as a function of speed and temperature

may be stated. First, the equivalent damping goes through an initial decrease followed by a gradual increase in damping with increasing speed. Secondly, the damping increases with increases in normal load. For instance, increasing the normal load by a factor of three resulted in an increase in damping about 2.5 times.

The maximum damper pad temperature rise (thermocouples were embedded near the contact surfaces), for example with a constant load of W_n = 111.2 N (25 lb) at 10,000 rpm, was measured to be 25°C (45°F). Generally, the pad temperature rise was linearly proportional to speed. Thermal behavior of the powder-lubricated damper provides further evidence that the powder film was carrying generated heat away from the contact as was discussed earlier (Fig. 1).

A set of two damper pads was tested in an unlubricated condition at room temperature. The test duration was about one minute under a load of 44.5 N (10 lb) and speeds up to 6000 rpm. During this run a high-pitched noise often developed, in particular when the speed was raised over 3000 rpm. Visual examination revealed abrasive and adhesive-type wear marks on the trailing portion of the pad.

Figure 13 shows the condition of the unlubricated test specimen after the one-minute run. As can be seen, considerable surface distress is evident. Figure 14(*a*) is a photograph of the damaged surface, indicating the wear pattern, while Fig. 14(*b*) shows a photograph of the distressed subsurface of the same damaged area. The latter photo was taken after preparation of the surface via lapping and removing wear debris and adhered film from the damper pad specimen as shown in Fig. 13(*a*). The severity of the surface distress shown in Figs. 14(*a*) and 14(*b*) was considered detrimental to the pure frictional damper life.

Figure 15 plots the measured damper frictional forces as a function of speed for both the powder-lubricated and unlubricated (dry) conditions. The characteristics of the two conditions differ considerably. The powder-lubricated frictional force data appear in many ways akin to the conventional hydrodynamic lubrication system (see Fig. 2). The unlubricated damper showed a constant shear force for much of the initial low-speed range, analogous to a dry frictional material behavior, followed by a rapid rise in shear force at a higher speed.

This sudden change in frictional force was attributed to the aforementioned surface damage (adhesive wear).

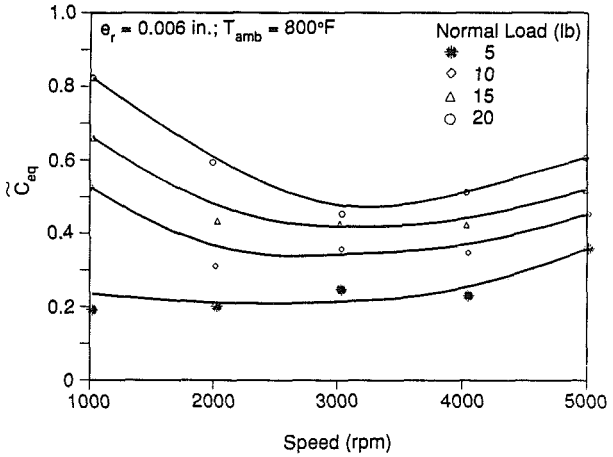

Fig. 12 Equivalent damper as a function of speed and load at 427°C

Conclusions

The damper performance, together with test observations and test specimen inspections, including powder-lubricated and unlubricated conditions, leads to the following conclusions with regard to the practical requirements of a powder lubrication system:

- *Film Adhesion.* An integral feature of powder lubrication is the permanent adhesion of the powder lubricant, either in pure form or in some altered state, to the interacting surfaces. Adhesion has wide-ranging effects on several tribological aspects of the lubrication process, namely: (*a*) morphology of the interacting surfaces, (*b*) surface roughness, (*c*) film thickness, and (*d*) characteristics of shear, friction, etc.

- *Intermediate Film.* It has been postulated by Heshmat (1989a), and is shown in the model of Fig. 1, that under powder lubrication conditions an intermediate film—a form of boundary layers—is created between the interacting surfaces and the lubricant film. The tests conducted under this program clarify

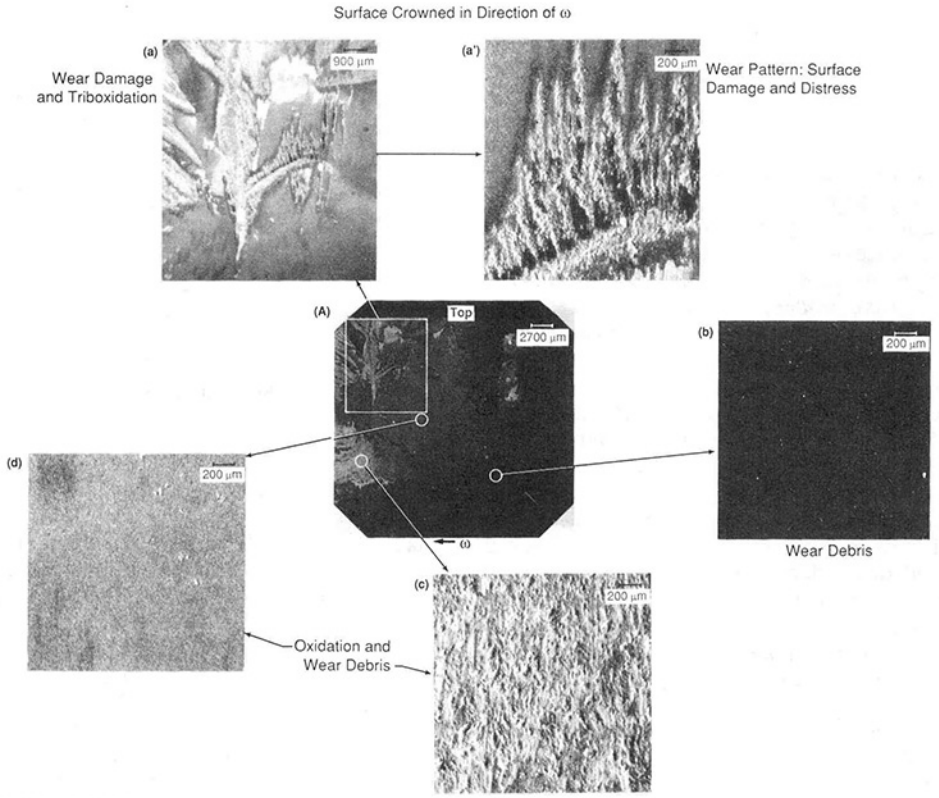

Fig. 13 Unlubricated damper pad surface appearance after 1.0-min test at room temperature (W_n = 44.48 N, speed to 6000 rpm, e_r = 0.24 mm)

Table 1 Comparison of PLD performance data—theory versus experiment; e_r = 152.4 μm, W_n = 44.5 N (10 lb)

SPEED (RPM)	THEORETICAL PREDICTION		EXPERIMENTAL DATA		
N	$\tilde{\tau}$† (-)	$\tilde{B}_{eq}$*	C_{eq}* (-)	C_{eq}** [lb-s)/in]	$(\frac{N-S}{m})\times 10^{+3}$
2,000	0.361	0.973	0.47	90.00	15.76
3,000	0.569	0.971	0.42	120.83	21.16
4,000	0.642	0.398	0.47	180.43	31.50
5,000	0.715	0.410	0.37	196.83	34.47
6,000	0.725	0.290	0.34	212.89	37.28

$\mu_o = 4 \times 10^{-4}$ lb-s/in^2, $h_o = 1.025 \times 10^{-4}$; $h_1 = .0006025$"
$h_1/h_o = 5.88$, $e_r = .006$ in; $R_2 = 3.99$ in., $R_1 = 2.99$ in.

† See Fig. 7
* Per unit area
** Total damping for damper element

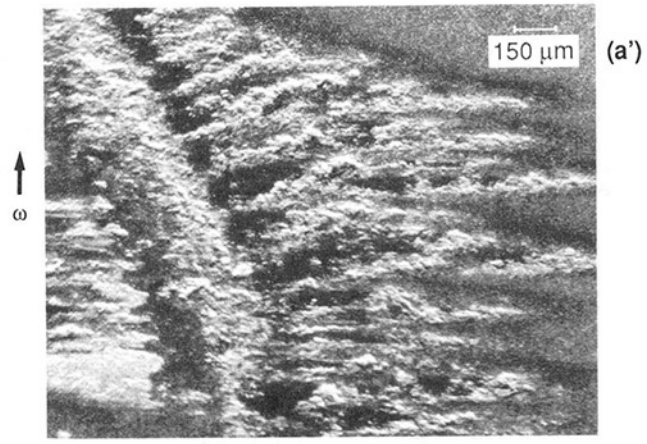

Fig. 14 Light micrograph of unlubricated damper pad surface after 1.0-min test (see Fig. 17 for test conditions)

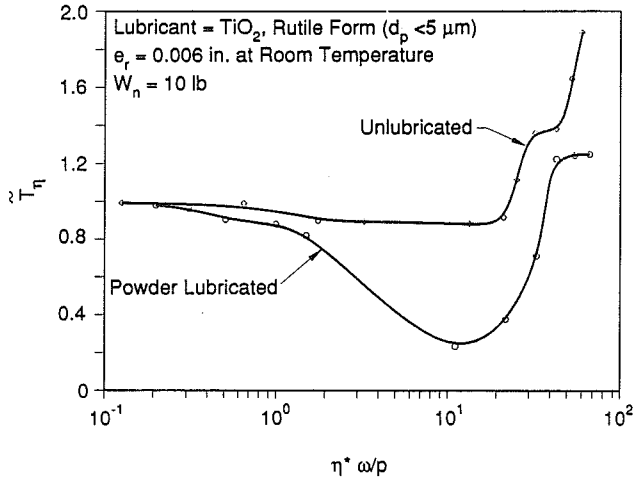

Fig. 15 Normalized shear force as a function of speed parameter for powder-lubricated and unlubricated damper tests

and amplify the mechanism of formation of these intermediate films.

• *Hydrodynamic Model.* Results of the series of experiments with powder indicate that the mechanism of powder flow seems to follow some of the basic features of hydrodynamic lubrication by exhibiting a layerlike shear, reminiscent of fluids. This shear is deemed responsible for the reduction in wear that accompanies the presence of debris between interacting surfaces. The nature of this sheared flow causes the least possible discontinuity between the various laminae of the powder bed. Thus, the basic feature of the quasi-hydrodynamic model is a layered flow of the powder bed, as portrayed in Fig. 1.

• *Damper Concept.* A novel high-temperature powder-lubricated damper with application to advanced turbine engines has been conceived and tested. Based on the experimental evidence and the theoretical development, it was shown that the equivalent damping of this concept is nearly constant with temperature and speed and increases with increasing normal load. Although tests were run with what may seem a severe lubricant (dry TiO_2 powder), no wear occurred. Long wear life for this damper is expected since powder lubrication produced no wear on the interacting surfaces.

References

Anson, D., et al., 1987, "Development Plan for a Coal-Water-Slurry-Fired Diesel Engine for Cogeneration Applications." U.S. DOE Report No. DOE/CE/40741-T1 (DE87012003), July.

Baskey, R. H., 1960, "An Investigation of Seal Materials for High-Temperature Applications," *ASLE Trans.*, Vol. 3, pp. 116–123.

Berthier, Y., Brendle, M., and Godet, M., 1987, "Boundary Conditions: Adhesions in Friction," *Leeds-Lyon Symposium, Interface Dynamics*, pp. 19–25.

Berthier, Y., Godet, M., and Brendle, M., 1988, "Velocity Accommodation in Friction," STLE Paper No. 88-TC-3A-C.

Bhat, S. T., Buono, D. F., and Hibner, D. H., 1981, "Analysis of High Load Dampers," NASA Report No. GR-165503, Aug.

Campbell, C., and Brennan, C. E., 1985, "Computer Simulation of Granular Shear Flows," *J. Fluid Mech.*, Vol. 151, pp. 167–168.

Cowin, S. C., 1974, "A Theory for the Flow of Granular Materials," *Powder Tech.*, Vol. 9, pp. 61–69.

Godet, M., and Berthier, Y., 1986, "Continuity and Dry Friction: Osborne Reynolds Approach," Fluid Film Lubrication—O. Reynolds Centenary, *Proceedings of the 13th Leeds-Lyon Tribology Symposium, Trib. Series 11*, pp. 653–663.

Heshmat, H., Shapiro, W., and Gray, S., 1982,"Development of Foil Journal Bearings for High-Load Capacity and High-Speed Whirl Stability," ASME *Journal of Lubrication Technology*, Vol. 104, pp. 149–156.

Heshmat, H., and Pinkus, O., 1986, "The Interaction of a Gas With Solid and Liquid Particles," *Proc. 6th Symposium on Transfer and Utilization of Particle Control Technology*, EPRI/EPA, CS-4918, 16.1–16.15, Feb.

Heshmat, H., 1988, "Powder-Lubricated Wedge Damper," U.S. Patent Application No. 1242-93 (2-D-814), Apr. 12.

Heshmat, H., 1989a, "Quasi-Hydrodynamic Lubrication With Dry Triboparticulate Matter: Experiment and Theory," Mechanical Technology Inc. Technical Report No. 89TR29.

Heshmat, H., 1989b, "Wear Reduction Systems: Powder-Lubricated Piston Rings for Coal-Fired Diesel Engines," *Proceedings DOE-METC Contractor's Review Meeting*, Oct.

Heshmat, H., Pinkus, O., and Godet, M., 1989, "On a Common Tribological Mechanism Between Interacting Surfaces," *STLE Trans.*, Vol. 32, No. 1, pp. 32–41.

Heshmat, H., 1990a, "The Rheology and Hydrodynamics of Dry Powder Lubrication," *Trans. of STLE*, Vol. 34, presented at the ASME/STLE Tribology Conference, Ontario, Canada.

Heshmat, H., 1990b, "High-Temperature Solid Lubricated Bearing Development—Dry-Powder-Lubricated Traction Testing," *Proc. 26th Joint Propulsion Conference*, sponsored by AIAA, SAE, and ASME, Paper No. 90-2047, July.

Heshmat, H., 1990c, "Diesel Wear: Powder-Lubricated Piston Rings for Coal-Fired Diesel Engines," *Proceedings DOE-METC Contractor's Review Meeting*, Mar.

Heshmat, H., and Walton, J. F., 1990, "High-Temperature Powder Lubricated Dampers for Gas Turbine Engines," *Proc. 26th Joint Propulsion Conference*, sponsored by AIAA, SAE, and ASME, Paper No. 90-2046, July.

Hibner, D. H., Bhat, S. T., and Buono, D. F., 1981, "Optimum Friction Damping of a Flexible Rotor," ASME Paper No. 81-GT-156.

Hsu, B. D., 1988, "Progress on the Investigation of Coal-Water-Slurry Fuel Combustion in a Medium-Speed Diesel Engine: Part II: Preliminary Full Load Test," presented at Energy-Sources Technology Conference and Exhibition, Jan.

Kaneta, M., Nishikawa, H., and Kameishi, K., 1990, "Observation of Wall Slip in Elastohydrodynamic Lubrication," ASME *Journal of Tribology*, Vol. 112, No. 3, pp. 447–452.

Nikolakakis, I., and Pilpel, N., 1988, "Effects of Particle Shape and Size on the Tensile Strengths of Powder,"*Journal of Powder Technology*, Vol. 56, No. 2, pp. 95–103.

Oike, M., Emori, N., and Sasada, T., 1985a, "Mild-Severe Wear Transition in Metal Rubbing With SiC Abrasive Grains Interposed Between Mating Surfaces," *Journal of JSLE*, International Edition, Tokyo.

Oike, M., Emori, N., and Sasada, T., 1985b, "Effect of Fine Ceramic Particles Interposed Between Sliding Surfaces on Wear of Metals," presented at the JSLE Int. Trib. Conference.

Rao, A. K., et al., 1988, "Operating Results of the Cooper-Bessemer JS-1 Engine on Coal Water Slurry," presented at ASME Energy-Sources Technology Conference and Exhibition, Jan.

Scott, B., and Winer, W. O., 1979a, "Shear Strength Measurements of Lubricants at High Pressure," ASME *Journal of Lubrication Technology*, Vol. 101, No. 3, pp. 251–257.

Scott, B., and Winer, W. O., 1979b, "A Rheological Model for Elastohydrodynamic Contacts Based on Primary Laboratory Data," ASME *Journal of Lubrication Technology*, Vol. 101, No. 3, pp. 258–265.

Tevaarwek, J. L., and Johnson, K. L., 1979, "The Influence of Fluid Rheology on the Performance of Traction Drivers," ASME *Journal of Lubrication Technology*, Vol. 101, No. 3, pp. 266–274.

Wallerstein, S., 1966a, "Application of a Powder Lubrication System to a Gas Turbine Engine—Part II," AFAPL-TR-65-43, Part II, Dec.

Wallerstein, S., 1966b, "Application of a Powder Lubrication System to a Gas Turbine Engine—Part III," AFAPL-TR-65-43, Part III.

A Gas-Operated Bearing Damper for Turbomachinery

J. M. Vance

B. P. Cardon

L. A. San Andres

Texas A&M University,
College Station, TX 77843

A. F. Storace

General Electric Aircraft Engines,
Cincinnati, OH 45215

A gas-operated bearing damper for turbomachinery has been designed, analyzed, and experimentally investigated in the laboratory. The damper utilizes air bled off from the compressor to power an actuator through orifices with area modulated by the vibratory displacement at the bearing support. The design objective for this passive device is to make the actuating dynamic gas pressure phase lead the vibratory displacement by 90 deg. Several variations of the basic concept have been tested. An analysis was performed to guide the experiments. All of the designs tested to date can produce positive damping, and one particular design has produced a damping coefficient of 8756 N-s/m (50 lb-sec/in.) with a power penalty of 5.2 kW (7 hp) at 310 KPa (45 psi). This design was installed on a laboratory rotor with flexibly supported ball bearings, and significant damping of the critical speed response was demonstrated. The experimental results to date suggest that further research can produce significant improvements in performance, and the device appears to be especially adaptable to high-temperature applications for aircraft engines.

Introduction

Future military engines, as well as engines for futuristic civil aircraft designs such as the National Aerospace Plane, are being designed to operate at higher efficiencies and Mach numbers. This requires lightweight rotor designs along with higher operating temperatures that will effectively eliminate oil from the engine. Squeeze film dampers will therefore no longer be viable devices for controlling engine dynamic response.

The increased specific power output and highly flexible rotor designs of these advanced engines will preclude the possibility of achieving acceptable rotordynamic behavior through structural mass and stiffness tuning. Dampers will be needed to achieve the required vibration control. Thus, a suitable replacement for the squeeze-film damper must be found for the non-oil high-temperature environment of this new generation of aircraft engines.

A gas-operated bearing damper, which used bleedoff air from the engine compressor, is being developed to meet this requirement. To replace the squeeze film damper, it must control response to rotor imbalance, allow operation through critical speeds, and suppress potential rotordynamic instabilities. Squeeze film dampers are limited to approximately 600°F even with new high-temperature lubricants. We see no reason why the gas damper cannot operate at temperatures exceeding 1000°F using well-known materials.

Design Variations

Two basic concepts for the gas damper have been investigated and evaluated analytically, and two versions of the most promising concept have been experimentally evaluated. The objective of this research to date has been to establish the feasibility of a gas damper for the application described above and to select the most promising design for further development. The two basic concepts are: (1) the swirl damper, and (2) the pocket damper.

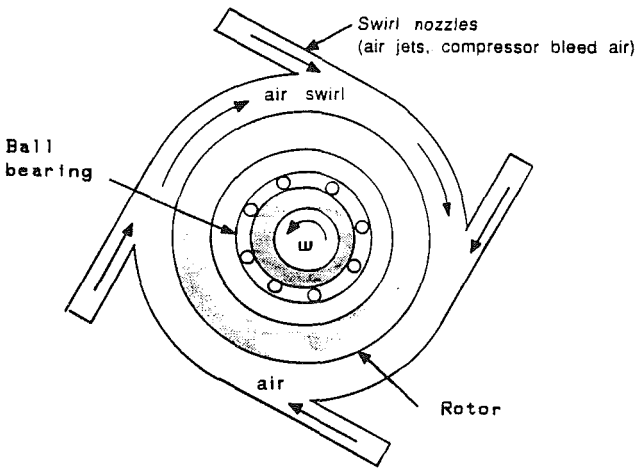

Fig. 1 Swirl damper concept

Figure 1 illustrates the swirl damper concept, which is based on the published work of Brown and Hart [1]. They showed experimental measurements on a small rotor, which demonstrates that a swirling gas flow around the rotating rotor surface (i.e., with no ball bearing in Fig. 1) will suppress synchronous response to imbalance if the direction of swirl is opposite to shaft rotation. Although the ball bearing in Fig. 1 is optional, the performance of the swirl damper is believed to be sensitive to the ratio of the nozzle exit fluid velocity to the tangential velocity of the rotor surface (the latter is zero with a ball bearing).

Contributed by the International Gas Turbine Institute and presented at the 36th International Gas Turbine and Aeroengine Congress and Exposition, Orlando, Florida, June 3–6, 1991. Manuscript received at ASME Headquarters March 4, 1991. Paper No. 91-GT-249. Associate Technical Editor: L. A. Riekert.

An elementary analysis predicts a very small amount of direct damping for the swirl damper, and mainly backward-driving cross-coupled stiffness, which is probably responsible for the demonstrated attenuation of response to imbalance. Synchronous response usually involves forward whirl and most rotordynamic instability mechanisms involve forward whirl. Therefore, a combination of backward-driving cross-coupled stiffness and small positive direct damping is adequate for rotordynamic control under most operating conditions.

From [1], the predicted cross-coupled stiffness for the swirl damper is

$$K_{xy} = RL\rho u^2 f\pi/c \tag{1}$$

where R is the radius; L is the axial length; ρ is the fluid density; u is the maximum fluid tangential velocity; f is the fluid friction factor ($0.01 < f < 0.1$); c is the radial clearance.

Division of Eq. (1) by the whirl frequency produces an equivalent damping coefficient, which is quite small when compared to a squeeze film damper. Nevertheless, the swirl damper can be installed at very advantageous locations along the rotor to improve its effectiveness greatly [2]. This is because it is not restricted to application at a bearing location since it does not need to be installed on a nonrotating part such as a squirrel cage bearing support [3]. On the other hand, the evolutionary nature of new engine developments would support an argument in favor of a stronger damper that could simply be installed on the squirrel cage to replace the traditional squeeze film.

The second basic concept is the pocket damper, in which the whirling rotor controls the flow of compressible gas (e.g., air) into and/or out of a control volume. The design objective is to produce a configuration in which the pocket pressure exerts a force on the rotor that opposes the vibratory velocity. Figure 2 illustrates a configuration in which the exit area 4 from the control volume 3 is controlled by the dynamic clearance δ between the rotor and stator. Air is supplied to the control volume through a fixed orifice 2. This design will be referred to here as the exit-varying pocket damper. In the laboratory test apparatus, there are eight pockets in a housing around the circumference of the test rotor. This design has the same advantage as the swirl damper, that is, it can act directly on the rotating rotor surface and therefore can be installed almost anywhere along the rotor.

Figure 3 illustrates an inlet-varying design, which is the most powerful gas damper actuator tested to date. One of the two actuators shown in the end view (looking along the axis of the rotor) is sectioned to show the flow path. As the slider head vibrates with the nonrotating bearing support, its displacement controls the flow of air from the stationary piston into the control volume. Thus the inlet area at location 2 in Fig. 2 is regulated by the vibratory displacement.

Since the pocket damper appears to be the most promising concept so far, the balance of this paper will be devoted to presenting the theory and test results for it.

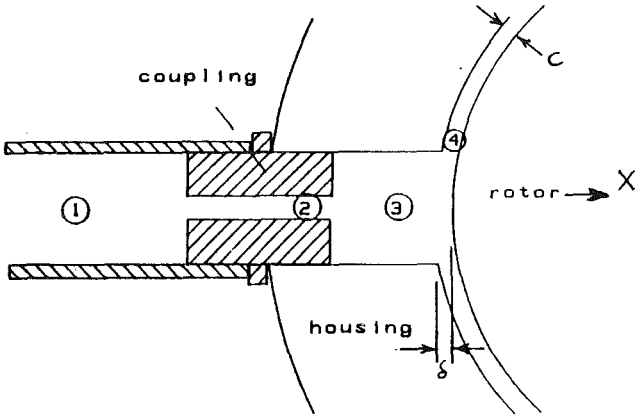

Fig. 2 Air pocket geometry for exit-varying pocket damper

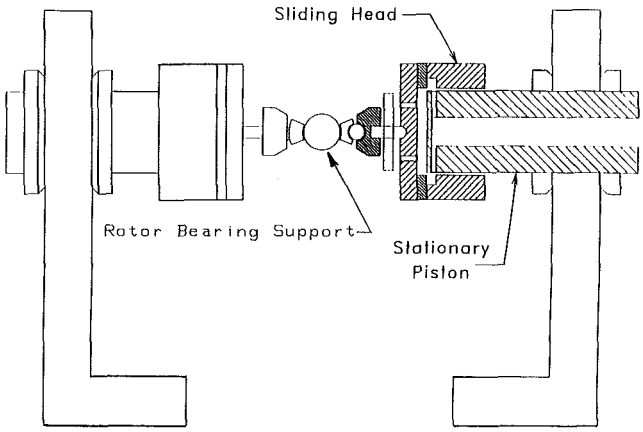

Fig. 3 Inlet-varying gas damper with two actuators (end view)

Nomenclature

A, A_i, A_e = area of pocket chamber, m^2; area of inlet and exit restrictions, m^2

a_{ie} = $\partial(\ln(A_i/A_e)/\partial\delta$, dynamic variation of inlet/exit area; $\overline{a}_{ie} = a_{ie} \cdot c$

a_s = $\delta_1 = \theta_1 + \phi$ sonic speed, m/s

C_1, C_2 = $P_i A/RT_i$, $V/\gamma RT_i$

c = nominal radial clearance, m

g_2, g_3 = $-\dot{m}\phi/P_s$, $\dot{m}a_{ie}$

K, C = stiffness and damping coefficients, N/m, Ns/m

l = length or depth of pocket chamber, m

$\dot{m}$ = mass flow rate across the pocket damper, kg/s

n = number of pockets on bearing circumference ($n \geq 3$)

P, p = absolute pressure, dynamic pressure, N/m^2

T = absolute temperature, K

V = $A(l + \delta(t))$ = volume of pocket chamber, m^3

$X, x, \dot{x}$ = amplitude of dynamic displacement, m = $X\sin(\omega t)$, $X\omega\cos(\omega t)$

z_i, z_e = P_i/P_s, P_e/P_i = inlet and exit pressure ratios

$$Z_i = \frac{[2z_i^{(2-\gamma)/\gamma} - (\gamma+1)z_i^{(1/\gamma)}]}{2\gamma[z_i^{2/\gamma} - z_i^{(\gamma+1)/\gamma}]}$$

$$Z_e = \frac{\gamma+1}{2\gamma} + \frac{1}{2\gamma} \cdot \frac{[(\gamma+1)z_e^{(\gamma+1)/\gamma} - 2z_e^{2/\gamma}]}{[z_e^{2/\gamma} z_e^{(\gamma+1)/\gamma}]}$$

$$\alpha = \frac{-\gamma z_i \phi}{a_{ie}(l/c+1)}$$

$$\beta = (A/A_e)\frac{\Gamma(l+c)}{a_s \gamma z_i}$$

γ = $Cp/Cv = 1.4$ = specific heat ratio for air

$\delta(t)$ = $c + X\sin(\omega t)$ = dynamic motion, m

$$\Gamma = \frac{z_i^{1/\gamma}\gamma(A_e/A_i)}{\Psi(z_i)\phi}$$

$$\Pi = \frac{\Gamma}{\gamma z_i \phi}$$

ϕ = $Z_e/z_i - Z_i$

ω = frequency of motion, rad/s

Subscripts

e = at discharge conditions

i = inlet, at pocket chamber

s = supply conditions

Theory

In an attempt to explain the rotordynamic effect of the labyrinth seals for compressible fluids, Alford [4] showed that, if the flow of gas into and out of a cavity is regulated by a vibratory motion, the dynamic pressure in the cavity can be out of phase with the vibratory motion.

Following his basic idea, and referring to the location numbers on Fig. 2, consider the flow of a perfect gas from a supply source at P_s, T_s (location 1), across restriction A_i (location 2), to a large volume (location 3) at conditions P_i, T_i, and then discharging through the exit restriction A_e (location 4) to exit conditions P_e, T_e. Unsteady flow conditions are determined by the dynamic displacement $\delta(t) = c + X\sin(\omega t)$ of a side of the volume, as shown in Fig. 2. Furthermore, both restrictions, at inlet and discharge, present flux areas (A_i, A_e) that can be dependent on the motion (i.e., as in Figs. 2 or 3). The conservation of mass equation in the pocket volumes states that

$$\frac{V}{\gamma T_i R}\frac{\partial P_i}{\partial t}+\frac{P_i A}{RT_i}\frac{\partial \delta}{\partial t}+\dot{m}_e(t)-\dot{m}_i(t)=0 \tag{2}$$

For small-amplitude dynamic motions, $X \ll C$, we assume the pressure and mass flow rates are given as the sum of a static and dynamic component, such that

$$P_i(t)=P_i+\hat{p}_i(t) \tag{3a}$$

$$\dot{m}_{i,e}(t)=\dot{m}+\frac{\partial \dot{m}_{i,e}}{\partial p_i}\hat{p}_i(t)+\frac{\partial \dot{m}_{i,e}}{\partial \delta}\delta(t) \tag{3b}$$

where $\dot{m}$ is the mass flow rate at equilibrium conditions, and given for a perfect gas as,

$$\dot{m}=\frac{P_s A_i \psi(z_i)}{\sqrt{\gamma R T_s}}=\frac{P_i A_e \psi(z_e)}{\sqrt{\gamma R T_i}} \tag{4}$$

where

$$\psi(z)=\left\{\frac{2\gamma^2}{(\gamma-1)}\left[z^{2/\gamma}-z^{(\gamma+1)/\gamma}\right]\right\}^{1/2} \tag{5}$$

and $z_i = P_i/P_s$, $z_e = P_e/P_i$ are the pressure ratios at inlet and discharge, respectively. From Eq. (4), a relationship between inlet and exit pressure ratios can be easily obtained. For air, the maximum pressure ratio, P_e/P_s, is equal to 0.27908, and occurs when both inlet and discharge areas are choked.

Substitution of Eq. (3) and Eq. (2) renders the equation

$$C_2\frac{\partial \hat{p}_i}{\partial t}+C_i X\omega\cos\omega t-g_2 p_i(t)-g_3 X\sin\omega t=0 \tag{6}$$

The coefficients C_1, C_2, g_2, and g_3 are given in the Nomenclature. A solution to Eq. (6) is easily obtained in the form,

$$\hat{p}_i(t)=p_{is}\sin(\omega t)+p_{ic}\cos(\omega t)=-\frac{S_p}{\Delta}x(t)-\frac{C_p}{\Delta}\dot{x}(t) \tag{7}$$

where

$$p_{is}=-XS_p/\Delta;\ p_{ic}=-X\omega C_p/\Delta \tag{8a}$$

and

$$S_p=(g_3g_2+C_1C_2\omega^2);\ C_p=(g_3C_2-g_2C_1)_i\Delta=g_2^2+C_2^2\omega^2 \tag{8b}$$

It is evident that if positive dynamic stiffness (opposed to displacement) and positive dynamic damping (opposed to velocity) are to be obtained, the following conditions must be satisfied for all frequencies and geometries used:

$$S_p=(g_3g_2+C_1C_2\omega^2)>0$$

$$C_p=(g_3C_2-g_2C_1)>0 \tag{9}$$

If the dynamic variation of volume in the pockets is neglected, then $C_1 = 0$, and thus, $S_p = g_3g_2$ and $C_p = g_3C_2$. Since $C_2 > 0$, and it can be shown that $g_2 < 0$ for all pressure ratios, then positive damping would be obtained if $g_3 > 0$. For positive flow through the volume ($\dot{m} > 0$), positive damping is obtained if

$$a_{ie}=\frac{1}{A_i}\left(\frac{\partial A_i}{\partial \delta}\right)-\frac{1}{A_e}\left(\frac{\partial A_e}{\partial \delta}\right)>0$$

We conclude then, as Alford [4] has previously shown, that

(*a*) If the exit area is varying, $\partial A_e/\partial\delta > 0$, while the inlet area remains fixed, $\partial A_i/\partial\delta = 0$, then $a_{ie} < 0$ and a negative damping coefficient will be obtained.

(*b*) If the inlet area is varying, $\partial A_i/\partial\delta > 0$, when the exit area is fixed, $\partial A_e/\partial\delta = 0$, then $a_{ie} > 0$ and a positive damping coefficient is obtained.

(*c*) If both inlet and exit areas are fixed, $\partial A_i/\partial\delta = \partial A_e/\partial\delta = 0$, then $a_{ie} = 0$ and no damping or stiffness will be obtained.

The opposite reasoning holds for the stiffness coefficient.

Also, if the change in volume is preserved, $C_1 \neq 0$, it can be shown that positive damping can be obtained even for an exit area varying and an inlet area fixed.

The local force exerted by the dynamic pressure $p_i(t)$ on the journal surface is equal to

$$f_x(t)=\hat{p}_i(t)A=-\frac{S_pA}{\Delta}x(t)-\frac{C_pA}{\Delta}\dot{x}(t) \tag{10}$$

If n equally spaced pocket chambers ($n \geq 3$) exist around the bearing circumference, then it can be shown that for circular centered orbits of radius e, the total radial and tangential forces are time independent and equal to:

$$F_r=-Ke$$

$$F_t=-Ce\omega \tag{11}$$

where the total stiffness (K) and damping (C) coefficients are given after some considerable algebraic manipulation as

$$K=-\frac{n}{2}\frac{AP_s}{c}\overline{\frac{a_{ie}}{\phi}}\frac{[1+\alpha(\beta\omega)^2]}{[1+(\beta\omega)^2]} \tag{12}$$

$$C=\frac{n}{2}\frac{AP_s}{a_s}*\left(\frac{A}{A_e}\right)\overline{a_{ie}}(l/c+1)\frac{\Pi(1-\alpha)}{[1+(\beta\omega)^2]} \tag{13}$$

Equations (12) and (13) show that the force coefficients, stiffness, and damping are highly dependent on the excitation frequency ω. Note that as $\omega \to \infty$, the damping coefficient vanishes regardless of the geometric configuration.

Also, it is pointed out that the analysis neglects any viscous effects that may arise in thin film lands between the volume discharge and sump reservoir. These effects are regarded as small due to the nature of the fluid considered. In any case, viscous effects, if present, will increase the damping coefficient.

As an example of the analysis, we consider a gas pocket damper with the following characteristics:

$T_s = 333.3$ K (600 R), $Ps = 745$ KPa(114.7 psi)

$l = 12.7$ mm (0.5 in.), $c = 0.254$ mm (0.010 in.), $l/c = 50$

$A_e/A_i = 1.5 \rightarrow P_e/P_s = .32322$,

$a_{ie} = 1/c$

$A = \pi De^2/4$, varies

The pressure ratio $P_e/P_s = 0.32322$, implies that the exit area is choked, so then for $A_e/A_i = 1.5$,

$z_c = P_e/P_i = 0.52828$; $z_i = P_i/P_s = 0.61182$; $\psi(z_i) = 0.7976$

$\phi = 1.7828$; $\Gamma = 1.0397$; $\Pi = 0.68085$;

$a_s = (\gamma R T_s)^{1/2} = 366.14$ m/s (14415in./s)

and $\alpha = -0.02994$; $\beta = (A/A_e) * 2.6983 \times 10^{-4}$ 1/Hz

Table 1

A cm^2	De cm	$\frac{A}{A_e}$	β 1/Hz	K KN/m	C N sec/m	ω^* Hz
6.45	2.866	28.20	.0076091	$-562.98 \cdot n\frac{(1+\alpha\beta^2\omega^2)}{(1+\beta^2\omega^2)}$	$\frac{1030.8\ n}{(1+\beta^2\omega^2)}$	759.51
12.9	4.053	39.894	0.01076	$-1125.90 \cdot n\frac{(1+\alpha\beta^2\omega^2)}{(1+\beta^2\omega^2)}$	$\frac{2918.11\ n}{(1+\beta^2\omega^2)}$	537.10
25.8	5.732	56.410	0.015221	$-2251.86 \cdot n\frac{(1+\alpha\beta^2\omega^2)}{(1+\beta^2\omega^2)}$	$\frac{8237.9\ n}{(1+\beta^2\omega^2)}$	379.69

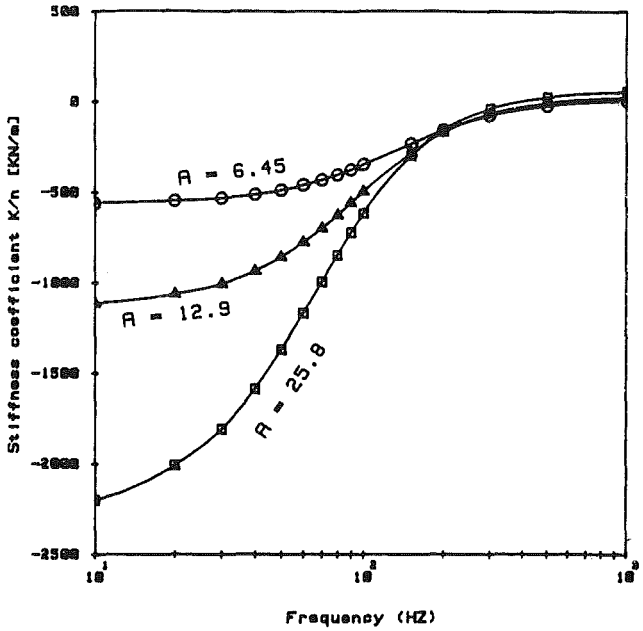

Fig. 4 Theoretical stiffness versus frequency for the example pocket damper

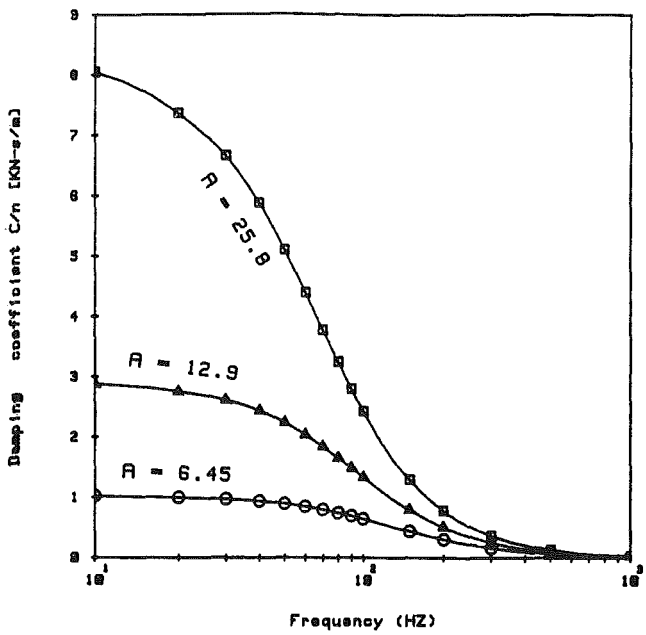

Fig. 5 Theoretical damping versus frequency for the example pocket damper

The ratio of pressure action area, A, to exit area, A_e, is given by:

$$\frac{A}{A_e}=\frac{\pi D_e^2/4}{\pi D_e C}=\frac{D_e}{4c}$$

For pocket areas A = 6.45 cm^2, 12.9 cm^2, 25.80 cm^2 (1, 2, 4 $in.^2$) the calculated values of stiffness and damping coefficients are given in Table 1. Notice that the dynamic stiffness is negative for low frequencies. The value of frequency ω^* denotes the frequency at which zero stiffness is obtained. Operation at $\omega > \omega^*$ would result in positive stiffness. Figures 4 and 5 show the stiffness (K) and damping (C) coefficients as functions of the frequency ω for the example case analyzed. Figure 5 shows that the damping coefficient decreases with increasing frequency. In a jet engine application where speeds are around 9000 rpm (ω = 150 Hz), for a gas damper with a pocket pressure area A = 6.45 cm^2 (1 $in.^2$) the damping coefficient is predicted to be 444.52 × n N-s/m. If a total damping of 17,501 N/m (100 lb-s/in.) is required, then 39 pocket dampers would be required. However, if the pocket area A is increased to 25.8 cm^2 (4 $in.^2$), only 14 pocket chambers would be required.

Thus, for a pocket damper with inlet area variation, $a_{ie} > 0$, we conclude that:

(a) Stiffness (K) is negative and increases with increasing frequency toward a positive value. The value of K at low frequencies is proportional to the supply pressure and the pocket area, while it is inversely proportional to the radial clearance or exit area. Negative direct stiffness lowers critical speeds but does not compromise rotor stability.

(b) Damping coefficient (C) is maximum at low frequencies and decreases with increasing frequencies. Damping at zero frequency is proportional to supply pressure and pocket volume while it is inversely proportional to the gas acoustic speed. The reduction in damping is a consequence of the fluid compressibility. In practice, a number of pockets or chambers with large volume will be required to provide substantial amounts of damping in a jet engine application.

Experiments

Preliminary testing to determine the most promising pocket damper design was carried out with a shaker attached to the nonrotating rotor.

Figure 6 shows the gas damper test rig in the Rotordynamics Laboratory at TAMU with the exit-varying damper (EVD) housing installed. There are eight pockets in the housing around the rotor of the type illustrated in Fig. 2. Three slight variations of the pocket geometry, illustrated in Fig. 7, were tested. The third variation has its inlet tube extended almost to the rotor surface, so it is labeled inlet-varying (IVD).

The measurement equipment used in these experiments consisted of a HP3582 spectrum analyzer, a signal generator,

power amplifier. Wilcoxon F4 shaker and impedance head, Bently Nevada proximity probes, a HP9816 computer with data aquisition card, and a digital plotter.

The transfer function of dynamic mass (F/a, "inertance") was used to determine the damping. Figure 8 shows the dynamic mass frequency response functions for EVD #1, at four different supply pressures. The minimum amplitude value, which is close to resonance (90 deg phase), is indicative of the modal damping. Notice that the damping increases with supply pressure. The measured mode shaped allows calculation of the gas damper coefficients shown in Fig. 9.

Using the same measurement procedure as for the exit-varying damper, the damping coefficients of Fig. 10 were obtained for the best inlet-varying damper with two IVD #2 horizontal actuators active in the configuration of Fig. 3. The data show poor repeatability primarily because the present design is difficult to adjust when more than one actuator is employed. The neutral position of the sliding head on the stationary piston is the critical adjustment. Plans for future work include the elimination or reduction of this sensitivity to adjustment of the neutral position.

Figure 11 shows the inlet-varying damper configuration IVD #2 with four actuators installed on the test rig for coastdown measurements through the first critical speed. The four actuators are rotated 45 deg relative to Fig. 3 to obtain more clearance above the base plate. Figure 12 is a photograph of the quad damper installation. The test rig setup for coastdown measurements is shown in Fig. 13. Horizontal and vertical eddy current proximity probes are installed at both ends of the rotor.

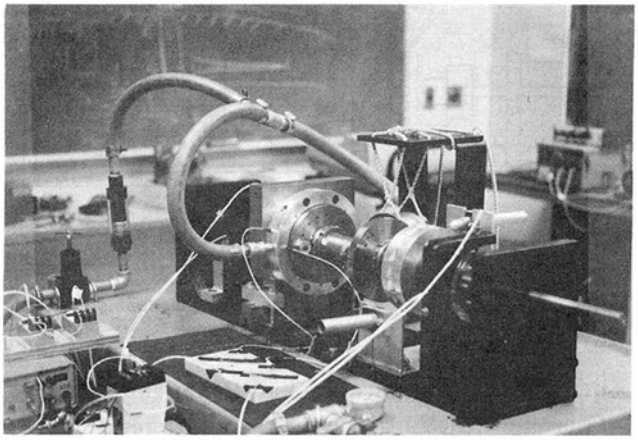

Fig. 6 Gas damper test rig with exit-varying damper installed

Coastdown vibration measurements with zero air supply pressure were used along with static stiffness measurements to determine the parameters for a computer simulation of the test rig rotordynamics. The right end vertical response to imbalance, measured and simulated, is shown in Fig. 14 for four different supply pressures to the damper. The damping coefficient values shown on the computer simulation are for the gas damper only and are the values found to produce the best agreement with the measured coastdown response for each supply pressure.

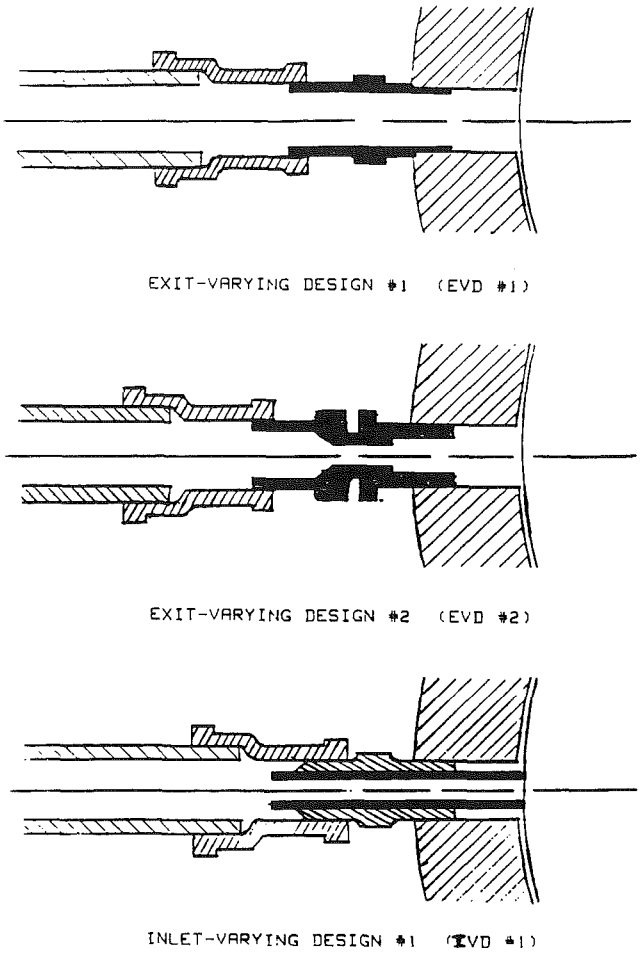

Fig. 7 Pocket damper design variations

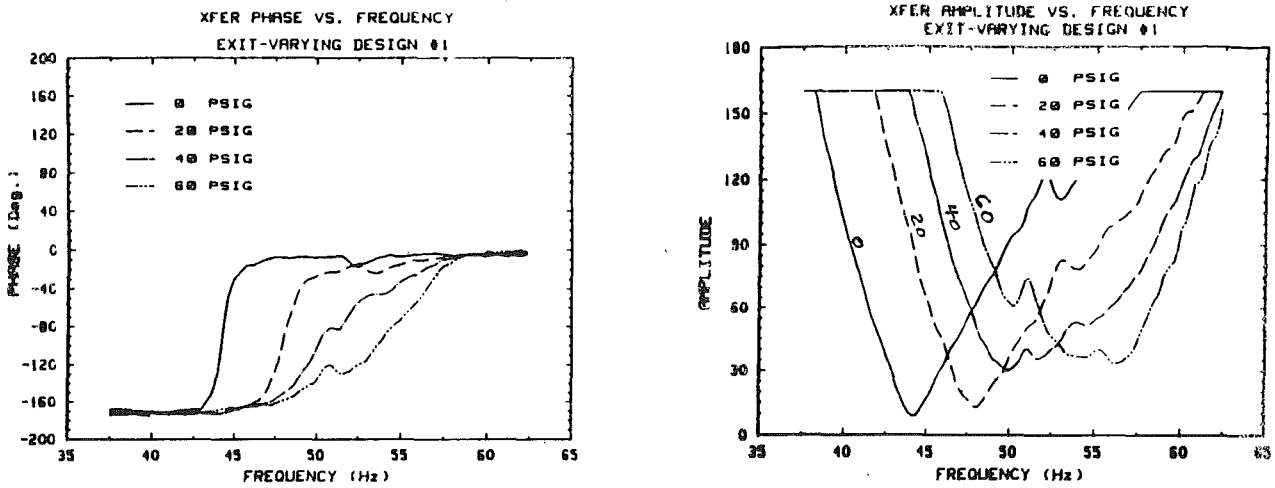

Fig. 8 Dynamic mass measurements for EVD #1

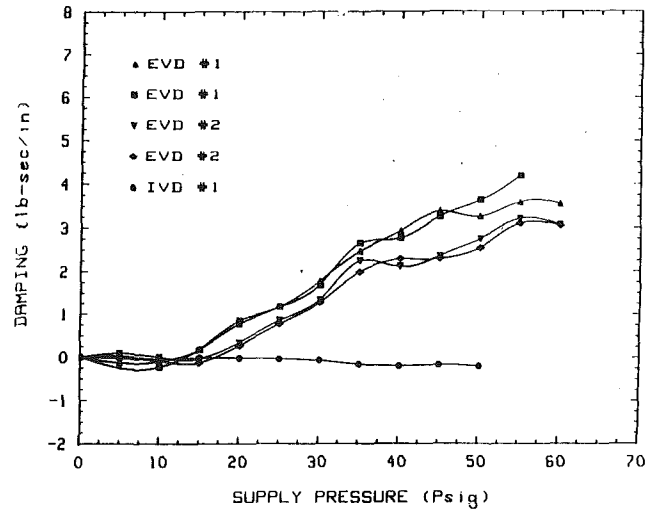

Fig. 9 Measured damping coefficients

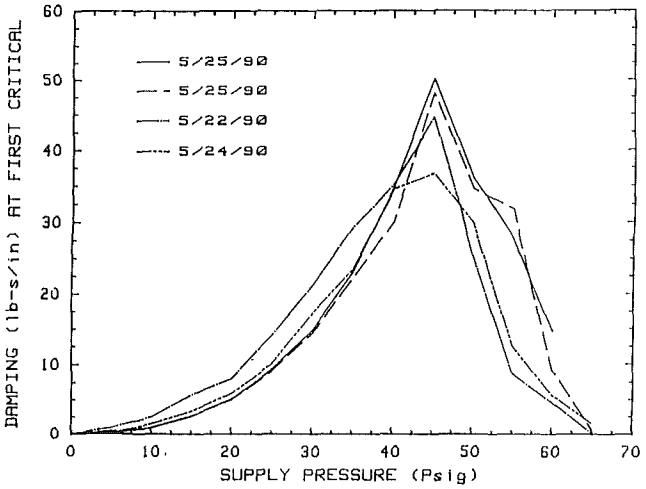

Fig. 10 Measured damping coefficients of IVD #2 pocket damper with two actuators

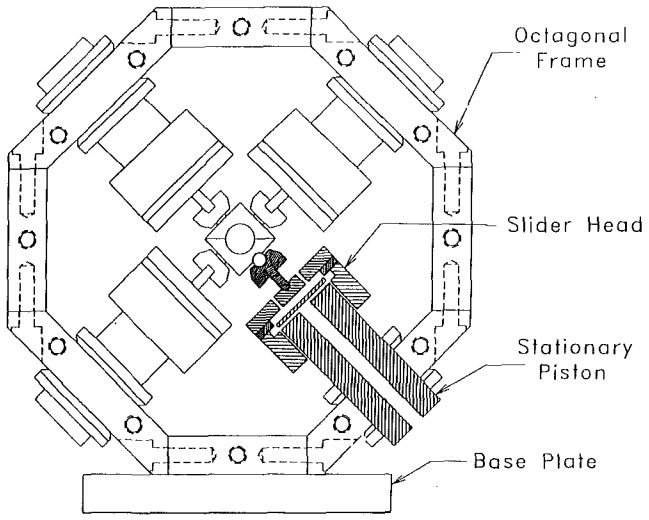

Fig. 11 For IVD #2 actuators installed for coastdown testing

Air flow rate measurements made with a flow meter showed that the theoretical predictions are accurate with less than 5 percent error. The compressor power absorbed by the gas damper is proportional to the product of flow rate and supply pressure. A typical value obtained from the flow measurements is 5.2 kW (7 hp) at a supply pressure of 310 kPa (45 psi).

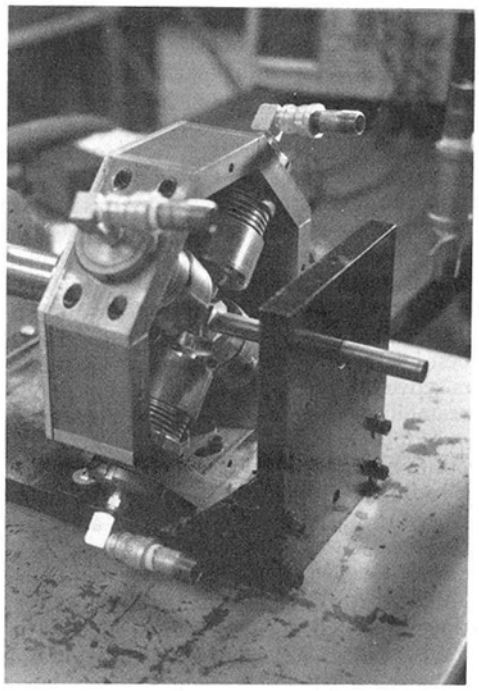

Fig. 12 Photograph of the Fig. 11 installation

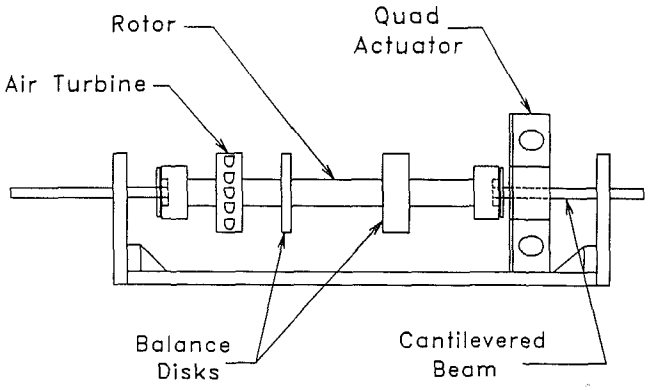

Fig. 13 Schematic of gas damper test rig set up for coastdown testing

Aircraft Engine Application and Requirements

General Electric Aircraft engines has performed studies to establish the requirements for high-temperature dampers in the context of large advanced technology engine concepts. The areas addressed in establishing the requirements included the damper location(s), required damping levels, synchronous and nonsynchronous vibration, damper weight and envelope, and damper reliability, durability, and maintainability. System vibration analyses were performed to establish the damper location(s) and the required damping levels. Figure 15 shows an example of an engine system vibration model and a fan rotor synchronous mode used in the establishment of damper requirements. The number 1 bearing is active in this mode, making it a good location for a damper to control fan rotor unbalance response. The forced-damp response characteristics were calculated to determine the required damping at the number 1 bearing damping to limit bearing loads, engine structure shears and moments, and clearance closures at the rotor stages to the desired values. It was established that a damping coefficient of approximately 43,800 N-s/m (250 lb-s/in.) is required, which translates to a peak damping force of approximately 1112 N (250 lb) in the operating speed range. The inlet-varying (pocket) gas damper has produced a measured damping coefficient of 8756 N-s/m (50 lb-sec/in.) with

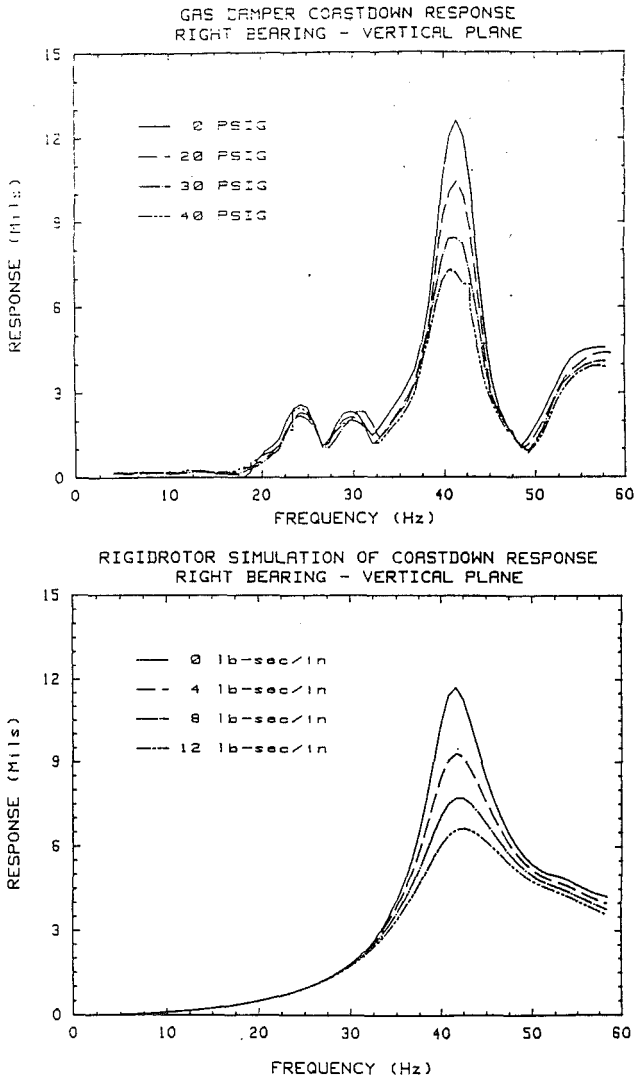

Fig. 14 Coastdown response (vertical probe), measured and simulated

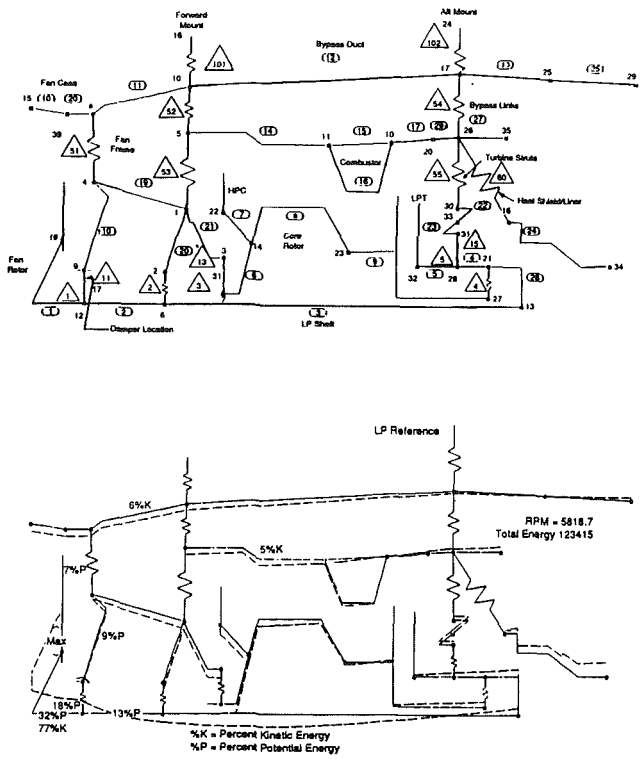

Fig. 15 System vibration model and responsive fan rotor mode for an advanced engine concept

only two actuators. This indicates that it can produce the damping levels needed (in the range of 43,800 N-s/m (250 lb-sec/in.)) for effective engine application. It appears that further refinement and optimization can be accomplished such that the capability of the pocket damper can be made consistent with the engine damping requirements. For example, improvements in the chamber porting, or the use of multiple pocket volumes placed in parallel along a given axis, hold promise of increasing the damping level achievable with this damper concept.

Discussion and Conclusions

Future advanced engine concepts will be designed to meet exceedingly challenging performance requirements, requiring high cycle temperatures and rotor speeds, advanced lightweight rotor structures, and high-temperature dry lube (non-oil) bearing sumps. In order to reduce vibration sensitivity to rotor imbalance and other stimuli, such as destabilizing (self-excited) forces and external excitation forces, it is essential that high-temperature dampers be integrated into the overall engine structural design.

Of the several gas damper concepts investigated, the inlet-varying pocket damper appears most promising unless aircraft engine design can be changed radically enough to consider installing a damper away from bearing locations, directly on a shrouded stage or the rotating shaft.

Measurements to date on the inlet-varying pocket damper indicate that it can produce significant damping with a reasonably small power penalty.

The theory predicts that the direct damping coefficient for the inlet-varying design drops off rapidly at frequencies above 100 Hz, but this issue remains to be investigated experimentally. For the exit-varying design, experiments showed that the dropoff can be moved out to much higher frequencies by simply changing the length of the supply piping to the damper.

Additional work remains to improve the performance of the pocket damper to meet the damping requirements for engine application. The sensitivity of the inlet-varying design to the adjustment of the sliding head position needs to be reduced. It seems likely that change to the porting of the chamber is a key to the solution of this problem.

If a higher temperature aircraft engine is to be developed, one of the many design challenges is to provide a rotor system damper that operates without oil. The gas damper must be considered as a prime candidate to meet this challenge.

References

1 Brown, R. D., and Hart, J. A., "A Novel Form of Damper for Turbomachinery," *Proceedings of the Fourth Biennial Workshop on Rotordynamic Instability Problems in High Performance Turbomachinery*, June 2-4, 1986, pp. 325-347.

2 Vance, J. M., *Rotordynamics of Turbomachinery*, Wiley, New York, 1988, pp. 287-289.

3 Vance, J. M., *Rotordynamics of Turbomachinery*, Wiley, New York, 1988, p. 39.

4 Alford, J. S., "Protecting Turbomachinery From Self-Excited Rotor Whirl," ASME JOURNAL OF ENGINEERING FOR GAS TURBINES AND POWER, Vol. 87, 1965, pp. 325-347.

Performance Characteristics of Brush Seals for Limited-Life Engines

R. E. Chupp
Teledyne CAE,
Toledo, OH 43612

C. A. Dowler
WL/POTX,
Wright Patterson Air Force Base, OH 45433

Brush seals are potential replacements for air-to-air labyrinth seals in gas turbine engines. An investigation has been conducted to determine the performance characteristics of brush seals for application in limited-life gas turbine engines. An elevated temperature, rotating test rig was designed and built to test labyrinth and brush seals in simulated subsonic and supersonic engine conditions. Results from initial tests for subsonic applications demonstrated that brush seals exhibit appreciably lower leakage compared to labyrinth seals, and thus offer significant engine performance improvements. Performance results have been obtained showing the effect of various brush seal parameters, including: initial interference, backplate gap, and multiple brush seals in series.

Introduction

Aggressive pursuit of increased performance in gas turbine engines is driving the thermodynamic cycle to higher pressure ratios, bypass ratios, and turbine inlet temperatures. As these three basic parameters increase, airflows in the internal air system and resultant thermodynamic cycle losses increase (Moore, 1975). This conflict of reducing internal airflows while increasing thermodynamic efficiency and performance is putting more emphasis on improvements to the internal flow system. Studies have shown that improvements to the internal flow system to reduce leakage can yield an increase in thrust by as much as 17 percent, or a decrease in the low-pressure turbine inlet temperature of 175 °F. One such improvement that is receiving renewed interest and research is the brush seal. The brush seal offers as much as an order of magnitude reduction in leakage flow over a conventional labyrinth seal.

A brush seal is shown schematically in Fig. 1. It has a set of densely packed, fine diameter (typically 0.003 in.) metallic fiber bristles sandwiched between inner and outer packing plates. The bristles are angled in the direction of rotation of the shaft to reduce friction and wear. The angle causes the bristles to bend rather than buckle when shaft excursions occur. The bristles run against a ceramic shaft coating to prevent/reduce wear on the shaft. These features allow the brush seal to retain its performance even after large excursions, whereas the labyrinth seal would incur a permanent increase in clearance under such conditions.

The purpose of this paper is to present results from a brush seal experimental investigation. The objectives of the investigation were to evaluate the performance improvements, wear characteristics, and cost impacts of replacing labyrinth seals with brush seals in a limited life engine. Initial results were published by Chupp and Nelson (1990).

Contributed by the International Gas Turbine Institute and presented at the 36th International Gas Turbine and Aeroengine Congress and Exposition, Orlando, Florida, June 3–7, 1991. Manuscript received at ASME Headquarters March 4, 1991. Paper No. 91-GT-281. Associate Technical Editor: L. A. Riekert.

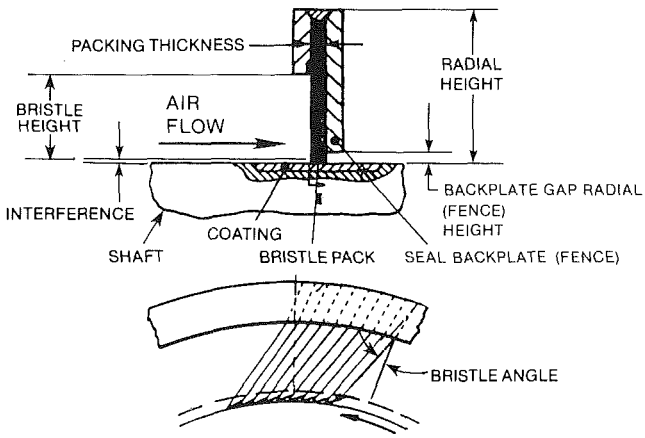

Fig. 1 Brush seal schematic

Background

For over 50 years now, labyrinth seals have been the primary seal used for air-to-air sealing in gas turbine engines. However, labyrinth seals have an intrinsic clearance associated with them due to the nature of their design. This clearance can initially be tight, but over time it increases appreciably due to shaft excursions and thermal growth. This increase in clearance increases parasitic leakage and engine performance losses. Ludwig and Bill (1980) point out that the losses associated with the increase in clearance of the labyrinth seal can result in as much as 17 percent loss in power and a 7-1/2 percent increase in specific fuel consumption (SFC) over time. With the demands of greater performance and reduced fuel consumption being placed on advanced engines, the need for improved sealing techniques is imperative.

The idea of replacing labyrinth seals with brush seals was first investigated in 1955 under the General Electric (GE) J-47 engine test, which proved unsuccessful. Rolls Royce success-

fully tested brush seals in some of their demonstrator engines in the 1980s, followed by a test on a production standard RB-199 in 1987. At present, the only production engine with brush seals is the IAE V2500, which was certified in 1987. This engine has brush seals in three locations, the high-pressure compressor delivery and the front bearing chamber as pressure balance seals. Allison has successfully tested brush seals in two of their engines to date (Holle and Krishnan, 1990). The first was the T800, which was tested with a brush seal at the power turbine discharge location. The second was the T406 Plus, which had 13 brush seals at compressor interstage locations and six in the engine hot section. These Allison tests demonstrated not only leakage flow reductions of up to an order of magnitude over labyrinth seals, but also the tolerance of brush seals to transient clearance changes.

Over the past couple of years, research on brush seals has increased with several papers published (Braun et al., 1990; Conner and Childs, 1990; Ferguson, 1988; Flower, 1990; Gorelov et al., 1988; Holle and Krishnan, 1990; Mullen et al., 1990). Results from these research programs have been very positive. They have shown that brush seals can offer dramatic reductions in parasitic leakage, improved flow metering capability, and better rotordynamic characteristics compared to conventional labyrinth seals.

Brush Seal Investigation

The brush seal investigation described in this paper was initiated in September 1988 and was completed July of 1990. The objective was to determine leakage and wear characteristics and cost impacts of brush seals compared to labyrinth seals. Limited-life engines were the primary applications considered. The investigation included: an engine study to identify potential locations to install brush seals; design and fabrication of an elevated temperature, rotating test rig; and testing of candidate brush seal configurations. The rig was designed to simulate subsonic and supersonic applications of limited-life engines, but the initial testing was limited to subsonic simulations.

In the engine study, selected state-of-the-art, limited-life engines were considered in determining potential locations for brush seals to replace labyrinth seals. Figure 2 summarizes the results of the study. This figure illustrates seven different locations to install brush seals and gives the corresponding operating conditions at these locations. Two prime locations, i.e., compressor backface (*B*) and turbine front face (*C*), were identified as the best locations to apply brush seals. These locations offer the maximum potential for reducing leakage and thus increasing engine performance.

Also in the study, engine cycle data were analyzed to determine a test cycle for the seal rig testing. The cycle chosen is representative for limited-life engines and has an initial maximum power condition (100 percent engine speed) for 10 minutes, corresponding to launch at altitude, followed by a cruise power condition (85 percent engine speed) for 35 minutes, corresponding to cruise operation at sea level.

Experiment

The brush seal test rig, designed and built in the investigation, is driven by an air turbine that rotates the rig up to

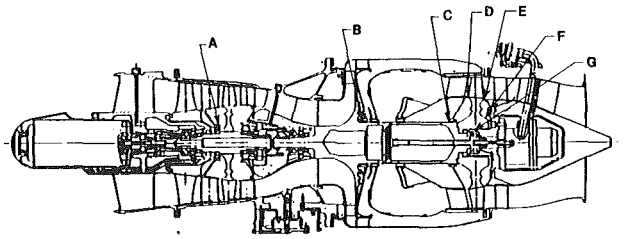

PARAMETER	LOCATION						
	A	B	C	D	E	F	G
Inlet temperature, F	305	490–920	500–1200	660–1250	1180	1260	1180
Seal material temperature, F	305	550–920	535–1220	900–1450	1200	1290	1190
Inlet pressure, psia	59	80–300	81–380	35–340	325	275	325
Seal pressure drop, psid	19	35–145	42–155	0.4–55	48	100	310
Disk surface velocity, ft/sec	720	570–915	570–915	1185–189	785	1185	500
Flow rate, lb/sec	minimal	.064–.140	.039–.780	.039–.780	.735	.735	.152
Δ P/Pin	0.320	0.34–0.48	.110–.570	.0055–.160	.150	.360	.955

Fig. 2 Summary of limited-life engine study

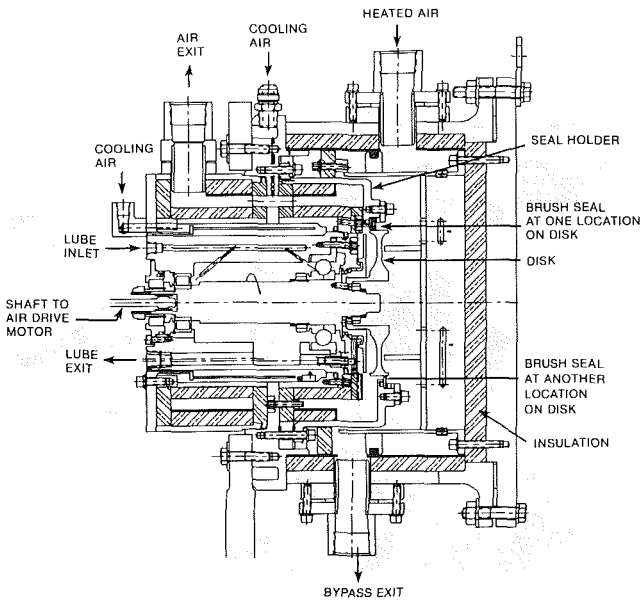

Fig. 3 Cross section of rotating test rig

40,000 rpm. The test disk diameter is 5.10 in. so that the maximum test surface speed is nearly 900 ft/sec. The rig is provided with various cooling and buffering air to protect the static structure. The bearings are lubricated and cooled by a circulating lubrication system. Heated air is supplied to the rig at temperatures up to 1500°F. The maximum allowable pressure of the test air is between 65 and 200 psia depending upon the air temperature level.

Figure 3 shows a cross section of the test rig with the various rig interfaces and features identified. Figure 4 is a photograph of the rig with a brush seal being installed and Fig. 5 is a photograph of a brush seal and test disk. The disks are coated to investigate the effect on performance and wear of the surface running against the brush seal. The seal holder as configured at the top of the disk in Fig. 3 can hold up to three brush seals so that multiple brush seals in series can be tested. The seal holder axial location is adjustable, as shown below the disk in

Nomenclature

CL = labyrinth seal radial clearance, in.
N = disk rotational speed, rpm
Pd, PD = exit air pressure, psia
Pu, Pin = inlet air pressure, psia
T, Ta = inlet air temperature, °F or R
Tm = seal material temperature, °F
V = disk surface speed, ft/sec
W = air flow rate, lb/sec
ΔP = pressure drop across seal, psid
ϕ = flow factor = $W\sqrt{T}/Pu$, lb$\sqrt{R}$/(psia * sec)

Fig. 3, so that the seal could be located at four different axial locations. This allowed up to four different individual brush seals to be tested separately with a given disk. A labyrinth seal ring that fit into the holder was provided so that flow comparison between labyrinth and brush seals could be made.

Rig instrumentation was provided to measure: shaft rotational speed, inlet and exit pressures, flow rate, air temperatures, and various rig monitoring temperatures, pressures and vibrations. Multiple probes were used for the seal inlet and exit pressure and the seal inlet temperature so that more accurate, representative data could be obtained. The seal flow rate was measured using an upstream orifice.

An initial series of tests was conducted on the brush seal rig. The testing was limited to investigating current brush seal designs as applied to subsonic, limited-life gas turbine engines. The maximum test temperature was approximately 600°F, which simulates subsonic applications. The initial test matrix included 15 brush seals and one reference labyrinth seal, as summarized in Table 1. The seal parameters investigated include: initial seal/disk interference, backplate gap height, repeatability, bristle surface finish operation, disk surface treatment, number of seals in series, operating temperature, and seal vendor. Brush seal configuration #1 in Table 1 was the baseline brush seal. It had nominal values for the various seal design parameters. The other configurations in Table 1 had variations in one or more of the seal/disk parameters to see their effect. All the seals tested except the last two listed were supplied by Cross Manufacturing Co. (1938) Ltd. of Devizes, Wilts, England. The last two seals were supplied by EG&G Sealol Engineering Products of Warwick, RI, and Textron Turbo Components of Walled Lake, MI. These last two seals replaced configurations #12 and #15, which were originally planned to be tested.

A four-phase approach was followed in testing each brush seal. First, an *ambient temperature flow performance* check was conducted at two moderate rotational speeds (15,000 and 25,000 rpm) to insure that the seal was properly installed. The

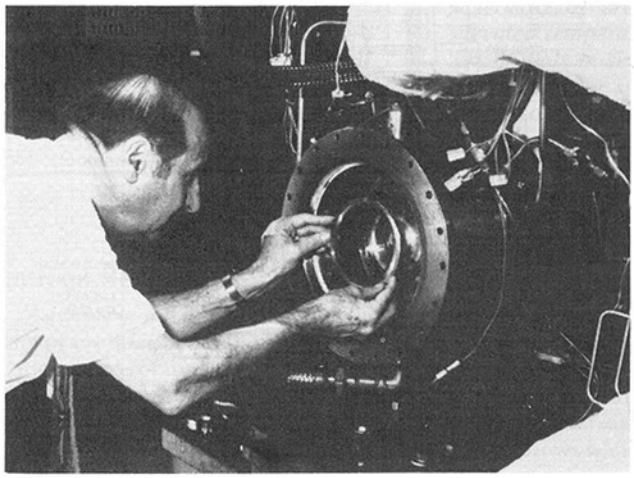

Fig. 4 Brush seal being installed in the rig

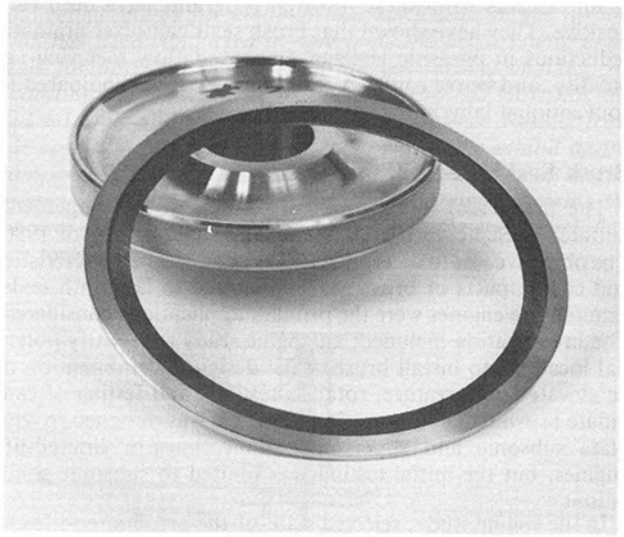

Fig. 5 Brush seal and coated test disk

Table 1 Initial seal test matrix

CONFIG #	INITIAL INTERF in	BACKPLATE HEIGHT in	BRISTLE HEIGHT in	BRISTLE ANGLE deg	BRISTLE DIA. in	BRISTLE DENSITY per in.circm	BRUSHES IN SERIES	PLATE/ BRISTLE MAT'L	BRISTLE SURFACE FINISH	SHAFT TREAT.	SHAFT INITIAL ROUGHNESS μin.	OPER. TEMP. F
1	0.005	0.030	0.286	45.0	0.0028	2450	1	N75/HA25	GROUND	Al O	30–40	600
2	"	"	"	"	"	"	"	"	"	"	"	400
3	0.001	"	"	"	"	"	"	"	"	"	"	600
4	0.005	0.020	"	"	"	"	"	"	"	"	"	"
5	"	0.030	"	"	"	"	"	"	"	"	"	"
6	"	"	"	30.0	"	"	"	"	"	"	"	"
7	"	"	"	45.0	"	"	"	"	"	Chr/Carb	20–30	"
8	"	"	"	"	"	"	2	"	"	Al O	30–40	"
9	"	"	"	"	"	"	1	"	NONE	NONE	10	"
10	"	"	"	"	"	"	"	"	GROUND	Al O	30–40	1300+
11	"	"	"	"	"	"	"	"	NONE	"	"	600
12 *	"	"	0.191	40	0.0020	4300	"	"	GROUND	"	"	"
13	0.008	"	0.286	45	0.0028	2450	"	"	"	"	"	"
14	0.005	"	"	"	"	"	"	X750	"	Chr/Carb	20–30	"
15 *	"	"	"	"	"	"	"	N75/HA25	"	Al O	30–40	"
A1	SIMILAR TO SEAL CONFIG. #1 EXCEPT SUPPLIED BY EG&G SEALOL									"	"	"
A2	TEXTRON 3-D BRAIDED COMPLIANT SEAL									"	"	"
REF	REFERENCE 4-KNIFE LABYRINTH SEAL WITH STATIC CL = 0.008 IN									"	"	"

" = Same as parameter value above
* = *Replaced by other vendor seals*
N75 = Nimonic 75
HA25 = Haynes 25
Seal Radial Height = 0.45 in
Seal Offset = 0.000 in
Bristle Packing Thickness = 0.027 in

Al O = Aluminum oxide coating
(Plasma sprayed METCO coating P105–13 per METCO Instruction 105NS to a thickness of 0.006 to 0.010 inches after final grind, over a 0.003 inch thickness of METCO 450 bond coat.)
Chr/Carb = Chromium carbide coating
(Plasma sprayed METCO chromium carbide P81VF–10 coating per METCO Bulletin 81VF–NS, to a thickness of 0.005 to 0.010 inches after final grind.)

running time for this check was short to minimize seal wear. Second, a *cycle simulation* was performed that modeled a limited-life engine cycle. The test cycle consisted of establishing the desired seal air temperature and upstream and downstream pressures, accelerating the rig to a designated maximum speed condition (35,000 rpm) and holding that speed for 10 minutes to model a launch condition. The speed was then lowered to 85 percent of maximum speed (30,000 rpm), the pressures reset to new values, and the lower speed maintained for an additional 35 minutes. This second speed condition modeled cruise operation. Third, *leakage flow performance* data were acquired by setting the speed at a desired value, lowering the pressure drop across the seal to nearly zero, and taking data points at successively higher pressure drops until a maximum of 115 psid (rig design limit) is reached. Data points were then acquired at successively lower pressure drops until nearly zero is reached again. Fourth, *wear evaluations* were made by testing a seal for a series of one hour time intervals at a higher speed (35,000 rpm) and making an abbreviated performance check after each hour. Most of the seals were tested for a total of four to eight hours. This total test time was established after it was determined for configuration #1 that most of the wear occurs in the first four hours. The rig rotational speeds were selected to match the limited-life engine applications and rig vibrational limits.

Results

Initial results from this investigation, reported earlier (Chupp and Nelson, 1990), showed that brush seals: (1) have significantly lower leakage (factor of 3 or more) compared to labyrinth seals; (2) have leakage characteristics that vary with rotational speed changes; (3) have an initial wear-in period (of about four hours) and then wear slowly; and (4) have performance and wear characteristics that vary with initial interference and disk surface finish/bristle final machining operation. These findings were based on data reported for configurations #1, #3, and #9 (see Table 1).

In this paper, results for four additional configurations will be presented and compared with the previous data. These four configurations are #4, #5, #8, and #A1, as listed in Table 1, and reflect the effects of backplate gap, repeatability, two seals in series, and seal vendor, respectively. The results presented will primarily involve leakage performance, i.e., seal flow factor versus seal pressure ratio parameter. Typical engine cycle simulation results also will be given. Wear testing data for these configurations are similar to that reported previously and will not be covered here.

Engine Cycle Simulation Results. Typical engine cycle simulation results for two brush seal configurations are given in Fig. 6. Configuration #1 is the baseline and configuration #5 has the same seal construction parameter values as the baseline to determine repeatability. This figure is a plot of leakage flow factor and disk rpm versus test time. The points are individual data points and the lines show approximately how the flow and speed vary between points. During the initial period, the speed is stepped up to 35,000 rpm and then maintained at that speed (launch condition). The leakage flow starts out low for the well-compacted brush with a moderate interference. As the disk diameter increases with increasing speed, the bristles adjust slowly to the diameter change because the pressure drop across the seal hold them in place. After the initial "launch" period, the change in flow is small, indicating that a nearly equilibrium condition has been reached. The rig speed is then decreased to 30,000 rpm (cruise condition). The leakage flow initially jumps up as the disk diameter decreases with the sudden decrease in speed, and the bristles respond slowly with the imposed pressure drop. Within about seven minutes steady state is reached. The leakage flow characteristics of configurations #1 and #5 in Fig. 6 are similar, with the final flows agreeing within 3 percent. Thus, the response of the bristle packing was very repeatable. The data in Fig. 6 demonstrate the performance repeatability obtainable from brush seals and from the test rig.

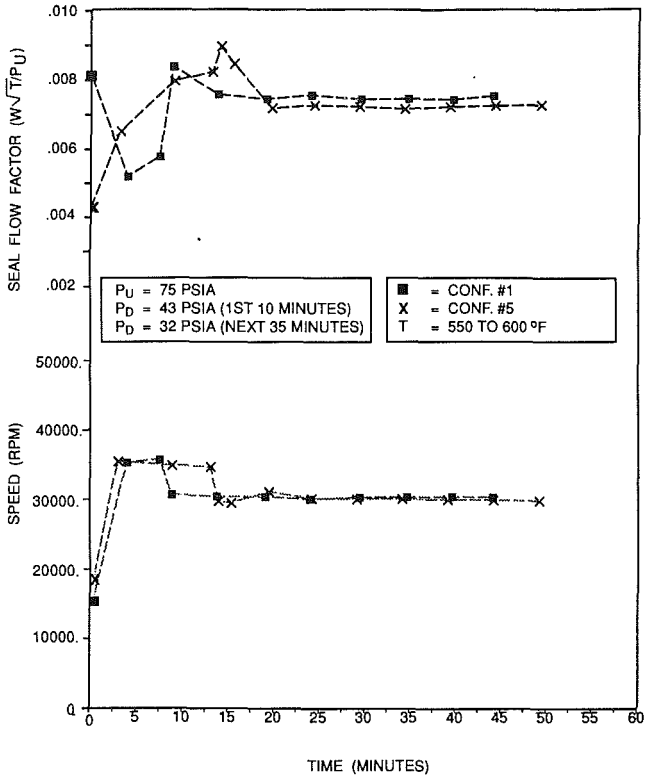

Fig. 6 Engine simulation cycle results for brush seal configurations #1 and #5

Performance Testing Results. Testing to acquire performance results was done immediately after the cycle simulation testing for most of the brush seals. Some seal wear would have occurred by then, but the flow characteristics should still be representative for limited-life engine applications. Figure 7 shows performance plots obtained for configurations #1 and #3 brush seals and the reference labyrinth seal at approximately 30,000 rpm and 500 to 600°F air temperature. These data were presented previously in separate plots (Chupp and Nelson, 1990) and are given here for comparison purposes. Figure 7 is a plot of flow factor versus a pressure ratio parameter that approximately linearizes the data at lower pressure ratios. The pressure drop parameter was derived from porous-wall flow expressions (Green and Duwez, 1951). The data points in Fig. 7 are stabilized ones taken three to six minutes after setting off a pressure drop condition. For the brush seal data, the first data point was for a very low pressure drop for which the bristles are in a relaxed position and a minimum flow factor is measured. Pressure drop was then successively increased, yielding the lower portion of the curve. The pressure drop was then successively decreased and the upper curve was obtained. The resulting brush seal data in Fig. 7 are classical hysteresis curves. The difference between the upper and lower curves is due in part to the bristles being displaced radially outward by the disk during the performance testing as the rig encounters small speed changes between test points. Speed increases cause the disk diameter to increase slightly and the bristles to be pushed out. Although the rig speed returns rapidly to the nominal value, the bristles respond slowly for the higher imposed pressure drops (higher values of pressure ratio parameter).

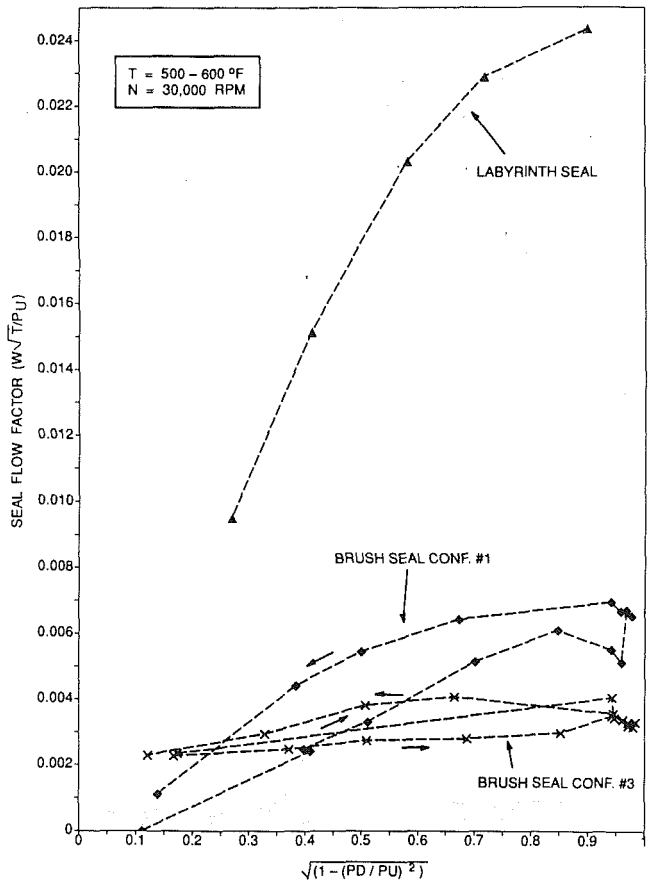

Fig. 7 Comparison of leakage flow performance results for brush seal configurations #1 and #3 versus the labyrinth seal

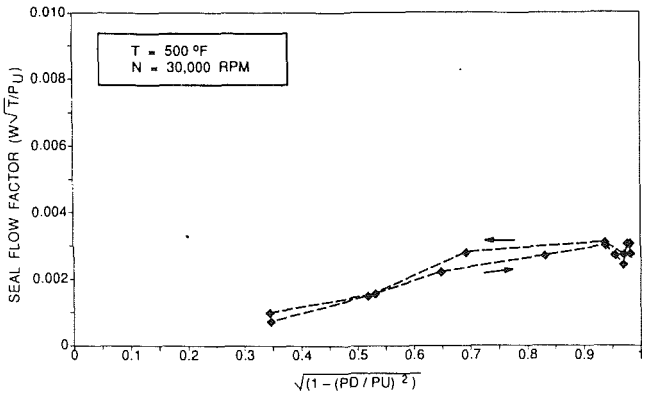

Fig. 8 Measured flow performance for brush seal configuration #8 with two seals in series

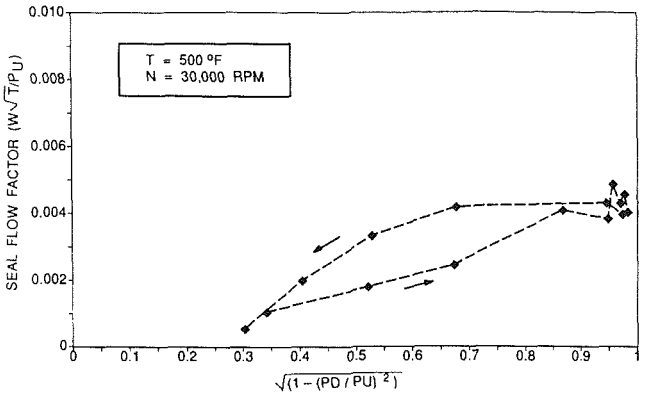

Fig. 9 Measured flow performance for brush seal configuration #A1 manufactured by a second vendor

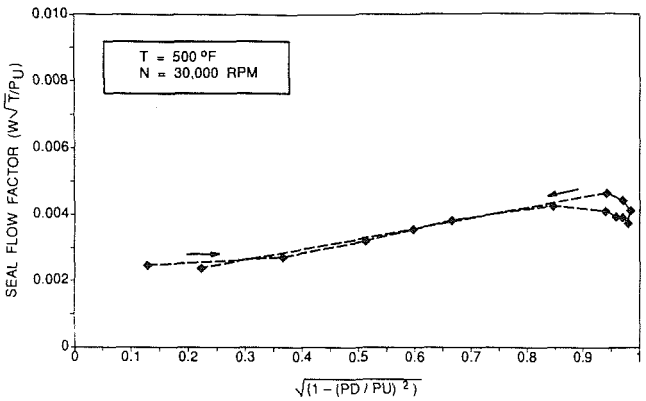

Fig. 10 Measured flow performance for brush seal configuration #4 with a smaller backplate gap

The data in Fig. 7 demonstrate the significantly lower leakage (factor of four to seven) of the brush seals compared to the reference labyrinth seal (with a radial clearance of about 0.006 in.). Further, these data show a significant difference in flow characteristics between the two brush seal configurations. Configuration #3 is identical with #1 except for the initial interference values (see Table 1). The difference in leakage was attributed primarily to seal-to-seal variations and amount of bristle wear incurred, and not the initial interference.

Two Seals in Series. Multiple brush seals in series were included in the test matrix because the pressure drop across any one seal is lower. This is important for higher pressure drop applications where higher forces on the bristles would deflect them under the backplate. Figure 8 gives flow performance results for configuration #8 that had two baseline configuration brush seals (#1) in series. The resultant hysteresis curve is similar to that for single brush seals except the level is lower and the variation between the upper and lower portions of the curve is less. In all the testing of this configuration, the leakage was not as sensitive to disk speed changes as it was for the single brush seals. Thus, two brush seals in series not only allow a higher pressure drop, but also reduce the flow leakage even for the lower pressure drops tested in this investigation and are less sensitive to disk speed changes than a single brush seal.

Different Seal Vendor. Figure 9 gives the leakage performance results for a brush seal manufactured by EG&G Sealol. It had dimensional parameter values approximately the same as those of the baseline configuration. The resultant hysteresis curve is similar to that of configurations #1 and #3 in Fig. 7. The leakage level is between that for these two configurations, but closer to the lower results of configuration #3. Thus, this brush seal from the second vendor yields leakage characteristics comparable to those of the baseline configurations.

Backplate Gap. Figure 10 gives the leakage performance results for configuration #4, which had a backplate gap of 0.020 in. compared to 0.030 in. for the baseline configuration. The resultant flow factor level is within the range of the other seals. The hysteresis curve in Fig. 10 has a very small difference between the upper and lower portions, but his seal in other testing reacted to disk speed changes similarly to the baseline one. Thus, lowering the backplate gap to 0.020 in. has little effect on the leakage flow characteristics.

To evaluate further the effect of backplate gap, a special series of tests was run at Cross Manufacturing facilities on

brush seal configuration #10. This configuration is the same as #1 and was to be rig tested later. The purpose of these tests was to quantify the relationship between maximum recommended pressure drop across a single brush seal and the backplate gap as the gap is increased above the nominal 0.030 in. Although Cross's rotating seal test rig operates with ambient temperature air and ambient downstream pressure, the results are representative of engine applications. The test approach was to evaluate the leakage performance for several backplate gaps of the same seal by successively removing material from the backplate inner surface and measuring performance. The backplate machining was done without affecting the bristles.

Figure 11 is a summary plot of the data obtained by Cross. It is a cross plot of the individual performance data curves and gives flow factor versus backplate gap for six pressure drop values. The smallest gap (0.032 in.) represents the nominal value for the baseline configuration. The data for this gap were obtained before removing any backplate material. The increase in flow factor with increasing pressure drop at the lower gap values is the expected effect of pressure ratio across the seal

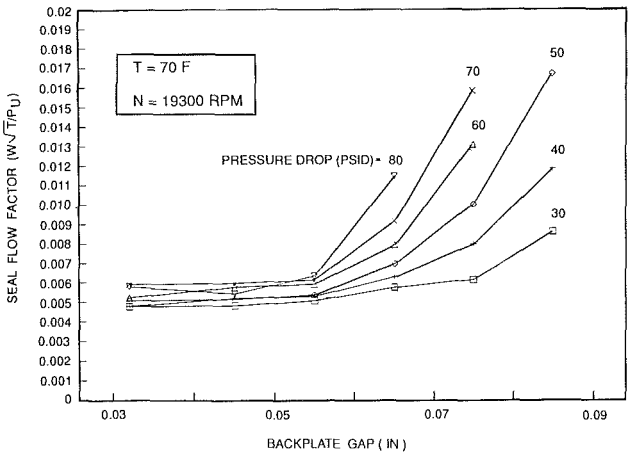

Fig. 11 Cross plot of flow performance data from Cross Manufacturing showing effect of increasing backplate gap

on leakage. For backplate gap values up to 0.055 in., the flow factor is essentially constant for a given pressure drop. As the gap increases above 0.055 in., the flow factor becomes a function of gap and a stronger function of pressure drop. Thus, at backplate gap of 0.055 in. the bristles begin to deflect under the backplate and the effective flow area increases. The amount of bristle deflection depends upon the pressure drop, but some increase in flow factor is noted even for the 30 psid data. The maximum recommended backplate gap for the bristle thickness and packing density considered in this investigation is then 0.055 in.

Performance Comparisons. Table 2 is a summary of leakage flow results obtained in this investigation. This table gives the available seal flow factor data measured at the end of the engine simulation test and at three pressure ratios in the performance testing. Also included are data for the labyrinth seal and results from the Cross testing with variable backplate gap. In the performance testing portion of the data in Table 2, the flow factor value listed is a mean value from the upper and lower portions of the hysteresis curve at a given pressure ratio.

Observations that can be drawn from the data comparison in Table 2 are:

- The performance testing gave a lower flow factor than that at the end of the simulation testing (i.e., pressure ratio near 2.3). This is due to differences in the pressure/speed history before acquiring the data points. Toward the end of the simulation testing, the bristles have come to an equilibrium point but are still not as close to the disk surface as they would be in the performance testing where the pressure drop has been decreased until the bristles are in a relaxed position. Thus, in engine applications the actual leakage may not be as low as measured in performance testing.
- The leakage flow factor for brush seals with baseline parameter values is between 0.0035 and 0.0060. The actual baseline configuration (#1) had a flow factor at the higher end of this range, but the other seals indicate that a more representative baseline flow factor is closer to 0.0040.
- Testing the baseline configuration at a test temperature near 400°F instead of 600°F (configuration #2 versus #1) had only a small effect on leakage flow factor.
- Decreasing the initial interference from a baseline value of

Table 2 Summary of leakage flow results for the various seals tested

CONFIG #	PARAMETER VARIED	BACKPLATE GAP (in)		FLOW FACTOR – W √T/PU			
			TEST:	SIMULATION	PERFORMANCE *		
			PRESSURE RATIO:	2.34	1.51	2.29	3.20
			PR. RAT. PARAMETER:	0.904	0.750	0.900	0.950
			TEMPERATURE (F)				
1	Baseline	0.030	600	0.0075	0.0061	0.0063	0.0062
2	Baseline at lower Temp.	0.030	400		0.0058	0.0060	0.0055
3	Initial interfer. = 0.001 in.	0.030	600	0.0066	0.0034	0.0035	0.0035
4	Backplate gap = 0.020 in	0.020	600	0.0057	0.0040	0.0044	0.0043
5	Repeat of baseline	0.030	600	0.0073			
8	Two seals in series	0.030	600	0.0036	0.0027	0.0029	0.0030
9	No I.D. grinding/shaft coating	0.030	600	0.0064	0.0033	0.0039	0.0040
A1	EG&G Sealol seal	0.030	600	0.0064	0.0036	0.0041	0.0041
Ref	Four-knife labyrinth seal	N/A	600		0.0234	0.0245	
10	Baseline seal tested at Cross	0.032	70			0.0048	0.0052
		0.045	70			0.0049	0.0052
		0.055	70			0.0051	0.0055
		0.065	70			0.0058	0.0070
		0.075	70			0.0062	0.0100
		0.085	70			0.0088	0.0168

* Flow factor for the Performance data are mean values of the upper and lower parts of the hysteresis curves at the given pressure ratios.

0.005 to 0.001 in. (configuration #3 versus #1) decreased the leakage, but the decrease is small considering the results from the other seals tested with near-baseline parameter values.

- The repeat simulation test of the baseline configuration (configuration #5) compared very closely with the baseline itself (configuration #1), thus proving brush seal and rig repeatability.
- Doubling the number of brush seals (configuration #8) yielded the lowest leakage performance (flow factor less than 0.003).
- Eliminating the final bristle grinding operation and running on an uncoated shaft (configuration #9) yielded flow performance close to the low end of the baseline range.

Conclusions

The results from the brush seal experimental investigation further demonstrate the potential of replacing labyrinth seal with brush seals, especially for subsonic, limited-life engine applications. The decreased leakage using brush seals would allow a better control of the cooling and leakage air flow rates that would decrease parasitic leakages and result in improved engine performance.

Specifically, the results of this investigation have shown that:

- Brush seals have a factor of four to seven less leakage than labyrinth seals.
- Performance characteristics, i.e., flow factor variations with pressure ratio across that seal, are a representative indication of the flow performance of brush seals, but actual flow leakage achieved in applications can be higher because of the pressure drop/shaft speed history.
- Brush seal leakage performance follows a hysteresis curve with the difference between upper and lower curve portions depending in part upon the disk speed excursions during the test.
- Changes in the initial bristle/disk interference for modest interference levels have marginal effect on the leakage characteristics.
- Multiple brush seals in series not only permit a higher pressure drop across the seals but also reduce the leakage level and sensitivity to disk speed changes.
- The maximum recommended backplate gap for the nominal bristle packing thickness and density is 0.055 in.
- Performance characteristics of brush seals manufactured by two different vendors were similar.

Acknowledgments

This investigation was sponsored by Aero Propulsion and Power Directorate (APPD), Wright Laboratory (WL), Aeronautical Systems Division (AFSC), United States Air Force, Wright-Patterson AFB, OH 45433-6563. Funding was also provided by Teledyne CAE. The authors would like to thank the many people who have contributed in this investigation. We would especially like to note the contributions of Air Force personnel: Lt. Paul Nelson and Lt. Gary Wilmes, previous contract technical monitors; vendor support from: Ralph Flowers of Cross Manufacturing, Chuck Nevola and Godwin Abele of EG&G Sealol, and Carlos Bailey of Textron Turbo Components; and many different individuals at Teledyne CAE.

References

Braun, M., Canacci V., and Hendricks, R., 1990, "Flow Visualization and Motion Analysis for a Series of Four Sequential Brush Seals," AIAA Paper No. 90-2482.

Chupp, R. E., and Nelson, P., 1990, "Evaluation of Brush Seals for Limited-Life Engines," AIAA Paper No. 90-2140.

Conner, K. J., and Childs, D. W., 1990, "Rotordynamic Coefficient Test Results for a 4-Stage Brush Seal," AIAA Paper No. 90-2139.

Ferguson, J. G., 1988, "Brushes as High Performance Gas Turbine Seals," ASME Paper No. 88-GT-182.

Flower, R., 1990, "Brush Seal Development System," AIAA Paper No. 90-2143.

Gorelov, G. M., Reznik, V. E., and Tsibizov, V. I., 1988, "Experimental Study of Brush Seal Flow Characteristics and Comparison With a Labyrinth Seal," *Izvestiya VUZ. Aviatsionnaya Tekhnika*, Vol. 31, No. 4, pp. 43–46.

Green L., Jr., and Duwez, P., 1951, "Fluid Flow Through Porous Metal," ASME *Journal of Applied Mechanics*, Vol. 18, pp. 39–45.

Holle, G. F., and Krishnan, M. R., 1990, "Gas Turbine Engine Brush Seal Applications," AIAA Paper No. 90-2142.

Ludwig, L. P., and Bill, R. C., 1980, "Gas Path Sealing in Turbine Engines," *ASLE Transactions*, Vol. 23, No. 1, pp. 1–22.

Moore, A., 1975, "Gas Turbine Engine Internal Air Systems: A Review of the Requirements and the Problems," ASME Paper No. 75-WA/GT-1.

Mullen, R. L., Braun, M. J., and Hendricks, R. C., 1990, "Numerical Modeling of Flows in Simulated Brush Seal Configuration," AIAA Paper No. 90-2141.

Brush Seal Leakage Performance With Gaseous Working Fluids at Static and Low Rotor Speed Conditions

J. A. Carlile

R. C. Hendricks

D. A. Yoder

NASA Lewis Research Center,
Cleveland, OH 44135

The leakage performance of a brush seal with gaseous working fluids at static and low rotor speed conditions was investigated. This report includes the leakage results for air, helium, and carbon dioxide at several bristle/rotor interferences. In addition, the effects of packing a lubricant into the bristles and also of reversing the pressure drop across the seal were investigated. Results were compared to that of an annular seal at similar operating conditions. In order to generalize the results, they were correlated using corresponding state theory. The brush seal tested had a bore diameter of 3.792 cm (1.4930 in.), a fence height of 0.0635 cm (0.025 in.), and 1800 bristles/cm-circumference (4500 bristles/in.-circumference). Various bristle/rotor radial interferences were achieved by using a tapered rotor. The brush seal reduced the leakage in comparison with the annular seal, up to 9.5 times. Reversing the pressure drop across the brush seal produced leakage rates approximately the same as that of the annular seal. Addition of a lubricant reduced the leakage by 2.5 times when compared to a nonlubricated brush seal. The air and carbon dioxide data were successfully correlated using the corresponding state theory. However, the helium data followed a different curve from the air and carbon dioxide data.

Introduction

A brush seal is a compliant seal and, as seen in Fig. 1, consists of a bristle pack held between two washers. The bristles have an initial radial interference with the rotor and are angled 30 to 60 deg from the radial centerline. This arrangement allows the seal to adapt easily to thermal effects, machining tolerances, and shaft excursions. In order for conventional seals (such as labyrinth and annular seals) to meet the same adaptability requirements, they require a clearance between the rotor and seal. Thus, brush seals have the potential to reduce the leakage over conventional seals significantly.

The back washer is designed as an annular seal so that it is as close to the rotor as possible while still accommodating shaft excursions and growth due to thermal and centrifugal effects. Since brush seals are a contacting seal, bristle material and rotor coating become a major design consideration. Because of this, the bristles are made of a superalloy (e.g., Haynes 25 and Hastelloy X), and the rotor is coated with a highly polished ceramic such as yttria-stabilized ZrO_2 or CrC.

Brush seals are currently being considered for such applications as gas turbine engines, turbopumps, gas compressors, and steam generators. Previous work demonstrates that brush seals reduce leakage from one-third to one-fourth that of four and five-cavity labyrinth seals (Flower, 1990; Gorelov et al., 1988). Ferguson (1988) found the leakage to be 1/10 to 1/20 that of labyrinth seals running in the same turbomachine with clearances of 0.75 mm. In addition, brush seals have been found by Childs (1990) to enhance rotor stability compared to labyrinth seals. For these investigations, air was used for the working fluid, and little information exists in the open literature for other working fluids. For this paper, the performance of a brush seal using gaseous air, carbon dioxide, and helium for the test fluids is presented.

Several analytical models for brush seals have been developed. A bulk flow model has been developed by Braun et al. (1990) and Hendricks et al. (1991a). Chupp et al. (1991) developed a model that generalizes the results over a range of conditions using the effective thickness of the bristle pack. The model is especially effective in accounting for fluid thermal effects at high pressure ratios. For this paper, the results are correlated using corresponding state theory. This method produces a single curve which is a function of the brush seal geometry, from which the leakage performance can be predicted for any fluid at any state.

Several other considerations were investigated for this report. The effect of reversing the pressure drop across the brush seal was studied for application to cases where the brush seal is installed improperly or reverse flow occurs during adverse

Contributed by the International Gas Turbine Institute and presented at the 37th International Gas Turbine and Aeroengine Congress and Exposition, Cologne, Germany, June 1-4, 1992. Manuscript received by the International Gas Turbine Institute February 24, 1992. Paper No. 92-GT-304. Associate Technical Editor: L. S. Langston.

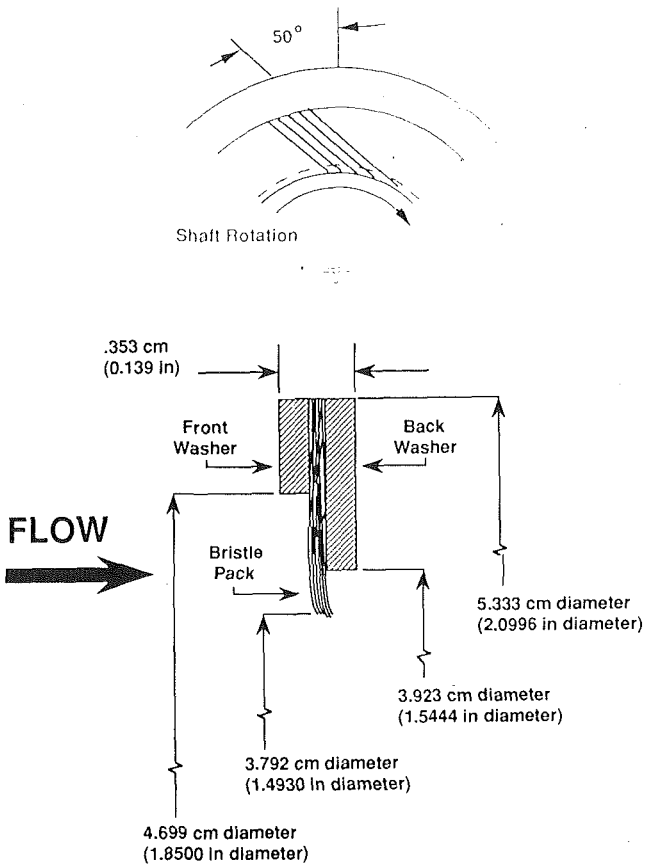

Fig. 1 Brush seal geometry

engine operation. In addition, the effect of putting a lubricant into the brush seal pack was examined.

Data for gaseous air, helium, and carbon dioxide are presented for static and dynamic rotor conditions. Air data are given for bristle/rotor radial interferences of 0.0018 and 0.0061 cm (0.0007 and 0.0024 in.). Helium data are given for bristle/rotor radial interferences of 0.0033 and 0.0061 cm (0.0013 and 0.0024 in.). Carbon dioxide data are given for a bristle/rotor radial interference of 0.0061 cm (0.0024 in.). The results of correlating the data using corresponding states theory are presented. For comparison purposes, an annular seal was tested in air and helium, and the results were compared to that of the brush seal. In addition, results of the seal packed with a lubricant and also of a seal tested with the pressure drop reversed are presented.

Seal Assembly

A bench-scale apparatus shown in Fig. 2 was used for this investigation. The apparatus consisted of a pressure vessel, rotor, and seal. The pressure vessel held the seal in position and acted as a circumferential seal on the outside diameter. There were two openings for the working fluid to enter near

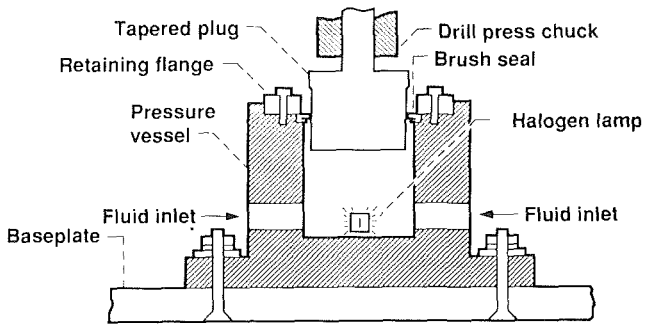

Fig. 2 Schematic of test apparatus

the base of the vessel located 180 deg apart. A halogen light was placed in the bottom of the pressure vessel for alignment purposes and to act as a back light for visualization of the bristle/rotor dynamics.

The 304 stainless steel rotor shown in Fig. 3 was driven by a drill press. It was tapered so that the bristle/rotor interference could be changed by adjusting the vertical height. The taper ranged from 38.6 to 37.8 mm (1.5202 to 1.4877 in.) in diameter over 25.36 mm (0.9986 in.). Since the seals axial lengths were small, the taper did not affect the leakage.

Seal Design

Both a brush seal and an annular seal were tested for comparison purposes. The geometry of the brush seal is given in Table 1 and is shown in Fig. 1. The brush seal was 0.353 cm (0.139 in.) thick and had a bore diameter of 3.792 cm (1.4930 in.). The outside diameter was 5.333 cm (2.0996 in.). The inside diameters of the front and back washers were 4.699 and 3.923 cm (1.8500 and 1.5444 in.), respectively. Thus, the fence height (i.e., the radial free length of the extension of the bristles beyond the back washer) was 0.0635 cm (0.025 in.) The bristles were made of Haynes 25 and angled 50 deg from the radial centerline. The bristles were 0.0051 cm (0.002 in.) in diameter and had a packing density of 1800/cm-circumference (4500 bristles/in.-circumference).

For comparison purposes, the annular seal was designed to have the same axial length as the brush seal, 0.353 cm (0.139 in.). It had an inside diameter of 3.8610 cm (1.5200 in.), which is equal to the diameter at the top of the rotor taper. Again, by changing the height of the rotor the clearance could be changed and a range of leakages could be determined.

Test Facility

A flow schematic of the system including instrumentation is shown by Schlumberger et al. (1991). Based on the flow rate, one of three parallel flow lines, each having a calibrated venturi meter, was used. The test fluid temperature and pressure were measured near the inlet to the pressure vessel (line losses were approximately 6 percent of the inlet pressure). The exit pressure was assumed to be equal to the measured ambient pressure. All temperatures were measured using type E (Cu/

Nomenclature

$a_1 \ldots a_5$ = const
$b_1 \ldots b_4$ = const
C_f = flow coefficient
f = ratio of fluid α temperature to fluid o temperature
G = mass flow rate
G^* = mass flow rate based on critical properties
g = Gibb's free energy
h = ratio of fluid α volume to fluid o volume
P = pressure
R = universal gas constant
T = temperature
V = volume
Z = compressibility
ρ = density
ω = acentric factor

Subscripts

c = critical constant
in = inlet
o = property of known fluid
r = reduced parameter
α = property of fluid to be predicted
θ = thermal correction factor
ϕ = volume correction factor

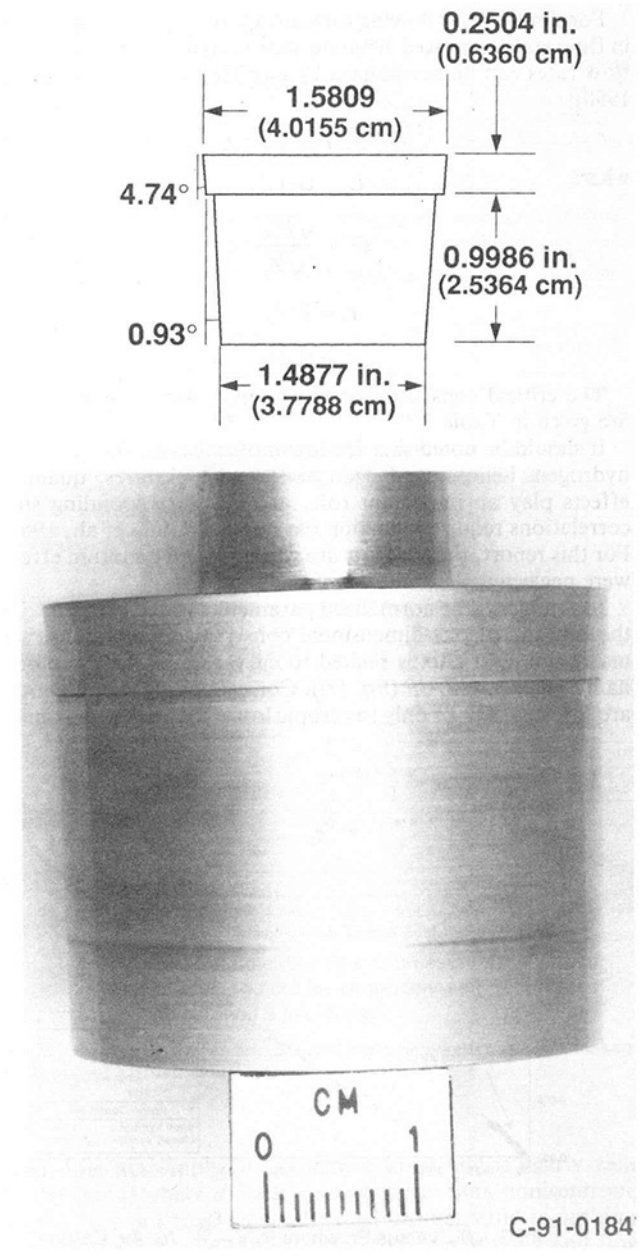

Fig. 3 Photo and schematic of the tapered rotor

Ni) thermocouples and pressures by strain-gage pressure transducers.

Test Configurations

The test configurations are summarized in Table 2. Data were first taken for the brush seal at a bristle/rotor radial interference of 0.0061 cm (0.0024 in.) with gaseous air, helium, and carbon dioxide for the test fluids. Additional data were taken at radial interferences of 0.0018 and 0.0033 cm (0.0007 and 0.0013 in.) for air and helium, respectively.

Next, the brush seal was inverted so that the pressure drop would be applied in the reverse direction. This configuration had a radial interference of 0.0053 cm (0.0021 in.) and was tested with air. Due to the direction of the bristle angle with the rotor, only data with a static rotor were taken.

A lubricant (halocarbon grease) was put into the bristle pack and along the inside diameter. This configuration was tested with air as the working fluid and a radial interference of 0.0061 cm (0.0024 in.).

Lastly, an annular seal was tested for comparison purposes.

Table 1 Brush seal system specification

Brush seal outside diameter	5.333 cm (2.0996 in.)
Brush seal inside diameter	3.792 cm (1.4930 in.)
Front washer inside diameter	4.699 cm (1.8500 in.)
Back washer inside diameter	3.923 cm (1.5444 in.)
Brush seal axial diameter	0.353 cm (0.139 in.)
Bristle diameter	0.0051 cm (0.0020 in.)
Pack density	1800/cm-circ (4500/in.-circ)
Angle of bristles from radial centerline	50°
Bristle material	Haynes 25
Rotor material	304 Stainless steel

Table 2 Test conditions

Configuration / radial clearance	Air	Helium	Carbon dioxide
Brush seal			
-0.0061 cm (-0.0024 in.)	x	x	x
-0.0018 cm (-0.0007 in.)	x		
-0.0033 cm (-0.0013 in.)		x	
Brush seal reversed			
-0.0053 cm (-0.0021 in.)	x		
Brush seal lubricated			
-0.0061 cm (-0.0024 in.)	x		
Annular seal			
0.0053 cm (0.0021 in.)	x		
0.0178 cm (0.0070 in.)	x		
0.0302 cm (0.0119 in.)		x	

For air, it was tested at radial clearances of 0.0053 and 0.0178 cm (0.0021 and 0.0070 in.). For helium, it was tested at a radial clearance of 0.0302 cm (0.0119 in.) These clearances were selected in order to obtain the leakage rates over a feasible working range.

Before each run, the pressure transducers were calibrated, and the system purged. A hand valve was opened to allow the working fluid to enter the pressure vessel, flow through the seal, and exit to ambient. Data were taken as the pressure was increased and then decreased to determine hysteresis effects. This procedure was repeated for static and dynamic rotor conditions. For the dynamic condition, the shaft rotation was 400 rpm. The gases were at ambient temperature [285–295 K (513–531 R)].

Corresponding States

An analysis was performed to generalize the various working fluid data using corresponding state theory. The extended van der Waals theory of corresponding states had been verified for several fluids and fluid mixtures by Mollerup (1978) and applied to two-phase choked flow by Hendricks and Simoneau (1973) and Simoneau and Hendricks (1977).

The premise of corresponding states is that all thermodynamic surfaces can be mapped to a single surface when expanded about the thermodynamic critical point. Thus, the properties of a fluid (α) can be predicted using another fluid (O) when the proper mapping is used. Equations (1) and (2) give the mapping for compressibility and Gibb's free energy, respectively (Hendricks and Sengers, 1980):

$$Z_\alpha(V, T) = Z_o(V/h, T/f) \quad (1)$$

$$g_\alpha(V, T) = g_o(V/h, T/f) - RT\ln(h) \quad (2)$$

where

$$h = [V_{\alpha c}/V_{oc}]\phi$$

$$f = [T_{\alpha c}/T_{oc}]\theta$$

$$\phi = 1 + (\omega_\alpha - \omega_o)[b_1(V_r - b_2 - b_3(V_r - b_4)\ln T_r]$$

$$\theta = 1 + (\omega_\alpha - \omega_o)[a_1 - a_2 \ln T_r + (a_3 - a_4/T_r)(V_r - a_5)]$$

Values for $a_1 \ldots a_5$, $b_1 \ldots b_5$, ϕ, and θ can be found from McCarty (1977).

From this, it can be seen that mass flow substitution into the conventional Bernoulli equation gives

$$G_\alpha = C_{f_c} \frac{\sqrt{\Delta P/V}}{\sqrt{(h^2/f)(Z_o/Z_\alpha)_c}} \quad (3)$$

Table 3 Critical constants (GASP)

Fluid	T_c (K)	P_c (MPa)	ρ_c (g/cc)	Z_c	G^* (g/cm^{2}s)
Air	132.55	3.766	0.313	0.3162	6106
He	5.19	0.227	0.0693	0.3039	720
CO_2	304.21	7.3835	0.464	0.2769	11123

For simple gases flowing through a venturi, over large ranges in fluid states removed from the thermodynamic critical point, flow rates can be normalized by (see Hendricks and Sengers, 1980):

$$G\sqrt{T_r}/P_r = C_f/5.0 \quad (4)$$

where

$$G_r = G/G^*$$

$$G^* = \frac{\sqrt{P_c \rho_c}}{\sqrt{Z_c}}$$

$$T_r = T/T_c$$

$$P_r = P/P_c$$

The critical constants for air, helium, and carbon dioxide are given in Table 3.

It should be noted that for low-molecular-weight fluids like hydrogen, helium, and neon at low temperatures, quantum effects play an important role, and the corresponding state correlations require reduction parameters (Gunn et al., 1966). For this report, the temperature was high and quantum effects were neglected.

In summary, the normalized parameters stated evolved from the solution of one-dimensional conservation equations. The maximum mass flux is related to curvature of the thermodynamic surface, dV/dP (Eq. (3)). Corresponding state relations are strictly valid for only isentropic losses. Thus, the maximum

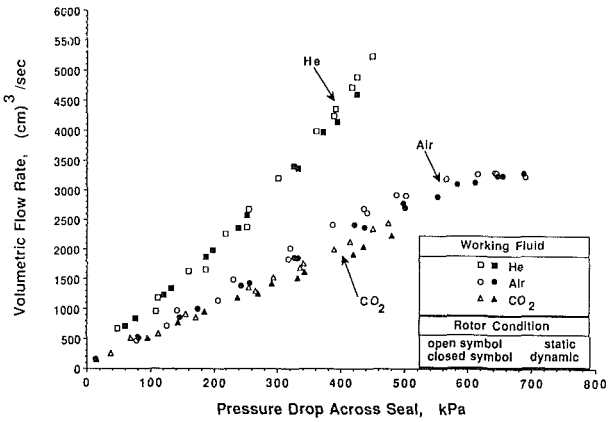

(a) Volumetric flow rate versus pressure drop across the brush seal for Helium, Air , and Carbon Dioxide.

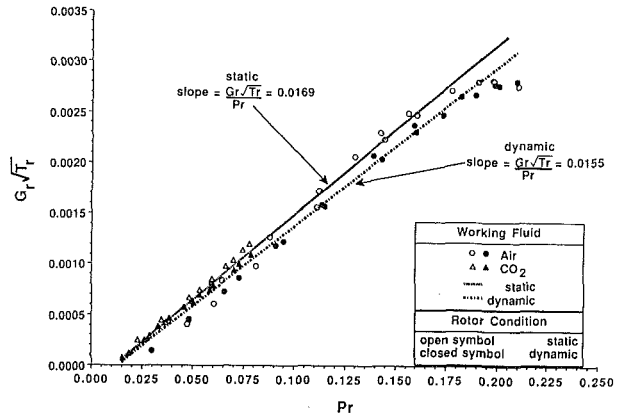

(b) $G_r\sqrt{T_r}$ versus Pr, where $P_r = \frac{P_{in}}{P_c}$, for Air and Carbon Dioxide.

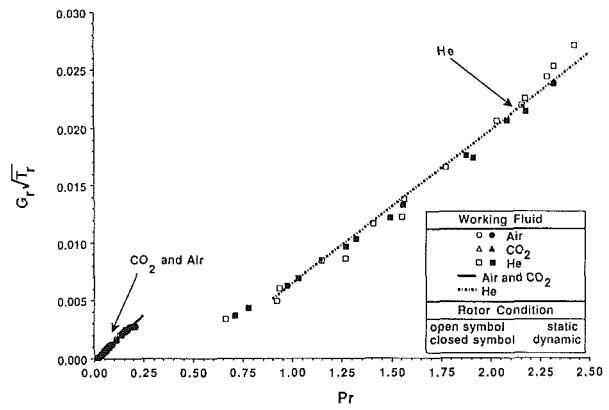

(c) $G_r\sqrt{T_r}$ versus Pr, where $P_r = \frac{P_{in}}{P_c}$, for Air, Carbon Dioxide, and Helium.

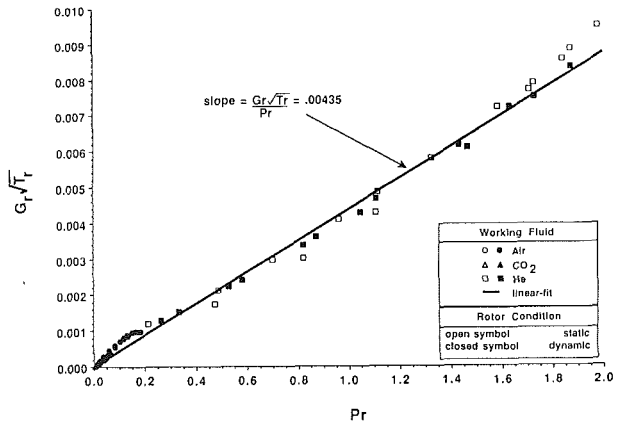

(d) $G_r\sqrt{T_r}$ versus Pr, where $P_r = \frac{\Delta P}{P_c}$, for Air, Carbon Dioxide, and Helium.

Fig. 4 Brush seal performance at static and dynamic rotor conditions and a bristle/rotor radial interference of +0.0061 cm (+0.0024 in.) for air, helium, and carbon dioxide

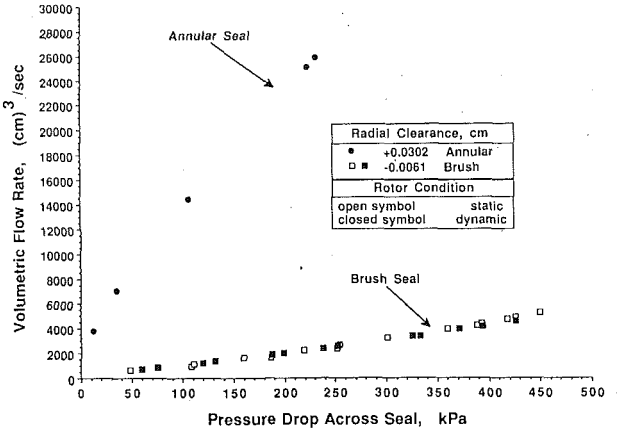

(a) Volumetric flow rate versus pressure drop with Helium as the working fluid for an annular seal and a brush seal.

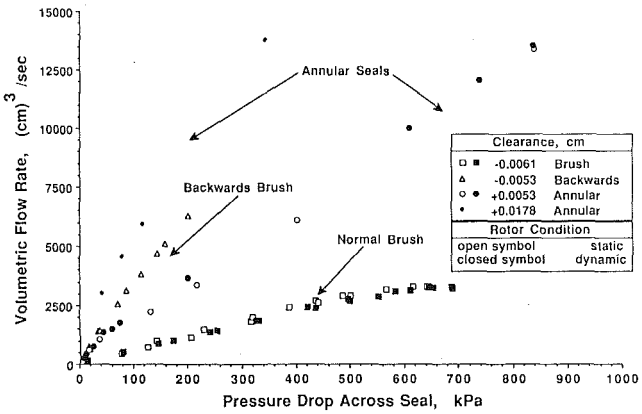

(b) Volumetric flow rate versus pressure drop with air as the working fluid for an annular seal, a reversed brush seal, and a brush seal.

Fig. 5 Comparison of an annular seal and a reversed brush seal leakage with that of a brush seal

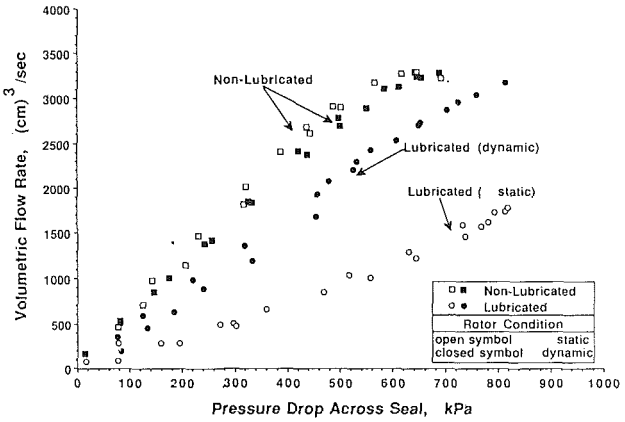

Fig. 6 Effect of lubrication on brush seals with air as the working fluid at a bristle/rotor radial interference of +0.0061 cm (+0.0024 in.)

mass flux maps only for isentropic flows and is nearly valid at the throat where dV/dP is much larger than nonisentropic losses. In a practical sense, the relations are valid to within a constant over a large range in thermodynamic states and flow geometries. Thus, if a single data point is found to establish this constant (which relates the working fluid and geometry), flow can be reliably predicted. For a fixed geometry, it appears that the nonisentropic losses for choked flows could be related to the thermodynamic surface, and the viscosity is correctable in terms of the extended theory of corresponding states. In addition, the direct solution of the conservation equations with an accurate equation of state does not require the use of the specific heat ratio (mass flux is proportional to the change in enthalpy).

Results and Discussion

The objectives of this investigation were: (1) to determine the performance of brush seals at several bristle/rotor interferences with various working fluids and to compare the results to an annular seal; (2) to generalize the results using corresponding state theory; (3) to determine the effect of packing lubricant into the bristles; and (4) to determine the effect of reversing the pressure drop across the seal.

Figure 4 presents the performance data of gaseous air, helium, and carbon dioxide at a bristle/rotor radial interference of 0.0061 cm (0.0024 in.). Figure 4(*a*) gives a plot of volumetric flow rate versus pressure drop across the seal for the various gases at static and dynamic (400 rpm) shaft conditions. All volumetric flow rates presented in this report are at standard temperature and pressure. For the carbon dioxide and air data, there was a slight decrease in leakage with shaft rotation; however, this effect was small (8 percent). Hysteresis effects were negligible. For the air and carbon dioxide data, the flattening at high pressure is not realistic and requires investigation. This is also the case in Fig. 7.

Figure 4(*b*) gives a plot of $G_r\sqrt{T_r}$ versus P_r for the gaseous air and carbon dioxide data; where $T_r = T_{in}/T_c$, $G_r = G/G^*$, $P_r = P_{in}/P_c$. Since the flow area was not known, it was taken to be a constant and set equal to 1.0 cm^2. The data fell onto a linear fit such that the slope $= G_r\sqrt{T_r}/P_r = 0.0169$ and 0.0155 for the static and dynamic shaft conditions, respectively. Figure 4(*c*) is the same plot with the helium data added. It can be seen that the helium data followed a different curve from that of the carbon dioxide and air data. An improvement in correlating the helium data with the air and carbon dioxide data can be seen if $G_r\sqrt{T_r}$ is plotted against $P_r = \Delta P/P_c$ as shown in Fig. 4(*d*). However, the helium data still follow a slightly different curve than that of the air and carbon dioxide data. The cause for this requires further investigation.

Figure 5 presents the results of the annular seal compared to the brush seal for gaseous air and helium for static and dynamic (400 rpm) shaft conditions. Figure 5(*a*) shows a plot of volumetric flow rate versus pressure drop for the brush and annular seals with helium as the working fluid. The radial clearances for the brush and annular seal were −0.0061 cm (−0.0024 in.) and 0.0302 cm (0.0119 in.), respectively. The annular seal leakage rate was 9.5 times greater than that of the brush seal.

Figure 5(*b*) shows a plot of volumetric flow rate versus pressure drop for the brush and annular seals with air as the test fluid for static and dynamic (400 rpm) shaft conditions. In addition, the plot includes the data for the brush seal with the pressure drop across the brush reversed. The radial interference for the brush was 0.0061 cm (0.0024 in.). Two radial clearances were tested for the annular seal: (0.0053 and 0.0178 cm (0.0021 and 0.0070 in.). For the brush seal with the pressure drop applied in the reverse direction, the seal had a radial interference of 0.0053 cm (0.0021 in.). Over this range of radial clearances, the annular seal leakage rate was between 3.5 and 7.5 times greater than the brush seal. The brush seal with the pressure drop applied in the reverse direction leaked 6.5 times that of the normal brush seal. With the pressure drop across the seal reversed giving the bristles no surface to press against, the reversed brush seal leaked approximately the same amount as that of the annular seal.

Figure 6 presents the results for the lubricated seal with air

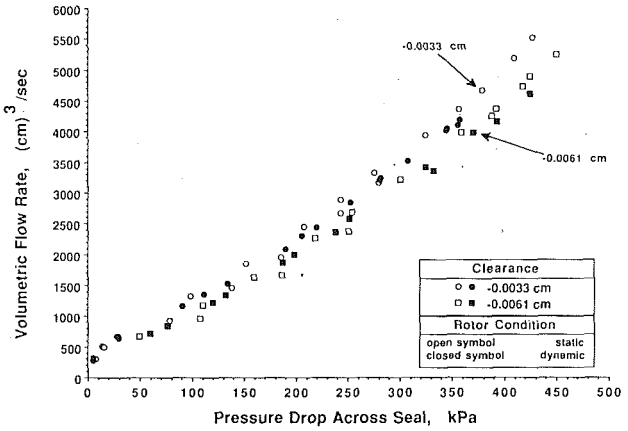

(a) Volumetric flow rate versus pressure drop across the seal with Helium as the working fluid.

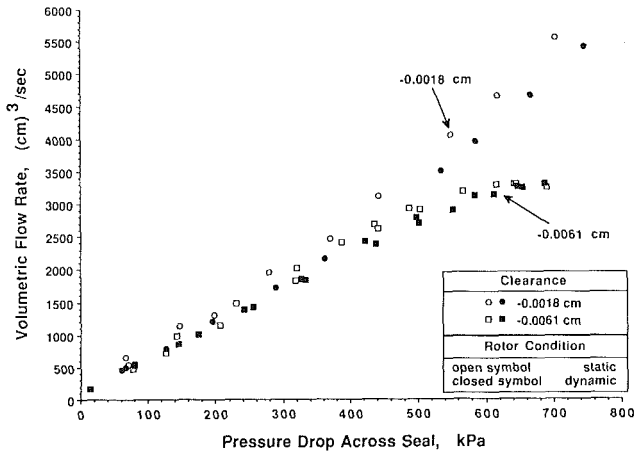

(b) Volumetric flow rate versus pressure drop across the seal with Air as the working fluid.

Fig. 7 Effect of bristle/rotor interference on brush seal leakage

as the test fluid compared to the nonlubricated brush seal static and dynamic (400 rpm) shaft conditions. It gives a plot of volumetric flow rate versus pressure drop across the seal at a radial interference of 0.0061 cm (0.0024 in.). For the static condition, the lubricated seal reduced the leakage 2.5 times that of the nonlubricated seal. For the dynamic condition, the lubricated seal reduced the leakage 1.5 times that of the nonlubricated seal. The lubricant served to hold the bristles in place and to block the porosity through the bristle pack. The static condition showed improvement over the dynamic case. This is the result of the lubricant acting as a seal at the bristle/rotor interface for the static case. This behavior can be seen in the steam data found from Schlumberger et al. (1991). The steam changed phases as it passed through the seal from vapor to liquid. The liquid became entrained in the bristles and blocked the fluid flow in the same manner as the lubricant.

Figure 7 presents the effect of bristle/rotor interference on leakage. Figure 7(*a*) gives a plot of volumetric flow rate versus pressure drop across the brush for helium at bristle/rotor radial interferences of 0.0033 and 0.0061 cm (0.0013 and 0.0024 in.). Figure 7(*b*) gives a plot of volumetric flow rate versus pressure drop across the brush for air at bristle/rotor radial interferences of 0.0018 and 0.0061 cm (0.0007 and 0.0024 in.). Both static and dynamic data are presented. As expected, the flow rate decreased with an increased interference.

A study of the bristle/rotor interface dynamics was made using high-speed film. Results show that as the pressure drop across the seal increased, the bristle pack would split at certain places along the circumference creating holes for a leak path. As the pressure drop decreased the bristle pack closed. Similar observations have been noted for a linear brush seal configuration ("rivering" effect) (Braun et al., 1990).

Summary of Results

The leakage performance of a brush seal with gaseous air, helium, and carbon dioxide for the test fluids was investigated for several bristle/rotor interferences at static and low rotor speeds. In addition, the effects of packing a lubricant into the bristles and of reversing the pressure drop across the seal were investigated. An annular seal was tested for comparison purposes. In order to generalize the results, they were correlated using corresponding state theory. A brush seal with an inside diameter of 3.792 cm (1.4930 in.) and a fence height of 0.635 cm (0.025 in.) was used. The following results were determined:

1 The air and carbon dioxide data showed a slight improved leakage rate at the rotating over the static condition. Hysteresis effects were negligible.

2 It was found that the air and carbon dioxide data had a flow coefficient equal to 0.0169 and 0.0155 for the static and dynamic shaft conditions, respectively. This was based on a $P_r = P_{in}/P_c$. The helium data did not follow the same trend.

3 A slight improvement in correlating the helium data with that of the air and carbon dioxide was seen if $P_r = \Delta P/P_c$ is used instead of $P_r = P_{in}/P_c$. The cause for the helium data behavior requires further investigation.

4 The brush seal leakage was between 3.5 and 9.5 times less than that of the annular seal, showing that the bristles make an effective seal.

5 The lubricated brush seal's leakage rate was up to 2.5 times less than that of the nonlubricated brush seal, indicating that the lubricant served to hold the bristles in place and block the porosity through the seal making a more effective seal.

6 For the lubricated seals, the static case showed a greater reduction in leakage than the rotating case. This is the result of the lubricant acting as a seal at the bristle/rotor interface for the static condition.

References

Braun, M. J., Hendricks, R. C., and Canacci, V. A., 1990, "Nonintrusive Qualitative and Quantitative Flow Characterization and Bulk Flow Model for Brush Seals," presented at the Japan International Tribology Conference, Nagoya.

Childs, D., 1990, "Brush Seal Rotordynamic Damping Characteristics," AIAA Paper No. 90-2139.

Chupp, R. E., Holle, G. F., and Dowler, C. A., 1991, "Simple Leakage Flow Model for Brush Seals," AIAA Paper No. 91-1913.

Ferguson, J. G., 1988, "Brushes as High Performance Gas Turbine Seals," ASME Paper No. 88-GT-182.

Flower, R., 1990, "Brush Seal Development System," AIAA Paper No. 90-2143.

Gorelov, G. M., Reznik, V. E., and Tsibizov, V. I., 1988, "An Experimental Study of the Rate Characteristics of Brush Seals in Comparison With Labyrinth Seals," *Aviatsionnaia Tekhnika*, No. 4, pp. 43-46 [in Russian].

Gunn, R. D., Chueh, P. L., and Prausnitz, J. M., 1966, "Prediction of Thermodynamic Properties of Dense Gas Mixtures Containing One or More of the Quantum Gases," *AIChE Journal*, Vol. 12, pp. 937-941.

Hendricks, R. C., and Simoneau, R. J., 1973, "Application of the Principle of Corresponding States to Two-Phase Choked Flow," NASA TM X-68193.

Hendricks, R. C., Baron, A. K., and Peller, I. C., 1975, "GASP—A Computer Code for Calculating the Thermodynamic and Transport Properties for Ten Fluids: Parahydrogen, Helium, Neon, Methane, Nitrogen, Carbon Monoxide, Oxygen, Fluorine, Argon, and Carbon Dioxide," NASA TN D-7808.

Hendricks, R. C., and Sengers, J. V., 1980, "Application of the Principle of Similarity to Fluid Mechanics—Water and Steam: Their Properties and Current Industrial Applications," *9th International Conference on the Properties of Steam*, J. Straub and K. Scheffler, eds., Pergamon Press, Oxford; unabridged version as NASA TM-79258, 1979.

Hendricks, R. C., Braun, M. J., and Mullen, R. L., 1990, "Brush Seal Configurations for Cryogenic and Hot Gas Applications," *Advanced Earth-to-*

Orbit Propulsion Technology, 1990, R. J. Richmond and S. T. Wu, eds., Vol. 2, NASA CP-3092-VOL-2, pp. 78–90.

Hendricks, R. C., et al., 1991a, "Some Preliminary Results of Brush Seal/Rotor Interference Effects on Leakage at Zero and Low RPM Using a Tapered-Plug Rotor," AIAA Paper No. 91-3390; NASA TM-104396.

Hendricks, R. C., et al., 1991b, "A Bulk Flow Model of a Brush Seal System," ASME Paper No. 91-GT-325.

McCarty, R. D., 1977, "A Comparison of Mathematical Models for the Prediction of LNG Densities," NBS IR 77-867.

Mollerup, J., 1978, "Thermodynamic Properties From Corresponding States Theory," *Proceedings of the American Institute of Chemical Engineers 71st Annual Meeting*, Miami Beach, FL., Paper No. 45 G.

Schlumberger, J. A., Proctor, M. P., and Hendricks, R. C., 1991, "Eccentricity Effects on Leakage of a Brush Seal at Low Speeds," presented at the Winter Annual Meeting of the ASME, Atlanta, GA; NASA TM-105141.

Simoneau, R. J., and Hendricks, R. C., 1977, "Generalized Charts for Computation of Two-Phase Choked Flow of Simple Cryogenic Liquids," *Cryogenics*, Vol. 17, pp. 73–76.

A Combined Experimental and Theoretical Study of Flow and Pressure Distributions in a Brush Seal

F. J. Bayley

C. A. Long

Thermo-Fluid Mechanics Research Centre,
School of Engineering,
University of Sussex,
Brighton, BN1 9QT,
Sussex, United Kingdom

A relatively simple theory is presented that can be used to model the flow and pressure distribution in a brush seal matrix. The model assumes laminar, compressible, isothermal flow and requires knowledge of an empirical constant: the seal porosity value. Measurements of the mass flow rate together with radial and axial distributions of pressure were taken on a nonrotating experimental rig. These were obtained using a 122 mm bore brush seal with 0.25 mm radial interference. The experimental data are used to estimate the seal porosity. Measurements of the pressure distributions along the backing ring and under the bristle tips and discussed. Predicted mass flows are compared with those actually measured and there is reasonable agreement considering the limitations of the model.

1 Introduction

A schematic diagram of a brush seal is shown in Fig. 1. The assembly comprises a bristle matrix clamped between a front plate on the upstream (high-pressure) side of the flow and a backing ring on the downstream (low-pressure) side. The bristles are inclined in the tangential direction; the angle between the bristle axis and a tangent to the contact point (the complement of the manufacturer's bristle lay angle) is θ. The axial width of the bristle matrix is Lx, and the radial distance from the bristle tips to the clamped end is Ly. The bristles overhang the backing ring by ΔH (measured in the radial direction); they are usually made from steel, and have a diameter d. Typical values of these parameters are: $\theta = 45$ deg, $Lx = 0.7$ mm, $Ly = 10$ mm, $\Delta H = 1.5$ mm, and $d = 0.0762$ mm.

The advantages of using brush seals in gas turbine engines were reported by Ferguson (1988). Compared with a conventional finned labyrinth seal, the brush seal offers a dramatic improvement (by five to ten times) in sealing. The compliance of the bristles also allows this improvement to be maintained when there are differential movements between shaft and seal casing, e.g., during engine transients. Rotation was found to decrease the leakage flow (by 35 percent at 3000 rad/s) but the author noted that further work was required to establish the cause of this effect. Braun et al. (1990) carried out flow visualization tests and pressure measurements using water and a linear (noncircular) brush seal. They identified several different patterns of flow between the bristles; the results illustrate the complex nature of the flow. Chupp and Dowler (1993) carried out performance tests on a number of different circular seals in a rotating test rig. Enhancements in the sealing performance compared to the conventional labyrinth seal were noted and found to be similar to those discussed by Ferguson. They also noted a hysteresis effect, where, for a given pressure ratio the flow rate was found to depend on whether the pressure ratio was arrived at by an increase or a decrease in the pressure. Hendricks et al. (1991) developed a theoretical model for predicting the mass flow, bristle displacements, and shaft load. This model uses established correlations for friction factors in porous media. The authors obtained reasonable agreement between their predicted mass flows and those supplied by a brush seal manufacturer.

The present paper discusses some theoretical and experi-

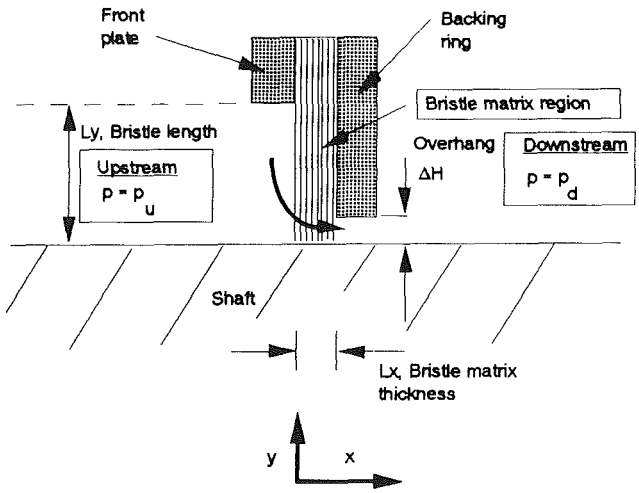

Fig. 1 A schematic diagram of a brush seal

Contributed by the International Gas Turbine Institute and presented at the 37th International Gas Turbine and Aeroengine Congress and Exposition, Cologne, Germany June 1-4, 1992. Manuscript received by the International Gas Turbine Institute February 24, 1992. Paper No. 92-GT-355. Associate Technical Editor: L. S. Langston.

mental aspects of research used to predict the operation of a brush seal. The experiments were conducted on a nonrotating brush seal rig, using a 122 mm bore brush seal, having a radial interference of 0.25 mm. The apparatus is described in Section 2. The theoretical work, which is discussed in Section 3, is based on a relatively simple model for the flow through the bristle matrix. The model calculates the pressure distributions, and hence bristle deflections, from the solution of Laplace's equation. The experimental measurements of pressure distribution, seal mass flow, and bristle deflections are discussed in Section 4.

2 Experimental Apparatus

The brush seal actually tested is shown in Fig. 2; the relevant dimensions are listed below:

Bristle bore diameter	121.76 mm
Backing ring inside diameter	124.56 mm
Front plate inside diameter	142.40 mm
Overall outside diameter	151.71 mm
Overall axial width	3.85 mm
Front plate and backing ring widths	1.625 mm
Bristle diameter	0.0762 mm
Backing ring overhang	1.4 mm
Bristle lay angle	45 deg

A section through the test rig is shown in Fig. 3. The seal is clamped between the front cover plate and spacer rings. The nonrotating test piece forms a dummy "rotor" and the outer diameter of this is machined to give the appropriate static radial interference between bristle tips and shaft. Flow is supplied to the rig from a 400 kW Howden screw compressor and the flow rate measured using an "Annubar." Air enters the rig through a hole in the rear cover plate. Thirty 10-mm-dia holes and a 0.1 mm mesh size stainless steel gauze distribute the incoming air evenly into an annular plenum chamber upstream of the seal.

The pressure distributions in the radial and axial directions are measured by pressure tappings located in the seal backing ring and in the rotor surface. The radial pressure tappings are located at four different circumferential locations. Each set comprises five separate, 0.25-mm-dia pressure tappings laser drilled in the backing ring at equispaced intervals between the front plate and backing ring inside diameters. The test piece, or rotor, contains 24, 0.25-mm-dia axial pressure tappings. These are located at angular intervals of 15 deg and separated by 0.06 mm in the axial direction. With this arrangement, 11 of the pressure tappings are expected to be under the bristle tips.

The remaining pressure tappings are to accommodate the expected axial deflection of the bristles and uncertainty in the exact location of the brush seal in the housing. Tests were carried out for the range of upstream absolute pressures (107 kPa $\leq P_u \leq$ 380 kPa). The pressures were measured by a 50-port Scanivalve. During a test, each of the measurement ports was opened for 0.5 seconds. Four complete sets of measurements would usually be made at a particular value of the upstream pressure. There were small differences in the measured pressure from a particular pressure tapping during these four scans, but these are considered to be negligible and for convenience the results discussed here are based on average values.

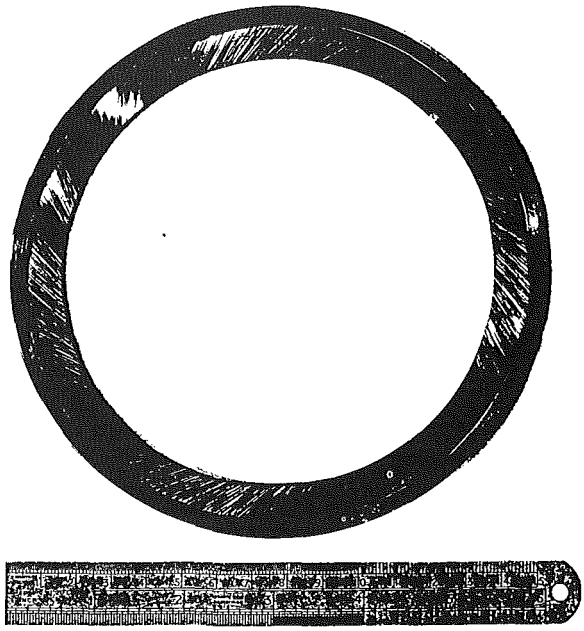

Fig. 2 The brush seal used in the experiments

Some test were conducted with superimposed vibration. To allow transmission of this vibration to the brush seal itself, the mass for the rig was supported on a separate frame, using four springs, and allowed to slide up and down on PTFE bushes. The velocity and amplitude of vibration were measured by a Bruel and Kjer 4339 accelerometer and Kistler M05-100 charge amplifier connected to a Gould Advance OS245A Oscilloscope. Tests with superposed vibrations were conducted using a frequency of 300 Hz and a velocity of 10 mm/s—values believed to be representative of engine conditions.

3 Theoretical Model

If the inertial terms in the boundary-layer equations are neglected, the resulting equations balance the pressure and viscous forces. For laminar flow of a perfect gas with viscosity μ, in the bristle matrix, the pressure field, $p(x,y)$, and hence mass flow, bristle loads, and deflections can be obtained from the solution of Laplace's equation. Density variations through-

Nomenclature

d = bristle diameter
h_x, h_y = characteristic passage widths in the axial and radial directions, respectively
Lx = axial width of bristle pack
Ly = radial height of bristle pack
m = mass flow rate
p = absolute pressure
p_s = pressure on shaft
P = $p^2/2RT$ general variable
P^* = $(p - p_d)/(p_u - p_d)$ = dimensionless pressure
r_s = radius of shaft
R = gas constant
R_p = p_u/p_d = pressure ratio
T = absolute temperature
x = coordinate in the axial direction
X = x/Lx = nondimensional axial coordinate
y = coordinate in the radial direction
Y = y/Ly = nondimensional radial coordinate
z = axial pressure tapping number
ΔH = bristle overhang
ΔR_s = static radial build interference ($\Delta R_s < 0$)
Δx = axial deflection
θ = angle between bristle axis and tangent to contact point
μ = dynamic viscosity
ρ = density
ϕ = $(h_y/h_x)^3$ = porosity value

Subscripts

d, u = pertaining to values downstream and upstream of the brush seal, respectively

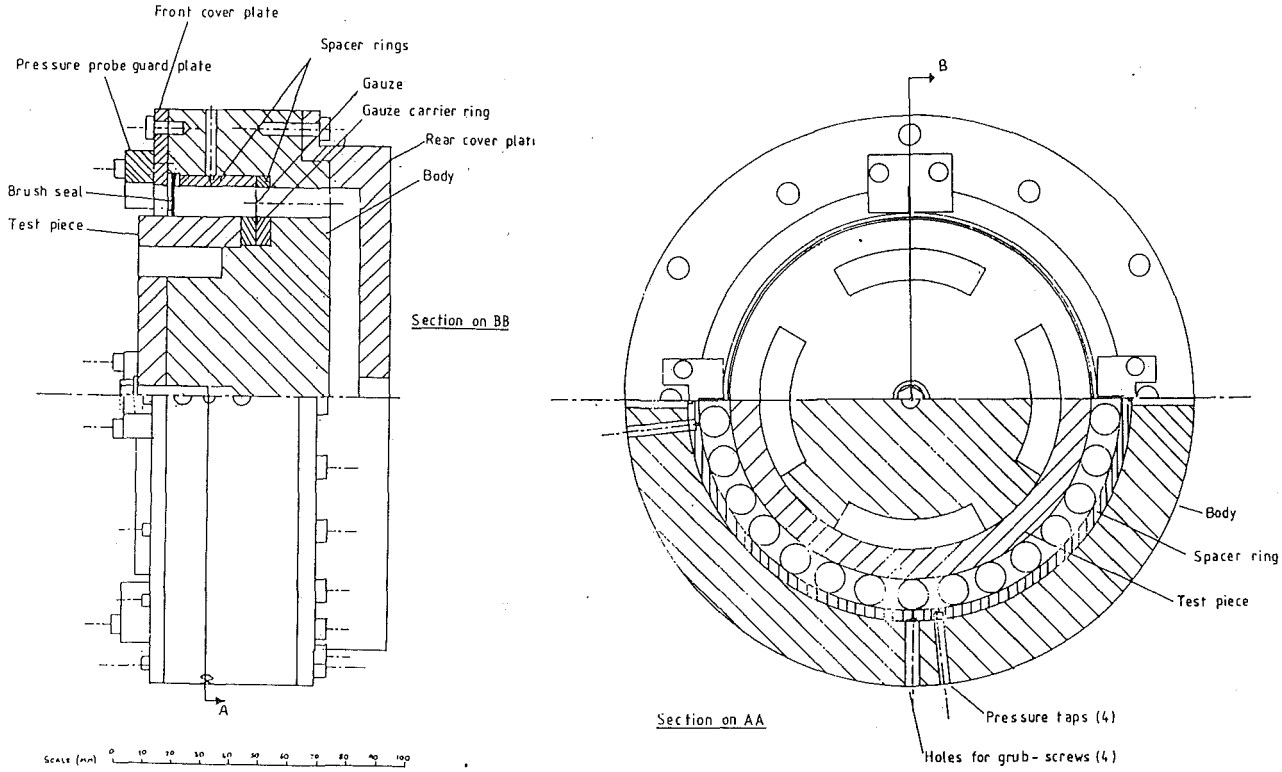

Fig. 3 Views and a section through the brush seal test rig

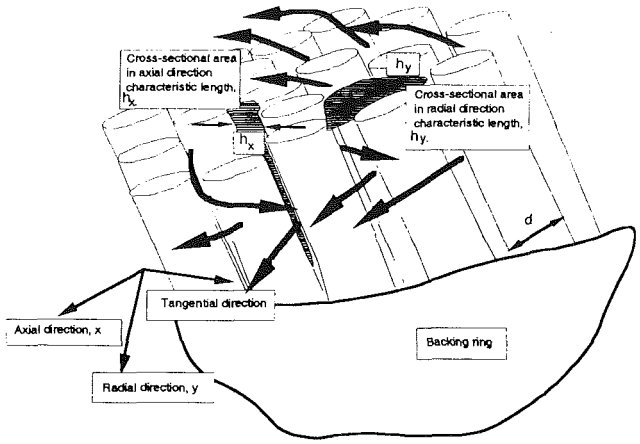

Fig. 4 Schematic diagram of flow through the bristle matrix

out the bristle matrix can be modeled by assuming isothermal flow and solving for the variable, $P = p^2/2T$, R being the appropriate gas constant and T, the absolute temperature.

Figure 4 shows a schematic diagram of flow in a brush seal matrix. Of particular interest are the axial and radial through-flow areas, which are shown shaded, and characterized by the respective lengths h_x and h_y. It is convenient to express these as a ratio: $\phi = (h_y/h_x)^3$, which can be thought of as a porosity value. It is of course expected that in a "real" brush seal, h_x and h_y are not constant throughout the bristle matrix. For this case, and using the above assumptions, the governing equation becomes:

$$\partial^2 P/\partial x^2 + \phi \partial^2 P/\partial y^2 + h_x^{-3}(\partial P/\partial y \partial h_y^3/\partial y + \partial P/\partial x \partial h_x^3/\partial x) = 0 \quad (1)$$

Equation (1) was discretized using finite differences and solved using Gausian-elimination. The boundary conditions specified for the solution are listed below:

1 On the upstream face of the seal, $x = 0$; $0 \le y \le Ly$ (see Fig. 1); the pressure is equal to the upstream pressure p_u.
2 On the outside diameter of the seal, $0 \le x \le Lx$; $y = Ly$, there is no flow in the radial direction and $(\partial p/\partial y)_{y=Ly} = 0$.
3 On the downstream face of the seal, $x = Lx$; $0 \le y \le Ly$: (i) in the overhang region, $0 \le y \le \Delta H$, the pressure is equal to the downstream pressure p_d, and (*ii*) next to the backing ring, $\Delta H < y \le Ly$, there is no axial flow $(\partial p/\partial x = 0)$.
4 At the bristle tips it is assumed that there is no radial flow: $(\partial p/\partial y)_{y=0} = 0$.

The computed pressure fields obtained from the computations with variable ϕ, with a variation from maximum to minimum of 64:1, are shown in Fig. 5. These were carried out for a seal with 0.25 mm radial build interference with upstream and downstream absolute pressure of $p_u = 2$ bar and $p_d = 1$ bar, respectively. The pressures, referred to as P^*, are non-dimensionalized with respect to the overall pressure difference across the seal: $P^* = (p - p_d)/(p_u - p_d)$. These are plotted against Y, the nondimensional radial coordinate ($Y = y/Ly$) and X ($X = x/Lx$), the nondimensional axial coordinate. The bristle overhang is indicated by the region $X = 1$ and $0 \le Y \le 0.14$, where $P^* = 0$.

There are three frames in this figure: (*a*) in which h_x increases linearly with distance from the upstream bristle row and $h_{x(x=Lx)} = 4h_{x(x=0)}$; (*b*) in which h_x decreases linear with distance from the bristle tips and $h_{x(y=0)} = 4h_{x(y=Ly)}$; and (*c*) which is for a constant value of ϕ equal to the average value of ϕ used in the above calculations. The results are presented for average values of $\phi = 1$ and 100, which are considered to span the range of realistic values.

Comparison between frames *c*(*i*) and *c*(*ii*) for constant values of $\phi = 1$ and 100, respectively, illustrates how the porosity value affects the pressure distribution in the bristle matrix. For $\phi = 1$, the bristle matrix had greater porosity in the axial direction than for $\phi = 100$. Consequently the pressure distri-

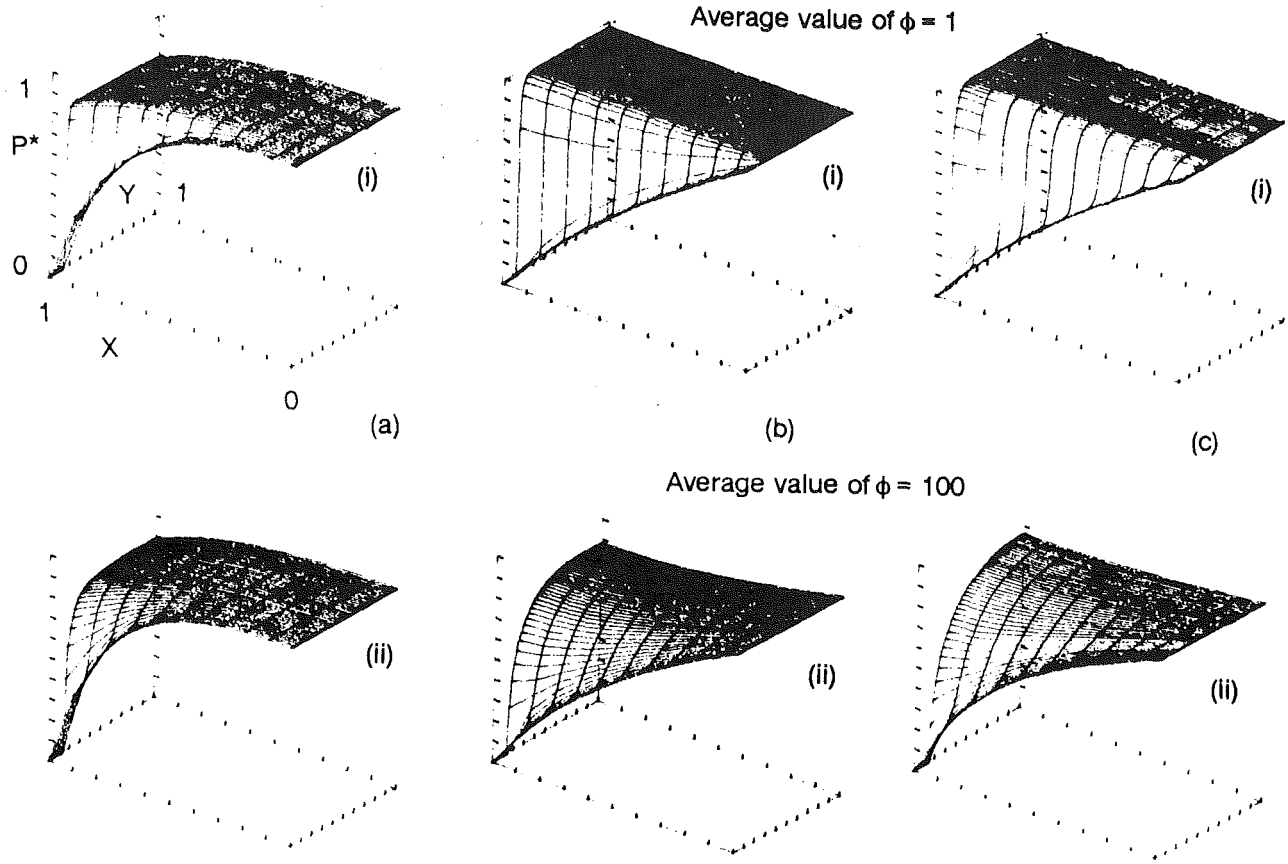

Fig. 5 Computed pressure fields in the bristle matrix: (*a*) $h_x = f(x)$; (*b*) $h_x = f(y)$; (*c*) h_x = const

bution imposed on the front plate of the seal ($p = p_u$ for $X = 0$ and $0 \leq Y \leq 1$) is almost entirely communicated to the backing ring. Increasing ϕ to $\phi = 100$ reduces the relative axial porosity and there is an increased radial pressure gradient along the backing ring. This effect has particular significance, as it means that the porosity of the bristle matrix can be estimated from measurements of the radial distribution of pressure along the backing ring.

As shown in Frames *b*(*i*) and *b*(*ii*), the radial pressure distributions on the backing ring, when h_x varies in the radial direction, are broadly similar to that obtained using a constant value of ϕ. When h_x varies in the axial direction, Frames *a*(*i*) and *a*(*ii*) show there is a larger difference. In this case the distribution at $X = 1$ is similar to that obtained from assuming a constant value of ϕ, equal to the local value for variable ϕ at $X = 1$. From this it may be inferred that the experimentally measured pressure distributions can still be used to estimate values of ϕ, the value being the value of ϕ on the backing ring. When h_x is made to vary with X, an increased overall axial pressure drop is also obtained. This is to be expected since the flow area in the axial direction increases in the streamwise direction, and hence the flow is almost entirely in this direction and the increased pressure drop occurs as a result of overcoming viscous forces. Comparing results for variable ϕ, using average values of $\phi = 1$ and $\phi = 100$ shows the same effects as noted for the case of constant ϕ in the bristle matrix: Increasing ϕ increases the overall pressure drop along the backing ring.

Since the bristles are in contact with the shaft, they must impose a load on it. This load will depend on the initial radial interference and (since the pressure distribution depends on ϕ) also the porosity value. Figure 6 summarizes these effects, where the shaft pressures are calculated for constant values of ϕ with $\phi = 1$ and 100. For each value of ϕ, the results are shown for four different initial radial interferences: $\Delta R_s = -0.1, -0.2, -0.4$, and -0.8 mm. The shaft pressure increases linearly with pressure ratio, and for any given radial interference the shaft pressure is greater at the lower value of ϕ. This is consistent with the results shown in Fig. 5. For a low value for ϕ, more of the radial pressure drop occurs at the bristle tips than for a large value of ϕ, and so the resulting load on the shaft is higher. Increasing the radial interference also increases the shaft pressure; this effect is due to the imposed preload of the interference fit between bristles and shaft.

4 Experimental Results

Measurements were taken of the variation of pressure along the backing ring and also under the bristle tips. These are referred to as radial and axial pressure distributions, respectively. The tests discussed below were conducted with and without superposed vibration and this was found to make no significant difference to either the mass flow through the seals, or the pressure distributions.

4.1 Radial Pressure Distributions. For the radial pressure distributions, the measurements are obtained from averaging pressures measured at four different circumferential locations. Tests were conducted over the range of upstream absolute pressures $107 < p_u < 380$ kPa and approximately 40 tests were conducted. For all the tests, the air inlet temperature was about 20°C; p_d, the downstream absolute pressure, was always at atmospheric pressure $\approx$ 100 kPa.

In order to show the physical behavior of the seal, it is convenient to present these results in *bands* of pressure ratio, Rp, where $Rp = p_u/p_d$. Figure 7 shows the measured radial pressure distributions of five tests in the range $2.23 < Rp < 2.65$. The pressures, referred to as P^*, are nondimensionalized with respect to the overall pressure difference across the seal: $P^* = (p - p_d)/(p_u - p_d)$. These are plotted against Y, the nondimensional distance from the shaft, and $Y = y/Ly$.

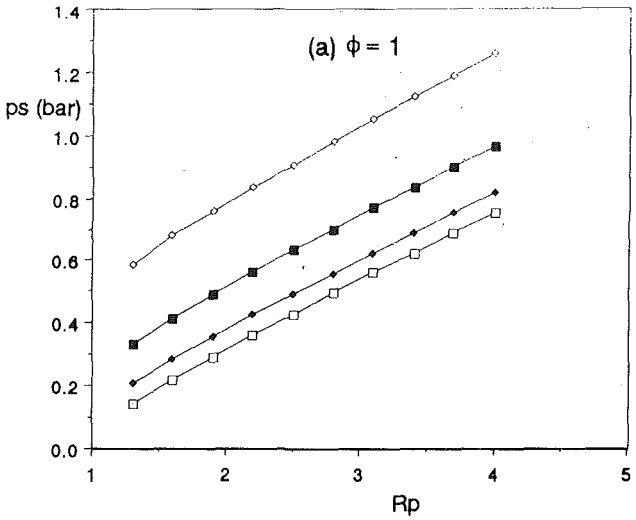

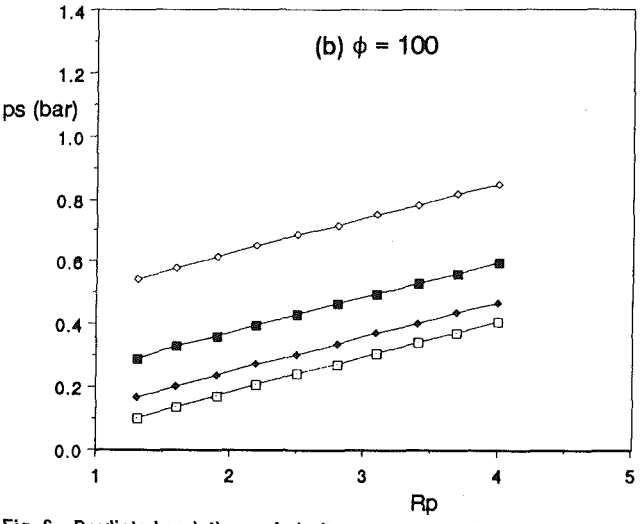

Fig. 6 Predicted variations of shaft pressure, p_s, with pressure ratio, Rp; bristle interference, ΔR_s; and seal porosity, ϕ;—□— $Rs = -0.1$ mm; —◆— $Rs = -0.2$ mm;—■— $Rs = -0.4$ mm;—◇— $Rs = -0.8$ mm

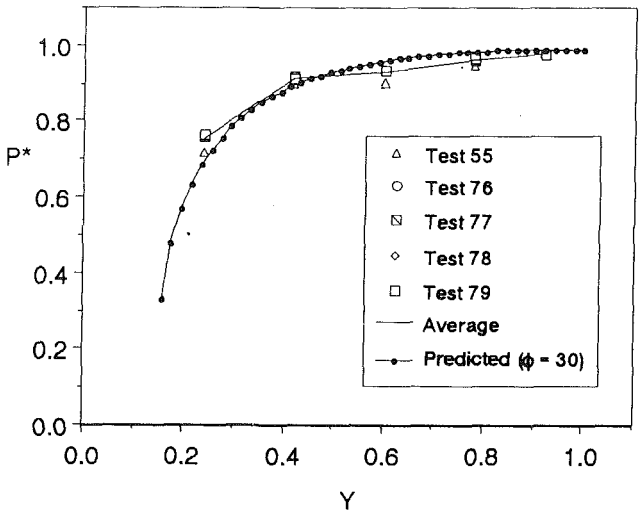

Fig. 7 Measured and predicted variations of radial pressure distribution along the backing ring

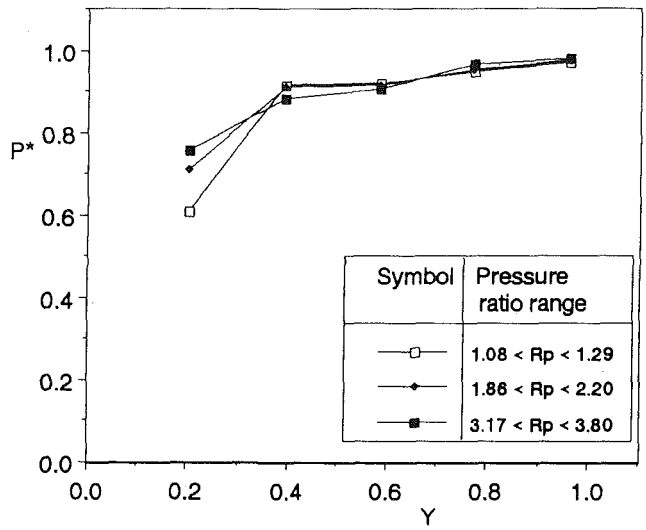

Fig. 8 Measured variations of the radial pressure distribution along the backing ring for different pressure ratios

The different symbols indicate the results from the different tests and the line gives the average value. There is relatively little scatter in the results and the average value gives a good representation of the distribution of pressure on the backing ring. It is worth noting that the pressure experienced on most of the backing ring is almost constant and at 0.9 to 0.95 p_u; most of the overall radial pressure drop occurs in the region $Y < 0.4$. Also shown in the graph is the predicted radial pressure distribution for $\phi = 30$, which can be seen to give a good overall fit to the experimental data.

The variation of radial pressure distribution with pressure ratio for all pressure ratios tested is summarized in Fig. 8, for tests at $1.08 < Rp < 1.29$; $1.86 < Rp$ 2.20 and $3.17 < Rp < 3.8$. At the lowest pressure ratio there is the largest overall drop in pressure from $Y = 1$, at the inner radius of the front plate to $Y = 0.2$ at the innermost pressure tapping. As the pressure ratio is increased this overall pressure gradient is reduced. Referring back to Fig. 5 it can be seen that a reduction in the overall pressure drop along the backing ring is consistent with a reduction of ϕ, the ratio of radial to axial porosity. This occurs in Fig. 8 and implies that the radial component of the total mass flow reduces as the pressure ratio is increased.

4.2 Axial Pressure Distributions. Measured axial pressure distributions for $\Delta R_s = -0.25$ mm are shown in Fig. 9. Each frame gives the results for tests conducted within a range of Rp: frame (*a*) $1.25 \leq Rp \leq 1.42$; (*b*) $2.20 \leq Rp \leq 2.70$; and frame (*c*) $Rp < 3.8$. Different symbols are used to denote the results obtained from separate tests within each pressure ratio range.

The axis abscissae, z, shows the pressure tapping number. At the lowest pressure ratios (see frame (*a*)), P^* is relatively constant for $z \leq 5$ and has a value of approximately unity indicating that this region is upstream of the bristle matrix. Since the pressure tappings are separated by 0.06 mm, the downstream face of the bristle matrix is expected to be located at $z = 16$. This is broadly where $P^* = 0$. There is some scatter in the measurements and it is considered that this occurs as a result of circumferential variations in the axial deflections of the brush seal. Despite this scatter, it appears that the form of the distributions does not change significantly with pressure ratio. The pressure appears to fall almost linearly with the distance through the bristle matrix. This is consistent with measurements carried out by Braun et al. (1990) on a linear brush seal with zero radial clearance.

4.3 Seal Mass Flows. It is of interest to compare measured and predicted mass flows for the brush seal. As previously noted, the measured radial pressure distributions indicate that

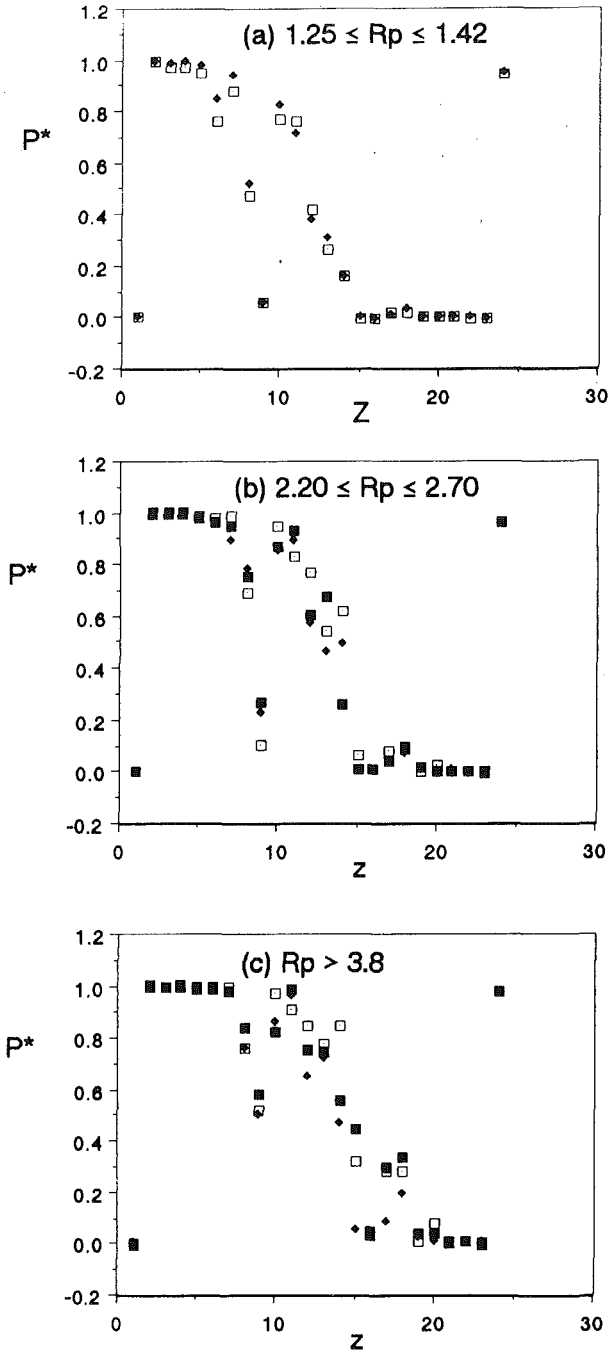

Fig. 9 Measured variations of the axial pressure distribution under the bristle tips for different pressure ratios

this particular seal has a porosity value of $\phi \approx 30$. Since $\phi = (h_y/h_x)^3$, a particular combination of h_x and h_y can be found to give correspondence between measured and predicted flows at just one value of pressure ratio. Predictions can be obtained using these values of h_x and h_y for the entire range of pressure ratios of interest.

The results of this are shown in Fig. 10. The overall agreement between measured and predicted flow rates is generally good. The theory underestimates the measurements at the lowest pressure ratios. This discrepancy could be improved, but it would result in an overestimate of the measured values at the higher pressure ratios.

The measurements of radial pressure distribution, shown in Fig. 8, suggest that ϕ increases as Rp is decreased. This may occur by either an decrease in h_x, or an increase in h_y. As shown

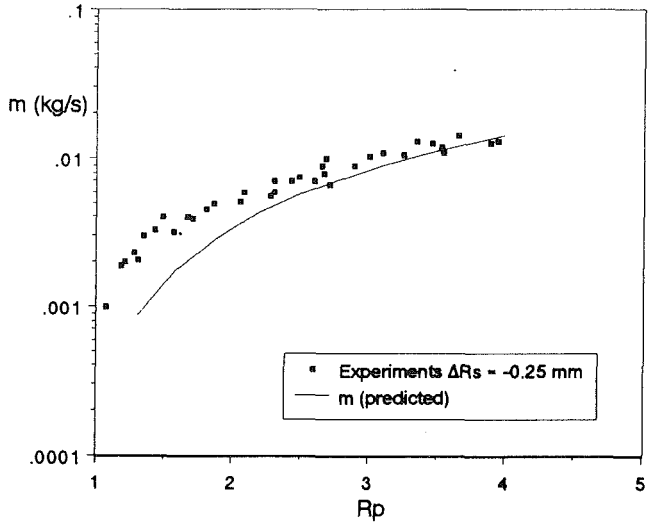

Fig. 10 Variation of measured and predicted mass flows, m, with pressure ratio, Rp

in Fig. 10, for a constant value of ϕ, the predicted and measured flow rates match at a high pressure ratio; but as the pressure ratio is reduced, the measured flow rate exceeds the predicted value. To obtain correspondence over the entire range of pressure ratio and consistency with the expected behavior of ϕ, implies that h_y should increase with decreasing pressure ratio.

4.4 Bristle Deflections. The pressure distributions shown in Fig. 9 can also be sued to estimate the axial deflection of the bristle pack. For this, it is assumed that the downstream face of the bristle pack is located at the point at which $P^* = 0$. It was found that at a pressure ratio of 3, the axial deflection was between 0.2 and 0.4 mm. It should be remembered that these results are based on a relatively subjective judgment and are therefore not considered to be of great accuracy. However, they are consistent with the expectation that as the pressure ratio is increased then so is the axial deflection. They are also consistent with the predicted axial deflection obtained from the model. For this, Eq. (1) is solved with $\phi = 30$. The predicted pressure distributions specify the loading on each bristle; the deflection can be obtained using the method of superposition (see Timoshenko and Gere, 1979), assuming the bristle to be a simple cantilever with a nonuniform distributed load.

5 Conclusions

This study has considered theoretical and experimental aspects of the operation of a brush seal. For the theoretical work, the pressure distribution in the bristle matrix was obtained by solving Laplace's equation. This requires an empirical constant describing the overall porosity of the bristle matrix (denoted by ϕ). The experiments were conducted using a nonrotating test rig with a 122 mm bore brush seal having 0.25 mm radial interference. Measurements were made of flow through the seal, together with the radial and axial pressure distributions (along the backing ring and under bristle tips, respectively). These were obtained with and without superimposed vibration for the range of upstream absolute pressures, $107 < p_u < 380$ kPa, and with a constant downstream exit absolute pressure, $p_d = 100$ kPa.

The principal conclusions from this work are summarized below:

1 The theoretical study has considered the case of constant ϕ, and also ϕ varying in the bristle matrix. Comparison between these two cases shows some difference in the distribution of pressure in the bristle matrix. Most significantly, the value of ϕ for a brush seal can be estimated from measuring the radial

pressure distribution on the backing ring. For the test considered here it was found that $\phi \approx 30$.

2 Theoretical predictions of the contact pressure of the bristles on the shaft show that this increases linearly with pressure ratio, and for a given radial interference the shaft pressure is increased when ϕ is decreased. Increasing the radial interference also increases the shaft contact pressure.

3 The pressure distribution under the bristle tips does not appear to change with pressure ratio, and decreases almost linearly with distance under the bristles.

4 Comparison between measured and predicted flows through the seal is generally good considering the overall simplicity of the theoretical model.

The effects of rotation have not been considered, either directly or by comparison of these current results with published data for rotating tests. To the present author's knowledge, these are the first published results of the radial pressure distributions and comparison is therefore not possible. Ferguson's data for the effect of rotation on the flow rate show a progressive reduction to 65 percent of the static flow at 3000 rad/s. The flow rate through the brush seal is governed by a overall porosity, so rotation could be expected to affect this, and therefore the radial pressure distributions, in a broadly similar way.

Acknowledgments

The authors would like to thank their former colleague, Prof. J. M. Owen, now at Bath University, for his analysis and derivation of the theoretical model used in this paper. Thanks must also go to Roll-Royce plc who funded the research work and granted permission to publish the results.

References

Braun, M. J., Hendricks, R. C., and Canacci, V., 1990, "Flow Visualization in an Simulated Brush Seal," ASME Paper No. 90-GT-217.

Chupp, R. E., and Dowler, C. A., 1993, "Performance Characteristics of Brush Seals for Limited Life Engines," ASME JOURNAL OF ENGINEERING FOR GAS TURBINES AND POWER, Vol. 115, this issue, pp. 390–396.

Ferguson, J. G., 1988, "Brushes as High Performance Gas Turbine Seals, ASME Paper No. 88-GT-182.

Hendricks, R. C., Schlumberger, S., Braun, M. J., Choy, F., and Mullen, R. L., 1991, "A Bulk Flow Model of a Brush Seal System," ASME Paper No. 91-GT-325.

Timoshenko, S. P., and Gere, J. M., 1979, *Mechanics of Materials*, Van Nostrand Reinhold Company, New York, p. 205.

Unusual Acoustic Vibration in Heat Exchanger and Steam Generator Tube Banks Possibly Caused by Fluid-Acoustic Instability

F. L. Eisinger
Mem. ASME

R. E. Sullivan

Foster Wheeler Energy Corporation,
Clinton, NJ 08809-4000

Flow channels of heat exchangers or steam generators containing tube arrays can be subject to acoustic vibration excited by flow of air, gas, or steam tranversely across the tubes. Such vibration occurs when a flow disturbance inside the tube bank excites a strong acoustic (standing wave) mode of the channel. The acoustic modes typically excited are those related to the dimension perpendicular to both the fluid flow direction and the tube axes. Preventive measures taken in the design stage are typically directed against these commonly existing standing waves. Evidence is presented of the unusual occurrence of standing waves that develop in the flow direction and in the tube axial direction. The causes for their development and methods of suppression are discussed.

Introduction

Acoustic waves can be excited by disturbances arising within the tube bundle but also away from the tube bundle in the ducting. Inside the tube bundle the excitation phenomena considered to be responsible for the development of acoustic vibration are primarily vortex shedding, but also turbulence, generated by crossflow. The effects of bends in the ducting, changes in cross section, turbulent swirling flow, and bluff bodies placed inside the duct are often the sources of acoustic vibration in the ducting away from the tube bundle.

Two types of acoustic modes are known to exist: those that are bound to the tube bundle and decay in the adjoining ducting, and those that exist primarily in the ducting and decay within the tube bundle. Both of these modes, as shown by Parker (1978) and Blevins (1986), can be excited by acoustic disturbances within the tube bundle. As mentioned earlier, the duct modes can also be excited by disturbances within the duct proper.

The acoustic modes typically excited by crossflow in tubular heat exchanger or steam generator tube banks are the transverse modes (modes $j = 1, 2, 3, \ldots$ in the y direction), which are perpendicular to the direction of flow and tube axes (Fig. 1). Longitudinal modes (i) in the flow direction (x), or transverse modes (k) in the direction of the tube axes (z) are rarely excited by crossflow and have not been reported in the literature. (The indices i, j, k give the number of acoustic waves in the flow (x), transverse (y), and tube axial (z) directions, respectively.)

In this paper we present evidence of unusual acoustic vibration in two cases: in one tubular air heater, acoustic vibration occurred in the longitudinal (flow) direction, and in the second, a steam generator economizer bank, acoustic vibration occurred in a direction transverse to flow, along the tubes.

Theories of Acoustic Vibration and Brief Review of Published Work

The publications on acoustic vibration or resonances in tube banks typically assume that vibration due to crossflow will occur only in the j modes, which are characterized by a fluc-

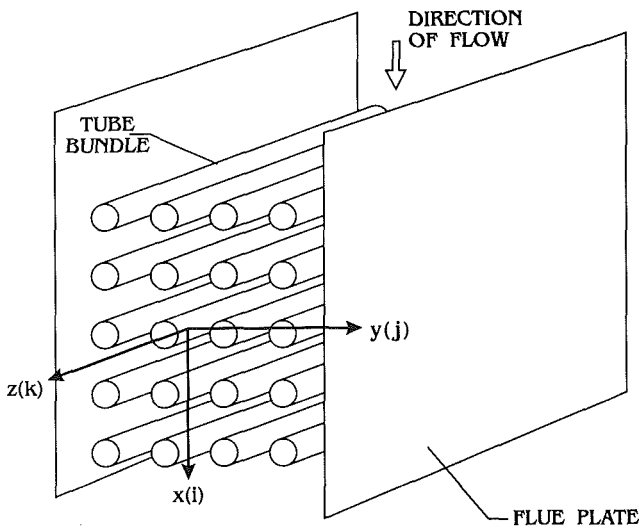

Fig. 1 Tube bundle in duct: orientation of axes *x, y, z* and modal indices *i, j, k* for acoustic modes

Contributed by the Nuclear Engineering Division and presented at the Western Pacific Regional Acoustics Conference IV, Brisbane, Australia, November 26–28, 1991. Manuscript received by the Nuclear Engineering Division August 13, 1991. Associate Technical Editor: S. M. Cho.

tuating particle velocity in the y direction (lift direction), which is perpendicular to the direction of flow and the tubes. Most of the experimental evidence, both laboratory and industrial does support this assumption.

Two principal sources causing acoustic vibration in tube bundles have been identified: vortex shedding and turbulence or turbulence-based instability.

The vortex theory is well established and its validity very well documented experimentally. It is also widely used in design practice. According to this theory, the vortex shedding-induced fluctuating lift forces are perfectly capable of interacting with the particle velocities of the fluid column standing waves vibrating in the same direction. At resonance intense noise and vibration can be generated. The works of Baird (1954), Grotz and Arnold (1956), Putnam (1959), Chen (1968), Chen and Young (1974), Parker (1978), Eisinger (1980), Blevins (1986), Blevins and Bressler (1987a, 1987b), and Parker and Stoneman (1989) all support the vortex shedding theory of acoustic vibration.

The turbulence-based theory postulates a triggering mechanism initiating the acoustic vibration and sustaining it by the energy contained within the turbulent flow inside the tube bank. An instability-like phenomenon is postulated. Although there is some experimental evidence that such a mechanism might be at work in certain cases, no proof of such a mechanism has so far been offered. The following works fall to some degree in this category: Owen (1965), Funakawa and Umakoshi (1970), Fitzpatick and Donaldson (1977), Fitzpatrick (1985, 1986), Rae and Murray (1987), and Ziada et al. (1988a, 1988b). A jet instability phenomenon for in-line arrays has recently been described by Ziada and Oengoren. Its origin seems to be associated with shear layer instability in jets between tube rows (Ziada and Oengoren, 1991; Oengoren and Ziada, 1991).

A large body of experimental and theoretical evidence has accumulated over the years in the field of solid propellant rocket combustion where the effect of a superimposed acoustic field upon the turbulent flame combustion process has been studied. Pressure- and velocity-coupled instability mechanisms have been shown to exist, initiating strong acoustic vibration in the enclosed spaces of the combustion chamber. Since acoustic waves in the enclosed space of a combustion chamber are always present, at certain conditions the coupling mechanism can give rise to intense acoustic vibration. We mention only a few of the publications in this field: Culick (1966), Price and Dehority (1967), Culick (1970), Price (1979), Culick and Magiawala (1981), Ma et al. (1990).

The instability mechanism of acoustic vibration in the combustion chamber seems to present supportive evidence for the turbulence-based theories of strong acoustic vibration in tube bundles. Although not proven yet, the interaction (coupling) of the acoustic waves always present inside a tube bundle (waves of different modes and magnitudes) with the turbulent flow field appears to be a plausible mechanism of excitation. It is this coupling mechanism that might have been responsible for the initiation of the unusual acoustic vibration described in this paper.

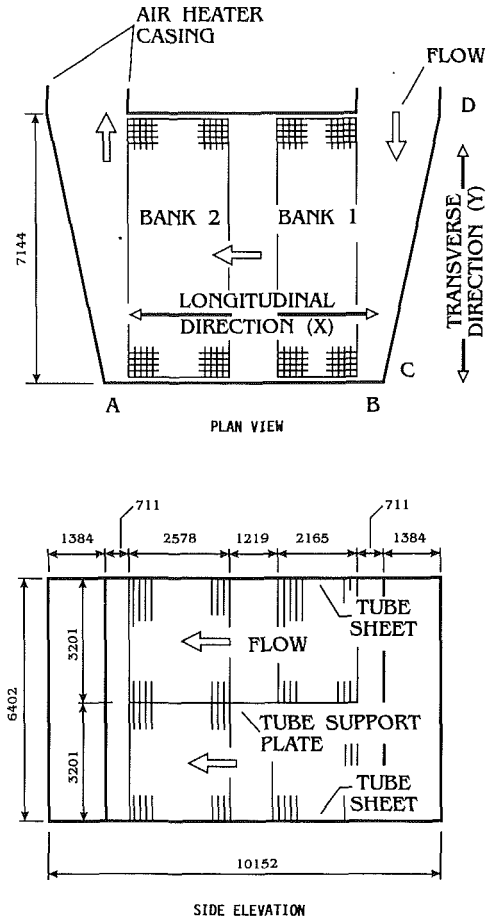

Fig. 2 Arrangement of tubular air heater (dimensions shown in mm)

Longitudinal Acoustic Vibration in a Full-Size Tubular Air Heater

Experimentally Observed Acoustic Vibration. The tubular air heater shown in Fig. 2 consists of two separate tube banks, bank 1 and bank 2. The tubes have an in-line arrangement and are supported by two tube sheets (at top and bottom), and by a tube support plate at midheight. The tubes are exposed to air flow on the outside and hot gas on the inside. The air enters the air heater at a right angle and as it makes a 90 deg turn enters bank 1 and bank 2 in crossflow. The heated air exits in a direction parallel to that of the inlet.

The air heater dimensions are given in Fig. 2. The geometry of the tube layout is given in Table 1. The air flow temperature increases as it passes through the air heater. Three flow conditions at three loads are specified, low (47 percent), medium (71 percent), and high (100 percent). The corresponding Helmholtz number He = vS/c_{eff} and Reynolds numbers Re = $vD/$

Nomenclature

c = speed of sound in free space
c_{eff} = speed of sound within tube bank
D = tube outside diameter
He = Helmholtz number
i, j, k = indices of acoustic modes in x, y, and z directions, respectively
L = tube longitudinal spacing
Re = Reynolds number
S = Strouhal number
T = tube transverse spacing
Te = temperature
v = flow velocity in gap between tubes
x = coordinate in flow direction
y = coordinate in transverse direction perpendicular to flow
z = coordinate in tube axial direction
ν = kinematic viscosity of air or gas

Table 1 Air heater tube bank geometry and flow parameters

Bank No.	Tube O.D. D	Side Spacing T	Longit. Spacing L	Air Flow							
				47% Load		71% Load		100% Load			
				He x 10^6 In/Out	Re In/Out	He x 10^6 In/Out	Re In/Out	Air Temp. In/Out T_e	Gap Vel. In/Out v	He x 10^6 In/Out	Re In/Out
	mm	mm	mm	—	—	—	—	C	m/s	—	—
1	64	79	75	4,600/ 5,280	10,818/ 8,737	6,950/ 7,980	16,341/ 13,199	37.8/ 139.3	6.08/ 8.05	9,780/ 11,240	23,016/ 18,590
2	64	79	89	3,460/ 3,990	8,737/ 7,323	5,230/ 6,030	13,199 11,062	139.3/ 273.9	8.05/ 10.68	7,360/ 8,490	18,590/ 15,563

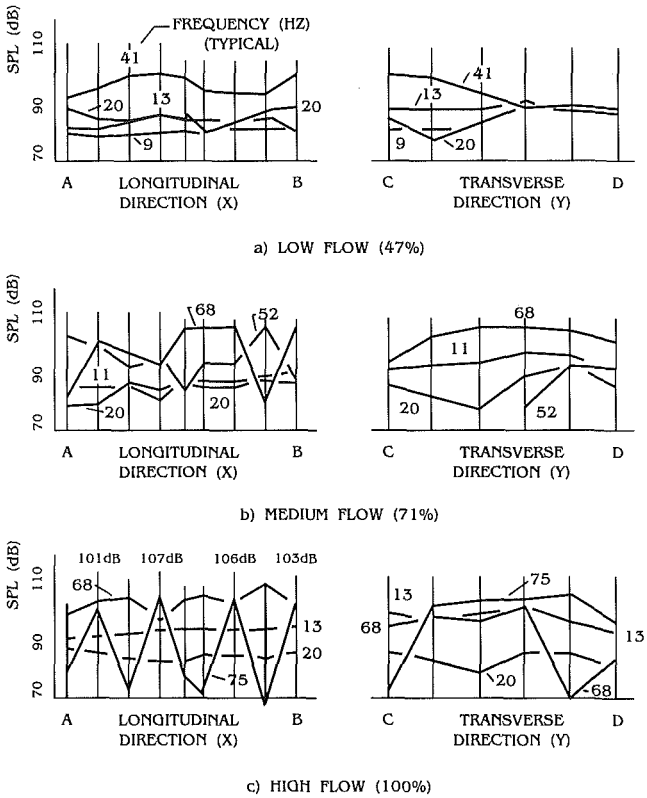

Fig. 3 Sound pressure levels at three air flow conditions measured around air heater at 1 m distance from casing (measured at elevation just above tube support plate; see Fig. 2 for location designations A, B, C, and D)

ν at the inlet and outlet of each bank and temperatures and velocities at 100 percent load are given in Table 1. Here v is the gap velocity, S is the Strouhal number, c_{eff} is the effective speed of sound within the tube bank, D is the tube diameter, and ν is the kinematic viscosity. The flow data were based on performance calculations of the air heater, correlated with control room data during operation. The tabulated data include Strouhal numbers based on the Fitzhugh map (Fitzhugh, 1973), and the effective speed of sound in the tube banks $c_{\text{eff}} = c(1 + \sigma)^{-1/2}$. Here c is the speed of sound in free space and σ is the fraction of space occupied by the tubes (Parker, 1978).

The air heater operated relatively quietly at low flows and became noisier at higher air flows. A particularly noisy vibratory condition developed when the air heater was exposed to the full-load flow.

Figure 3 shows plots of sound readings taken at a 1 m distance from the casing in the longitudinal (AB) and transverse (CD) directions at low, medium, and high flow conditions. The measurements were taken at an elevation just above the tube support plate using a Bruel and Kjaer (B&K) type 2230 precision integrating sound level meter in conjunction with a B&K type 2515 vibration analyzer. From these measurements, it can be seen that the acoustic environment around the air heater was relatively noisy. There was, however, no clearly developed standing wave pattern observed throughout the range of flow velocities, except at the high flow condition, when suddenly an intense acoustic vibratory condition developed. This condition was characterized by a single frequency noise and a clearly defined standing wave. As shown in Fig. 3(*c*), the standing wave was established in the flow direction (x) at a frequency of 75 Hz in the third mode. There was some variation of the 68 Hz frequency sound in the transverse (y) and longitudinal (x) directions; however, this did not represent a fully developed standing wave. A wave pattern in the longitudinal direction is already indicated at the medium flow at the frequencies of 68 Hz and 52 Hz.

The presence of the longitudinal acoustic vibration was considered unusual and was treated with concern as the suppression of this type of vibration is more difficult than the typically occurring transverse acoustic wave in the y (lift) direction, which is easily treated by placing acoustic baffles within the tube bank in the direction of flow (Eisinger, 1980).

Comparison of Predicted and Measured Acoustic Frequencies and Mode/Response Shapes. The air heater tube bank, including its untubed cavities, was modeled by finite elements using the effective speed of sound approach described by Parker (1978) and Blevins (1986). A two-dimensional model consisting of 1600 elements representing the plan view of the air heater (with a dimension equal to unity in the vertical (z) direction) was constructed. The temperature gradient, both tube banks, and untubed cavities were included in this model. The temperature of the air entering bank 1 was 37.8°C and increased linearly to 139.5°C within this bank. Air entered bank 2 at 139.5°C and increased linearly within this bank to a maximum temperature of 274°C. The temperature in the untubed cavities corresponded to the inlet and outlet temperatures of the corresponding tube banks. The speed of sound and the density of air (parameters needed for the numerical analysis) were specified for each bank and the untubed spaces. The effective speed of sound at atmospheric pressure was modified inside the tube banks by the solidity ratios of 0.535 and 0.449 for banks 1 and 2, respectively. Acoustic natural frequencies and mode shapes were determined. The results are given in Table 2. The measured frequencies are also given in this table for comparison. The measured frequencies of 20 Hz, 41 Hz, 52 Hz, 68 Hz, and 75 Hz compare well with those predicted. The measured response at 75 Hz (Fig. 3*c*) compares well with the predicted mode shape at 73.4 Hz with $ijk = 3, 1, 0$ in the longitudinal direction. The transverse component, however, appears distorted. The measured response at 68 Hz resembles to some degree the predicted one at 67.7 Hz, showing a not fully developed and somewhat distorted standing wave with $ijk = 2, 2, 0$.

Transverse Acoustic Vibration Along Tube Axes in Steam Generator Economizer Banks

Experimental Results. The economizer tube banks are located at the bottom of a large steam generator with the tubes

Table 2 Comparison of predicted and measured frequencies and mode shapes within air heater tube banks

Predicted Frequency (Hz)	20.0	24.9	33.0	40.0	49.6	52.5	55.3	60.6	67.7	73.4	80.0
Predicted Mode i, j, k (Approximated)	1, 0, 0	0, 1, 0	1, 1, 0	2, 0, 0	2, 1, 0	2, 1, 0	1, 2, 0	3, 0, 0	2, 2, 0	3, 1, 0	0, 3, 0
Measured Frequency (Hz)	20			41		52			68	75	

oriented from side-to-side of the unit. Bank 1 is located in the front, and bank 2 in the rear pass. Figure 4 shows the arrangement. There is one acoustic baffle located within each tube bank extending over the entire length of the banks from top to bottom. The economizer tubes are exposed to vertically oriented crossflow of hot gases leaving the steam generator heat recovery area tube banks. The tube banks above the economizer are perpendicular to the economizer tubes. There is an untubed cavity above the economizer banks with the lowest bank located 3200 mm above the economizer. An untubed discharge duct is located below. The tube layout is in-line with a constant side spacing and an alternating, narrow and wider longitudinal spacing. A division wall separates pass 1 from pass 2, making the flows through these passes relatively independent but regulated by dampers located 1575 mm below the banks.

The economizer tube banks developed strong acoustic vibration when exposed to full-load gas flow. The parameters of the gas flow at the vibratory condition are given in Table 3. These were based on boiler performance calculations correlated with experimentally determined operating parameters.

During the noisy period of acoustic vibration, sound measurements were taken using the sound meter and vibration analyzer described in the preceding section. A complete sound survey was performed at several elevations all around the steam generator. There was no evidence of acoustic standing waves in any of the steam generators upper banks. The strong vibratory condition was confined to the economizer area giving the highest readings. Figure 5 gives the results of the sound measurments taken at a 1 m distance from the boiler casing at locations 1 and 2 at the front, and at location 3 at the rear of the unit, in the side-to-side direction. The dominant frequency of the acoustic vibration was 42 Hz. At location 1 a relatively mild wave developed (Fig. 5*a*), indicating that bank 1 was not experiencing an intense noise condition at the 42 Hz frequency. The measurements at location 3 at the rear of the unit revealed a well-developed fourth mode standing wave extending in the side-to-side direction, thus a *standing wave established along the tube axes* (z) $i = 0, j = 0, k = 4$ (Fig. 5*c*). The measured maximum sound pressure level (SPL) at the 42 Hz frequency was 99.7 dB. This corresponds to a SPL higher by about 20–25 dB on the inside, considering the sound transmission losses through the casing and insulation. At location 2 at the discharge duct, the measured sound levels were somewhat higher, with a maximum of 104.3 dB (Fig. 5*b*). The plot at this location is indicative of a wave similar to that at location 3 with a distortion. The relative difference between the strength of the waves at locations 3 and 2 can perhaps be partially attributed to the presence of tube supports, a total of four, located at about the points of the maximum acoustic velocity in the fourth mode standing wave. Although the area at these supports was 35–40 percent open, some effect on the acoustic amplitude could be expected.

The results show that the intense acoustic vibration developed primarily in bank 2 in the rear pass. The onset of this vibration was sudden, caused by slightly reducing the gas flow in pass 2 (and correspondingly increasing the flow in pass 1).

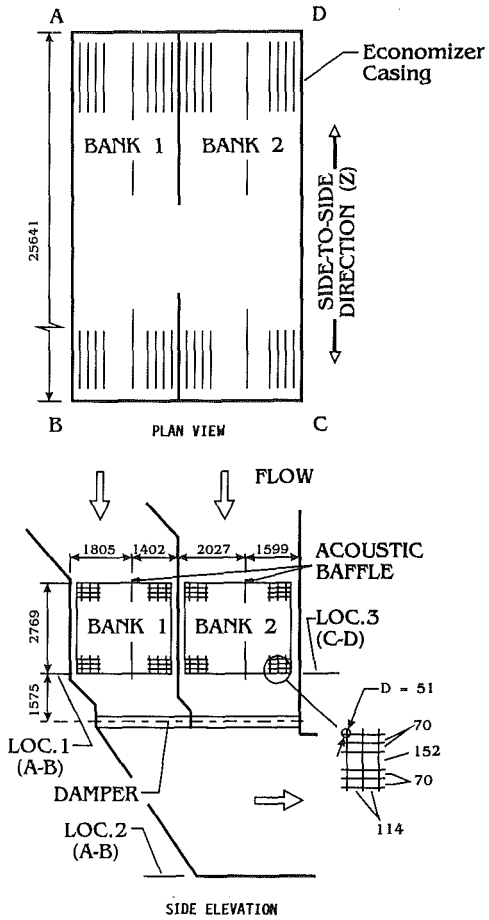

Fig. 4 Arrangement of economizer tube banks in lower portion of steam generator (dimensions shown are in mm)

By reversing this procedure, the vibratory condition could be abruptly stopped. This vibration is indicative of the type of excited instability since a triggering effect of a sudden reduction in gas flow was necessary to initiate it. (A slow increase in gas flow to full load did not cause this vibration.)

Acoustic vibration of this unusual type is again of concern to heat exchanger designers not only because it is difficult to predict but also because it is more difficult to suppress when it occurs.

Comparison of Predicted and Measured Parameters. Due to the presence of acoustic baffles, which were designed to eliminate the typical j-mode acoustic vibration, no such vibration occurred. The gas columns within the tube banks extended 25.64 m from side-to-side along the tubes. Table 4 gives the predicted acoustic frequencies, modes 1 through 4, and the measured fourth mode ($ijk = 0, 0, 4$) frequency at 42 Hz. The comparison between the predicted and measured values is very good.

Table 3 Economizer tube bank geometry and flow parameters at full load

Bank No.	Tube O.D. D	Side Spacing T	Longit. Spacing L	Gas Temp. In/Out T_e	Gap Vel. In/Out v	He x 10^6 In/Out	Re In/Out
	mm	mm	mm	C	m/s	—	—
1	51	114	70 152	533/ 412	14.3/ 12.2	4,530 - 6,540/ 4,170 - 6,030	9,198/ 10,302
2	51	114	70 152	458/ 385	18.1 16.3	6,012 - 8,685/ 5,700 - 8,245	13,760/ 14,816

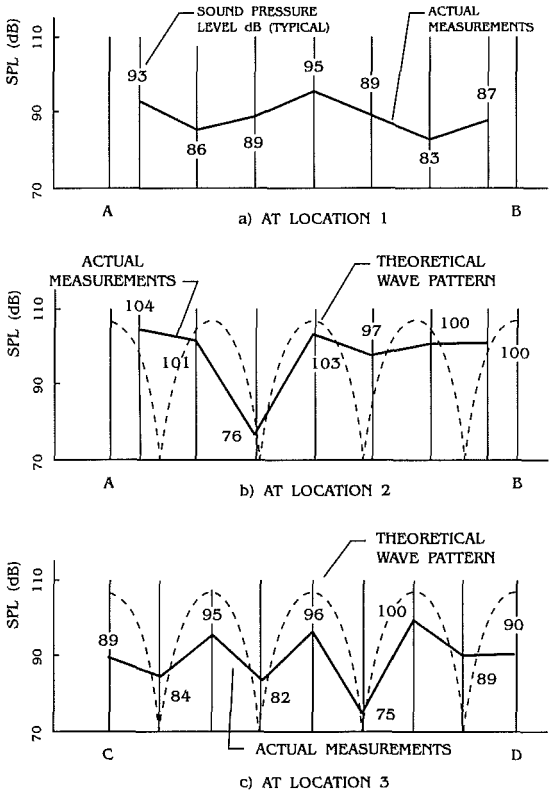

Fig. 5 Sound pressure levels at full-load gas flow measured at 1 m distance from economizer casing at three locations in side-to-side direction; all readings at dominant frequency of 42 Hz

Table 4 Comparison of predicted and measured frequencies and mode shapes within economizer tube banks

Predicted Freq. (Hz)	Bank 1	10.7	21.4	32.0	42.7
	Bank 2	10.3	20.6	30.9	41.3
Predicted Mode i, j, k (Approximated)		0, 0, 1	0, 0, 2	0, 0, 3	0, 0, 4
Measured Freq. (Hz)					42

Prediction of Intense Acoustic Vibration

The presently available criteria for the prediction of flow-induced acoustic vibration (called damping criteria) were all developed for the most commonly occurring j modes (Chen and Young, 1974; Fitzpatrick, 1986; Ziada et al., 1988b; Blevins, 1990). None of these criteria would predict the described vibration with certainty. More complete criteria that will include all acoustic modes (i, j, k) clearly need to be developed.

Means of Eliminating the Unusual Acoustic Vibration

Suppression of i Mode Acoustic Vibration. This mode of vibration is relatively difficult to suppress. We mention structural modifications that might help.

1 Increase acoustic damping, preferably by modifying the duct casing. Here a double wall casing with a perforated inner wall and the space between the two walls filled with acoustic damping material could be used.
2 Use overlapping single or double segmental baffles inserted inside the tube bank. A tortuous path of a single stream or a two-stream flow, respectively, will be created. This will change the acoustic frequencies and increase damping. The negative effect is an increased pressure drop across the tube bank.
3 Increase acoustic damping in the flow direction by using screens or perforated baffles. The negative effect again is increased pressure drop.
4 If the acoustic mode is not a pure i mode but has some j-mode component incorporated, the use of acoustic baffles parallel with the flow may change the frequency and the damping sufficiently to eliminate the vibration.

Suppression of k-Mode Acoustic Vibration. This acoustic mode is easier to suppress. Acoustic barriers in planes perpendicular to the tubes, parallel with the flow can be inserted to form porous baffles with as low an open area as possible. The number and location of these barriers depends on the mode(s) that need to the suppressed.

Corrective Measures Implemented

Suppression of Air Heater Acoustic Vibration. The vibration in the air heater was suppressed by using the conventional approach of installing acoustic baffles in the flow direction in combination with turning vanes on the flow inlet side. Three parallel equally spaced acoustic baffles were installed in banks 1 and 2 in conjunction with three turning vanes as shown in Fig. 6. This arrangement, which was dictated by the need to avoid increasing the pressure drop through the air heater, did eliminate the acoustic vibration. Although the baffles did not affect the 75 Hz i mode directly, their effect was significant in that the space inside the air heater was essentially split into four parallel spaces, each having a slightly different frequency in the i mode. The new frequencies were in the range between minus 8 percent to plus 6 percent relative to the computed

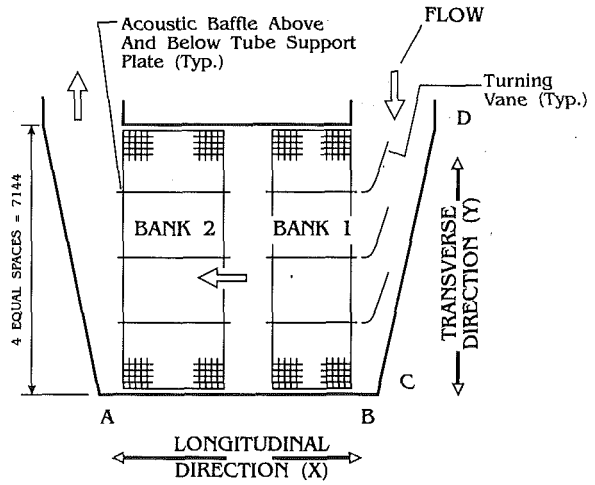

Fig. 6 Arrangement of acoustic baffles and turning vanes in air heater tube banks eliminating *i*-mode acoustic vibration

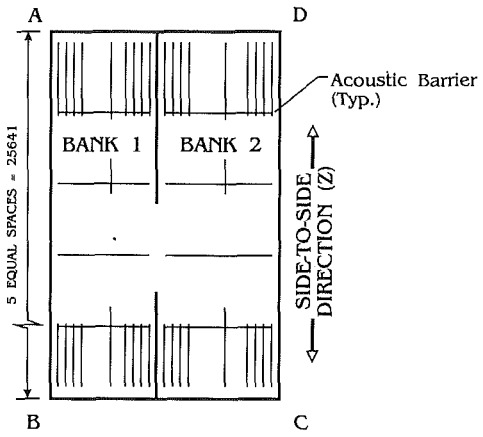

Fig. 7 Arrangement of acoustic barriers in economizer tube banks suppressing *k*-mode acoustic vibration

frequency of 73.4 Hz before the baffles were installed. Although the frequency change was relatively small, it did contribute to the elimination of the vibration when it was combined with an increased acoustic damping provided by the baffles.

Suppression of Economizer Acoustic Vibration. The *k*-mode vibration that occurred in the tube axial direction was suppressed by the installation of acoustic barriers placed along the 25.64 m side-to-side dimension. Four barriers dividing the 25.64 m distance into five approximately equal spaces were installed in both banks of the economizer. Figure 7 shows the arrangement. The barriers were built in place and were made of cylindrical tubes extending vertically and covering the entire height of the tube banks. Care was taken to fill in the remaining gaps between the tubes. This was accomplished by tabs welded to the inserted tube grid elements. In this way the original tube bank porosity of 81.8 percent in the tube axial direction was reduced to only 17.5 percent. The low porosity barriers changed the *k*-mode acoustic frequency and also introduced acoustic damping, which effectively suppressed the initially occurring 42 Hz acoustic vibration.

Discussion of Results and Working Theory

The excitation mechanism for the unusual acoustic vibration experienced in full-size heat exchangers is not fully understood at this time. If one postulated a vortex-excited system, one would find that at the vibration experienced, the maximum vortex shedding frequency was 30 percent below the 75 Hz vibration in the air heater, and a minimum of 47 percent above the 42 Hz frequency in the vibrating economizer bank using Fitzhugh's (1973) Strouhal numbers. These have been well correlated with experiments (Blevins and Bressler, 1987a, 1987b). Thus it appears that this vibration was not caused by the classical vortex shedding phenomenon.

Further, still within the vortex shedding theory, a shift of vortex shedding frequency in the tube bank by an acoustic field could occur. According to Blevins' study (Blevins, 1985) on a single cylinder, an 8 percent shift required a 150 dB sound field. We would have needed a much greater shift and thus an even stronger sound field before the onset of the vibration. There was no evidence of this in the test data.

The prediction of acoustic frequencies and mode shapes was good considering the complexity of the arrangement of the heat exchangers. The theoretical mode shapes formed a good basis for the interpretation of the experimental data.

In cases like this, one would explore all other possible sources that could be responsible for the onset of the acoustic conditions. We were not able to exclude the influence of many of the possible external sources, such as the effects of bends in the ducting, tube flexibility, and in the case of the economizer banks, the effect of the distant upper steam generator tube banks and the effect of the downstream damper. It is conceivable that these effects may have played some role, both in contributing to the level of turbulence, and, perhaps, in providing the stimulus for initiation of the acoustic vibration.

Considering all the available evidence, it would appear that the vibration experienced falls in the category of the coupling phenomena demonstrated to exist in enclosures with turbulent flow. Based on this theory, the underlying cause of this vibration would be the presence of turbulence in conjunction with vortex shedding—a condition always present inside a tube bank. The superimposed acoustic waves of many different frequencies and amplitudes, also always present, would interact and couple with the turbulent flow field and at proper conditions initiate the acoustic vibration. Within this context, it appears, the mechanism that caused the unusual vibration in the tube banks was one of a *fluid-acoustic instability*.

Summary and Conclusions

Unusual acoustic vibration in heat exchanger tube banks that developed in full-size operating units was described and evaluated using presently available methodology. The vibration did not meet the test of being excited by the traditional vortex shedding, or vortex shedding modified by an acoustic field. A *fluid-acoustic (coupling) mechanism* is put forward as the probable cause of the intense acoustic vibration experienced. Further studies of this theory are clearly needed.

Acknowledgments

The authors gratefully acknowledge the permission of Foster Wheeler Energy Corporation to publish the results contained in this paper.

References

Baird, R. C., 1954, "Pulsation-Induced Vibration in Utility Steam Generation Units," *Combustion*, Apr., pp. 38-44.

Blevins, R. D., 1985, "The Effect of Sound on Vortex Shedding From Cylinders," *Journal of Fluid Mechanics*, Vol. 161, pp. 217-237.

Blevins, R. D., 1986, "Acoustic Modes of Heat Exchanger Tube Bundles," *Journal of Sound and Vibration*, Vol. 109 (1), pp. 19-31.

Blevins, R. D., and Bressler, M. M., 1987a, "Acoustic Resonance in the Heat Exchanger Tube Bundles—Part I: Physical Nature of the Phenomenon," ASME *Journal of Pressure Vessel Technology*, Vol. 109, pp. 275-281.

Blevins, R. D., and Bressler, M. M., 1987b, "Acoustic Resonance in the Heat Exchanger Tube Bundles—Part II: Prediction and Suppression of Resonances," ASME *Journal of Pressure Vessel Technology*, Vol. 109, pp. 282-299.

Blevins, R. D., 1990, *Flow-Induced Vibration*, 2nd ed., Van Nostrand Reinhold Co., New York, pp. 370–375.

Chen, Y. N., 1968, "Flow Induced Vibration and Noise in the Tube Bank Heat Exchanger Due to von Karman Streets," ASME *Journal of Engineering for Industry*, pp. 134–146.

Chen, Y. N., and Young, W. C., 1974, "The Orbital Movement and the Damping of the Fluidelastic Vibration of Tube Banks Due to Vortex Formation, Part 3—Damping Capability of Tube Bank Against Vortex-Excited Sonic Vibration in the Fluid Column," ASME *Journal of Engineering for Industry*, Vol. 96, pp. 1072–1075.

Culick, F. E. C., 1966, "Acoustic Oscillations in Solid Propellant Rocket Chambers," *Astronautica Acta*, Vol. 12, No. 2, pp. 114–126.

Culick, F. E. C., 1970, "Stability of Longitudinal Oscillations With Pressure and Velocity Coupling in a Solid Propellant Rocket," *Combustion Science and Technology*, Vol. 2, pp. 179–201.

Culick, F. E. C., and Magiawala, K. R., 1981, "Measurements of Energy Exchange Between Acoustic Fields and Non-uniform Steady Flow Fields," *Journal of Sound and Vibration*, Vol. 75(4), pp. 503–517.

Eisinger, F. L., 1980, "Prevention and Cure of Flow-Induced Vibration Problems in Tubular Heat Exchangers," ASME *Journal of Pressure Vessel Technology*, Vol. 102, pp. 138–145.

Fitzhugh, J. S., 1973, "Flow Induced Vibration in Heat Exchangers," *Proceedings of UKAEA/NPL International Symposium on Vibration Problems in Industry*, Keswick, Apr., Paper No. 427.

Fitzpatrick, J. A., and Donaldson, I. S., 1977, "A Preliminary Study of Flow and Acoustic Phenomena in Tube Banks," ASME *Journal of Fluids Engineering*, Vol. 99, pp. 681–686.

Fitzpatrick, J. A., 1985, "The Prediction of Flow Induced Noise in Heat Exchanger Tube Arrays," *Journal of Sound and Vibration*, Vol. 99(3), pp. 425–435.

Fitzpatrick, J. A., 1986, "A Design Guide Proposal for Avoidance of Acoustic Resonance in In-Line Heat Exchangers,," ASME *Journal of Vibration, Acoustics, Stress, and Reliability in Design*, Vol. 108, pp. 296–300.

Funakawa, M., and Umakoshi, R., 1970, "The Acoustic Resonance in a Tube Bank," *Bulletin of the Japan Society of Mechanical Engineers*, Vol. 13, No. 57, pp. 348–355.

Grotz, B. J., and Arnold, F. R., 1956, "Flow Induced Vibration in Heat Exchangers," Technical Report No. 31 Mech. Engineering Department, Stanford University, Stanford, CA.

Ma, Y., Van Moorhern, W. K., and Shorthill, R. W., 1990, "An Innovative Method of Investigating the Role of Turbulence in the Velocity Coupling Phenomenon," ASME *Journal of Vibration and Acoustics*, Vol. 112, pp. 550–555.

Oengoren, A., and Ziada, S., 1991, "Vorticity Shedding and Acoustic Resonance in an In-Line Tube Bundle, Part II—Acoustic Resonance," *Flow-Induced Vibration and Wear*, ASME PVP-Vol. 206, pp. 135–145.

Owen, P. R., 1965, "Buffeting Excitation of Boiler Tube Vibration," *Journal of Mechanical Engineering Science*, Vol. 7, No. 4, pp. 431–439.

Parker, R., 1978, "Acoustic Resonances in Passages Containing Banks of Heat Exchanger Tubes," *Journal of Sound and Vibration*, Vol. 57(2), pp. 245–260.

Parker, R., and Stoneman, S. A. T., 1989, "The Excitation and Consequences of Acoustic Resonances in Enclosed Fluid Flow Around Solid Bodies," *Proceedings, Institution of Mechanical Engineers*, Vol. 203, C18187, pp. 9–19.

Price, E. W., and Dehority, G. L., 1967, "Velocity Coupled Axial Mode Combustion Instability in Solid Propellant Rocket Motors," presented at the Second ICRPG/AIAA Solid Propulsion Meeting, Anahiem, CA, June.

Price, E. W., 1979, "Velocity Coupling in Oscillatory Combustion of Solid Propellants," *AIAA Journal*, Vol. 17, pp. 799–800.

Putnam, A. A., 1959, "Flow Induced Noise in Heat Exchangers," ASME *Journal of Engineering for Power*, Vol. 81, pp. 417–422.

Rae, G. J., and Murray, B. G., 1987, "Flow Induced Acoustic Resonances in Heat Exchangers," *Proceedings International Conference on Flow Induced Vibrations Bowness-on-Windermere*, sponsored by BHRA, England, Paper E3, pp. 221–231.

Ziada, S., Oengoren, A., and Buhlmann, E. T., 1988a, "On Acoustical Resonance in Tube Arrays, Part I—Experiments," *International Symposium on Flow Induced Vibration and Noise*, Vol. 3, ASME Winter Annual Meeting, Chicago, IL, pp. 219–243.

Ziada, S., Oengoren, A., and Buhlmann, E. T., 1988b, "On Acoustical Resonance in Tube Arrays, Part II—Damping Criteria," *International Symposium on Vibration and Noise*, Vol. 3, ASME Winter Annual Meeting, Chicago, IL, pp. 245–254.

Ziada, S., and Oengoren, A., 1991, "Vorticity Shedding and Acoustic Resonance in an In-Line Tube Bundle, Part I: Vorticity Shedding," *Proceedings of the Institution of Mechanical Engineers, Flow Induced Vibrations*, I Mech E, May, pp. 497–509.

E. C. Cobb

T.-C. Cheu

J. Hoffman

Textron Lycoming,
Stratford, CT 06497

Optimal Circumferential Placement of Cylindrical Thermocouple Probes for Reduction of Excitation Forces

This paper presents a design methodology to determine the optimal circumferential placement of cylindrical probes upstream of a turbine stage for reduced excitation forces. The potential flow forcing function generated by the probes is characterized by means of a Fourier analysis. A finite difference formulation is used to evaluate the sensitivity of the forcing function to the probe positions. An optimization scheme, based on the linear programming method, uses the sensitivity analysis results to reposition the probes such that the Fourier amplitudes of critical excitation orders are reduced. The results for a sample design situation are presented.

Introduction

Technological advances in material science and internal aerodynamics are quickly exploited by the gas turbine industry to produce more efficient and lighter weight products. This results in engine operation at higher mechanical stress levels, thus demanding more accurate estimations of stress in both steady and dynamic states. This has resulted in continuous efforts to improve the state of the art in stress analysis.

The need for more sophisticated approaches, with regard to structural dynamics and vibratory stress, is particularly strong. Estimation of vibratory stress in the turbine or compressor blades of an engine during the paper design phase was once considered to be extremely difficult. Now, however, such considerations are becoming a matter of routine. In advancing such effort, methods for determining critical speeds and the deformations and stress profiles of particular modes of vibration have been developed. In short, significant progress has been made in addressing the response side of this issue. In this paper the forcing function side of vibratory stress analysis is addressed.

The vibratory response of a structural system can be mitigated by reducing the magnitude of the dynamic force that impels its motion. In general, such an approach has not been considered practical. However, for certain rather common causes, this approach can be put to use with good results. Specifically, for the case of upstream flow obstructions, produced by essential instrumentation (such as thermocouple probes), the vibratory stress induced on turbine blades resulting from wake perturbations can be estimated and systematically altered by analytic methods. Such a method is the subject of this paper. This is accomplished by application of linear programming techniques [1, 2], through which optimal values of forcing function spectral distribution and magnitude may be obtained.

It is well known that obstructions in a flow stream will create wakes behind the obstructions. Within the wakes, the pressure can drop from that of the free-stream pressure to the thermodynamic static pressure. A turbine blade passing through such a wake will be subject to a pressure variation, which can induce the unwanted vibratory response of the blade. In this paper we consider a set of cylindrical thermocouple probes placed immediately upstream of the turbine blades. These probes will create wakes, which give rise to a variable circumferential pressure, which in turn acts as forcing function on the blade.

The probe wake widths are assumed proportional to the diameter of the probes. The wake is also assumed to maintain a constant width as it travels downstream. That is, the wake does not spread out or decay. For small axial distances between the probes and the blades, as is the case in most modern turbine engines, this closely represents the true physical situation.

The general equation of motion for the blade considered as a multiple degree of freedom system is

$$[M]\ddot{\mathbf{U}} + [C]\dot{\mathbf{U}} + [K]\mathbf{U} = \mathbf{F}(t) \tag{1}$$

The excitation forces generated by the variable circumferential pressure may be characterized by means of a Fourier series analysis. Thus, the right-hand side of Eq. (1) is given by

$$\mathbf{F}(t) = \mathbf{P} \sum_{n=1}^{\infty} C_n \cos\left(n\Omega t + \phi_{n_r}\right) \tag{2}$$

With the excitation forces in this form, the steady-state solution to Eq. (1) is given by

Contributed by the International Gas Turbine Institute and presented at the 37th International Gas Turbine and Aeroengine Congress and Exposition, Cologne, Germany, June 1–4, 1992. Manuscript received by the International Gas Turbine Institute February 11, 1992. Paper No. 92-GT-423. Associate Technical Editor: L. S. Langston.

$$\mathbf{U}(t)=\sum_{n=1}^{\infty}\sum_{r=1}^{N_m}\left(\frac{\Phi_r(\Phi_r^T\cdot\mathbf{P})}{K_r}\right)[D_r]C_n\cos(n\Omega t-\phi_{n_r}) \quad (3)$$

where

$$D_r=\left[\frac{1}{\sqrt{(1-R_r^2)^2+(2\zeta_r R_r)^2}}\right]$$

$$R_r=\frac{n\Omega}{\omega_r} \quad (4)$$

as presented by Craig [3]. The complete solution to Eq. (1) will include the transient response of the system to the initial conditions. Transient response is an important part of the impulsive reaction to probe perturbation. However, transient response analysis is not treated in this paper in order that the impact of the optimization scheme on the steady-state response may be clearly demonstrated.

If the excitation forces generated by the variable circumferential pressure coincide with a natural frequency of the blade, then large resonant responses will occur. The usual solution to this problem is to redesign the turbine blades such that the blade is insensitive to the exciting forces. Since aerodynamic design constraints on the blades do not generally allow radical changes in the blade geometry, an effective design change is often hard to come by. This is particularly true of power turbine blades where there are no internal cavities that could be modified to provide some relief [4].

When modification of the blade structure is not possible, the only feasible solution is to reduce or change the forcing function acting on the blades. To accomplish this effectively, a systematic technique of parameter iteration must be used, whereby an optimization of effects is achieved. By using such optimization techniques, design parameters that are not aerodynamically related to performance can be adjusted to alter the shape of circumferential pressure variations. The adjustments are made such that a reduction of the amplitudes of those Fourier components of the forcing function (produced by that shape) can be effected. Most important among these are the ones that can generate blade resonance. In effect, the energy associated with the resonant components is shifted to less critical modes.

In this study, the design parameters selected are the circumferential locations of the thermocouple probes. The locations of each probe is assumed to be unrestricted, except that the probes may not physically overlap or have excessive movement such that the proper measurements of circumferential temperature distributions for engine control are lost. Additional proscriptions may be imposed on the specific probe locations by some other design criteria, such as avoiding fuel lines or oil service lines.

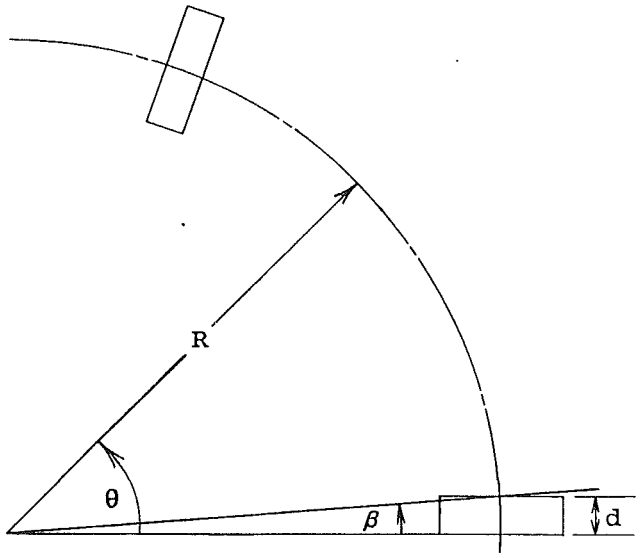

Fig. 1 Geometry parameters for circumferential placement of the thermocouple probes

The circumferential pressure pattern in a plane downstream of the probes is defined as a specific pressure, P_p, at a given angle of circumference. The circumferential pressure pattern between the probes is assumed to be constant and is equal to the free-stream pressure, P_s. The pressure in the wake behind the probes is assumed to drop to a minimum pressure equal to the thermodynamic static pressure, P_0.

The width of the pressure wake downstream of a probe is assumed to be equal to the diameter of the probe. Figure 1 shows the geometry definitions used in defining the wake width at the midspan of the probe. The angle that subtends the circumferential arc length at the probe midspan radius is defined as β and is given by

$$\beta=2\tan^{-1}\frac{d}{2R} \quad (5)$$

This angle will increase as the radial position from the engine

Nomenclature

A_n = coefficients of the Fourier cosine terms
B_n = coefficients of the Fourier sine terms
C_n = vector amplitude of the Fourier coefficients
$[C]$ = structural damping matrix
D_r = modal amplification factor
d = probe diameter
f = objective function
$\mathbf{F}(t)$ = vector of time-dependent forcing function
g = constraint functions
i, j = indices
$[K]$ = structural stiffness matrix
K_r = modal stiffness
$[M]$ = structural mass matrix
M = number of spatial divisions within a wake
N = number of movable probes
N_m = number of modes to be used in the modal analysis
N_f = number of frequencies to be constrained
n = integer value of the excitation order
$\mathbf{P}$ = vector defining the spatial dependence of the loading
P_0 = minimum pressure within the wake behind a probe
P_p = pressure magnitude within the wake behind a probe
P_s = free-stream pressure between probes
q = number of spatial increments
r = variable index of the natural frequency mode number
R_r = frequency ratio = Ω/ω_r
$\mathbf{U}(t)$ = displacement vector of physical coordinates
α = design variable
β = angle subtending the arc length of the probe diameter
ϵ = integration error
θ = circumferential angle
ζ_r = modal damping factor for the rth mode
Φ_r = normal mode shape for the rth mode
ϕ_{nr} = phase angle of the nth excitation order in the rth normal mode
Ω = rotational speed of the rotor
ω_r = natural frequency of the rth mode

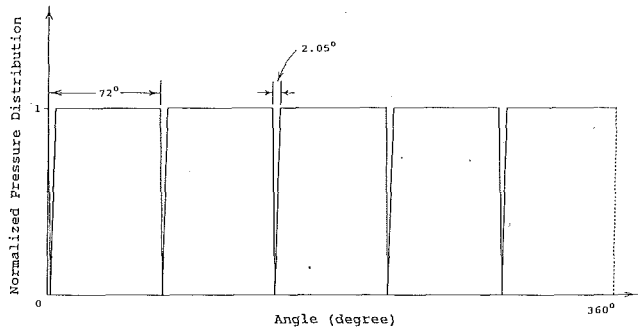

Fig. 2 Pressure pattern for five equally spaced circumferential thermocouple probes with 0.25 in. probe diameter and 7.0 in. radius at midspan of the probes

centerline is decreased. Thus, the optimization analysis is also a function of the particular radius from the engine centerline used. The methodology presented here does not currently account for the change in the Fourier coefficients as a function of the radius. However, this was judged to be a tolerable modeling expedient. The analysis for the example given in this paper was performed at the midspan radius of the probe, which gives a good approximation of the total forcing function.

The pressure in the wake downstream of a probe varies with the circumferential angle. The angle β is normalized to range from zero to π so that the pressure is represented by a sine squared function using the normalized angle, that is

$$P_p = (P_s - P_0)\left(1 - \sin^2\left(\frac{i\pi}{M}\right)\right) \quad i = 0 \ldots M \tag{6}$$

where M is the number of divisions of β. Experimental testing has shown that this mathematical definition of the pressure is quite accurate [5].

As an example, the circumferential pressure distribution shown in Fig. 2 is given for the case where the pressure difference between the free-stream pressure and the static pressure is normalized to one. There are five identical probes of 0.635 cm (0.25 in.) diameter, spaced 72 deg apart, and at a radius of 17.78 cm (7.0 in.).

Fourier Analysis

For a given number of probes at specified circumferential locations, the resulting pressure versus circumferential angle for a complete traverse of the turbine stage can be developed and represented by a Fourier series [6]. In the general case, this pressure pattern will have a spatial period equal to the probe mid span circumference, or in angular measure, 2π. Thus:

$$P_p(\theta) = A_o + \sum_{n=1}^{\infty} \{A_n \cos(n\theta) + B_n \sin(n\theta)\} \tag{7}$$

The Fourier coefficients of the pressure pattern may now be evaluated using the well-known Euler formulas:

$$A_o = \frac{1}{2\pi}\int_{-\pi}^{\pi} P_p(\theta)d\theta$$

$$A_n = \frac{1}{\pi}\int_{-\pi}^{\pi} P_p(\theta)\cos(n\theta)d\theta$$

$$B_n = \frac{1}{\pi}\int_{-\pi}^{\pi} P_p(\theta)\sin(n\theta)d\theta \tag{8}$$

The pressure pattern may also be described in the vector amplitude form:

$$P_p(\theta) = \sum_{n=1}^{\infty} C_r \cos(n\theta + \phi_n) \tag{9}$$

where

$$C_n = \sqrt{A_n^2 + B_n^2}$$

$$\phi_n = \tan^{-1}\frac{B_n}{A_n} \tag{10}$$

Using simple numerical integration methods, the Fourier series coefficients described in Eq. (8) can be easily obtained for a specific pressure distribution. A Simpson's rule numerical integration scheme was used in this study to evaluate the Fourier coefficients.

In the frequency domain, the forcing function can be specified conveniently by these Fourier coefficients. Derivatives of the Fourier coefficients with respect to the locations of the probes provide the trend of variation of the amplitudes of various excitation modes due to the change of probe locations. These derivatives are required by the linear programming technique to find the optimal placement of the probes for reduced excitation.

Analysis Procedure

The problem of the optimal placement of thermocouples can be stated as to minimize an objective function, f, which can be selected as the amplitude of the most critical mode, subject to the design constraints on selected modal amplitudes, of:

$$g_j^L \le g_j \le g_j^U \qquad j = 1, \ldots, N_f \tag{11}$$

and the side constraints of the design variables

$$\alpha_i^L \le \alpha_i \le \alpha_i^U \qquad i = 1, \ldots, N \tag{12}$$

where N is the total number of movable probes and the design variables are selected as angular locations of the probes.

Using the first-order Taylor series expansion centered at the current locations, f and g of the new placement can be approximated as

$$f = f_0 + \sum_{i=1}^{N} \frac{\partial f}{\partial \alpha_i}(\alpha_i - \alpha_{io}) \tag{13}$$

$$g_i = g_{jo} + \sum_{i=1}^{N} \frac{\partial g_i}{\partial \alpha_i}(\alpha_i - \alpha_{io}) \quad j = 1, \ldots, N_f \tag{14}$$

to form a linear programming problem over a limited range of design variables. Calculations of the derivatives of the objective function and the constraint functions are called sensitivity analyses because these derivatives provide the trend of variations of those functions due to the change in the design variables. In this paper these derivatives are calculated using a central finite difference formulation presented in the following.

When using central finite difference to perform sensitivity analysis, the derivatives are calculated for each design variable one at a time. All of the probes except the one for which the derivative is being calculated are considered fixed. For the design variable associated with the movable probe, a small perturbation in the circumferential location is added to and to and subtracted from the current probe location. The Fourier coefficients are evaluated for the modified circumferential pressure patterns resulting from these positive and negative perturbations. The derivatives of the coefficients with respect to the probe location are approximated by the change in the Fourier coefficient amplitudes divided by twice the perturbation. For the nth vector amplitude, the derivative with respect to the ith design variable is:

$$\frac{\partial C_n}{\partial \alpha_i} \approx \frac{C_n(+\Delta\alpha_i) - C_n(-\Delta\alpha_i)}{2\Delta\alpha_i} \quad \begin{matrix} n = 0, 1, \ldots, \infty \\ i = 1, 2, \ldots, N \end{matrix} \tag{15}$$

The derivatives of A_n and B_n may also be calculated in the same manner.

Sample Problem

The methodology developed above was implemented by a FORTRAN program for automatic computation. As a sample case, the situation of a thermocouple harness containing five probes upstream of a turbine stage in a small gas turbine engine was analyzed. The probes were uniformly spaced at 0, 72, 144, 216, and 288 deg. All five probes were given the same diameter, 0.635 cm (0.25 in.). The pressure difference between the free-stream pressure and the static pressure was normalized to one. The analysis is carried out at the midspan radius of the probes which was defined as 17.78 cm (7.0 in.). Figure 2 shows the resulting idealized circumferential pressure distribution for this example. The turbine blades were considered to be sensitive to the fifth-order excitation at the operating rotational speed. The design goal was to reduce the magnitude of the fifth-order excitation generated by the thermocouple probe wakes.

As a practical matter, it is not feasible to compute every term in the displacement solution summation of Eq. (3). In addition, for practical engineering problems, not every Fourier coefficient is required to be constrained. Thus, we impose limits only on the excitation orders immediately above and below the critical excitation order. This is an acceptable approximation as a result of the inverse square relationship of the response to the frequency ratio given in Eq. (3). Because of this relationship, energy transferred to excitation orders other than those in immediate proximity of the critical order will have little effect on the response. Therefore, because the fifth-order excitation was specified as the critical excitation order in the example, only the fourth and sixth excitation order coefficients are required to be constrained. However, in order to demonstrate the capacity of the software developed, the first through fourth and the sixth through ninth excitation order coefficients are constrained to have an upper limit of 0.01 on their amplitudes.

Additional constraints due to the locations of other mechanical components were: Because of an oil supply line, the number one probe (located at 0.0 deg) was not permitted to move in the clockwise direction, and, because of a structural support, the number five probe (located at 288 deg) was also not allowed to move in the clockwise direction.

To perform the numerical integration to calculate the Fourier coefficients, an initial spatial increment of ten points per degree of circumference was selected. Using the selected spatial increment, the circumferential pressure pattern was discretized. The discretization process yields a total of 3600 spatial points in one period and allows 1800 Fourier coefficients to be computed. The reconstruction of the actual pressure distribution requires an infinite series summation of the Fourier coefficients and their associated functionals. However, as indicated before, each of the individual Fourier coefficients is calculated with a high degree of accuracy because of the number of points used to define the function in the spatial domain. Therefore, only those coefficients and their derivatives pertinent to the objective and constraint functions require calculation.

The present example used three design variables. The three design variables selected, α_1, α_2, and α_3, were the locations of probe numbers 1, 3, and 5, respectively. The objective was to reduce the amplitude of the fifth-order coefficient while constraining the amplitudes of the first through fourth and the sixth through ninth-order coefficients to be less than or equal to 0.01 psi. At the same time, geometry constraints are placed on the maximum motion (in degrees) that the design variables may move.

Therefore, the objective function is stated simply as:

$$f = C_5 \tag{16}$$

while the constraint functions are defined by:

$$C_i \le 0.01 \qquad \begin{matrix} i = 1, 2, 3, 4, \\ 6, 7, 8, 9, \end{matrix} \tag{17}$$

and the side constraints on the probe locations are given by:

$$\begin{aligned} -1 \le \alpha_1 \le 0 \\ -1 \le \alpha_2 \le 1 \\ -1 \le \alpha_3 \le 0 \end{aligned} \tag{18}$$

These side constraints prevent the first and fifth probes from moving in the clockwise direction (positive changes of α_1 and α_3) but allow the third probe to move in either direction. These side constraints also serve as the maximum move limits of design variables used for each iteration in the linear programming. By experience, these move limits allow the functions to be linearized to give a good approximation of the nonlinear characteristics of the problem while retaining a reasonable computation cost.

The computation results for this example are presented in Tables 1–7. The computation proceeded through three global iterations, each with a different integration increment size. There are a number of local iterations within each global iteration. The local iterations of each global iteration are considered converged when all the movable probes cannot move with an angle larger than the integration increment size of the associated global iteration. A final global iteration is performed with a very small integration increment size to verify that the analysis has converged.

The integration increment size is fixed within each global iteration. However, the integration increment size is reduced by an order of magnitude when computation proceeds from

Table 1 Change of probe locations (deg) for the first global iteration

Iteration Number	Probe Number 1	2	3	4	5
1	0.0000000	0.0000000	1.0000000	0.0000000	0.0000000
2	-1.0000000	0.0000000	1.0000000	0.0000000	-1.0000000
3	-1.0000000	0.0000000	1.0000000	0.0000000	-1.0000000
4	-1.0000000	0.0000000	1.0000000	0.0000000	-1.0000000
5	0.0000000	0.0000000	1.0000000	0.0000000	-1.0000000
6	0.0000000	0.0000000	1.0000000	0.0000000	-0.2000000
7	0.0000000	0.0000000	0.1000000	0.0000000	0.0000000
8	0.0000000	0.0000000	0.0000000	0.0000000	0.0000000

Table 2 Change of probe locations (deg) for the second global iteration

Iteration Number	Probe Number 1	2	3	4	5
1	0.0000000	0.0000000	0.9500000	0.0000000	0.0000000
2	0.0000000	0.0000000	0.0400000	0.0000000	0.0000000
3	0.0000000	0.0000000	0.0000000	0.0000000	0.0000000

Table 3 Change of probe locations (deg) for the third global iteration

Iteration Number	Probe Number 1	2	3	4	5
1	0.0000000	0.0000000	1.0000000	0.0000000	0.0000000
2	0.0000000	0.0000000	0.2470000	0.0000000	0.0000000
3	0.0000000	0.0000000	0.0290000	0.0000000	0.0000000
4	0.0000000	0.0000000	0.0230000	0.0000000	0.0000000
5	0.0000000	0.0000000	0.0080000	0.0000000	0.0000000
6	0.0000000	0.0000000	0.0000000	0.0000000	0.0000000

Table 4 Probe locations (deg) for the global iterations

Iteration Number	Probe Number 1	2	3	4	5
0	0.000000	72.000000	144.000000	216.000000	288.000000
1	-3.000000	72.000000	150.100000	216.000000	283.800000
2	-3.000000	72.000000	151.090000	216.000000	283.800000
3	-3.000000	72.000000	152.397000	216.000000	283.800000

Table 5 Harmonic amplitudes for the first global iteration

Iteration Number	Harmonic Amplitude (10^{-3}) C_0	C_1	C_2	C_3	C_4	C_5	C_6	C_7	C_8	C_9
1	985.7877	0.1513	0.1540	0.1564	0.1578	28.3848	0.1648	0.1641	0.1678	0.1683
2	985.7877	0.2398	0.2026	0.3030	0.5238	28.3647	0.7463	0.6293	0.7930	1.0074
3	987.0519	2.7436	2.2826	2.9369	1.8656	25.7641	3.9559	1.8865	3.6298	1.9934
4	988.6292	6.0608	5.3680	6.2035	4.3708	22.4301	7.9151	4.9831	7.0553	3.4160
5	988.6302	6.2201	5.3172	6.3213	3.9343	22.1718	8.8021	5.3040	7.2367	3.6619
6	988.6302	6.3781	5.2760	6.4329	3.6155	21.8331	9.6281	5.8870	7.2993	4.5743
7	988.6302	6.4572	5.1481	6.6901	3.4842	21.5772	9.9717	6.2187	7.7950	5.0551
8	988.6307	6.4622	5.1341	6.7193	3.4732	21.5527	9.9928	6.2495	7.8548	5.0863

Table 6 Harmonic amplitudes for the second global iteration

Iteration Number	Harmonic Amplitude (10^{-3}) C_0	C_1	C_2	C_3	C_4	C_5	C_6	C_7	C_8	C_9
1	988.6312	6.4019	5.2564	6.7752	3.0852	21.5775	9.8151	6.4922	7.8632	4.9003
2	988.6312	6.4509	5.1348	7.0473	2.9659	21.3475	9.9924	6.8554	8.4022	5.2290
3	988.6312	6.4527	5.1303	7.0594	2.9613	21.3373	9.9992	6.8729	8.4241	5.2429

Table 7 Harmonic amplitudes for the third global iteration

Iteration Number	Harmonic Amplitude (10^{-3}) C_0	C_1	C_2	C_3	C_4	C_5	C_6	C_7	C_8	C_9
1	988.6312	9.2801	8.6817	9.0439	2.2201	21.5067	9.8259	7.1561	8.3794	4.8395
2	988.6312	9.2473	8.6910	9.2649	1.8381	21.2365	9.9703	7.6561	8.8714	5.2421
3	988.6312	9.2408	8.6975	9.3132	1.7462	21.1676	10.0020	7.7924	8.9865	5.3408
4	988.6312	9.2433	8.6971	9.3072	1.7570	21.1757	9.9983	7.7761	8.9730	5.3293
5	988.6312	9.2410	8.6976	9.3122	1.7484	21.1692	10.0012	7.7890	8.9838	5.3384
6	988.6312	9.2415	8.6972	9.3105	1.7513	21.1716	10.0002	7.7845	8.9800	5.3353

one global iteration to the next. The analysis within the first global iteration uses an integration increment size of 0.1 deg. Once the local iterations converge, the step size is reduced to 0.01 deg. The second global iteration then continues beginning from the probe positions determined in the last global iteration. The smaller integration increment size increases the accuracy of the Fourier coefficient calculation and the sensitivity analysis. Therefore, the algorithm may move the probes a larger amount in the local iteration immediately following the integration increment size change. However, the trend of convergence is always in toward the order of the step size. The analysis proceeds within the seconds global iteration until the local iterations converge. The integration increment size is reduced further to 0.001 deg and the analysis continues until the local iteration converges. Tables 2 and 3 clearly show this behavior occurring in the first local iteration after the integration increment size change for both the second and third global iterations.

In our example, the overall program was considered converged when the change in location of any one of the movable probes was less than 0.001 deg. This limit was set from the practical consideration that angles smaller than this cannot easily be measured in a manufacturing situation. This convergence criterion was reached after the third global iteration. A final global iteration was run with a very small integration step size of 0.0005 deg. Since the changes of all of the probe locations were zero at the first local iteration of the fourth global iteration, it was verified that the algorithm had converged.

Table 4 shows an iteration history of the probe locations. For each iteration, the change in the angular location of each probe is given. Because their position specifications are fixed, there are no changes in the locations of the number 2 and 4 probes.

Tables 5–7 show the iteration history of the harmonic amplitudes. Figure 3 is a histogram showing the change in the

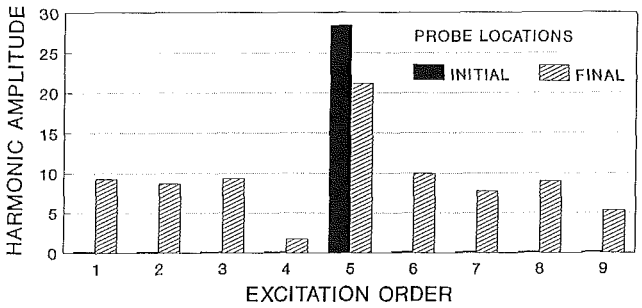

Fig. 3 Initial and final vector amplitudes for the example

vector amplitudes of the first nine excitation orders between the condition at the beginning of the analysis and the condition at the conclusion of the analysis. After three global iterations, amplitude of the fifth-order excitation has been reduced by 26 percent. The amplitudes of all other excitation orders have been increased and are approaching the constraint upper limit. The amplitudes of the first, second, third, sixth, and eighth-order excitations have closely approached the constraint upper limit of 0.01 psi. Because the amplitudes of these coefficients are approaching the upper limit, an alternate convergence criterion could be specified by defining a tolerance bound on these constraint amplitudes.

Three simple examples of the application of the methodology are represented in the Goodman diagram shown in Fig. 4. For a linear system, a 26 percent reduction in the excitation force will result in a 26 percent reduction in the alternating stress.

Consider the following three hypothetical cases. The first case is an engine component with a mean stress of 25 ksi, and an alternating stress of 11 ksi, point A in Fig. 4. Assuming that the contributions to the alternating stress from excitation orders other than the fifth order are negligible, a reduction of 26 percent in the alternating stress brings the alternating stress

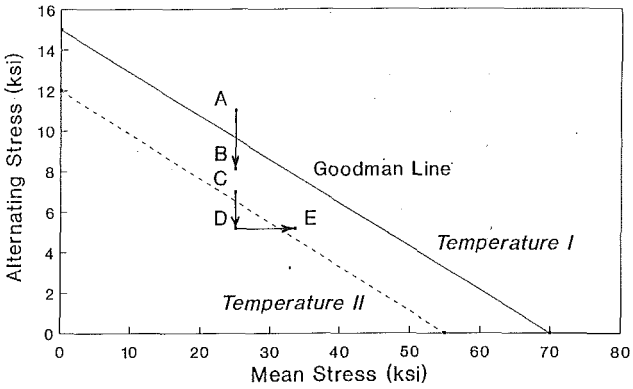

Fig. 4 Goodman diagram for the sample problem

to 8.14 ksi, or point B in Fig. 4. Using the Goodman line at temperature I, Fig. 4 clearly shows that such a reduction in alternating stress brings the component from the finite life region to the infinite life region.

The second case again uses the Goodman line at temperature I. This case is that of an engine component with a mean stress of 25 ksi and an alternating stress of 7 ksi, point *C* in Fig. 4. This stress condition provides a vibratory margin of 2.64 ksi. A reduction of the alternating stress by 26 percent brings the alternating stress to 5.18 ksi, point *D*. In this case the mean stress may safely be increased to 33.5 ksi while retaining an infinite life of the component and maintaining a vibratory margin of 2.64 ksi. This increase in allowable mean stress means that the component could be operated safely at a speed 16 percent higher, thus improving performance without sacrificing component life or vibratory margin.

The third case is that where the engine component also has an alternating stress of 7 ksi and a mean stress of 25 ksi. With a 26 percent reduction of the alternating stress, from 7 ksi to 5.18 ksi, and a constant mean stress, the temperature of the component could be increased. With an increase in temperature, the Goodman line would move from that given by the temperature *I* line to that at temperature *II*, the dashed line shown in Fig. 4. An increase in the overall temperature of the engine will result in improved performance. By reducing the forcing function acting on the blades, the alternating stress in the blades will be reduced. A temperature increase to improve engine performance can then be made without sacrificing component life.

All three of these examples demonstrate a marked improvement in the quality of the components resulting from reduction of the forcing function driving the vibration of the components. The application of this methodology allows any one or a combination of all three improvements to be made to an engine component.

Conclusion

A methodology has been presented that provides a simple and powerful automated tool for use in reducing the amplitude of the excitation generated by thermocouple probes upstream of a turbine rotor. Using this methodology, the aerodynamic parameters upstream of the probes are not altered. Therefore, the aerodynamic performance of the engine is impacted minimally. The methodology presented is capable of handling a large spectrum of complex design situations. The methodology associated with this type of problem. This is accomplished by providing a computational approach for determining the locations of thermocouple probes to reduce the downstream wake excitation amplitudes. The algorithm itself is highly efficient. The example given in this paper was executed on an IBM 3090 mainframe computer using 14.4, 53.4, 460.2 CPU seconds for the first, second, and third global iterations respectively. The verification run required 145.2 CPU seconds to confirm the convergence of the solution.

The methodology can be extended in the following manner. First, the methodology can be adapted to consider other objects in the flow path. The methodology has general applicability if the pressure wake downstream of the obstruction can be described in a piecewise analytic manner. Thus excitations generated by stator vanes or inlets or inlet struts may also be considered by the methods presented here. Secondly, a pseudo-three-dimensional analysis may be conducted by including the effects of various radii on the Fourier coefficients. Finally, a transient response analysis can be included, if desired, by including the system initial conditions in the solution of Eq. (1).

In summary, this paper presents an effective and efficient methodology to improve the quality and reliability of gas turbine engine components. The software developed to implement this methodology is highly accurate and cost effective. Therefore, component quality assurance can be achieved with reduced design effort.

References

1 Fox, R. L., *Optimization Methods for Engineering Design*, Addison-Wesley, Reading, MA, 1973.

2 Zienkiewicz, O. C., and Campbell, J. S., *Shape Optimization and Sequential Linear Programming, Optimum Structural Design Theory and Applications*, R. H. Gallagher and O. C. Zienkiewicz, eds., Wiley, New York, 1973.

3 Craig, R. R., *Structural Dynamics*, Wiley, New York, 1981.

4 Cheu, T. C., "Sensitivity Analysis and Shape Optimization of Axisymmetric Structures," *International Journal for Numerical Methods in Engineering*, Vol. 28, 1989, pp. 95–108.

5 Kerrebrock, J. L., and Mikolajczak, A. A., "Intra-stator Transport of Rotor Wakes and Its Effect on Compressor Performance," ASME JOURNAL OF ENGINEERING FOR POWER, Vol. 92, 1970, pp. 359–368.

6 Brigham, E. O., *The Fast Fourier Transform*, Prentice-Hall, Inc., Englewood Cliffs, NJ, 1974.

7 Ralston, A., and Rabinowitz, P., *A First Course in Numerical Analysis*, McGraw-Hill, New York, 1978.

Development of a Regenerator for an Automotive Gas Turbine Engine

J. Sayama

T. Morishita

Higashi-Fuji Technical Center,
TOYOTA Motor Corporation,
Shizuoka, Japan

It is vital to estimate the temperature effectiveness and pressure loss of the regenerator accurately when designing a gas turbine engine because these characteristics basically determine the size, weight, and fuel consumption of the regenerative gas turbine engine. In operation of an actual engine, regenerators often fail to attain the characteristics predicted by conventional methods, because there are many performance-reducing irregularities such as the nonuniform velocity distribution of gases flowing into the core. In this paper, a prediction method that is based on data from actual engine tests is examined as a way to predict regenerator temperature effectiveness and pressure losses when there are causes for deterioration of these characteristics. This method resulted in a system, taking the deterioration of these characteristics into consideration as they occur in an actual engine, that represents temperature effectiveness and pressure loss as the function of core specifications such as the core size and the core matrix. This prediction method was then used to predict the regenerator characteristics of actual engines with more than satisfactory results (the accuracy is ±1.25 percent for temperature effectiveness and ±4 percent for pressure loss).

Introduction

Regenerators are indispensable to automotive gas turbine engines since they greatly influence the engines' size, weight, and fuel consumption characteristics [7-15]. Thus, it is important to estimate characteristics such as temperature effectiveness and pressure loss accurately from the regenerator core specifications.

For ideal conditions, the regenerator characteristics can be calculated with the values of the core characteristics, which are Nusselt number and friction factor: $f \cdot \mathrm{Re}$. However, the nonuniformity of velocity distribution of the gas flowing into the regenerator of an actual engine occurs in both the radial and circumferential directions along the surface of the core [1].

This nonuniformity of velocity decreases the temperature effectiveness, particularly in the high efficiency region ($\eta_{HE} \geq 0.8$), and increases pressure loss, which is a main factor for the deterioration of the engines' regenerator performance.

The high-efficiency region is critical for automotive gas turbine engines and it is undoubtedly important to the development of gas turbine engines to be able to grasp and predict the regenerator characteristics under such conditions. Furthermore, it is desirable that the temperature effectiveness can be calculated without using the Nusselt number, since it is considered to be difficult to find a reliable value of the Nusselt number. (The Nusselt number can be calculated under some boundary conditions. However, it is difficult to obtain reliable boundary conditions. Furthermore, passage-to-passage nonuniformity in matrix shape exists.) With these points in mind, a new prediction method based on engine data was studied.

The method in this paper represents, first, the temperature effectiveness in actual engines as a function of the core specification using simulated results that take variables such as nonuniform gas velocity into consideration. Second, pressure loss characteristics of various ceramic cores are measured and represented as a function of core specifications. Then, methods for applying the results obtained from the above to actual engines are studied.

Regenerator Under Development

Figure 1 shows the GTV, which TOYOTA developed as an experimental gas turbine powered passenger car. The two-shaft regenerative gas turbine engine as shown in Fig. 2 is installed in the GTV and its basic specifications are shown in Table 1 [17].

A schematic diagram of the regenerator is shown in Fig. 3. The MAS (Magnesium Aluminum Silicate) core is driven by a peripheral ring gear.

As the MAS and AS (Aluminum Silicate) material strengths were low compared with the LAS (Lithium Aluminum Silicate) material, a pin-type support system[1] was not feasible with the MAS and AS materials. However, the pin-type support system has high reliability during high-temperature operation and excellent potential for withstanding temperature increase in fu-

Contributed by the International Gas Turbine Institute and presented at the 37th International Gas Turbine and Aeroengine Congress and Exposition, Cologne, Germany, June 1-4, 1992. Manuscript received by the International Gas Turbine Institute January 28, 1992. Paper No. 92-GT-27. Associate Technical Editor: L. S. Langston.

[1] In this paper, "pin-type support system" indicates a method where pins, located along the periphery of the matrix core, supported by two metallic springs each couple the core with the peripheral ring gear.

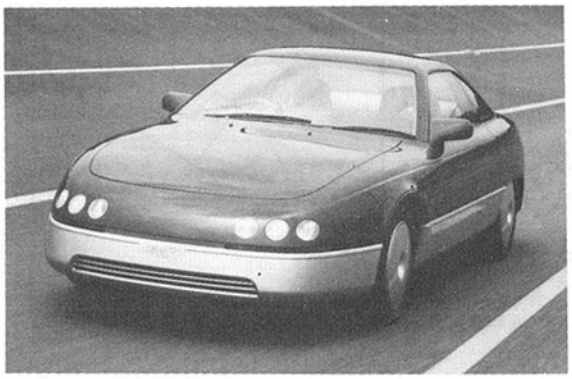

Fig. 1 Toyota GTV

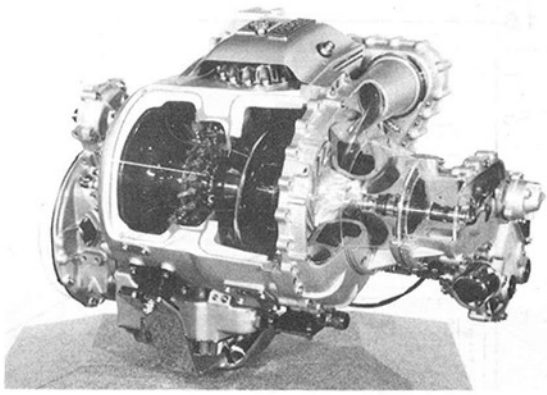

Fig. 2 GT41 gas turbine engine

ture turbine systems because the support is mechanical. Thus, we developed a pin-type support system regenerator with a core made of the MAS material that has superior characteristics at high temperature and low leakage characteristics through the walls [4].

The development of a pin-type support system with the MAS core was achieved by matching the thermal expansion coefficient of the pin material with that of the matrix material ($\alpha_{pin} = \alpha_{matrix} = 0.4 \times 10^{-6}$ 1/°C) and by developing an improved adhesive for joining the pin to the matrix. A heat exchanger equipped with the MAS core that uses such a pin-type support system is in the GTV now being road tested. Cores of various matrix specifications are being used in engine tests. The core shown in Fig. 4 has a density of 1240 cells/in.^{2} and its specifications are shown in Table 2. The cells are rectangular in shape, with an aspect ratio of 1:1.7.

Table 1 Specifications of GT41 engine

Type		Two-Shaft
Gas Generator	Compressor	Centrifugal
	Turbine	Radial Inflow
	Ratational Speed	68,000 rpm
Power Turbine	Turbine	Axial (with Variable Nozzle)
	Ratational Speed	53,000 rpm
Heat Exchanger		Rotary Regenerative Type
Reduction Gear Ratio		10.13
Maximun Output		150 Ps / 5300 rpm

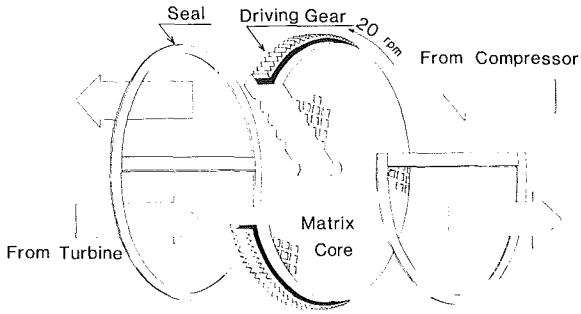

Fig. 3 Schematic of flow pattern through regenerator

Temperature Effectiveness

The purpose herein is to show regenerator temperature effectiveness as a function of core specifications, based on engine data. First, temperature effectiveness was represented as a function of core specifications, without considering performance deterioration. Then the equations were modified by taking into account the effects of nonuniform gas velocity distributions. The validity of the altered equations was verified by testing engines with different core specifications.

Nomenclature

A = heat transfer area, m^2
C_{min}, C_{max} = heat capacity rate, kcal/h·K
Cp = specific heat at constant pressure, kcal/kg·K
f = friction factor
g = acceleration due to gravity = 9.80665 m/s^2
Ga = gas flow rate, kg/s
h = unit conductance of thermal convection heat transfer, kcal/h·m^{2}K
K = pressure loss coefficient defined in Eq. (3)
NTU_o = overall number of heat transfer units
Nu = Nusselt number = $h \cdot Hd/\lambda$
P = pressure, kg/cm^2
ΔPa = pressure loss in air side, mmAq
ΔPg = pressure loss in gas side, mmAq
Re = Reynolds number = $v \cdot Hd/\nu$
T = temperature, K
v = gas velocity, m/s
α_a, α_g, β_a, β_g = empirical constants defined in Eqs. (5) and (6)
γ = specific weight, kg/m^3
η_{HE} = temperature effectiveness of regenerator
λ = thermal conductivity, kcal/(h•m^{2}K/m)
ν = kinetic viscosity, m^2/s

Core Specification

L = thickness of regenerator core
D = core diameter
H_d = hydraulic diameter, m
n = cell density, cell/in.^{2}
t = wall thickness of matrix
V_{eff} = effective volume of core, m^3
β = heat transfer area per unit volume, m^2/m^3
σ = ratio of free area to frontal area

Subscripts

a = air side in regenerator
g = gas side in regenerator
l = laminar flow
t = turbulent flow
3 = outlet of compressor
3.5 = outlet of regenerator in air side
6 = outlet of power turbine
7 = outlet of regenerator in gas side

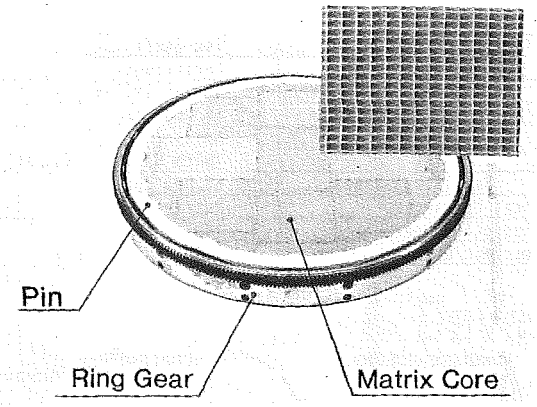

Fig. 4 Regenerator core of GT41 engine

Table 2 Specifications of regenerator core

Cell Density	; n (1/inch²)	1240
Hydraulic Diameter	; Hd (mm)	0.58
Open Area Ratio	; σ	0.71
Heat transfer area per unit volume	; β (m²/m³)	4920
Matrix shape		Rectangular (Aspect Ratio=1.7)
Material		MAS
Wall Thickness	; t (mm)	0.109

Table 3 Calculating conditions

No.	Symbol	Core Diameter D_2 (mm)	Core Thickness L (mm)	Cell Density n (1/inch²)	Wall Thickness t (mm)	T_6 (°C)	Matrix Shape
1	○	400	70	1000	0.10	700	Square
2	◎	500	70	1000	0.10	700	Square
3	※	600	70	1000	0.10	700	Square
4	⬠	700	70	1000	0.10	700	Square
5	▽	600	50	1000	0.10	700	Square
6	人	600	90	1000	0.10	700	Square
7	△	600	110	1000	0.10	700	Square
8	□	600	70	800	0.10	700	Square
9	×	600	70	1200	0.10	700	Square
10	◇	600	70	1400	0.10	700	Square
11	+	600	70	1000	0.09	700	Square
12	*	600	70	1000	0.10	900	Square
13	★	600	50	1000	0.10	1100	Square
14	◯	600	90	1000	0.10	700	Equilateral Triangular

T_3=250 (° C), Core Rotational Speed = 25 (rpm),
Air Flow Rate=0.05, 0.1, 0.2 0.3, 0.4, 0.5, 0.6, 0.7, 0.8, 1.0 (Kg/sec)
Nusselt Number ; Nu = 3.63 for Square Matrix,
3.11 for Equilatelal Triangular Matrix

Empirical Equation of Temperature Effectiveness in the Case of Uniform Velocity Distribution. Papers on methods to calculate the performance of regenerators have been published [2, 3] that showed a way whereby the temperature effectiveness can be found numerically by dividing the core into many cells and then taking the heat transfer and heat balance of each cell into consideration. This method was used to find numerical values for the temperature effectiveness of various core specifications, and usage conditions, as shown in Table 3. (This condition was determined from the usage conditions of automotive gas turbine engines.)

As a result of study on the empirical equation, temperature effectiveness obtained from these calculations can be expressed as a function of core specifications. The results are shown in Fig. 5. The terms $\{H_d/(\mathrm{Nu}\beta V_{\mathrm{eff}})\}Ga/T_m^{0.73}$ and $\eta_{HE}/(1-\eta_{HE})$ $(=1/\mathrm{NTU}_o)$ were estimated from the analysis shown in the Appendix. It can be seen that under the conditions covered by these calculations, the temperature effectiveness is expressed univocaly by $\{H_d/(\mathrm{Nu}\beta V_{\mathrm{eff}})\}Ga/T_m^{0.73}$. Thus, it is considered that the term $\{H_d/(\mathrm{Nu}\beta V_{\mathrm{eff}})\}Ga/T_m^{0.73}$ can be used as an indicator of temperature effectiveness.

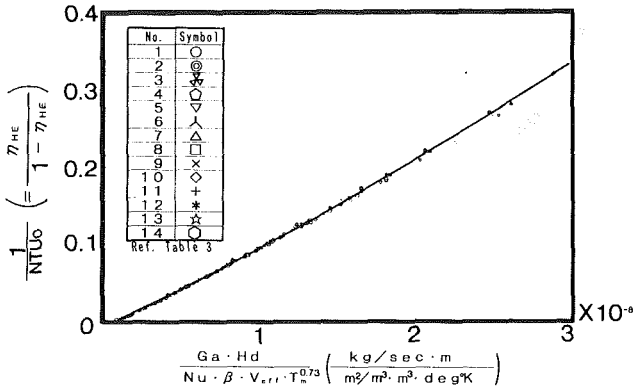

Fig. 5 Numerical solution for various core specifications

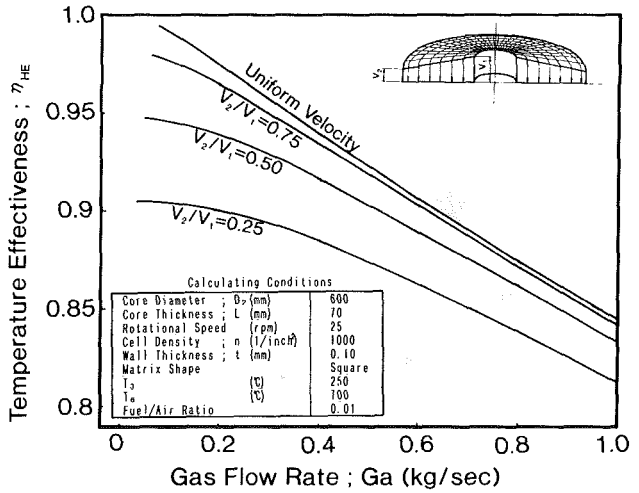

Fig. 6 Temperature effectiveness versus gas flow rate (nonuniformity in radial direction)

Nonuniform Gas Velocities Flowing Into the Core. In the case of a nonuniform velocity distribution of gases flowing into the core, simulations were performed by applying the above-cited numerical calculation method. Then a study was made of the results of these calculations to determine whether $\{H_d/(\mathrm{Nu}\beta V_{\mathrm{eff}})\}Ga/T_m^{0.73}$ can be used as an indicator similar to the previous section.

It is assumed that the distribution of the velocity of air and gases flowing into the core would be nonuniform in two directions, radial and circumferential. These distributions are further divided into three kinds:

1 Distribution on the air side.
2 Distribution on the gas side.
3 Distribution on both the air and gas sides.

Because there seems to be no essential difference between the above three items, distribution on the gas side is considered here.

Nonuniformity in the Radial Direction. Figure 6 compares the results of calculations on the basis of uniform gas velocity distribution and nonuniform distribution in the radial direction, on the gas side. As can be seen in this figure, three kinds of nonuniformities in the radial direction were considered here (strong toward the center), i.e., v_1/v_2 = 0.25, 0.50, and 0.75.

The difference of temperature effectiveness from uniform velocity distribution is small in the region of a large flow. However, with uniform velocity distribution, when *Ga* approaches zero, then η_{HE} approaches 100 percent. In comparison, as nonuniformity grows larger and as *Ga* approaches zero, then η_{HE} tends to decrease.

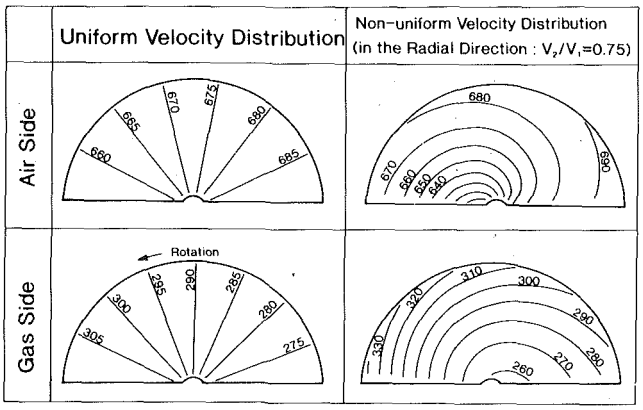

Fig. 7 Temperature distribution at the exit face of core

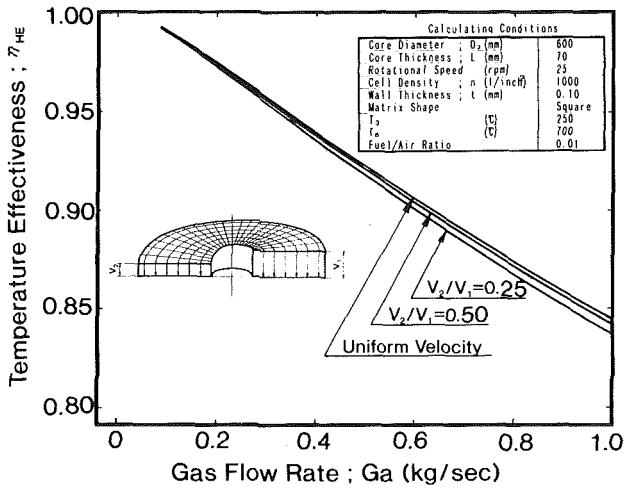

Fig. 8 Temperature effectiveness versus gas flow rate (nonuniformity in circumferential direction)

Figure 7 shows the results of calculations of the operational gas temperature at the exit face on both the air and gas sides when Ga is 0.4 (kg/s). When the gas is distributed uniformly, the distribution of temperatures in the radial direction of the core is also small. The temperatures at the center on the gas side, however, increase in the case of nonuniformity. This means that effective heat transfer has not occurred in these areas, so high-temperature gas is exhausted.

Nonuniformity in the Circumferential Direction. Figure 8 compares the results of calculations carried out when there is nonuniformity in the circumferential direction and complete uniformity. (As can be seen in this figure, two kinds of nonuniformities were considered, i.e., $v_1/v_2 = 0.25$ and 0.5.) Compared to results obtained when no nonuniformity is present, the deterioration of the temperature effectiveness is small on the low flow side and large on the high flow side.

Empirical Equation When Nonuniformity Is Present. When nonuniformity is present, as previously discussed, it is assumed that the temperature effectiveness can be expressed as some function of the term $\{H_d/(\mathrm{Nu}\beta V_{\mathrm{eff}})\}Ga/T_m^{0.73}$. Figures 9 and 10 show the results of calculations for various core specifications. Figure 9 is a case of nonuniform distribution in the radial direction. Figure 10 is one of nonuniform distribution in the circumferential direction, and also for nonuniform distribution in both the radial and circumferential directions. These results show us that $1/\mathrm{NTU}_o$ is a principal function of the term $\{H_d/(\mathrm{Nu}\beta V_{\mathrm{eff}})\}Ga/T_m^{0.73}$, which indicates core specifications and engine operating conditions.

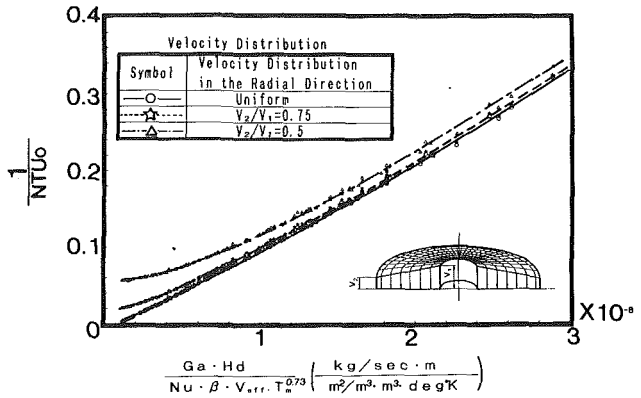

Fig. 9 Temperature effectiveness calculated for various core specifications (nonuniformity in radial direction)

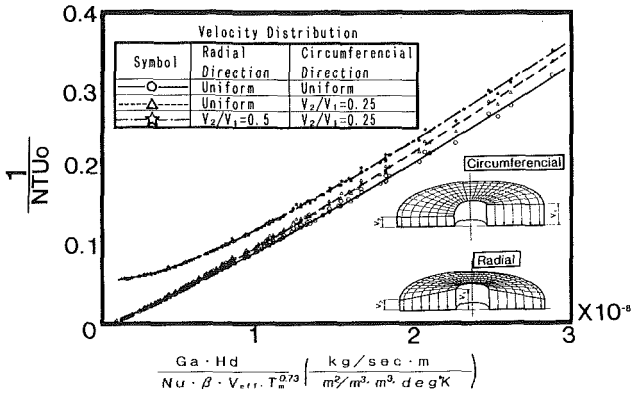

Fig. 10 Temperature effectiveness calculated for various core specifications (nonuniformity in circumferential and both radial and circumferential direction)

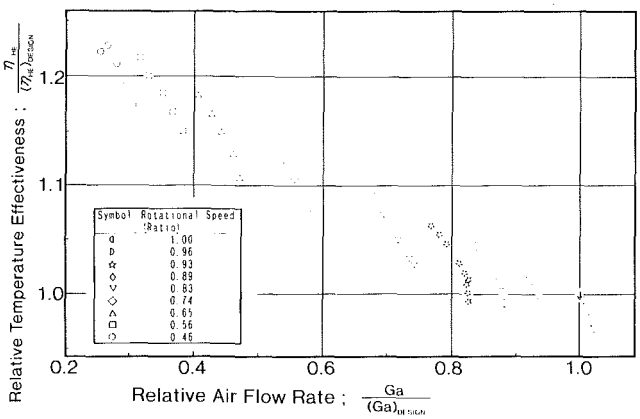

Fig. 11 Temperature effectiveness measured in engine

Accordingly, if this relationship is obtained with a certain engine, temperature effectiveness can be predicted by using this relationship even if matrix specifications and core sizes are changed. Furthermore, temperature effectiveness of the regenerator can be approximated as follows with an accuracy of ±0.5 percent within a range of $0.8 \leq \eta_{HE} \leq 0.94$:

$$\frac{1}{\mathrm{NTU}_o} = \alpha_1 \cdot \frac{H_d}{\mathrm{Nu}\beta V_{\mathrm{eff}}} \cdot \frac{Ga}{T_m^{0.73}} + \alpha_2 \qquad (1)$$

where α_1 and α_2 are empirical constants determined by the regenerator.

Practical Application of Equation (1). Figure 11 shows temperature effectiveness η_{HE} versus relative air flow rate meas-

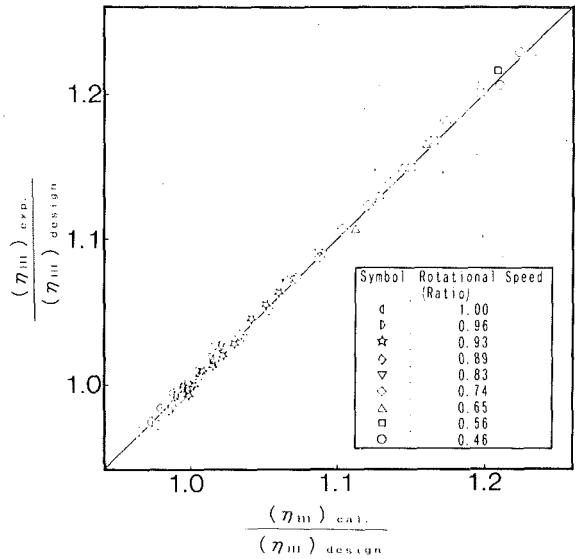

Fig. 12 Accuracy of empirical equation

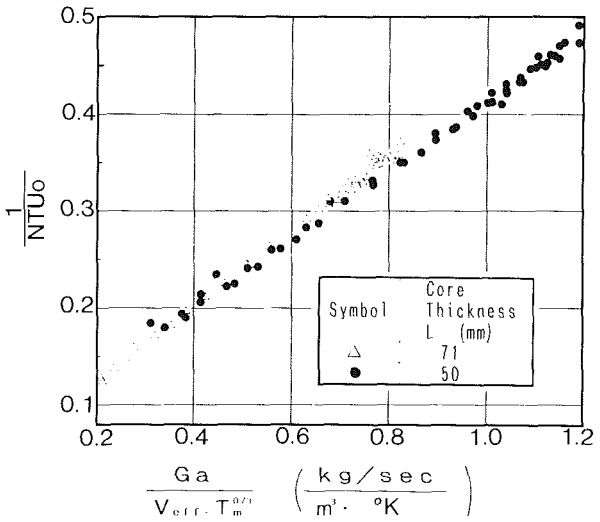

Fig. 13 Engine test results with different core thicknesses

ured in an engine, and Fig. 12 shows the application of Eq. (1) to these results in order to prepare an empirical equation of temperature effectiveness. Obviously, the temperature effectiveness seen in Fig. 12 approximates the temperature effectiveness in an actual engine with nonuniform gas velocity distribution and other factors that lower effectiveness.

Thus, we can say that if empirical Eq. (1) of the regenerator temperature effectiveness is prepared with a certain engine, the temperature effectiveness can be predicted with this equation even if matrix specifications and core size are changed. The following verifies the validity of this prediction method when core specifications of the regenerators in engines are changed.

Engine Verification Results. Tests for two different cases were performed with engines. In one, the core thickness was changed; in the other, the matrix specifications were changed.

In the Case of a Core Thickness Change. Figure 13 shows $1/\mathrm{NTU}_o$ for $Ga/(V_{\mathrm{eff}}T_m^{0.73})$ obtained with the engine test (as the core matrix was unchanged, this term was used instead of $\{H_d/(\mathrm{Nu}\beta V_{\mathrm{eff}})\}Ga/T_m^{0.73}$ as the horizontal axis of the graph). Note that both sets of data are virtually in a straight line, despite the change of core thickness. Thus, change of core thickness can be predicted effectively by Eq. (1) with an accuracy of ±1.25 percent, even when the engine has factors such as nonuniform gas velocity distribution that lower the temperature effectiveness.

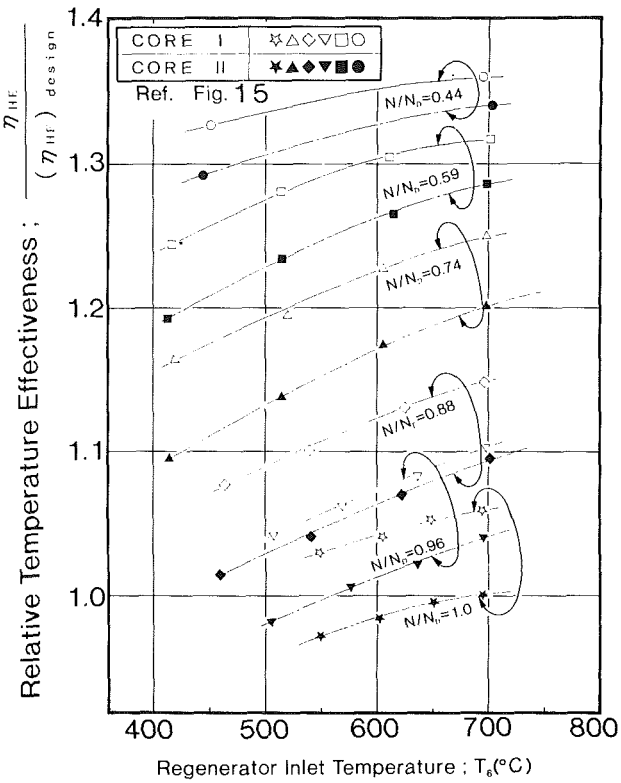

Fig. 14 Temperature effectiveness measured in engine

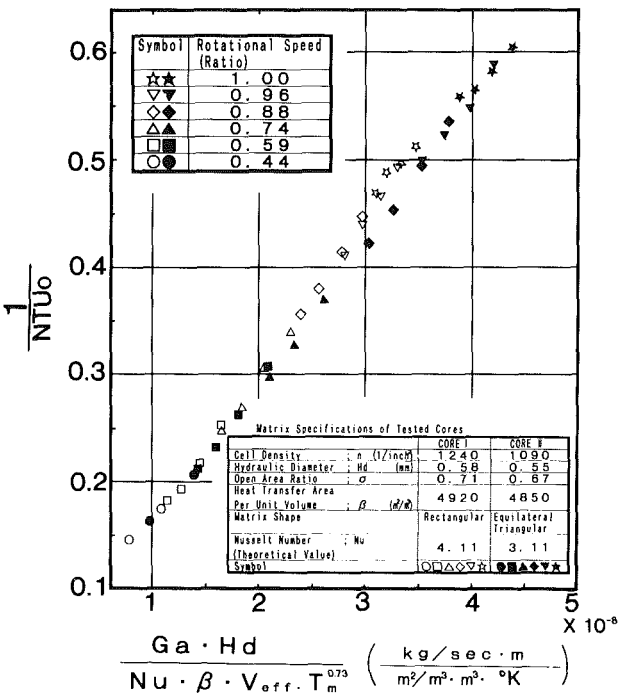

Fig. 15 Verification of prediction method

In the Case of a Matrix Specifications Change. Figure 14 shows the results of tests in which the matrix specifications were changed. The two kinds of cores were tested.

Figure 15 shows $1/\mathrm{NTU}_o$ for $\{H_d/\mathrm{Nu}\beta V_{\mathrm{eff}}\}Ga/T_m^{0.73}$. It can be seen that the data from the two engines are virtually spread

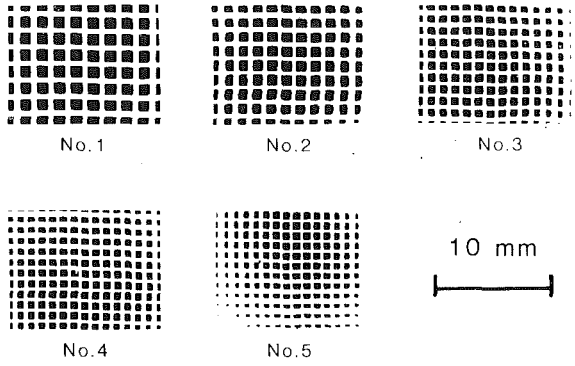

Fig. 16 Cores used for pressure loss measurement

Table 4 Comparison of flow friction characteristics (square matrix)

	Empirical	Numerical
f·Re	13.6	14.23

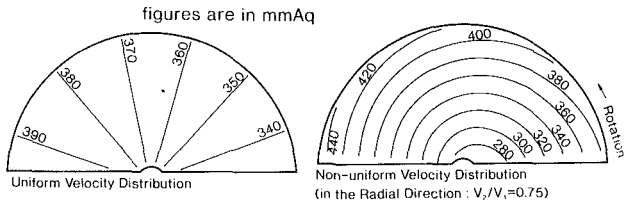

Fig. 17 Example of pressure loss distribution calculated

over a single line, which means that we can assume that changes in matrix specifications can be accurately predicted by Eq. (1) with an accuracy of ±1.25 percent.

Pressure Loss

The objective herein is to determine the pressure loss in an engine as a function of core specifications of a regenerator. First, the pressure loss of ceramic cores with various matrix specifications (with square matrices) was measured. Analysis of these measurements allowed pressure losses to be divided into laminar and turbulent pressure losses and expressed as a function of the core specifications.

Next, practical application of the results in predicting the pressure loss of the regenerators in engines were studied.

Core Pressure Loss. It is considered that there are four contributing factors to pressure loss of the core: passage friction, entrance/exit effects, and flow acceleration [16]. Within the scope of automotive gas turbine engines, the major part of core pressure loss is due to passage friction. As a result of the study in [1], the pressure loss of cores was explainable by using the two terms representing laminar and turbulent components, as follows:

$$\Delta P = \Delta P_l + \Delta P_t$$

$$\begin{cases} \Delta P_l = 4f \cdot \dfrac{L}{H_d} \cdot \dfrac{\gamma v^2}{2g} & (2) \\ \Delta P_t = K \cdot \dfrac{\gamma v^2}{2g} & (3) \end{cases}$$

Reference [1] contains the figures obtained through measurement of pressure loss in ceramic cores of various matrix specifications (Fig. 16). As a result of the analysis, the laminar and turbulent components of the core pressure loss could be expressed as a function of core specifications.

On the other hand, the numerical value of laminar pressure loss coefficients f•Re can be obtained by computing. (As the laminar pressure loss accounts for the majority of total pressure loss, the laminar pressure loss is discussed here.) The numerical and empirical values of f•Re for a square matrix are compared in Table 4. The empirical value is 4.5 percent lower than the numerical value. This difference may be attributed to passage-to-passage nonuniformity of the matrix core. Although further study will be necessary to establish precisely the cause of the above difference, the authors consider that if the ratio of the numerical value to empirical value is taken into account, laminar pressure loss for matrix shapes other than square can be obtained accurately enough for practical use. (Numerical values of laminar pressure loss with various shapes can be calculated [5, 6].)

Pressure Loss During Actual Engine Operation. Pressure loss in actual engine operation tends to be greater than that registered by the core alone because of several conditions under which regenerator cores are actually used:

1 The temperature gradient along the core passage is sharp.
2 Because temperature dispersion occurs along the face of the regenerator core, pressure loss tends to follow these dispersion characteristics.
3 The distribution of velocities (and temperature) of air and gas flowing into the regenerator tend to be nonuniform.
4 In addition to pressure losses attributable to the core, there are pressure losses caused by the ducts before and after the core.

In order to calculate the pressure loss of the regenerator by use of pressure loss coefficients of the core mentioned above, the influence of these factors must be corrected. Therefore, regenerator and engine tests were both carried out and the influence of the above factors studied quantitatively.

Regenerator Testing. When the inside of the core exhibits a temperature gradient, the laminar pressure loss can be calculated with the following equation:

$$\Delta P_l = 4 \int \left(\frac{f_z}{H_d} \cdot \frac{\gamma_z v_z^2}{2g} \right) dz$$

where γ_z and v_z are the functions of the distance Z from the core entrance and f_z can be calculated with $f_z = (f \cdot \mathrm{Re})/\mathrm{Re}$.

Also, as shown in Fig. 17 (the results of numerical calculations), the pressure loss distribution is not uniform because of nonuniformity of the temperature distribution along the surface of the core, even if the velocity distribution is uniform. Therefore, the average pressure loss of the core can be obtained by integrating and averaging the values obtained from the equation above.

In practice, however, this calculation is inconvenient. Therefore, with the results of simulations of various conditions, it is considered that sufficient accuracy can be obtained with Eq. (4), which uses average physical property values at the core entrance and exit:

$$\Delta P_l = 4 f_m \cdot \frac{L}{H_d} \cdot \frac{\gamma_m v_m^2}{2g} \quad (4)$$

In order to verify Eq. (4), a full-size test rig was built and pressure loss was measured. Figure 18 shows a schematic flow diagram of the test rig.

Figure 19 compares the measured pressure losses with Eq. (4) predictions (the turbulent pressure loss value was derived from Eq. (3)). The close agreement shown in this figure confirms the accuracy of the prediction method, making it possible to calculate the pressure loss for the regenerator, which has factors (1) and (2) mentioned above.

Engine Testing. Not only does the engine have nonuni-

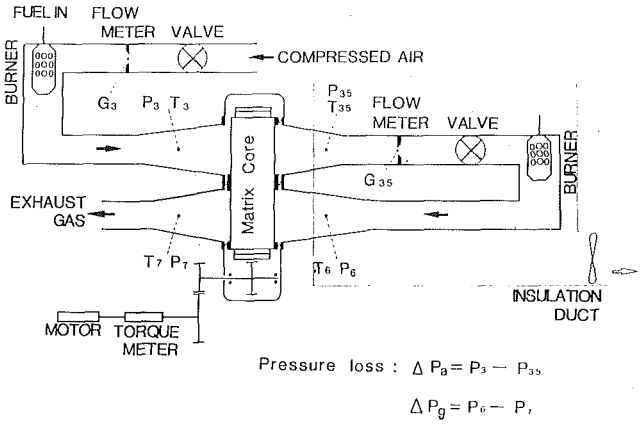

Fig. 18 Schematic diagram of regenerator test rig

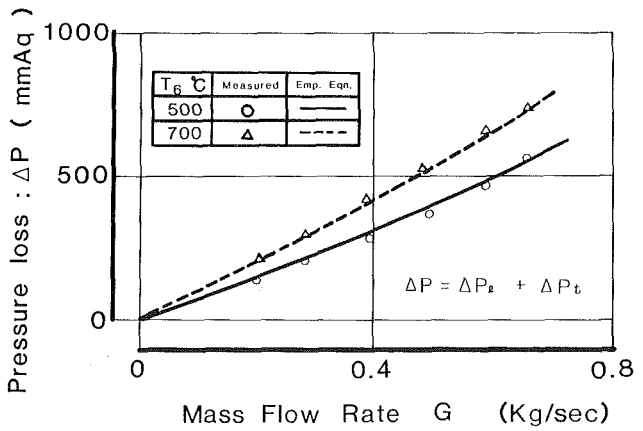

Fig. 19 Comparison of pressure loss

formity of gas flow distribution in the regenerator, but it also incurs pressure losses caused by the engine duct systems located before and after the core. As with the core itself, measured pressure loss in the engine was classified into laminar and turbulent components, and expressed as follows (α_a, α_g, β_a, and β_g are empirical constants derived from analysis of data from the engine):

$$\Delta P_a = (\Delta P_a)_l + (\Delta P_a)_t = \alpha_a \left(\frac{T_{am}^{1.66}}{P_3} \right) G_3 + \beta_a \left(G_3 \sqrt{\frac{T_{am}}{P_3}} \right)^2 \quad (5)$$

$$\Delta P_g = (\Delta P_g)_l + (\Delta P_g)_t = \alpha_g \left(\frac{T_{gm}^{1.66}}{P_6} \right) G_6 + \beta_g \left(G_6 \sqrt{\frac{T_{gm}}{P_6}} \right)^2 \quad (6)$$

where $T_{am} = (T_3 + T_{35})/2$, $T_{gm} = (T_6 + T_7)/2$.

In the above equation, the subscript l represents the laminar pressure loss in the core passage and the subscript t represents the sum of turbulent pressure loss caused by the core entrance/exit and the engine duct system. To clarify the amount of pressure loss increase resulting from the aforementioned factors (3) and (4), the laminar and turbulent core pressure loss coefficient $f \cdot \mathrm{Re}$ and K, previously discussed, were converted and introduced into these equations as α, β. Table 5 compares two α and β (gas side only).

The following is clarified by this Table 5:

1 The ratio of $(\alpha)_{\text{engine}}$ to $(\alpha)_{\text{core}}$ is 1.11. Since nonuniformity of the velocity exists, it is assumed to cause an increase in laminar pressure loss.

Table 5 Comparison of pressure loss coefficients

	α_g	β_g
Measured in Engine	0.020	2.24
Core Characteristics	0.018	0.156

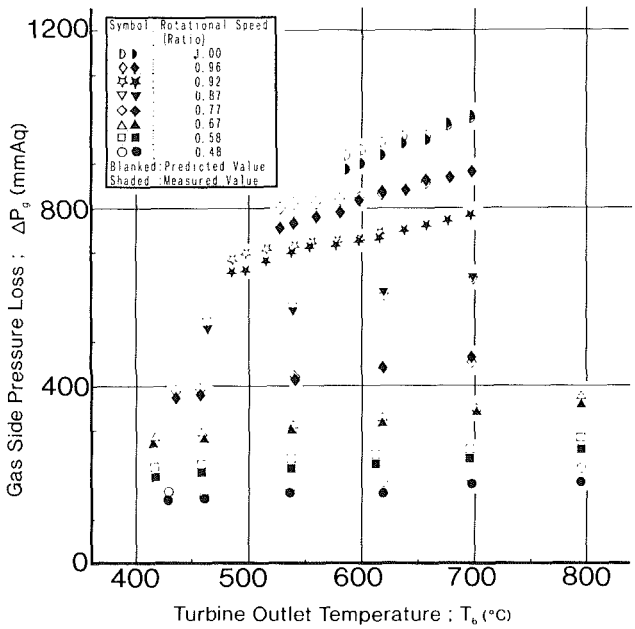

Fig. 20 Comparison of predicted and measured values

2 The difference between $(\beta)_{\text{engine}}$ and $(\beta)_{\text{core}}$ (2.24 − 0.156 = 2.084) indicates the turbulent pressure loss due to the engine ducts.

Accordingly, the aforementioned factors (3) and (4) can be corrected with the above items, and the regenerator pressure loss in this engine can be determined as a function of the core specifications.

Verification Using An Actual Engine. Engine tests were conducted to verify the prediction method obtained above. Figure 20 compares measured values with predicted results for pressure loss on the gas side. In this figure, blanked symbols show predicted values and shaded symbols show measured values. The predicted value is found by using Eq. (6) above. The empirical constants α_g, β_g in the equation are obtained by correcting the core pressure loss coefficients with the method mentioned previously. Note that the figures for both values are in accord with the accuracy of ±4 percent.

Conclusion

Methods for predicting the main characteristics of automotive gas turbine engine regenerators, i.e., temperature effectiveness and pressure loss, based on data obtained from actual engine tests, were investigated.

1 The empirical equation of regenerator temperature effectiveness in an actual engine having nonuniform gas velocity distribution was expressed as a function of core specifications, which was obtained with simulation results that take the influence of nonuniform gas velocity into consideration. The results were satisfactorily verified in actual engine tests.

2 Pressure losses of various ceramic cores were measured and classified into laminar and turbulent components by analysis of the test results. These components were then expressed as functions of core specifications. Next, regenerator and engine tests were conducted and the pressure loss increase factors were analyzed quantitatively so as to be able to apply the core pressure loss to an actual engine. As a result, regenerator

pressure loss in the engine was found to be a function of the core specifications. This prediction method was satisfactorily verified with actual engine tests.

This study resulted in a new method, representing the regenerator characteristics as the function of core specifications, which can be used to predict the temperature effectiveness and pressure loss of regenerators operating in actual engines.

Acknowledgments

The authors obtained cooperation from the NGK Insulators, Ltd. for the development of the pin type regenerator core.

References

1 Sayama, J., Iwai, M., et al., "Effects of Regenerator Performance on an Automotive GT Engine," 1987-TOKYO-IGTC-61, pp. 125–132.

2 Lamberston, T. J., "Performance Factors of a Periodic-Flow Heat Exchanger," *Trans. ASME*, Vol. 80(3), 1958, pp. 586–592.

3 Coppage, J. E., and London, A. L., "The Periodic-Flow Regenerator—A Summary of Design Theory," *Trans. ASME*, Vol. 75(7), 1953, p. 779.

4 Matsuhisa, T., and Oda, I., "Heat Transfer and Flow Friction Characteristics for Fin Geometries of Extruded Ceramic Regenerator Core," Tokyo Int. Gas Turbine Congress, 1983.

5 Shah, R. K., "Laminar Flow Friction and Forced Convection Heat Transfer in Ducts of Arbitrary Geometry," *Int. J. Heat Mass Transfer*, Vol. 18, 1975, pp. 848–862.

6 Sparrow, E. M., and Haji-Sheikh, A., "Flow and Heat Transfer in Ducts of Arbitrary Shape With Arbitrary Thermal Boundary Conditions," ASME *Journal of Heat Transfer*, Vol. 88, 1966, pp. 351–358.

7 Collman, J. S., Amann, C. A., Matthews, C. C., Stettler, R. J., and Verkamp, F. J., "The GT-225—An Engine for Passenger-Car Gas Turbine Research," SAE Paper No. 750167, 1975.

8 Cadwell, R. G., Chapman, W. I., and Walch, H. C., "The Ford Turbine—An Engine Designed to Compete With the Diesel," SAE Paper No. 720168, 1992.

9 Fucinari, C. A., Rahnke, C. J., Rao, V. D. N., and Vallance, J. K., "Ceramic Regenerator Systems Development Program—Final Report," DOE/NASA/0008-12, NASA CR-165139.

10 Wagner, C. E., and Pampreen, R. C., "Upgraded Automotive Gas Turbine Engine Design and Development Program Final Report," NASA CR-159671, Vol. 2, June 1979.

11 Walzer, P., Grotrian, J. M., and Buchheim, R., "The VW-GT150—An Experimental Automotive Gas Turbine Engine," SAE Paper No. 800190, 1980.

12 "Der Mercedes-Benz Forshungs-Personenwagen Auto 2000," *Automobiltechnishe Zeitschrift* (*ATZ*), Vol. 83-9, 1981, pp. 395–401.

13 Kronogard, S. O., "Three-Shaft Automotive Turbine-Transmission Systems of the KTT Type—Performance and Features," ASME JOURNAL OF ENGINEERING FOR POWER, Vol. 100, 1978, pp. 95–110.

14 Kutchey, J. A., and Julien, H. L., "The Measured Influence of Flow Distribution on Regenerator Performance," SAE Paper No. 740164, 1974.

15 Winter, J. M., and Nussle, R. C., "Experimental Performance of the Regenerator for the Chrysler Upgraded Automotive Gas Turbine Engine," DOE/NASA/51040-32 NASA TM-82671, Feb. 1982.

16 Kays, W. M., and London, A. L., *Compact Heat Exchangers*, 3rd ed., McGraw Hill Book Company, New York, 1984.

17 Tsutsui, T., Watanabe, A., and Morishita, T., "Control System for a Gas Turbine Powered Passenger Car," 1991-YOKOHAMA-IGTC.

APPENDIX

Study on Empirical Equation of Temperature Effectiveness

Assuming uniformity in gas velocity distribution and virtually infinite core rotation speed, the temperature effectiveness of a regenerator can be found analytically and represented by the following equations in the same manner as for counterflow direct type regenerators:

$$\eta_{HE}=\frac{1-\exp\{-\mathrm{NTU}_o(1-C_{\min}/C_{\max})\}}{1-(C_{\min}/C_{\max})\exp\{-\mathrm{NTU}_o(1-C_{\min}/C_{\max})\}} \tag{A1}$$

$$\mathrm{NTU}_o=\frac{1}{C_{\min}}\left\{\frac{1}{1/(hA)_{\mathrm{air}}+1/(hA)_{\mathrm{gas}}}\right\} \tag{A2}$$

In addition, when Eq. (A1) is applied to a gas turbine engine, it will become Eq. (A3), because $C_{\min}/C_{\max}$ approaches unity.

$$\eta_{HE}=\frac{\mathrm{NTU}_o}{1+\mathrm{NTU}_o} \tag{A3}$$

From Eq. (A2),

$$\mathrm{NTU}_o=\frac{1}{(C_p)_{\mathrm{air}}G_3}\cdot\left\{\frac{1}{1/\left(\frac{\mathrm{Nu}\lambda\beta V}{H_d}\right)_{\mathrm{air}}+1/\left(\frac{\mathrm{Nu}\lambda\beta V}{H_d}\right)_{\mathrm{gas}}}\right\}$$

where $\lambda_{\mathrm{air}} \doteqdot \lambda_{\mathrm{gas}}$, then set to λ_m, and $V_{\mathrm{air}} \doteqdot V_{\mathrm{gas}} \doteqdot 2.0\ V_{\mathrm{eff}}$, the above equation is as follows:

$$\frac{1}{\mathrm{NTU}_o}=\alpha\cdot\frac{H_d}{\mathrm{Nu}\lambda_m\beta V_{\mathrm{eff}}}\cdot Ga$$

where α = constant determined for each regenerator; V_{eff} = volume of effective portion of core ($=(R_2^2-R_1^2)\pi L$; R_1, R_2 are the inner and outer radii of the core, respectively).

In addition, the above equation can be represented as Eq. (A4) because the thermal conductivity of air can be set approximately as $\lambda_m = CT_m^{0.73}$ in the region where the actual engines operate (C is a proportional constant and T_m is a mean temperature of the regenerator: $T_m = (T_3 + T_6)/2$).

$$\frac{1}{\mathrm{NTU}_o}=\alpha\cdot\frac{H_d}{\mathrm{Nu}\beta V_{\mathrm{eff}}}\cdot\frac{Ga}{T_m^{0.73}} \tag{A4}$$